UNIVERSITY OF IOANNINA

SCHOOL OF SCIENCES

DEPARTMENT OF PHYSICS

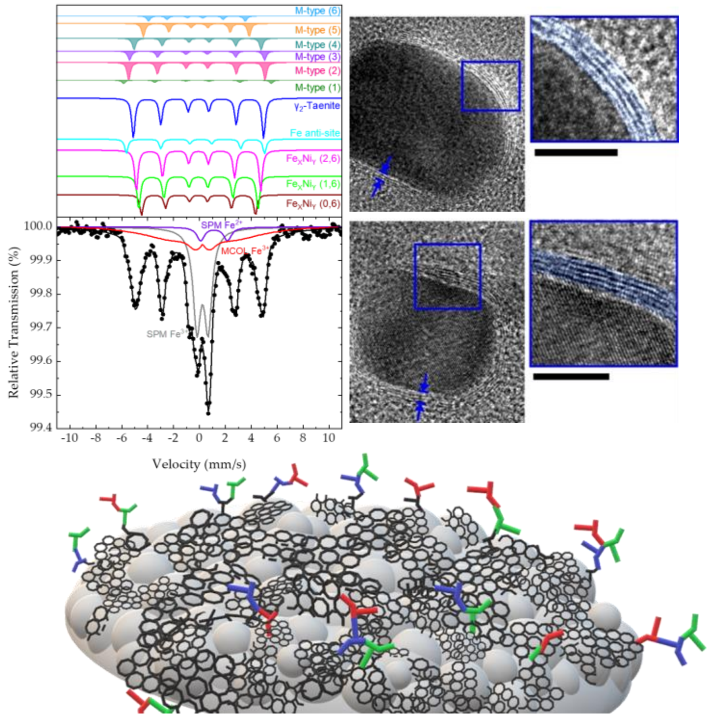

SYNTHESIS, CHARACTERIZATION AND STUDY OF THE PROPERTIES OF NEW HYBRID MAGNETIC NANOSTRUCTURED MATERIALS OF BIMETALLIC IRON ALLOYS (Fe-Rh, Fe-Co, Fe-Ni) GROWN ON NANODIAMONDS

ZIOGAS PANAGIOTIS

PhD THESIS

IOANNINA 2025

ΠΑΝΕΠΙΣΤΗΜΙΟ ΙΩΑΝΝΙΝΩΝ

ΣΧΟΛΗ ΘΕΤΙΚΩΝ ΕΠΙΣΤΗΜΩΝ

ΤΜΗΜΑ ΦΥΣΙΚΗΣ

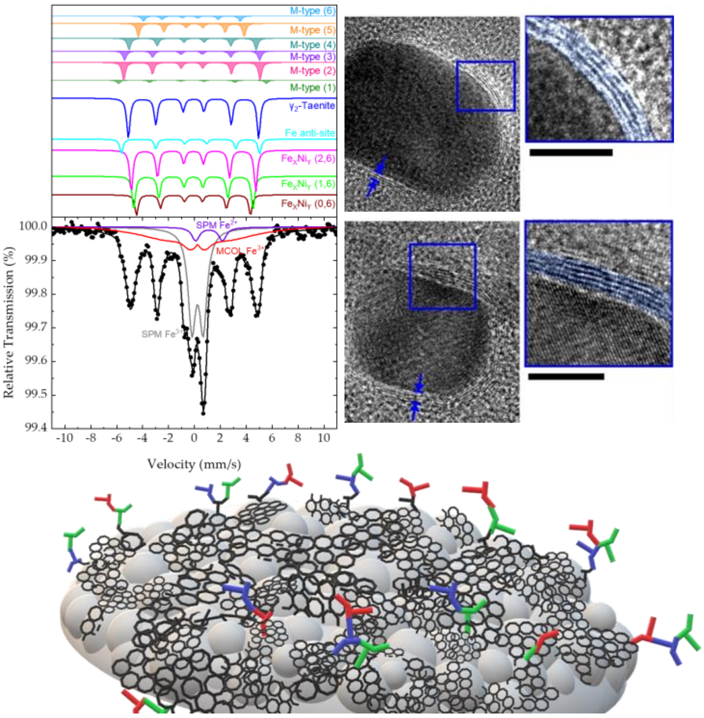

ΣΥΝΘΕΣΗ, ΧΑΡΑΚΤΗΡΙΣΜΟΣ ΚΑΙ ΜΕΛΕΤΗ ΤΩΝ ΙΔΙΟΤΗΤΩΝ ΝΕΩΝ ΥΒΡΙΔΙΚΩΝ ΜΑΓΝΗΤΙΚΩΝ ΝΑΝΟΔΟΜΗΜΕΝΩΝ ΥΛΙΚΩΝ ΔΙΜΕΤΑΛΛΙΚΩΝ ΚΡΑΜΑΤΩΝ ΣΙΔΗΡΟΥ (Fe-Rh, Fe-Co, Fe-Ni) ΑΝΑΠΤΥΓΜΕΝΩΝ ΣΕ ΝΑΝΟΔΙΑΜΑΝΤΙΑ

ΖΙΩΓΑΣ ΠΑΝΑΓΙΩΤΗΣ

ΔΙΔΑΚΤΟΡΙΚΗ ΔΙΑΤΡΙΒΗ

ΙΩΑΝΝΙΝΑ 2025

Three-member advisory committee

1. Alexios P. Douvalis (Supervisor), Professor, Department of Physics, University of Ioannina, Greece

2. Athanasios B. Bourlinos, Professor, Department of Physics, University of Ioannina, Greece

3. Ioannis Panagiotopoulos, Professor, Department of Materials Science and Engineering, University of Ioannina, Greece

Seven-member assessment committee

1. Alexios P. Douvalis (Supervisor), Professor, Department of Physics, University of Ioannina, Greece

2. Athanasios B. Bourlinos, Professor, Department of Physics, University of Ioannina, Greece

3. Ioannis Panagiotopoulos, Professor, Department of Materials Science and Engineering, University of Ioannina, Greece

4. Yiannis Deligiannakis, Professor, Department of Physics, University of Ioannina, Greece

5. Anastasios Markou, Assistant Professor, Department of Physics, University of Ioannina, Greece

6. Michael Karakassides, Professor, Department of Materials Science and Engineering, University of Ioannina, Greece

7. George Litsardakis, Professor, Department of Electrical and Computer Engineering, Aristotle University of Thessaloniki, Greece

Ευχαριστίες

Η παρούσα διδακτορική διατριβή είναι το αποτέλεσμα μιας συνεχούς προσπάθειας να κατανοήσω και να ερμηνεύσω όλες εκείνες τις διεργασίες και φαινόμενα σε μέρος των υβριδικών μαγνητικών υλικών στη νανοκλίμακα, πάντα με οδηγό τις αρχές της Φυσικής Στερεάς Κατάστασης και της Επιστήμης των Υλικών. Κατά τη διάρκεια αυτής, καταλυτική ήταν η συνεισφορά ενός πλήθους ανθρώπων τόσο πάνω σε θέματα επιστημονικού και ερευνητικού ενδιαφέροντος όσο και σε θέματα ήθους, στάσης ζωής και διαμόρφωσης του χαρακτήρα μου σε επιστημονικό και προσωπικό επίπεδο. Έτσι, αν κάποιος θεωρούσε ότι η εκπόνηση της παρούσας διατριβής αφορά τον δικό μου προσωπικό μόχθο, σας διαβεβαιώ ότι η ολοκλήρωση της αφορά μια συλλογική προσπάθεια, όπου ο κάθε παράγοντας συνεισέφερε μοναδικά και με τον δικό του τρόπο.

Πιο συγκεκριμένα, θα ήθελα να εκφράσω την ευγνομοσύνη μου στον Επιβλέπωντα μου, κύριο **Καθηγητή Αλέξιο Π. Δούβαλη** που μου έδωσε την ευκαιρία να εργαστώ δίπλα του και μου έδειξε τον δρόμο και τον τρόπο να ακολουθήσω το όνειρο μου σαν νέος Φυσικός προς την επιστημονική-ερευνητική μου πορεία. Στο πρόσωπο σας γνώρισα τι πάει να πεί πάθος για τη δουλειά μου, και πως για να γίνει αυτή σωστά δεν πρέπει να γίνονται εκπτώσεις, παρά μόνο αξιοπρεπείς, συνεπείς και συστηματικές προσπάθειες. Οι αρετές αυτές μπορούν μόνο να αποδείξουν το ποιόν του ανθρώπου πίσω από τον Καθηγητή, ενός ανθρώπου με περισσή θέληση, υπομονή και επιμονή, πάντα διατεθιμένος να μου αφιερώσει, αμέτρητες φορές, ώρες στο γραφείο και το εργαστήριο από τον προσωπικό του χρόνο του για να μου μεταλαμπαδεύσει τις γνωσεις και τις διδαχές του. Για όλα αυτά και όλα όσα με το καλό έρθουν στο μέλλον, σας εκτιμώ και σας ευχαριστώ και σας θεωρώ σαν πρότυπο και μέντορα μου.

Απέραντη είναι η εκτίμηση και ευγνωμοσύνη μου και για τα δύο μέλη της τριμελούς συμβουλευτικής επιτροπής μου, τον κύριο **Καθηγητή Αθανάσιο Β. Μπουρλίνο** για την στήριξη του καθόλη την διάρκεια της διατριβής, η εξειδίκευση και κατάρτιση του οποίου κατάφερε να ξεκλειδώσει πολλά μυστήρια στα υπό μελέτη συστήματα μας. Ένας άνθρωπος του οποίου η εφευρετικότητα, το πάθος για τη σπουδή του και η ανιδιοτέλεια του είναι παραδείγματα προς μίμηση, που θα φέρω για πάντα μαζί μου. Καθώς επίσης ευχαριστώ και τον κύριο **Καθηγητή Ιωάννη Παναγιωτόπουλο** για τις εποικοδομητικές συζητήσεις μας πάνω στα μαγνητικά υλικά, την στήριξη του καθώς και για την αξιολόγηση της διατριβής μου.

Πολλά ευχαριστώ και στα υπόλοιπα μέλη της επταμελούς εξεταστικής επιτροπής μου, κύριο **Καθηγητή Ιωάννη Δελληγιαννάκη** για τις εποικοδομητικές συζητήσεις και συμβουλές του, καθώς και για την ευκαιρία που μου προσέφερε να συνεργαστούμε τόσο κατά την επιμέλεια του βιβλίου Υλικά και Περιβάλλον, Περιβαλλοντικές Επιπτώσεις & Αρχές Ανάλυσης Κύκλου Ζωής, όσο και στα πλαίσια ενός ερευνητικού προγράμματος με τη συμμετοχή μου σε πειράματα μαγνητικών μετρήσεων και της ανάλυσης τους. Τον κύριο **Επίκουρο Καθηγητή Αναστάσιο Μάρκου**, για το ευχάριστο κλίμα στο γραφείο μας καθώς και για τις αμέτρητες συμβουλές πάνω στην επιστήμη και τις εμπειρίες του από το εξωτερικό, που μοιράστηκε μαζί μου. Τον ευχαριστώ πολύ και του εύχομαι καλή σταδιοδρομία, σαν νεότερο μέλος της επταμελούς. Τον κύριο **Καθηγητή Μιχάλη Καρακασίδη**, με τον οποίον δεν είχα την τιμή να αλληλεπιδράσω πολύ, ωστόσο τον ευχαριστώ για τον χρόνο και τη κριτική του για την αξιολόγηση της παρούσας διατριβής. Επίσης θα ήθελα να ευχαριστήσω και τον κύριο

Καθηγητή Γεώργιο Λιτσαρδάκη, η συμμετοχή του οποίου στην επταμελή εξεταστική επιτροπή με τιμά ιδιαίτερα, καθώς είχα την τιμή να γνωριστούμε και να με φιλοξενήσει στο ερευνητικό εργαστήριο Ηλεκτροτεχνικών Υλικών του Τμήματος Ηλεκτρολόγων Μηχανικών & Μηχανικών Υπολογιστών στο Αριστοτέλειο Πανεπιστήμιο Θεσσαλονίκης στα πλαίσια συνεργασίας για την μελέτη των μαγνητικών ιδιοτήτων μέρους των δειγμάτων που παρουσιάζω στη διατριβή μου. Σας ευχαριστώ πολύ για το υπέροχο κλίμα εντός και εκτός εργαστηρίου, τις εποικοδομητικές συζητήσεις μας πάνω στα μαγνητικά υλικά καθώς και για την εμπιστοσύνη που μου δείξατε στο χειρισμό του συστήματος μέτρησης φυσικών ιδιοτήτων.

Επιπλέον, θα ήθελα να ευχαριστήσω θερμά και τον κύριο **Καθηγητή Γεώργιο Δημητρακόπουλο** του Τμήματος Φυσικής του Αριστοτελείου Πανεπιστημίου Θεσσαλονίκης, την **Υποψήφια Διδάκτορα Πολυξένη Χατζοπούλου** καθώς και ολόκληρη ερευνητική ομάδα του κ. Δημητρακόπουλου, για την υπέροχη συνεργασία πάνω στις παρατηρήσεις ηλεκτρονικής μικροσκοπίας διέλευσης των υπό μελέτη συστημάτων της διδακτορικής διατριβής μου καθώς και για την φιλοξενία στους χώρους των ερευνητικών εργαστηρίων. Η συνεισφορά σας ήταν κομβικής σημασίας και σας ευχαριστώ πολύ.

Πολλά ευχαριστώ και στην κυρία **Δόκτορα Χριστίνα Παπαχριστοδούλου**, μέλος ΕΔΙΠ του Τμήματος Φυσικής για το φιλικό κλίμα και την αμέριστη βοήθεια της στα πρώτα μου βήματα στον χώρο της ερευνητικής διάταξης περίθλασης ακτίνων-Χ. Πολλά ευχαριστώ και στον κύριο **Δόκτορα Αλέξανδρο Πολύμερο**, μέλος ΕΔΙΠ του Τμήματος Φυσικής για το φιλικό κλίμα και συμπαράσταση στο χώρο του ερευνητικού εργαστηρίου φασματοσκοπίας Mössbauer και Φυσικής Υλικών. Επιπλέον, θα ήθελα να ευχαριστήσω και τον εκλιπών **Παναγιώτη Τριανταφύλλου**, μέλος Ε.Τ.Ε.Π. του Τομέα «Φυσικής Στερεάς Κατάστασης και Φυσικής Υλικών και Επιφανειών» του Τμήματος Φυσικής. Ήταν τιμή μου να γνωρίσω τον πιο εφευρετικό και γεμάτο όρεξη για διδαχή άνθρωπο του ορόφου μας, που σε κάθε συνάντηση μας πέρα των λύσεων που έδινε σε κάθε τεχνικό, ηλεκτρονικό, μηχανικό, κατασκευαστικό ζήτημα παρέδιδε και μαθήματα ζωής, που θα κουβαλώ και θα προσπαθώ και εγώ να μεταδώσω.

Πολλά ευχαριστώ και στα παιδιά του ορόφου μας, μέλη της ερευνητικής ομάδας του κ. Δεληγιαννάκη. Ήταν μεγάλη μου χαρά να γνωριστούμε και να αφουγκραστούμε τις ανησυχίες μας, κάνοντας τις μέρες μας 'στον αγώνα' ευχάριστες. Επίσης πολλά ευχαριστώ και στα παιδία που πέρασαν από την επίβλεψη του Καθηγητή μου, τόσο στα πλαίσια της διπλωματικής τους εργασίας όσο και σε μεταπτυχιακό επίπεδο, πιο συγκεκριμένα τους Φυσικούς δεσποινίς **Ελπινίκη Μπόμπολη** και κύριο **Θεοδόση Σούλιο**, για τις αμέτρητες ώρες που περάσαμε μαζί στο γραφείο και το εργαστήριο και την ευκαιρία να τους διδάξω όλα όσα διδάχθηκα.

Σε αυτό το σημείο θα ήθελα να ευχαριστήσω και τους ανθρώπους από το στένο φιλικό και οικογενειακό περιβάλλον μου. Παρά το γεγονός ότι ο καθένας μας διάλεξε τον δικό του δρόμο, πάντα στις δύσκολες μας στιγμές ήμαστε και είμαστε εκεί ο ένας για τον άλλον, εκφράζοντας ο καθένας με τον δικό του τρόπο τη συμπαράσταση του. Και όσον αφορά εμένα, ομολογώ πως ήταν απλές οι κουβέντες και οι πράξεις, ώστε να μου δώσουν τη δύναμη για να συνεχίσω το δικό μου έργο. Για αυτά και πολλά άλλα σας ευχαριστώ, φίλε/φίλη μου **Αρχοντή**, **Άγγελε**, **Σωτήρη**, **Γιώργο Φ.**, **Νίκο Δ.**, **Γιώργο Β.**, **Γιώργο Κ.**, **Σάββα**, **Νάγια**, **Μυρσίνη**, **Δώρα**, **Αλεξάνδρα**, **Κώστα Μ.**, **Κώστα Ν.**, **Ηλία**, **Πέτρο**, **Χρήστο Λ.**, **Αλέξανδρε**, **Χριστίνα Κ.**, **Νίκο Η.**, **Μάριε** και **Χρήστο Ντ**.

Επιπλέον, θα ήθελα να ευχαριστήσω και τα αδέρφια μου, **Ορέστη** και **Χριστίνα**. Πιστεύω πολύ στις δυνατότητες σας, και αυτό το αποδεικνύουν καθημερινά οι πράξεις σας, και αν μπορούσε να πεί κάτι αυτή μου η προσπάθεια, αυτό θα ήταν να μην τα βάζετε κάτω και να προσπαθείτε ο καθένας για τη δική του σπουδή. Οι δύσκολες καταστάσεις θέτουν τα θεμέλια για μεγάλα πράγματα, αρκεί να υπάρχει θέληση, υπομονή και επιμονή.

Για το τέλος θα ήθελα να εκφράσω την απέραντη ευγνομοσύνη μου στους ανθρώπους που με στηρίζουν και πιστεύουν σε εμένα καθημερινά, την σύντροφο μου και **Υποψήφια Διδάκτορα Καραγιάννη Βασιλική**, για την αμέριστη αγάπη και πίστη στις δυνατότητες μου, αλλά κυριώς την ευχαριστώ που είναι πάντα δίπλα μου, στήριγμα και συνοδοιπόρος, κάνοντας τη ζωή μου πάντα πιο γλυκιά. Τέλος, θα ήθελα να ευχαριστήσω μέσα από τα βάθη της καρδιάς μου τους γονείς μου, **Γιώργο** και **Σούλα**, τους αφανείς ήρωες και πρότυπα μου, που με στηρίζουν σε κάθε μου βήμα και είναι πάντοτε στο πλευρό μου σε κάθε όμορφη αλλά και δύσκολη πτυχή της ζωής μου. Αν η μεγαλύτερη χαρά για ένα γονιό που στερείται, είναι οι επιτυχίες των παιδιών του, τότε η μεγαλύτερη χαρά για ένα παιδί που κοπιάζει, είναι η παρουσία των γονιών του στις επιτυχίες του.

Ευχαριστώ πολύ την Επιτροπή Ερευνών και Διαχείρησης του ΕΛΚΕ του Πανεπιστημίου Ιωαννίνων για την υποτροφία στα πλαίσια της εκπόνησης της διδακτορικής διατριβής μου στο πλαίσιο του προγράμματος με κωδικό 82561 και τίτλο 'ΠΡΟΓΡΑΜΜΑ ΥΠΟΤΡΟΦΙΩΝ ΥΠΟΨΗΦΙΩΝ ΔΙΔΑΚΤΟΡΩΝ ΚΑΙ ΜΕΤΑΔΙΔΑΚΤΟΡΩΝ', καθώς και το Ελληνικό Ίδρυμα Έρευνας και Καινοτομίας (ΕΛ.ΙΔ.Ε.Κ.) για την υποστήριξη της διατριβής μου.

ΕΛ.ΙΔ.Ε.Κ.
Ελληνικό Ίδρυμα Έρευνας & Καινοτομίας

Η ερευνητική εργασία υποστηρίχτηκε από το Ελληνικό Ίδρυμα Έρευνας και Καινοτομίας (ΕΛ.ΙΔ.Ε.Κ.) στο πλαίσιο της «3ης Προκήρυξης ΕΛ.ΙΔ.Ε.Κ. για Υποψήφιους/ες Διδάκτορες» (Αριθμός Υποτροφίας: 06623)

Αφιερωμένο σε όσους προσπαθούν να κυνηγήσουν όσα τους προστάζει η περιέργια τους...

Περίληψη

Τις τελευταίες δεκαετίες, τα σωματίδια στη νανοκλίμακα έχουν γίνει αντικείμενο έντονης επιστημονικής έρευνας τόσο σε θεωρητικό όσο και σε πειραματικό επίπεδο, αναδεικνύοντας τις ιδιαίτερες ιδιότητες που διαθέτουν ως υλικά μεγάλης επιστημονικής και τεχνολογικής σημασίας. Η αξιοποίηση τους από ένα εύρος τεχνολογικά εξελισσόμενων τομέων όπως η αποθήκευση πληροφορίας, η κατάλυση, η πράσινη ενέργεια, η ηλεκτρονική, η χημική βιομηχανια,η βιοϊατρική και η βιοφαρμακευτική, αποκαλύπτει τις νέες και ιδιαίτερες δυνατότητες που μπορούν να προσφέρουν σε σχέση με τα συμβατικά μαζικά (bulk) υλικά. Μια πολύ σημαντική κατηγορία νανοϋλικών είναι τα υβριδικά νανοϋλικά. Τα νανοϋλικά αυτά αναδεικνύουν την δυνατότητα συνένωσης διαφορετικών νανοϋλικών μεταξύ τους, συνδυάζοντας τις ιδιαίτερες ξεχωριστά ιδιότητες τους προς τον σχηματισμό μιας υβριδικής νανοδομής με συνδυασμένες ιδιότητες.

Στο πλαίσιο αυτό, η εκπόνηση της παρούσας διδακτορικής διατριβής επικεντρώθηκε στην σύνθεση, τον χαρακτηρισμό και την μελέτη των ιδιοτήτων νέων υβριδικών μαγνητικών νανοδομημένων υλικών. Οι νανοδομές αυτές συγκαταλέγονται στην υποκατηγορία των μεταλλικών υβριδικών ενώσεων και σχετίζονται με την ανάπτυξη μαγνητικών διμεταλλικών κραμμάτων με βάση τον σιδήρο (Fe) πάνω στην επιφάνεια κατάλληλων υποστρωμμάτων ανάπτυξης νανοδιαμαντιών (NDs).

Οι στόχοι που θέσαμε στη παρούσα διατριβή, ήταν η σύνθεση νέων υβριδικών νανοδομημένων μαγνητικών υλικών με ιδιαίτερες μαγνητικές ιδιότητες που αφορούν διμερή κράματα μεταλλικών στοιχείων με βάση τον σίδηρο (Fe) και συγκεκριμένα τα κράματα Fe-Rh, Fe-Co και Fe-Ni, χρησιμοποιώντας ως υποδομή ανάπτυξής τους μήτρες νανοδιαμαντιών. Στο πλαίσιο αυτό δόθηκε ιδιαίτερη έμφαση στην προσπάθεια για σχηματισμό νανοκρυστάλλων υψηλής ποιότητας διμερών κραμάτων σιδήρου με διατεταγμένη στοιχειακά δομή και καλή διασπορά στη μήτρα των νανοδιαμαντιών, καθώς και στην ανάπτυξη ιδιαίτερων μαγνητικών ιδιοτήτων όπως υψηλές τιμές συνεκτικού πεδίου, μέσω της πρόκλησης τετραγωνικών παραμορφώσεων της κυβικής κρυσταλλικής δομής τους, διατηρώντας παράλληλα τα νανοδιάστατα χαρακτηριστικά των σωματιδίων, χωρίς δηλαδή αύξηση του μεγέθους τους και σχετικά υψηλή μαγνήτιση κόρου.

Ο λόγος που επιλέξαμε τα συγκεκριμένα μαγνητικά κράματα είναι τα πολύ ενδιαφέροντα και σημαντικά μαγνητικά χαρακτηριστικά που διαθέτουν οι αντίστοιχες μαζικές (bulk) δομές και η προοπτική που υπάρχει να αναδειχθούν επιπλέον ιδιαίτερα δομικά και μαγνητικά χαρακτηριστικά με την ανάπτυξη των φάσεων αυτών στην νανοκλίμακα, σε συνδυασμό με την βάση ανάπτυξης των νανοδιαμαντιών. Το κύριο μέρος αυτής της διάτριβης καλύπτεται από τον περαιτέρω χαρακτηρισμό, μελέτη και ερμηνεία των δομικών, μορφολογικών, ηλεκτρονιακών και μαγνητικών ιδιοτήτων των μαγνητικών αυτών νανοδομημένων φάσεων σε σχέση με την κρυσταλλική τους δομή, την μορφολογία των νανοδομών και τις συνθήκες σύνθεσης. Η χρήση των υποστρωμάτων των νανοδιαμαντιών ως πλαισίων-υποδομών ανάπτυξης νέων

νανοδομημένων μαγνητικών υλικών, αναδεικνύει αυτή την μέθοδο σύνθεσης ως μία απλή, εύκολη και χαμηλού κόστους τεχνική σύνθεσης νέων μαγνητικών υβριδικών νανοδομημένων υλικών.

Επιπρόσθετα επιδιώκουμε να προβάλουμε την ερευνητική καινοτομία της ανάπτυξης αυτών των μαγνητικών νανοδομών πάνω σε μήτρες νανοδιαμαντιών, καθώς είναι η πρώτη φορά που επιχειρείται μία τέτοια προσπάθεια με τα συγκεκριμένα μαγνητικά υλικά. Επιπλέον επιθυμούμε να καταστήσουμε γνωστή στην ευρύτερη επιστημονική κοινότητα την δυναμική των δυνατοτήτων που μπορεί να προσφέρει η βάση ανάπτυξης αυτών των σημαντικών υλικών που είναι τα νανοδιαμάντια σε συνδυασμό με τις ιδιαίτερες μαγνητικές νανοδομές, ως πρόταση για την ανάπτυξη νέας τεχνολογίας η οποία εκτιμούμε ότι έχει ιδιαίτερη δυναμική να αξιοποιηθεί σε εφαρμογές σε πεδία όπως η ηλεκτρονική και μαγνητο-ηλεκρονική, η βιοϊατρική, η βιοφαρμακευτική και σχετικά διασυνδεόμενα αντικείμενα.

Στην παρούσα διατριβή, ασχοληθήκαμε με την σύνθεση, χαρακτηρισμό και ανάλυση τριών υβριδικών μαγνητικών νανοδομημένων συστημάτων:

I. **Το σύστημα Fe-Rh/NDs**
II. **Το σύστημα Fe-Co/NDs**
III. **Το σύστημα Fe-Ni/NDs**

Συγκεκριμένα, για την ανάπτυξη των υβριδικών κρυσταλλικών μαγνητικών νανοδομών Fe-Co/NDs, Fe-Ni/NDs και Fe-Rh/NDs ακολουθήσαμε την στρατηγική του συνδυασμού μεθόδων σύνθεσης υγρής χημείας και ανόπτησης υπό ελεγχόμενες συνθήκες. Οι συνθέσεις υγρής χημείας βασίζονται στη μέθοδο του βοροϋδριδίου ($NaBH_4$) και τη μέθοδο γονιμοποίησης της μήτρας (impregnation method). Παράλληλα παρασκευάστηκαν πρόδρομα δείγματα ελεύθερων νανοσωματιδίων Fe-(Rh/Co/Ni) της ίδιας στοιχειομετρίας με αυτής των υβριδικών ώστε να συγκριθούν οι ιδιότητές τους, να εκτιμηθεί και να ερμηνευτεί, ο ρόλος και οι ιδιότητες της βάσης-μήτρας των νανοδιαμαντιών στην διαδικασία σύνθεσης των μαγνητικών φάσεων στις υβριδικές νανοδομές.

Για την σύνθεση των πρόδρομων υβριδικών δειγμάτων αρχικά χρησιμοποιείται το πρώτο από τα δύο συστατικά (NDs) σε προπαρασκευασμένη μορφή, συνδυαζόμενο με τα υδατικά διαλύματα των κατάλληλων αλάτων του κοινού μεταλλικού στοιχείου (Fe) και του δεύτερου συστατικού (Rh/ Co/ Ni). Τα τελικά υβριδικά δείγματα προκύπτουν ύστερα από θερμική ανόπτηση των πρόδρομων δειγμάτων σε υψηλές θερμοκρασίες, σφραγισμένα υπό συνθήκες κενού (10^{-3} Torr) σε αμπούλες χαλαζία. Η διαδικασία αυτή είναι απαραίτητη αφενός για την δημιουργία αναγωγικών συνθηκών για την δημιουργία των επιθυμητών μεταλλικών νανο-κραμάτων με τις ιδιαίτερες κρυσταλλικές δομές και αφετέρου για την αποφυγή οξείδωσης των μαγνητικών νανοσωματιδίων κατά την ανάπτυξή τους. Το είδος των νανοδομημένων φάσεων, η κρυσταλλική τους δομή, η μορφολογία, το μέγεθος τους, η αυτό-οργάνωση και η διασπορά στις μήτρες των νανοδιαμαντιών καθορίζουν σε μεγάλο βαθμό και τις μαγνητικές ιδιότητες των παρασκευασθέντων υβριδικών υλικών, χαρακτηριστικά που μπορούν να ελεγχθούν μέσω των συνθηκών σύνθεσης (διαδικασία και θερμοκρασίες ανόπτησης, συγκέντρωση νανοσωματιδίων πάνω στα νανοδιαμάντια).

Ο χαρακτηρισμός και η ανάλυση των δομικών, μορφολογικών, ηλεκτρονιακών και μαγνητικών ιδιοτήτων των δειγμάτων που παρασκευάστηκαν για την διερεύνηση των υπό μελέτη μαγνητικών υβριδικών νανοδομημέων συστημάτων έγινε μέσω της χρήσης ειδικών τεχνικών χαρακτηρισμού όπως περίθλαση ακτίνων-X (XRD), ηλεκτρονική μικροσκοπία διέλευσης (TEM), TEM υψηλής ανάλυσης (HRTEM), ηλεκτρονική μικροσκοπία σάρωσης και διέλευσης (STEM) με δυνατότητα χρήσης μεθόδου λήψης υψηλής γωνίας δακτυλιοειδών εικόνων σκοτεινού πεδίου (HAADF) και φασματοσκοπικής ανάλυσης ακτίνων-X με ενεργειακή διασπορά (EDS), μαγνητικές μετρήσεις σε τυπικό μαγνητόμετρο δονούμενου δείγματος (VSM) καθώς και σε σύστημα μέτρησης μαγνητικών ιδιοτήτων (MPMS) με χρήση VSM και φασματοσκοπία Mössbauer ^{57}Fe σε γεωμετρία διέλευσης και σε διάφορες θερμοκρασίες (300 K-11 K).

Ειδικότερα, το σύστημα Fe-Rh/NDs αναπτύχθηκε μέσω του συνδυασμού της μεθόδου υγρής χημείας του βοροϋδριδίου ($NaBH_4$) και ανόπτησης υπό ελεγχόμενες συνθήκες κενού σε σφραγισμένες αμπούλες χαλαζία (700°C για 30 λεπτά). Συντέθηκαν επίσης δείγματα ελεύθερων (χωρίς παρουσία νανοδιαμαντιών) μαγνητικών νανοσωματιδίων με την ίδια στοιχειομετρία των υβριδικών δειγμάτων. Στα υβριδικά δείγματα τα νανοσωματίδια Fe-Rh που αναπτύσσονται στις επιφάνειες των νανοδιαμαντιών είναι σιδηρομαγνητικά και έχουν οργανωμένη κυβική δομή τύπου CsCl B2-bcc α'-Fe-Rh, πλούσια σε Rh στοιχειομετρία (60-70 at.%) με μέσο μέγεθος 4 nm, και κατανέμονται ομοιόμορφα στις επιφάνειες των προτύπων νανοδιαμαντιών. Επίσης παρουσιάζουν σταθερή σιδηρομαγνητική συμπεριφορά σε ένα ευρύ φάσμα θερμοκρασιών από 2 K έως 400 K, χωρίς παρατηρήσιμη αντισιδηρομαγνητική σε σιδηρομαγνητική μετάβαση. Υπό τις ίδιες συνθήκες, στα ελεύθερα δείγματα (χωρίς νανοδιαμάντια), αναπτύχθηκαν παραμαγνητικά νανοσωματίδια Fe-Rh με fcc δομή, τα οποία αποκτούν αντισιδηρομαγνητικά χαρακτηριστικά σε χαμηλές θερμοκρασίες (<77 K). Τα αποτελέσματα αυτά, υπογραμμίζουν τον κρίσιμο ρόλο της μήτρας νανοδιαμαντιών, καθώς τα άτομα άνθρακα στα γραφιτικά επιφανειακά στρώματα αυτών διευκολύνουν τη διάχυση και ανάπτυξη της σιδηρομαγνητικής φάσης τύποθ CsCl B2-bcc α'-Fe-Rh. κατά την ανόπτηση.

Το σύστημα Fe-Co/NDs αναπτύχθηκε μέσω συνδυασμού μεθόδων υγρής χημείας ($NaBH_4$ και γονιμοποίησης) και θερμικής επεξεργασίας σε εύρος θερμοκρασιών (600–700°C) και χρόνων ανόπτησης (2 s–32 h). Για την πλήρη κατανόηση των μαγνητικών ιδιοτήτων των μαγνητικών νανοδομών, συντέθηκαν επίσης δείγματα εμπλουτισμένα σε το ισότοπο ^{57}Fe, ακολουθώντας στο πρώτο στάδιο τη μέθοδο γονιμοποίησης, της ίδιας ονομαστικής στοιχειομετρίας με τα μη εμπλουτισμένα, με σκοπό να διευκολυνθεί περαιτέρω η ανάλυση με την τεχνική της φασματοσκοπίας Mössbauer ^{57}Fe. Τα ευρήματα δείχνουν ότι τόσο τα υβριδικά όσο και τα ελεύθερα δείγματα (χωρίς νανοδιαμάντια) που συντέθηκαν με τη μέθοδο $NaBH_4$ περιείχαν κράμα Fe-Co και νανοσωματίδια οξειδίου σιδήρου-κοβαλτίου τύπου σπινελίου, με τα πρώτα να παρουσιάζουν ισχυρές διασωματιδιακές αλληλεπιδράσεις. Αυτές οι αλληλεπιδράσεις υποδηλώνουν μεγαλύτερα μεγέθη νανοσωματιδίων ή/και συνάθροιση σε συστάδες (clusters), που θα επηρεάζουν την κατανομή τους στη μήτρα των νανοδιαμαντιών στα υβριδικά δείγματα, γεγονός που απέτρεψε την περαιτέρω χρήση της διαδικασίας ανόπτησης. Αντίθετα, η διαδρομή της γονιμοποίησης στο πρώτο στάδιο της σύνθεσης, απέδωσε μετά το δεύτερο στάδιο της ανόπτησης νέα μαγνητικά νανοϋβριδικά υλικά, αποτελούμενα από σιδηρομαγνητικά οργανωμένης κυβικής κρυσταλλικής δομής (bcc) νανοσωματίδια Fe-Co που αναπτύσσονται στη μήτρα των νανοδιαμαντιών. Αυτά τα νανοσωματίδια Fe-Co, παρουσιάζουν μέση διάμετρο μεταξύ 6 και 10 nm, κατανέμονται ομοιόμορφα στις επιφάνειες των νανοδιαμαντιών και εμφανίζουν υψηλή περιεκτικότητα σε κοβάλτιο (~65 at. % Co). Επίσης εμφανίζουν σταθερή σιδηρομαγνητική συμπεριφορά σε ένα εύρος θερμοκρασιών από 400 K έως 2 K, με τιμές συνεκτικών πεδίων από περίπου 110 Oe στους 400 K σε περίπου 850 Oe στους 2 K. Παράλληλα με την ανάπτυξη της κύριας κρυσταλλικής φάσης Fe-Co, παρατηρείται και ο συστηματικός σχηματισμός μιας τετραγωνικά στρεβλωμένης (tetragonally distorted) από την κυβική συμμετρία δομής μαρτενσιτικού τύπου Fe-Co, η εμφάνιση της οποίας οφείλεται στις φυσικά αναπτυσσόμενες δομές ατόμων άνθρακα χαρακτήρα sp^2 (δομές τύπου γραφενίου) στην επιφάνεια των νανοδιαμαντιών. Οι δομές αυτές ευνοούν διάφορους επιφανειακούς δομικούς μετασχηματισμούς των κυρίαρχων εσωτερικών sp^3 υβριδικών νανοδομών των νανοδιαμαντιών σε sp^2 κατά το δεύτερο στάδιο της θερμικής κατεργασίας των υβριδικών υλικών. Οι νανοδομές τύπου γραφενίου αποτελούν πλούσια πηγή ατόμων άνθρακα, τα οποία κατά τη διάρκεια θερμικής κατεργασίας πάνω από τους 600°C μπορούν, λόγω διαδικασιών γραφιτικοποίησης, να διαχυθούν ενδοπλεγματικά στη δομή των μαγνητικών νανοσωματιδίων Fe-Co επιφέροντας επιφανειακούς μη-εκτεταμένους τετραγωνικούς δομικούς μετασχηματισμούς μαρτενσιτικού-τύπου σε μέρος αυτών των μεταλλικών νανοσωματιδίων. Αυτό αποδεικνύεται, τόσο από την παρουσία των αντίστοιχων μαρτενσιτικών συνιστωσών στα φάσματα Mössbauer ^{57}Fe, όσο και από την διαπιστωμένη μέσω μετρήσεων TEM και HRTEM ανάπτυξη στρωμάτων γραφιτικού-τύπου, τα οποία περιτυλίγουν τα μαγνητικά νανοσωματίδια Fe-Co καθώς αναπτύσσονται πάνω στην επιφάνεια των νανοδιαμαντιών.

Για το σύστημα Fe-Ni/NDs, η ανάπτυξη των υβριδικών κρυσταλλικών μαγνητικών νανοδομών έγινε μέσω του συνδυασμού μεθόδων σύνθεσης υγρής χημείας και ανόπτησης υπό ελεγχόμενες συνθήκες. Αρχικά επιλέχθηκε η μέθοδος του βοροϋδριδίου ($NaBH_4$) και όπως και στην περίπτωση του συστήματος Fe-Co/NDs, καταλήξαμε στη μέθοδο γονιμοποίησης και ανόπτησης υπό ελεγχόμενες συνθήκες κενού (700°C, 30 min–8 h). Τα αποτελέσματα έδειξαν την ανάπτυξη σιδηρομαγνητικών νανοσωματιδίων Fe-Ni, πλούσιων σε νικέλιο (~64 at.%), με μέσο μέγεθος 10 nm και κρυσταλλική δομή τύπου $AuCu_3$ γ'-fcc, ομοιόμορφα διασπαρμένων στις επιφάνειες νανοδιαμαντιών. Τα νανοσωματίδια παρουσιάζουν σιδηρομαγνητική συμπεριφορά (2 K–400 K) με μαγνήτιση κόρου 11.9 emu/g και συνεκτικά πεδία 10–490 Oe. Η φασματοσκοπία Mössbauer ^{57}Fe αποκάλυψε συμμετοχή του σιδήρου τόσο στη βασική fcc σιδηρομαγνητική φάση όσο και σε μια δευτερεύουσα μαρτενσιτικού τύπου Fe-Ni φάσης, η οποία σχετίζεται με τη διάχυση ατόμων άνθρακα από τις γραφιτικές δομές sp^2 στις επιφάνειες των νανοδιαμαντιών προς τις ενδοπλεγματικές θέσεις της Fe-Ni δομής, καθώς οι sp^2 δομές υποβάλλονται σε διαδικασίες περαιτέρω γραφιτικοποίησης κατά το δεύτερο στάδιο της θερμικής κατεργασίας. Όπως και στη περίπτωση του συστήματος Fe-Co/NDs, έτσι και εδώ οι μετρήσεις TEM και

HRTEM έδειξαν ότι γραφιτικά στρώματα τύπου γραφενίου περιβάλλουν τα νανοσωματίδια Fe-Ni, επιβεβαιώνοντας τη σύνδεση μεταξύ της μήτρας νανοδιαμαντιών και των μοναδικών δομικών χαρακτηριστικών των νανοσωματιδίων.

Ο συνδυασμός των αποτελεσμάτων για τα συστήματα Fe-Co/NDs και Fe-Ni/NDs καταδεικνύει ότι η σύνθεση σε δύο στάδια και οι εσωτερικοί μηχανισμοί ανάπτυξης των μεταλλικών νανοκραμάτων οδηγούν σε ιδιαίτερα νανοϋβριδικά μαγνητικά συστήματα με παρόμοια και επαναλαμβανόμενα μορφολογικά χαρακτηριστικά. Η επαναληψιμότητα αυτή αποδίδεται στη βήμα-προς-βήμα διαδικασία σύνθεσης που ακολουθείται και στα δύο συστήματα.

Ο σχηματισμός των μεταλλικών νανοσωματιδίων στις μήτρες νανοδιαμαντιών, καθώς και η ανάπτυξη γραφιτικών νανοδομών στη διεπιφάνεια των μαγνητικών νανοσωματιδίων και αυτών των νανοδιαμαντιών, συνδέεται άμεσα με τη διαδικασία γραφιτικοποίησης των sp^2 ατόμων άνθρακα που υπάρχουν στις επιφάνειες των νανοδιαμαντιών. Αυτή η διαδικασία λαμβάνει χώρα σε υψηλές θερμοκρασίες και ενισχύεται από την παρουσία των μεταλλικών στοιχείων (Co, Ni) στα διμεταλλικά κράματα. Επιπλέον, η ανάπτυξη της μαρτενσιτικού τύπου φάσης και στα δύο συστήματα θεωρείται αναμενόμενη, καθώς σχετίζεται με τις θερμικές συνθήκες και τη γραφιτικοποίηση κατά το δεύτερο στάδιο της σύνθεσης. Τα συνολικά αποτελέσματα υποδεικνύουν ότι το μορφολογικό περιβάλλον, το οποίο περιλαμβάνει τις αλληλοσυνδεόμενες μαρτενσιτικού και γραφιτικού τύπου φάσεις, επηρεάζεται από τη δράση των μαγνητικών νανοσωματιδίων, των νανοδιαμαντιών και το είδος του μεταλλικού στοιχείου στο κράμα σιδήρου. Η παρουσία του Co ή Ni φαίνεται να παίζει καταλυτικό ρόλο στη διαμόρφωση αυτών των χαρακτηριστικών. Αντίθετα, η παρουσία του Rh σαν δεύτερο στοιχείο κραματοποίησης, φαίνεται πως δεν επιδρά στη διαμόρφωση παρόμοιων χαρακτηριστικών στο σύστημα Fe-Rh/NDs. Αυτό οφείλεται στις φυσικοχημικές ιδιότητες του στοιχειακού Rh, που το καθιστούν λιγότερο επιδραστικό σε δεσμούς άνθρακα σε αντίθεση με τα άλλα στοιχεία μετάπτωσης (Fe, Co, Ni). Συνεπώς, στα πλούσια σε συγκέντρωση Rh νανοσωματίδια Fe-Rh που σχηματίζονται κατά την ανόπτηση, φαίνεται ότι η καταλυτική δράση του Fe περιορίζεται από την επίδραση του Rh που υπερισχύει στη σύσταση της μαγνητικής φάσης, και έτσι δεν μπορεί να ευνοήθει η διαδικασία της γραφιτικοποίησης.

Abstract

Over recent decades, nano-scaled materials have been the focus of extensive scientific research, both theoretical and experimental, due to their remarkable properties with significant scientific and technological potential. Their applications span a wide array of advanced fields, from information storage, catalysis, and green energy to electronics, food science, construction, biomedicine, and biopharmaceutics. These materials offer exceptional advantages compared to traditional bulk counterparts, revealing unique properties that support innovations across these sectors.

A particularly valuable class of these materials is nanohybrids, which combine distinct nanomaterials into a single hybrid structure, thereby merging their advantageous properties. This PhD thesis centers on synthesizing, characterizing, and analyzing new hybrid magnetic nanostructured materials, specifically magnetic nanohybrids based on bimetallic iron (Fe) alloys, and more specifically the Fe-Rh, Fe-Co and Fe-Ni alloys, grown on nanodiamonds (NDs) substrates. Particular emphasis was placed on the formation of high-quality nanocrystals of binary iron alloys with an ordered elemental structure and good dispersion within the nanodiamond matrix. Additionally, the development of distinctive magnetic properties, such as high coercive field values, was pursued by inducing tetragonal distortions in their cubic crystalline structure while maintaining the nanoscale characteristics of the particles—ensuring no increase in their size—and achieving relatively high saturation magnetization. We selected these magnetic alloys due to their intriguing magnetic properties in bulk form and the potential to display even more distinctive structural and magnetic characteristics when synthesized at the nanoscale on NDs substrates.

The main body of this thesis delves into the structural, morphological, electronic, and magnetic properties of these nanostructured magnetic phases. By exploring how their crystal structure and morphology evolve under specific synthesis conditions, we highlight the role of nanodiamonds as growth templates. This synthetic approach offers a straightforward, cost-effective pathway to creating novel hybrid magnetic nanomaterials with high potential for diverse technological applications.

This work aims to present the pioneering synthesis of these magnetic nanostructures on nanodiamonds templates, as this approach has not previously been applied to the specific magnetic materials under investigation. We also aim to demonstrate the unique capabilities that NDs nanotemplates contribute to these magnetic nanohybrids, showcasing their relevance for applications in fields such as electronics, magneto-electronics, biomedicine, and beyond.

This thesis involves the synthesis, characterization, and analysis of three distinct hybrid magnetic nanostructured systems:

- **I. Fe-Rh/NDs system**
- **II. Fe-Co/NDs system**
- **III. Fe-Ni/NDs system**

More specific, each of these systems was developed using a two-stage synthesis process that combines wet-chemical techniques with controlled thermal treatments. The synthesis protocols involve $NaBH_4$ reduction and impregnation techniques, where the NDs nanotemplates are combined with precise amounts of iron and second metal salts (Rh, Co, or Ni). Additionally, unsupported Fe-(Rh/Co/Ni) nanoparticle precursor samples with equivalent stoichiometry were synthesized for comparison. This allowed us to evaluate the impact of NDs nanotemplates on the growth and properties of the nanoalloy magnetic phases. For the synthesis of the precursor hybrid samples, the first component (NDs) is initially used in its pre-prepared form and combined with aqueous solutions of the appropriate salts of the primary metallic element (Fe) and the second component (Rh/Co/Ni). Final samples obtained after annealing the precursors at high temperatures in vacuum-sealed quartz ampoules (10^{-3} Torr), a step necessary both to maintain reducing conditions favorable for alloy formation and to prevent oxidation of the magnetic nanoparticles. The type of nanostructured phases, their crystalline structure, morphology, size, self-organization, and dispersion within the nanodiamond matrices largely determine the magnetic properties of the synthesized hybrid materials. These characteristics can be controlled through the synthesis conditions, including the annealing process and temperatures, as well as the concentration of nanoparticles on the nanodiamonds.

The characterization and analysis of the structural, morphological, electronic, and magnetic properties of these materials were performed using a comprehensive suite of experimental techniques. These included X-ray diffraction (XRD), transmission electron microscopy (TEM), high-resolution TEM (HRTEM) and scanning-transmission electron microscopy (STEM) with high-angle annular dark-field (HAADF) imaging, energy-dispersive X-ray spectroscopy (EDS), vibrating sample magnetometry (VSM), magnetic property measurement system (MPMS), and ^{57}Fe Mössbauer spectroscopy in transmission geometry at different temperatures (300 K-11 K).

Specifically, the Fe-Rh/NDs system was developed through a combination of the wet-chemical borohydride method ($NaBH_4$) and annealing under controlled vacuum conditions in sealed quartz ampoules (700°C for 30 minutes). Additionally, samples of free magnetic nanoparticles (without the presence of nanodiamonds) with the same stoichiometry as the hybrid samples were synthesized.

In the hybrid samples, Fe-Rh nanoparticles formed on the surfaces of the nanodiamonds exhibit ferromagnetic properties and an ordered cubic CsCl-type B2-bcc α'-Fe-Rh structure. These nanoparticles are rich in Rh stoichiometry (60-70 at.%) with an average size of 4 nm and are uniformly distributed on the surfaces of the nanodiamond templates. They also display stable ferromagnetic behavior over a broad temperature range from 2 K to 400 K, without any observable transition from antiferromagnetic to ferromagnetic behavior. Under the same conditions, free samples (without nanodiamonds) developed paramagnetic Fe-Rh nanoparticles with an fcc structure, which acquire antiferromagnetic characteristics at low temperatures (<77 K). These results underscore the critical role of the nanodiamond matrix, as the carbon atoms in the graphitic surface layers of the nanodiamonds facilitate the diffusion and development of the ferromagnetic CsCl-type B2-bcc α'-Fe-Rh phase during annealing.

The Fe-Co/NDs system was developed through a combination of wet-chemical methods ($NaBH_4$ and impregnation) and thermal treatment over a range of temperatures (600–700°C) and annealing times (2 seconds to 32 hours). To thoroughly understand the magnetic properties of the magnetic nanostructures, isotope-enriched samples with ^{57}Fe were synthesized using the impregnation method during the first stage. These samples had the same nominal stoichiometry as the non-enriched ones, facilitating further analysis via ^{57}Fe Mössbauer spectroscopy. The findings indicate that both hybrid and free samples (without nanodiamonds) synthesized using the $NaBH_4$ method contained Fe-Co alloy and cobalt-iron oxide nanoparticles with spinel-like structures. The Fe-Co alloy nanoparticles exhibited strong interparticle interactions, as evidenced by Mössbauer spectroscopy, suggesting larger particle sizes and/or aggregation into clusters. These characteristics impacted their distribution in the nanodiamond matrix in hybrid samples, making further annealing impractical.

In contrast, the impregnation route in the first synthesis stage yielded new magnetic nanohybrid materials after the second annealing stage. These materials comprised ferromagnetic Fe-Co nanoparticles with an ordered cubic (bcc) crystalline structure that developed on the nanodiamond matrix. The Fe-Co nanoparticles, with an average diameter between 6 and 10 nm, were uniformly distributed on the nanodiamond surfaces and exhibited high cobalt content (~65 at.% Co). They demonstrated stable ferromagnetic behavior across a temperature range from 400 K to 2 K, with coercive field values increasing from approximately 110 Oe at 400 K to about 850 Oe at 2 K.

In addition to the development of the primary Fe-Co crystalline phase, a systematic formation of a tetragonally distorted martensitic-like Fe-Co structure was observed. This phase is attributed to the naturally occurring sp^2 (graphene-like) carbon structures on the nanodiamond surfaces. These structures promote surface structural transformations of the dominant internal sp^3 hybridized nanostructures of the nanodiamonds into sp^2 during the second stage of thermal processing of the hybrid materials. The graphene-like nanostructures serve as a rich source of carbon atoms, which, during thermal treatment above 600°C, can diffuse into the lattice of the Fe-Co magnetic nanoparticles. This diffusion, facilitated by graphitization processes, induces localized tetragonal martensitic-like structural transformations in some of these metallic nanoparticles. This is evidenced by the presence of corresponding martensitic components in the ^{57}Fe Mössbauer spectra and by TEM and HRTEM measurements, which reveal the development of graphene-like layers wrapping around the Fe-Co magnetic nanoparticles as they form on the nanodiamond surfaces.

For the Fe-Ni/NDs system, the development of hybrid crystalline magnetic nanostructures was achieved through a combination of wet-chemical synthesis methods and annealing under controlled conditions. Initially, the borohydride method ($NaBH_4$) was employed. However, similar to the Fe-Co/NDs system, the process was later optimized using the impregnation method followed by annealing under vacuum conditions (700°C for 30 minutes to 8 hours). The results revealed the formation of ferromagnetic Fe-Ni nanoparticles, rich in nickel (~64 at.%), with an average size of 10 nm and an $AuCu_3$ γ'-fcc crystalline structure. These nanoparticles were uniformly distributed across the surfaces of nanodiamonds. The nanoparticles exhibited ferromagnetic behavior over a broad temperature range (2 K–400 K), with a saturation magnetization of 11.9 emu/g and coercive field values between 10 and 490 Oe. ^{57}Fe Mössbauer spectroscopy indicated that iron contributed not only to the primary fcc ferromagnetic phase but also to a secondary martensitic-like Fe-Ni phase. The formation of this martensitic-like phase is attributed to the diffusion of carbon atoms from the sp^2 graphitic structures on the surfaces of nanodiamonds into the interstitial positions of the Fe-Ni structure. This diffusion occurs during the second stage of thermal processing, where the sp^2 structures undergo further graphitization.

As in the Fe-Co/NDs system, TEM and HRTEM measurements confirmed that graphene-like graphitic layers enveloped the Fe-Ni nanoparticles, underscoring the link between the nanodiamond matrix and the unique structural characteristics of the nanoparticles.

The combined findings for the Fe-Co/NDs and Fe-Ni/NDs systems demonstrate that the two-stage synthesis process, along with the intrinsic mechanisms governing the development of the metallic nanocomposites, leads to unique hybrid magnetic systems with similar and reproducible morphological characteristics. This reproducibility is attributed to the step-by-step synthesis approach applied to both systems. The formation of metallic nanoparticles on nanodiamond matrices and the development of graphitic nanostructures at the interface between the magnetic nanoparticles and the nanodiamonds are directly linked to the graphitization process of the sp^2 carbon atoms present on the nanodiamond surfaces. This process occurs at high temperatures and is enhanced by the presence of metallic elements (Fe, Co, Ni) in the bimetallic alloys.

Moreover, the development of the martensitic-like phase in both systems is considered expected, as it is associated with the thermal conditions and graphitization occurring during the second stage of synthesis. The overall results suggest that the morphological environment, characterized by interconnected martensitic and graphitic phases, is influenced by the interaction of the magnetic nanoparticles, nanodiamonds, and the type of metallic element in the iron-based alloy. The presence of Co or Ni appears to play a catalytic role in shaping these characteristics.

In contrast, the presence of Rh as the secondary alloying element in the Fe-Rh/NDs system does not seem to contribute to the formation of similar characteristics. This discrepancy is attributed to the physicochemical properties of elemental Rh, which make it less interactive in carbon bonding processes compared to other transition metals (Fe, Co, Ni). Consequently, in the Rh-rich Fe-Rh nanoparticles formed during annealing, the catalytic activity of Fe is limited by the dominance of Rh within the magnetic phase, thereby inhibiting the graphitization process.

Table of Contents

Chapter 1. Hybrid Nanomaterials

1.1 Introduction

In modern society, technological advancements provide humanity with numerous ways to tackle its most pressing challenges. However, as technology progresses at a fast pace, it demands more complex and interconnected materials and processes. This growing complexity emphasizes the need for advanced materials capable of performing challenging tasks with greater efficiency. Consequently, a new generation of high-performance materials, produced through sustainable and cost-efficient methods, is emerging as a more effective solution to meet the requirements of modern technologies than traditional materials.

Hybrid materials stand out as a promising class that offers these advantages. They showcase the possibility of merging different materials to combine their favorable properties into a single hybrid structure. This combination of properties gives hybrid materials the versatility to be applied in a broad range of sectors, from automotive and construction to electronics, pharmaceuticals, and biomedicine [1].

Current research on hybrid materials can be categorized into two main types [1], [2], [3]. The first classification is based on the nature of the interactions between the components of the hybrids, while the second focuses on the roles each component plays in the hybrid system (e.g., as a host or guest). According to the first classification, there are two subtypes. Class I hybrids are formed through weak interactions such as hydrogen bonding, van der Waals forces, or electrostatic interactions. Common preparation methods of Class I hybrids involve sol-gel processes [4], self-assembly [5] and in situ polymerization methods [6].

In contrast, Class II hybrids are characterized by strong chemical bonds, such as covalent bonds, though in some cases, both strong and weak interactions can coexist in a single material. Typical methods for the preparation of Class II hybrids are self-assembly synthesis methods [7], template-assisted synthesis [8], and hydrothermal processes [9].

The second classification system divides hybrid materials into four subgroups based on the dominant matrix/host and guest structure: organic-inorganic hybrids (where the matrix is the first component in the expression, here organic) [10], inorganic-organic hybrids [11], inorganic-inorganic hybrids [12], and organic-organic hybrids [13].

Two critical aspects of hybrid material research are the composition and structure of their components. A wide variety of materials can be used to create hybrids, leading to an extensive range of possible compositions. Frequently used materials include polymers [14], silica (SiO_2) [15], biomaterials [16], metals (especially transition metals) [17], metal-organic frameworks (MOFs) [18], and perovskites [19]. Additionally, the synthesis techniques used to produce hybrid materials have advanced significantly in recent decades, evolving to meet the growing demands in various scientific fields. This evolution highlights the potential of hybrid materials to impact numerous applications, especially when they are engineered at the nanoscale.

Common methods for synthesizing hybrid materials include sol-gel techniques [11], self-assembly [20], in-situ polymerization [7], template-assisted synthesis [21], solvothermal and hydrothermal methods [22], microwave-assisted synthesis [23], atomic layer deposition [24], chemical vapor deposition [25], co-precipitation/impregnation [9], and spray pyrolysis [26].

The broad range of possible combinations of organic and inorganic components results in hybrid materials being an excellent choice for various applications. Furthermore, tailoring synthesis methods allows for specific properties to be achieved, offering a versatile solution to many of today's technological challenges. Hybrid materials are widely used in fields such as energy storage, catalysis, sensing, photonics, and biomedicine, with extensive applications in each [27].

In this regard, M. G. Kanatzidis et al. were the first to report the synthesis of a novel type of organic-inorganic hybrid material, combining pyrrole, a polymer well-known for its electrical properties, with a 2D layered inorganic solid, FeOCl. This combination, achieved through the oxidative intercalation of the organic molecules and the simultaneous reduction of the inorganic layered structure, resulted in a new class of polymer-inorganic hybrids that exhibit high electrical conductivity, in contrast to other FeOCl intercalation compounds. This group's endeavor is a part of a broader effort that has led to the development of organic-inorganic hybrids [28].

This thesis investigates hybrid nanomaterials belonging to the inorganic-inorganic category, with a particular focus on metal compound hybrids with magnetic properties. These nanohybrids (NHDs) comprise iron-based bimetallic alloys—specifically Fe-Rh, Fe-Co, and Fe-Ni compounds—developed on suitable growth substrates, as illustrated in Figure 1.1. Nanodiamonds (NDs) are chosen as growth platforms due to their exceptional physical properties, making them highly suitable for this purpose. The selected magnetic alloys exhibit remarkable bulk magnetic properties, and their nanoscale synthesis on NDs offers the potential to reveal even more distinctive structural and magnetic features. This study examines how crystal structures and morphologies of these alloys evolve under controlled synthesis conditions, emphasizing the critical role of nanodiamonds as growth matrices. This synthesis strategy provides a simple, cost-effective method to produce innovative hybrid magnetic nanomaterials with significant potential for a wide range of technological applications.

The primary goal of this research is to introduce a novel synthesis approach for these magnetic nanostructures, employing nanodiamonds as templates—a strategy not previously applied to these specific materials. Additionally, it aims to highlight the unique contributions of ND templates to the development of magnetic nanohybrids, emphasizing their suitability for applications in various fields, including electronics, magneto-electronics, and biomedicine.

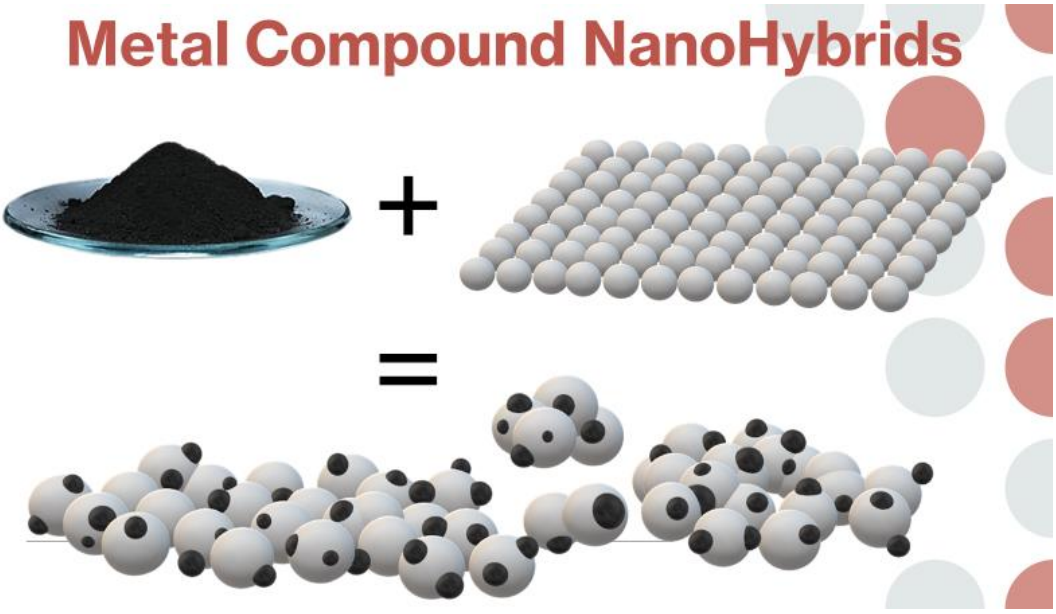

Figure 1.1 Graphical illustration of a metal compound nanohybrid material, where a metal compound (Fe-Rh, Fe-Co and Fe-Ni alloy compound) develops on an appropriate growth nanotemplate material (nanodiamonds).

1.2 Nanodiamonds and Other Carbon Allotropes

1.2.1 Introduction

Carbon, one of the most abundant elements in the universe by mass after hydrogen, helium and oxygen, serves as a fundamental element of all known life. The first meet of carbon with the earliest human civilizations was in prehistory in the forms of soot and charcoal, with the former to be exploited since the first person could handle it from fire. Since then, elemental carbon was found to exist in several forms, each of which has its own physical characteristics. In nature, two of its well-defined and most exploited forms, diamonds and graphite are crystalline in structure, but they differ in physical properties because the arrangements of the atoms in their structures are dissimilar. Therefore, carbon is known to exhibit allotropy, a property of a chemical element to exist in two or more distinct stable (under certain conditions) structural forms varying in the crystal structure and having thus significantly distinct physical properties.

The last forty years the rapid evolution of technology led to the design and development of many new materials full of potentialities. A class of them comprises some synthetic and structurally distinct forms of carbon which are not found as abundant materials in nature, and due to their decreased dimensions are often referred to as carbon nanomaterials. Such well-known nowadays carbon nano-allotropes include fullerene, carbon nanotubes, graphene, carbon quantum dots and NDs. These carbon nanomaterials have garnered significant interest due to their existing or potential use in catalytic processes, electronics, biomedicine, and biopharmaceutics applications, all favored by their low cost, tunable structure, high durability, unique electronic properties, and diverse functionality [29].

With respect to their dimensions, carbon nanomaterials can be classified into three groups: (i) zero-dimensional (0D) structures such as fullerene, carbon quantum dots, and NDs, (ii) one-dimensional (1D) structures such as carbon nano-horns and carbon nanotubes, and (iii) two-dimensional (2D) structures such as graphene and few-layered graphenes. Graphite and diamond are classified as the characteristic bulk 3D carbon allotropes, from the typical structure of which these nano-allotropes originate. Other classification factors pertain to the type of covalent bonding between the carbon atoms in a respective carbon nano-allotrope. Generally, in terms of orbital hybridization, carbon can display sp^3, sp^2 and sp configurations, allowing the existence of a great variety of crystalline and structurally disordered materials [30], [31]. The structures of the most significant carbon nano-allotropes are depicted in Figure 1.2.

Although carbon nano-allotropes exhibit unique functionalities, such as significantly enhancing certain catalytic processes in an environmentally friendly and sustainable manner, they also have notable shortcomings that limit their practical applications. For instance, they often suffer from layer stacking and aggregation, which reduces their surface area and catalytic activity. Graphene, in particular, is prone to structural defects during synthesis, negatively impacting its electronic and mechanical properties. Similarly, carbon nanotubes tend to bundle and agglomerate, hindering their uniform dispersion in matrices or solutions. Nanodiamonds, on the other hand, are susceptible to surface oxidation or graphitization under certain conditions, which can compromise their desired properties. These limitations restrict the versatility and applicability of carbon nano-allotropes in some specific technological and industrial fields [31], [32], [33].

Therefore, carbon nanomaterials are frequently subjected to surface modifications by suitable functional groups to enable attachment of various organic and/or inorganic compounds in order to enrich the properties and, hence, the application potential of the resulting hybrid system [32], [34], [35], [36]. Therefore, the physicochemical properties of the carbon nanomaterials may be adjusted and improved by the covalent or noncovalent bonding of various chemical groups or compounds due to synergetic effects and, thus, bring new characteristics that cannot be shown by the carbon nanostructures alone. In this case, these nanohybrid systems can become competitive materials in various fields where carbon nanomaterials themselves are not so preferable or they can offer a good substitute for other nanomaterials with decreased efficiency for a given application.

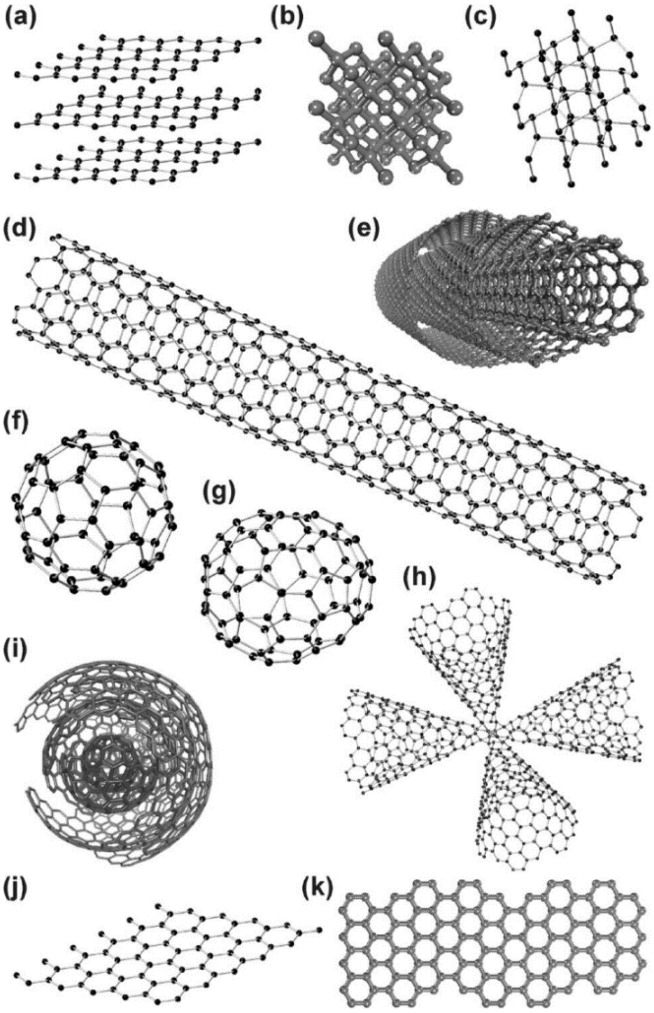

Figure 1.2 Allotropes of carbon: (a) graphite; (b) diamond; (c) lonsdaleite; (d) single-walled carbon nanotube; (e) multiwalled carbon nanotube; (f) fullerene C_{60}; (g) fullerene C_{76}; (h) carbon nanohorns; (i) onion-like carbon; (j) graphene; (k) carbon nanoribbons [30].

In this respect, carbon nanomaterials typically lack a magnetic response when subjected to external magnetic fields, which prompts numerous endeavors to confer this property onto them. Recent results have shown successful efforts in imparting magnetic characteristics to carbon-based nanostructured hybrid materials [37], [38], [39], [40], [41]. The combination of magnetic materials with carbon nanostructures yields synergistic effects, enhancing the electrochemical performance and catalytic capabilities of the hybrids [31]. This enhancement makes them highly promising for applications such as the chemical degradation of diverse organic and/or inorganic compounds and energy storage [32]. Additionally, hybrid composites comprising magnetic materials and carbon nanostructures exhibit improved sensing properties, enabling the detection of various organic compounds and biomolecules for applications like MRI imaging, biological imaging, and therapy [42], [43], [44].

1.2.2 Overview of the Basic Carbon Nano-Allotropes

1.2.2.1 Fullerene

In 1985, Kroto's research team discovered a novel carbon allotrope named fullerene while investigating carbon's properties in extraterrestrial composites [45]. Among many fullerene variants C_{60} stands out for its symmetry and stability, comprising carbon atoms arranged in hexagonal and pentagonal patterns. Alongside C_{60}, other fullerenes like C_{70}, C_{76}, C_{82}, and C_{84} have been identified [46]. These fullerenes are typically produced through low-pressure methods involving electric discharge between carbon electrodes in a helium atmosphere, or via laser or arc vaporization of carbon or graphite in an inert atmosphere [46], [47]. Fullerenes and their derivatives have attracted significant attention for their optical properties [48], heat resistance [49], superconductivity [50], and ferromagnetic behavior, with Curie temperatures reaching approximately 33 K, surpassing those of any reported organic magnets [51]. Functionalized fullerenes, where various organic and inorganic compounds are added, have emerged as promising candidates in medicine [52], electronics [53], and catalysis [54]. The discovery of fullerenes sparked a notable surge in carbon chemistry interest, fueling endeavors to create novel carbon-based nanostructures.

1.2.2.2 Carbon Nanotubes

In 1991, Iijima et al. made a breakthrough by discovering a novel carbon structure termed multiwalled carbon nanotubes in carbon soot generated via an arc-discharge method [55]. Two years later, he also identified single-walled carbon nanotubes [56]. A single-walled carbon nanotube is essentially a graphene sheet rolled into a cylinder, typically with a diameter ranging from approximately 0.4 to 2 nm. In contrast, multiwalled carbon nanotubes consist of concentric cylinders with an interlayer spacing of 0.34 nm and a diameter varying from about 2 to 25 nm; these rolled graphene sheets are held together by van der Waals interactions [57]. Both single-walled and multiwalled carbon nanotubes can extend to lengths of hundreds of micrometers or even centimeters. With aspect ratios (length-to-diameter ratio) frequently exceeding 10000, carbon nanotubes are regarded as among the most anisotropic materials ever produced. Carbon nanotubes possess exceptional strength and stiffness, with properties significantly influenced by factors such as the way graphene sheets are rolled, their dimensions, morphology, and defects. They exhibit impressive mechanical properties, boasting a Young's modulus of around 1.2 TPa and a tensile strength of about 100 GPa, approximately 100 times greater than steel [57]. The electrical properties of carbon nanotubes are primarily dictated by chirality and diameter; single-walled carbon nanotubes can act as metals, semiconductors, or small-gap semiconductors. Due to their nanometer-scale diameter, electron transport occurs predominantly along the nanotube axis, involving quantum effects, hence carbon nanotubes are sometimes referred to as one-dimensional conductors.

Carbon nanotubes demonstrate remarkable optical properties including absorption, photoluminescence, and Raman scattering, alongside excellent thermal and chemical stability [57], [58], [59]. Their large surface area facilitates easy functionalization through covalent attachment of chemical groups, noncovalent adsorption of functional molecules, or endohedral filling of their inner cavity. Various production methods exist including electric arc-discharge, laser ablation, and chemical vapor deposition [58], [59], with the latter being employed for commercial high-purity carbon nanotube production. Carbon nanotubes have been proposed for various applications across diverse fields such as strength reinforcement in composites, energy and gas storage, nanoelectronics (transistors, logic, memory, sensors), polymer matrix fillers, drug delivery systems, gene delivery components, and photothermal therapy tools [58], [59]. Beyond practical applications, carbon nanotubes serve as an ideal model system for investigating quantum phenomena in quasi-1D solids, including single-electron charging [60] and quantum interference [61].

1.2.2.3 Graphene

Graphene, often acknowledged as "the thinnest material in our universe," is a flat, two-dimensional monolayer of sp^2-bonded carbon atoms arranged in a hexagonal honeycomb lattice. It was first been proven that it can be handled and studied as an isolated material in 2004 [62]. Graphene can be considered as the fundamental unit for the construction of 3D graphite (stacking of graphene sheets), 1D carbon nanotubes (rolling of a graphene sheet), or 0D fullerenes (wrapping of a graphene sheet). High-quality graphene demonstrates semimetal or zero-gap semiconductor behavior and possesses remarkable physical properties, including intrinsic mobility (approximately 200000 $cm^2 \cdot V^{-1} \cdot s^{-1}$), Young's modulus (approximately 1 TPa), theoretical surface area (approximately 2630 $m^2 \cdot g^{-1}$), thermal conductivity (approximately 5000 $W \cdot m^{-1} \cdot K^{-1}$), and optical transmittance (approximately 97.7%) [63], [64], [65]. In physics, graphene has facilitated the study of diverse phenomena such as room-temperature quantum Hall effect [66], single-molecule adsorption events [67] and giant magnetoresistance [68]. Reducing the size of graphene sheets below 100 nm in all dimensions yields graphene quantum dots, exhibiting size- and edge crystallography-dependent physical phenomena.

Graphene can be produced through mechanical exfoliation, epitaxial growth, chemical vapor deposition, and chemical exfoliation, with mechanical exfoliation currently considered the most convenient method for producing high-quality samples [62], [63], [64], [65], [69], [70]. Similar to carbon nanotubes, graphene (and graphene oxide) can be covalently and/or noncovalently functionalized with various groups for secondary attachment of organic or inorganic compounds [71], [72]. Covalent modification generates oxygenated species like carboxyl, epoxy, and hydroxyl, forming graphene oxide, which then facilitates the covalent attachment of other compounds [72].

Due to their outstanding properties, graphene and its derivatives have found applications across a broad spectrum, including lightweight, thin, and flexible yet durable display screens [73], electrochromic devices (utilizing graphene oxide) [74], transparent conducting electrodes in liquid-crystal displays [75], optical modulators [76], and conductive plates in ultracapacitors [77].

Additionally, graphene, graphene oxide, and graphene quantum dots hold promise in medicine for drug/gene delivery [78], cancer therapy [79], biosensing [80], and bioimaging [81]. However, challenges such as low production yields and product purity hinder the widespread incorporation of graphene into composite materials.

1.2.2.4 Carbon Quantum Dots

Carbon quantum dots, also known as carbon nanoparticles, have recently garnered considerable attention due to their distinctive quantum size effects and strongly size-dependent electronic, optical, and electrochemical properties [82]. These nanocrystals, with dimensions in all axes less than 10 nm, consist of graphitic sp^2 carbon. In addition to their intriguing optical characteristics such as tunable photoluminescence based on dot size and surface functional groups [83], nonlinear optical response [84], photoinduced electron transfer [85], and electrochemiluminescence [86], carbon quantum dots offer several advantages over heavy-metal-containing semiconductor-based quantum dots [82]. These advantages include chemical inertness, biocompatibility, and low toxicity [87].

Carbon quantum dots can be synthesized using both bottom-up and top-down approaches [88]. Bottom-up methods involve utilizing molecular precursors like citric acid, glucose, or resin, while top-down synthesis procedures start with larger carbon-based materials such as NDs, graphite, carbon nanotubes, carbon soots, activated carbon, or graphene oxide.

Carbon quantum dots, along with their functionalized derivatives, have found significant applications primarily in the medical field for diagnostic purposes, particularly in bioimaging and biosensing [89].

1.2.2.5 Nanodiamonds

Nanoscale diamond particles were initially created through detonation processes in the Soviet Union during the 1960s. However, their existence was largely concealed from the global scientific community until the late 1980s [32]. Despite being shrouded in secrecy for many years, the widespread commercial production of synthetic nano-powders at affordable prices has now made this material readily accessible for research and development purposes. Consequently, this availability has inflicted a rapid growth in the field [36].

Diamond nanocrystals stand out among many materials, including other nanocarbon allotropes. Typically, they exhibit exceptional mechanical strength and outstanding thermal conductivity, rendering them valuable for applications such as cutting, drilling, and semiconductor manufacturing. Moreover, diamond nanocrystals demonstrate notable biocompatibility, minimal toxicity, and superior chemical stability compared to other carbon nanostructures [31]. Therefore, they represent promising candidates for biomedical and biopharmaceutical applications, such as bioimaging [90], biosensing [91], drug delivery[92], hyperthermia [93], and as contrast agents [94].

Presently, there is a diverse array of NDs available for research. These have been synthesized using various techniques, including detonation (Figure 1.3) [95], laser ablation [96], high-energy ball milling of high-pressure high-temperature diamond microcrystals [97], plasma-assisted chemical vapor deposition [98], autoclave synthesis from supercritical fluids [99], chlorination of carbides [100], ion irradiation of graphite [101], electron irradiation of carbon 'onions' [102], and ultrasound cavitation [103].

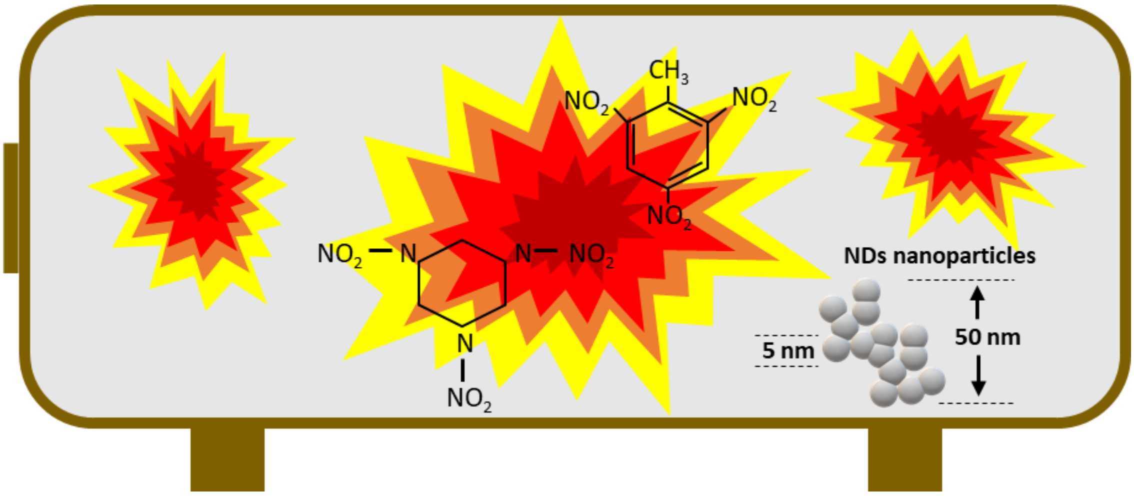

Figure 1.3 Representation of the synthesis of detonation nanodiamonds combining explosive detonations in a closed metallic chamber in an N_2, CO_2 and liquid or solid H_2O atmosphere.

The prosperous utilization of NDs across various technological domains can be attributed to their exceptionally stable crystal structure. This structural stability arises from their unique sp^3 hybridization, which, coupled with their versatile morphology, gives rise to several intriguing characteristics. In terms of morphology, pristine ND NPs typically exhibit spherical, crystalline structures with a narrow size distribution, averaging around 4 to 5 nm [31], [32]. Additionally, ND NPs often aggregate closely, forming coarse and close-up agglutinates with fractal morphologies, spanning from a few NPs in thickness to several hundred nanometers in length [31], [33], [36]. Consequently, NDs can be organized into robust substrates comprising clustered diamond NPs, providing favorable conditions for various applications as growth nanoplatforms, where particle aggregation and surface interactions play pivotal roles [36].

Furthermore, diamond NPs exhibit an ultrahigh surface-to-volume ratio at the nanoscale. This characteristic exposes a significant portion of diamond carbon atoms at the surface and subsurface regions. However, these nano-sized regions are prone to imperfections and defects, commonly originating from the detonation explosion during ND production, leading to deviations from the ideal crystal periodicity. Transmission electron microscopy observations reveal that ND particles typically consist of polyhedra with a diamond core composed of sp^3 carbon, potentially partially coated by a graphitic shell or amorphous carbon with dangling bonds terminated by functional groups (as illustrated in Figure 1.4) [104], [105]. Consequently, a substantial number of unsaturated carbon atoms are observed at the surface and sub-surface sites of NDs. As a result, the dangling bonds of these unsaturated atoms at the grain boundaries undergo significant surface relaxation through stabilization via termination with hydrogen and oxygen functional groups or through reconstruction, particularly at elevated temperatures, into full and/or partial sp^2 hybridized domains to minimize surface energy [31]. Notably, similar surface relaxation phenomena occur when the surface shape of NDs deviates from the typical cubic crystal to octahedral, cuboctahedral, and spherical clusters. Thus, in addition to size and shape, surface terminations play a crucial role in determining the stability of diamond NPs [32].

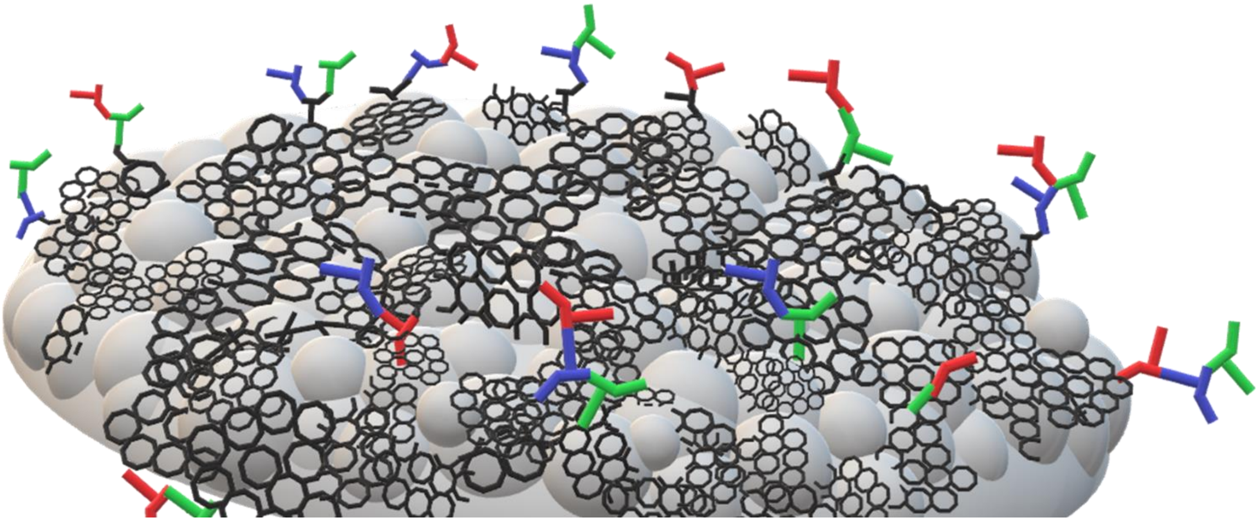

Figure 1.4 Graphical illustration of the structure of a cluster of diamond nanoparticles. This scheme displays the structure of a nanodiamond nanoparticles cluster at ambient conditions. The diamond sp^3-type core nanoparticles (colored grey) are covered by layers of unsaturated surface sp^2-type carbon atoms (colored black), arising from imperfections and defects at the surface and subsurface nano-scaled regions of the nanodiamond nanoparticles, forming uncompensated graphitic domains with dangling bonds, which undergo surface relaxation phenomena through stabilization with functional groups (hydrogen, oxygen, and nitrogen colored green, red and blue).

To elucidate the sequence of surface relaxation phenomena in carbon nanostructures, thermal annealing proves to be more suitable. This process facilitates the decomposition of surface functionalities and promotes the phase transition from diamond terminations to graphitic-type sp^2 nanostructures. Specifically, this transition involves the conversion of sp^3 hybridized carbon atoms into either a partial or uniform core/shell (sp^3/sp^2) configuration of NDs or a concentric sp^2 hybridized graphitic carbon arrangement (resembling onion-like nanocrystals). The nature of these conversions can be controlled by adjusting the annealing conditions, including temperature and time duration [31], [32], [33]. Consequently, engineered NDs hold promise as versatile growth nanoplatforms for leveraging interfacial-surfactant effects, opening up intriguing opportunities across various technological applications.

Considering this, diamond nanocrystals, due to their tunable surface chemistry, can undergo surface modification with appropriate functional groups, enabling the attachment of various organic and/or inorganic compounds to enhance their properties and broaden the application potential of the resulting hybrid system. The bonding of various compounds to the surface of diamond nanocrystals defines their physicochemical properties and introduces novel characteristics not exhibited by the diamond nanostructures alone [30], [31], [33], [34].

In this thesis, I focus on the unique properties and capabilities of diamond nanostructures in order to implement them as growth nanotemplates for the development of novel hybrid magnetic nanostructures composed of iron-based metallic compound alloys (as it will be further described) grown on the surfaces of NDs nanotemplates.

1.3 Advanced Magnetic Nanomaterials based on binary Iron-alloys

1.3.1 Introduction

Iron-based bimetallic compounds are important magnetic materials exhibiting robust magnetic characteristics that make them ideal for a wide range of applications. From advanced magnetic storage devices and transformers to biomedical technologies like magnetic resonance imaging (MRI) and targeted drug delivery [106], iron-based metallic compounds are becoming indispensable. Their versatility and adaptability also make them highly attractive for emerging scientific and technological fields such as spintronics and energy harvesting technologies [107].

In this context, selecting an appropriate iron-based bimetallic alloy to be combined with a promising growth platform like the nanodiamonds is an important strategic issue for the development of such new nanohybrid magnetic materials. One criterion for this selection is related to the specific magnetic properties these materials already hold, as well as the prospects of enhancing these properties, which combined with NDs' properties can ultimately pave the way for the exploration of their novel physical and chemical properties and the exploitation of such NHDs in numerous scientific and technological related fields and applications.

In this thesis, within the category of iron-based magnetic nanoalloys, I concentrate my focus into the combination of the iron-rhodium (Fe-Rh), iron-cobalt (Fe-Co) and iron-nickel (Fe-Ni) bimetallic compound nanoalloys, respectively, with the NDs growth nanotemplates. This dissertation specifically emphasizes the development of high-purity bcc and fcc nanocrystallites in the Fe-Co and Fe-Ni systems, targeting nearly equiatomic stoichiometry to achieve well-ordered nanostructures. It also investigates the formation of tetragonally distorted structures within these systems to enhance magnetic properties while retaining their nanoscale features. For the Fe-Rh system, the focus was on synthesizing high-purity nanocrystallites of the well-ordered bcc-B2 crystal phase, which exhibits metamagnetic properties at compositions approaching equiatomic ratios.

1.3.2 The Iron-Rhodium (Fe-Rh) bimetallic compound system

Among the transition-metal binary alloys based on iron with significant magnetic properties utilized in many technological applications [108], the Fe-Rh system has attracted renewed interest due to its unique characteristics. In 1938, Fallot et al. discovered that the Fe-Rh bimetallic compound with an equiatomic composition could increase its magnetization values with rising temperature, up to a critical transition temperature that varies with compositional changes [109]. Since then, it has been established that this magnetic change is accompanied by a temperature hysteresis, suggesting a first-order isostructural transition from an antiferromagnetic (CsCl-type AFM B2 α' phase) to a ferromagnetic (CsCl-type FM B2 α phase) state upon annealing in alloys containing compositions approximately between 48-to-52 at. % Rh (Figure 1.5) [110], [111], [112], [113], [114], [115]. Moreover, this magnetic transition is accompanied by a volume expansion of about 1% [116]. Nonetheless, in the near-equiatomic stoichiometries, the bulk Fe-Rh system can also be found in a disordered γ fcc structure, which exhibits paramagnetic (PM) characteristics at room temperature (RT).

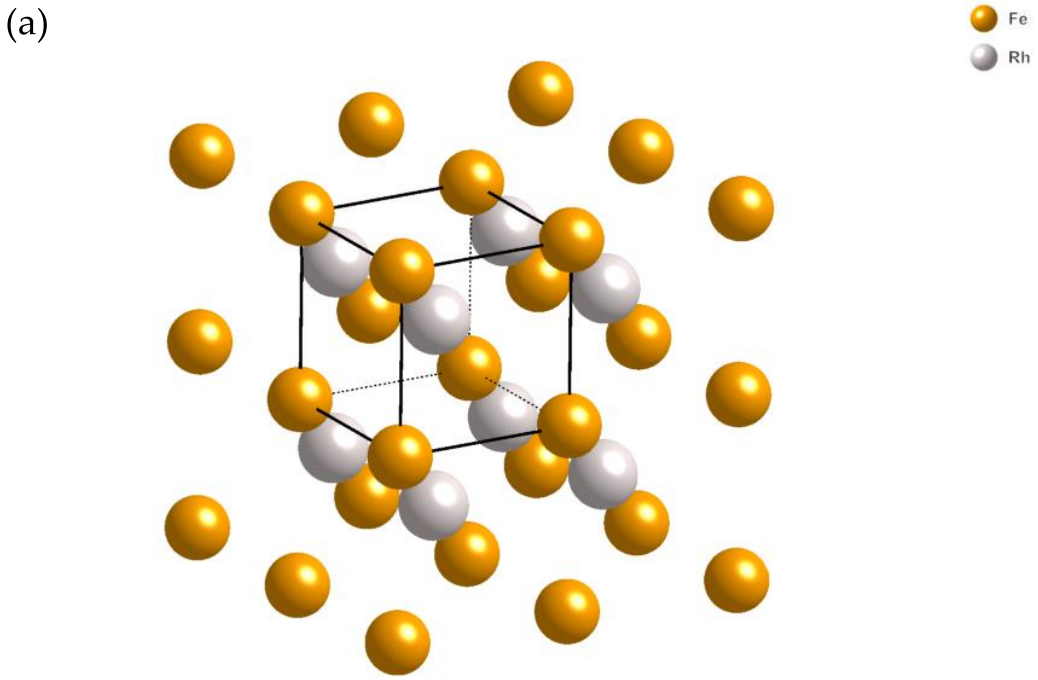

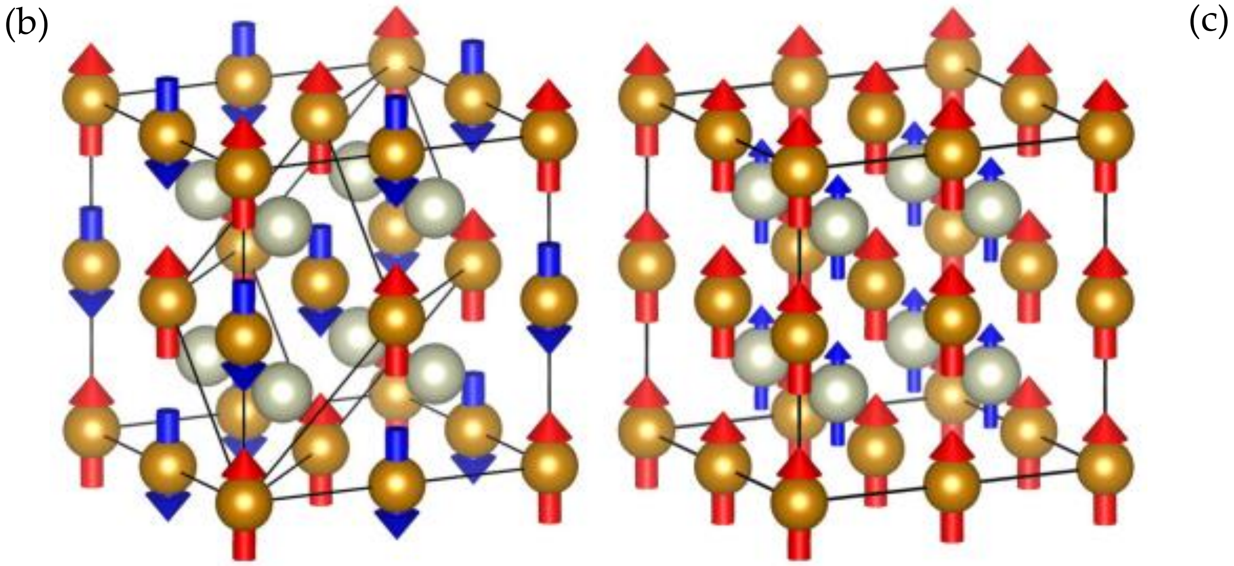

Figure 1.5 (a) Crystal structure of B2 bcc CsCl-type FeRh where iron atoms are represented in gold and rhodium is silver color. (b) B2 AFM α' phase of the FeRh structure showing also the magnetic moment configuration, where iron atoms are in the [111] lattice planes and possess antiferromagnetic alternating sip-up (red) and spin-down (blue) moments. (c) B2 FM α' phase of the FeRh structure, where also the rhodium atoms possess magnetic moments, shown with blue colored arrows with less intensity than the iron atoms which are shown with red arrows; all moments are aligned ferromagnetically [117].

Since then, many researchers have given considerable efforts to understand this intriguing magnetic behavior, both experimentally and theoretically [110], [114], [115], [118], [119]. These studies demonstrated that in the bulk Fe-Rh alloy system, the CsCl-type phase is retained below a critical temperature $T_{transition}$, and as the temperature increases, the first-order transition is accompanied by a rapid and uniform expansion of the ordered cubic structure of about 1% in volume change. This first-order transition in ordered $Fe_{50}Rh_{50}$ alloys corresponds to an antiferromagnetic-ferromagnetic (AFM-to-FM) transformation at $T_{AFM\text{-}to\text{-}FM}$ of approximately 80 °C (~ 353 K).

Studies made by J.S. Kouvel et al. revealed that $Fe_{48}Rh_{52}$ ingots and fillings, prepared by induction-melting at 950°C for 24 hours and cooled slowly at RT, exhibited a highly ordered B2 CsCl-type structure (a = 2.99 Å) along with residues of an fcc phase (a = 3.74 Å). Magnetization measurements showed a remarkably sharp transition during tempering at 77 °C (350 K) with significant temperature hysteresis. In the temperature range of 77 K to 350 K (below this transition), the magnetization increased very slowly and linearly with the applied field. However, above the transition temperature, the magnetization increased rapidly, attaining a near-saturated value, with the bulk saturation magnetization (Ms) being 130 emu/g, which decreased with increasing temperature in a manner characteristic of a typical ferromagnet, and a Curie point (Tc) of about 675 K (or 402 °C). It has been noted that external magnetic fields and pressures can alter this transition temperature ($T_{AFM\text{-}to\text{-}FM}$) [115].

Hofer et al. conducted another significant study on the magnetic properties of Fe-Rh alloys with 50 to 64 at. % Rh content. Their samples, $Fe_{100-x}Rh_x$ ingots, were prepared by induction-melting at 1600 °C followed by heat treatment at 1000 °C for 50 hours, and then cooled slowly to RT to obtain the desired AFM α'-phase free from residual stresses and strains. In the 51 to 61 at. % Rh concentration range, the PM Tc remained stable at (367 ± 3) °C, while for compositions with 62 and 63 at. % Rh, this temperature was slightly lower at 344°C. Moreover, increasing Rh content from 51 to 63 at. % led to the rising of the average transition temperature values, $T_{AFM\text{-}to\text{-}FM}$, from 26 to 78 °C, accompanied by increasing thermal hysteresis. In contrast, the $Fe_{36}Rh_{64}$ alloy was found to be completely paramagnetic. Subsequent XRD measurements in these alloys indicated the presence of a fully ordered AFM CsCl-type α' phase (a = 2.986 Å) and a PM fcc γ phase (a = 3.764 Å), while in the alloy containing 64 at. % Rh, only the γ phase was observed, indicating the absence of any α' phase.

It is concluded that the consistency of the lattice parameters of both α' bcc (AFM) and γ fcc PM phases in the alloys, regardless of atomic composition, suggests a subsequent stability of the individual compositions of these two alloys, and that it is the relative amount of the two phases that is varying with composition. This is confirmed by the consistency of the values of Tc. On the other hand, the variation in $T_{AFM\text{-}to\text{-}FM}$ and the existence of thermal hysteresis at high Rh concentrations may be attributed to inhomogeneous strains in the α'phase's grains due to the increasing amounts of the γ phase in them, which could delay the AFM-to-FM transition, in the sense of the increase of $T_{AFM\text{-}to\text{-}FM}$ values [111].

Another significant study on the effects of mechanical and thermal treatment on the structure and the magnetic transition in Fe-Rh alloys was conducted by J.M. Lommel et al. In their work they focused on the effect of sample dimensions on the first-order transition by preparing $Fe_{49}Rh_{51}$ fillings, which were vacuum annealed at 975 °C for 48 hours and quenched at RT. XRD measurements showed that the Fe-Rh fillings exhibited a disordered fcc structure with a = 3.736 Å [112]. Generally, plastic deformation induced during quenching can lead to the conversion of the normal CsCl-type phase to a disordered fcc phase, which is weakly magnetic and does not exhibit the first-order transition. Magnetic measurements indicated that between 78-to-500 K, the magnetization was nearly temperature-independent, and there was no evidence of the first-order transition near 26 to 78 °C [111]. However, at 510 K (237 °C), a rapid increase in magnetization occurred, and further heating to 700 K (427 °C) showed normal Tc behavior typical of a FM material. Subsequent cooling led to the appearance of stable first-order transition characteristics upon repeated temperature cycling.

This result prompted an investigation into the kinetics of the transformation from the fcc phase to the CsCl-type phase, by measuring the Ms as a function of time at 510 K. XRD patterns of the fcc $Fe_{49}Rh_{51}$ alloy undergoing the annealing cycle at 510 K for 10 minutes showed a gradual reduction of the fcc phase and the emergence of a highly ordered CsCl-type structure. Additionally, X-ray results showed a complete formation of the CsCl-type phase at the expense of the fcc phase after an annealing cycle of 1 hour. After 40 hours of annealing, the transition was incomplete, with large magnetization values even at 78 K, and broad and hysteretic tendencies. Extended annealing times (approximately 1300 hours) resulted in a more complete, sharper and less hysteretic transition. However, the first-order transition remained incomplete compared to bulk material, indicating that imperfections in the long-range order and/or defects induced by plastic deformation significantly affect the magnetic transition.

Sputter-deposited Fe-Rh thin films exhibit similar magnetic behavior. Y. Ohtani et al. investigated the magnetic and microstructural properties of sputter-deposited $Fe_{100-x}Rh_x$ alloy thin films. For their experiments, thin films of $Fe_{100-x}Rh_x$ ($28 < x < 57$ at. % Rh) and 200 nm thickness were deposited on glass substrates at 100 °C (as-sputtered films), which were then annealed at 300 °C and 600 °C for 4 hours [120]. XRD results, compared with magnetic measurements, indicated that the as-sputtered films transform from an FM bcc phase to a PM fcc phase at a Rh concentration of 35 at. %, highlighting the difficulty in obtaining a CsCl-type ordered equiatomic FeRh thin film directly. The literature reports that the fcc single phase is obtained by rapid quenching from the liquid state in the Rh content range of 30 at. % to 90 at. % [111], [112], [120], [121], [122], [123].

After annealing at 600 °C for 4 hours, the formation of bcc CsCl-type diffraction peaks were clearly observed in $Fe_{55}Rh_{45}$, $Fe_{52}Rh_{48}$ and $Fe_{46}Rh_{54}$ films, while an fcc diffraction peak attributed to the γ phase was observed only for films with Rh content greater than 50 at. %. Magnetic measurements of the annealed films showed a continuous decrease in Ms values as the Rh content increased from 30 to 57 at. %. This continuous change contrasts sharply with the abrupt drop observed in bulk FeRh at 50 at. % Rh. Moreover, the three thin films displayed a broad transition with large thermal hysteresis and a remaining FM behavior typical of a FM phase even below $T_{AFM\text{-to-}FM}$. This broad transition feature in thin films is continuous throughout the stoichiometric FeRh composition and agrees with similar characteristics observed in smaller-than-bulk samples reported in the literature [111].

Additionally, Ohtani et al. demonstrated that the AFM-to-FM transition occurs over a broader composition range in thin films compared to bulk materials. This finding highlights the significant impact of intrinsic structural features on the compositional distribution and magnetic properties of thin films. To gain deeper insights, the microstructure of the films was analyzed in detail using Mössbauer spectroscopy. The spectra of the three annealed films revealed the presence of two ferro/ferrimagnetic components: a dominant component associated with Fe sites in the perfectly ordered CsCl phase and a secondary component linked to Fe anti-site configurations. In the $Fe_{52}Rh_{48}$ and $Fe_{46}Rh_{54}$ films, these magnetic components were accompanied by two additional nonmagnetic components, identified as the fcc phase. Notably, the concentration of the fcc phase, reflected by its absorption area, increased with higher Rh content, corresponding to a reduction in the ferro/ferrimagnetic components.

Thus, it is evident that compositional inhomogeneity is retained in sputter-deposited and nearly equiatomic FeRh thin films. This inhomogeneity is responsible for the existence of many defects and anti-phase regions across the grain boundaries of the main CsCl-type structure, significantly destabilizing the AFM-to-FM transition.

Considering that the well-studied Fe-Rh system exhibits rather interesting magnetic properties, one would expect an established phase diagram to describe the unique microstructure of this system (Figure 1.6). However, this is not the case, and only portions of a rather tentative diagram have been developed [124], [125], [126], [127], [128]. Moreover, these investigations indicate the existence of miscible regions of the α' and γ phases extending between 20 to 64 at. % Rh concentration at low temperatures in many non-bulk form cases.

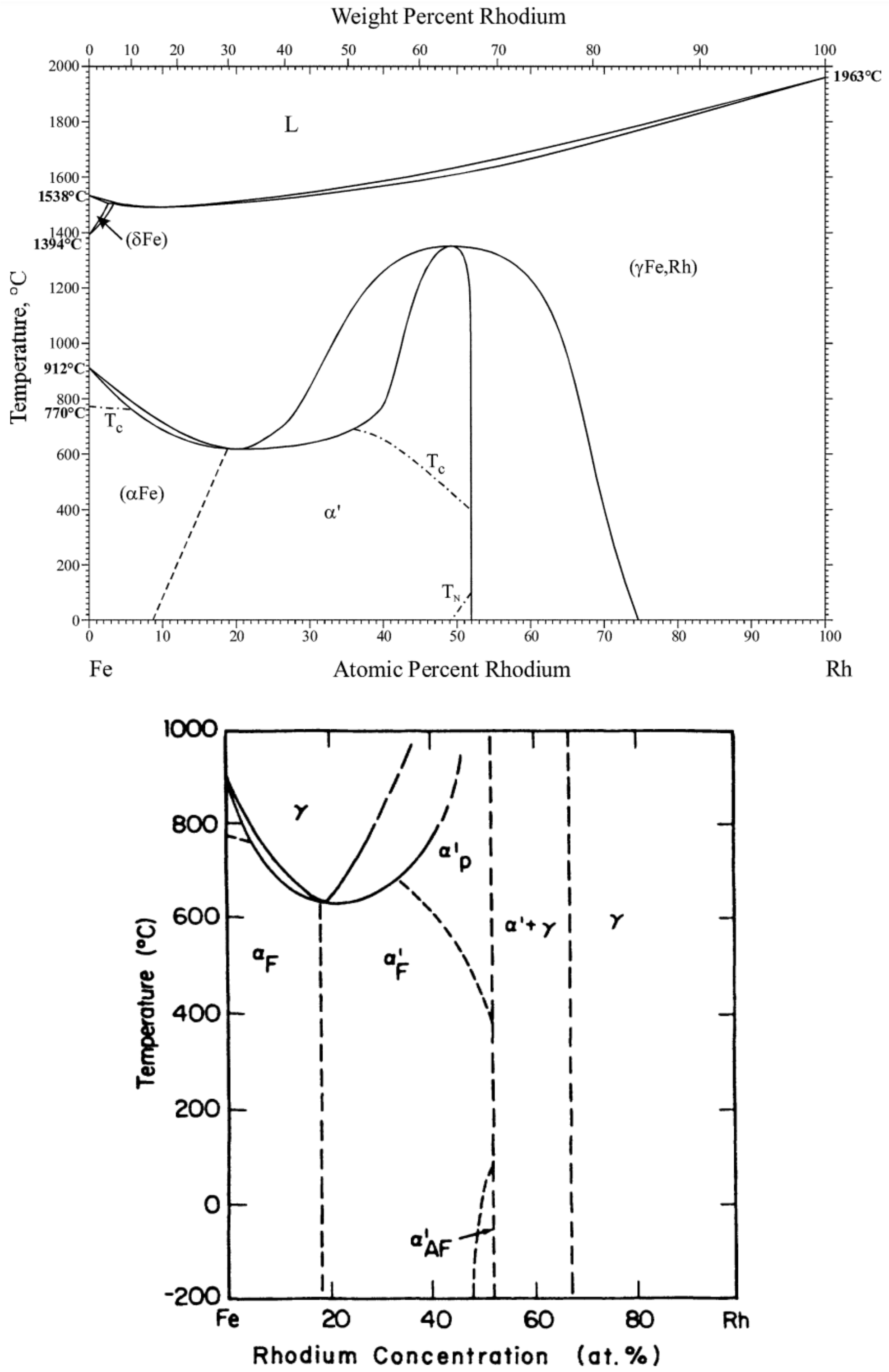

Figure 1.6 Approximate phase diagrams of the Fe-Rh system [126] (top), [128] (bottom).

For non-bulk Fe-Rh alloys, it is crucial to carry out synthetic procedures that minimize the formation of the γ phase, which is known to significantly influence the sample's magnetic properties. Moreover, over the past decades, several studies have highlighted the difficulty of achieving a stable critical temperature point in nanostructured Fe-Rh, as the preparation of such Fe-Rh samples is influenced by factors such as particle morphology, phase composition, heat treatment, presence of external magnetic fields and pressure [116], [120], [121], [129]. Various strategies have been implemented to achieve the desired magnetically ordered B2-bcc phase through different physical and chemical routes, involving bulk, nanoparticle or thin film forms. In most cases, this has led to the additional presence of non-magnetic γ-fcc residues.

This γ-fcc variant form in such Fe-Rh systems is known to possess PM characteristics at RT. As the temperature drops below the magnetic critical-freezing transition temperature (T_f) of about 80 K for this phase, it exhibits a magnetically spin-glass (SG) behavior [122], [123], [124]. For fcc Fe-Rh NPs, the disordered atomic nature of the fcc structure coincides with a random orientation of uncompensated moments of the nanostructured grains. At low temperatures, below the T_f range, the exchange interaction width exceeds the domain size of the fcc Fe-Rh NPs, causing the magnetic moments to freeze in cluster-glass arrangements. In this temperature range, the sample magnetizes collectively, resulting in low susceptibility. As the temperature increases, the exchange interaction weakens, which is indicative of the weaker exchange coupling of atoms at the grain boundaries or interfaces of the NPs. When the grains of the NPs become uncoupled, a peak in the susceptibility value is observed. Therefore, the decoupling between the grains at the interface results in the conversion between the static magnetic arrangement and the PM or superparamagnetic (SPM) state [122], [130].

Furthermore, the stabilization of the Fe-Rh FM phase at RT and below is of great interest [131]. Since nanosized crystals could exhibit significant deviations in interatomic distances and unit-cell distortions compared to bulk materials [132], achieving this stabilization could combine the significant magnetic characteristics of bulk structures with the unique structural and magnetic properties of equivalent nanophases. This could enable the exploitation of these nanostructures in a vast field of new and emerging technological applications. To date, Fe-Rh systems have been proposed as materials for uses in thermally assisted magnetic recording [133], [134], storage media applications [135], thin films for antiferromagnetic spintronics [117], [136], novel applications in medicine like magnetic hyperthermia [137], [138] and as magnetocaloric materials for switchable high contrast ratio MRI labels [106], as well as RT AFM memory resistors [139] and high magnetostrictive applications [140], [141].

1.3.3 The Iron-Cobalt (Fe-Co) bimetallic compound system

A significant type of magnetic nanoparticle (MNP) system, which is considered an essential component for applications targeting specific magnetic properties is based on the iron-cobalt (Fe-Co) bimetallic compound, which stands out as a competitive option due to its soft magnetic characteristics. Bulk Fe-Co alloys are known to form solid bcc bimetallic compounds (Fe_xCo_{100-x}) over a wide temperature range. Specifically, Fe-Co alloys with a cobalt concentration of 30 to 70 at. % Co exhibit a chemically ordered B2 (CsCl-type) body-centered cubic (bcc α-phase) crystal structure over a broad temperature range. This phase undergoes an order-disorder (O-D) phase transformation to a chemically disorder A2 bcc phase, where the iron and cobalt atoms occupy randomly the atomic positions (Figure 1.7) [142], [143].

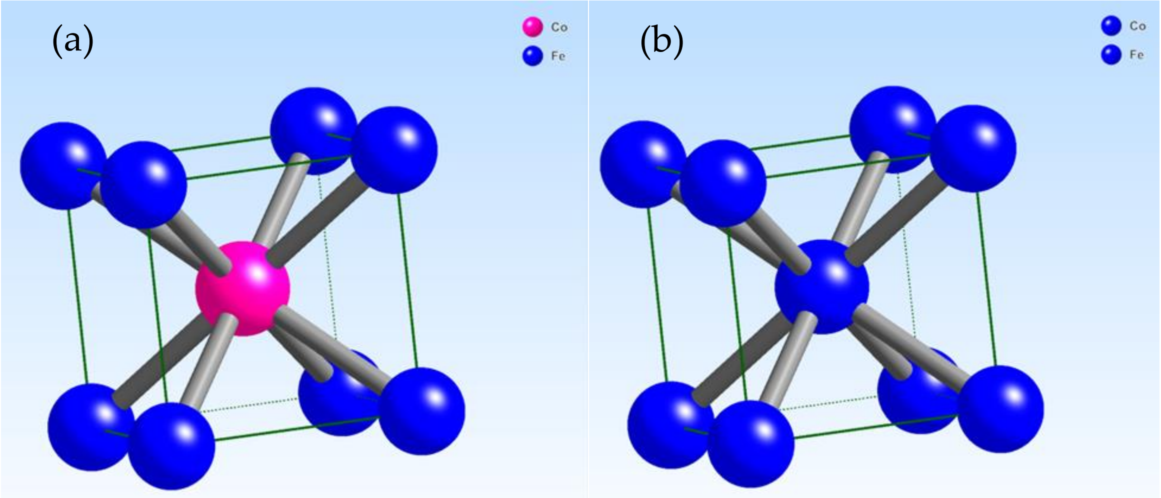

Figure 1.7 Typical crystal structures of the ordered B2-bcc Fe-Co alloy (a) and of the disordered A2-bcc Fe-Co alloy (b).

More specifically, in a nearly equiatomic Fe-Co alloy the O-D transition occurs at 730 °C and is accompanied by a magnetic-to-nonmagnetic α (bcc)-to-γ (face-centered cubic fcc) transition at approximately 965 °C (Figure 1.8) [144], [145], [146]. Both the O-D and the α-to-γ transitions depend on the cobalt concentration.

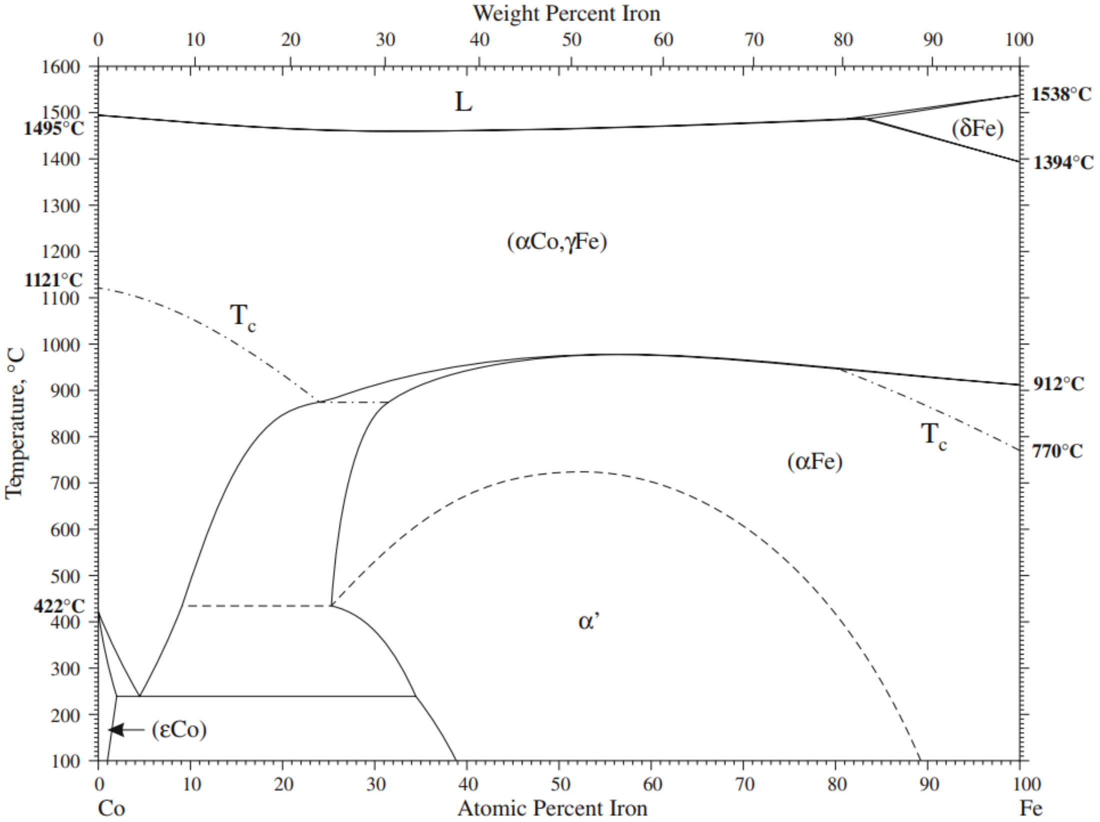

Figure 1.8 Typical Fe-Co phase diagram [147].

The ordered FM B2-type Fe-Co alloys present significant combination of high M_S, reaching up to 240 emu/g in the bulk form when the cobalt content reaches approximately 30 at. %, with low coercivity (H_C) values in the range of 10-65 Oe. They also exhibit high Tc of up to 1500 K, a low uniaxial magnetic anisotropy constant K_u of about 2×10^4 J/m^3, and large permeability, depending on their composition [142], [148], [149], [150], [151], [152]. These excellent soft magnetic compounds have attracted significant interest for various soft magnetic materials applications. Specifically, Fe-Co alloys have been proposed for use in catalysis [37], electromagnetic wave absorption [153], spintronic devices [154], enhanced-permeability-dielectrics for reducing switching field in arrays of single-layer magnetoresistive-random-access-memory bits [155], heat-assisted magnetic recording for achieving greater storage density in hard disk drives [156], magnetic bearing and turbine engine components [143], building blocks for nanostructured thin films or bulk magnetic materials [151], magnetic particle imaging [157], and as magnetic carriers for drug targeting, cancer therapy, and hyperthermia [38], [158].

Various techniques are available to synthesize such MNPs, including mechanical alloying [149], impregnation followed by subsequent heat and chemical treatments [38], one-pot polyol pathway based on the addition of precursors at elevated temperatures [142], pulsed-laser ablation combined with inert gas condensation [159], carbothermal reduction via impregnated chitosan beads with Fe and Co ions [160], high-throughput magnetron sputtering [155], ethanol dehydrogenation through chemical vapor deposition [37], high-throughput thermal plasma synthesis [161], pulsed-laser deposition for thin films growth [154], hydrothermal [39] and microemulsion methods [162]. In all synthesis methods it is crucial to choose the appropriate approach that leads to the desired morphology, arrangement, size, and long-term stability of the MNPs for their intended application.

As mentioned before, typical cubic Fe-Co alloys possess soft magnetic characteristics and exhibit low K_u values. These properties render them unsuitable for applications as hard magnetic materials. However, if K_u could be increased considerably to sufficiently high values, the Fe-Co alloys could potentially become paradigms of non-rare-earth hard metal ferromagnets. Indeed, recent first-principles calculations have predicted high K_u values exceeding 10^6 J/m^3 for the Fe-Co alloys with the body-centered tetragonal (bct) crystal structure. The bct crystal lattice is considered an intermediate metastable lattice between the bcc and the fcc crystal lattices into which Fe-Co alloys can crystallize [163], [164], [165]. This bcc-bct-fcc transformation is known as the Bain transformation.

In real samples, two known synthetic methods can be employed to stabilize the bct Fe-Co structure, a phase not explicitly evident in the equilibrium phase diagram of the Fe-Co system [166]. As proposed by T. Hasegawa's group, this can be achieved either by applying uniaxial stress to the Fe-Co cubic lattices through epitaxial effects or by introducing a third element such as boron (B), nitrogen (N), or carbon (C) interstitially into the Fe-Co cubic structure [167], [168], [169].

Epitaxially grown pure Fe-Co thin films on various buffer layers have shown K_u magnitudes up to 10^6 J/m^3 when their crystal lattice constants c to a ratio (c/a) is slightly above 1.0 ($1.0 < c/a < 1.2$), and the Co concentration is about 50-60 at % [164], [170], [171]. However, structural relaxation in epitaxially grown Fe-Co thin films limits the occurrence of bct structures with c/a ratio of about 1.2 to film thicknesses below approximately 1-3 nm [172]. Another crucial consideration is the chemical ordering of Fe and Co atoms in the crystal structure of the Fe-Co alloys, given by the ordering parameter S. To achieve high K_u values in the Fe-Co compounds, S is required to be high ($S > 0.8$) [164].

Alternatively, adding a specific third element such as B, C, or N, is expected to induce a tetragonal distortion in the Fe-Co cubic lattice. Computational studies by D. Odkhuu et al. on Fe-Co alloys have predicted an induced tetragonal distortion of Fe-Co structures through interstitial N doping, leading to a considerable K_u value of 2×10^6 J/m^3 [25] in the B2-ordered tetragonal Fe-Co alloy [165]. This is achieved by the phase transition from ordered Fe-Co CsCl-type B2-bcc to bct upon a small addition of N, which tends to transform to an fcc phase at higher levels of N doping. Notably, based on their studies, T. Hasegawa's group has experimentally achieved the stabilization of a bct Fe-Co phase at the boundaries between ordered B2 bcc and disordered fcc phases with increasing content of a third doped element (V and N). In their work, the formation of the bct-like Fe-Co phase is inferred from the effect of the c/a ratio on K_u, when the c/a ratio ranges between 1.05 and 1.30, at 1.0 up to 5.5 at. % concentration of the third element [168]. These findings were later confirmed by TEM-based observations, showing the formation of a bct-FeCo:VN single crystallite with a lattice constant c/a ratio of about 1.07 and a lattice fringe [167]. The atomic configuration of the Fe-Co-V-N unit cell corresponds to that of the B2-type Fe-Co.

Regarding tetragonally distorted iron alloy phases, the Fe-based alloy martensites are another significant class of materials with excellent mechanical and magnetic properties. These materials emerge from the austenite-to-martensite transformation, a diffusionless rearrangement of the atoms contained in the original fcc crystal lattice into the bcc crystal lattice, triggered by a homogeneous structural deformation, e.g., the Bain or Kurdyumov γ-to-α transformation [173], [174]. Many investigations have demonstrated that the tetragonal symmetry of the martensite phase results from the preferential occupation of a third element like N and C in one of the three (x-, y-, z-) available octahedrally coordinated interstitial site sublattices (Figure 1.9).

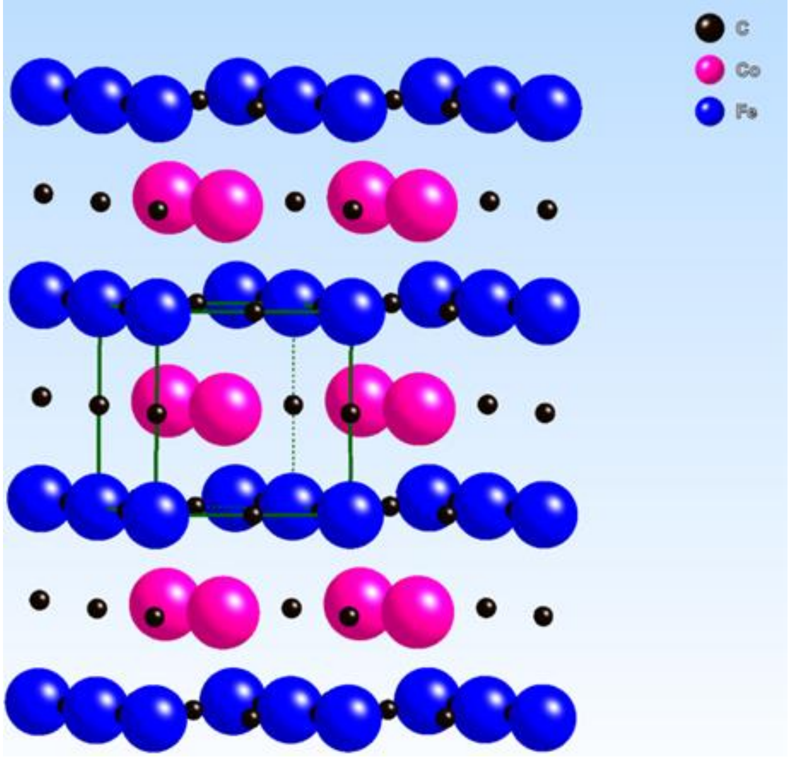

Figure 1.9 Schematic presentation of the crystal structure of the ordered B2-type FeCo phase, with carbon atoms (black spheres) in the octahedral interstitial sites.

In the case of carbon, this preferential occupancy arises from its higher solubility (up to about 9 at. % concentration) in the fcc austenitic (γ) Fe-based phase, compared to the bcc ferritic (α) Fe-based phase (up to about 1 at. % concentration). The formation of martensite occurs as the crystal structure undergoes the γ-to-α transformation over a limited range of thermal treatments (slow or rapid cooling, aging, or tempering). When the transformation happens too quickly for the carbon atoms to be able to diffuse forming either graphite or iron carbide (Fe_3C), the C atoms are trapped in the octahedral interstitial sites [175], [176], [177], [178].

Efforts to adequately describe the primary transition and subsequent martensite phase formation often involve complicated crystallographic mechanisms, which deviate from the primary purposes of this study. However, ^{57}Fe Mössbauer spectroscopy, as an atomic-level-probing characterization technique, is considered more proficient in elucidating these mechanisms. This technique has been used extensively to investigate the specific electronic and magnetic modifications imposed on the Fe-sites by the carbon interstitials, which depend on the proximity of iron atoms to the carbon interstitials and the specific local structures. The literature suggests that the presence of carbon at the octahedral interstitial sites in the initial austenite structure significantly determines the aspect ratio (c/a) of the final bct martensite lattice and its tetragonality yield, independent of the presence of other alloying elements [175], [179].

Regarding the two combined nanomaterial types in this study, namely NDs and Fe-Co alloy NPs, many researchers have conducted studies that deal with the synthesis, characterization, and applications of such nanomaterials. These studies often use different nanocarbon allotropes in core/shell models [37], [38], [172], as thin film substrates [159], or as interstitial dopants [40], [41], [179], [180].

1.3.4 The Iron-Nickel (Fe-Ni) bimetallic compound system

Within the scope of discovering new technologies and materials for humanity's ever-increasing needs and demands, a significant type of compound is the bimetallic iron-nickel (Fe-Ni) system. The Fe-Ni alloy system stands out as a prime example of human ingenuity, presenting lately renewed interest due to its potential to enhance its properties and versatility through interventions in its crystal structure, as well as to serve as component in metal compound hybrids.

Charles Edouard Guillaume was the first scientist to systematically develop and study the properties of Fe-Ni alloys, and he received the Nobel Prize in Physics for his discovery of the Invar alloy. This iron-nickel alloy, containing 36% at. Ni, exhibits an extremely low thermal expansion coefficient over a wide range of temperatures around ambient temperature. The discovery of Invar led to numerous technological advancements, including the manufacturing of thermostats and precision instruments. Invar alloy is utilized in electronics, circuit breakers, motor controls, temperature-compensating springs, and more. Its thermal properties also make it suitable for use in glass-metal and ceramic-metal joints. Advanced applications further utilize Fe-Ni Invar alloy in the aerospace industry and in precision laser optical measuring systems [181].

In addition to the interesting and widely exploited thermal properties of Fe-Ni Invar alloy, this system has garnered immense interest for its magnetic properties over the last decades.

The equilibrium Fe-Ni phase diagram generally exhibits two major phases, α and γ, and a two-phase $\alpha+\gamma$ region. The α phase refers to a bcc ordered crystal structure, called Kamacite, which does not accept more than 5 to 7 at. % Ni concentration. The γ phase refers to a fcc disordered crystal phase, called Taenite, which occurs in a wide range of Ni concentrations and extends at high temperatures above 400°C. Kamacite exhibits soft FM characteristics, while Taenite, due to its disordered crystal nature, presents PM order at high temperatures. However, the high-temperature PM γ-phase decomposes into two disordered phases as the temperature decreases. One is the PM fcc disordered γ_1-phase with low Ni concentration up to 28 at. % Ni, named Anti-taenite [182]. The other is a FM fcc disordered γ_2-phase with high Ni concentration from 45 up to 70 at. % Ni, called high-Ni taenite, which is encountered across the phase diagram above 330 °C [183]. Studies on the Fe-Ni phase diagram below 400 °C demonstrate an extensive asymmetrical miscibility gap associated with magnetically induced spinodal decomposition for alloys containing 28-to-45 at. % Ni [184], [185], [186]. Moreover, between the metastable phase boundaries of low Ni compositions (7-to-27 at. % Ni), martensitic transformations are also observed (Figure 1.10) [187].

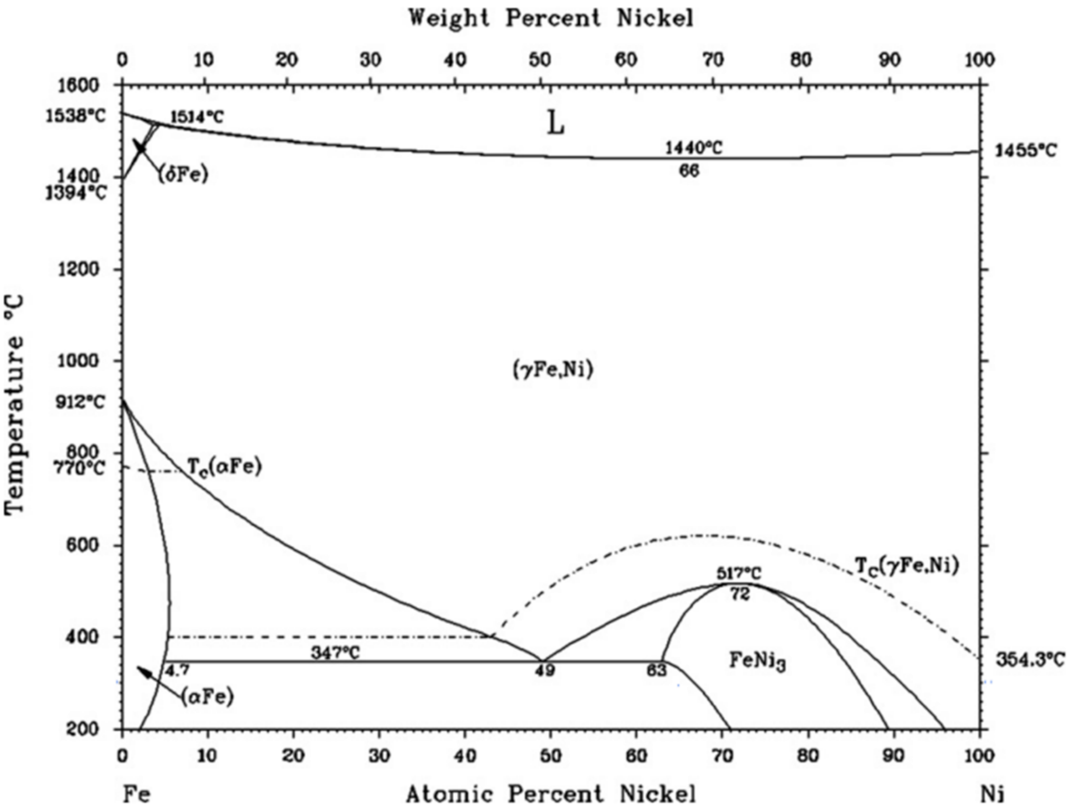

Figure 1.10 The Fe-Ni phase diagram [188].

For a considerable time, the phase transformations of the Fe-Ni system at low temperatures were shrouded in ambiguity, rendering this phase diagram complex and not well understood. Another significant challenge in studying these alloys was the slow diffusion rates of the Fe-Ni system at such low temperatures. R.B. Scorzelli et al. and many other groups have reported that as cooling occurs, the diffusion coefficient of Ni decreases from 1.5×10^{-16} $cm^2{\cdot}s^{-1}$ at 600 °C to 1×10^{-21} $cm^2{\cdot}s^{-1}$ at 500°C. Remarkably, at 300°C, it would take more than 10^4 years for one atomic jump to occur [184], [189], [190], [191].

For that reason, many scientists were called upon to shed light on and to resolve the low-temperature phase transformations of the Fe-Ni system. In 1962, P.J. Pauvele et al. demonstrated for the first time, by conducting neutron irradiation experiments in the presence of a magnetic field on equiatomic Fe-Ni alloys, a new order-disorder transition to an ordered crystal phase of the AuCu-type at 320 °C (Figure 1.11) [192].

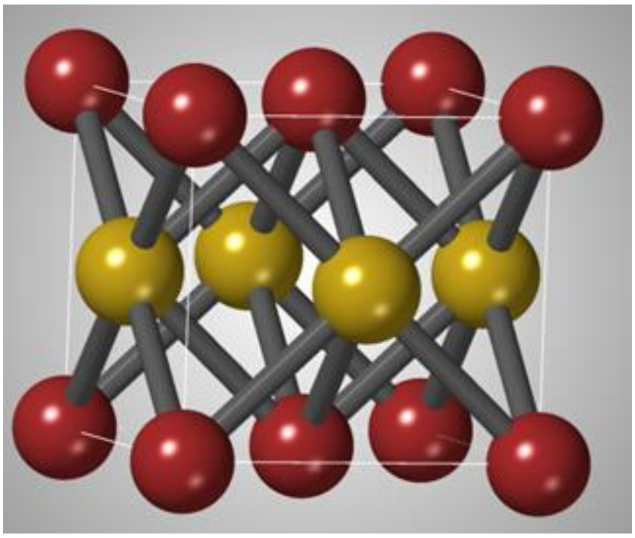

Figure 1.11 Crystal structure of the chemically ordered AuCu-type FeNi γ''-phase, iron atoms are illustrated by the red colored spheres and the nickel atoms by the dark yellow spheres.

This chemically ordered FeNi γ''-phase, called Tetrataenite or $L1_0$, exhibits a tetragonal structure with a lattice constant α= 3.582 Å and c/a ratio very close to 1. Magnetic studies have revealed that the tetragonal $L1_0$ FeNi phase is a promising hard magnet, offering a large uniaxial magnetic anisotropy constant, $K_u \sim 2.1 \times 10^6$ J/m^3, and a high Curie temperature ($T_C \sim 550$ °C) [193].

Such a significant discovery led to the study of the ordered FeNi alloy with the $L1_0$ structure by several groups [187], [192], highlighting neutron irradiation as a non-conventional method enhancing diffusion in sluggish systems at low temperatures.

It is generally accepted that both diffusion effects and fast particle irradiation are closely connected. In particular, as an excess number of defects can be produced by irradiation, defects tend to maintain a steady concentration during irradiation at elevated temperatures. This steady-state concentration of excess defects is directly related to atomic diffusion, and therefore, regulating particle irradiation can subsequently improve the diffusion rate in samples such as Fe-Ni alloys [194].

Despite the extensive studies of the ordered $L1_0$ FeNi phase at that time, there were still unanswered questions concerning the characteristics of the phases cohabiting in the renewed Fe-Ni phase diagram. However, answers were more likely emerged from an unexpected source, literally falling from the sky, as they came in the form of meteorites, providing tons of insightful information regarding this challenging system.

Iron meteorites are interesting natural systems composed of Fe-Ni alloys that have cooled at a rate of about 1-10 °C per 10^6 years [187]. This unique cooling rate provides an opportunity to thoroughly study Fe-Ni alloys in thermodynamic equilibrium, compared to alloys prepared in the laboratory. Therefore, iron meteorites have played a significant role in the study of the Fe-Ni phase diagram.

Most meteorites are composed mainly of two phases: one corresponding to Kamacite with an ordered bcc structure (α-phase) and one corresponding to Taenite with a disordered fcc structure (γ-phase).

These two phases possess definite crystallographic orientations relative to each other, forming a pattern called Widmannstätten. This pattern can be arranged with unchanged orientations throughout the entire meteorite, showing that originally the meteorite, in a higher temperature state, was a single fcc crystal. However, the very slow cooling process allowed plates of Kamacite to precipitate along the appropriate planes of the fcc crystal. Subsequent growth of the Kamacite regions led the meteorite to be composed of alternating and/or intersecting regions of Kamacite and Taenite of the original fcc crystal [185].

Many investigations have pointed out that meteoritic Taenite, generally occurring as thin plates called lamellae, decomposes into an ordered FM equiatomic FeNi phase (Tetrataenite) with the $L1_0$ superstructure (γ''-phase) and a disordered PM fcc Ni-poor γ_1-phase Fe-Ni alloy (Anti-taenite). Structural studies show that both FM γ'' and PM γ_1 phases have the same lattice constants, about 3.582 Å, forming together a pseudo-monocrystal whose axes are those of the original high-temperature fcc crystal, as mentioned above.

Many studies on meteoritic samples have shown that Kamacite consists of up to 8 at. % Ni concentration and is well defined in the Fe-Ni phase diagram. These studies also indicate instabilities regarding Taenite lamellae, which present steep nickel concentration gradients near the interface between Kamacite and Taenite. Moving inwards from this interface into Taenite, a wide layer containing 40-50 at. % Ni is encountered. This surface layer of the lamellae is composed mainly of the ordered $L1_0$ FeNi phase. Deeper in the lamellae follows a dark-etching layer containing about 28-45 at. % Ni. This layer consists of fine domains of the ordered FeNi phase and a PM disordered γ_1-alloy with less than 28 at. % Ni in between, rather than an fcc Fe-Ni alloy with continuously varying composition.

The observation of a monomineralic layer of Tetrataenite and of Anti-taenite/Tetrataenite intergrowths indicates that the stability range of Tetrataenite at the equilibration temperature (320 °C) is between 46 to 53 at. %Ni. Furthermore, bulk fcc Fe-Ni alloys with less than about 28 at. % Ni transform by a diffusion-less process to another metastable state called Martensite (α_2-phase). Nonetheless, well-distributed small crystallites of disordered γ_1-phase Fe-Ni alloy (with less than 28 at. % Ni) are known to be unstable towards martensitic transformation at RT and below. This instability is likely due to the intimate intergrowth of the γ_1-phase with the ordered $L1_0$ phase on the same Bravais lattice, thereby stabilizing both of them in the fcc structure [185].

Finally, an inner layer found only in thick lamellae is entirely transformed into Martensite (α_2-phase). The occurrence of Martensite in the middle of the lamella is consistent with the decreasing Ni-concentration towards the center of the lamellae, as fcc Fe-Ni alloys with low nickel content are unstable towards martensitic transformations [195]. Moreover, in the center of some thick lamellae, the α_2-phase decomposes into α and γ-phase (Plessite). In contrast, thin lamellae contain no martensitic α_2-phase.

Apart from the ordered FeNi crystal structure, another ordered structure exists in the Fe-Ni alloy system. This intermetallic compound, with a high Ni concentration of about 75 at. % Ni, possesses an ordered soft FM γ'-fcc crystal $L1_2$ structure ($AuCu_3$-type, Pm3m space group) called Awaruite (Figure 1.12) [187], [196].

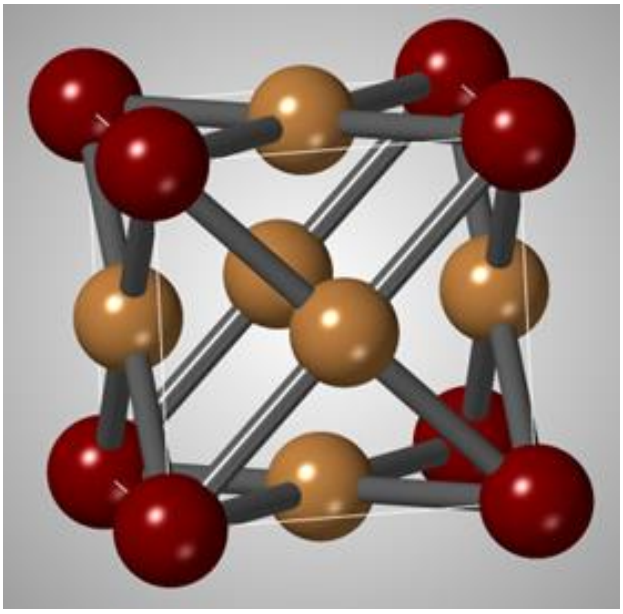

Figure 1.12 Crystal structure of the chemically ordered $AuCu_3$-type $FeNi_3$ γ'-phase, iron atoms are depicted with red spheres and nickel atoms with dark yellow spheres.

Comprehensive studies undertaken on many iron-meteoritic samples have led to a thorough characterization of the Fe-Ni phases observed in the low-temperature phase diagram range and have helped to reveal the elusive and complicated interconnections between them.

Thus, the discovery and interpretation of the ordered $L1_0$ FeNi Tetrataenite, whether by artificial or natural means, has intensified interest in exploiting its unique magnetic properties.

Compared to other metallic minerals, tetragonal $L1_0$ Tetrataenite features very high coercivity (between 1500 and 3000 Oe at RT) and a RT uniaxial magnetic anisotropy constant K_u of about 1.9×10^6 J/m^3 [197], [198], [199], [200], associated with strong perpendicular magnetocrystalline anisotropy. This significant anisotropy energy value is attributed to Tetrataenite's chemically ordered tetragonal crystal structure, positioning γ''-FeNi as a promising permanent magnet candidate with a theoretical maximum energy product of 335 kJ·m^{-3}, roughly 66% of that of NdFeB-based supermagnets [201]. Moreover, many studies based on a wide variety of iron-meteoritic samples report Tetrataenite RT coercivity values in the range of 1100 to 3000 Oe and saturation magnetization values of about 135 to 150 emu/g [198]. Additionally, Tetrataenite presents a high Curie temperature (T_C = 550 °C); however, due to its chemical stabilization at low temperatures, it exhibits a low chemical order-disorder temperature ($T_{O\text{-}D}$ = 320°C). These favorable magnetic properties render Tetrataenite a superior magnetic material free of rare-earth elements. Furthermore, this ideal permanent magnet is comprised of inexpensive, easy-to-process, and readily available elements. These appealing features position Tetrataenite as a feasible and promising permanent magnet candidate with the potential to supplement and/or replace rare-earth permanent magnets for energy transformation and generation. Additionally, this intriguing magnetic material can provide effective magnetic properties, making it suitable for exploitation in electronics, such as in microwave devices and electromagnetic wave-absorbing materials [202], or in medical science applications such as ferrofluids in magnetic hyperthermia [35] and drug delivery [203].

Engineering the fabrication and stabilization of tetragonality and long-range chemical ordering in the chemically disordered fcc parent phase to form Tetrataenite has proven to be very challenging. Since atomic diffusion is extremely slow at the order-disorder temperature point, an inconceivably long amount of time would be required to synthesize $L1_0$-FeNi. Therefore, $L1_0$-FeNi with a significantly high long-range order parameter, S, cannot be derived through the conventional equilibrium process that promotes the formation of $L1_0$ through a mutual diffusion of Fe and Ni, utilizing the stability of $L1_0$-FeNi as the driving force for ordering [197], [198], [201].

As mentioned earlier, to enhance diffusivity towards the γ''-FeNi phase formation, it is necessary to increase the material's defect concentration, which has primarily been managed through neutron irradiation. Considering this, many research groups have tried to implement similar tactics using different synthetic routes. In some cases, the importance of induced tetragonal distortion towards the stabilization of the peculiar tetragonal $L1_0$ FeNi alloy phase is highlighted. This mechanism can be achieved in two ways: by applying uniaxial stress to the parent Fe-Ni lattice through epitaxial effects or by introducing a third element such as boron (B), nitrogen (N), or carbon (C) interstitially into the parent Fe-Ni structure (Figure 1.13) [167], [168].

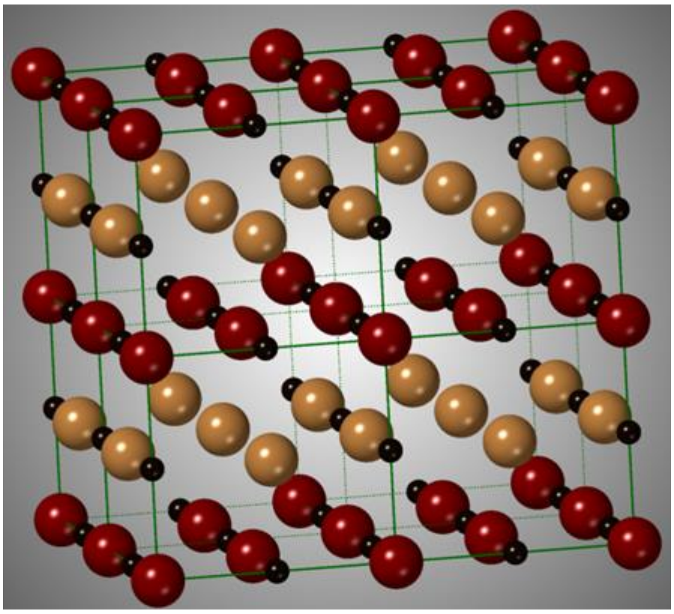

Figure 1.13 Crystal structure of the chemically ordered $L1_0$ FeNi γ''-phase (iron atoms colored red and nickel atoms colored dark yellow), with carbon atoms (black spheres) occupying the octahedral interstitial sites.

Regarding the latter method, Goto et al. proposed an ordered-alloy formation process involving a stable ordered intermediate material. In this method, the ordered configuration of FeNi with nitriding as the trigger is combined with topotactic de-nitriding to extract nitrogen atoms from the FeNi nitrides without damaging the crystal structure. $L1_0$-FeNi fabricated by this method showed a high coercive field (1800 Oe) along with a high K_u value (about 1×10^6 J/m^3), which is directly correlated with the high degree of order (S ~ 0.7) in the material. While this K_u value is less than that of Nd-Fe-B (4.9×10^6 J/m^3), it is still an extremely high value considering that the material is free of rare-earth elements. The proposed method, called nitrogen insertion and topotactic extraction, is demonstrated as an effective alternative for fabricating $L1_0$-FeNi, differentiating from the conventional thermally activated process in that the ordered alloys can be derived directly by de-nitriding [198]. Since that effort, many other studies have followed based on this synthetic process. Recently, F. Takata et al. developed for the first time single-phase tetragonal Fe_2Ni_2N films by molecular beam epitaxy, which, after a subsequent extraction of N atoms, led to the formation of FeNiN films with an $L1_0$ tetragonal crystal structure. This approach, proceeding from the fabrication of high uniaxial magnetic anisotropy $L1_0$ FeNiN epitaxial films followed by a 100 % extraction of N atoms, could advance the development of well-ordered tetragonal FeNi films.

Similarly, M. Gong and S. Ren, reported a rational epitaxial core-shell compound based on the heteroepitaxial growth of AuCu/FeNi nanostructures, which stabilizes tetragonal FeNi nanostructures, revealing enhanced coercivity and anisotropy. The key element for achieving unique magnetic performance (H_C ~ 1010 Oe and M_S ~ 122 emu/g) is the realization of a tetragonal distortion induced by the $L1_0$ phase transformation of the AuCu core. This transformation transfers the necessary strain energy on the epitaxial interface to trigger and stabilize the tetragonal FeNi structures [197].

Significant theoretical research has also provided a robust platform for studying alloying effects with the ultimate goal to stabilize the tetragonal FeNi compound. For instance, L. Y. Tian and his group, focusing on the phase transformation of the tetragonal FeNi phase based on first-principles theory, found a strong dependence of the $T_{O\text{-}D}$ on the configurational and vibrational degrees of freedom. Their calculations yield a final $T_{O\text{-}D}$ = 286 °C compared to the experimental value of 320°C. Their results open up the possibility of developing an effective and accurate method for modeling tetragonal ordered forms of FeNi alloys [193].

In this context, many other theoretical studies have emphasized the need to stabilize $L1_0$-FeNi compounds by introducing tetragonal distortions. To promote the formation of $L1_0$-FeNi crystal structure, researchers have proposed co-doping with other elements, like carbon, boron, and hydrogen, in addition to nitrogen [199], [204], [205], [206]. In particular, P. Rani et al. in their study, investigated the regulation of the magnetocrystalline anisotropy (MCA) energy of $L1_0$-FeNi by the diffusion of interstitial carbon-doped atoms using a full-potential approach within the generalized gradient approximation. Their calculated results showed a significant K_u value increase to 1.9×10^6 J/m^3, due to a feasible tetragonal distortion induced by interstitial carbon-doping followed by a slight decrease in saturation magnetization.

1.4 Brief outline of the targets and work done in this PhD Thesis

The hereunto doctoral dissertation (D.D.) entitled 'Synthesis, characterization and study of the properties of new hybrid magnetic nanostructured materials of bimetallic iron alloys (Fe-Rh, Fe-Co, Fe-Ni) grown on nanodiamonds' focuses on the synthesis, the characterization and the analysis of the morphological, structural, electronic and magnetic properties of new hybrid magnetic nanostructured materials based on nanodiamond matrices. The coalescence is referred to two very significant nanostructures, that of nanodiamonds in combination with selected magnetic binary metallic alloys based on Iron. In my thesis I emphasize, that the selection of those nanostructured materials comes both from the uniquely exceptional properties of each component of this hybrid nanomaterial and the special interest of the wider scientific community, that has been focused in general around the exploitation of nanoparticles, which find fertile ground in an increasing number of technological applications. The magnetic NPs component of the hybrid nanostructured samples synthesized during the current D.D. was chosen to be bimetallic alloys of Iron-Cobalt (Fe-Co), Iron-Nickel (Fe-Ni) and Iron-Rhodium (Fe-Rh), based on the very interesting magnetic properties found for the corresponding bulk structures and the perspective to point out extra remarkable characteristics through the preparation of some of their unique phases in nano-scale in combination with the ND matrices. In particular, for the Fe-Co and Fe-Ni bimetallic alloys we concentrated on the formation of the body centered crystal (bcc) and face centered crystal (fcc) structures for each system, respectively. These phases feature prominently in soft ferrimagnets and can be exploited in many applications, where such features are demanded such as coil cores, high and low frequency converters, electron beam focusing magnetic lenses etc. Moreover, I aimed forward to the formation of the corresponding tetragonal structures of these two alloys, the body centered tetragonal structures (bct) for the Fe-Co and Fe-Ni alloys, respectively. About these tetragonal structures, it is already known that they can present enhanced magnetic characteristics, such as strong values of MCA, which overcome even the corresponding MCA values of the typical permanent magnets based on Iron-Platinum (Fe-Pt). Furthermore, these tetragonal structures can hold inflated values of M_S. Such magnetic characteristics render these structures possible candidates, capable of outplacing the typical permanent magnet structures, which mostly are based on rare earth (RE) elements, in order to avail themselves in applications such as magnetic recording or magnetic storage along with green energy applications. Regarding the Fe-Rh alloy, I targeted to the special nature of the metamagnetic transition, during which there is an interaction between the structural and magnetic properties as the temperature alters. Responsible for this interesting and unusual metamagnetic transition is the ordered crystal structure (bcc-B2) of the Fe-Rh alloy in equiatomic composition, which is subjected to a remarkable first-order isostructural (B2-B2) metamagnetic transition from the antiferromagnetic state to the ferromagnetic state in temperatures about 77-97 °C. The challenge that was set regarding the investigation of the Fe-Rh system was the desire of focusing to the formation of high-quality nanocrystals of the ordered bcc-B2 crystal phase, which could present the metamagnetic transition and also of setting the mechanism through which the critical metamagnetic temperature could be controlled or could be modified via the synthesis conditions.

In total the goals I pose in the current PhD dissertation are, on the one hand the synthesis of new nanostructured magnetic materials with exceptional magnetic properties, which concern binary metallic alloys based on Fe, such as Fe-Co, Fe-Ni and Fe-Rh deposited on nanodiamond matrices and on the other hand the characterization and the analysis of their structural, morphological, electronic and magnetic properties. The utilization of nanodiamond substrates as growing frames of new nanostructured magnetic materials is expected to give prominence to this synthesis method as a simple, ease and low-budget preparation technique of new magnetic hybrid nanostructured materials. In addition, through this dissertation I wish to designate this novel research of developing these magnetic nanostructures on nanodiamond matrices, since this is the first time an endeavor like this is ever ventured with these specific magnetic materials. Moreover, this dissertation aims to promote to the wider scientific community the dynamics of the potentials which the developing matrix of these hybrid materials, i.e. the nanodiamonds, can offer in combination with the special magnetic nanostructures, as a proposal for the development of new technology in fields such as biomedicine, biopharmaceutics, electronics, magneto-electronics and relative interconnected subjects.

In order to accomplish all these, samples of magnetic nanoparticles free of NDs, of the same stoichiometry as the hybrid ones have also been prepared, to compare their properties and to evaluate, to delineate and to interpret the role and the properties of the nanodiamond matrix-substrate during the synthesis procedure of the magnetic phases in the hybrid nanostructures. The syntheses of the hybrid and the free NPs samples of all systems have been realized with a combination of synthetic methods, including wet chemistry methods, namely, the Borohydride ($NaBH_4$) and the Impregnation methods and thermal annealing at high temperatures under vacuum (10^{-3} Torr) in quartz (SiO_2) ampoules. This procedure is necessary on the one hand for the forging of the reduction conditions, which must prevail for the formation of the desired metallic alloys and on the other hand for the avoidance of oxidation of the magnetic nanoparticles during their growth.

For the nanohybrid samples, the type of the nanostructured phases, their crystal structure, morphology, size, auto-arrangement and dispersion on the NDs matrices determine the magnetic properties of the produced hybrid materials, features that can be controlled through the synthesis conditions (wet chemistry procedure, annealing time and temperatures, magnetic nanoparticle concentration).

The characterization of the structural, morphological, electric and magnetic properties of the prepared samples was deployed via characterization techniques such as X-ray diffraction (XRD), magnetic measurements at high and low temperatures with vibrating sample magnetometery (VSM) and ^{57}Fe Mössbauer Spectroscopy. In addition, electron microscopy techniques such as (transmission and scanning electron microscopy (TEM and SEM), high-resolution TEM (HRTEM), scanning TEM (STEM) and energy dispersive X-ray spectroscopy (EDS) were utilized, for further characterization of the morphological and structural properties of the samples.

The results contribute to the understanding of the mechanisms responsible for the special features that these new hybrid magnetic nanostructured materials present.

1.5 References

[1] P. Gómez-Romero and C. Sanchez, Eds., *Functional Hybrid Materials*, 1st ed. Wiley, 2003. doi: 10.1002/3527602372.

[2] P. Gomez-Romero, A. Pokhriyal, D. Rueda-García, L. N. Bengoa, and R. M. González-Gil, "Hybrid Materials: A Metareview," *Chem. Mater.*, vol. 36, no. 1, pp. 8–27, Jan. 2024, doi: 10.1021/acs.chemmater.3c01878.

[3] P. Judeinstein and C. Sanchez, "Hybrid organic–inorganic materials: a land of multidisciplinarity," *J. Mater. Chem.*, vol. 6, no. 4, pp. 511–525, 1996, doi: 10.1039/JM9960600511.

[4] M. Faustini, D. Grosso, C. Boissière, R. Backov, and C. Sanchez, "'Integrative sol–gel chemistry': a nanofoundry for materials science," *J Sol-Gel Sci Technol*, vol. 70, no. 2, pp. 216–226, May 2014, doi: 10.1007/s10971-014-3321-9.

[5] J. Ma, J. Wang, X. Ai, and S. Zhang, "Biomimetic self-assembly of apatite hybrid materials: From a single molecular template to bi-/multi-molecular templates," *Biotechnology Advances*, vol. 32, no. 4, pp. 744–760, Jul. 2014, doi: 10.1016/j.biotechadv.2013.10.014.

[6] T. Premkumar and K. E. Geckeler, "Graphene–DNA hybrid materials: Assembly, applications, and prospects," *Progress in Polymer Science*, vol. 37, no. 4, pp. 515–529, Apr. 2012, doi: 10.1016/j.progpolymsci.2011.08.003.

[7] W. Al Zoubi, M. P. Kamil, S. Fatimah, N. Nashrah, and Y. G. Ko, "Recent advances in hybrid organic-inorganic materials with spatial architecture for state-of-the-art applications," *Progress in Materials Science*, vol. 112, p. 100663, Jul. 2020, doi: 10.1016/j.pmatsci.2020.100663.

[8] A. L. M. Reddy, S. R. Gowda, M. M. Shaijumon, and P. M. Ajayan, "Hybrid Nanostructures for Energy Storage Applications," *Advanced Materials*, vol. 24, no. 37, pp. 5045–5064, Sep. 2012, doi: 10.1002/adma.201104502.

[9] J.-M. Rueff, M. Poienar, A. Guesdon, C. Martin, A. Maignan, and P.-A. Jaffrès, "Hydrothermal synthesis for new multifunctional materials: A few examples of phosphates and phosphonate-based hybrid materials," *Journal of Solid State Chemistry*, vol. 236, pp. 236–245, Apr. 2016, doi: 10.1016/j.jssc.2015.09.018.

[10] P. Gomez-Romero, "Hybrid Organic-Inorganic Materials—In Search of Synergic Activity," *Adv. Mater.*, vol. 13, no. 3, pp. 163–174, Feb. 2001, doi: 10.1002/1521-4095(200102)13:3<163::AID-ADMA163>3.0.CO;2-U.

[11] M. M. Adnan, A. R. M. Dalod, M. H. Balci, J. Glaum, and M.-A. Einarsrud, "In Situ Synthesis of Hybrid Inorganic–Polymer Nanocomposites," *Polymers*, vol. 10, no. 10, p. 1129, Oct. 2018, doi: 10.3390/polym10101129.

[12] T. Sirinakorn, K. Imwiset, S. Bureekaew, and M. Ogawa, "Inorganic modification of layered silicates toward functional inorganic-inorganic hybrids," *Applied Clay Science*, vol. 153, pp. 187–197, Mar. 2018, doi: 10.1016/j.clay.2017.12.011.

[13] T. Vijayakanth, D. J. Liptrot, E. Gazit, R. Boomishankar, and C. R. Bowen, "Recent Advances in Organic and Organic–Inorganic Hybrid Materials for Piezoelectric Mechanical Energy Harvesting," *Adv Funct Materials*, vol. 32, no. 17, p. 2109492, Apr. 2022, doi: 10.1002/adfm.202109492.

[14] L. Qiu, X. Han, C. Xing, and U. Glebe, “Polymerization-Induced Self-Assembly: An Emerging Tool for Generating Polymer-Based Biohybrid Nanostructures,” *Small*, vol. 19, no. 18, p. 2207457, May 2023, doi: 10.1002/smll.202207457.

[15] J. Oshiro Junior, M. Paiva Abuçafy, E. Berbel Manaia, B. Lallo Da Silva, B. Chiari-Andréo, and L. Aparecida Chiavacci, “Drug Delivery Systems Obtained from Silica Based Organic-Inorganic Hybrids,” *Polymers*, vol. 8, no. 4, p. 91, Mar. 2016, doi: 10.3390/polym8040091.

[16] M. Catauro and S. V. Ciprioti, “Characterization of Hybrid Materials Prepared by Sol-Gel Method for Biomedical Implementations. A Critical Review,” *Materials*, vol. 14, no. 7, p. 1788, Apr. 2021, doi: 10.3390/ma14071788.

[17] S. Al-Saadi and R. K. Singh Raman, “Silane Coatings for Corrosion and Microbiologically Influenced Corrosion Resistance of Mild Steel: A Review,” *Materials*, vol. 15, no. 21, p. 7809, Nov. 2022, doi: 10.3390/ma15217809.

[18] S. Yuan *et al.*, “Stable Metal–Organic Frameworks: Design, Synthesis, and Applications,” *Advanced Materials*, vol. 30, no. 37, p. 1704303, Sep. 2018, doi: 10.1002/adma.201704303.

[19] B. Hwang and J. Lee, “Recent Advances in Memory Devices with Hybrid Materials,” *Adv Elect Materials*, vol. 5, no. 1, p. 1800519, Jan. 2019, doi: 10.1002/aelm.201800519.

[20] C. Mendoza, V. P. Nirwan, and A. Fahmi, “Nanofabrication of hybrid nanomaterials: Macroscopically aligned nanoparticles pattern via directed self-assembly of block copolymers,” *J of Applied Polymer Sci*, vol. 140, no. 5, p. e53409, Feb. 2023, doi: 10.1002/app.53409.

[21] M. R. Horn *et al.*, “Polyoxometalates (POMs): from electroactive clusters to energy materials,” *Energy Environ. Sci.*, vol. 14, no. 4, pp. 1652–1700, 2021, doi: 10.1039/D0EE03407J.

[22] V. I. Karagianni *et al.*, “From Simple Packaging Materials to Smart Sensors: Sunlight Exposure Sensing in Bubble Wraps Incorporating a Layered Metal Selenide Photocatalyst,” *Advanced Optical Materials*, vol. 12, no. 20, p. 2400373, Jul. 2024, doi: 10.1002/adom.202400373.

[23] S. Atri and R. Tomar, “A Review on the Synthesis and Modification of Functional Inorganic-Organic-Hybrid Materials via Microwave-Assisted Method,” *ChemistrySelect*, vol. 6, no. 34, pp. 9351–9362, Sep. 2021, doi: 10.1002/slct.202102030.

[24] L. Nicole, C. Laberty-Robert, L. Rozes, and C. Sanchez, “Hybrid materials science: a promised land for the integrative design of multifunctional materials,” *Nanoscale*, vol. 6, no. 12, pp. 6267–6292, 2014, doi: 10.1039/C4NR01788A.

[25] K. Ashurbekova, K. Ashurbekova, G. Botta, O. Yurkevich, and M. Knez, “Vapor phase processing: a novel approach for fabricating functional hybrid materials,” *Nanotechnology*, vol. 31, no. 34, p. 342001, Aug. 2020, doi: 10.1088/1361-6528/ab8edb.

[26] D. S. Jung, Y. N. Ko, Y. C. Kang, and S. B. Park, “Recent progress in electrode materials produced by spray pyrolysis for next-generation lithium ion batteries,” *Advanced Powder Technology*, vol. 25, no. 1, pp. 18–31, Jan. 2014, doi: 10.1016/j.apt.2014.01.012.

[27] M. Faustini, L. Nicole, E. Ruiz-Hitzky, and C. Sanchez, “History of Organic–Inorganic Hybrid Materials: Prehistory, Art, Science, and Advanced Applications,” *Adv Funct Materials*, vol. 28, no. 27, p. 1704158, Jul. 2018, doi: 10.1002/adfm.201704158.

[28] M. G. Kanatzidis, L. M. Tonge, T. J. Marks, H. O. Marcy, and C. R. Kannewurf, “In situ intercalative polymerization of pyrrole in Fe0Cl: a new class of layered, conducting polymer-inorganic hybrid materials,” *J. Am. Chem. Soc.*, vol. 109, no. 12, pp. 3797–3799, Jun. 1987, doi: 10.1021/ja00246a057.

[29] Y. Kubozono, Ed., *Physics and Chemistry of Carbon-Based Materials: Basics and Applications*. Singapore: Springer Singapore, 2019. doi: 10.1007/978-981-13-3417-7.

[30] J. Tuček, K. C. Kemp, K. S. Kim, and R. Zbořil, “Iron-Oxide-Supported Nanocarbon in Lithium-Ion Batteries, Medical, Catalytic, and Environmental Applications,” *ACS Nano*, vol. 8, no. 8, pp. 7571–7612, Aug. 2014, doi: 10.1021/nn501836x.

[31] X. Duan *et al.*, “sp ^{2} /sp ^{3} Framework from Diamond Nanocrystals: A Key Bridge of Carbonaceous Structure to Carbocatalysis,” *ACS Catal.*, vol. 9, no. 8, Art. no. 8, Aug. 2019, doi: 10.1021/acscatal.9b01565.

[32] V. N. Mochalin, O. Shenderova, D. Ho, and Y. Gogotsi, “The properties and applications of nanodiamonds,” *Nature Nanotech*, vol. 7, no. 1, Art. no. 1, Jan. 2012, doi: 10.1038/nnano.2011.209.

[33] M. Zeiger, N. Jäckel, V. N. Mochalin, and V. Presser, “Review: carbon onions for electrochemical energy storage,” *J. Mater. Chem. A*, vol. 4, no. 9, pp. 3172–3196, 2016, doi: 10.1039/C5TA08295A.

[34] M. Alahmadi and M. Siaj, “Graphene-Assisted Magnetic Iron Carbide Nanoparticle Growth,” *ACS Appl. Nano Mater.*, vol. 1, no. 12, pp. 7000–7005, Dec. 2018, doi: 10.1021/acsanm.8b01794.

[35] A. Salati, A. Ramazani, and M. Almasi Kashi, “Deciphering magnetic hyperthermia properties of compositionally and morphologically modulated FeNi nanoparticles using first-order reversal curve analysis,” *Nanotechnology*, vol. 30, no. 2, p. 025707, Jan. 2019, doi: 10.1088/1361-6528/aae7f3.

[36] A. B. Bourlinos *et al.*, “Fabrication of fluorescent nanodiamond@C core–shell hybrids via mild carbonization of sodium cholate–nanodiamond complexes,” *J Mater Sci*, vol. 46, no. 24, Art. no. 24, Dec. 2011, doi: 10.1007/s10853-011-5911-z.

[37] A. M. S. Lopes, F. F. Barbosa, M. A. M. Torres, S. B. C. Pergher, and T. P. Braga, “In situ synthesis of highly stable FeCo alloy encapsulated in carbon from ethanol,” *Materials Today Communications*, vol. 32, p. 103900, Aug. 2022, doi: 10.1016/j.mtcomm.2022.103900.

[38] W. S. Seo *et al.*, “FeCo/graphitic-shell nanocrystals as advanced magnetic-resonance-imaging and near-infrared agents,” *Nature Mater*, vol. 5, no. 12, Art. no. 12, Dec. 2006, doi: 10.1038/nmat1775.

[39] J. Ding, L. Cheng, and W. Zhao, “Self-Assembly Magnetic FeCo Nanostructures on Oxide Graphene for Enhanced Microwave Absorption,” *J. Electron. Mater.*, vol. 51, no. 6, pp. 2856–2866, Jun. 2022, doi: 10.1007/s11664-022-09552-4.

[40] L. V. Kozhitov, D. G. Muratov, V. G. Kostishin, V. I. Suslyaev, E. Yu. Korovin, and A. V. Popkova, “FeCo/C nanocomposites: Synthesis, magnetic and electromagnetic properties,” *Russ. J. Inorg. Chem.*, vol. 62, no. 11, pp. 1499–1507, Nov. 2017, doi: 10.1134/S0036023617110110.

[41] R. Ghunaim *et al.*, “Single-crystalline FeCo nanoparticle-filled carbon nanotubes: synthesis, structural characterization and magnetic properties,” *Beilstein J. Nanotechnol.*, vol. 9, pp. 1024–1034, Mar. 2018, doi: 10.3762/bjnano.9.95.

[42] A. S. Barnard, “Predicting the impact of structural diversity on the performance of nanodiamond drug carriers,” *Nanoscale*, vol. 10, no. 19, pp. 8893–8910, 2018, doi: 10.1039/C8NR01688G.

[43] X. Zhang, R. Lam, X. Xu, E. K. Chow, H. Kim, and D. Ho, “Multimodal Nanodiamond Drug Delivery Carriers for Selective Targeting, Imaging, and Enhanced Chemotherapeutic Efficacy,” *Advanced Materials*, vol. 23, no. 41, pp. 4770–4775, Nov. 2011, doi: 10.1002/adma.201102263.

[44] P. Maletinsky *et al.*, “A robust scanning diamond sensor for nanoscale imaging with single nitrogen-vacancy centres,” *Nature Nanotech*, vol. 7, no. 5, pp. 320–324, May 2012, doi: 10.1038/nnano.2012.50.

[45] H. W. Kroto, J. R. Heath, S. C. O’Brien, R. F. Curl, and R. E. Smalley, “C60: Buckminsterfullerene,” *Nature*, vol. 318, no. 6042, pp. 162–163, Nov. 1985, doi: 10.1038/318162a0.

[46] M. Prato, “[60]Fullerene chemistry for materials science applications,” *J. Mater. Chem.*, vol. 7, no. 7, pp. 1097–1109, 1997, doi: 10.1039/a700080d.

[47] F. Diederich and Y. Rubin, “Synthetic Approaches toward Molecular and Polymeric Carbon Allotropes,” *Angew. Chem. Int. Ed. Engl.*, vol. 31, no. 9, pp. 1101–1123, Sep. 1992, doi: 10.1002/anie.199211013.

[48] Y. Wang and L. T. Cheng, “Nonlinear optical properties of fullerenes and charge-transfer complexes of fullerenes,” *J. Phys. Chem.*, vol. 96, no. 4, pp. 1530–1532, Feb. 1992, doi: 10.1021/j100183a007.

[49] M. Kawauchi, T. Kawauchi, and T. Takeichi, “Solubilization of [60]Fullerene Owing to Inclusion Complex Formation between Syndiotactic Poly(methyl methacrylate) and the Fullerenes in Polar Solvents,” *Macromolecules*, vol. 42, no. 16, pp. 6136–6140, Aug. 2009, doi: 10.1021/ma901235b.

[50] A. F. Hebard *et al.*, “Superconductivity at 18 K in potassium-doped C60,” *Nature*, vol. 350, no. 6319, pp. 600–601, Apr. 1991, doi: 10.1038/350600a0.

[51] P. W. Stephens *et al.*, “Lattice structure of the fullerene ferromagnet TDAE–C60,” *Nature*, vol. 355, no. 6358, pp. 331–332, Jan. 1992, doi: 10.1038/355331a0.

[52] D. Y. Lyon, J. D. Fortner, C. M. Sayes, V. L. Colvin, and J. B. Hughes, “Bacterial cell association and antimicrobial activity of a C_{60} water suspension,” *Enviro Toxic and Chemistry*, vol. 24, no. 11, pp. 2757–2762, Nov. 2005, doi: 10.1897/04-649R.1.

[53] Z. He, C. Zhong, S. Su, M. Xu, H. Wu, and Y. Cao, “Enhanced power-conversion efficiency in polymer solar cells using an inverted device structure,” *Nature Photon*, vol. 6, no. 9, pp. 591–595, Sep. 2012, doi: 10.1038/nphoton.2012.190.

[54] B. S. Sherigara, W. Kutner, and F. D’Souza, “Electrocatalytic Properties and Sensor Applications of Fullerenes and Carbon Nanotubes,” *Electroanalysis*, vol. 15, no. 9, pp. 753–772, Jun. 2003, doi: 10.1002/elan.200390094.

[55] S. Iijima, “Helical microtubules of graphitic carbon,” *Nature*, vol. 354, no. 6348, pp. 56–58, Nov. 1991, doi: 10.1038/354056a0.

[56] S. Iijima and T. Ichihashi, “Single-shell carbon nanotubes of 1-nm diameter,” *Nature*, vol. 363, no. 6430, pp. 603–605, Jun. 1993, doi: 10.1038/363603a0.

[57] B. H. Hong *et al.*, “Extracting subnanometer single shells from ultralong multiwalled carbon nanotubes,” *Proc. Natl. Acad. Sci. U.S.A.*, vol. 102, no. 40, pp. 14155–14158, Oct. 2005, doi: 10.1073/pnas.0505219102.

[58] H. Dai, “Carbon Nanotubes: Synthesis, Integration, and Properties,” *Acc. Chem. Res.*, vol. 35, no. 12, pp. 1035–1044, Dec. 2002, doi: 10.1021/ar0101640.

[59] R. Andrews, D. Jacques, D. Qian, and T. Rantell, “Multiwall Carbon Nanotubes: Synthesis and Application,” *Acc. Chem. Res.*, vol. 35, no. 12, pp. 1008–1017, Dec. 2002, doi: 10.1021/ar010151m.

[60] M. Bockrath *et al.*, “Single-Electron Transport in Ropes of Carbon Nanotubes,” *Science*, vol. 275, no. 5308, pp. 1922–1925, Mar. 1997, doi: 10.1126/science.275.5308.1922.

[61] K. Liu *et al.*, “Quantum-coupled radial-breathing oscillations in double-walled carbon nanotubes,” *Nat Commun*, vol. 4, no. 1, p. 1375, Jan. 2013, doi: 10.1038/ncomms2367.

[62] K. S. Novoselov *et al.*, “Electric Field Effect in Atomically Thin Carbon Films,” *Science*, vol. 306, no. 5696, pp. 666–669, Oct. 2004, doi: 10.1126/science.1102896.

[63] C. N. R. Rao, A. K. Sood, K. S. Subrahmanyam, and A. Govindaraj, “Graphene: The New Two-Dimensional Nanomaterial,” *Angew Chem Int Ed*, vol. 48, no. 42, pp. 7752–7777, Oct. 2009, doi: 10.1002/anie.200901678.

[64] M. J. Allen, V. C. Tung, and R. B. Kaner, “Honeycomb Carbon: A Review of Graphene,” *Chem. Rev.*, vol. 110, no. 1, pp. 132–145, Jan. 2010, doi: 10.1021/cr900070d.

[65] A. H. Castro Neto, F. Guinea, N. M. R. Peres, K. S. Novoselov, and A. K. Geim, “The electronic properties of graphene,” *Rev. Mod. Phys.*, vol. 81, no. 1, pp. 109–162, Jan. 2009, doi: 10.1103/RevModPhys.81.109.

[66] Y. Zhang, Y.-W. Tan, H. L. Stormer, and P. Kim, “Experimental observation of the quantum Hall effect and Berry’s phase in graphene,” *Nature*, vol. 438, no. 7065, pp. 201–204, Nov. 2005, doi: 10.1038/nature04235.

[67] F. Schedin *et al.*, “Detection of individual gas molecules adsorbed on graphene,” *Nature Mater*, vol. 6, no. 9, pp. 652–655, Sep. 2007, doi: 10.1038/nmat1967.

[68] W. Y. Kim and K. S. Kim, “Prediction of very large values of magnetoresistance in a graphene nanoribbon device,” *Nature Nanotech*, vol. 3, no. 7, pp. 408–412, Jul. 2008, doi: 10.1038/nnano.2008.163.

[69] K. S. Kim *et al.*, “Large-scale pattern growth of graphene films for stretchable transparent electrodes,” *Nature*, vol. 457, no. 7230, pp. 706–710, Feb. 2009, doi: 10.1038/nature07719.

[70] X. Li *et al.*, “Large-Area Synthesis of High-Quality and Uniform Graphene Films on Copper Foils,” *Science*, vol. 324, no. 5932, pp. 1312–1314, Jun. 2009, doi: 10.1126/science.1171245.

[71] V. Georgakilas *et al.*, “Functionalization of Graphene: Covalent and Non-Covalent Approaches, Derivatives and Applications,” *Chem. Rev.*, vol. 112, no. 11, pp. 6156–6214, Nov. 2012, doi: 10.1021/cr3000412.

[72] K. P. Loh, Q. Bao, P. K. Ang, and J. Yang, “The chemistry of graphene,” *J. Mater. Chem.*, vol. 20, no. 12, p. 2277, 2010, doi: 10.1039/b920539j.

[73] S. Bae *et al.*, “Roll-to-roll production of 30-inch graphene films for transparent electrodes,” *Nature Nanotech*, vol. 5, no. 8, pp. 574–578, Aug. 2010, doi: 10.1038/nnano.2010.132.

[74] O. Ö. Ekiz, M. Ürel, H. Güner, A. K. Mizrak, and A. Dâna, “Reversible Electrical Reduction and Oxidation of Graphene Oxide,” *ACS Nano*, vol. 5, no. 4, pp. 2475–2482, Apr. 2011, doi: 10.1021/nn1014215.

[75] D. S. Hecht, L. Hu, and G. Irvin, “Emerging Transparent Electrodes Based on Thin Films of Carbon Nanotubes, Graphene, and Metallic Nanostructures,” *Advanced Materials*, vol. 23, no. 13, pp. 1482–1513, Apr. 2011, doi: 10.1002/adma.201003188.

[76] M. Liu *et al.*, “A graphene-based broadband optical modulator,” *Nature*, vol. 474, no. 7349, pp. 64–67, Jun. 2011, doi: 10.1038/nature10067.

[77] M. D. Stoller, S. Park, Y. Zhu, J. An, and R. S. Ruoff, “Graphene-Based Ultracapacitors,” *Nano Lett.*, vol. 8, no. 10, pp. 3498–3502, Oct. 2008, doi: 10.1021/nl802558y.

[78] Z. Liu, J. T. Robinson, X. Sun, and H. Dai, “PEGylated Nanographene Oxide for Delivery of Water-Insoluble Cancer Drugs,” *J. Am. Chem. Soc.*, vol. 130, no. 33, pp. 10876–10877, Aug. 2008, doi: 10.1021/ja803688x.

[79] L. Zhang, J. Xia, Q. Zhao, L. Liu, and Z. Zhang, “Functional Graphene Oxide as a Nanocarrier for Controlled Loading and Targeted Delivery of Mixed Anticancer Drugs,” *Small*, vol. 6, no. 4, pp. 537–544, Feb. 2010, doi: 10.1002/smll.200901680.

[80] S. Myung *et al.*, “Label-Free Polypeptide-Based Enzyme Detection Using a Graphene-Nanoparticle Hybrid Sensor,” *Advanced Materials*, vol. 24, no. 45, pp. 6081–6087, Nov. 2012, doi: 10.1002/adma.201202961.

[81] S. Zhu *et al.*, “Strongly green-photoluminescent graphene quantum dots for bioimaging applications,” *Chem. Commun.*, vol. 47, no. 24, p. 6858, 2011, doi: 10.1039/c1cc11122a.

[82] L. Cao, M. J. Meziani, S. Sahu, and Y.-P. Sun, “Photoluminescence Properties of Graphene versus Other Carbon Nanomaterials,” *Acc. Chem. Res.*, vol. 46, no. 1, pp. 171–180, Jan. 2013, doi: 10.1021/ar300128j.

[83] H. Li *et al.*, “Water-Soluble Fluorescent Carbon Quantum Dots and Photocatalyst Design,” *Angew Chem Int Ed*, vol. 49, no. 26, pp. 4430–4434, Jun. 2010, doi: 10.1002/anie.200906154.

[84] A. B. Bourlinos *et al.*, “Synthesis, characterization and non-linear optical response of organophilic carbon dots,” *Carbon*, vol. 61, pp. 640–643, Sep. 2013, doi: 10.1016/j.carbon.2013.05.017.

[85] H. Li *et al.*, “Carbon quantum dots with photo-generated proton property as efficient visible light controlled acid catalyst,” *Nanoscale*, vol. 6, no. 2, pp. 867–873, 2014, doi: 10.1039/C3NR03996J.

[86] Y. Dong, C. Chen, J. Lin, N. Zhou, Y. Chi, and G. Chen, “Electrochemiluminescence emission from carbon quantum dot-sulfite coreactant system,” *Carbon*, vol. 56, pp. 12–17, May 2013, doi: 10.1016/j.carbon.2012.12.086.

[87] L. Cao *et al.*, “Competitive Performance of Carbon ‘Quantum’ Dots in Optical Bioimaging,” *Theranostics*, vol. 2, no. 3, pp. 295–301, 2012, doi: 10.7150/thno.3912.

[88] F. Bruno *et al.*, “A Comparative Study of Top-Down and Bottom-Up Carbon Nanodots and Their Interaction with Mercury Ions,” *Nanomaterials*, vol. 11, no. 5, p. 1265, May 2021, doi: 10.3390/nano11051265.

[89] A. B. Bourlinos *et al.*, “Gd(iii)-doped carbon dots as a dual fluorescent-MRI probe,” *J. Mater. Chem.*, vol. 22, no. 44, p. 23327, 2012, doi: 10.1039/c2jm35592b.

[90] X. Wang *et al.*, “Multiple Bioimaging Applications Based on the Excellent Properties of Nanodiamond: A Review,” *Molecules*, vol. 28, no. 10, p. 4063, May 2023, doi: 10.3390/molecules28104063.

[91] S. A. Qureshi, W. W.-W. Hsiao, L. Hussain, H. Aman, T.-N. Le, and M. Rafique, “Recent Development of Fluorescent Nanodiamonds for Optical Biosensing and Disease Diagnosis,” *Biosensors*, vol. 12, no. 12, p. 1181, Dec. 2022, doi: 10.3390/bios12121181.

[92] S. Chauhan, N. Jain, and U. Nagaich, “Nanodiamonds with powerful ability for drug delivery and biomedical applications: Recent updates on in vivo study and patents,” *Journal of Pharmaceutical Analysis*, vol. 10, no. 1, pp. 1–12, Feb. 2020, doi: 10.1016/j.jpha.2019.09.003.

[93] A. M. Vervald *et al.*, “Boron-Doped Nanodiamonds as Anticancer Agents: En Route to Hyperthermia/Thermoablation Therapy,” *ACS Biomater. Sci. Eng.*, vol. 6, no. 8, pp. 4446–4453, Aug. 2020, doi: 10.1021/acsbiomaterials.0c00505.

[94] W. Hou *et al.*, “Nanodiamond–Manganese dual mode MRI contrast agents for enhanced liver tumor detection,” *Nanomedicine: Nanotechnology, Biology and Medicine*, vol. 13, no. 3, pp. 783–793, Apr. 2017, doi: 10.1016/j.nano.2016.12.013.

[95] V. V. Danilenko, “On the history of the discovery of nanodiamond synthesis,” *Phys. Solid State*, vol. 46, no. 4, pp. 595–599, Apr. 2004, doi: 10.1134/1.1711431.

[96] G.-W. Yang, J.-B. Wang, and Q.-X. Liu, “Preparation of nano-crystalline diamonds using pulsed laser induced reactive quenching,” *J. Phys.: Condens. Matter*, vol. 10, no. 35, pp. 7923–7927, Sep. 1998, doi: 10.1088/0953-8984/10/35/024.

[97] J.-P. Boudou *et al.*, “High yield fabrication of fluorescent nanodiamonds,” *Nanotechnology*, vol. 20, no. 23, p. 235602, Jun. 2009, doi: 10.1088/0957-4484/20/23/235602.

[98] M. Frenklach, W. Howard, D. Huang, J. Yuan, K. E. Spear, and R. Koba, “Induced nucleation of diamond powder,” *Applied Physics Letters*, vol. 59, no. 5, pp. 546–548, Jul. 1991, doi: 10.1063/1.105434.

[99] Y. G. Gogotsi, K. G. Nickel, D. Bahloul-Hourlier, T. Merle-Mejean, G. E. Khomenko, and K. P. Skjerlie, “Structure of carbon produced by hydrothermal treatment of β-SiC powder,” *J. Mater. Chem.*, vol. 6, no. 4, pp. 595–604, 1996, doi: 10.1039/JM9960600595.

[100] S. Welz, Y. Gogotsi, and M. J. McNallan, “Nucleation, growth, and graphitization of diamond nanocrystals during chlorination of carbides,” *Journal of Applied Physics*, vol. 93, no. 7, pp. 4207–4214, Apr. 2003, doi: 10.1063/1.1558227.

[101] T. L. Daulton, M. A. Kirk, R. S. Lewis, and L. E. Rehn, “Production of nanodiamonds by high-energy ion irradiation of graphite at room temperature,” *Nuclear Instruments and Methods in Physics Research Section B: Beam Interactions with Materials and Atoms*, vol. 175–177, pp. 12–20, Apr. 2001, doi: 10.1016/S0168-583X(00)00603-0.

[102] F. Banhart and P. M. Ajayan, “Carbon onions as nanoscopic pressure cells for diamond formation,” *Nature*, vol. 382, no. 6590, pp. 433–435, Aug. 1996, doi: 10.1038/382433a0.

[103] É. M. Galimov *et al.*, “Experimental corroboration of the synthesis of diamond in the cavitation process,” *Dokl. Phys.*, vol. 49, no. 3, pp. 150–153, Mar. 2004, doi: 10.1134/1.1710678.

[104] S. Osswald, G. Yushin, V. Mochalin, S. O. Kucheyev, and Y. Gogotsi, “Control of sp ^{2} /sp ^{3} Carbon Ratio and Surface Chemistry of Nanodiamond Powders by Selective Oxidation in Air,” *J. Am. Chem. Soc.*, vol. 128, no. 35, pp. 11635–11642, Sep. 2006, doi: 10.1021/ja063303n.

[105] O. Shenderova *et al.*, “Surface Chemistry and Properties of Ozone-Purified Detonation Nanodiamonds,” *J. Phys. Chem. C*, vol. 115, no. 20, pp. 9827–9837, May 2011, doi: 10.1021/jp1102466.

[106] M. Barbic *et al.*, “Magnetocaloric materials as switchable high contrast ratio MRI labels,” *Magn. Reson. Med.*, vol. 81, no. 4, pp. 2238–2246, Apr. 2019, doi: 10.1002/mrm.27615.

[107] J. Puebla, J. Kim, K. Kondou, and Y. Otani, “Spintronic devices for energy-efficient data storage and energy harvesting,” *Commun Mater*, vol. 1, no. 1, p. 24, May 2020, doi: 10.1038/s43246-020-0022-5.

[108] W. Pepperhoff and M. Acet, *Constitution and Magnetism of Iron and its Alloys*. in Engineering Materials. Berlin, Heidelberg: Springer Berlin Heidelberg, 2001. doi: 10.1007/978-3-662-04345-5.

[109] M. Fallot, “Les alliages du fer avec les métaux de la famille du platine,” *Ann. Phys.*, vol. 11, no. 10, pp. 291–332, 1938, doi: 10.1051/anphys/193811100291.

[110] G. Shirane, C. W. Chen, P. A. Flinn, and R. Nathans, “Hyperfine Fields and Magnetic Moments in the Fe–Rh System,” *Journal of Applied Physics*, vol. 34, no. 4, pp. 1044–1045, Apr. 1963, doi: 10.1063/1.1729362.

[111] E. M. Hofer and P. Cucka, “Magnetic properties of Rh-rich FeRh alloy,” *Journal of Physics and Chemistry of Solids*, vol. 27, no. 9, pp. 1552–1555, Sep. 1966, doi: 10.1016/0022-3697(66)90151-X.

[112] J. M. Lommel and J. S. Kouvel, “Effects of Mechanical and Thermal Treatment on the Structure and Magnetic Transitions in FeRh,” *Journal of Applied Physics*, vol. 38, no. 3, pp. 1263–1264, Mar. 1967, doi: 10.1063/1.1709570.

[113] J. Kim, R. Ramesh, and N. Kioussis, “Revealing the Hidden Structural Phases of FeRh,” *Phys. Rev. B*, vol. 94, no. 18, p. 180407, Nov. 2016, doi: 10.1103/PhysRevB.94.180407.

[114] L. Muldawer and F. deBergevin, “Antiferromagnetic-Ferromagnetic Transformation in FeRh,” *The Journal of Chemical Physics*, vol. 35, no. 5, pp. 1904–1905, Nov. 1961, doi: 10.1063/1.1732175.

[115] J. S. Kouvel and C. C. Hartelius, “Anomalous Magnetic Moments and Transformations in the Ordered Alloy FeRh,” p. 3.

[116] A. M. Kadomtseva, “MAGNETIC AND MAGNETOELASTIC PROPERTIES OF A METAMAGNETIC IRON-RHODIUM,” p. 6.

[117] M. Wolloch *et al.*, “Impact of lattice dynamics on the phase stability of metamagnetic FeRh: Bulk and thin films,” *Phys. Rev. B*, vol. 94, no. 17, p. 174435, Nov. 2016, doi: 10.1103/PhysRevB.94.174435.

[118] S. Lounis, M. Benakki, and C. Demangeat, “Ferromagnetic stabilization of ordered B2 FeRh thin films,” *Phys. Rev. B*, vol. 67, no. 9, p. 094432, Mar. 2003, doi: 10.1103/PhysRevB.67.094432.

[119] F. Pressacco, V. Uhlíř, M. Gatti, A. Bendounan, E. E. Fullerton, and F. Sirotti, “Stable room-temperature ferromagnetic phase at the FeRh(100) surface,” *Sci Rep*, vol. 6, no. 1, p. 22383, Mar. 2016, doi: 10.1038/srep22383.

[120] Y. Ohtani and I. Hatakeyama, “Antiferro-ferromagnetic transition and microstructural properties in a sputter deposited FeRh thin film system,” *Journal of Applied Physics*, vol. 74, no. 5, pp. 3328–3332, Sep. 1993, doi: 10.1063/1.354557.

[121] H. Miyajima and S. Yuasa, “Structural phase transition and magnetic properties of FeRh1−xCox alloys,” *Journal of Magnetism and Magnetic Materials*, vol. 104–107, pp. 2025–2026, Feb. 1992, doi: 10.1016/0304-8853(92)91652-A.

[122] M. Rosenberg, V. Kuncser, O. Crisan, A. Hernando, E. Navarro, and G. Filoti, “A Mössbauer spectroscopy and magnetic study of FeRh,” *Journal of Magnetism and Magnetic Materials*, vol. 177–181, pp. 135–136, Jan. 1998, doi: 10.1016/S0304-8853(97)00662-8.

[123] L. S.-J. Peng and G. S. Collins, “Point Defects And The B2 To Fcc Transformation In Milled FeRh,” *MRS Proc.*, vol. 481, p. 631, 1997, doi: 10.1557/PROC-481-631.

[124] C. C. Chao, P. Duwez, and C. C. Tsuei, “Metastable fcc Fe–Rh Alloys and the Fe–Rh Phase Diagram,” *Journal of Applied Physics*, vol. 42, no. 11, pp. 4282–4284, Oct. 1971, doi: 10.1063/1.1659766.

[125] L. H. Lewis, C. H. Marrows, and S. Langridge, “Coupled magnetic, structural, and electronic phase transitions in FeRh,” *J. Phys. D: Appl. Phys.*, vol. 49, no. 32, p. 323002, Aug. 2016, doi: 10.1088/0022-3727/49/32/323002.

[126] H. Okamoto, “Fe-Rh (Iron-Rhodium),” *J. Phase Equilib. Diffus.*, vol. 32, no. 5, pp. 472–472, Oct. 2011, doi: 10.1007/s11669-011-9934-6.

[127] G. Shirane, R. Nathans, and C. W. Chen, “Magnetic Moments and Unpaired Spin Densities in the Fe-Rh Alloys,” *Phys. Rev.*, vol. 134, no. 6A, pp. A1547–A1553, Jun. 1964, doi: 10.1103/PhysRev.134.A1547.

[128] L.-Y. Chen and D. W. Lynch, “Ellipsometric studies of magnetic phase transitions of Fe-Rh alloys,” *Phys. Rev. B*, vol. 37, no. 18, pp. 10503–10509, Jun. 1988, doi: 10.1103/PhysRevB.37.10503.

[129] H. Y. Y. Ko, T. Suzuki, N. N. Phuoc, and J. Cao, “Fabrication and characterization of FeRh nanoparticles,” *Journal of Applied Physics*, vol. 103, no. 7, p. 07D508, Apr. 2008, doi: 10.1063/1.2832440.

[130] E. Navarro *et al.*, “Low Temperature Magnetic Properties of FCC FeRh Obtained by Ball Milling,” *MSF*, vol. 269–272, pp. 133–138, Jan. 1998, doi: 10.4028/www.scientific.net/MSF.269-272.133.

[131] A. Hillion *et al.*, “Low Temperature Ferromagnetism in Chemically Ordered FeRh Nanocrystals,” *Phys. Rev. Lett.*, vol. 110, no. 8, p. 087207, Feb. 2013, doi: 10.1103/PhysRevLett.110.087207.

[132] U. Herr, J. Jing, R. Birringer, U. Gonser, and H. Gleiter, “Investigation of nanocrystalline iron materials by Mössbauer spectroscopy,” *Appl. Phys. Lett.*, vol. 50, no. 8, pp. 472–474, Feb. 1987, doi: 10.1063/1.98177.

[133] J.-U. Thiele, S. Maat, and E. E. Fullerton, “FeRh/FePt exchange spring films for thermally assisted magnetic recording media,” *Appl. Phys. Lett.*, vol. 82, no. 17, pp. 2859–2861, Apr. 2003, doi: 10.1063/1.1571232.

[134] C. Bordel *et al.*, “Fe Spin Reorientation across the Metamagnetic Transition in Strained FeRh Thin Films,” *Phys. Rev. Lett.*, vol. 109, no. 11, p. 117201, Sep. 2012, doi: 10.1103/PhysRevLett.109.117201.

[135] J.-U. Thiele, S. Maat, J. L. Robertson, and E. E. Fullerton, “Magnetic and Structural Properties of FePt–FeRh Exchange Spring Films for Thermally Assisted Magnetic Recording Media,” *IEEE Trans. Magn.*, vol. 40, no. 4, pp. 2537–2542, Jul. 2004, doi: 10.1109/TMAG.2004.829325.

[136] B. Yu, M. Liu, P. W. Egolf, and A. Kitanovski, “A review of magnetic refrigerator and heat pump prototypes built before the year 2010,” *International Journal of Refrigeration*, vol. 33, no. 6, pp. 1029–1060, Sep. 2010, doi: 10.1016/j.ijrefrig.2010.04.002.

[137] V. I. Zverev, A. P. Pyatakov, A. A. Shtil, and A. M. Tishin, “Novel applications of magnetic materials and technologies for medicine,” *Journal of Magnetism and Magnetic Materials*, vol. 459, pp. 182–186, Aug. 2018, doi: 10.1016/j.jmmm.2017.11.032.

[138] I. Astefanoaei, R. Gimaev, V. Zverev, and A. Stancu, “Modelling of working parameters of Gd and FeRh nanoparticles for magnetic hyperthermia,” *Mater. Res. Express*, vol. 6, no. 12, p. 125089, Dec. 2019, doi: 10.1088/2053-1591/ab5c4a.

[139] X. Marti *et al.*, “Room-temperature antiferromagnetic memory resistor,” *Nature Mater*, vol. 13, no. 4, pp. 367–374, Apr. 2014, doi: 10.1038/nmat3861.

[140] M. R. Ibarra and P. A. Algarabel, “Giant volume magnetostriction in the FeRh alloy,” *Phys. Rev. B*, vol. 50, no. 6, pp. 4196–4199, Aug. 1994, doi: 10.1103/PhysRevB.50.4196.

[141] P. A. Algarabel *et al.*, “Giant room-temperature magnetoresistance in the FeRh alloy,” *Appl. Phys. Lett.*, vol. 66, no. 22, pp. 3061–3063, May 1995, doi: 10.1063/1.114278.

[142] P. Karipoth, A. Thirumurugan, S. Velaga, J.-M. Greneche, and R. Justin Joseyphus, “Magnetic properties of FeCo alloy nanoparticles synthesized through instant chemical reduction,” *Journal of Applied Physics*, vol. 120, no. 12, Art. no. 12, Sep. 2016, doi: 10.1063/1.4962637.

[143] R. H. Yu, S. Basu, Y. Zhang, and J. Q. Xiao, “Magnetic domains and coercivity in FeCo soft magnetic alloys,” *Journal of Applied Physics*, vol. 85, no. 8, Art. no. 8, Apr. 1999, doi: 10.1063/1.369073.

[144] P. A. Montano and M. S. Seehra, “Mössbauer study of the order-disorder and $\alpha-\gamma$ transitions in FeCo,” *Phys. Rev. B*, vol. 15, no. 5, pp. 2437–2441, Mar. 1977, doi: 10.1103/PhysRevB.15.2437.

[145] J. M. MacLaren, T. C. Schulthess, W. H. Butler, R. Sutton, and M. McHenry, “Electronic structure, exchange interactions, and Curie temperature of FeCo,” *Journal of Applied Physics*, vol. 85, no. 8, pp. 4833–4835, Apr. 1999, doi: 10.1063/1.370036.

[146] M. Ležaić, Ph. Mavropoulos, and S. Blügel, “First-principles prediction of high Curie temperature for ferromagnetic bcc-Co and bcc-FeCo alloys and its relevance to tunneling magnetoresistance,” *Applied Physics Letters*, vol. 90, no. 8, p. 082504, Feb. 2007, doi: 10.1063/1.2710181.

[147] H. Okamoto, “Co-Fe (Cobalt-Iron),” *J Phs Eqil and Diff*, vol. 29, no. 4, pp. 383–384, Aug. 2008, doi: 10.1007/s11669-008-9345-5.

[148] J. M. D. Coey, *Magnetism and Magnetic Materials*, 1st ed. Cambridge University Press, 2001. doi: 10.1017/CBO9780511845000.

[149] F. Sánchez-De Jesús, A. M. Bolarín-Miró, C. A. Cortés Escobedo, G. Torres-Villaseñor, and P. Vera-Serna, “Structural Analysis and Magnetic Properties of FeCo Alloys Obtained by Mechanical Alloying,” *Journal of Metallurgy*, vol. 2016, pp. 1–8, Jul. 2016, doi: 10.1155/2016/8347063.

[150] M. Delshad Chermahini, M. Zandrahimi, H. Shokrollahi, and S. Sharafi, “The effect of milling time and composition on microstructural and magnetic properties of nanostructured Fe–Co alloys,” *Journal of Alloys and Compounds*, vol. 477, no. 1–2, pp. 45–50, May 2009, doi: 10.1016/j.jallcom.2008.10.163.

[151] G. S. Chaubey *et al.*, “Synthesis and Stabilization of FeCo Nanoparticles,” *J. Am. Chem. Soc.*, vol. 129, no. 23, Art. no. 23, Jun. 2007, doi: 10.1021/ja0708969.

[152] B. deMayo, D. W. Forester, and S. Spooner, “Effects of Atomic Configurational Changes on Hyperfine Interactions in Concentrated Iron-Cobalt Alloys,” *Journal of Applied Physics*, vol. 41, no. 3, pp. 1319–1320, Mar. 1970, doi: 10.1063/1.1658920.

[153] R. Lv *et al.*, “Carbon nanotubes filled with ferromagnetic alloy nanowires: Lightweight and wide-band microwave absorber,” *Applied Physics Letters*, vol. 93, no. 22, p. 223105, Dec. 2008, doi: 10.1063/1.3042099.

[154] H. Ito *et al.*, “Fabrication of $L1_0$-type FeCo ordered structure using a periodic Ni buffer layer,” *AIP Advances*, vol. 9, no. 4, Art. no. 4, Apr. 2019, doi: 10.1063/1.5079982.

[155] C. V. Falub *et al.*, “Enhanced permeability dielectric FeCo/Al_2O_3 multilayer thin films with tailored properties deposited by magnetron sputtering on silicon,” *AIP Advances*, vol. 9, no. 3, Art. no. 3, Mar. 2019, doi: 10.1063/1.5079477.

[156] A. Jakobsson *et al.*, “Tuning the Curie temperature of FeCo compounds by tetragonal distortion,” *Applied Physics Letters*, vol. 103, no. 10, p. 102404, Sep. 2013, doi: 10.1063/1.4819773.

[157] G. Song *et al.*, “Carbon-coated FeCo nanoparticles as sensitive magnetic-particle-imaging tracers with photothermal and magnetothermal properties,” *Nat Biomed Eng*, vol. 4, no. 3, pp. 325–334, Feb. 2020, doi: 10.1038/s41551-019-0506-0.

[158] A. Hütten *et al.*, “New magnetic nanoparticles for biotechnology,” *Journal of Biotechnology*, vol. 112, no. 1–2, pp. 47–63, Aug. 2004, doi: 10.1016/j.jbiotec.2004.04.019.

[159] N. Patelli *et al.*, “Structure and magnetic properties of Fe-Co alloy nanoparticles synthesized by pulsed-laser inert gas condensation,” *Journal of Alloys and Compounds*, vol. 890, p. 161863, Jan. 2022, doi: 10.1016/j.jallcom.2021.161863.

[160] R. B. Da Silva *et al.*, “Influence of the gas atmosphere on the obtention of cobalt and iron based nanocomposites and core/shell nanoparticles by calcination in the presence of chitosan,” *Journal of Solid State Chemistry*, vol. 312, p. 123225, Aug. 2022, doi: 10.1016/j.jssc.2022.123225.

[161] M.-S. Jang *et al.*, “High-throughput thermal plasma synthesis of Fe_xCo_{1-x} nano-chained particles with unusually high permeability and their electromagnetic wave absorption properties at high frequency (1–26 GHz),” *Nanoscale*, vol. 13, no. 27, pp. 12004–12016, 2021, doi: 10.1039/D1NR01845K.

[162] A. Shokuhfar and S. S. S. Afghahi, “Size Controlled Synthesis of FeCo Alloy Nanoparticles and Study of the Particle Size and Distribution Effects on Magnetic Properties,” *Advances in Materials Science and Engineering*, vol. 2014, pp. 1–10, 2014, doi: 10.1155/2014/295390.

[163] T. Burkert, L. Nordström, O. Eriksson, and O. Heinonen, “Giant Magnetic Anisotropy in Tetragonal FeCo Alloys,” *Phys. Rev. Lett.*, vol. 93, no. 2, Art. no. 2, Jul. 2004, doi: 10.1103/PhysRevLett.93.027203.

[164] Y. Kota and A. Sakuma, “Degree of Order Dependence on Magnetocrystalline Anisotropy in Body-Centered Tetragonal FeCo Alloys,” *Appl. Phys. Express*, vol. 5, no. 11, Art. no. 11, Oct. 2012, doi: 10.1143/APEX.5.113002.

[165] D. Odkhuu and S. C. Hong, “First-Principles Prediction of Possible Rare-Earth Free Permanent Magnet of Tetragonal Fe Co with Enhanced Magnetic Anisotropy and Energy Product through Interstitial Nitrogen,” *Phys. Rev. Applied*, vol. 11, no. 5, Art. no. 5, May 2019, doi: 10.1103/PhysRevApplied.11.054085.

[166] T. Nishizawa and K. Ishida, “The Co−Fe (Cobalt−Iron) system,” *Bulletin of Alloy Phase Diagrams*, vol. 5, no. 3, pp. 250–259, Jun. 1984, doi: 10.1007/BF02868548.

[167] T. Hasegawa and Y. Seki, “TEM-based crystal structure analysis of body-centered tetragonal structure in non-epitaxial FeCo film with added V and N,” *Materials Letters*, vol. 313, p. 131734, Apr. 2022, doi: 10.1016/j.matlet.2022.131734.

[168] T. Hasegawa, T. Niibori, Y. Takemasa, and M. Oikawa, “Stabilisation of tetragonal FeCo structure with high magnetic anisotropy by the addition of V and N elements,” *Sci Rep*, vol. 9, no. 1, Art. no. 1, Dec. 2019, doi: 10.1038/s41598-019-41825-7.

[169] J. Shen, M. Gong, Q. Dai, and S. Ren, “Surface-Stress-Induced Phase Transformation of Ultrathin FeCo Nanowires,” *ACS Appl. Mater. Interfaces*, vol. 8, no. 1, pp. 31–36, Jan. 2016, doi: 10.1021/acsami.5b10991.

[170] P. Warnicke, G. Andersson, M. Björck, J. Ferré, and P. Nordblad, “Magnetic anisotropy of tetragonal FeCo/Pt(001) superlattices,” *J. Phys.: Condens. Matter*, vol. 19, no. 22, Art. no. 22, Jun. 2007, doi: 10.1088/0953-8984/19/22/226218.

[171] L. Zhang, L. Liu, and S. Ishio, “Investigation of magnetic anisotropy and magnetization process of tetragonal distorted FeCo multilayer films,” *Materials Letters*, vol. 160, pp. 238–241, Dec. 2015, doi: 10.1016/j.matlet.2015.07.087.

[172] M. Gong, A. Kirkeminde, M. Wuttig, and S. Ren, “Phase Transformation-Induced Tetragonal FeCo Nanostructures,” *Nano Lett.*, vol. 14, no. 11, Art. no. 11, Nov. 2014, doi: 10.1021/nl5030485.

[173] *The Structures of Alloys of Iron*. Elsevier, 1966. doi: 10.1016/C2013-0-01893-2.

[174] W. Pepperhoff and M. Acet, *Constitution and Magnetism of Iron and its Alloys*. in Engineering Materials. Berlin, Heidelberg: Springer Berlin Heidelberg, 2001. doi: 10.1007/978-3-662-04345-5.

[175] G. V. Kurdjumov and A. G. Khachaturyan, “Nature of axial ratio anomalies of the martensite lattice and mechanism of diffusionless γ → α transformation,” *Acta Metallurgica*, vol. 23, no. 9, pp. 1077–1088, Sep. 1975, doi: 10.1016/0001-6160(75)90112-1.

[176] G.V. Kurdyumov Institute for Metal Physics, NAS of Ukraine, 36 Academician Vernadsky Blvd., UA-03680 Kyiv-142, Ukraine *et al.*, “Carbon Distribution in Low-Temperature Isothermal Iron-Based Martensite and Its Tetragonality,” *Metallofiz. Noveishie Tekhnol.*, vol. 38, no. 4, pp. 455–475, Jun. 2016, doi: 10.15407/mfint.38.04.0455.

[177] V. G. Gavriljuk, A. V. Tarasenko, and A. I. Tyshchenko, “Low temperature ageing of the freshly formed Fe-C and Fe-N martensites,” *Scripta Materialia*, vol. 43, no. 3, pp. 233–238, Jul. 2000, doi: 10.1016/S1359-6462(00)00396-1.

[178] Y. Gao and Y. Wang, “Hidden pathway during fcc to bcc/bct transformations: Crystallographic origin of slip martensite in steels,” *Phys. Rev. Materials*, vol. 2, no. 9, Art. no. 9, Sep. 2018, doi: 10.1103/PhysRevMaterials.2.093611.

[179] W. K. Choo and R. Kaplow, “Mössbauer measurements on the aging of iron-carbon martensite,” *Acta Metallurgica*, vol. 21, no. 6, pp. 725–732, Jun. 1973, doi: 10.1016/0001-6160(73)90036-9.

[180] P. M. Gielen and R. Kaplow, “Mossbauer effect in iron-carbon and iron-nitrogen alloys,” *Acta Metallurgica*, vol. 15, no. 1, pp. 49–63, Jan. 1967, doi: 10.1016/0001-6160(67)90155-1.

[181] A. Sahoo and V. R. R. Medicherla, “Fe-Ni Invar alloys: A review,” *Materials Today: Proceedings*, vol. 43, pp. 2242–2244, 2021, doi: 10.1016/j.matpr.2020.12.527.

[182] D. G. Rancourt and R. B. Scorzelli, “Low-spin γ-Fe⍰Ni(γLS) proposed as a new mineral in Fe⍰Ni-bearing meteorites: epitaxial intergrowth of γLS and tetrataenite as a possible equilibrium state at ∼20–40 at% Ni,” *Journal of Magnetism and Magnetic Materials*, vol. 150, no. 1, pp. 30–36, Sep. 1995, doi: 10.1016/0304-8853(95)00089-5.

[183] L. J. Swartzendruber, V. P. Itkin, and C. B. Alcock, “The Fe-Ni (iron-nickel) system,” *JPE*, vol. 12, no. 3, pp. 288–312, Jun. 1991, doi: 10.1007/BF02649918.

[184] Y. A. Abdu, T. Ericsson, and H. Annersten, “Coexisting antiferromagnetism and ferromagnetism in mechanically alloyed Fe-rich Fe–Ni alloys: implications regarding the Fe–Ni phase diagram below 400°C,” *Journal of Magnetism and Magnetic Materials*, vol. 280, no. 2–3, pp. 395–403, Sep. 2004, doi: 10.1016/j.jmmm.2004.03.036.

[185] J. F. Albertsen, J. M. Knudsen, N. O. Roy-Poulsen, and L. Vistisen, “Meteorites and Thermodynamic Equilibrium in f.c.c. Iron-Nickel Alloys (25-50% Ni),” *Phys. Scr.*, vol. 22, no. 2, pp. 171–175, Jan. 1980, doi: 10.1088/0031-8949/22/2/014.

[186] J. F. Albertsen, H. P. Nielsen, and V. F. Buchwald, “On the Fine Structure of Meteoritical Taenite/Tetrataenite and its Interpretation,” *Phys. Scr.*, vol. 27, no. 4, pp. 314–320, Apr. 1983, doi: 10.1088/0031-8949/27/4/015.

[187] J. F. Albertsen, J. M. Knudsen, and G. B. Jensen, “Structure of taenite in two iron meteorites,” *Nature*, vol. 273, no. 5662, pp. 453–454, Jun. 1978, doi: 10.1038/273453a0.

[188] B. Zhang, N.-E. Fenineche, H. Liao, and C. Coddet, “Magnetic properties of in-situ synthesized FeNi3 by selective laser melting Fe-80%Ni powders,” *Journal of Magnetism and Magnetic Materials*, vol. 336, pp. 49–54, Jun. 2013, doi: 10.1016/j.jmmm.2013.02.014.

[189] R. B. Scorzelli and J. Danon, “Mössbauer Spectroscopy and X-Ray Diffraction Studies of Fe-Ni Order-Disorder Processes in a 35% Ni Meteorite (Santa Catharina),” *Phys. Scr.*, vol. 32, no. 2, pp. 143–148, Aug. 1985, doi: 10.1088/0031-8949/32/2/010.

[190] R. B. Scorzelli, “[No title found],” *Hyperfine Interactions*, vol. 110, no. 1/2, pp. 143–150, 1997, doi: 10.1023/A:1012679517295.

[191] R. B. Scorzelli and E. Dos Santos, “Meteoritic Fe-Ni alloys: A review of 57Fe Mössbauer spectroscopy studies,” *Geochemistry*, vol. 79, no. 4, p. 125547, Dec. 2019, doi: 10.1016/j.chemer.2019.125547.

[192] J. Paulevé, D. Dautreppe, J. Laugier, and L. Néel, “Une nouvelle transition ordre-désordre dans Fe-Ni (50-50),” *J. Phys. Radium*, vol. 23, no. 10, pp. 841–843, 1962, doi: 10.1051/jphysrad:019620023010084100.

[193] L.-Y. Tian *et al.*, “Density Functional Theory description of the order-disorder transformation in Fe-Ni,” *Sci Rep*, vol. 9, no. 1, p. 8172, Jun. 2019, doi: 10.1038/s41598-019-44506-7.

[194] G. J. Dienes and A. C. Damask, “Radiation Enhanced Diffusion in Solids,” *Journal of Applied Physics*, vol. 29, no. 12, pp. 1713–1721, Dec. 1958, doi: 10.1063/1.1723032.

[195] A. Christiansen, L. Larsen, H. Roy-Poulsen, N. O. Roy-Poulsen, L. Vistisen, and J. M. Knudsen, “Iron-Nickel Alloys in a Taenite Lamella from the Iron Meteorite Cape York as Measured by Conversion

Electron Mössbauer Spectroscopy," *Phys. Scr.*, vol. 29, no. 1, pp. 94–96, Jan. 1984, doi: 10.1088/0031-8949/29/1/016.

[196] A. Kovács *et al.*, "Discovery and Implications of Hidden Atomic-Scale Structure in a Metallic Meteorite," *Nano Lett.*, vol. 21, no. 19, pp. 8135–8142, Oct. 2021, doi: 10.1021/acs.nanolett.1c02573.

[197] M. Gong and S. Ren, "Phase Transformation-Driven Surface Reconstruction of FeNi Nanostructures," *Chem. Mater.*, vol. 27, no. 22, pp. 7795–7800, Nov. 2015, doi: 10.1021/acs.chemmater.5b03736.

[198] S. Goto *et al.*, "Synthesis of single-phase L10-FeNi magnet powder by nitrogen insertion and topotactic extraction," *Sci Rep*, vol. 7, no. 1, p. 13216, Oct. 2017, doi: 10.1038/s41598-017-13562-2.

[199] Y. Miura, S. Ozaki, Y. Kuwahara, M. Tsujikawa, K. Abe, and M. Shirai, "The origin of perpendicular magneto-crystalline anisotropy in L1 $_0$ –FeNi under tetragonal distortion," *J. Phys.: Condens. Matter*, vol. 25, no. 10, p. 106005, Mar. 2013, doi: 10.1088/0953-8984/25/10/106005.

[200] M. Werwiński and W. Marciniak, "*Ab initio* study of magnetocrystalline anisotropy, magnetostriction, and Fermi surface of L1 $_0$ FeNi (tetrataenite)," *J. Phys. D: Appl. Phys.*, vol. 50, no. 49, p. 495008, Dec. 2017, doi: 10.1088/1361-6463/aa958a.

[201] A. M. Montes-Arango *et al.*, "Discovery of process-induced tetragonality in equiatomic ferromagnetic FeNi," *Acta Materialia*, vol. 116, pp. 263–269, Sep. 2016, doi: 10.1016/j.actamat.2016.06.050.

[202] X. G. Liu, D. Y. Geng, C. J. Choi, J. C. Kim, and Z. D. Zhang, "Magnetic properties, complex permittivity and permeability of FeNi nanoparticles and FeNi/AlO x nanocapsules," *J Nanopart Res*, vol. 11, no. 8, pp. 2097–2104, Nov. 2009, doi: 10.1007/s11051-008-9575-9.

[203] E. Kaniukov *et al.*, "FeNi nanotubes: perspective tool for targeted delivery," *Appl Nanosci*, vol. 9, no. 5, pp. 835–844, Jul. 2019, doi: 10.1007/s13204-018-0762-4.

[204] D. Guenzburger and J. Terra, "Theoretical study of magnetism and Mössbauer hyperfine interactions in ordered FeNi and disordered fcc Fe-rich Fe–Ni alloys," *Phys. Rev. B*, vol. 72, no. 2, p. 024408, Jul. 2005, doi: 10.1103/PhysRevB.72.024408.

[205] H. Piet *et al.*, "Superstoichiometric Alloying of H and Close-Packed FeNi under High Pressures: Implications for Hydrogen Storage in Planetary Cores," In Review, preprint, Nov. 2020. doi: 10.21203/rs.3.rs-103113/v1.

[206] P. Rani, J. Thakur, A. Taya, and M. K. Kashyap, "Effect of tetragonal distortion induced by interstitial C-doping in L10-FeNi," presented at the DAE SOLID STATE PHYSICS SYMPOSIUM 2018, Hisar, Haryana, India, 2019, p. 030497. doi: 10.1063/1.5113336.

Chapter 2. Experimental Characterization Techniques

2.1 X-ray Diffraction from Polycrystalline Materials

2.1.1 General description

The study of X-ray diffraction from polycrystalline materials constitutes the first, most common and simple procedure used to identify qualitatively and quantitatively the crystal phases observed in solid materials. For that reason, X-ray diffraction is denoted as the most popular characterization technique for the analysis of the atomic structure and composition of such crystalline materials. This technique has been implemented to characterize the synthetic polycrystalline samples produced in this thesis, and the fundamental principles, as well as the means of the appropriate experimental setups are described here.

The diffraction of X-rays is essentially a scattering phenomenon in which the atoms of a crystal scatter incident X-rays in all directions and in some of these directions the scattered beams are completely in phase and so reinforce each other to form an interference pattern of diffracted beams.

This phenomenon is based on the production of high energetic photons, derived from the interactions of the fast moving, accelerated from a high-voltage (~35 – 40 kV), electrons emitted from a tungsten filament, with the atoms of a metallic target inside the X-ray tube. These electrons bombard (and decelerate in) the metallic target (e.g. copper- Cu, cobalt-Co, molybdenum-Mo). From this procedure a continuous spectrum of photons (white radiation or Bremsstrahlung) is produced, since the fast-moving electrons are scattered inelastic and decelerate, together with the characteristic emission lines of the atomic electronic transitions (K_α, K_β, L_α, L_β, M_α etc.) in specific wavelengths. The emission lines are attributed to the ionization effect of those fast-moving electrons possessing the appropriate kinetic energy to knock electrons of the target's metal atoms out of the inner shells (K, L, M). This effect prompts an immediate inner shell electron replacement from an outer shells' electron, emitting energy in the process. The energy emitted is in the form of a photon with a definite wavelength, attributed to the characteristic K, L, M radiation. The existence of strong and sharp characteristic radiation lines disposed with definite wavelengths is the reason that makes the X-ray diffraction possible, since diffraction experiments require the use of monochromatic and coherent radiation [1], [2], [3].

X-rays interact with the materials they collide, in different ways, nevertheless, scattering is attained mostly from electrons having atomic (localized) or conductive (free) characteristics. Scattering may be elastic, in which the wavelength is preserved, and the scattered ray is coherent with the incident ray, or inelastic (e.g. Compton). It is known that the localized electrons of the atoms in a material can scatter coherently X-rays, in contrast to the loosely connected or free electrons, which scatter incoherently. The ability of X-rays to be scattered from atoms or ions elastically and coherently depends on the number of localized electrons on them, therefore from the type of element and its valence, as well as the wavelength and the scattering angle via the atomic scattering factor (*f*). Therefore, X-rays can be utilized for the examination and analysis of the periodic atomic crystalline structure of solid materials through diffraction phenomena [1], [2], [3].

In the powder X-ray diffraction method, the solid material to be examined is ground to a very fine powder comprised of small crystallites in a mosaic morphology, which is placed in an appropriate holder. The atoms of each crystallite are arranged in a periodic long-range order in the form of planes and thus, this arrangement creates the Bragg's law conditions for constructive interference of the X-rays scattered coherently from all the atoms in all the planes of a crystal. For this reason, the wavelength of the diffracted X-rays has to be in the same order of magnitude (~Å) as the interatomic distances between the scattering centers and consequently the normal distances between the parallel atomic planes of a crystal. This requirement follows from Bragg's law,

$$n\lambda = 2dsin\theta, \quad (2.1)$$

where λ is the wavelength of the incident and diffracted beam, d is the perpendicular distance between the parallel atomic lattice planes in the crystal, θ is the incident and diffracted angle formed by the corresponding directions of the X-ray incident and diffracted beams and the parallel crystal planes, Figure 2.1. Since sinθ cannot exceed unity,

$$\frac{n\lambda}{2d} = sin\theta < 1 \quad (2.2)$$

nλ must be less than 2d. For diffraction, the smallest value of n is 1. Therefore, the condition for diffraction at any observable angle 2θ is,

$$\lambda < 2d \Rightarrow \lambda = 2dsin\theta. \quad (2.3)$$

$$QK - PR = PKcos\theta - PKcos\theta = 0. \quad (2.4)$$

$$ML + LN = d'sin\theta + d'sin\theta. \quad (2.5)$$

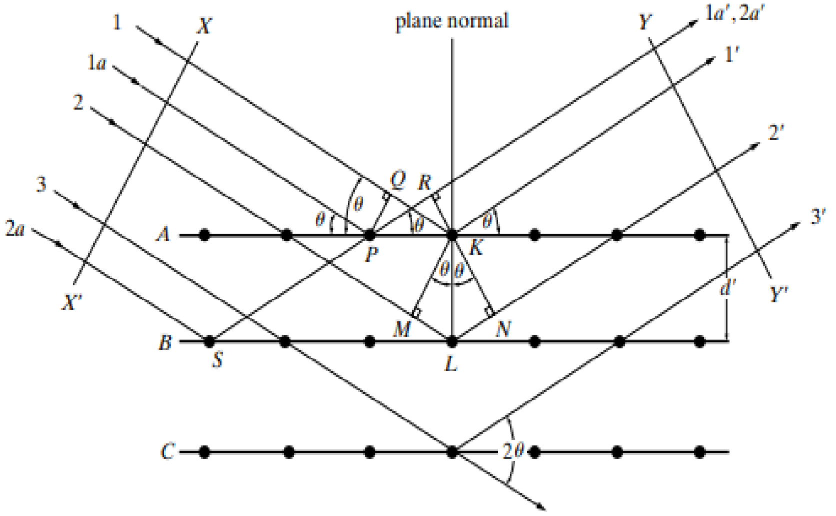

Figure 2.1 Diffraction of X-rays by the parallel atomic planes of a crystal and the respective path differences of the reflected X-rays beam following Bragg's law [1].

By means of elastic beam scattering of X-rays, from the periodic atomic crystal lattices of the sample, the appropriate diffraction conditions are developed, resulting in constructive superposition of the diffracted X-rays in specific spatial locations.

There are many advanced geometries regarding the diffraction from polycrystalline powder samples and the most popular instrumentation refers to the Bragg-Brentano geometry. In this geometry the material to be examined is spread and formed to a very fine powder comprised of small (~ μm) crystallites or consolidated microscopic aggregates in a mosaic morphology, where the atoms of each crystallite are arranged in a periodic long-range order in the form of planes and thus, this arrangement creates the Bragg's law conditions for constructive interference of the X-rays scattered coherently from all the atoms in all the appropriate planes of a crystal powder sample, which is spread in the form of a horizontal parallel plane on a suitable formed holder. This plane is considered to coincide with the atomic lattice planes of the crystallites with Miller indices (hkl). However, due to their small size and large number, these crystallites are randomly oriented within the powder sample. This means, that for every possible and available atomic lattice plane of a crystal with Miller indices (hkl) there will be a subset of crystallites which are properly oriented with their atomic planes parallel to the samples' plane in order to diffract the incident monochromatic beam (K_α) at the appropriate angle θ as shown in Figure 2.2 [1], [2], [3]. Due to the very large number of crystallites the statistical probabilities of the number of crystallites in each subgroup are expected to be roughly equal to each other, unless other conditions as preferred orientation of some particular atomic planes occurs, which disturbs the statistical equality [1].

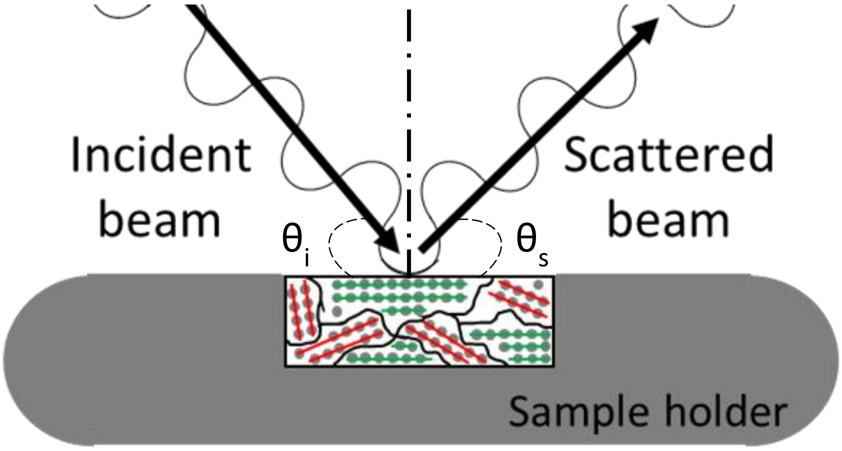

Figure 2.2 Diffraction of X-rays at the particular incident and diffracted angles θ occurs only when the incident X-ray beam is scattered by the subgroup of crystallites' appropriate lattice planes with Miller indices (hkl) (grey atoms bisected by green lines), that coincide with the parallel to the holder's horizontal plane and fulfill Bragg's law conditions. The same crystallites' lattice planes which are however randomly oriented (grey atoms bisected by red lines) do not scatter the X-rays in a constructive manner. Other subgroups of crystals with different (hkl) indices and different d-spacings give constructive interference at different θ angles when also their corresponding lattice planes coincide with the parallel to the holder's horizontal plane.

To provide the necessary equality between the incident and diffracted θ angles and the sample's horizontal plane, the diffractometer parts, source and detector, of the Bruker Advance D8 diffractometer setup used in our experiments, are moving coherency while the powder specimen is kept firm in the form of a horizontal flat plate (θ - θ geometry), Figure 2.3.

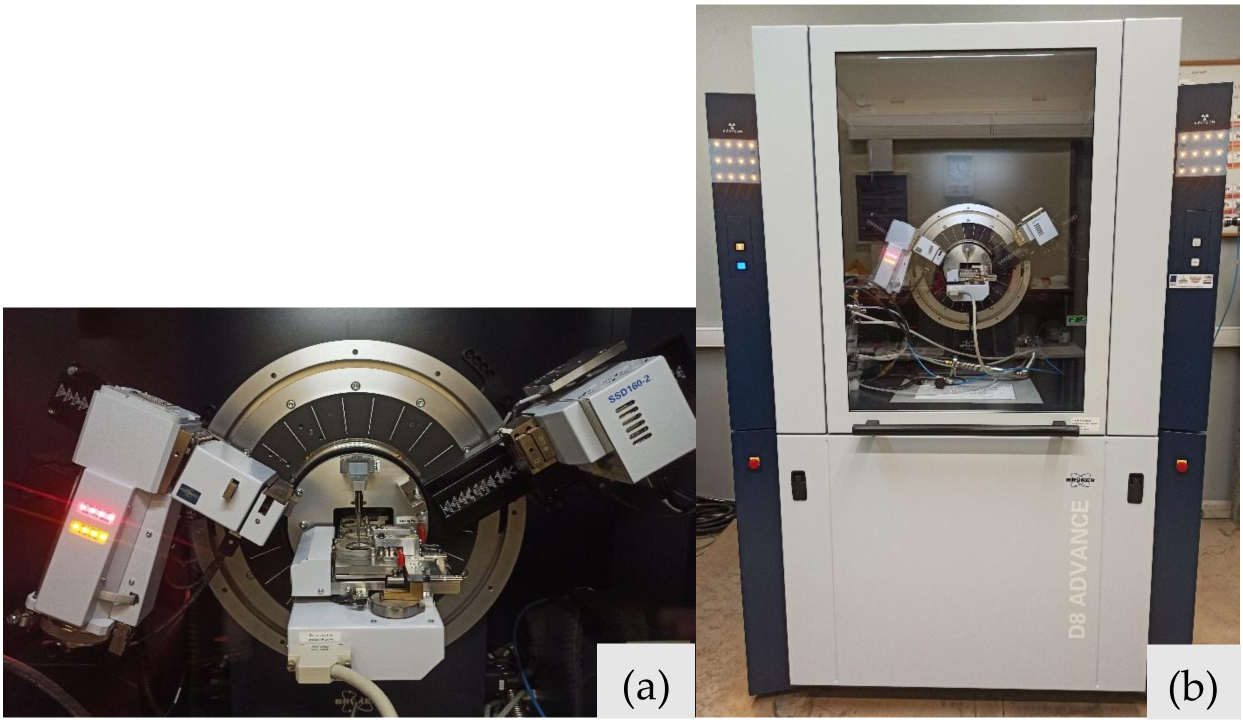

Figure 2.3 Schematic representation of the moving parts of the θ-θ goniometer in the X-ray diffraction setup inside the dome of the diffractometer, during scanning in a range of angles with a stable holder's plane and moving X-ray source and detector (a). General view of the Bruker Advance D8 diffractometer (b).

2.1.2 Diffraction Peak Broadening from Nanostructured Samples

In a real powder X-ray diffraction diagram the shape of the diffraction peaks acquires broadenings. There is a variety of factors contributing to this broadening, more important of which is the presence of various types of defects that can modulate the peaks' shape formation. To this manner,small crystal or grain size can be thought of as a kind of defect and can alter the widths of diffraction peaks. In the limit of 'grain' size approaching that of a finite number of unit cells, as are the cases found in nanostructured materials, sharp diffraction peaks no longer exist, and important information about this kind of materials can be received from how they diffract X-rays. This can be better described by the form of the curve of diffracted intensity vs. 2θ (Figure 2.4), which on the one hand, (2.4a) illustrates the X-ray diffraction diagram of a real sample and on the other hand, (2.4b) the X-ray diffraction diagram of an ideal sample, emerging only at the exact Bragg angle.

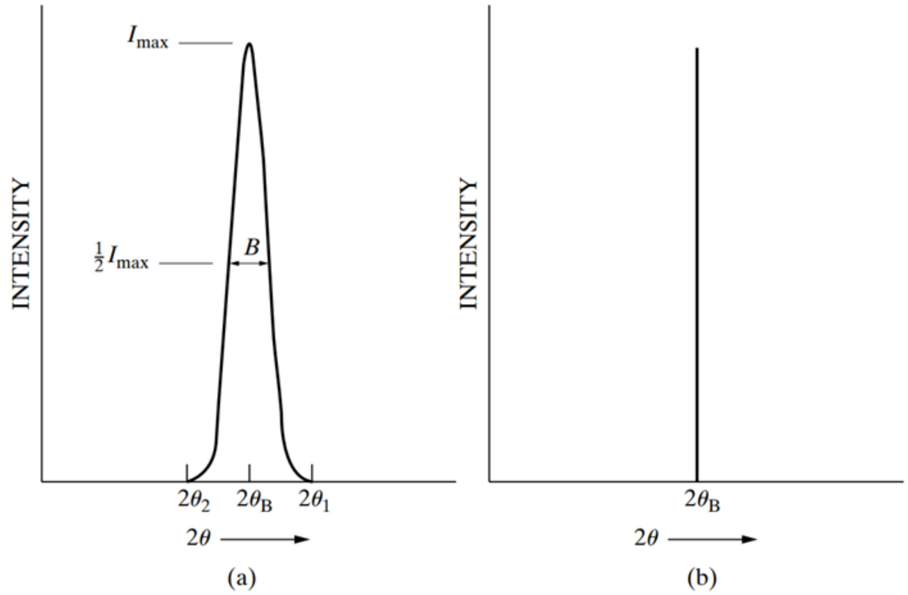

Figure 2.4 Schematic representation of the effect of fine crystalline size on the diffraction curve around the Bragg angle (a), and hypothetical case where diffraction occurs only exact at the Bragg angle (b) [1].

Based on this argument, the presence of two limiting angles around the Bragg angle $2\theta_B$, $2\theta_1$ and $2\theta_2$, are therefore defined, at which the diffracted intensity is taken to be attenuated to zero, or to the background value. The width of the diffraction curve (B) is measured in radians at the intensity equal to the half of the peak's maximum intensity, and this measure of B is defined as the full-width at half maximum (FWHM). From the measured widths B of a series of diffraction peaks belonging to a specific crystalline nanostructured phase it is easy to estimate the size of very small crystals of this phase using the relation known as the Scherrer's formula (equation 2.6) [1], [2], [3].

$$t = \frac{\lambda}{B cos\theta_B}. \quad (2.6)$$

2.2 Transmission Electron Microscopy

2.2.1 General Description

In recent years, the transmission electron microscope (TEM) has become the preferred instrument for generating atomic-resolution images of materials, identifying defects, and providing spectroscopic and diffraction data from sub-nanometer areas. Significant progress in electron microscopy has greatly enhanced the ability to examine atomic structures in detail, benefiting research in physics, chemistry, materials science, biology, and medicine. TEMs are offered with a wide range of characterization techniques with high spatial and analytical resolution, techniques which render them crucial for the comprehensive study of nanoscale materials.

Today, TEMs are arguably the most efficient and versatile tools for characterizing materials across spatial ranges from the atomic scale, through the expanding 'nano' regime (from < 1 nm to ~100 nm), up to the micrometer level and beyond [4]. The fundamental principle behind electron microscopy techniques is the interaction between an electron beam, which has much shorter wavelengths than visible light, and the atoms in a sample, in order to resolve much smaller features than traditional optical microscopy. Since electrons are a form of ionizing radiation, one key benefit of their use is that they generate a variety of secondary signals when they collide with the sample. These interactions result in various phenomena, including directly transmitted electrons, secondary and backscattered electrons, elastically and inelastically scattered electrons, characteristic and continuum X-rays, Auger electrons, visible light, and photons across different energy levels (Figure 2.5) [4].

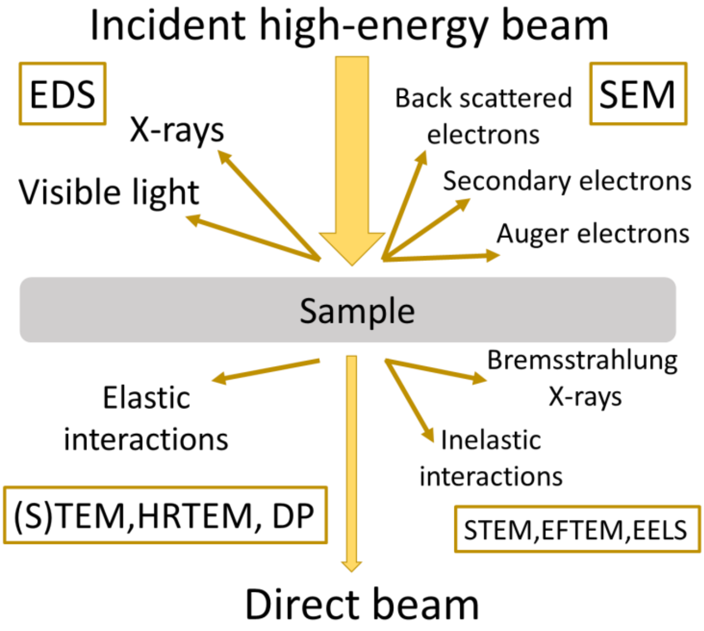

Figure 2.5 Signals generated when a high-energy beam of electron interacts with a thin specimen. Most of these signals can be detected in different analytical methods [reference 4].

TEMs instrumentation can be divided into three main components: the illumination system, the objective lens and specimen stage, and the imaging system [4]. The illumination system comprises the electron gun, which can be either a thermionic or field-emission source, and the concentric magnetic lenses (condenser lenses). To avoid electron emission instabilities and maintain good TEM performance, the gun section must operate under ultra-high vacuum (10^{-10} mbar) conditions. The emitted electron beam is accelerated to the desired energy using high-voltage (typically between 80 – 300 kV), giving the electron the energy needed to pass through the entire specimen. The first condenser lens controls the beam's spot size, while the second manages the beam's convergence angle, with their role being to take electrons from the source and transfer them to the specimen. The objective lens and the specimen holder/stage system form the heart of the TEM. This is where all beam-specimen interactions occur. The electron beam is directed through a very thin sample (typically less than 100 nanometers thick). As the electrons pass through the specimen, they interact with the atoms within it, and some are scattered, while others pass through unaffected, creating the various images and diffraction patterns that are subsequently magnified for viewing and recording. The objective lens is the most important lens in a TEM because its quality determines the quality of all the information about the specimen. After passing through the sample, the unscattered and scattered electrons are focused by several electromagnetic lenses to magnify the image or diffraction pattern produced by the objective lens and to focus these on the viewing screen or computer display via a detector or TV camera (Imaging system). The magnifying lenses are referred to as intermediate and diffraction lenses, and the final lens is the projector lens, which projects the final image or diffraction pattern onto the viewing screen or detector. The so-called bright field image generated is based on the interactions between the electrons and the structures of the sample, such as its atomic arrangement, density and composition (Figure 2.6) [4], [5].

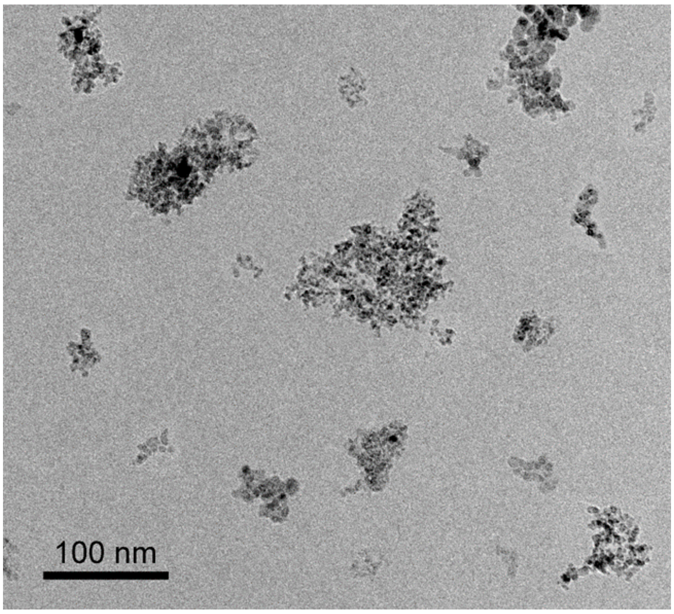

Figure 2.6 Bright-field conventional TEM image of a nanostructured hybrid sample composed of the Fe-Co nanoparticles grown on nanodiamonds synthesized in this work.

These three components—the illumination system, specimen stage, and imaging system—are often collectively called the "column" for obvious reasons. In most TEMs, the electrons travel "down" the column due to its vertical construction (Figure 2.7) [4].

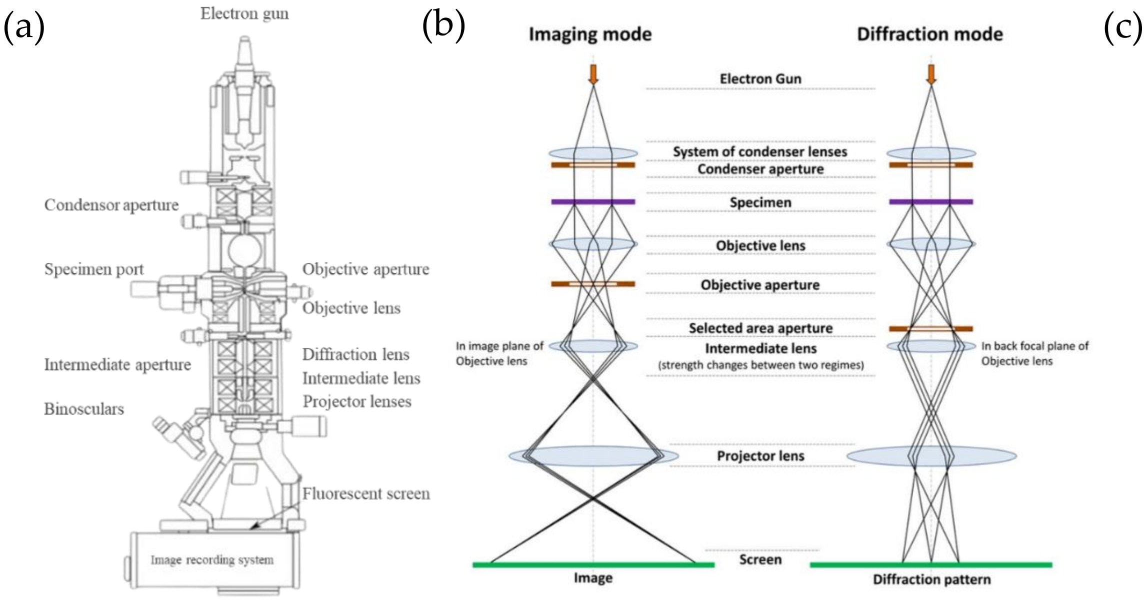

Figure 2.7 Optical components of a TEM (a). Schematic representation of the ray-path diagrams of the two basic operation modes, image (b) and diffraction (c) [4].

2.2.2 TEM Techniques

2.2.2.1 Scanning Transmission Electron Microscopy

Scanning TEM (STEM) is a variation of TEM, where the electron beam is focused into a fine probe and scanned across the sample, similar to the way scanning electron microscope (SEM) works. Instead of forming an image from electrons passing through the entire sample at once, the electron beam is moved in a scanning pattern across the sample and the detector collects the transmitted or scattered electrons at each point. STEM is often combined with techniques like electron energy loss spectroscopy and energy dispersive X-ray spectroscopy (EDS) to gather detailed elemental and chemical information from the sample. Moreover, STEM provides atomic-scale resolution imaging because the small probe size can resolve individual atoms. Also, by using different detectors STEM can create images using a variety of signals (bright-field, dark-field, high-angle annular dark-field (HAADF)) (Figure 2.8) [4], [5].

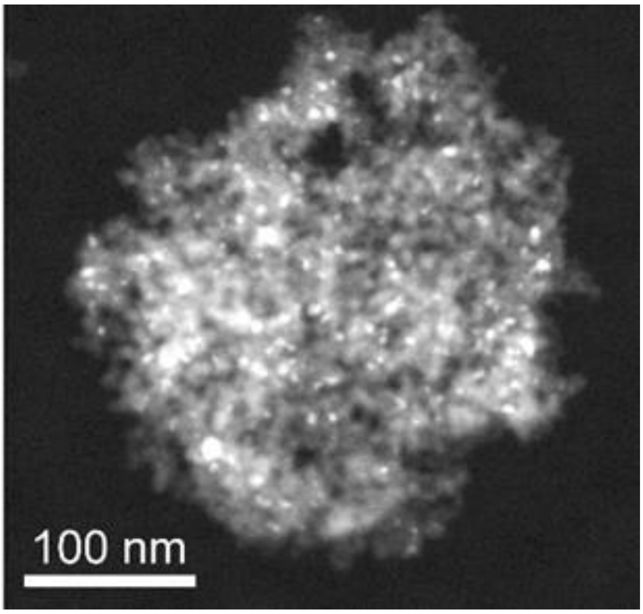

Figure 2.8 HAADF STEM image from a nanohybrid cluster of a nanostructured hybrid sample composed of Fe-Co nanoparticles grown on nanodiamonds synthesized in this work.

2.2.2.2 High-Resolution TEM

High-resolution TEM (HRTEM) refers to a mode of TEM that is optimized to achieve resolutions high enough to directly image the atomic structure of a sample, often to sub-Angstrom level. HRTEM allows the visualization of the arrangement of the atoms and the crystal structure of materials. HRTEM uses phase contrast, where the electron wave interference patterns form images of the atomic lattice planes in the sample. These patterns arise because of the small phase shifts in electron waves as the pass-through areas of different atomic potential within the sample. In HRTEM, the resolving power can be less than 1 Å meaning that individual atomic columns can be often distinguished (Figure 2.9). Both STEM and HRTEM are techniques that are used to extend the functionality of a conventional TEM for detailed atomic and structural analysis [4], [5].

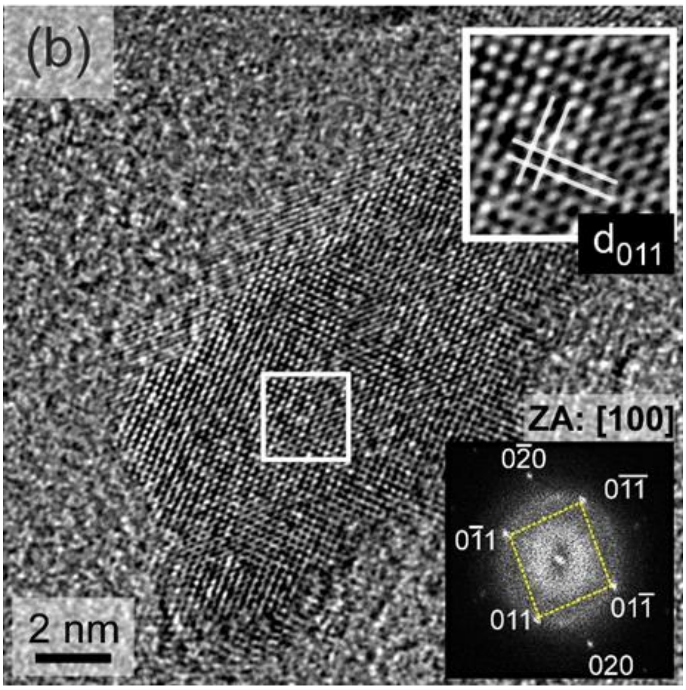

Figure 2.9 HRTEM image of a typical metallic Fe–Co alloy nanoparticle projected along the [100] direction of the cubic bcc lattice in a nanostructured hybrid sample composed of Fe-Co nanoparticles grown on nanodiamonds synthesized in this work. The closed packed {011} planes of a bcc Fe-Co metallic nanoparticle are distinguished in the white inset, while the fast Fourier transform of the specific area is also presented and the bcc Fe-Co $0\bar{1}1$, $0\bar{1}\bar{1}$, $01\bar{1}$ and 011 periodicities are annotated in the bottom right inset.

2.2.2.3 Energy Dispersive X-ray Spectroscopy

Energy dispersive X-ray spectroscopy (EDS or EDX) is an analytical technique used in combination with electron microscopy (TEM or SEM) to determine the elemental composition of a sample. It works by detecting X-rays emitted from the sample when it is bombarded by the electron beam. In particular, when the high-energy electron beam strikes the atoms in the sample is causes the ejection of inner-shell electrons from these atoms. To restore stability, electrons from higher-energy shells fall into the vacant lower-energy shell. During this transition the energy difference between the two shells is released as an X-ray photon. The energy of these emitted X-rays is characteristic of the specific element because each element has unique energy levels. From this process the EDS detector collects and measures the energy of these emitted X-rays. By analyzing the energy and intensity of the X-rays, the detector can determine what elements are present in the sample and their relative concentrations. EDS can be also used to create elemental maps by scanning the electron beam over an area of the sample and by recording the distribution of the elements (Figure 2.10). However, EDS is less sensitive to light elements (like H, C, N and O) compared to heavier elements, as X-ray emission from light elements can be weak and difficult to detect [4], [5].

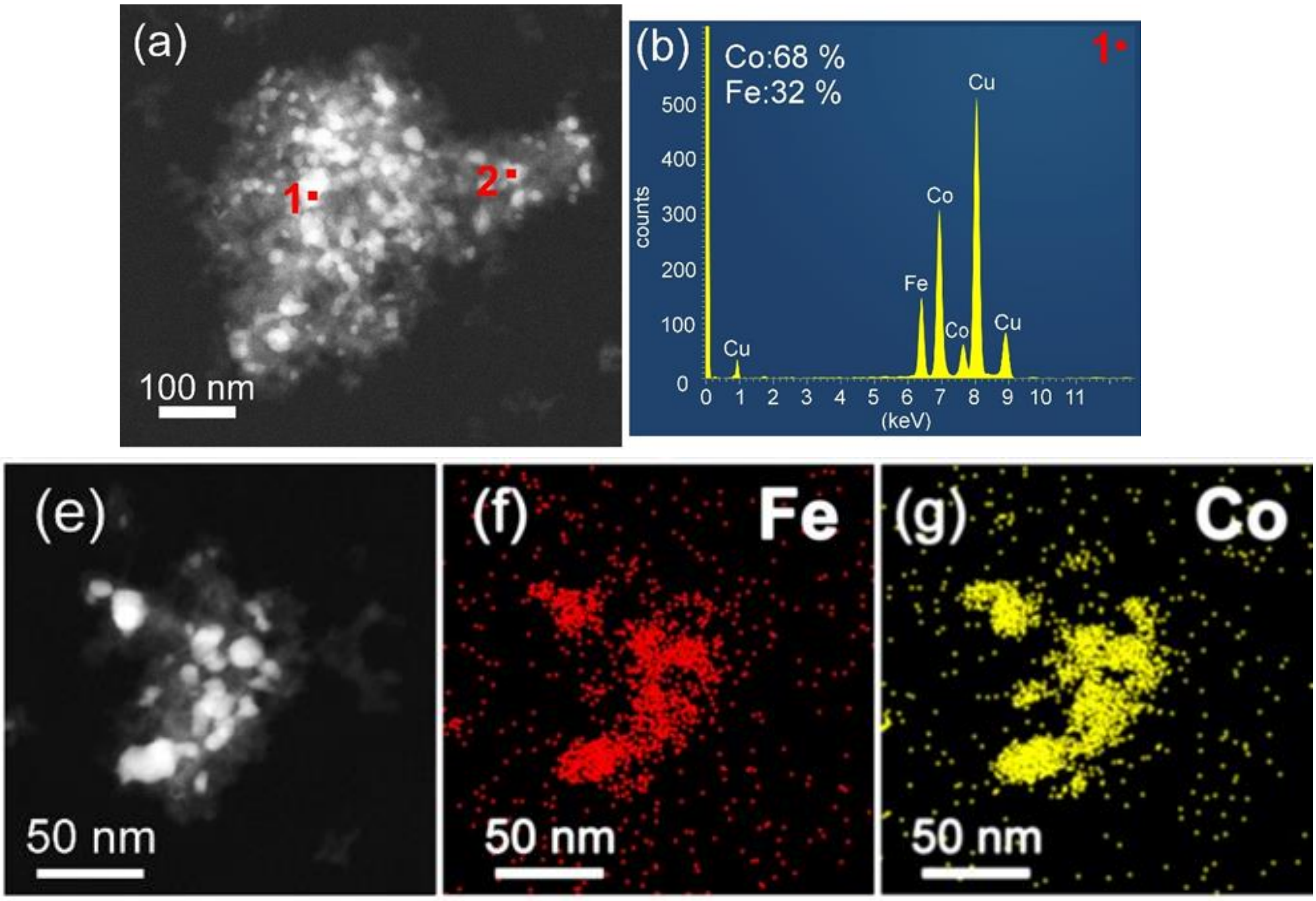

Figure 2.10 (a) HAADF-STEM image from a Fe-Co alloy nanoparticles/nanodiamonds hybrid cluster from a sample composed of Fe-Co nanoparticles grown on nanodiamonds synthesized in this work, showing positions with red color where point-EDX spectra were collected. (b) The spectrum from position point 1 of (a) and the corresponding atomic percentage. HAADF STEM image of another hybrid Fe–Co nanoparticles/nanodiamonds cluster (e) and the corresponding elemental distribution-mapping of Fe (f) and Co (g).

The characterization and study of the structural and morphological properties, stoichiometry, and particle size of the samples, under investigation in this thesis, were performed by using analytical TEM/STEM observations, which were carried out using a JEOL JEM 2011 TEM/HRTEM microscope with resolution capability of 0.19 nm and a 200 kV JEOL JEM F200 TEM/STEM microscope equipped with a Cold Field Emission Gun (CFEG) and an OXFORD X-Max 65T EDS detector (Figure 2.11).

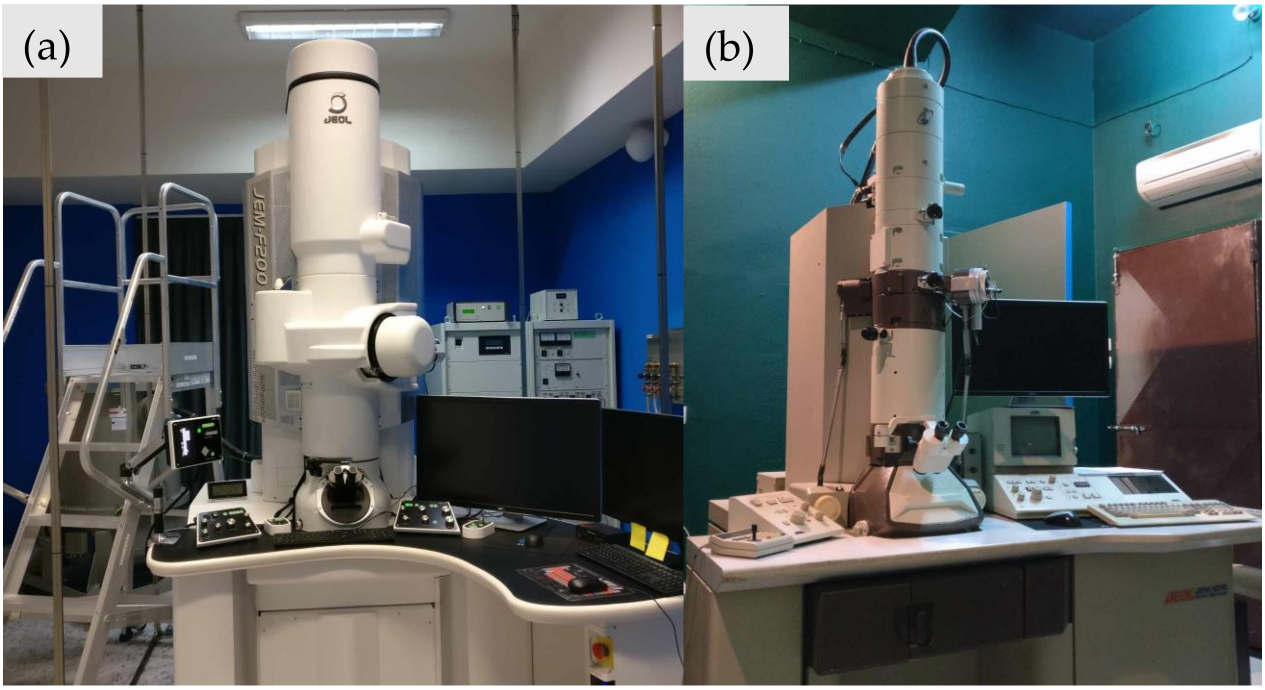

Figure 2.11 200kV JEOL JEM F200 TEM/STEM microscope (a) and JEOL JEM 2011 TEM/HRTEM microscope (b).

Prior to TEM observations, the samples were dispersed in ethanol and suspended in ultrasound for up to 60 min, while a single drop of a very dilute suspension of each sample was placed on a carbon-coated Cu grid and left to dry naturally by evaporation at ambient conditions.

2.3 Magnetic Measurements

2.3.1 General Description

Magnetic measurements are indispensable for understanding the electronic and magnetic properties of materials, both for fundamental study of the physical mechanisms responsible for their appearance, as well as for developing new applications which are contributing in the design of a wide range of procedures and devises used for navigation, electricity generation, energy conversion, magnetic data storage, sensors, catalysis, to refer to some, which are used in daily life. The most common instrument used for measuring the magnetic properties of materials is the vibrating sample magnetometer (VSM).

2.3.2 Vibrating Sample Magnetometer

A VSM device measures the magnetic properties of a material by detecting the magnetic moment of a sample. VSM’s operation is based on the magnetic flux change occurring in a coil when a magnetized sample is vibrating next to it. The sample, typically in the form of a small sphere, cylinder, disk, or arbitrary shaped specimen, is affixed to one end of a nonmagnetic rod, while the other end of the rod is attached to a precision mechanical vibrator. The sample is placed in a uniform applied magnetic field (H), generated by an electromagnet or a superconducting magnet, and vibrates at a fixed frequency, typical in a sinusoidal motion mode, in a direction (z) perpendicular to the applied magnetic field. As the sample vibrates, its magnetic moment generates a time-varying magnetic flux in the pickup coils positioned near the sample (Figure 2.12).

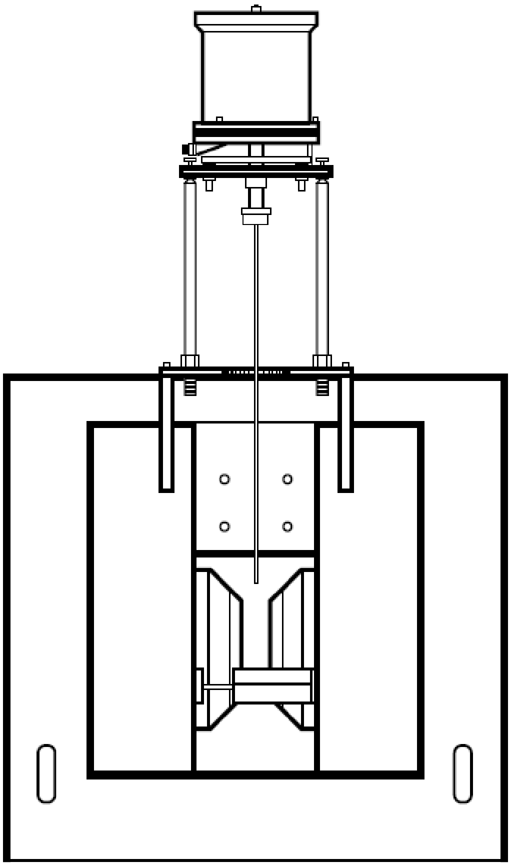

Figure 2.12 Typical VSM system (a), independent adjustment of the coarse sample along the X, Y and Z direction (b), and model of the coil sets fitted on the poles of the electromagnets (c). Lake Shore Cryotronics model 7300.

This changing flux induces a voltage (generated from the induced electromotive force (emf)) proportional to the magnetic moment of the sample. The induced voltage is detected and converted, through a system of lock-in amplifiers to remove the background vibration contribution, to a magnetic moment value produced by the sample alone. The magnetic moment of the sample can be measured at different applied field values, alignments of sample’s orientation to the direction of the applied magnetic field and temperatures, allowing thus to obtain different types of magnetic responses, like isothermal magnetization (M) vs. H (magnetic hysteresis) loops, M vs. temperatures curves, M vs. time curves, and other magnetic characteristics [6], [7].

The VSM is highly versatile and sensitive, capable of measuring both weak and strong magnetic substances. Standard versions can detect a magnetic moment of about 10^{-5} electromagnetic units (emu) or 10^{-8} A·m^2. This sensitivity necessitates strict cleanliness protocols when measuring small or weakly magnetic samples. VSMs can be suitable for measuring the magnetic properties of a wide range of materials allowing the study of saturation magnetization, coercivity, remanence and other high-field effects, of different types of magnetic materials, such as ferromagnetic, ferrimagnetic, antiferromagnetic, paramagnetic and diamagnetic materials. VSMs are also suitable for measuring and studying the magnetic properties both for bulk and nano-scaled materials, as well as magnetic thin films and multilayers. Moreover, since the vibration frequency is high, data collection is relatively a quick procedure. The VSM can be adapted for measurements at high and low temperatures, as only the sample placed at the tip of the vibrating rod need to be heated or cooled [8].

Measurements of the magnetic properties of the samples synthesized and studied in this thesis, were performed initially on a conventional VSM manufactured by LakeShore, model 7300 equipped with a 12 inch electromagnet, capable of delivering applied fields from a few G to 20 kG, a sensitivity ranging from $5\text{x}10^{-6}$ to 10^3 emu, and vector magnetic moment (both x and y directions) measuring ability (Figure 2.13).

Figure 2.13 Conventional Vibrating Sample Magnetometer setup, Lake Shore Cryotronics model 7300.

Apart from the stand-alone VSM setup, as the LakeShore's 7300 described above, magnetic measurements using a VSM can be performed on a probe-hosting system, such as Quantum Design's Physical Properties Measuring System (PPMS), using an appropriate VSM probe. Quantum Design's PPMS is a versatile and highly automated probe-hosting system designed to measure a variety of physical properties, including magnetic, electrical, thermal and optical properties of materials. The PPMS consists of different measurement options and probes that can measure a wide range of properties under controlled temperature, magnetic field and pressure conditions. The system can operate over a wide temperature range (typically from few K to room temperature or higher) and can apply magnetic fields up to several Tesla using superconducting magnets. Regarding the magnetic properties, in the PPMS, they can be measured by both direct current (DC) magnetometry (which measures static magnetic moments) and alternative current (AC) susceptibility (which measures the material's magnetic moment response to a time-varying magnetic field). The VSM probe of a PPMS performs measurements with even higher versatility and sensitivity than conventional VSMs, working in a DC magnetic hysteresis measurement with a magnetic moment sensitivity of 10^{-9} A·m^2 (10^{-6} emu) over the full 14 T field range. Sample rods for thin films, bulk materials, powder, or liquid samples are available, and samples up to 6.3 mm in diameter can be accommodated. A larger detection coil set can accommodate samples up to 12 mm in diameter but with reduced magnetic moment sensitivity. Furthermore, a sample heater can increase the temperature range up to 1000 K. AC susceptibility measurements in a PPMS device exhibit a magnetic moment sensitivity of 10^{-11} A·m^2 (10^{-8} emu). Such advantages render PPMS as high precision devices providing extremely accurate control over temperature and magnetic field, making them ideal for experiments requiring precise environmental conditions (Figure 2.14). In addition, PPMS are highly automated operating systems, allowing complex measurement sequences and data analysis to be performed, designed for a broader scope of material characterization with precise control [8].

The investigation of the magnetic properties of the samples were also performed on a VSM-equipped Physical Property Measurement System (Quantum Design PPMS equipped with an EverCool II dewar option) and a VSM-equipped Magnetic Property Measurement System (Quantum Design MPMS 3) through mass magnetization (M) and magnetic susceptibility (χ_g) measurements (Figure 2.14).

Figure 2.14 Physical Property Measuring System equipped with an EverCool II dewar option (a) and Magnetic Property Measurement System devices (b) (Quantum Design).

2.4 ^{57}Fe Mössbauer Spectroscopy

2.4.1 General Description

^{57}Fe Mössbauer spectroscopy is a powerful technique that offers valuable insights into the atomic, electronic, and magnetic structure of materials, especially to those containing iron. The Mössbauer effect, identified by Rudolph L. Mössbauer in 1957 [9], refers to the recoil-free emission and absorption of γ-ray photons by atomic nuclei bound in a solid. This effect has had a profound impact on fields such as physics, chemistry, biology and geology. Its distinctive characteristic is the production of resonance spectra with exceptionally narrow energy resolution, providing valuable information of the local environment of iron atoms or ions in a sample.

In chemistry, the practical use of the Mössbauer effect lies in its ability to identify subtle changes in energy interactions between the nucleus and neighboring nuclei electrons, which were previously deemed insignificant [10].

2.4.2 The Mössbauer Effect

For many years, the phenomenon of resonant absorption of electromagnetic radiation has been recognized through observations of light-induced electronic transitions in atoms or molecules. For such resonant absorption to occur, the quantum energy of the light must match the energy difference between the involved atomic or molecular electronic states. A similar mechanism applies to γ-radiation, involving nuclear states as emitters and absorbers. In these experiments, γ-ray emission is generally initiated by the decay of a radioactive precursor of the resonance nuclei with Z protons and N neutrons (Figure 2.15).

The nuclear reaction (such as α-decay, β-decay, or K-capture) results in the formation of an isotope (Z, N) in an excited state (e) with energy E_e. This excited nucleus has a finite mean lifetime τ and eventually transits to its ground state (g) with energy E_g, following an exponential decay law. This transition leads to the emission of a γ-photon with quantum energy $E_0 = E_e - E_g$, assuming the process occurs without recoil. Consequently, this γ-photon can be reabsorbed by a nucleus of the same type in its ground state, resulting in a transition to the excited state with energy E_e. [10], [11], [12]. This phenomenon, known as nuclear recoil-free resonance emission and absorption of γ-rays or the Mössbauer effect, earned Rudolf L. Mössbauer the Nobel Prize in Physics in 1961.

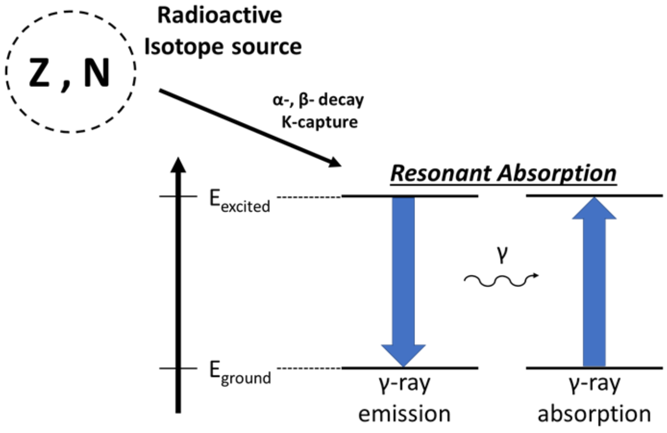

Figure 2.15 Recoilless nuclear resonance emission and absorption of γ-rays (Mössbauer effect).

To highlight the significance of recoilless emission and absorption on the experimental detection of the Mössbauer effect, it is essential to consider several factors, particularly the high quantum energy of the γ-radiation used in Mössbauer spectroscopy (E_0=10−100 keV), which is much higher than the typical energies encountered in optical spectroscopy (1-10 eV). Although the absolute widths of the energy levels involved in both spectroscopies are quite similar, the relative resolution resulting from the ratios of the widths of the nuclear levels to the transition energies are very small due to the high mean E_0 energies $\Delta E/E_0 = 10^{-13}$ or less (see Figure 2.16).

As a result, the recoil associated with the emission or absorption of a photon poses a significant challenge for nuclear transitions in gases and liquids. The energy loss for the γ-quanta is so substantial that emission and absorption lines do not overlap, making nuclear γ-resonance virtually impossible [10].

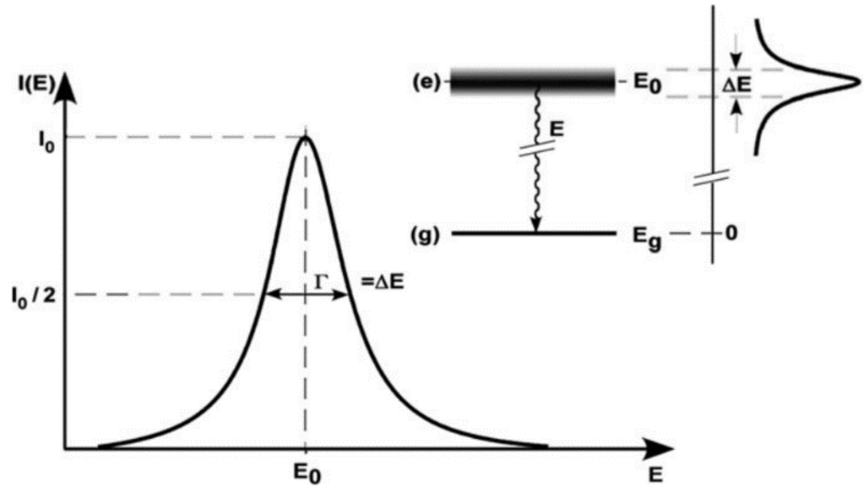

Figure 2.16 Intensity distribution I(E) for the emission of γ-rays with mean transition energy E0. The Heisenberg natural line width of the distribution, Γ = ħ/t, is determined by the mean lifetime τ (=t) of the excited state (e) [10].

The energy E0 of a nuclear or electronic excited state with an average lifetime τ can be measured with a precision limited by the time interval Δt available for the measurement. The energy E0 is subjected to an inherent uncertainty ΔE as described by the Heisenberg uncertainty principle applied to energy and time, which are conjugate variables:

$$\Delta E \cdot \Delta t \geqslant \hbar, \qquad (2.7)$$

where h = 2πħ is Planck's constant.

The relevant time interval Δt is approximately equal to the mean lifetime, Δt ~ τ. Consequently, ground states with an infinite lifetime have zero uncertainty in energy. As a result, when a group of identical nuclei, fixed in space, transitions from excited states (e) to ground states (g), the energy E of the emitted photon fluctuates around a central energy $E_0 = E_e - E_\gamma$. The intensity distribution of the emitted radiation follows a Lorentzian curve as a function of energy E, described by the Breit-Wigner equation [13]:

$$I(E) = \frac{\Gamma/(2\pi)}{(E-E_0)^2+(\Gamma/2)^2}. \qquad (2.8)$$

The emission line is centered at the mean transition energy E0 (see Figure 2.16). It can be noted that $I(E) = 1/2\, I(E_0)$ for $E = E_0 \pm \Gamma/2$, which defines Γ as the FWHM of the spectral line. Γ is referred to as the natural width of the excited nuclear state. Weisskopf and Wigner [14], demonstrated that the natural width Γ is related to the mean lifetime τ of the excited state by:

$$\Gamma \cdot \tau = \hbar. \qquad (2.9)$$

The ratio Γ/E_0, which represents the precision required in nuclear γ-absorption to align emission and absorption resonances, is crucial. For example, the first excited state of ^{57}Fe has a mean lifetime $\tau = t_{1/2}/\ln 2 = 1.43 \cdot 10^{-7}$ s. Using $\hbar = 6.5826 \cdot 10^{-16}$ eV s, the line width Γ is calculated as $4.55 \cdot 10^{-9}$ eV.

In nuclear γ-resonance it is assumed that a photon emitted by a nucleus with mean energy $E_0 = E_e - E_g$ carries the entire energy $E_0 = E_\gamma$. However, this assumption does not hold for free atoms or molecules, as photon emission imparts recoil to the nucleus. When a photon is emitted from a nucleus of mass M, the nucleus recoils moving with a velocity u in the opposite direction of the photon's propagation (Figure 2.17) [10].

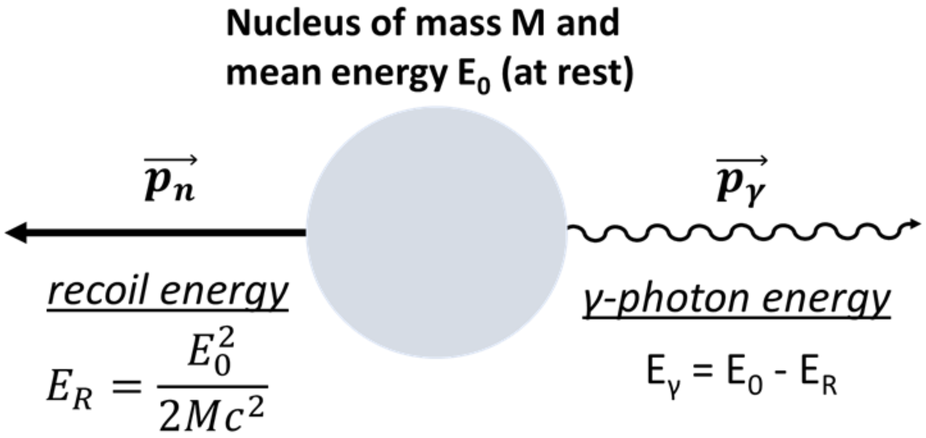

Figure 2.17 Recoil momentum $\overrightarrow{p_n}$ imparted on a nucleus during a γ-ray emission.

If the nucleus is initially at rest the recoil energy gained is:

$$E_R = \frac{1}{2}M\upsilon^2. \quad (2.10)$$

Momentum conservation dictates:

$$p_n = -p_\gamma, \quad (2.11)$$

where $p_n = M\upsilon$ is the momentum of the nucleus, and p_γ is the photon's momentum, which is given by its quantum energy:

$$p_\gamma = -\frac{E_\gamma}{c}, \; E_\gamma = E_o - E_R. \quad (2.12)$$

Because the nucleus has a large mass, the recoil velocity is small and the non-relativistic approximation can be used:

$$E_R = \frac{1}{2}Mv^2 = \frac{(Mv)^2}{2M} = \frac{p_n^2}{2M} = \frac{E_\gamma^2}{2Mc^2}. \quad (2.13)$$

Since E_R is negligible compared to E_0, it is reasonable to approximate $E_\gamma \sim E_0$, which leads to the recoil energy formula for a nucleus in an isolated atom or molecule:

$$E_R = \frac{E_0^2}{2Mc^2}. \quad (2.14)$$

For example, for the ^{57}Fe Mössbauer transition (with $E_0 = 14.4$ keV) the recoil energy is $E_R = 1.95 \cdot 10^{-3}$ eV, which is significantly larger than the natural width $\Gamma = 4.55 \cdot 10^{-9}$ eV. The recoil effect causes a shift in the emission energy from E_0 to lower energies by E_R so the photon carries energy $E_\gamma = E_0 - E_R$. Similarly, in absorption the photon must supply $E_\gamma = E_0 + E_R$ to account for both the energy transition and recoil. As a result, nuclear γ-resonance absorption (the Mössbauer effect) cannot occur between free atoms due to recoil energy loss. In solids the Mössbauer-active nucleus is tightly bound preventing free recoil. Instead, the recoil energy is shared with the entire crystal, which has a much larger mass, rendering the translational recoil energy negligible. If the recoil excites or annihilates a lattice vibration (phonon), the energy difference is still much larger than the natural width Γ preventing resonance absorption. However, quantum mechanics allows for a finite probability f of "zero-phonon" processes, where no phonon is involved in this process. The statistical mean fraction of the number of "zero-phonon" processes to the total number of occurring processes, known as the Lamb-Mössbauer factor, represents the recoil-free fraction. Typical values include f= 0.91 for the 14.4 keV transition in ^{57}Fe at room temperature and f = 0.06 for the 129 keV transition in ^{191}Ir [10], [11], [15], [16]. The recoil-free fraction depends on temperature, and the Debye model for phonon spectra provides a reasonable estimate of f. The temperature dependence is given by:

$$f(T) = exp\left[\frac{-3E_\gamma^2}{k_B \Theta_D Mc^2}\left\{\frac{1}{4} + \left(\frac{T}{\Theta_D}\right)^2 \int_0^{\Theta/T} \frac{x}{e^x - 1} dx\right\}\right], \qquad (2.15)$$

where $E_\gamma^2/2Mc^2$ is the recoil energy E_R, k_B is the Boltzmann constant and Θ_D is the Debye temperature. The factor *f* is essential for determining the intensity of a Mössbauer spectrum [10], [15], [16].

In conclusion:

1. *f* increases as the transition energy E_γ decreases;

2. *f* increases as the temperature decreases;

3. *f* increases as the Debye temperature Θ_D increases.

2.4.3 Hyperfine Interactions

In ideal situations, transitions occur between unaltered energy levels of "bare" nuclei with a mean transition energy E_0. However, in reality nuclei are subject to electric and magnetic fields generated by the electrons of the Mössbauer atom and surrounding atoms. These fields interact with the electric charge distribution and the magnetic moment of the Mössbauer nucleus affecting its nuclear energy states. This effect, known as nuclear hyperfine interaction, can either shift the nuclear energy levels as seen in the electric monopole interaction (e_0), or split degenerate states, as observed with the electric quadrupole (e_2) and magnetic dipole (m_1) interactions. In practice, in Mössbauer spectroscopy only these three interactions are significant.

The Mössbauer spectrum generally provides information about the type and strength of these hyperfine interactions. The e_0 interaction shifts the position of the resonance lines in terms of Doppler velocity, leading to the se-called isomer shift (δ), while e_2 and m_1 interactions cause splitting of the resonance lines reflecting the allowed transitions between ground and excited states. These hyperfine interactions provide key insights into the chemical and physical properties of the sample under study [10], [16], [17].

2.4.3.1 Overview of Electric Hyperfine Interactions

The total energy of the electrostatic interaction between a nucleus with charge Ze and the surrounding charges can be expressed classically as:

$$E_{el} = V_0 \cdot \int \rho_n d\tau - \sum_{i=1}^{3} E_i \cdot \int \rho_n x_i d\tau + \frac{1}{2}\sum_{i,j=1}^{3} V_{ij} \cdot \int \rho_n x_i x_j d\tau + \cdots. \quad (2.16)$$

The first term represents the total electrostatic energy of the nucleus considered as a point charge, and is irrelevant here. Since the nucleus remains fixed at the atom's center it does not experience an electric field and the second term can be ignored (also, nuclei with well-defined parity have no electric dipole moment, meaning $\int \rho_n x_i d\tau = 0$). The higher-order terms can be disregarded because the associated nuclear moments and interaction energies are extremely small, leaving only the term:

$$E_{el}^{(2)} = \frac{1}{2}\sum_{i,j=1}^{3} V_{ij} \int \rho_n(\vec{r}) x_i x_j d\tau. \quad (2.17)$$

The superscript (2) indicates that this is a second-order approximation of electrostatic energy. This integral can be divided into isotropic and anisotropic parts by adding and subtracting $r^2 = \sum x_i^2$, resulting in:

$$\int \rho_n(\vec{r}) r^2 \, x_i x_j d\tau = \frac{1}{3} \int \rho_n(\vec{r}) d\tau + \frac{1}{3} \int \rho_n(\vec{r}) \left(3x_i x_j - \delta_{ij} r^2\right) d\tau. \text{ (2.18)}$$

The first term, $\int \rho_n(\vec{r}) r^2 d\tau$, depends only on the radial distribution of the nuclear charge and is called the nuclear monopole moment. The second term, which describes the orientation-dependent part of the charge distribution in second power, is the nuclear quadrupole moment Q. The isotropic part of the nuclear charge distribution (the monopole moment) cannot be exactly calculated because the precise distribution is unknown. However, for simplicity the nucleus can be modeled as a uniform charged sphere with radius R and a total charge +Ze. By making the necessary conversions the energy of the electrostatic monopole interaction between a finite nucleus and its electrons becomes:

$$E_1 = -\frac{2\pi}{5} Z e^2 R^2 |\psi(0)|^2 = \delta E, \text{ (2.19)}$$

where e^2 is the charge of the electron and $|\psi(0)|^2$ is the finite probability density at r = 0 for the s-electrons to penetrate the finite nucleus of radius R.

This term uniformly shifts the nuclear energy levels with different shifts for the ground and excited states due to differences in nuclear volume and mean square nuclear radius. This gives rise to the isomer shift δ observed in Mössbauer spectra [10], [16].

By inserting the nuclear quadrupole moment tensor $Q_{ij} = \int \rho_n(\vec{r}) \left(3x_i x_j - \delta_{ij} r^2\right) d\tau$, into the equations (2.18) and (2.17), we obtain the quadrupole interaction energy:

$$E_Q = \frac{1}{6} \sum_{i,j=1}^{3} V_{ij} \cdot Q_{ij}. \text{ (2.20)}$$

Quadrupole interaction removes the degeneracy of nuclear states with spin quantum numbers I > ½ causing quadrupole splitting ΔE_Q in the Mössbauer spectrum. According to equation (2.16) the total electrostatic energy is the sum of the monopole and quadrupole interaction energies: $E_{el}^{(2)} = E_1 + E_Q$.

In Mössbauer spectroscopy, the nuclear eigenstates are characterized by total angular momentum with quantum number I, also known as nuclear spin. The electric quadrupole interaction is often expressed using angular momentum operators, as the properties of the quadrupole moment allow Clebsch-Gordon coefficients and the Wigner-Eckart theorem to simplify the calculation. This results in a convenient spin Hamiltonian for the quadrupole interaction:

$$\hat{H}_Q = \frac{eQ}{6I(2I+1)}\sum_{i,j=1}^{3} V_{ij} \cdot \left[\frac{3}{2}\left(I_iI_j + I_jI_i\right) + \delta_{ij}I^2\right]. \quad (2.21)$$

This equation requires only one nuclear constant, Q, to describe the quadrupole moment. The simplification arises because the nucleus's angular momentum imposes cylindrical symmetry on the charge distribution.

By choosing the symmetry axis as $x_i = z$, the energy variation caused by nuclear reorientation depends only on the charge distribution difference along the z-axis compared to the x- or y-axis. As a result, the off-diagonal elements Q_{ij} of the quadrupole moment operator are zero for i≠j. These elements are defined by the integrals $\int \rho_n(\vec{r})z^2 d\tau$ and $\int \rho_n(\vec{r})r^2 d\tau$, leading to the classical expression:

$$Q = \frac{1}{e}\int \rho_n(\vec{r})(z^2 - x^2)d\tau = \frac{1}{e}\int \rho_n(\vec{r})(3z^2 - r^2)d\tau = \frac{1}{e}\int \rho_n(\vec{r})r^2(3cos^2\theta - 1)d\tau, \quad (2.22)$$

where θ is the polar angle between the symmetry axis (z) and vector r, with z = r·cosθ. This equation shows that the nuclear quadrupole moment Q is positive for elongated nuclei, negative for oblate nuclei and zero for spherical charge distributions. Nuclear states with spin quantum numbers I = 0, or I = 1/2 do not have an observable quadrupole moment [10], [16].

2.4.3.2 Mössbauer Isomer Shift

The electric monopole interaction between a nucleus (with an average square radius R^2) and its surrounding environment results from the nuclear charge distribution ZeR^2 and the electronic charge density $e|\psi(0)|^2$ at the nucleus. The energy shift, $\delta E = const \cdot R^2|\psi(0)|^2$, applies to nuclei with identical mass and charge but in different nuclear states (isomers), which have different charge distributions ($ZeR_g^2 \neq ZeR_e^2$). The nuclear volume and average radius vary with excitation state ($R_g^2 \neq R_e^2$) leading to distinct energy shifts for the Mössbauer nucleus in both the ground (g) and the excited (e) states. This effect, as illustrated in Figure 2.18, is responsible for the Mössbauer isomer shift, δ [10], [16].

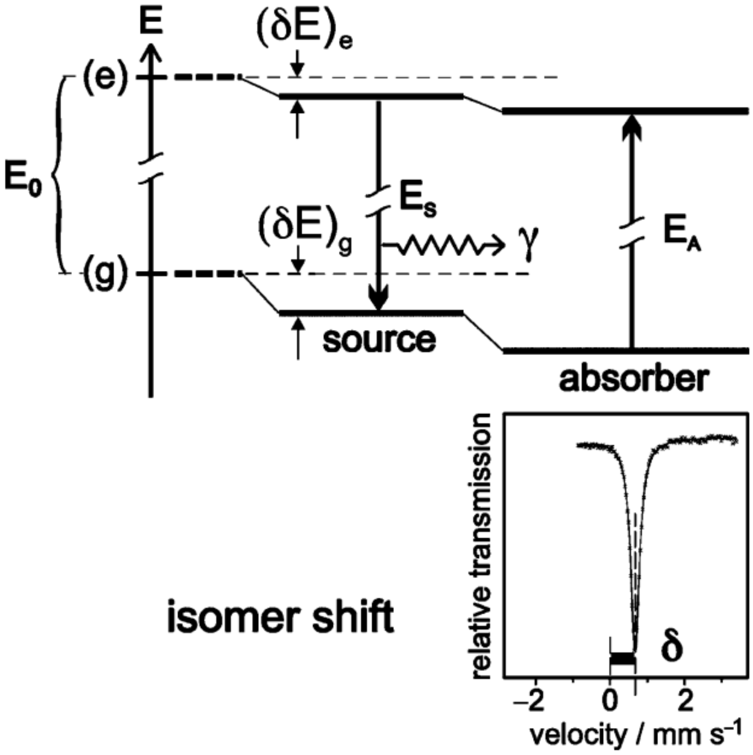

Figure 2.18 The electric monopole interaction between the nuclear charge and the electron density at the nucleus shifts the energy of the nuclear states and gives the Mössbauer isomer shift [10].

The energy of a γ-photon emitted by an excited Mössbauer nucleus in the source is given by the transition energy:

$$E_S = E_0 - [(\delta E)_e - (\delta E)_e]_{source} = E_0 + \tfrac{2\pi}{5} Ze^2 |\psi(0)|_S^2 \left(R_e^2 - R_g^2\right), \quad (2.23)$$

where E_0 is the transition energy of a bare nucleus and $|\psi(0)|_S^2$ represents the electronic charge density in the source material. For the absorber nucleus holds a similar expression:

$$E_A = E_0 - [(\delta E)_e - (\delta E)_e]_{absorber} = E_0 + \tfrac{2\pi}{5} Ze^2 |\psi(0)|_A^2 \left(R_e^2 - R_g^2\right). \quad (2.24)$$

Since the electron densities $|\psi(0)|_S^2$ and $|\psi(0)|_A^2$ differ due to distinct chemical compositions, the transition energies E_S and E_A are also different. This difference causes a shift in the γ-resonance, which is observed as the isomer shift δ in the Mössbauer experiment:

$$\delta = E_A - E_S = \tfrac{2\pi}{5} Ze^2 \{|\psi(0)|_A^2 - |\psi(0)|_S^2\} \left(R_e^2 - R_g^2\right). \quad (2.25)$$

By assuming $R_e - R_g = \Delta R$ and $R_e + R_g \sim 2R$, the equation (6.19) simplifies to:

$$\delta = \frac{4\pi}{5} Ze^2\{|\psi(0)|_A^2 - |\psi(0)|_S^2\} \cdot R^2\left(\frac{\Delta R}{R}\right). \qquad (2.26)$$

This equation demonstrates that the isomer shift δ, related to the chemical bond formation between two atoms is influenced by the electron distribution between them. More specifically, it is affected by how the total electron density is shared across the atoms. The isomer shift reflects the difference in electron density at the nucleus between the absorber and the source and is indirectly impacted by the relative change in nuclear radius between the excited and the ground states (δR/R). For most nuclei, the excited state has a larger radius, though in some cases, such as the ^{57}Fe, the opposite is true. In transition metals, where changes in oxidation state involve alterations in the number of d-electrons the sensitivity of the isomer shift is greatly reduced. However, for widely studied isotopes like ^{57}Fe the proportionality constant $a = \frac{4\pi}{5} Ze^2R^2\left(\frac{\Delta R}{R}\right)$ is large enough that changes in oxidation state are easily observed. As the number of d-electrons increases the isomer shift becomes more positive indicating that the nuclear radius change δR/R is negative [10], [16].

Second-Order Doppler Shift (S.O.D.)

In Mössbauer spectroscopy the experimentally observed isomer shift δ_{exp} also includes a relativistic component known as the second-order Doppler shift δ_{SOD}:

$$\delta_{exp} = \delta + \delta_{SOD}. \ (2.27)$$

This shift arises from the relativistic energy change of the γ-photon caused by the thermal motion of the emitting and absorbing nuclei, proportional to the mean square velocity $<u^2>$. The second-order Doppler shift is expressed as:

$$\delta_{SOD} = -E_\gamma \frac{<\upsilon^2>}{2c^2}. \ (2.28)$$

The value of δ_{SOD} decreases with temperature and becomes negligible at low temperatures, such as in liquid helium. However, at room temperature it may reach values as large as -0.1 mm/s. According to the Debye model, the second-order Doppler shift is given by:

$$\delta_{SOD} = -\frac{9k_BE_\gamma}{16M_{eff}c^2}\left(\Theta_M + 8T\left(\frac{T}{\Theta_M}\right)^3 \int_0^{\frac{\Theta_M}{T}} \frac{x^3}{e^x-1}dx\right), \ (2.29)$$

where M_{eff} is the effective vibrating mass and Θ_M is the Mössbauer temperature representing the specific environment surrounding the Mössbauer nucleus [10], [16].

2.4.3.3 Quadrupole Splitting

Quadrupole Splitting is a prominent characteristic of Mössbauer spectra. It generally occurs when a nucleus with an electric quadrupole moment interacts with an electric field gradient (EFG) at the nucleus. The EFG describes the variations in rotational conformations that a non-spherical nucleus can feel within a non-uniform electric field, which is produced by the asymmetrical charge distribution of surrounding electrons. A quadrupole moment arises in nuclei with spin greater than one-half, and since all Mössbauer nuclei have a quadrupole moment in either their ground or excited state (or both), they are prone to exhibit quadrupole splitting. The spectra can be quantified by the nuclear quadrupole coupling constant, which is the product of V_{zz} (the primary component of the EFG) and eQ (the electric quadrupole moment of the nucleus), where e represents the elementary charge of a proton. The shape of the nucleus is best approximated by a power series, with the significant term representing the nuclear quadrupole moment. In quantum mechanics, spatial operations for individual nucleons can be replaced by angular momentum operators that act on the total spin I of the nucleus [10], [16]. The spin-Hamiltonian operator typically used to compute quadrupole interactions is expressed as:

$$\hat{H}_Q = \frac{eQV_{zz}}{4I(2I-1)}\left[3\hat{I}^2 - I(I+1) + \frac{\eta}{2}(\hat{I}_+^2 + \hat{I}_-^2)\right], (2.30)$$

where I is the nuclear spin number, number, $\hat{I}_\pm = \hat{I}_x \pm i\hat{I}_y$ are shift operators, and $\hat{I}_x, \hat{I}_y, \hat{I}_z$ represent the projections of nuclear spin along the principal axes. Q is the quadrupole moment of the nucleus, while V_{zz} and η denote the primary component and the asymmetry parameter of the EFG at the nucleus, respectively. The product eQV_{zz} is referred to as the nuclear quadrupole coupling constant (NQCC). Like all hyperfine coupling constants, the NQCCs represents the interaction between a nuclear property and an electronic one.

In equation (2.30), only one nuclear constant, Q, is required to parameterize the nuclear properties. This is largely because the nuclear charge distribution possesses cylindrical symmetry, due to the nucleus having a well-defined angular momentum. By selecting z as the symmetry axis, the quadrupole moment Q corresponds, in classical terms, to the difference between the charge distribution along and perpendicular to z. The sign of Q is determined by the nature of the nuclear deformation: a positive quadrupole moment suggests an elongated, cigar-like nucleus, while a negative Q signifies an oblate, pancake-shaped nucleus (Figure 2.19). Only nuclear states with spin $I > 1/2$ display a non-zero quadrupole moment [10], [16].

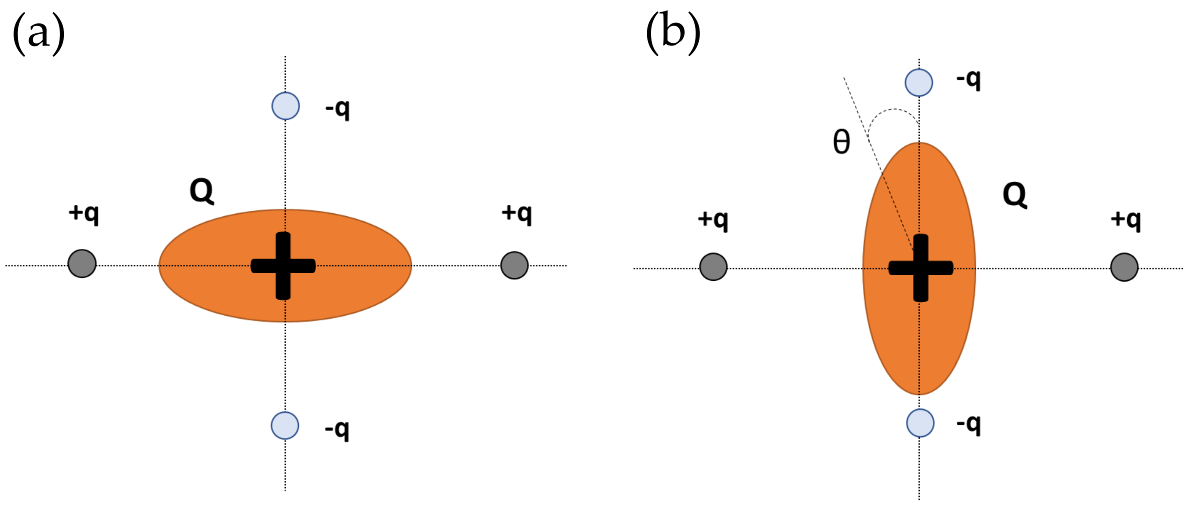

Figure 2.19 Rotational configurations of a cigar-shaped nucleus with quadrupole moment Q between of two positive charges (+q) and two negative charges (-q). The configuration (**b**) is energetically more favorable than (**a**) because the positive tips of the elongate nucleus are closer to the negative charges. The rotational energy of the system depends on the strength of Q, the EFG and the rotation angle (θ). The rotation angle and the energy of the system are quantized.

The electrons around the Mössbauer atom, along with the surrounding charges on the ligands, generate an electric potential $V(\overrightarrow{r})$ at the nucleus (located at $\vec{r} = (0, 0, 0)$). The electric field $\vec{E}$ is equal to the negative gradient of this potential, expressed as $\vec{E} = -\vec{\nabla}V$. In Cartesian coordinates, this becomes $\vec{E} = -(\frac{\partial V}{\partial x}, \frac{\partial V}{\partial y}, \frac{\partial V}{\partial z})$. The EFG at the nucleus corresponds to the second derivative of the potential $V(\vec{r})$ at $\vec{r} = 0$, which can be written as:

$$EFG = \left[-\vec{\nabla}\vec{E}\right] = \left[\vec{\nabla}\vec{\nabla}V\right] = \begin{bmatrix} V_{xx} & V_{xy} & V_{xz} \\ V_{yx} & V_{yy} & V_{yz} \\ V_{zx} & V_{zy} & V_{zz} \end{bmatrix}, (2.31)$$

where $V_{ij} = (\frac{\partial^2 V}{\partial x_i \partial x_j})$ are the nine components of the second-rank, 3x3 EFG tensor. In cases where the EFG has an axial symmetry, the components satisfy the condition $V_{xx} = V_{yy} = -\frac{V_{zz}}{2}$, which follows from the Laplace condition that $V_{xx} + V_{yy} + V_{zz} = 0$. Since the EFG tensor is symmetric, it can be diagonalized by rotating it to a principal axis system (PAS) where the off-diagonal elements vanish, i.e., $V_{i \neq j} = 0$. By convention, the principal axes are labeled such that the tensor components are ordered as V_{zz}, V_{yy}, and V_{xx}, with $|V_{zz}| \geqslant |V_{yy}| \geqslant |V_{xx}|$. For systems lacking axial symmetry, an additional parameter called the asymmetry parameter η is needed to describe the EFG, defined as:

$$\eta = (V_{xx} - V_{yy})/V_{zz}, 0 \leq \eta \leq 1. (2.32)$$

In systems with three- or fourfold symmetry axes passing through the Mössbauer nucleus, the EFG is symmetric, leading to $V_{xx} = V_{yy}$, and thus $\eta = 0$. Moreover, in cases where two mutually perpendicular axes exhibit threefold or higher symmetry, the EFG must be zero.

In the simplest scenario, where the EFG exhibits axial symmetry ($V_{xx} = V_{yy}$, or $\eta = 0$), the Schrödinger equation can be solved using spin wavefunctions $|I,m_I\rangle$, characterized by the magnetic quantum number $m_I = I, I-1, \ldots, -I$. For $\eta = 0$, the corresponding energies are given by:

$$E_Q(m_I) = \frac{eQV_{zz}}{4I(2I-1)}[3m_I^2 - I(I+1)]. \quad (2.33)$$

The electric quadrupole interaction leads to a splitting of the (2I+1) magnetic substates without altering the overall mean energy of the nuclear spin states. In this case, substates with identical absolute values of $|m_I|$ remain degenerate when $\eta = 0$. This phenomenon is illustrated for ^{57}Fe in Figure 2.20 [10], [16].

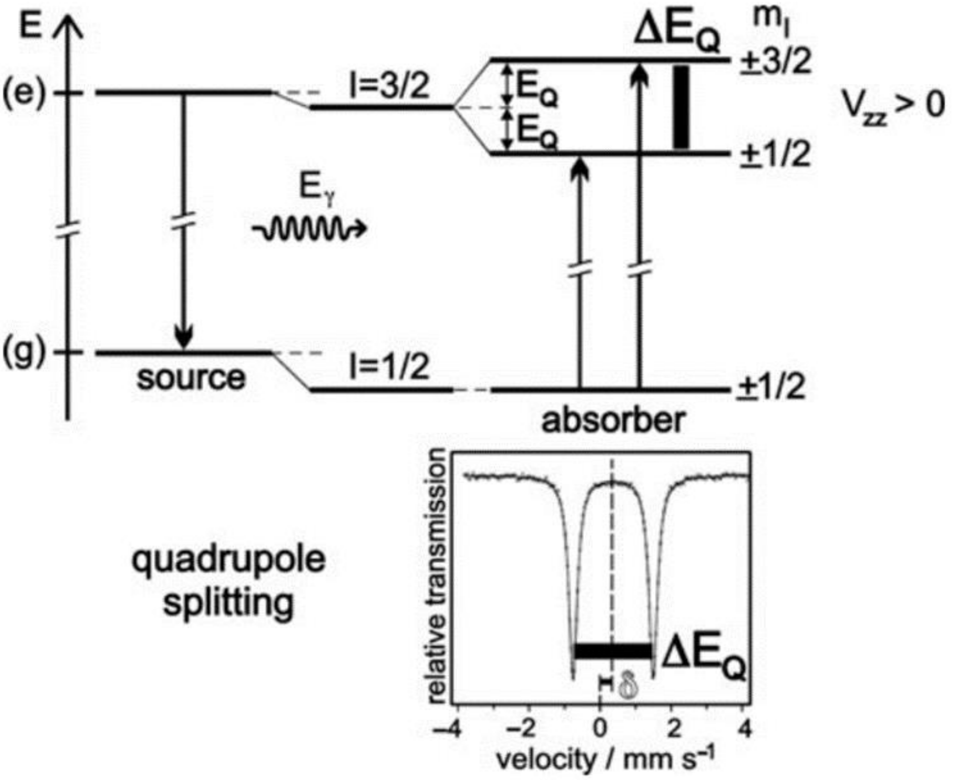

Figure 2.20 Quadrupole splitting of the excited state of ^{57}Fe with I = 3/2 and the resulting Mössbauer spectrum [10].

Specifically, the ground state (I = 1/2) remains unsplit, as it lacks a quadrupole moment. Meanwhile, the excited state (I = 3/2) splits into two doubly degenerate states, $|3/2, \pm 3/2\rangle$ and $|3/2, \pm 1/2\rangle$, due to the m_I^2 dependence of the quadrupole energy:

$$E_Q\left(\pm\frac{3}{2}\right) = {}^{3eQV_{zz}}/_{12},\ E_Q\left(\pm\frac{1}{2}\right) = -{}^{3eQV_{zz}}/_{12}\ \text{, for I = 3/2. (2.34)}$$

The energy difference (ΔE_Q) between the two sets of substates is given by:

$$\Delta E_Q = E_Q\left(\pm\frac{3}{2}\right) - E_Q\left(\pm\frac{1}{2}\right) = \frac{eQV_{zz}}{2}. \quad (2.35)$$

In a typical Mössbauer experiment involving a ^{57}Fe powder sample this splitting results in a quadrupole doublet, two resonance lines of equal intensity. The separation between these lines corresponds to the quadrupole splitting ΔE_Q. This parameter is crucial for understanding the chemical environment, as it provides insight into bonding characteristics and local symmetry around the iron site. Additionally, the isomer shift (δ), representing the displacement of the quadrupole spectrum center from zero velocity can also be inferred from the spectrum, as the quadrupole interaction does not affect the mean energy of the nuclear states [10], [16].

When the EFG lacks axial symmetry ($\eta \neq 0$), the quadrupole interaction becomes more complex. The shift operators $\vec{I}_{\pm}^2$ associated with η introduce off-diagonal elements in the Hamiltonian matrix, like $\langle m_I|\hat{H}_Q|m_I \pm 2\rangle$. For $I = 3/2$, the exact solution for the energy levels is:

$$E_Q\left(I = \frac{3}{2}, m_I\right) = \frac{eQV_{zz}}{4I(2I-1)}\left[3m_I^2 - I(I+1)\sqrt{1+\frac{\eta^2}{3}}\right]. \quad (2.36)$$

Comparing (2.33) and (2.36), it is evident that η can alter the quadrupole splitting by up to ~ 15%, as η is restricted to values between 0 and 1 [10], [16].

2.4.3.4 Magnetic Dipole Interaction and Magnetic Splitting

A nucleus with spin quantum number $I > 0$ interacts with a magnetic field through is magnetic dipole moment μ. This magnetic dipole interaction, or nuclear Zeeman effect, is described by the Hamiltonian:

$$\vec{H}_m = -\vec{\mu}\cdot\vec{B} = -g_N\mu_N\vec{I}\cdot\vec{B}, \quad (2.37)$$

where $\vec{B}$ represents the magnetic induction, g_N is the nuclear Lande′ factor, and $\mu_N = e\hbar/2M_Pc$ is the nuclear magneton (M_P being the proton mass). The magnetic hyperfine splitting allows us to determine the effective magnetic field acting on the nucleus, which may result from a combination of an external field B_{ext} and an internal field B_{int}, typically generated by the magnetic moments of the valence electrons.

It is well-established that hyperfine interactions for a nucleus "A" involve three primary contributions: (a) the isotropic Fermi contact term, (b) the spin-dipolar interaction and (c) the spin-orbit correction. These contributions are often of similar magnitude but can differ in sign. The Fermi contact term arises from spin density localized at a point in space, such as the iron nucleus and is highly sensitive to core-level spin polarization. In contrast, the dipolar hyperfine tensor depends primarily on the spin distribution in the valence shell making it easier to calculate. The spin-orbit coupling term, being a response property, reflects how the system reacts to external perturbations influenced by the excitation spectrum [10], [12], [16].

Spin polarization is particularly useful in understanding the magnetic hyperfine coupling of organic radicals, where the Fermi contact dominates. However, transition metal complexes behave differently. The electron-electron repulsion experienced by a given electron results from the summation of contributions from all other electrons with interactions dependent on their spin. Consequently, the spatial configuration of spin-up and spin-down orbitals differs, leading to a net spin density that arises from this imbalance. In general, orbitals that have little spatial overlap with the singly occupied orbitals are distorted towards the singly occupied orbitals and orbitals that occupy the same region in space are "repelled." In transition metal complexes the singly occupied orbitals, typically derived from metal 3d orbitals. Thus, the 3s shell is polarized to leave positive spin-density at the nucleus because the 3s and 3d shells occupy a similar region of space. By contrast, the 2s shell is polarized in the opposite direction and leaves a negative spin-density at the nucleus. The 1s shell is also polarized to give negative spin-density but here the spin-polarization is found to be very small.

The dipolar hyperfine interaction mirrors the quadrupole interaction in many ways. Both the dipolar magnetic hyperfine coupling and the EFG tensor use similar integrals with the main difference being the contraction of these integrals with spin density in the former and the total electron density in the latter. This means the dipolar interaction is not influenced by distant nuclei and the same partitioning applies as for the EFG tensor allowing a similar interpretation in terms of one-center, two-center and multi-center interactions. Finally, the spin-orbit contribution to magnetic hyperfine coupling stems from the orbital motion of unpaired electrons. This effect, introduced into the ground state wavefunction via spin-orbit coupling with excited states, allows the angular momentum in the ground state to produce a magnetic dipole moment, which interacts with the nuclear dipole moment, thereby contributing to magnetic hyperfine coupling [10], [16].

Diagonalizing the Hamiltonian matrix gives the eigenvalues for the nuclear Zeeman effect:

$$E_M(m_I) = -\frac{\mu B m_I}{I} = -g_N \mu_N B m_I. \quad (2.38)$$

This interaction splits the nuclear state with spin quantum number I into 2I+1 equally spaced, nondegenerate substates $|I, m_I>$, defined by the sign and the magnitude of m_I. In ^{57}Fe, for example, the excited state (I = 3/2) splits into four magnetic substates, while the ground state (I = 1/2) splits into two substates. The allowed γ-transitions between these sublevels follow the magnetic dipole selection rules ($\Delta I = 1$, $\Delta m = 0, \pm 1$). In a Mössbauer experiment this results in a sextet of resonance lines with relative intensities following a 3:2:1:1:2:3 pattern under isotropic magnetic field distribution (Figure 2.21) [10].

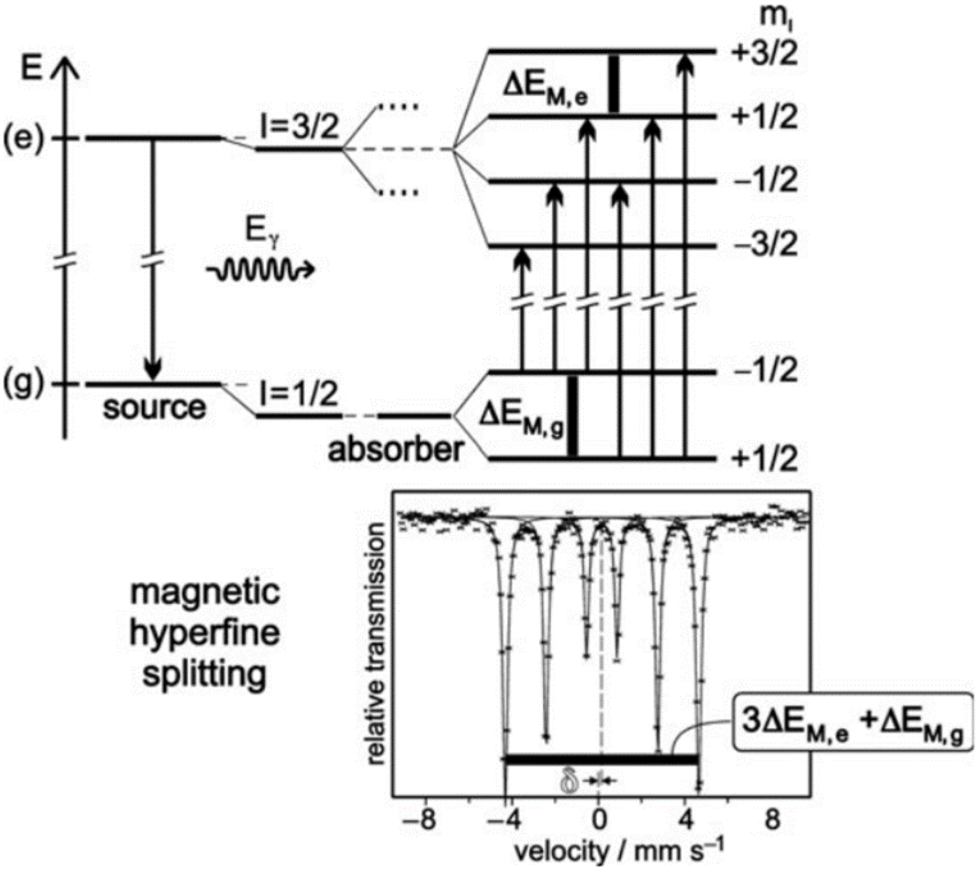

Figure 2.21 Magnetic dipole splitting (nuclear Zeeman effect) in ^{57}Fe and resultant Mössbauer spectrum (schematic) [10].

Pure nuclear magnetic hyperfine interaction without the influence of electric quadrupole interaction is rarely observed in chemical applications of the Mössbauer effect, with metallic iron being a notable exception. More commonly, a nuclear state is simultaneously affected by all three types of hyperfine interactions: electric monopole, magnetic dipole and electric quadrupole interactions, described by the Hamiltonian:

$$\hat{H} = \delta E + \hat{H}_Q + \hat{H}_M. \quad (2.39)$$

The monopole interaction, δE, responsible for the isomer shift is straightforward to handle as it simply adds uniformly to all transition energies. As a result, the Mössbauer spectrum displays a consistent shift (isomer shift) across all resonance lines without altering their relative separations. However, both the magnetic dipole ($\widehat{H}_M$) and electric quadrupole ($\widehat{H}_Q$) interactions depend on the nuclear spin's magnetic quantum numbers making their combined Hamiltonian more complex to evaluate.

In case of ^{57}Fe, competing hyperfine interactions do not occur for the ground state because there is no quadrupole moment for I = 1/2. For the excited state (I =3/2) the Schrödinger equation can be simplified when one of the hyperfine interactions is weak enough to be treated as a perturbation. Although this approach is seldom used for precise quantitative analyses of Mössbauer spectra it is educational and can often provide insights into the origins of complex spectra [10], [12], [16].

High-field Condition: $g_N\mu_N B >> eQV_{zz}/2$

The combined effects of strong nuclear magnetic (Zeeman) interaction and weak electric quadrupole interaction in the excited state of ^{57}Fe are illustrated in Figure 2.22. The left side of the figure represents the initial condition of pure Zeeman splitting, as described by equation 2.38 and previously shown in figure 2.21. In this example the external magnetic field $\vec{B} = (0, 0, B)$, defining the quantization axis, is oriented along the z-direction, that is coaxial with the principal component of EFG, V_{ZZ}. The additional quadrupole interaction, illustrated on the right side of Figure 2.22, causes the Zeeman states with $m_I = \pm 3/2$ and $m_I = \pm 1/2$ to shift in opposite directions, both upward and downward. In first-order approximation, all states experience the same energy shift $E_Q^{(1)}$, as predicted by the m_I^2-dependence of the electric quadrupole interaction (see equation 2.33). Here, the superscript (1) denotes the first-order perturbation. The value of $E_Q^{(1)}$ is determined by the component of the EFG tensor along the quantization axis. For this case, where the EFG exhibits axial symmetry (η = 0) and the principal component is V_{zz}, the quadrupole shift $E_Q^{(1)}$ is given by:

$$E_Q^{(1)} = \frac{eQV_{zz}}{4}. \quad (2.40)$$

This value represents half the quadrupole splitting that would be observed in the absence of a magnetic field at the nucleus in a purely quadrupole-affected spectrum [10], [16].

In this case the eigenvalues are:

$$E = -g\mu_N H m_I + (-1)^{|m_I|+1/2} \cdot \frac{eQV_{zz}}{4}\left(\frac{3cos^2\theta - 1}{2}\right) \quad (2.41)$$

and the respective level splitting is illustrated for a 3/2 ⇒1/2 decay in the right side of Figure 2.22 ($V_{zz} > 0$). In this case the angle θ is not necessarily determined. However, if cosθ = 1/√3 then the quadrupole interaction is fortunately absent. The expression

$$\frac{eQV_{zz}}{4}\left(\frac{3cos^2\theta-1}{2}\right) \quad (2.42)$$

is often denoted as ε if θ is unknown.

If the EFG tensor is not axially symmetric but the magnetic axis lies along one of its principal axes, then the excited-state splitting for I = 3/2 gives the four energies

$$\frac{1}{2}g\mu_N H \pm \frac{eQV_{zz}}{4}\left[\left(1+\frac{4g\mu_N H}{eQV_{zz}}\right)^2+\frac{\eta^2}{3}\right]^{1/2} \text{and} -\frac{1}{2}g\mu_N H \pm \frac{eQV_{zz}}{4}\left[\left(1-\frac{4g\mu_N H}{eQV_{zz}}\right)^2+\frac{\eta^2}{3}\right]^{1/2} \quad (2.43)$$

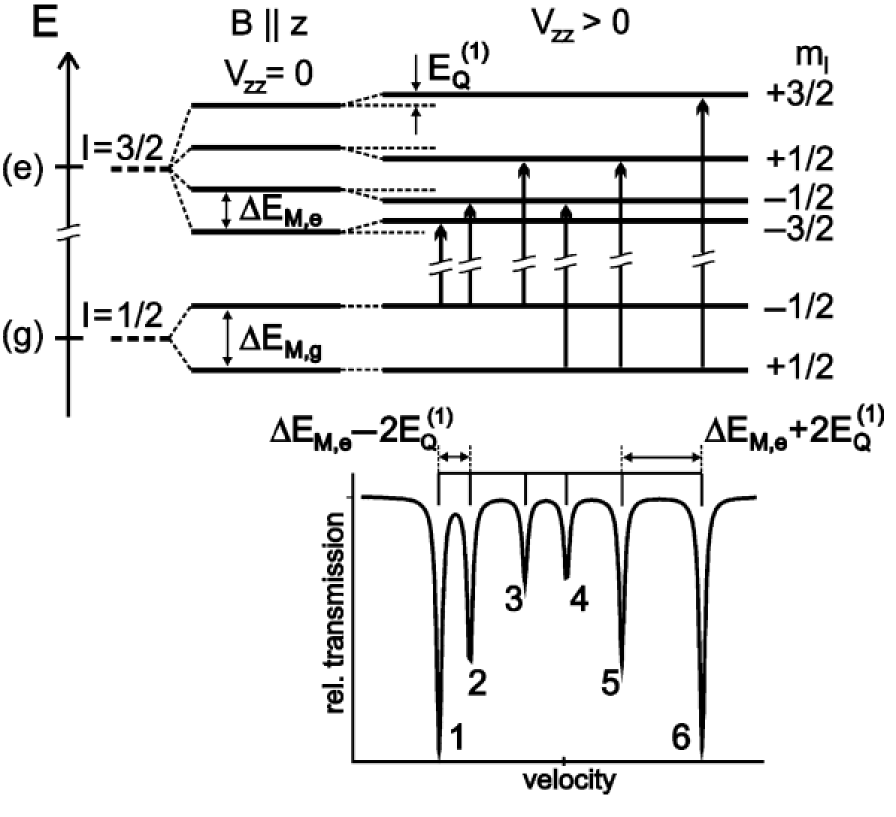

Figure 2.22 Level scheme for ^{57}Fe of a combined hyperfine interaction with a strong magnetic interaction and a weak quadrupole interaction having V_{zz}>0 (top right), compared to a seldom magnetic interaction (top left) [10] and the resulting spectrum (bottom).

2.4.4 The ^{57}Fe Mössbauer Spectrometer

^{57}Fe Mössbauer spectra are typically recorded using transmission geometry, where the sample, acting as the absorber, contains the stable (non-radioactive) isotope of the Mössbauer element. A schematic of a standard spectrometer setup is shown in Figure 2.23. The radioactive Mössbauer source is mounted on an electro-mechanical velocity transducer, also known as the Mössbauer drive, which moves in a controlled manner to modulate the emitted γ-radiation via the Doppler effect. The drive is powered by an electronic control unit that operates based on a reference voltage ($V_{reference}$) supplied by a digital function generator.

Most Mössbauer spectrometers operate in constant-acceleration mode, where the drive velocity is linearly varied in a periodic manner, either in a saw-tooth or triangular waveform. In this mode, the source moves back and forth in a repeating cycle. The γ-photons emitted by the source are detected by a γ-detector, which converts them into electrical signals. These signals are then amplified, shaped, and processed through a series of electronic components, including a preamplifier, main amplifier, and a single-channel analyzer (SCA).

The SCA is a pulse discrimination device tuned to pass only the 14.4 keV Mössbauer radiation, allowing resonance energy pulses to be directed to the multi-channel analyzer (MCA) for data acquisition, while non-resonant radiation adjacent to 14.4 keV is cut-out. The MCA serves as the core of the Mössbauer spectrometer, responsible for acquiring and storing the data. It consists of an array of digital counters equipped with input logic to register discrete electrical pulses, in a sequence that eventually corresponds to the velocities of the source's movement relative to the sample [10].

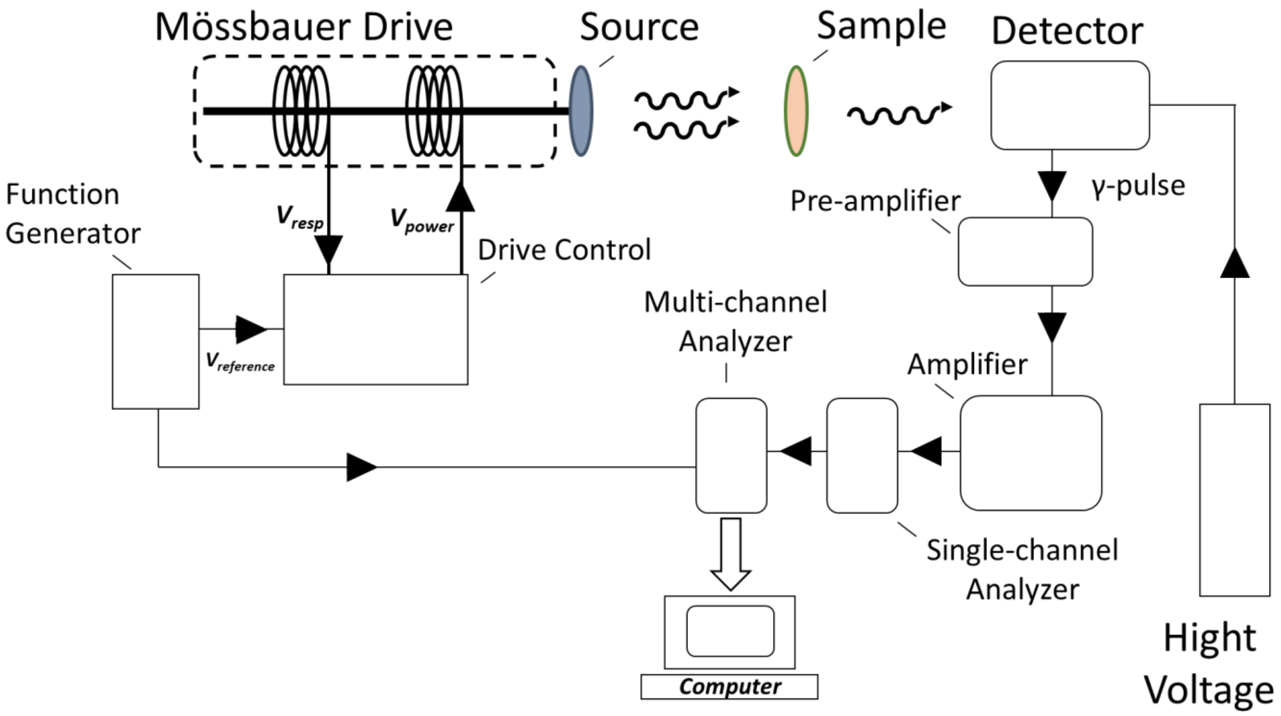

Figure 2.23 Diagrammatic representation of a Mössbauer spectrometer for transmission geometry measurements.

2.4.4.1 The ^{57}Fe Mössbauer Drive System

To resolve the fine Mössbauer spectral lines, such as those for ^{57}Fe, which have a full width of about $2\Gamma_{nat} \approx 0.2$ mm/s, it is essential to control the motion of the Mössbauer source with a precision of at least 0.01 mm/s. Most Mössbauer spectrometers use electromechanical velocity transducers of the "loudspeaker" variety, which can handle velocity ranges from under 1 mm/s to several cm/s, covering the full hyperfine splitting range of many common isotopes.

All necessary reference and trigger signals for operating a Mössbauer spectrometer are generated by a digital function generator. This unit supplies two key outputs: (a) an oscillating reference voltage to the drive control unit, and (b) a set of trigger pulses to the MCA for synchronizing data recording (see Figure 2.23). The reference voltage ($V_{reference}$) is applied to one input of a differential amplifier in the drive control unit. The amplified signal then powers the drive coil, facilitating the motion of the Mössbauer source [10], [16].

The Mössbauer drive is a linear motor designed for precise oscillating movement. The moving component is a rod or tube that holds the radioactive source at one end. This motion is restricted to one dimension by two-disc springs, ensuring the movement occurs only along the axial direction. Two magnets, attached to the rod, are positioned within the drive and pick-up coils. The magnetic field from the drive coil accelerates the magnets, while the pick-up coil monitors the source's movement by inducing a response voltage (V_{resp}), which reflects the actual motion. This response is fed back into the second input of the differential amplifier in the drive control unit [10]. In our experiments, we utilized the WissEl Drive System 360, comprising the Mössbauer Drive Unit MR-360 and the WissEl Mössbauer Velocity Transducer MA-260 S or MVT-1000.

The frequency of the triangular drive motion should be slightly higher than the system's first mechanical resonance, typically between 10 and 30 Hz. This frequency determines how often the source moves through the full velocity range during spectrum accumulation. The velocity sweep's amplitude is controlled by scaling the $V_{reference}$ in the drive control unit. Adjustments to the feedback loop, such as amplifier gain and frequency response settings, further enhance the velocity control.

To collect a Mössbauer spectrum, the gamma-ray detection system's electrical pulses must be synchronized with the source's velocity. This is achieved by operating the MCA in multi-channel scaling (MCS) mode. In this mode, the function generator sequentially triggers the MCA's digital counters (channels), with each channel accumulating incoming gamma-ray pulses.

The process begins when the MCA receives a "start" pulse from the function generator, which is synchronized with the source's minimum velocity. Following this start pulse, a series of 512 "channel advance" pulses are generated, with delays of around 100 μs each. Upon receiving each pulse, the MCA closes the current channel, moves to the next one, and opens it for gamma-ray pulse recording. Once the last channel is closed, the MCA resets and repeats the cycle. This synchronization ensures each channel corresponds to a specific velocity point, providing accurate velocity increments. At the end of the measurement, the counts stored in each MCA channel create the Mössbauer spectrum, which is typically displayed as counts versus channel number, or more precisely relative transmission of radiation through the sample versus Doppler velocity, after applying the folding and calibration constants from a relative channel to velocity calibration and transform procedure [10], [16]. In our study, the data collected from the Mössbauer spectrometers in multi-channel scaling mode were imported through a data acquisition hardware/software system, such as The Nucleus Personal Computer Analyzer (PCA-II) from Nucleus INC., Oak Ridge, USA, or the custom-made MossCard hardware/software system developed in our lab. For the analysis of the Mössbauer spectra the IMSG09 57Fe-119Sn Mössbauer fitting program [18] was used.

2.4.4.2 The ^{57}Fe Mössbauer Light Source

In conventional nuclear γ-resonance emission and absorption, the 14.4 keV γ-radiation is emitted by nuclei of a radioactive isotope situated at the source, and is absorbed by nuclei of a relevant isotope embedded in the sample-absorber, which is typically a stable isotope. The parent radioactive nuclei in the source decay into the excited state suitable for γ-emission. For example, in ^{57}Fe spectroscopy, ^{57}Co serves as the γ-source (Figure 2.24). With a half-life of 270 days, ^{57}Co decays via K-capture, where a K-shell electron is captured by the nucleus, converting cobalt into iron and leaving ^{57}Fe in a 136 keV excited state.

This excited ^{57}Fe state can transit to the ground state in two ways: directly, by emitting a 136 keV γ-photon (9% of the emission events), or via an intermediate 14.4 keV Mössbauer state (91% of the emission events) by first emitting a 122 keV photon, followed by a 14.4 keV γ-photon [10].

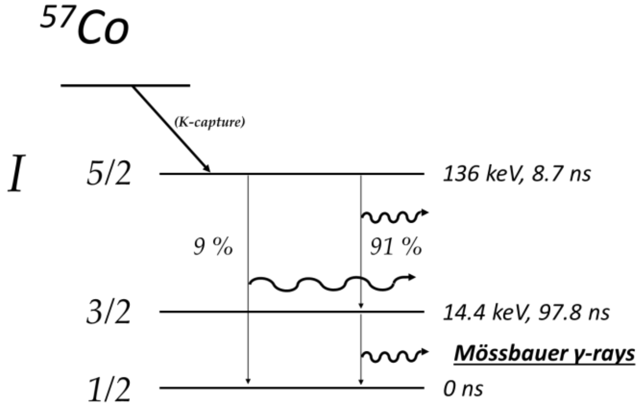

Figure 2.24 Decay scheme of ^{57}Co. The nuclear levels are labeled with spin quantum numbers and lifetime.

2.4.4.3 Absorber Sample

In Mössbauer transmission geometry measurements, the sample can be a solid thin foil, compacted powder, or frozen solution, as long as it contains sufficient concentrations of the Mössbauer isotope and allows γ-radiation to penetrate and transit through it. The need for optimum concentration of the Mössbauer active isotope in the sample is related to various factors related to the sample's thickness, like the number N_M of Mössbauer nuclei per square centimeter, the Debye–Waller factor f_A of the absorber material, and the resonance cross-section σ_0 of the Mössbauer isotope. Low isotope concentration leads to weak signals and long acquisition times, while the ability of γ-radiation to pass through the sample can be challenging in some cases. Mössbauer γ-rays are soft and can be strongly absorbed by non-resonant mass absorption, especially in materials with heavy elements like chlorine or beyond. Choosing an optimal absorber thickness is a balance between achieving a strong signal and avoiding a low count rate caused by non-resonant γ-attenuation. The sample thickness influences both the Mössbauer signal strength and resonant linewidth, as well as the intensity of the radiation reaching the detector, as γ-rays are attenuated due to non-resonant absorption via the photoelectric effect and Compton scattering. The Mössbauer signal increases almost linearly with sample thickness, but thick absorbers are producing undesirable increment in the resonant linewidth which decreases the resolution of the spectrum, while the count rate decreases exponentially, making it crucial to optimize the absorber's thickness to obtain a sufficient spectrum in a reasonable measurement time [10], [16]. A rule of thumb however is suggested, which states that a typical concentration of about 10 mg/cm^2 of total Fe in the sample seems to be close to the optimum concentration of the resonant isotope for ^{57}Fe Mössbauer spectroscopy [16].

In this thesis, the samples were fine polycrystalline powders, evenly spread in the form of thin layers inside the Mössbauer sample holders. If the sample was granular or had agglomerated grains, it was pulverized to fine powder form using an agate mortar and pestle for the holder preparation. For natural iron samples, which contain 2.17% ^{57}Fe, a concentration of about 5 mg/cm^2 was used in the Mössbauer holders. When synthesized samples lacked enough mass for even distribution on the holder's surface, they were mixed with inert, low-γ-absorption materials such as fine sugar or coal. The Mössbauer holders themselves were made of materials with low atomic numbers, like plexiglass or ABS polymer, to minimize γ-radiation absorption (Figure 2.25). The fine powder was kept firmly in place to the sample holder inner surface by putting and pressing a properly cut styrofoam disk on top of it before sealing the holder with the appropriate cup.

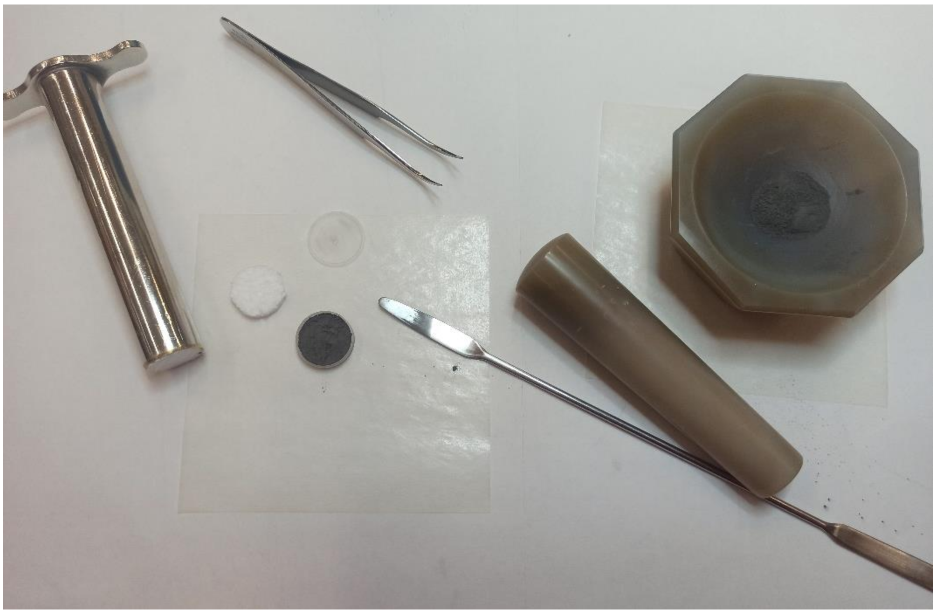

Figure 2.25 Picture of the tools for preparation and form of a fine powder Mössbauer holder used in this thesis.

2.4.4.4 Mössbauer Detectors

Mössbauer γ-radiation detectors convert photons transmitted through a sample into electrical pulses. Ideally, the detector should be highly sensitive to Mössbauer radiation while minimizing detection of other photon types. This helps to reduce the counter's dead time and protects downstream electronics from unnecessary strain, enabling fast counting events with strong pulses and high-count rates. For transmission measurements, Mössbauer spectrometers typically use gas-filled proportional counters, which offer good energy resolution, can handle high count rates, and can be tuned for sensitivity to specific Mössbauer radiation by adjusting the type of gas and the chamber dimensions. These detectors are also affordable and durable [10], [16].

Proportional counters are filled with gases such as argon, krypton, or xenon, often mixed with about 10% of a quench gas like methane. For the 14.4 keV radiation from ^{57}Co, their efficiency typically ranges from 60–80%. In our studies, we used two types of gas-filled proportional counters: one filled with a mixture of 90% argon and 10% methane, supplied by Karl-Heinz Finder, with an efficiency of over 65% for 14.4 keV γ-rays, and another, a krypton-carbon dioxide detector with a 97%-to-3% ratio at 2 atm pressure, from Reuter Stokes, with an efficiency of around 80% [11].

2.4.4.5 The ^{57}Fe Mössbauer Transmission Spectrum

In a Mössbauer transmission experiment, the stable isotope-containing absorber is positioned between the radiation source and detector (Figure 2.26).

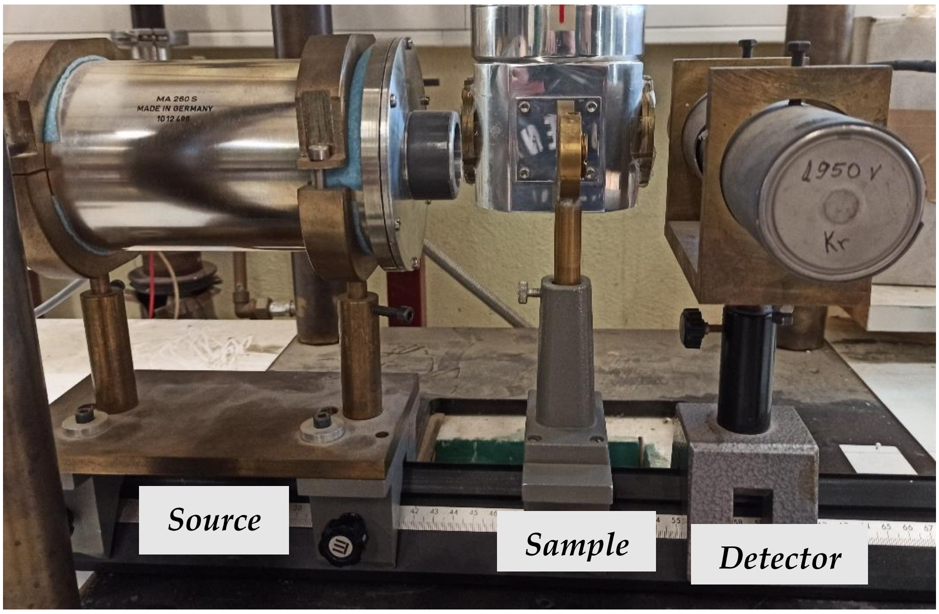

Figure 2.26 Picture of the Mössbauer drive/source-sample-detector experimental setup of a ^{57}Fe Mössbauer spectrometer.

The 14.4 keV γ-rays passing through the absorber are attenuated by resonant absorption from all the Mössbauer nuclei (such as iron atoms or ^{57}Fe ions) in the sample. If all these nuclei are subject to the same hyperfine interactions, their contributions combine to form a single spectrum that reflects those interactions. However, when the Mössbauer nuclei are subjected to various types of hyperfine interactions, the total spectrum is a superposition of individual components, each corresponding to a different interaction.

The total absorption area under the spectrum curve (measured from the baseline) is proportional to the total number of Mössbauer nuclei present in the absorber (Figure 2.27).

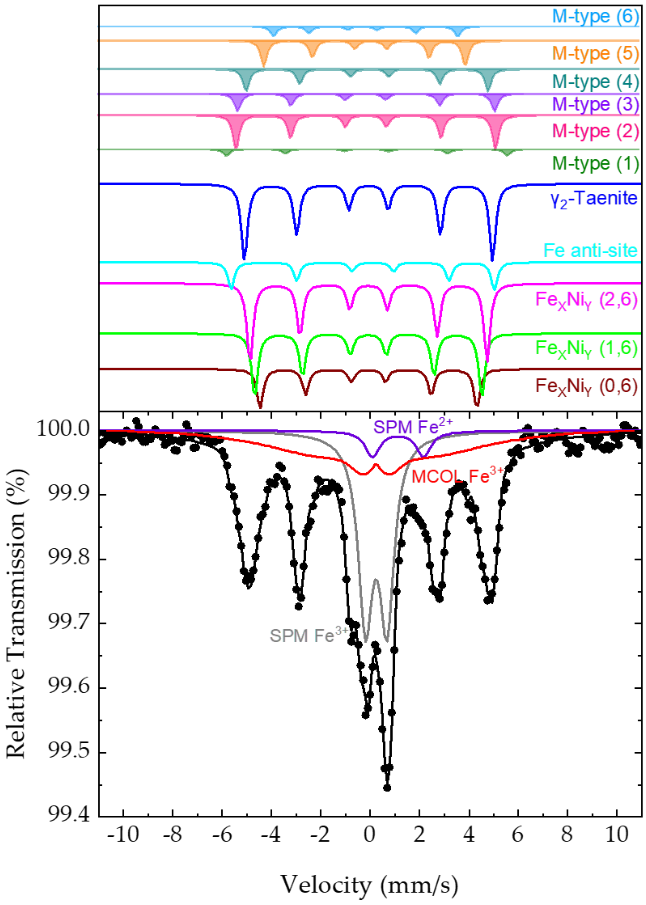

Figure 2.27 ^{57}Fe Mössbauer spectrum of a Fe-Ni NPs/NDs hybrid sample, collected at room temperature. The total spectrum is a superposition of individual components, each corresponding to a different interaction.

The proportion of each component in the total spectrum is proportional to the absorption area of the individual component, which is influenced by both the number of the related ^{57}Fe Mössbauer nuclei contained in the sample and the Debye-Waller (or Lamb-Mössbauer) factor (*f*) of the particular site corresponding to this component, which affect the resonant absorption. If the Debye-Waller factor is thought to be similar for all Mössbauer nuclei in the sample, which is the most commonly adopted case, then the absorption percentage of each component is directly related to the percentage of ^{57}Fe Mössbauer nuclei corresponding to that specific hyperfine interaction [10].

The electronic and magnetic properties of iron atoms or ions in the absorber are independent of the specific isotope within the sample, in the sense that all iron isotopes participate in the hyperfine interactions with the same manner. In naturally occurring materials however, the abundance of the ^{57}Fe isotope is consistently 2.17%. Therefore, the total number of iron atoms or ions with identical electronic and magnetic properties is proportional to the number of ^{57}Fe nuclei present. If the concentration of iron is low, it may be beneficial to enrich the absorber with reactants containing a higher proportion of ^{57}Fe nuclei to enhance the signal.

2.4.4.6 Mössbauer Cryostats

In many Mössbauer spectroscopy applications, cryostats are essential for low-temperature and temperature-dependent measurements. They are used to maintain samples at low temperatures or to improve Debye–Waller factors in absorbers, particularly for isotopes with high γ-energy. Paramagnetic samples are often studied at liquid-helium temperatures to slow down spin relaxation and investigate electronic ground states. Additionally, phase transitions and spin crossover phenomena require exploration over a wide range of temperatures. With a basic helium bath or flow cryostat, temperatures can be controlled between 1.2 K and 500 K.

For experiments requiring absorber temperatures below room temperature in this thesis, Mössbauer spectra were recorded using two types of cryostats. The liquified gas N_2 bath type (Oxford Instruments Variox 760) and the closed-loop He gas type cryocooler (ARS DMX-20). In these setups, the desired temperature is achieved by cooling the sample via its thermal contact with a proper gas that transfers the cooling power either from the liquified gas contained in the cryostat's reservoir (bath type N_2), or from a cold tip which is refrigerated through the cooling cycles of the refrigerating gas (He gas type cryocooler). Liquid nitrogen can achieve minimum temperatures of 78 K, while helium gas can cool samples to as low as 9 K (see Figure 2.28). Intermediate temperatures between the minimum and room temperature can be achieved through transfer of heating power with the use of appropriate electrical resistances housed in the cryostats. The temperature is monitored and adjusted using sensors like thermocouples and thin film resistances (Cernox), and temperature variation is managed by applying the electrical power to the electrical resistance circuit using a specialized temperature controller.

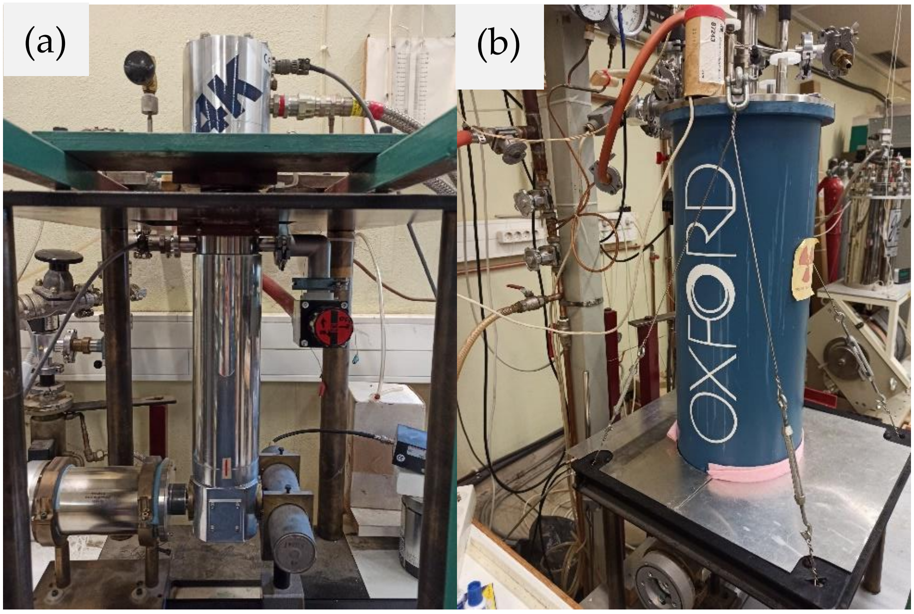

Figure 2.28 (a) He gas closed-loop ARS DMX-20 and (b) liquid N_2 bath Oxford Instruments Variox 760 Mössbauer cryostats.

2.5 References

[1] B. D. Cullity and S. R. Stock, *Elements of X-ray diffraction*, 3. ed. Upper Saddle River, NJ: Prentice Hall, 2001.

[2] C. Suryanarayana and M. G. Norton, *X-Ray Diffraction*. Boston, MA: Springer US, 1998. doi: 10.1007/978-1-4899-0148-4.

[3] H. P. Klug and L. E. Alexander, *X-Ray diffraction procedures: for polycrystalline and amorphous materials*. New York: Wiley, 1976.

[4] D. B. Williams and C. B. Carter, *Transmission Electron Microscopy*. Boston, MA: Springer US, 2009. doi: 10.1007/978-0-387-76501-3.

[5] N. I. Φλωρίνη, "Study of the structure and mechanical behavior of low-dimensional III-V semiconductor heterostructures," 2021, doi: 10.26262/HEAL.AUTH.IR.327655.

[6] B. D. Cullity and C. D. Graham, *Introduction to magnetic materials*, 2nd ed. Hoboken, N.J: IEEE/Wiley, 2009.

[7] J. M. D. Coey, *Magnetism and Magnetic Materials*, 1st ed. Cambridge University Press, 2001. doi: 10.1017/CBO9780511845000.

[8] V. Franco and B. Dodrill, Eds., *Magnetic Measurement Techniques for Materials Characterization*. Cham: Springer International Publishing, 2021. doi: 10.1007/978-3-030-70443-8.

[9] R. L. M�ssbauer, "Kernresonanzfluoreszenz von Gammastrahlung in Ir191," *Z. Physik*, vol. 151, no. 2, pp. 124–143, Apr. 1958, doi: 10.1007/BF01344210.

[10] P. Gütlich, E. Bill, and A. X. Trautwein, *Mössbauer Spectroscopy and Transition Metal Chemistry*. Berlin, Heidelberg: Springer Berlin Heidelberg, 2011. doi: 10.1007/978-3-540-88428-6.

[11] N. Tsoulfanidis and S. Landsberger, *Measurement & Detection of Radiation*, 5th ed. Boca Raton: CRC Press, 2021. doi: 10.1201/9781003009849.

[12] *Applications of Mossbauer Spectroscopy*. Elsevier, 1976. doi: 10.1016/B978-0-12-178401-0.X5001-X.

[13] G. Breit and E. Wigner, "Capture of Slow Neutrons," *Phys. Rev.*, vol. 49, no. 7, pp. 519–531, Apr. 1936, doi: 10.1103/PhysRev.49.519.

[14] V. Weisskopf and E. Wigner, "Berechnung der nat�rlichen Linienbreite auf Grund der Diracschen Lichttheorie," *Z. Physik*, vol. 63, no. 1–2, pp. 54–73, Jan. 1930, doi: 10.1007/BF01336768.

[15] U. Gonser, Ed., *Mössbauer Spectroscopy II: The Exotic Side of the Method*, vol. 25. in Topics in Current Physics, vol. 25. Berlin, Heidelberg: Springer Berlin Heidelberg, 1981. doi: 10.1007/978-3-662-08867-8.

[16] N. N. Greenwood and T. C. Gibb, *Mössbauer Spectroscopy*. Dordrecht: Springer Netherlands, 1971. doi: 10.1007/978-94-009-5697-1.

[17] E. Murad and J. Cashion, *Mössbauer Spectroscopy of Environmental Materials and Their Industrial Utilization*. Boston, MA: Springer US, 2004. doi: 10.1007/978-1-4419-9040-2.

[18] A. P. Douvalis, A. Polymeros, and T. Bakas, "IMSG09: A ^{57} Fe- ^{119} Sn Mössbauer spectra computer fitting program with novel interactive user interface," *J. Phys.: Conf. Ser.*, vol. 217, p. 012014, Mar. 2010, doi: 10.1088/1742-6596/217/1/012014.

Chapter 3. Interpretation of Superparamagnetic Relaxation Phenomena in Magnetic Nanoparticles

3.1 Introduction

In recent decades, the physics of nanoscale magnetic materials has garnered significant research attention, as magnetic NPs have played a crucial role in both fundamental research and technological innovations. For example, extensive studies on nanoscale magnetic particles have been conducted due to their potential in biomedical applications, such as enhancing MRI contrast agents, treating cancer cells with hyperthermia, targeted drug delivery, and manipulating cell membranes [1], [2], [3], [4].

Based on P. Weiss' hysteresis behavior [5], [6], [7], the magnetization ($\vec{M}$), of a bulk FM material, measured as a function of the applied magnetic field ($\vec{H}$), shows a characteristic hysteresis loop. This occurs due to the finite time required for the alignment of magnetic domains with the field at temperatures below the Curie point. These domains are separated by domain walls, which attempt to minimize the system's free energy. The magnetostatic energy increases with the volume of the material, while domain wall energy is proportional to the surface area. Therefore, a critical size exists below which domain formation becomes energetically unfavorable, resulting in a uniformly magnetized single domain. In this state, the particle behaves like a small permanent magnet. The size of this single-domain particle depends on various material properties, especially different anisotropy energy terms (Figure 3.1) [8], [9].

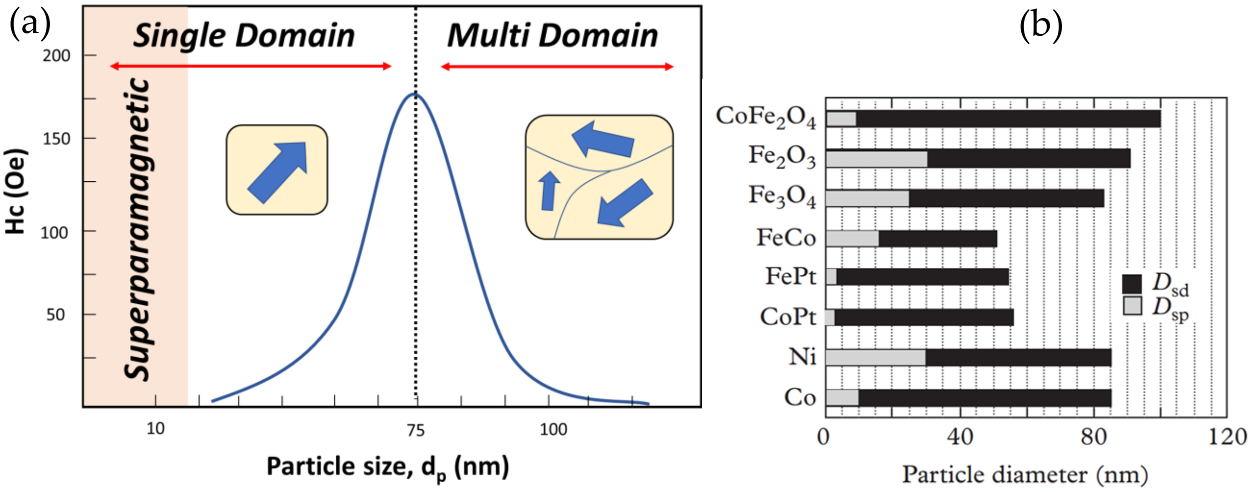

Figure 3.1 Schematic illustration of the particle size dependence of the coercivity of magnetite nanoparticles measured at 300 K (a), and critical sizes (in diameter) of superparamagnetic, D_{sp}, and single domain, D_{sd}, metal, alloy and oxide nanoparticles of spherical shape (b) [7].

Additionally, single-domain particles exhibit another notable feature: their magnetization reversal mechanism. This involves the rotation of $\vec{M}$, from one magnetic easy axis to another, passing through a magnetically hard direction. This rotation allows for control over the coercivity of magnetic nanoparticles, which typically falls between that of soft magnetic and conventional permanent magnet materials. The ability to regulate coercivity has led to significant technological advancements, particularly in data storage. However, one limitation of MNPs is the instability of their magnetization direction due to environmental thermal energy, which can overcome the energy barrier between easy magnetization directions. This effect, known as superparamagnetic (SPM) relaxation, causes each NP to behave like a paramagnetic atom, a crucial factor in the development of high-density magnetic data storage systems [5], [9].

3.2 Relaxation Phenomena in Magnetic Nanoparticles

To better understand relaxation phenomena in MNPs, it is essential to recall some basic magnetic concepts [5], [6], [7]. Magnetic anisotropy refers to the dependence of internal energy on the direction of spontaneous magnetization, creating easy and hard magnetization axes. The system's total magnetization tends to align along the easy axis. This energy difference between easy and hard axes arises from two microscopic interactions: the spin-orbit interaction and the long-range dipolar coupling of magnetic moments. Spin-orbit coupling causes intrinsic magnetocrystalline (MCA) anisotropy, surface anisotropy, and magnetostriction, while dipolar interactions contribute to shape anisotropy. Anisotropy is stronger in lattices with low symmetry and weaker in high-symmetry lattices. In bulk materials, MCA and magnetostatic energies are the primary sources of anisotropy. However, in fine particles, thin films, and nanostructures, shape and surface anisotropies become increasingly relevant.

Shape anisotropy results from the specimen's geometry. A single-domain spherical particle has no shape anisotropy, as the demagnetizing factors are isotropic in all directions. In contrast, non-spherical samples are easier to magnetize along the longer axis due to a smaller demagnetizing field, as the surface poles are farther apart.

Surface anisotropy arises from broken symmetry and reduced coordination at the surface. As particle size decreases, surface contributions become more significant than bulk contributions, leading surface anisotropy to dominate over MCA and magnetostatic energies.

Thus, the magnetic anisotropy of nanoparticles is complex. It is often assumed that nanoparticles exhibit dominant uniaxial anisotropy, with the magnetic energy expressed as:

$$E = KV \sin\theta, \text{ (3.1)}$$

where K is an effective magnetic anisotropy constant, V is the particle volume and θ is the angle between the magnetization direction and the easy axis of the magnetization [8], [9]. In this case, there are two energy minima at θ = 0° and θ = 180° separated by an energy barrier of height KV. In very small particles at finite temperatures, thermal energy can be comparable to the energy barrier leading to SPM relaxation, where the magnetization direction fluctuates spontaneously between the two easy directions. The SPM relaxation time τ is approximately described by the Neel–Brown expression [5], [7]:

$$\tau = \tau_0 exp\left({KV}/{k_B T}\right), \text{ (3.2)}$$

where τ_0 is typically of about 10^{-12} ~ 10^{-9} s, k_B is the Boltzmann's constant and T is the temperature. This equation applies to well-separated particles, where magnetic interactions between these particles are considered negligible [5], [7].

In principle, the SPM relaxation time describes the time needed for thermal excitations of a particle's magnetic moment to occur over an energy barrier, KV. It is generally agreed that τ_0, that is the attempt time or inverse attempt frequency, is related to the Larmor pre cession frequency of the moment, $\omega_L = \gamma\mu_0 H_{eff}$, where $\gamma = \frac{2}{2m_e}$ and H_{eff} is the resultant of the applied field, H_{app}, and the anisotropy field, $H_K = \frac{2K}{\mu_0 M_s}$, where Ms is the saturation magnetization. For weak applied fields, $H_{app} << H_K$ and $H_{eff} = H_K$. Thus,

$$\tau_0 \sim \frac{1}{\mu_0 \alpha\gamma H_K} = \frac{M_S}{2\alpha\gamma K}, \text{ (3.3)}$$

where α is the dimensionless Gilbert damping parameter, that ensures that the particle magnetization is eventually aligned with the magnetic field, instead of rotating forever around the applied field axis [7].

SPM relaxation can be studied using various experimental techniques, where the timescale of the technique is critical. If the relaxation time is longer than the experimental timescale, the magnetization appears static; if it is shorter, an average magnetization is observed. As the SPM relaxation is temperature-dependent, the temperature at which the relaxation time matches the experimental timescale is known as the blocking temperature (T_B). Each experimental technique defines its own blocking temperature based on its timescale. In real samples which are often composed of an assembly of particles with different sizes and shapes, a distribution of particle size and anisotropy constants is often observed, leading to a distribution of energy barriers and thus relaxation times. The median blocking temperature is the point at which half the sample's particles have relaxation times shorter than the experimental timescale, and the other half have longer times. In DC magnetization measurements, the timescale is in seconds or longer, while AC magnetization allows the timescale to be adjusted based on the frequency of the alternating applied field. Mössbauer spectroscopy, with a timescale in the vicinity of nanoseconds, is commonly used for nanoparticles with short relaxation times [8], [9].

Furthermore, below the blocking temperature, where the SPM relaxation is slow, thermal fluctuations can still influence the magnetic properties through collective magnetic excitations. These involve small fluctuations of the magnetization direction near the easy axis, where the magnetic moments of all atomic or ionic spins within the magnetic domain remain parallel (Figure 3.2) [10].

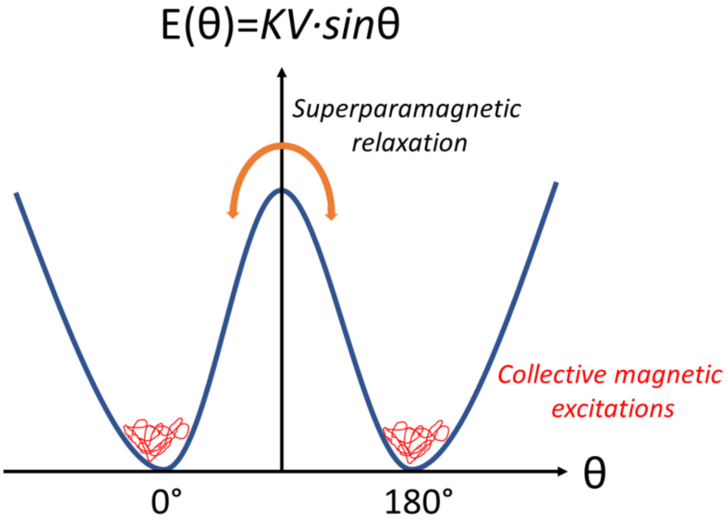

Figure 3.2 Schematic illustration of the free energy of a single domain particle with uniaxial anisotropy as a function of magnetization direction. E_B is the energy barrier KV, and θ is the angle between the magnetization and the easy axis.

3.3 Characterization of Nanoparticles

3.3.1 Structural and Morphological Characterization

In studies of magnetic nanoparticles, it is essential that they are well characterized with respect to purity, size, shape, and so on. A standard technique for characterization of nanoparticles is X-ray diffraction, which is used to identify the crystalline phases in a sample. Analysis of a sample by powder XRD provides important information that is complementary to various microscopic and spectroscopic methods, such as phase identification, sample purity, crystallite size, and, in some cases, morphology [11], [12]. As a bulk technique, the information it provides can be correlated with microscopy data to test if microscopic observations on a small number of particles are representative of the majority of the sample.

Powder XRD analyses can provide insights about many properties of nanostructured materials, since they can be influenced from the structure, size and shape effects. When the crystallite size decreases from bulk to nanoscale dimensions, the XRD peaks broaden. The Scherrer equation (3.3) quantitatively describes the broadening of a peak at a particular diffraction angle θ_B, as it relates the crystalline domain size t to the width of the peak at half of its height B. The Scherrer constant, K, is typically considered to be 0.91 but can vary with the morphology of the crystalline domains.

$$t = {}^{K\lambda}\!/_{Bcos\theta_B}. \quad (3.4)$$

The X-ray wavelength (λ) remains constant based on the type of X-rays used. Each peak in the XRD pattern can be analyzed independently and should consistently reflect the crystalline domain size, assuming the sample can be approximated as having uniform, spherical particles [11].

It is important to understand that the crystalline domain size does not always equate to the particle size, as some particles may be polycrystalline and contain multiple domains. If the crystalline domain size calculated through the Scherrer equation aligns with the average particle diameter measured by TEM or other sizing techniques, this indicates that the particles are likely single crystals rather than polycrystalline.

As the size decreases from bulk material to the nanoscale, the XRD peaks broaden slightly. With further size reduction, the broadening becomes more significant, resulting in lower signal intensity, overlapping peaks, and difficulty in distinguishing individual peaks. Therefore, particles with very small crystalline domains are harder to analyze due to the combination of broadened peaks and low signal-to-noise ratios (Figure 3.3) [12].

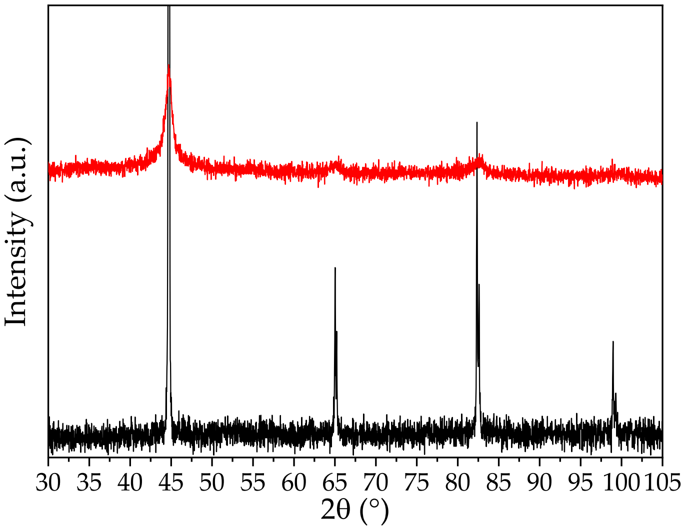

Figure 3.3 Peak line broadening between bulk a-Fe (bottom black curve) and nanostructured a-Fe (top red curve) materials through XRD measurements.

This size-dependent broadening of XRD peaks is crucial for nanomaterial characterization. For example, if TEM shows spherical particles with an average diameter of 10 nm, but the XRD pattern has sharp peaks typical of larger crystalline domains, this would suggest that most of the bulk sample is not composed of 10 nm particles. Instead, the observed 10 nm particles are likely a minority within the sample.

TEM is a commonly used method for characterizing nanoparticles, providing details on both particle size and morphology. In the analysis of crystalline nanoparticles, electron diffraction helps identify the crystal structure (Figure 3.4). High-resolution TEM can often reveal lattice planes, enabling further investigation of the crystal structure.

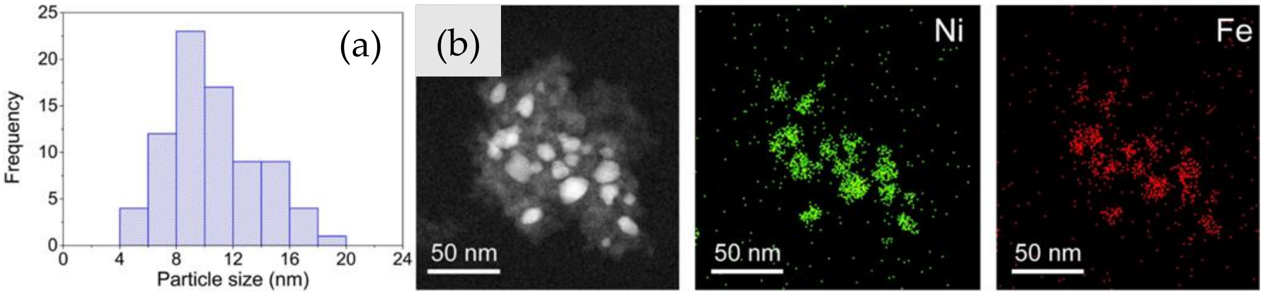

Figure 3.4 Distribution of Fe-Ni metallic nanoparticles sizes in a hybrid FeNi NPs/NDs sample (a), and HAADF STEM images of a particular hybrid Fe-Ni NPs/NDs cluster (b) with the corresponding elemental distribution of Ni and Fe.

3.3.2 DC Magnetic Measurements of Noninteracting Magnetic Nanoparticles

When a sample of SPM particles is exposed to an applied magnetic field above the blocking temperature, the measured magnetization equals its thermal equilibrium value, that is, the particles are magnetized in a way that is similar to a paramagnetic material. However, the magnetic moments that interact with the applied magnetic field are the moments of whole particles, which can be hundreds or thousands of Bohr magnetons. This is in contrast to paramagnetic materials in which only the magnetic moments of individual ions (typically a few Bohr magnetons) interact with the field. Therefore, at a given temperature, the magnetization of a sample of superparamagnetic particles will approach the saturation value much faster than for a paramagnetic material [8], [9].

Often, the superparamagnetic relaxation in samples of magnetic nanoparticles is studied by measuring the so-called zero-field-cooled (ZFC) and the field-cooled (FC) magnetization curves. A ZFC magnetization curve is obtained by cooling the sample in zero applied magnetic field from a temperature, where the entire sample shows a superparamagnetic response. Then the magnetic field, with low or high strength depending on the magnitude of the magnetization response of the sample, is applied and the magnetization of the sample is measured as a function of temperature during heating. Usually the FC magnetization curve is measured sequentially after the ZFC measurement, by applying the magnetic field and the measurement is done as a function of decreasing temperature (Figure 3.5) [5].

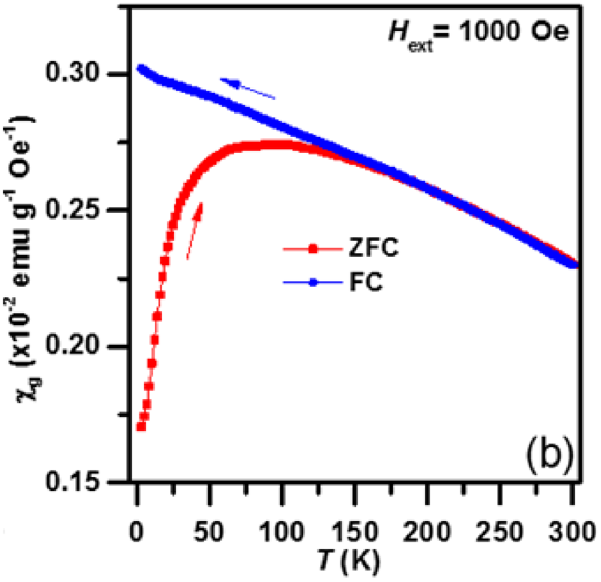

Figure 3.5 ZFC and FC magnetization curves measured on a ferromagnetic hybrid nanostructured material of iron carbide nanoparticles grown on nanodiamond nanoparticles nanotemplates.

At temperatures well below the blocking temperature, the zero-field cooled (ZFC) magnetization is low because the sample is not in thermal equilibrium. In this state, the magnetization directions of the particles, when subjected to a small applied field, are largely influenced by the randomly oriented easy magnetization directions. As the temperature rises, smaller particles begin to enter the superparamagnetic state, increasing the likelihood of their magnetization aligning with the applied field, which results in higher magnetization. With continued temperature increases, more particles become superparamagnetic, leading to further magnetization increases. On the other side, as the temperature increases further the increasing thermal energy causes a decline in magnetization due to the overall effect of increased fluctuations of all particles. Thus, a maximum in the ZFC magnetization curve is typically observed in Figure 3.5.

In the field-cooled (FC) state, the magnetization of the majority of particles remains frozen in directions that align closely due to the simultaneous application of the external magnetic field and the cooling procedure, making it significantly larger than that observed in the ZFC state. The ZFC and FC curves converge at the bifurcation temperature, which is the temperature above which all particles achieve a superparamagnetic state [5].

ZFC magnetization curves are often modeled to indicate that well below the blocking temperature, the magnetic moments are frozen in random easy directions. The effect of an applied external field, in this case, is to slightly alter the directions of minimum energy.

When analyzing ZFC susceptibility curves for real samples, it is commonly assumed that their response is influenced by the particle size distribution on the relaxation time, which notably smooths out the sharp transition between the blocked and superparamagnetic states. Typically, the timescale for such measurements is around $\tau_m \approx 100$ s. It is essential to note that the peak in the ZFC magnetization curve corresponds to the blocking temperature for particles of uniform size.

However, in samples with a distribution of particle sizes, the peak temperature can be as much as twice the blocking temperature of the particles of uniform size [9].

3.3.3 ^{57}Fe Mössbauer Spectroscopy

^{57}Fe Mössbauer spectroscopy is frequently employed to investigate the magnetic properties of nanoparticles. Due to its high sensitivity to relaxation processes occurring on a nanosecond timescale, this technique is ideal for studying relaxation phenomena that cannot be examined using methods like AC and DC susceptibility measurements.

In bulk magnetic materials, the ^{57}Fe Mössbauer spectra typically feature spectral sextets with narrow linewidths, depending on the number of different iron atomic sites present. The spacing between these spectral lines reflects the strength of the magnetic field at the nucleus. However, in studies involving magnetic nanoparticles, SPM relaxation can significantly impact the shape of the spectra, depending on the relaxation time. The timescale of Mössbauer spectroscopy, τ_M, is linked to the Larmor precession time of the nuclear magnetic moment in the magnetic hyperfine field [13], [14]. In ^{57}Fe Mössbauer spectroscopy, τ_M is typically a few nanoseconds. When the relaxation time is long compared to τ_M (slow relaxation), the spectra exhibit sharp sextets. As the relaxation time approaches τ_M, the lines become increasingly broader, and the magnetic splitting begins to collapse. For extremely short relaxation times, less than 10^{-10} s (fast relaxation), the spectra show only singlets or doublets (Figure 3.6) [9].

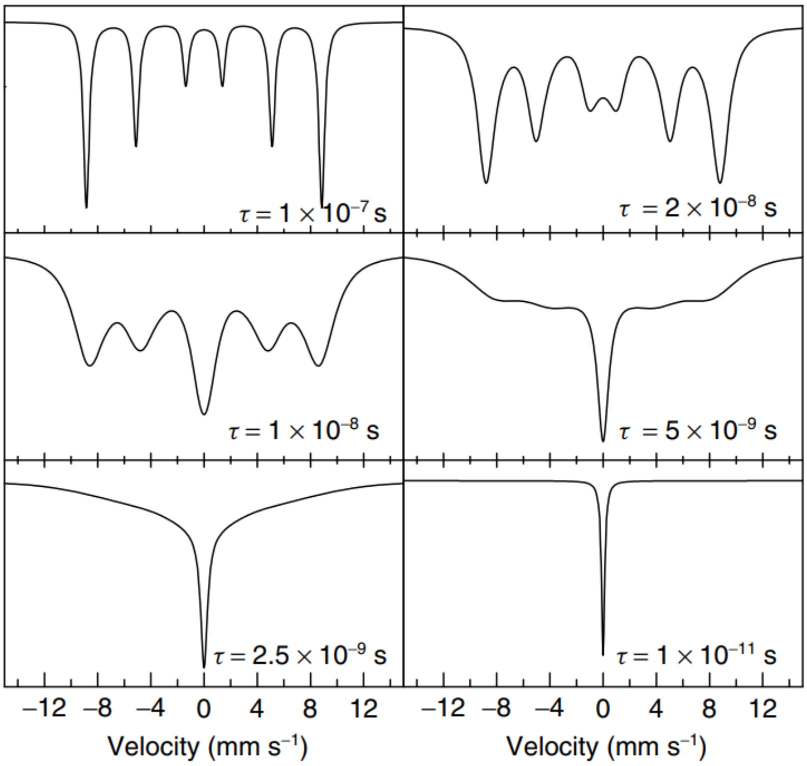

Figure 3.6 Theoretical calculated ^{57}Fe Mössbauer spectra of a typical magnetically oriented sample of nanoparticles of identical sizes at different superparamagnetic relaxation times τ [9].

Due to the inevitable variation in particle size, a wide range of relaxation times is observed in nanoparticle samples. This causes a broadening of the spectral lines in the corresponding Mössbauer spectra, as different groups of nanoparticles are contributing different shapes of subspectra in superposition. When τ_0 is small in comparison to τ_M, the typical particle size distribution produces a broad spread of relaxation times, especially near the blocking temperature, where the average relaxation time is close to τ_M. As a result, only a small proportion of the particles have relaxation times similar to τ_M. Therefore, the spectra primarily consist of a sextet with narrow lines, corresponding to particles well below their blocking temperature ($\tau >> \tau_M$), alongside to a sharp singlet or doublet from particles undergoing fast SPM relaxation ($\tau << \tau_M$) [9]. However, at higher temperatures additional contributions of from components with collapsing magnetic splitting characteristics can also be observed due to the increase of the portion of particles that have comparable relaxation time values to τ_M.

3.4 References

[1] I. Astefanoaei, R. Gimaev, V. Zverev, and A. Stancu, “Modelling of working parameters of Gd and FeRh nanoparticles for magnetic hyperthermia,” *Mater. Res. Express*, vol. 6, no. 12, Art. no. 12, Dec. 2019, doi: 10.1088/2053-1591/ab5c4a.

[2] M. Barbic *et al.*, “Magnetocaloric materials as switchable high contrast ratio MRI labels,” *Magn. Reson. Med.*, vol. 81, no. 4, Art. no. 4, Apr. 2019, doi: 10.1002/mrm.27615.

[3] V. I. Zverev, A. P. Pyatakov, A. A. Shtil, and A. M. Tishin, “Novel applications of magnetic materials and technologies for medicine,” *Journal of Magnetism and Magnetic Materials*, vol. 459, pp. 182–186, Aug. 2018, doi: 10.1016/j.jmmm.2017.11.032.

[4] G. Song *et al.*, “Carbon-coated FeCo nanoparticles as sensitive magnetic-particle-imaging tracers with photothermal and magnetothermal properties,” *Nat Biomed Eng*, vol. 4, no. 3, pp. 325–334, Feb. 2020, doi: 10.1038/s41551-019-0506-0.

[5] J. M. D. Coey, *Magnetism and Magnetic Materials*, 1st ed. Cambridge University Press, 2001. doi: 10.1017/CBO9780511845000.

[6] D. Jiles, *Introduction to magnetism and magnetic materials*, Third edition. Boca Raton: CRC Press, Taylor & Francis Group, 2016.

[7] K. M. Krishnan, *Fundamentals and applications of magnetic materials*, First edition. Oxford, United Kingdom: Oxford University Press, 2016.

[8] S. Bedanta and W. Kleemann, “Supermagnetism,” *Journal of Physics D: Applied Physics*, vol. 42, p. 013001, Dec. 2008, doi: 10.1088/0022-3727/42/1/013001.

[9] S. Mørup and M. Hansen, “Superparamagnetic Particles,” 2007. doi: 10.1002/9780470022184.hmm409.

[10] S. Mørup, C. Frandsen, and M. F. Hansen, “Uniform excitations in magnetic nanoparticles,” *Beilstein J. Nanotechnol.*, vol. 1, pp. 48–54, Nov. 2010, doi: 10.3762/bjnano.1.6.

[11] B. D. Cullity and S. R. Stock, *Elements of X-ray diffraction*, 3. ed. Upper Saddle River, NJ: Prentice Hall, 2001.

[12] C. F. Holder and R. E. Schaak, “Tutorial on Powder X-ray Diffraction for Characterizing Nanoscale Materials,” *ACS Nano*, vol. 13, no. 7, pp. 7359–7365, Jul. 2019, doi: 10.1021/acsnano.9b05157.

[13] N. N. Greenwood and T. C. Gibb, *Mössbauer Spectroscopy*. Dordrecht: Springer Netherlands, 1971. doi: 10.1007/978-94-009-5697-1.

[14] P. Gütlich, E. Bill, and A. X. Trautwein, *Mössbauer Spectroscopy and Transition Metal Chemistry*. Berlin, Heidelberg: Springer Berlin Heidelberg, 2011. doi: 10.1007/978-3-540-88428-6.

Chapter 4. Sample Synthesis

4.1 Materials Synthesis of the Fe-Rh/NDs System

The synthesis of hybrid magnetic crystalline Fe-Rh/NDs nanostructures involved the combination of two steps (Scheme 4.1), an initial wet chemistry step, aiming to the delivery of the as-made (AM) chemical precursors, followed by thermal treatments of these precursors under controlled conditions. A nominal Fe:Rh atomic ratio of 1:1 was implemented using appropriate amounts of the corresponding metal salts, while a total ~10 wt.% of combined Fe and Rh metal-to-ND mass ratio was also considered. For the first stage, alongside the as-made hybrid sample (FeRh-AM-ND), an as-made unsupported Fe-Rh sample (FeRh-AM-NP), with the same nominal Fe:Rh=1:1 atomic stoichiometry was also prepared. The comparison between the properties of the hybrid and unsupported samples is designed to evaluate the effect of the presence of NDs, leading thus to a deeper understanding and a better interpretation of the NDs' matrix role in the growth of the nanoalloy phases during th synthesis procedure. In this work, the wet chemical route is based on the use of the ($NaBH_4$) reducing agent [1].

In particular, in the first stage, 270 mg NDs (⩾ 97 % Aldrich 636428, St. Louis, MO, USA) were suspended in a beaker containing 30 mL deionized H_2O to afford a fine aqueous slurry. In another beaker, 200 mg NaOH were dissolved in 20 mL of deionized H_2O followed by the addition of 40 mg $RhCl_3$ (98 % Aldrich 307866). The mixture was stirred for 2 hours until full dissolution of the rhodium salt ($RhCl_3$ is insoluble in water but soluble in alkaline solutions). At this point the pH of the solution was brought to 6-7 by concentrated HCl (37 %) prior to the addition of 30 mg anhydrous $FeCl_3$ (97 % Aldrich 157740) dissolved in 1 mL of deionized H_2O. The pH-adjustment was necessary in order to avoid alkaline precipitation of iron (III). The resulting solution was further diluted with water until a total volume of 40 mL. After combining the salt solution with the NDs slurry, 300 mg $NaBH_4$ (99 % Aldrich 213462) were rapidly added and the mixture was stirred for 20 minutes at ambient conditions. The material was centrifuged and washed with deionized water and acetone prior to air drying to afford the as-made hybrid sample FeRh-AM-ND. In the second stage, the FeRh-AM-ND sample was sealed under vacuum (10^{-3} Torr) in a quartz ampoule, that was then thermally treated at 700 °C for 30 minutes, affording the FeRh-AN-ND sample (Scheme 4.1(a)).

For the sample of unsupported NPs, 40 mg $RhCl_3$ (98 % Aldrich 307866) and 30 mg anhydrous $FeCl_3$ (97 % Aldrich 157740) were dissolved in deionized water, as also described above for the hybrid sample, to afford 40 mL of salt solution. The latter was poured into 30 mL deionized H_2O, followed by the rapid addition of 300 mg $NaBH_4$ (99 % Aldrich 213462) under vigorous stirring. The mixture was stirred for 20 minutes under ambient conditions. The as-formed precipitate was allowed to settle and rinsed with deionized water and acetone prior to air drying, acquiring the as made unsupported sample FeRh-AM-NP. In the same manner as for its hybrid counterpart, a following annealing process of the FeRh-AM-NP sample sealed in a quartz ampoule under vacuum (10^{-3} Torr) at 700 °C for 30 minutes took place, affording the FeRh-AN-NP sample (Scheme 4.1(b)). The nature of the nanostructured phases, including their crystal structure, morphology, particle size, self-organization, and dispersion on the NDs matrices, is expected to critically affect the magnetic properties of the prepared hybrid materials. These characteristics can be controlled through the preparation conditions, such as the synthesis procedure, annealing temperature and duration, and the concentration of NPs grown on the NDs substrate.

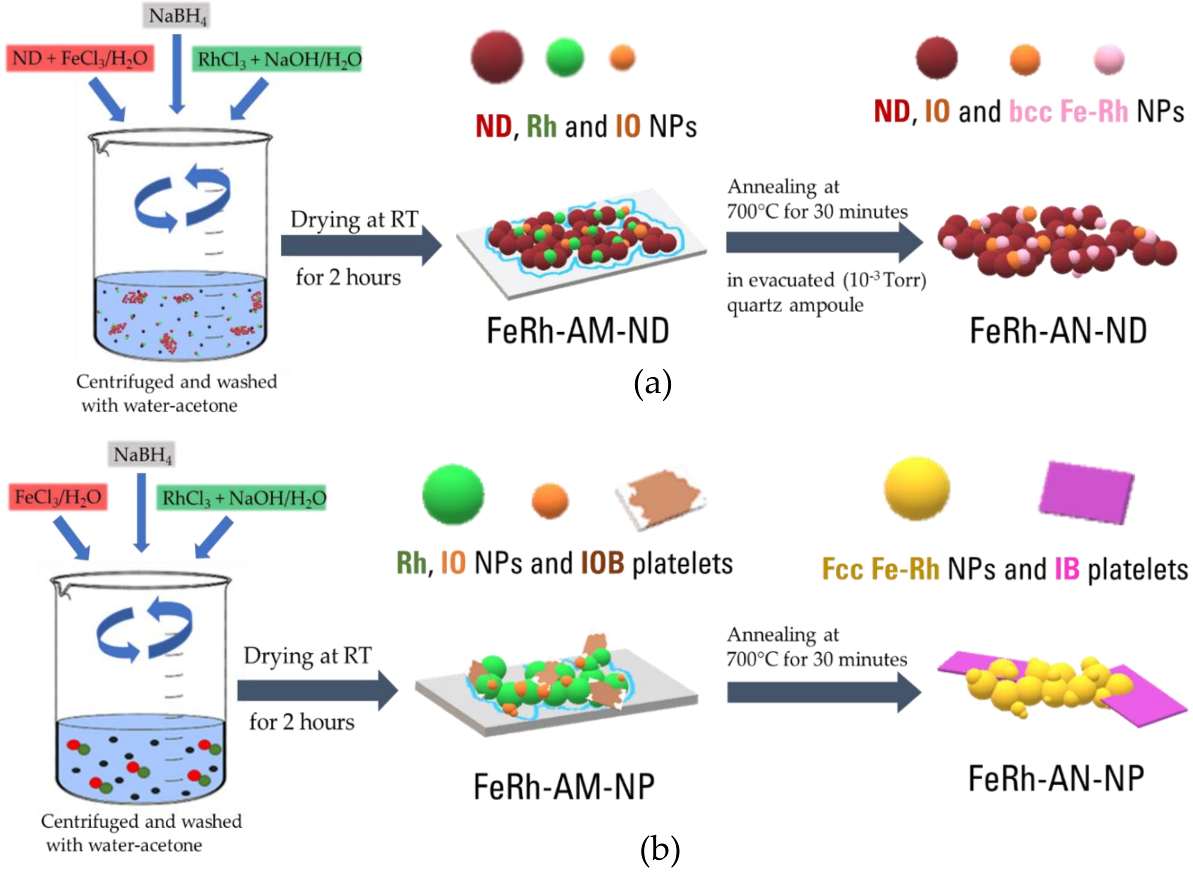

Scheme 4.1 Graphic representation of the synthesis procedure of the as-made and annealed samples for the hybrid Fe-Rh/NDs (a) and unsupported Fe-Rh NPs (b) cases.

The synthesis of the magnetic hybrid crystalline Fe-Rh/NDs and unsupported Fe-Rh nanostructures yielded four as-prepared precursor samples, from which three annealed samples were subsequently derived. For simplicity, we use the abbreviated notation codes listed in Table 4.1 to refer to the samples discussed.

Table 4.1 Abbreviated code names of the prepared samples of the Fe-Rh/NDs system.

Samples	Code Names	Brief Description
FeRh-BH-AM1-NHD	BH-AM1-NHD	Precursor (01)
FeRh-BH-AM1-NP	BH-AM1-NP	Free as-made unsupported NPs (01)
FeRh-BH-AN(700C,30m)-NHD	BH-NHD1-700C,30m	Fe-Rh NPs/NDs Nanohybrids annealed at 700 °C for 30 min

FeRh-BH-AN(700C,30m)-NP	BH-NP1-700C,30m	Free unsupported NPs annealed at 700 °C for 30 min
FeRh-BH-AM2-NHD	BH-AM2-NHD	Precursor (02)
FeRh-BH-AM2-NP	BH-AM2-NP	Free as-made unsupported NPs (02)
FeRh-BH-AN(700C,30m)-NHD	BH-NHD2-700C,30m	Fe-Rh NPs/NDs Nanohybrids annealed at 700 °C for 30 min

Following this, the properties of these representative samples of the Fe-Rh/NDs system are discussed in Chapter 5.

4.2 Materials Synthesis of the Fe-Co/NDs System

Similar to the synthetic procedure used for the Fe-Rh/NDs system, the synthesis of the Fe-Co/NDs nanohybrids system involved also two main steps. The first step was a wet chemistry process aimed to deliver the AM chemical precursors, followed by annealing of these precursors under controlled conditions. In this synthesis however, two different wet chemistry synthetic routes were employed: one utilizing the $NaBH_4$ reducing agent and the other using the impregnation method [1], [2], [3]. The goal of implementing both methods was to evaluate their effectiveness in producing the desired magnetic nanohybrid and unsupported nanostructures for comparison of their properties and effect of the NDs supporting matrix, as done for the Fe-Rh/NDs system, and to determine which method provides the highest yield of these magnetic nanoalloy materials.

In the $NaBH_4$ reducing agent synthetic route, a nominal Fe:Co atomic ratio of 1:1 was implemented using appropriate amounts of the corresponding metal salts, while a total ~10 wt.% of combined Fe and Co metal-to-ND mass ratio was also considered for the preparation of the as-made hybrid precursor sample. For the first step, alongside the as-made hybrid precursor sample (FeCo-BH-AM-ND), an as-made unsupported Fe-Co precursor sample (FeCo-BH-AM-NP), with the same nominal Fe:Co = 1:1 atomic stoichiometry was also prepared.

In particular, in the first stage, 185 mg NDs (⩾ 97 % Aldrich 636428) were suspended in a beaker containing 20 mL deionized H_2O and 48 mg of hydrous $FeCl_3$ (97 % Aldrich 157740) mixed with 42 mg hydrous $CoCl_2$ (97 % Aldrich 769495) in order to afford a fine aqueous material. After combining the salt solution with the NDs, 200 mg $NaBH_4$ (99 % Aldrich 213462) combined with 5 mL H_2O were rapidly added and the mixture was stirred for 20 minutes at ambient conditions. Then the material was centrifuged and washed with deionized water and acetone prior to air drying in a hood, to afford the as-made hybrid precursor sample FeCo-BH-AM-ND.

In the second stage, the FeCo-BH-AM-ND precursor sample was sealed under vacuum (10^{-3} Torr) in quartz ampoules, that would be afterwards thermally treated at the proper annealing conditions (annealing at 600 °C, 650 °C and 700 °C for 2 seconds, in case of the 700 °C thermal treatment, 30 minutes, 2, 8 and 32 hours in all cases), affording the FeCo-BH-AN-ND sample (Scheme 4.2(a)).

For the unsupported NPs sample, 423 mg of hydrous $CoCl_2$ (97 % Aldrich 769495) and 480 mg of hydrous $FeCl_3$ (97 % Aldrich 157740) were dissolved in 200 mL of deionized water to create the salt solution. This solution was poured into 50 mL deionized H_2O, followed by the rapid addition of 2 g $NaBH_4$ (99 % Aldrich 213462) under vigorous stirring. The mixture was stirred for 20 minutes at room temperature. The resulting precipitate was allowed to settle, then rinsed with deionized water and acetone, and air dried at room temperature for 2 hours, yielding the as-made unsupported precursor sample FeCo-BH-AM-NP. In a similar manner to its hybrid counterpart, the FeCo-BH-AM-NP precursor sample underwent an annealing process in a sealed quartz ampoule under vacuum (10^{-3} Torr) at the appropriate conditions (annealing at 600 °C, 650 °C and 700 °C for 2 seconds, in case of the 700 °C thermal treatment, 30 minutes, 2, 8 and 32 hours in all cases), resulting in the FeCo-BH-AN-NP sample (Scheme 4.2(b)). The synthesis of both hybrid and unsupported samples and the investigation of their properties aim to highlight the unique role of the NDs nanotemplates and their influence on the formation of magnetic nanoalloys during the synthetic process.

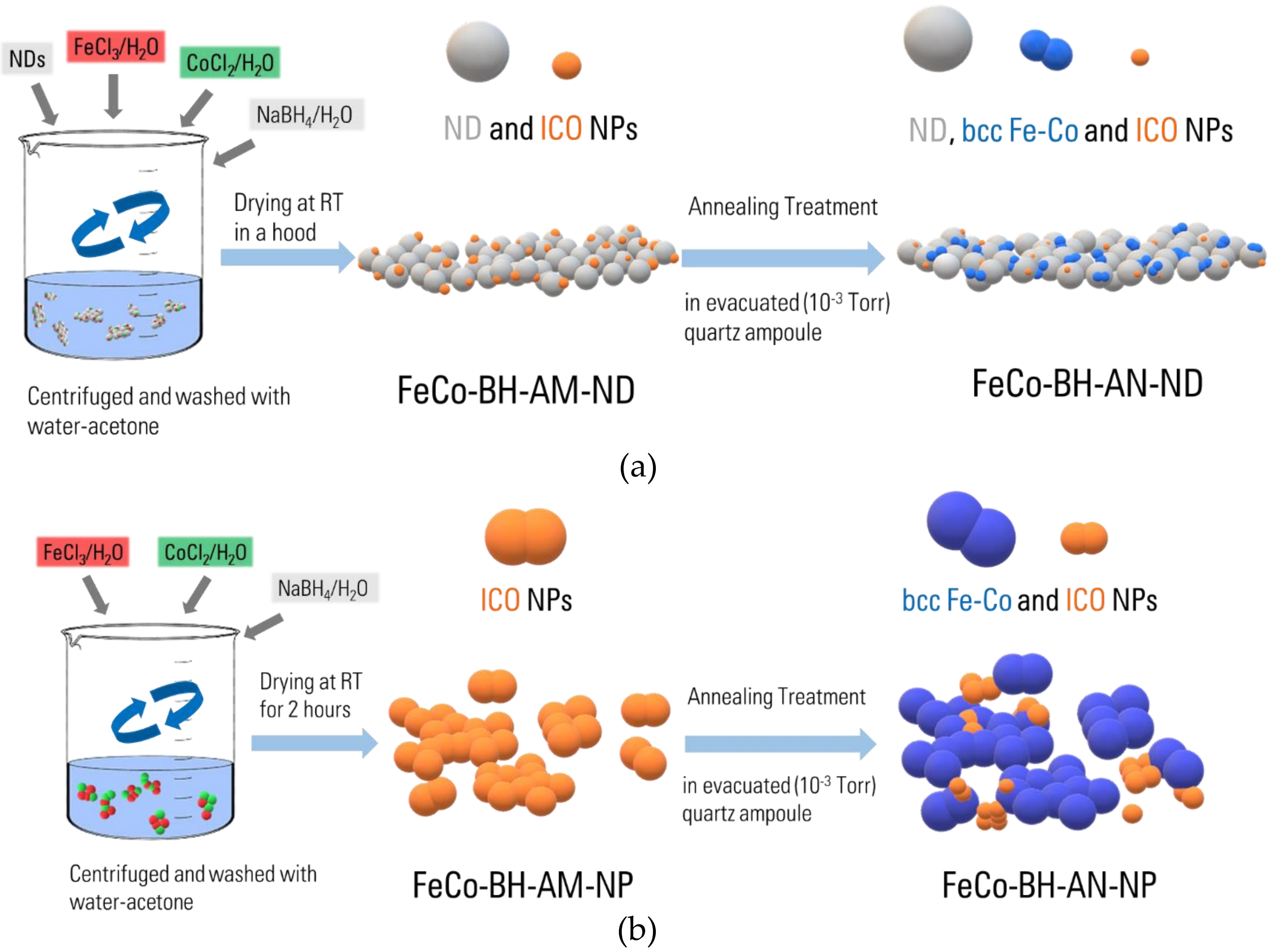

Scheme 4.2 Graphic representation of the synthesis procedure of the as-made and annealed hybrid Fe-Co/NDs (a) and unsupported Fe-Co NPs (b) samples using the $NaBH_4$ reducing agent method.

The synthesis of magnetic hybrid crystalline Fe-Co/NDs and unsupported Fe-Co nanostructures using $NaBH_4$ as a reducing agent resulted in the preparation of two as-made precursor samples, which are denoted more simply in Table 4.2.

Table 4.2 Abbreviated code names of the samples of the Fe-Co/NDs system prepared with the $NaBH_4$ reducing agent.

Sample	Code Names	Brief Description
FeCo-BH-AM1-NHD	BH-AM1-NHD	As-made Fe-Co NPs/NDs Nanohybrids
FeCo-BH-AM1-NP	BH-AM1-NP	Free as-made unsupported Fe-Co NPs

A similar two-step procedure was employed for the production of hybrid magnetic crystalline Fe–Co/NDs nanostructures using the wet chemistry impregnation method [2], [3]. This method initially aimed to produce the as-made chemical precursors, followed by annealing the precursors under controlled conditions. A nominal Fe:Co atomic ratio of 1:1 was implemented using appropriate amounts of the corresponding metal salts. A total ~10 wt.% of combined Fe and Co metal-to-ND mass ratio was considered, while both conventional (FeCo-IM-AM-NHD) and ^{57}Fe-enriched (En-FeCo-IM-AM-NHD) reactants were used for the preparation of the corresponding AM nanohybrid precursor samples (Scheme 4.3). The use of ^{57}Fe-enriched reactants was chosen to enhance the resolution of the Mössbauer spectra (MS) transmission signals, given the low Fe content of the samples.

For the preparation of a typical conventional FeCo-IM-AM-NHD precursor, 58 mg of $Fe(NO_3)_3{\cdot}9H_2O$ (99.99+%, Aldrich 254223-50G) and 42 mg of $Co(NO_3)_2{\cdot}6H_2O$ (>99.0%, Fluka 60832, Morris Plains, NJ, USA) were dissolved in 0.8 mL of deionized water. This solution was mixed with 150 mg of detonation ND powder (98%, Aldrich 636428-1G). The mass concentrations of all components were calculated so that the final as-made hybrid precursor contained approximately 10 wt. % of equiatomic Fe–Co metal. The mixture was blended and homogenized into a moist paste using an agate mortar, and then allowed to dry at 100° C for 24 h. After dehydration, the material was re-homogenized into a fine powder and calcined in air at 400 °C for 1 h. This process aimed to remove the nitrates and produce homogeneous well-dispersed iron–cobalt oxide (ICO) NP seeds on the surfaces of the ND nanotemplates (see Scheme 4.3). Subsequently, thermal treatments of the typical conventional FeCo-IM-AM-NHD precursor were conducted in sealed under-vacuum (10^{-3} Torr) quartz ampoules at specific temperature and durations.

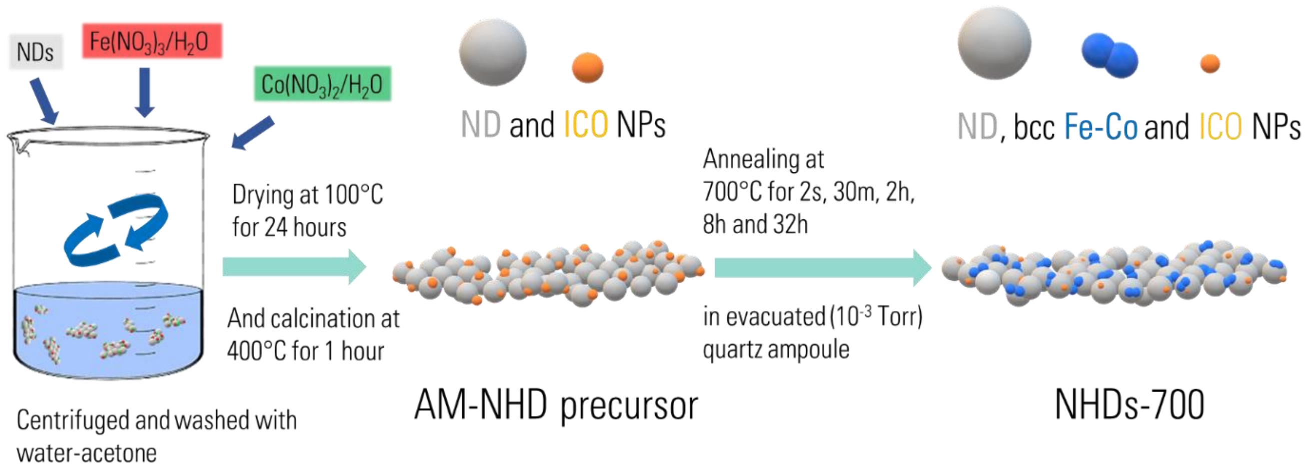

Scheme 4.3 Graphic representation of the synthesis procedure of as-made hybrid and annealed nanohybrid samples of the Fe-Co/NDs system based on the impregnation method.

The conceptualization and study of the characteristics and properties developed for the samples resulting after the second-step synthetic procedure for the Fe-Co/NDs system, was crucial to be investigated over a wide annealing temperature range and with different annealing intervals. This was necessary to achieve the growth of the desired and unique magnetic hybrid nanostructured materials, as indicated by numerous other studies cited in the literature and a thorough examination of the respective phase diagram. Consequently, the annealing process of the proposed conventional synthesis was conducted at three different temperatures, at 600°C, 650°C and 700°C. For each temperature, four different annealing durations were selected, except for 700°C, which had five different annealing intervals. This approach provided our study with five conventional as-made precursor samples, from which seventeen conventional annealed samples were derived, resulting in twenty-one samples in total. The abbreviated notation code names of the discussed samples are listed in Table 4.3.

Table 4.3 Abbreviated code names of the conventional samples of the Fe-Co/NDs system prepared with the Impregnation method.

Samples	Code Names	Brief Description
FeCo-IM-AM1-NHD	IM-AM1-NHD	As-made Fe-Co NPs/NDs Nanohybrids precursor (01)
FeCo-IM-AN(700C,30m)	IM-NHD1-700C,30m	Fe-Co NPs/NDs Nanohybrids annealed at 700 °C for 30 min
FeCo-IM-AM2-NHD	IM-AM2-NHD	As-made Fe-Co NPs/NDs Nanohybrids precursor (02)
FeCo-IM-AN(700C,30m)	IM-NHD2-700C,30m	Fe-Co NPs/NDs Nanohybrids annealed at 700 °C for 30 min

FeCo-IM-AM3-NHD	IM-AM3-NHD	As-made Fe-Co NPs/NDs Nanohybrids precursor (03)
FeCo-IM-AN(650C,30m)	IM-NHD3-650C,30m	Fe-Co NPs/NDs Nanohybrids annealed at 650 °C for 30 min
FeCo-IM-AN(650C,8h)	IM-NHD3-650C,8h	Fe-Co NPs/NDs Nanohybrids annealed at 650 °C for 8 h
FeCo-IM-AN(700C,30m)	IM-NHD3-700C,30m	Fe-Co NPs/NDs Nanohybrids annealed at 700 °C for 30 min
FeCo-IM-AM4-NHD	IM-AM4-NHD	As-made Fe-Co NPs/NDs Nanohybrids precursor (04)
FeCo-IM-AN(600C,30m)	IM-NHD4-600C,30m	Fe-Co NPs/NDs Nanohybrids annealed at 600 °C for 30 min
FeCo-IM-AN(600C,32h)	IM-NHD4-600C,32h	Fe-Co NPs/NDs Nanohybrids annealed at 600 °C for 32 h
FeCo-IM-AN(650C,2h)	IM-NHD4-650C,2h	Fe-Co NPs/NDs Nanohybrids annealed at 650 °C for 2 h
FeCo-IM-AN(650C,32h)	IM-NHD4-650C,32h	Fe-Co NPs/NDs Nanohybrids annealed at 650 °C for 32 h
FeCo-IM-AM5-NHD	IM-AM5-NHD	As-made Fe-Co NPs/NDs Nanohybrids precursor (05)
FeCo-IM-AN(600C,2h)	IM-NHD5-600C,2h	Fe-Co NPs/NDs Nanohybrids annealed at 600 °C for 2 h
FeCo-IM-AN(600C,8h)	IM-NHD5-600C,8h	Fe-Co NPs/NDs Nanohybrids annealed at 600 °C for 8 h
FeCo-IM-AN(700C,2sec)	IM-NHD5-700C,2s	Fe-Co NPs/NDs Nanohybrids annealed at 700 °C for 2 sec
FeCo-IM-AN(700C,30m)	IM-NHD5-700C,30m	Fe-Co NPs/NDs Nanohybrids annealed at 700 °C for 30 min
FeCo-IM-AN(700C,2h)	IM-NHD5-700C,2h	Fe-Co NPs/NDs Nanohybrids annealed at 700 °C for 2 h
FeCo-IM-AN(700C,8h)	IM-NHD5-700C,8h	Fe-Co NPs/NDs Nanohybrids annealed at 700 °C for 8 h
FeCo-IM-AN(700C,32h)	IM-NHD5-700C,32h	Fe-Co NPs/NDs Nanohybrids annealed at 700 °C for 32 h

For the preparation of the ^{57}Fe En-FeCo-IM-AM-NHD precursor, 51 mg of $Fe(NO_3)_3 \cdot 9H_2O$ (99.99+%, Aldrich 254223-50G) along with 0.1 mL of metallic ^{57}Fe dissolved in HNO_3 solution with C(^{57}Fe) = 7 mg/mL concentration, and 42 mg of $Co(NO_3)_2 \cdot 6H_2O$ (>99.0%, Fluka 60832) were dissolved in 1 mL of deionized water. This solution was then mixed with 150 mg of ND powder (98%, Aldrich 636428-1G). The nominal ^{57}Fe-to-Fe^{3+} atomic ratio in the relative reactants was calculated to be approximately 0.1. Subsequently, the mixture followed the same process of dehydration and calcination as that of the non-enriched FeCo-IM-AM-NHD precursor.

In the final step, the En-FeCo-IM-AM-NHD precursor was thermally treated in vacuum (10^{-3} Torr)-sealed quartz ampoules at 700 °C for varying annealing time intervals of 30 min, 2 h, and 8 h. Additionally, we also examined the influence of a slow cooling (SC) procedure after annealing in the specific time interval of 30 min, from 700 °C to room temperature (RT), under controlled conditions (30 °C/h) using the En-FeCo-IM-AM-NHD precursor to produce the En-NHD-700,30m-SC sample. This was performed to explore the possibility of further enhancing the Fe–Co atomic ordering of the resulting crystalline alloy phases in this sample and to compare the results with the relative results on other samples that lacked the SC step feature [4], [5]. The resulting abbreviated notation code names of the enriched conventional and annealed samples, are listed in Table 4.4.

Table 4.4 Abbreviated code names of the ^{57}Fe enriched samples of the Fe-Co/NDs system prepared with the Impregnation method.

Samples	Code Names	Brief Description
En-FeCo-IM-AM6-NHD	En- IM-AM6-NHD	^{57}Fe enriched as-made Fe-Co NPs/NDs Nanohybrids precursor (06)
En-FeCo-IM-AN(700C,30m)	En- IM-NHD6-700C,30m	^{57}Fe enriched Fe-Co NPs/NDs Nanohybrids annealed at 700 °C for 30 min
En-FeCo-IM-AN(700C,30m)-SC	En- IM-NHD6-700C,30m-SC	^{57}Fe enriched Fe-Co NPs/NDs Nanohybrids annealed at 700 °C for 30 min with Slow Cooling (SC)
En-FeCo-IM-AN(700C,2h)	En- IM-NHD6-700C,2h	^{57}Fe enriched Fe-Co NPs/NDs Nanohybrids annealed at 700 °C for 2 h
En-FeCo-IM-AN(700C,8h)	En- IM-NHD6-700C,8h	^{57}Fe enriched Fe-Co NPs/NDs Nanohybrids annealed at 700 °C for 8 h

Following this concept, the properties of the conventional and enriched samples of the Fe-Co/NDs system are investigated in Chapter 6.

4.3 Materials Synthesis of the Fe-Ni/NDs System

For the synthesis of the Fe-Ni/NDs system the same two-step process of wet chemistry followed by annealing was used, similar to the approach for the Fe-Co/NDs system. As before, both the $NaBH_4$ reducing agent and the impregnation synthesis methods were applied to assess which technique produces better the desired magnetic hybrid and unsupported nanostructures, as well as to determine which method yields the highest amount of these magnetic nanoalloy materials [1], [2], [3].

Using the $NaBH_4$ reducing agent synthetic route, a nominal Fe:Ni atomic ratio of 1:1 was implemented using appropriate amounts of the corresponding metal salts. A total ~10 wt.% of combined Fe and Ni metals to the ND mass ratio was also considered for the preparation of the as-made hybrid precursor sample. For the first step of this synthetic route, alongside to the as-made hybrid precursor sample (FeNi-BH-AM-ND), an as-made unsupported Fe-Ni precursor sample (FeNi-BH-AM-NP), with the same nominal Fe:Ni = 1:1 atomic stoichiometry was also prepared.

In particular, in the first stage, 180 mg NDs ($\geqslant$ 97 % Aldrich 636428) were suspended in a beaker containing 20 mL deionized H_2O and 48 mg of hydrous $FeCl_3$ (97 % Aldrich 157740) mixed with 42 mg hydrous $NiCl_2$ (97 % Aldrich 654507) in order to afford a fine aqueous material. After mixing, 200 mg $NaBH_4$ (99 % Aldrich 213462) combined with 5 mL H_2O were rapidly added and the mixture was stirred for 20 minutes at ambient conditions. Then the material inside the beaker was left in rest for one hour in a hood, prior to its centrifuge and wash with deionized water and acetone and then dried in room temperature, to afford the as-made hybrid precursor sample FeNi-BH-AM-ND.

In the second stage, the FeNi-BH-AM-ND sample was sealed under vacuum (10^{-3} Torr) in a quartz ampoule, that would be afterwards thermally treated at the proper annealing conditions, affording the FeNi-BH-AN-ND sample (Scheme 4.4(a)).

For the unsupported NPs sample, 420 mg of hydrous $NiCl_2$ (97 % Aldrich 654507) and 480 mg of hydrous $FeCl_3$ (97 % Aldrich 157740) were dissolved in 200 mL of deionized water to create the salt solution. This solution was poured into 50 mL deionized H_2O, followed by the rapid addition of 2 g $NaBH_4$ (99 % Aldrich 213462) under vigorous stirring. The mixture was stirred for 20 minutes at room temperature. The resulting precipitate was allowed to settle, then rinsed with deionized water and acetone, and air dried at room temperature, yielding the as-made unsupported precursor sample FeNi-BH-AM-NP. Similarly, to its hybrid counterpart, the FeNi-BH-AM-NP precursor sample underwent an annealing process in a sealed quartz ampoule under vacuum (10^{-3} Torr) at the appropriate conditions, resulting in the FeNi-BH-AN-NP sample (Scheme 4.4(b)). The synthesis of both hybrid and unsupported samples and the investigation of their properties aim to highlight the unique role of the NDs nanotemplates and their influence on the formation of the magnetic nanoalloys during the synthetic process.

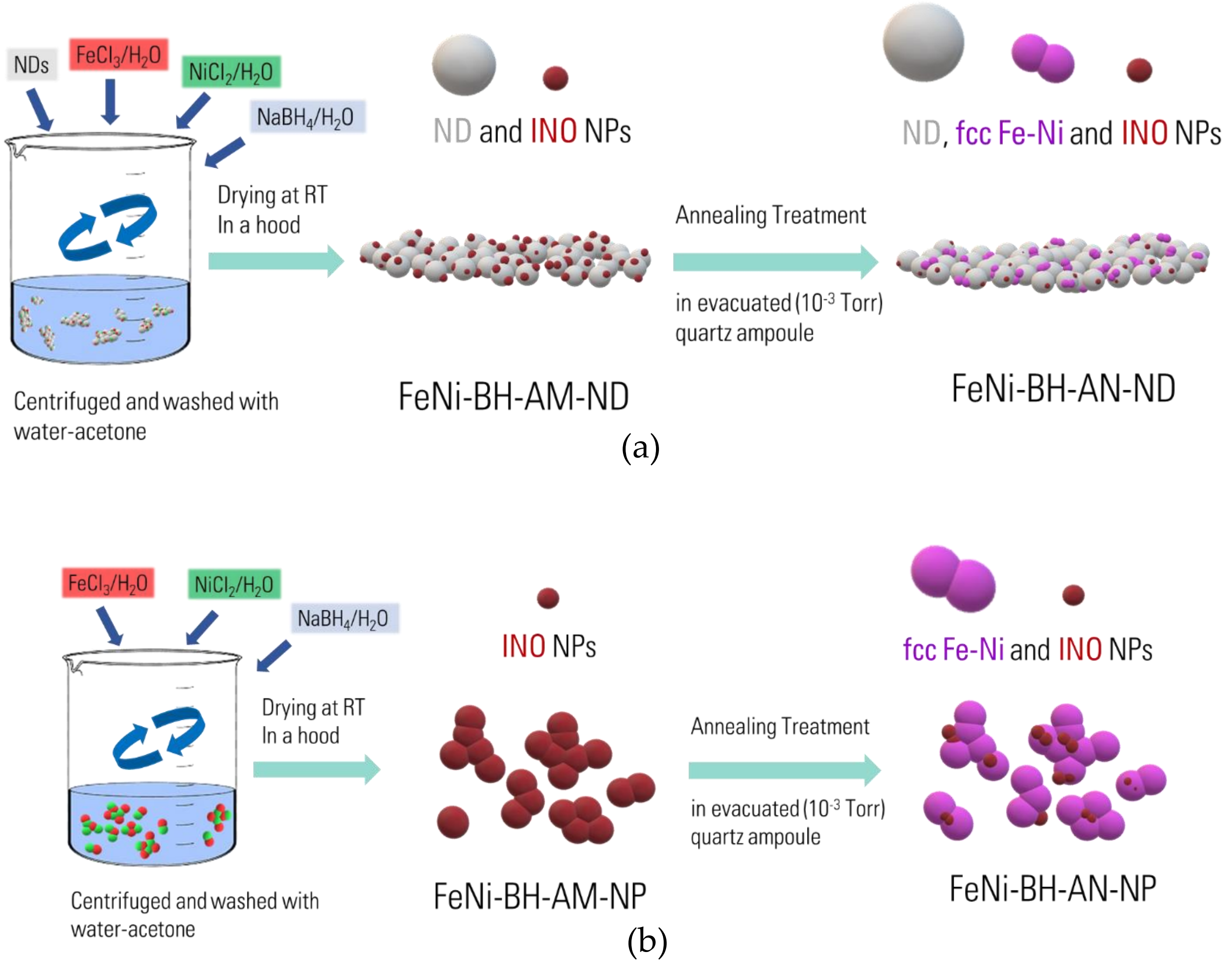

Scheme 4.4 Graphic representation of the synthesis procedure of the as-made and annealed hybrid Fe-Ni/NDs (a) and unsupported Fe-Ni NPs (b) samples using the $NaBH_4$ reducing agent method.

The synthesis of magnetic hybrid crystalline Fe-Ni/NDs and unsupported Fe-Ni nanostructures using $NaBH_4$ as a reducing agent resulted in the preparation of two as-made precursor samples, which are denoted more simply in Table 4.5.

Table 4.5 Abbreviated code names of the samples of the Fe-Ni/NDs system prepared with the $NaBH_4$ reducing agent.

Samples	Code Names	Brief Description
FeNi-BH-AM1-NHD	BH-AM1-NHD	As-made Fe-Ni NPs/NDs Nanohybrids precursor
FeNi-BH-AM1-NP	BH-AM1-NP	Free as-made unsupported Fe-Ni NPs
FeNi-BH-AN(700C,4h)-NHD	BH-NHD1-700C,4h	Fe-Ni NPs/NDs Nanohybrids annealed at 700 °C for 4h
FeNi-BH-AN(700C,4h)-NP	BH-NP1-700C,4h	Free unsupported NPs annealed at 700 °C for 4h

FeNi-BH-AN(300C,96h)-NHD	BH-NHD1-300C,96h	Fe-Ni NPs/NDs Nanohybrids annealed at 300 °C for 96h
FeNi-BH-AN(300C,96h)-NP	BH-NP1-300C,96h	Free unsupported NPs annealed at 300 °C for 96h

The second synthesis of the hybrid magnetic crystalline Fe–Ni/NDs nanostructures involved as well a two-step procedure. Initially a wet chemistry impregnation method was implemented [2], [3]. This method aimed to produce the as-made chemical precursor samples, followed by their annealing under controlled conditions. A nominal Fe:Ni atomic ratio of 1:1 was considered using appropriate amounts of the corresponding metal salts, while a total ~10 wt.% of combined Fe and Ni metal to the ND mass ratio was considered, while both conventional (FeNi-IM-AM-NHD) and ^{57}Fe-enriched (En-FeNi-IM-AM-NHD) reactants were used for the preparation of the corresponding AM nanohybrid precursor samples (Scheme 4.5). The use of ^{57}Fe-enriched reactants was chosen to enhance the resolution of the Mössbauer spectra (MS) transmission signals, given the low Fe content of the samples.

The preparation of a typical conventional FeNi-IM-AM-NHD precursor involved the combination of 35 mg of $Fe(NO_3)_3{\cdot}9H_2O$ (99.99+%, Aldrich 254223-50G) and 25 mg of $Ni(NO_3)_2{\cdot}6H_2O$ (>99.99+%, Aldrich 13478-00-7) dissolved in 0.5 mL of deionized water. The solution was then mixed with 90 mg of detonation NDs powder (98%, Aldrich 636428-1G). The mass concentrations of all components were calculated to ensure that the final AM hybrid precursor contained ~ 10 wt.% of equiatomic combined Fe and Ni metals percentage. The mixture was blended and homogenized in a moist paste form using an agate mortar and pestle, and then allowed to dry at 100°C for 24 h. After dehydration, the material was re-homogenized into a fine powder and calcined in air at 400°C for 1 h. This process aimed to remove the nitrates and produce uniform well dispersed iron-nickel oxide (INO) NPs seeds on the surfaces of the NDs nanotemplates (see Scheme 3). Afterwards, thermal treatments of the AM-NHD precursor were conducted in sealed under vacuum (10^{-3} Torr) quartz ampoules at temperatures of 700°C (NHD-700C) for varying time intervals of 30 min and 4 h.

The investigation and analysis of the Fe-Ni/NDs system and more specifically the second annealing step of the synthetic procedure, relied on the results derived from the respectively annealing step applied in the Fe-Co/NDs system. Therefore, the annealing process of the proposed conventional synthesis of the Fe-Ni/NDs system, was conducted at 700°C. For this temperature, two different annealing duration intervals were selected. This methodology provided our study with two conventional as-made precursor samples, from which four conventional annealed samples were derived, resulting in six samples in total. The abbreviated notation code names of the discussed samples are listed in Table 4.6.

Table 4.6 Abbreviated code names of the samples of the Fe-Ni/NDs system prepared with the Impregnation method.

Samples	Code Names	Brief Description
FeNi-IM-AM1-NHD	IM-AM1-NHD	As-made Fe-Ni NPs/NDs Nanohybrids precursor (01)
FeNi-IM-AN(700C,30m)	IM-NHD1-700C,30m	Fe-Ni NPs/NDs Nanohybrids annealed at 700 °C for 30m min
FeNi-IM-AN(700C,4h)	IM-NHD1-700C,4h	Fe-Ni NPs/NDs Nanohybrids annealed at 700 °C for 4 h
FeNi-IM-AM2-NHD	IM-AM2-NHD	As-made Fe-Ni NPs/NDs Nanohybrids precursor (02)
FeNi-IM-AN(700C,30m)	IM-NHD2-700C,30m	Fe-Ni NPs/NDs Nanohybrids annealed at 700 °C for 30m min
FeNi-IM-AN(700C,4h)	IM-NHD2-700C,4h	Fe-Ni NPs/NDs Nanohybrids annealed at 700 °C for 4 h
FeNi-IM-AN(700C,30m-to-300C,64h)	IM-NHD2-(700C,30m/300C,64h)	Fe-Ni NPs/NDs Nanohybrids annealed at 700 °C for 30m min followed by annealing at 300 °C for 64 h
FeNi-IM-AN(700C,4h-to-300C,96h)	IM-NHD2-(700C,4h/300C,96h)	Fe-Ni NPs/NDs Nanohybrids annealed at 700 °C for 4h min followed by annealing at 300 °C for 96 h

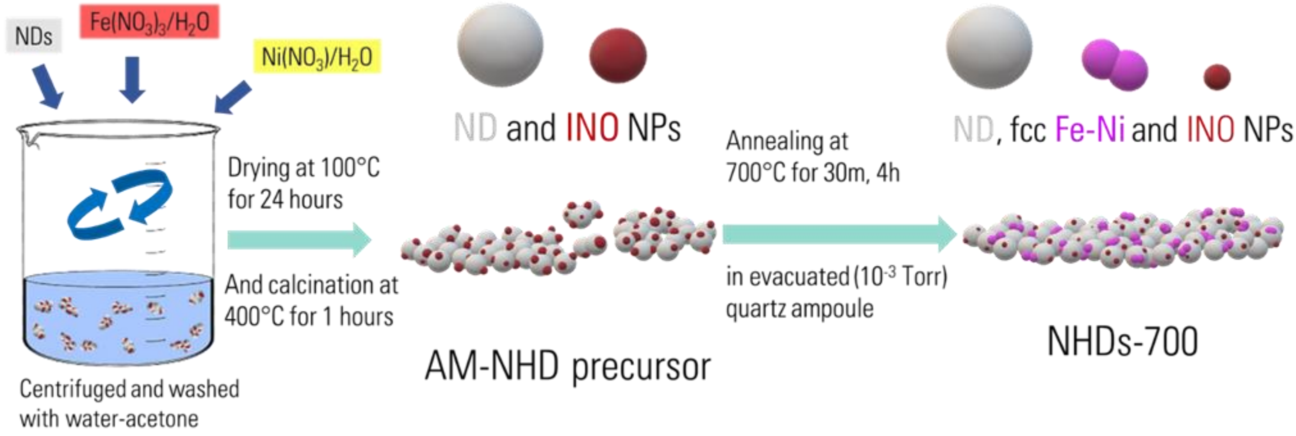

Scheme 4.5 Graphic representation of the synthesis procedure of as-made hybrid chemical precursor and the final annealed nanohybrid samples.

For the preparation of second ^{57}Fe En-FeNi-IM-AM-NHD precursor, 28 mg of $Fe(NO_3)_3·9H_2O$ (99.99+%, Aldrich 254223-50G) and 25 mg of $Ni(NO_3)·6H_2O$ (>99.99+%, Aldrich 13478-00-7) were dissolved in 0.5 mL of deionized water, along with two drops of an HNO_3 solution enriched with ^{57}Fe isotopes (C = 10 mg/mL). This solution was then mixed with 90 mg of NDs powder (98%, Aldrich 636428-1G). The nominal ^{57}Fe-to-Fe^{3+} reactants atomic ratio was calculated to be approximately 0.1.

Subsequently, the mixture followed the same dehydration and calcination processes as that of the non-enriched FeNi-IM-NHD precursor sample.

In the final step, the En-FeNi-IM-AM-NHD precursor was thermally treated in vacuum (10^{-3} Torr)-sealed quartz ampoules at 700 °C for varying annealing time intervals of 30 min and 4h. Additionally in our study, we examined the influence of quenching (Q) the enriched samples, from 700°C to RT, by removing the ampoule from the furnace at 700°C and placing it on a thick bronze plate in order to induce heat rapidly, in the case of En-NHDs-700,30m and En-NHDs-700,4h samples. Quenching the samples in a bronze plate let the heat to attenuate from 700°C to RT within 15 minutes. This step carried out in order to investigate if instant cooling from RT can influence the crystallinity of the hybrid samples, and to study any possible interaction between the crystal ordering and the magnetic properties of the formatted crystal phases in the quenched samples, to compare them with the other hybrid samples, which are lacking the Q feature. The resulting abbreviated notation code names of the enriched conventional and annealed samples, are listed in Table 4.7.

Table 4.7 Abbreviated code names of the ^{57}Fe enriched samples of the Fe-Ni/NDs system prepared with the Impregnation method.

Samples	Code Names	Brief Description
En-FeNi-IM-AM3-NHD	En- IM-AM3-NHD	^{57}Fe enriched as-made Fe-Ni NPs/NDs Nanohybrids precursor
En-FeNi-IM-AN(700C,30m)	En- IM-NHD3-700C,30m	^{57}Fe enriched Fe-Ni NPs/NDs Nanohybrids annealed at 700 °C for 30m min
En-FeNi-IM-AN(700C,30m)-Q	En- IM-NHD3-700C,30m-Q	^{57}Fe enriched Fe-Ni NPs/NDs Nanohybrids annealed at 700 °C for 30m min with Quenching (Q)
En-FeNi-IM-AN(700C,4h)	En- IM-NHD3-700C,4h	^{57}Fe enriched Fe-Ni NPs/NDs Nanohybrids annealed at 700 °C for 4 h
En-FeNi-IM-AN(700C,4h)-Q	En- IM-NHD3-700C,4h-Q	^{57}Fe enriched Fe-Ni NPs/NDs Nanohybrids annealed at 700 °C for 4 h with Quenching (Q)

Following this concept, the properties of the conventional and enriched samples of the Fe-Ni/NDs system are investigated in Chapter 7.

4.4 References

[1] A. B. Bourlinos, I. Panagiotopoulos, D. Niarchos, and D. Petridis, “Hydrophilic Co–Pt Alloy Nanoparticles: Synthesis, Characterization, and Perspectives,” *Journal of Materials Research*, vol. 19, no. 4, pp. 1227–1233, Apr. 2004, doi: 10.1557/JMR.2004.0159.

[2] A. B. Bourlinos *et al.*, "Fabrication of fluorescent nanodiamond@C core–shell hybrids via mild carbonization of sodium cholate–nanodiamond complexes," *J Mater Sci*, vol. 46, no. 24, Art. no. 24, Dec. 2011, doi: 10.1007/s10853-011-5911-z.

[3] A. Bourlinos, A. Simopoulos, D. Petridis, H. Okumura, and G. Hadjipanayis, "Silica-Maghemite Nanocomposites," *Adv. Mater.*, vol. 13, no. 4, pp. 289–291, Feb. 2001, doi: 10.1002/1521-4095(200102)13:4<289::AID-ADMA289>3.0.CO;2-U.

[4] A. Shokuhfar and S. S. S. Afghahi, "Size Controlled Synthesis of FeCo Alloy Nanoparticles and Study of the Particle Size and Distribution Effects on Magnetic Properties," *Advances in Materials Science and Engineering*, vol. 2014, pp. 1–10, 2014, doi: 10.1155/2014/295390.

[5] Y. Kota and A. Sakuma, "Degree of Order Dependence on Magnetocrystalline Anisotropy in Body-Centered Tetragonal FeCo Alloys," *Appl. Phys. Express*, vol. 5, no. 11, Art. no. 11, Oct. 2012, doi: 10.1143/APEX.5.113002.

Chapter 5. Study of the Fe-Rh/ND system

5.1 XRD

The XRD diagrams of pristine NDs, as-made nanohybrid and unsupported samples, prepared using the $NaBH_4$ reducing agent (BH), are shown in Figure 5.1. Figure 5.1a depicts two main broad diffraction peaks of the cubic ND structure at 43.9° (111) and 75.4° (220) degrees 2θ (lattice constant a= 3.567 Å, ICDD PDF 00-006-0675). Moreover, at 21.6° degrees 2θ a diminished diffraction peak, attributed to impurity residuals, can also be observed. An estimation of the average NP crystalline domain size <D> for each peak of this phase based on the most resolvable widths of its main diffraction peaks was made using the Scherrer formula [1], providing an average size of $<D_{NDs}>$ = 5 nm for the NDs, as depicted in this pattern. This result indicates that the pristine NDs sample is composed of very small ND NPs following the nominal nanocrystalline structure and purity provided by Aldrich. The XRD pattern of BH-AM1-NHD sample in Figure 5.1b reveals the dominant contributions of the broad diffraction peaks attributed to NDs, along with two quite inferior and very broad diffraction contributions centered at 36° and 42° degrees 2θ, which are attributed to the (311) main diffraction peak of a spinel-type γ-Fe_2O_3 (maghemite) iron oxide (IO) phase (lattice constant a= 8.352 Å, ICDD PDF 00-039-1346) [2], and the (111) main diffraction peak of either an fcc Fe-Rh equiatomic alloy phase at 41.8° degrees 2θ (lattice constant a= 3.740 Å, ICDD PDF 01-074-5849) and/or an fcc metallic elemental Rh phase at 41.1° (111) degrees 2θ (lattice constant a= 3.803 Å, ICDD PDF 00-005-0685). The presence of this metallic phase in the BH-AM1-NHD sample can be justified mainly by the asymmetric broadening of the NDs' main (111) diffraction peak at 43.9 2θ, which acquires larger broadening towards its lower 2θ values, where the main (111) diffraction peak of the metallic phase contributes. The application of Scherrer's formula affords the ND phase of the BH-AM1-NHD sample an average crystalline domain size of about $<D_{NDs}>$ = 3 nm, while the estimation of the average crystalline domain size $<D_{Fe\text{-}Rh}>$ for the metallic Fe-Rh alloy and/or elemental Rh phase is not feasible, due to their non-resolvable diffraction peak width. The XRD pattern of BH-AM1-NP sample in Figure 5.1c exhibits a very broad diffraction peak centered at approximately 42° degrees 2θ, attributed to the main diffraction peak of either the fcc Fe-Rh alloy phase and/or the fcc metallic elemental Rh phase. A secondary broad diffraction peak is also observed at approximately 36° degrees 2θ, which is attributed to the same spinel-type IO phase found in the BH-AM1-NHD sample. An average crystalline domain size of about $<D_{Fe\text{-}Rh}>$ = 2 nm was estimated for the metallic Fe-Rh or elemental Rh alloy phase found for the BH-AM1-NP sample by applying the Scherrer's formula. The aspects of the nature, morphology, and stoichiometry of the developed phases in both BH-AM1-NHD and BH-AM1-NP precursor samples are revealed by TEM analysis (vide infra).

Following this context, Figures 5.1d and 5.1e shows the XRD diagrams of the BH-AM2-NHD and BH-AM2-NP samples, respectively. These patterns present resembling structural characteristics to those found for the former samples. In particular, the XRD pattern of BH-AM2-NHD sample in

Figure 5.1d depicts the dominant contribution of the broad diffraction peaks attributed to NDs, along with the less intense contributions from the broad diffraction peaks of the spinel-type IO and Fe-Rh and/or elemental Rh fcc phase at ~36° and ~42° degrees 2θ respectively. In case of the BH-AM2-NP sample, the main contribution from the fcc Fe-Rh and/or elemental Rh phase is dominant, while an indication for the presence of the spinel-type IO phase can also be observed (Figure 5.1e). An estimation of the average crystalline domain size renders the NDs with $<D_{NDs}>$ = 4 nm in the BH-AM2-NHD sample, while the Fe-Rh and/or elemental Rh NPs obtained average sizes of $<D_{Fe-Rh}>$ = 2 nm in the BH-AM2-NP sample. These results are in good agreement with those observed for the BH-AM1-NHD and BH-AM1-NP samples, rendering the proposed synthesis, as a method capable to produce consistent nanostructured phases, regardless the AM precursor. Moreover, the wide widths of the diffraction peaks corresponding to the Fe-Rh and/or elemental Rh phases and the reduced intensities of the diffraction peaks attributed to the IO phases observed in the patterns of all AM precursor samples indicate, besides their extreme small NP sizes, that they can also feature low crystallinity.

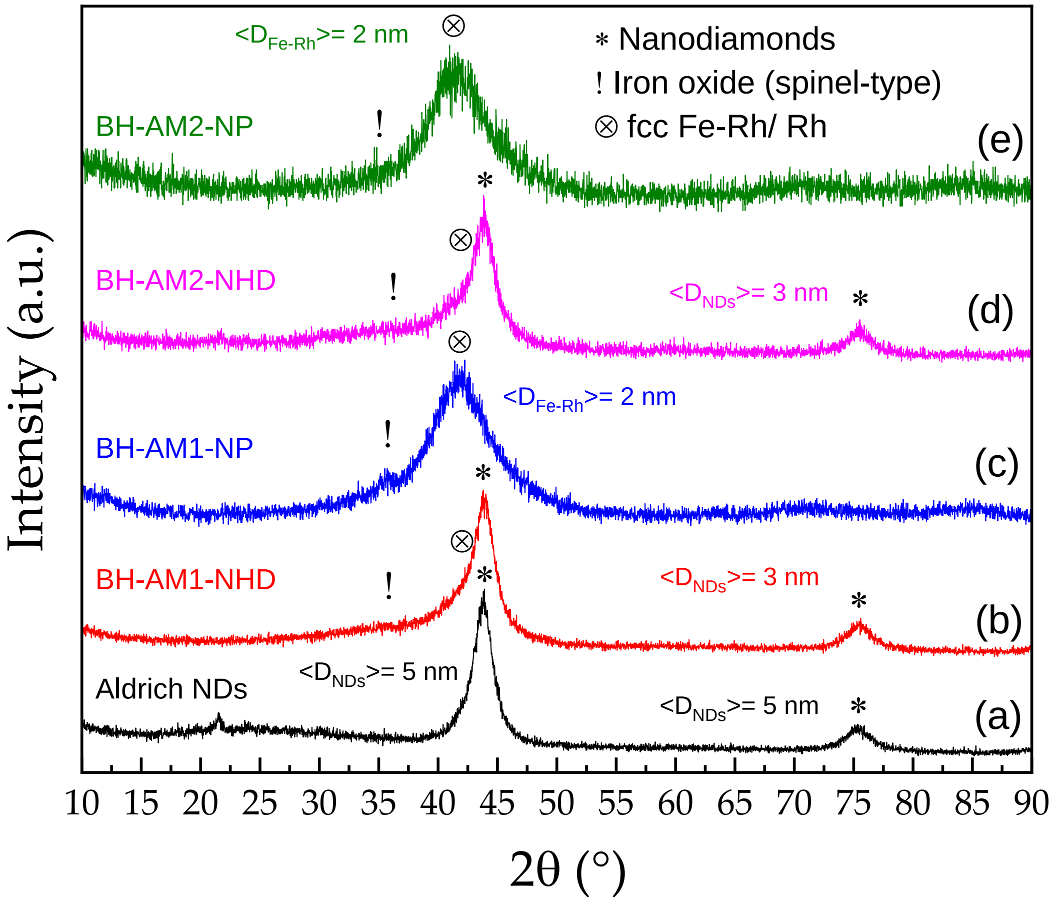

Figure 5.1 XRD patterns of the pristine NDs (a), BH-AM1-NHD (b), BH-AM1-NP (c), BH-AM2-NHD (d) and BH-AM2-NP (e) samples. The crystalline phases in the samples are depicted by respective different symbols denoting the angular positions of their main diffraction peaks. The average crystalline domain size <D> of the nanodiamonds phase for the as-made nanohybrid precursor samples and that of the iron-rhodium and/or metallic rhodium phases for the as-made unsupported samples are denoted in each pattern.

From the XRD diagrams presented in Figure 5.2, it is evident that the annealing of the as-made nanohybrid and unsupported precursors at the chosen temperature of 700°C and time duration of 30 minutes is capable to induce the formation of some new nanocrystalline phases. At the same time, the presence of the ND phase is completely retained, while that of the spinel-type IO phase is diminished. In particular, the XRD diagram of the BH-NHD1-700C,30m sample in Figure 5.2a, designates the presence of two main contributions corresponding to two different crystal structures, one of the fcc NDs with relative broad diffraction peaks, and a second one with relative sharp diffraction peaks observed at 29.9° (100), 42.8° (110), 53.1° (111), 62.1° (200), 70.4° (210) and 78.4° (211) degrees 2θ corresponding to the equiatomic FeRh B2 bcc phase (lattice constant a= 2.987 Å, ICDD PDF 04-002-1337). In the case of the BH-NP1-700C,30m sample, the XRD diagram in Figure 5.2b exhibits two main contributions. One of them presents four sharp diffraction peaks at 41.5° (111), 48.3° (200), 70.6° (220) and 85.3° (311) degrees 2θ corresponding to the fcc Fe_3Rh_7 phase (lattice constant a= 3.772 Å, ICDD PDF 03-065-6840). The other contribution is attributed to the orthorhombic crystal structure of the iron oxyborate (IOB) Fe_3BO_5 (Vonsenite) phase with its main diffraction peaks appearing at 35.1° (240), 37.8° (150), 38.1° (400), 43.7° (321), 46.9° (350), 57.6° (441), 60.2° (002), 61.6° (112), 61.9° (550), 66.7° (601) and 71.5° (281) degrees 2θ (lattice constants a= 9.452 Å, b= 12.287 Å and c= 3.072 Å, ICDD PDF 00-025-0395). The formation of this phase may be attributed to residual boron (B) originating from the $NaBH_4$ reducing agent, most probably in the form of amorphous boron oxide (B_2O_3) (BO) in the corresponding as-made sample, in combination with the presence of IO NPs and the influence of the annealing conditions (vide infra). In Figure 5.2c the XRD diagram of the BH-NHD2-700C,30m sample depicts similar structural characteristics to those found for the BH-NHD1-700C,30m sample. More specifically, the main diffraction peaks of the fcc ND and bcc B2 Fe-Rh phases are exhibited in the same angular positions to the equivalent phases observed in BH-NHD1-700C,30m sample. It is revealed that for both annealed nanohybrid samples the diffraction peaks of the IOB Fe_3BO_5 phase are completely absent.

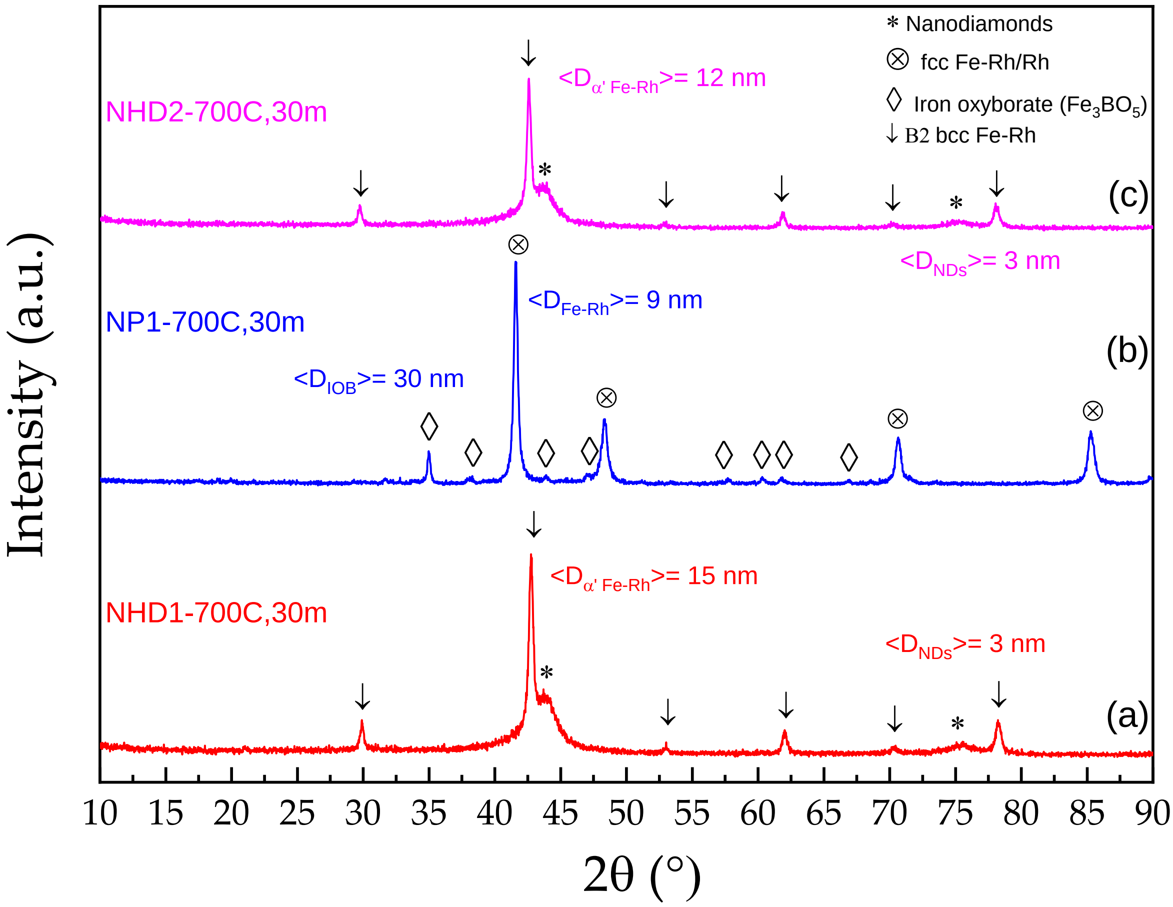

Figure 5.2 XRD patterns of the BH-NHD1-700C,30m (a), BH-NP1-700C,30m (b) and BH-NHD2-700C,30m (c) samples. The crystalline phases in the samples are depicted by respective different symbols denoting the angular positions of their main diffraction peaks. The average crystalline domain size <D> of the nanodiamonds and bcc iron–rhodium phase for the annealed nanohybrid samples and that of the fcc iron-rhodium and iron-oxyborate phase for the annealed unsupported samples are denoted in each pattern.

An estimation of the average crystalline domain size <D> extracted out of the best resolvable widths of the main diffraction peaks of the main phases presented in each pattern can be made using the Scherrer formula, and the results are depicted in each pattern. It is evident that the average size of the bcc B2 FeRh NPs ranges between 12 and 15 nm in both annealed nanohybrid samples, and that of the fcc Fe_3Rh_7 NPs is 9 nm, while that of the IOB NPs is of about 30 nm. These features render the annealed samples with noticeable differences in their XRD diagrams compared to the parent as-made precursor samples, which concern mainly the sharper and more intense diffraction peaks of the Fe-Rh alloy phases, indicating their high crystallinity. The average size of the ND NPs is consistent with the expected characteristics, preserving its nanoscale features both in the as-made and annealed hybrid samples. Thus, heating at 700°C seems not to affect the morphology of the NDs nanotemplates, which is important and indicates the structural and chemical stability of the NDs' substrate. From these results it is concluded that as regards the formation of the Fe-Rh alloy phase originating from the reduction of the IO NP seeds in the presence of the Fe-Rh and/or metallic Rh NP seeds of the as-made and unsupported Fe-Rh samples, the annealing of the precursors under the specific conditions can trigger the formation of well crystalized nanostructured Fe-Rh alloy phases in the corresponding samples, despite the presence of secondary impurity phases found in the case of the BH-NP1-700C,30m sample. The aspects of the nature, morphology, and stoichiometry of the metallic phases developed in the annealed sample originating from the BH-AM1-NHD precursor will be revealed by following TEM observations (vide infra).

5.2. TEM, STEM and EDS Analysis Results

The determination of the of the nanophases' dispersion, morphology and structure was revealed by TEM/STEM observations. TEM and HAADF-STEM-EDS images, which thoroughly determine the chemical and structural details of the respective samples, HRTEM images and additional EDS spectra from the samples, namely BH-AM1-NHD, BH-AM1-NP, BH-NHD1-700C,30m and BH-NP1-700C,30m are displayed in Figures 5.3 to 5.23.

Figure 5.3 displays the morphology of the BH-AM1-NHD sample, showing a nanohybrid system consisting of well-dispersed ND clusters. These ND cluster nanotemplates contain relatively spherical shaped metallic NPs grown on their surfaces, appearing in darker contrast than the rest of the material in the bright field images, with sizes ranging from 1 to about 6 nm, and averaging (as evident from several images) at (3 ± 1) nm. These metallic NPs are deposited on close packed ND NPs of individual sizes in the range of 4 nm forming roughly round as well as irregular-shaped nanotemplate clusters, with sizes ranging from 30 to about 400 nm (Figures 5.3 and 5.4).

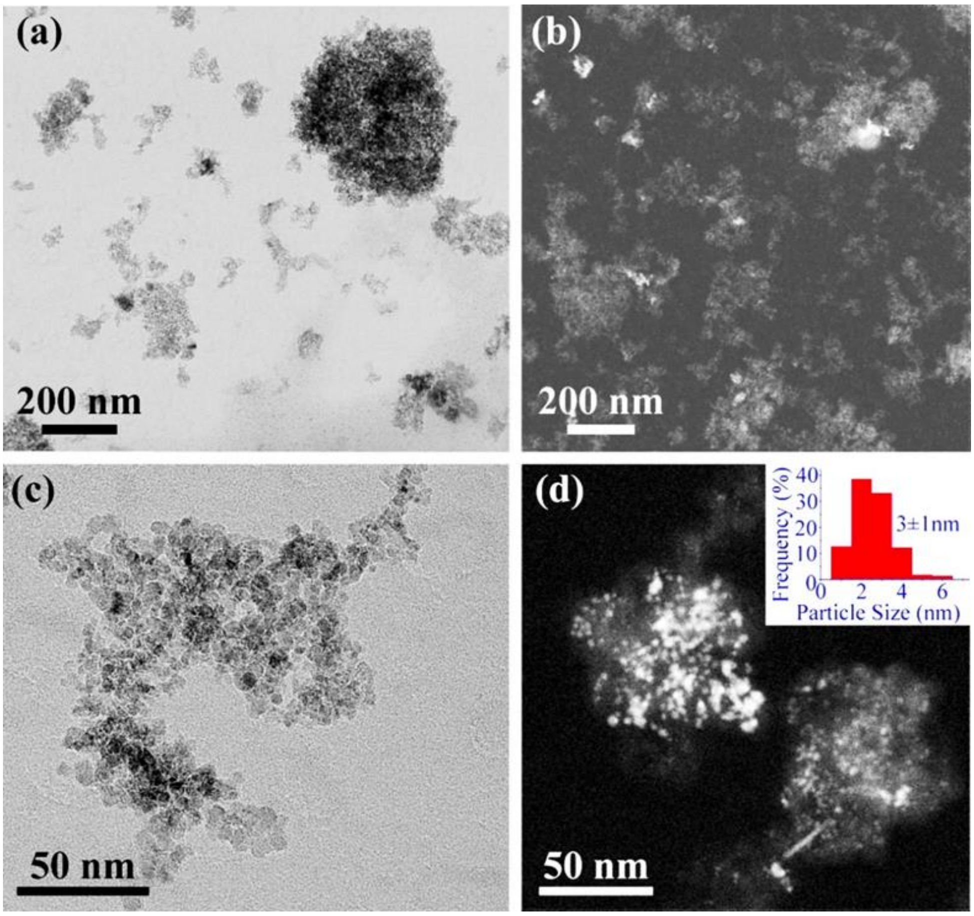

Figure 5.3 Low (a, b) and high (c, d) magnification TEM/STEM images of the BH-AM1-NHD sample. The HAADF/STEM images (b) and (d) show metallic NPs clustering within the larger ND clusters, where individual metallic NPs are discernible within the NDs nanotemplate through their increased Z-contrast. The inset in (d) is a histogram of the metallic NPs size distribution.

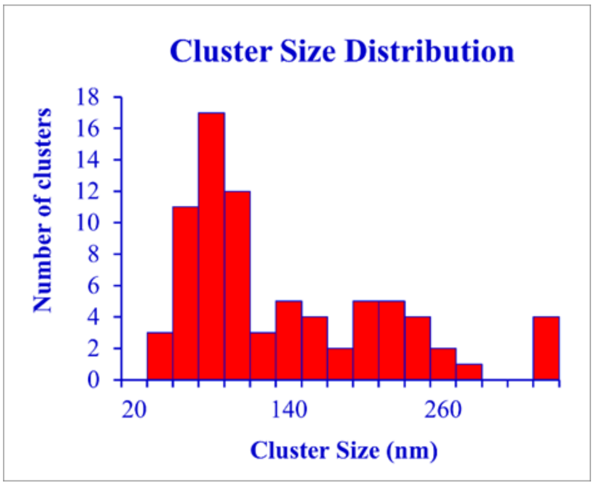

Figure 5.4 Histogram of the NDs' nanotemplate clusters size distribution appearing in the BH-AM1-NHD sample measured from TEM.

Z-contrast imaging by HAADF/STEM in Figures 5.3b, 5.3d reveals that the metallic NPs are well distributed on the NDs nanotemplates. EDS spectra from this sample shown in Figure 5.5 denote a

Fe:Rh atomic ratio between 1:9 and 2:8. EDS spot analysis was performed on the larger NPs shown in Figure 5.6, and indicative results are given in Table 5.1, while elemental distribution mappings of Fe and Rh shown in Figure 5.7a denote the coexistence of the two elements in the regions of the clusters where the metallic NPs are detected. Figure 5.8 displays an HRTEM image of different metallic Fe-Rh NPs grown on the surface of the ND nanotemplates, where the characteristic *d*-spacings corresponding to the close-packed {111} lattice planes of the ND (0.21 nm) and the metallic NP fcc (0.22 nm) structures are resolved. The latter *d*-spacing corresponds either to elemental Rh or to Rh-rich γ-Fe_xRh_{1-x} alloy NPs.

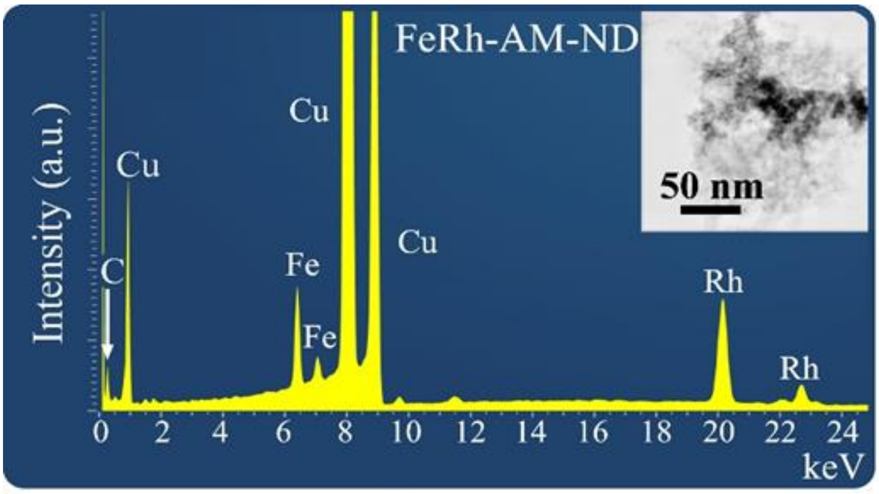

Figure 5.5 Overall EDS spectrum of the BH-AM1-NHD sample, collected from the region presented as inset. The Fe at% composition of the Fe-Rh metallic alloys was calculated to be 10% from the respective K_α peaks. Cu peaks are due to the TEM supporting grids.

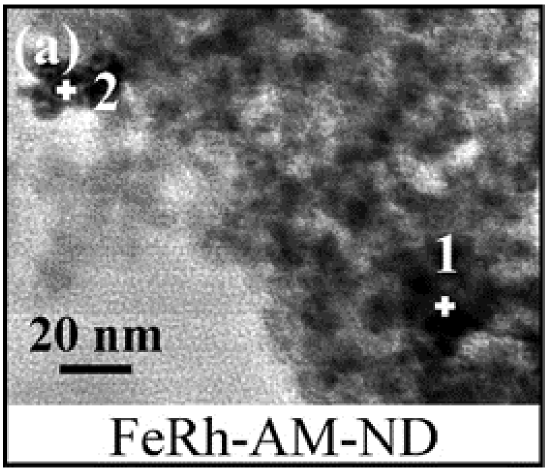

Figure 5.6 Indicative bright field STEM image from the BH-AM1-NHD sample showing positions where EDS point analysis was performed. The corresponding measurements are given in **Table 5.1**.

Table 5.1 Fe at% composition of the Fe-Rh metallic alloy calculated from the K_α peaks of point-spectra acquired from the points marked in **Figure 5.6**.

a. BH-AM1-NHD	
Spot	**Fe %at**
1	23
2	12

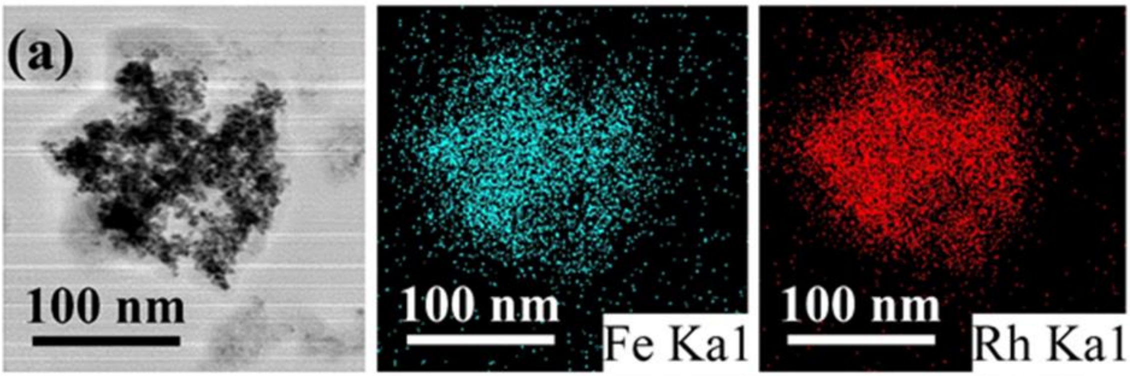

Figure 5.7 EDS Fe and Rh elemental maps obtained from the BH-AM1-NHD sample.

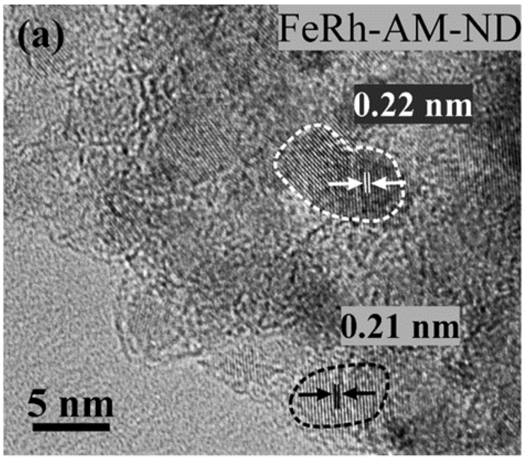

Figure 5.8 HRTEM images from the BH-AM1-NHD sample (a). In (a) the {111}-lattice fringes measured at ~0.22 nm periodicity are shown in white, from fcc elemental Rh or Rh-rich γ-Fe-Rh alloy NPs. In (a), ND {111}-lattice fringes with similar periodicity are shown in black (due to their similar {111} d-spacing, NPs and NDs are differentiated based on absorption contrast).

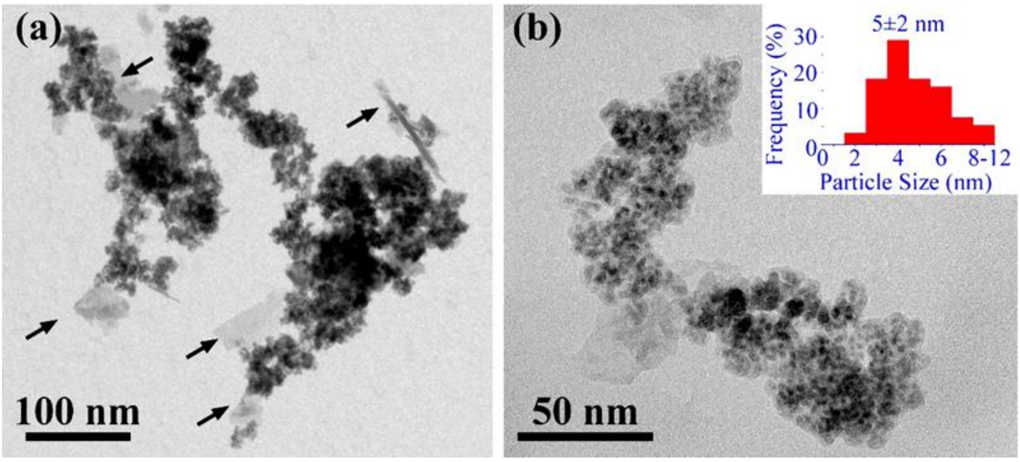

Figure 5.9 Bright field TEM images of characteristic aggregated metallic NPs clusters found in the BH-AM1-NP sample. Arrows in (a) point to sheet-like, low-contrast platelets, distinguished from the rather spherical aggregated NPs. The inset in (b) is the histogram of the particle-size distribution of the individual metallic NPs.

Figure 5.9 reveals the morphology of the BH-AM1-NP sample. The developed metallic NPs present roughly rounded shapes with a size distribution manly occurring between 2 to 8 nm, averaging at 5 nm, while larger NPs are also detected. These NPs are accumulated into close packed clusters in the range of 100-300 nm. From Figure 5.9b it is shown that the NPs located closer to the center of the clusters are depicted sharper and denser, suggesting relatively higher crystallinities and sizes of the corresponding nanostructured phases in comparison to the outer paled/fainted NPs of the clusters, which seem to possess more of a 'core-shell' structure. Due to their quite small sizes and lower crystallinity these shells may correspond to a partial oxidized or fully oxidized IO of the maghemite (γ-Fe_2O_3) composition. In some cases, as shown by the black arrows in Figure 5.9a, low-contrast platelets with thickness ≤ 20 nm and widths of the order of 100-200 nm are observed in this sample.

From EDS analysis (Figures 5.10, 5.11 and Table 5.2), the average Fe:Rh atomic ratio was found to be 2:8, similar to that observed for the BH-AM1-NHD sample. However, the signals from the platelets, point EDS analyses and chemical mapping on them (Figure 5.11 point 3, and area indicated by arrow in Figure 5.12), indicate a high depletion of Rh content in these formations, compared to a uniform distribution of Fe and Rh in the metallic NPs region. This shows that these platelets probably contain an iron-bearing phase in this sample, possibly of the maghemite type, as evidenced by XRD and ^{57}Fe Mössbauer spectroscopy (vide infra). Moreover, the presence of the crystalline IOB Fe_3BO_5 phase in the BH-NP1-700C,30m sample (originating from the annealing of the BH-AM1-NP sample), as evidenced by XRD and ^{57}Fe Mössbauer spectroscopy (vide infra), suggests that these platelets could also contain an amorphous-glassy BO (B_2O_3) phase as residual of the $NaBH_4$ reducing agent, which is not contributing in XRD. This glassy phase could serve as the source of B for the development of the IOB phase in the BH-NP1-700C,30m sample during annealing. Structural characterization by HRTEM of the accumulated metallic NPs in the BH-AM1-NP sample (Figure 5.13) reveals *d*-spacings of lattice fringes equal to approximately 0.22 nm on average, indicating the presence of corresponding {111} planes of either an fcc Rh-rich γ-Fe_xRh_{1-x} alloy or elemental Rh structure [3].

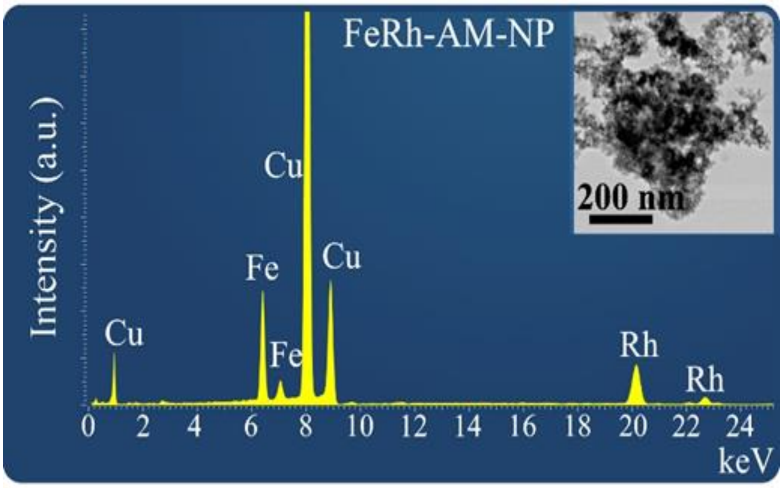

Figure 5.10 Overall EDS spectrum of the BH-AM1-NP sample, collected from the region presented as inset. The Fe at% composition of the Fe-Rh metallic alloys was calculated to be 23% from the respective K_α peaks. Cu peaks are due to the TEM supporting grids.

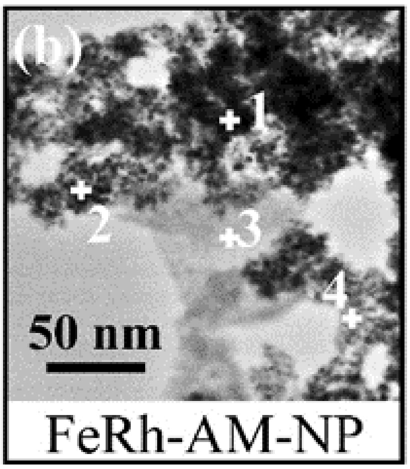

Figure 5.11 Indicative bright field STEM image from the BH-AM1-NP sample showing positions where EDS point analysis was performed. The corresponding measurements are given in **Table 5.2**.

Table 5.2 Fe at% composition of the Fe-Rh metallic alloy calculated from the K_α peaks of point-spectra acquired from the points marked in **Figure 5.11**.

b. BH-AM1-NP	
Spot	**Fe %at**
1	9
2	14
3	41
4	15

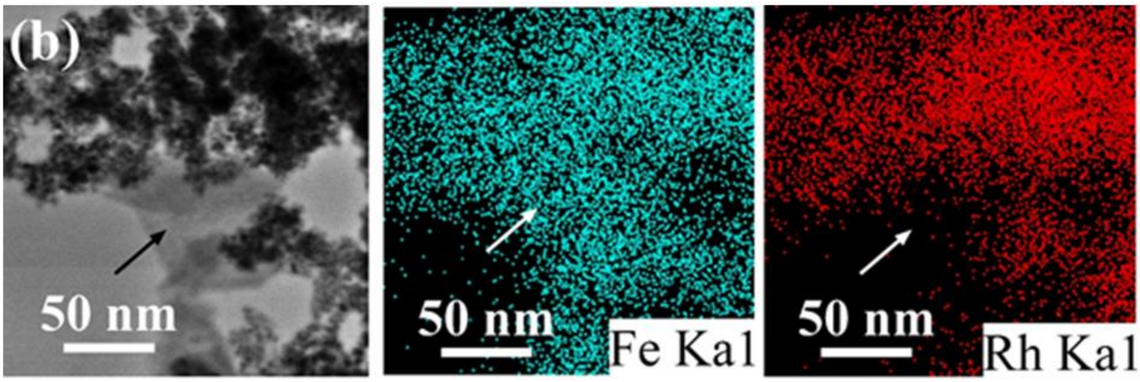

Figure 5.12 EDS Fe and Rh elemental maps obtained from the BH-AM1-NP sample. Arrows point at Fe-rich platelets, possibly connected to IOs and IOBs.

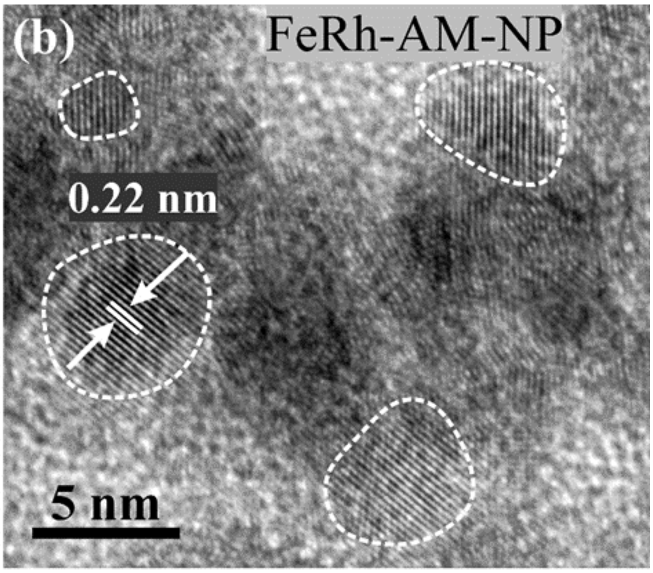

Figure 5.13 HRTEM image from the BH-AM1-NP sample where the periodicity of he {111}-lattice fringes measured at ~0.22 nm is shown in white, indicating fcc elemental Rh or Rh-rich γ-Fe-Rh alloy NPs.

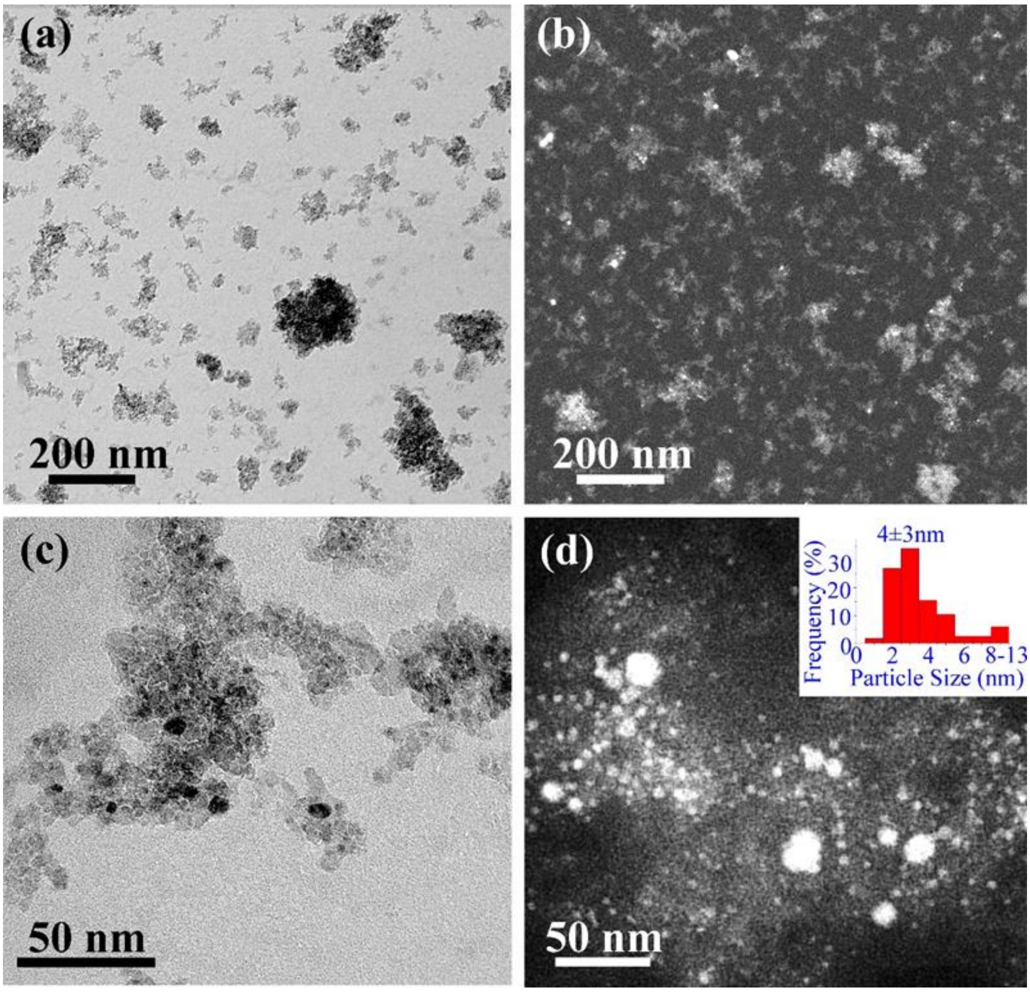

Figure 5.14 Low (a, b) and high (c, d) magnification TEM/STEM images of the BH-NHD1-700C,30m sample. Z-contrast HAADF/STEM images showing the Fe-Rh/NDs hybrid clusters (b) as well as individual Fe-Rh NPs in the hybrids (d) after annealing. The Fe-Rh NP size distribution histogram is presented as an inset in (d).

Moving on, Figure 5.14 reveals the morphology of the BH-NHD1-700C,30m sample. This system exhibits a better spatial and well-resolved dispersion of the formed hybrid nanostructures in comparison to the previous precursor samples. Both ND and metallic Fe-Rh NPs here possess roughly spherical shapes. We observed a reduction in the NDs nanotemplate cluster size after the thermal annealing process relative to that of the BH-AM1-NHD sample, which now ranges between 20 and 80 nm. Z-contrast imaging by HAADF/STEM in Figures 5.14b and 5.14d revealed that the metallic NPs are evenly distributed on the NDs nanotemplates. For the majority of metallic NPs, the average diameter increased only slightly from that of the BH-AM1-NHD sample as a consequence of the thermal annealing treatment and was measured at (4 ± 3) nm, becoming simultaneously slightly broader. Moreover, most of the metallic NPs in this sample are more round-shaped and well-formed compared to those of the BH-AM1-NHD sample. However, there are also some larger spherical metallic NPs with diameters exceeding 8 nm.

EDS spectra of some hybrid Fe-Rh/NDs clusters in this sample reveal average Fe:Rh atomic ratios from about 3:7 up to 4:6, with the latter being determined in clusters comprising only small metallic NPs with average diameter < 5 nm (Figure 5.15). On the other hand, larger metallic NPs showed ratios between 2:8 and 3:7 (Figure 5.16 and Table 5.3). Chemical mapping of hybrid Fe-Rh/NDs clusters (Figure 5.17) reveal the presence of both Fe and Rh at the same spatial positions where the metallic NPs are detected. The HRTEM image of Figure 5.18, shows a metallic NP embedded in a ND/NPs cluster of the BH-NHD1-700C,30m sample with lattice fringe *d*-spacing of ~0.30 nm, corresponding to the {100} planes of the CsCl-type B2 α'-Fe-Rh phase. These features provide yet another proof of the NDs nanotemplates' ability to grow and host very small metallic NPs of high crystallinity uniformly distributed on their surfaces after thermal annealing [4], [5], [6], [7].

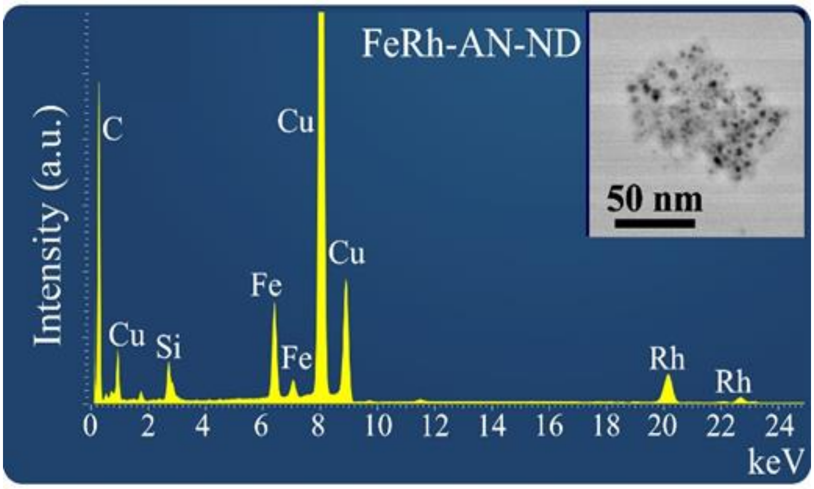

Figure 5.15 Overall EDS spectrum of the BH-NHD1-700C,30m sample, collected from the region presented as inset. The Fe at% composition of the Fe-Rh metallic alloys was calculated to be 37% from the respective K$_\alpha$ peaks. Cu peaks are due to the TEM supporting grids. The Si peak is attributed to contamination from the quartz ampule during the annealing.

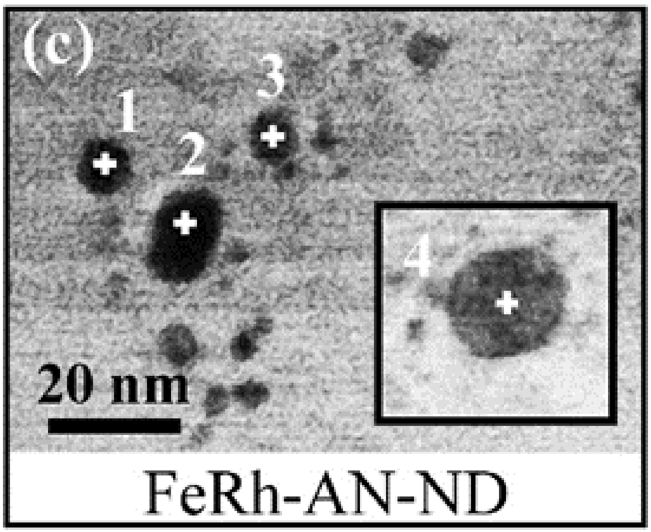

Figure 5.16 Indicative bright field STEM image from the BH-NHD1-700C,30m sample showing positions where EDS point analysis was performed. The corresponding measurements are given in **Table 5.3**.

Table 5.3 Fe at% composition of the Fe-Rh metallic alloy calculated from the K$_\alpha$ peaks of point-spectra acquired from the points marked in **Figure 5.16**.

c. BH-NHD1-700C,30m	
Spot	**Fe %at**
1	22
2	23
3	23
4	29

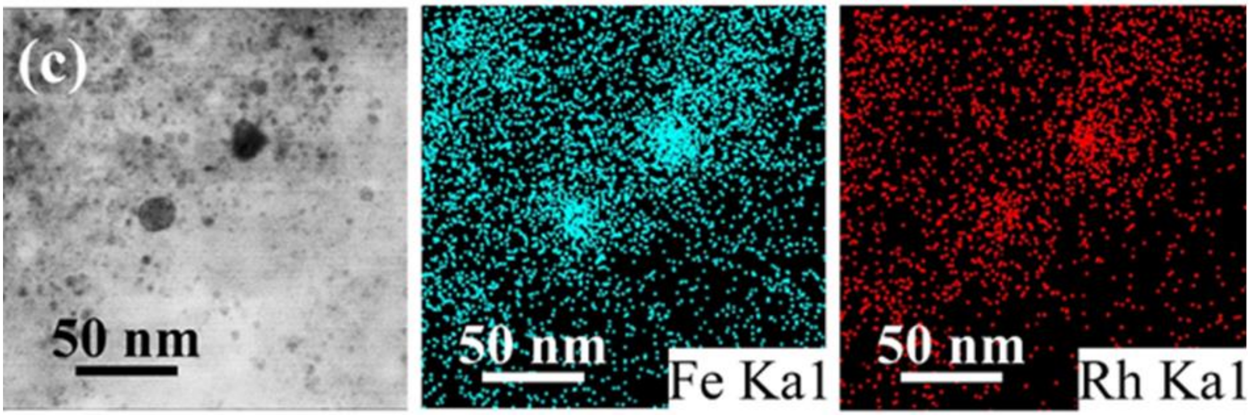

Figure 5.17 EDS Fe and Rh elemental maps obtained from the BH-NHD1-700C,30m sample.

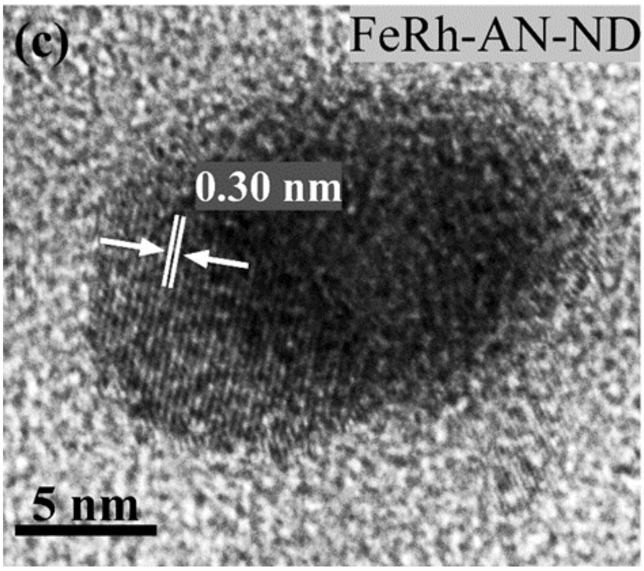

Figure 5.18 HRTEM image from the BH-NHD1-700C,30m sample. The {100}-lattice fringes of the CsCl-type α'-Fe-Rh phase of a metallic NP after the annealing process, with ~0.30 nm spacing, are illustrated.

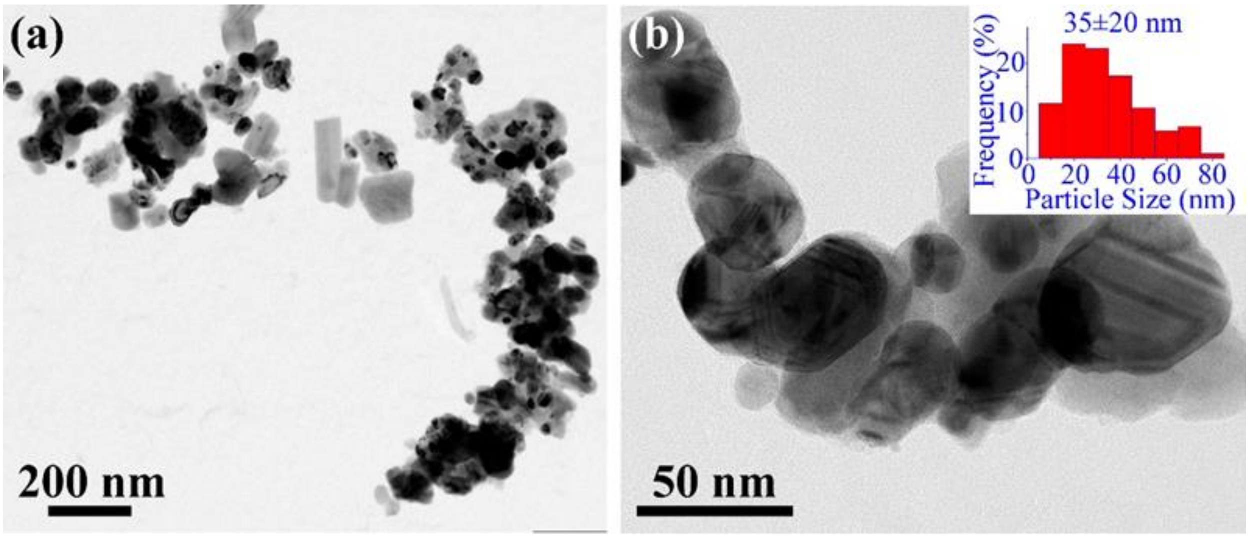

Figure 5.19 Bright field TEM images from the BH-NP1-700C,30m sample (a and b). The size distribution of the spherical-type NPs is presented as inset in (b).

On the other hand, annealing under vacuum at 700 °C of the BH-AM1-NP precursor sample changes considerably its morphology. This is revealed by the conventional TEM images of the BH-NP1-700C,30m sample presented in Figure 5.19. A mix of aggregated almost spherical NPs on the one hand and larger elongated platelets on the other hand were observed. Diffraction contrast from the spherical NPs in Figure 5.19b indicates the presence of twin boundaries, which are characteristic structural defects of fcc metallic crystals. On the other hand, the platelets appearing in Figure 5.19a did not exhibit such defects. The metallic NPs in this sample are considerably larger than those of the BH-AM1-NP sample. This is attributed to the unhindered NPs' growth which is a consequence of thermal annealing at high temperatures in combination with the high NP proximity and aggregation found already in the parent BH-AM1-NP sample before annealing. The size of the spherical metallic NPs presented a broad distribution as displayed in the inset of Figure 5.19b. The average metallic NP diameter was found at (35 ± 20) nm, i.e. there is a 7-fold increase compared to those of the BH-AM1-NP sample.

An overall EDS spectrum from the BH-NP1-700C,30m sample presented in Figure 5.20 suggests an average Fe:Rh atomic ratio of 3:7. EDS spot analyses (Figure 5.21 and Table 5.4), as well as elemental mapping (Figure 5.22) revealed also that the platelets contain only Fe as metallic element, indicating that they are composed of IOs, and in particular IOBs, as suggested by XRD, while the high contrast spherical NPs are Rh-rich with Fe:Rh atomic ratio of 1:9. This was further confirmed by the HRTEM observations, as shown in Figure 5.23, whereby a {111} lattice spacing of ~0.22 nm was again measured in the spherical metallic NP, corresponding to the fcc Fe-Rh metallic structure, while lattice fringes of ~0.38 nm *d*-spacing in the platelets are attributed to the {220} planes of the IOB Fe_3BO_5 structure [8], [9].

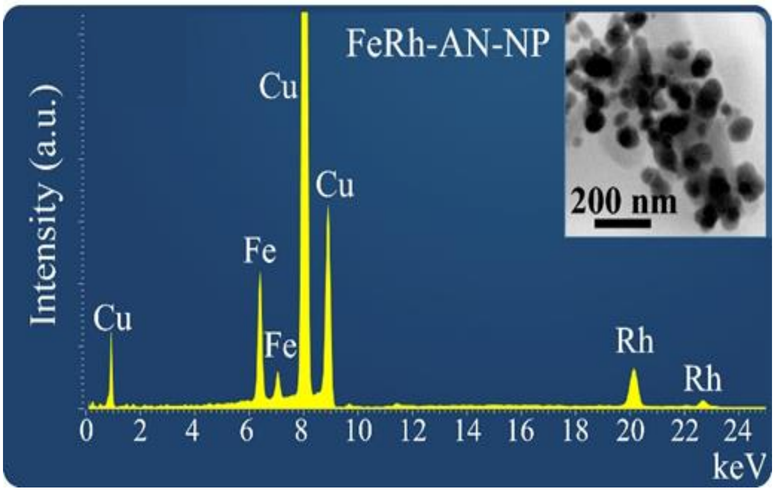

Figure 5.20 Overall EDS spectrum of the BH-NP1-700C,30m sample, collected from the region presented as inset. The Fe at% composition of the Fe-Rh metallic alloys was calculated to be 27% from the respective K_α peaks. Cu peaks are due to the TEM supporting grids.

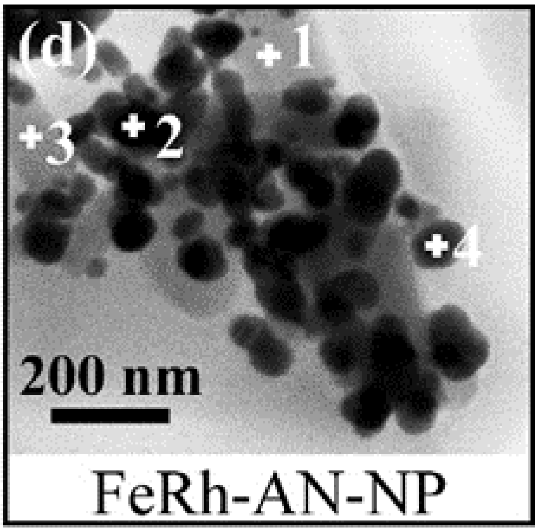

Figure 5.21 Indicative bright field STEM image from the BH-NP1-700C,30m sample showing positions where EDS point analysis was performed. The corresponding measurements are given in **Table 5.4**.

Table 5.4 Fe at% composition of the Fe-Rh metallic alloy calculated from the K_α peaks of point-spectra acquired from the points marked in **Figure 5.21**.

d. BH-NP1-700C,30m	
Spot	**Fe %at**
1	100
2	17
3	100
4	8

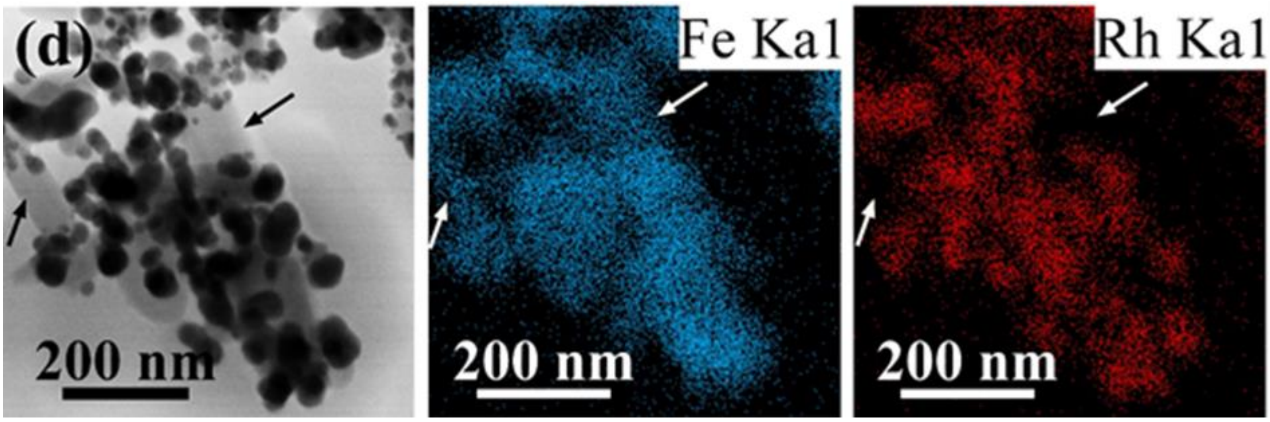

Figure 5.22 EDS Fe and Rh elemental maps obtained from the BH-NP1-700C,30m sample. Arrows in the annealed unsupported NP sample, point at Fe-rich platelets, possibly connected to IOs and IOBs.

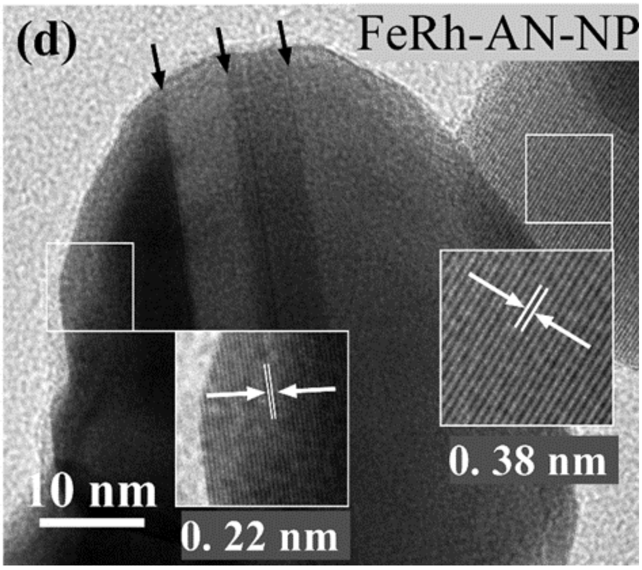

Figure 5.23 HRTEM image from the BH-NP1-700C,30m sample. The Fe-Rh {111}- lattice fringes with spacing ~0.22 nm are measured in a spherical NP that exhibits twinning (black arrows), as well as lattice fringes of ~0.38 nm spacing in another NP, attributed to the {220} planes of iron oxyborate Fe_3BO_5.

5.3 Magnetization and Magnetic Susceptibility

The magnetic properties of the hybrid and unsupported nanostructured samples before and after annealing are delineated by their M vs. H under constant T and χ_g vs. T under constant H measurements. These measurements taken for the as-made precursors and annealed samples, appear in Figures 5.24 to 5.27. From these measurements the compositions, stoichiometries, structures and morphologies, as well as the dispersions of the nanostructures are reflected through the magnetic interactions and interconnections of the NPs developed in each sample.

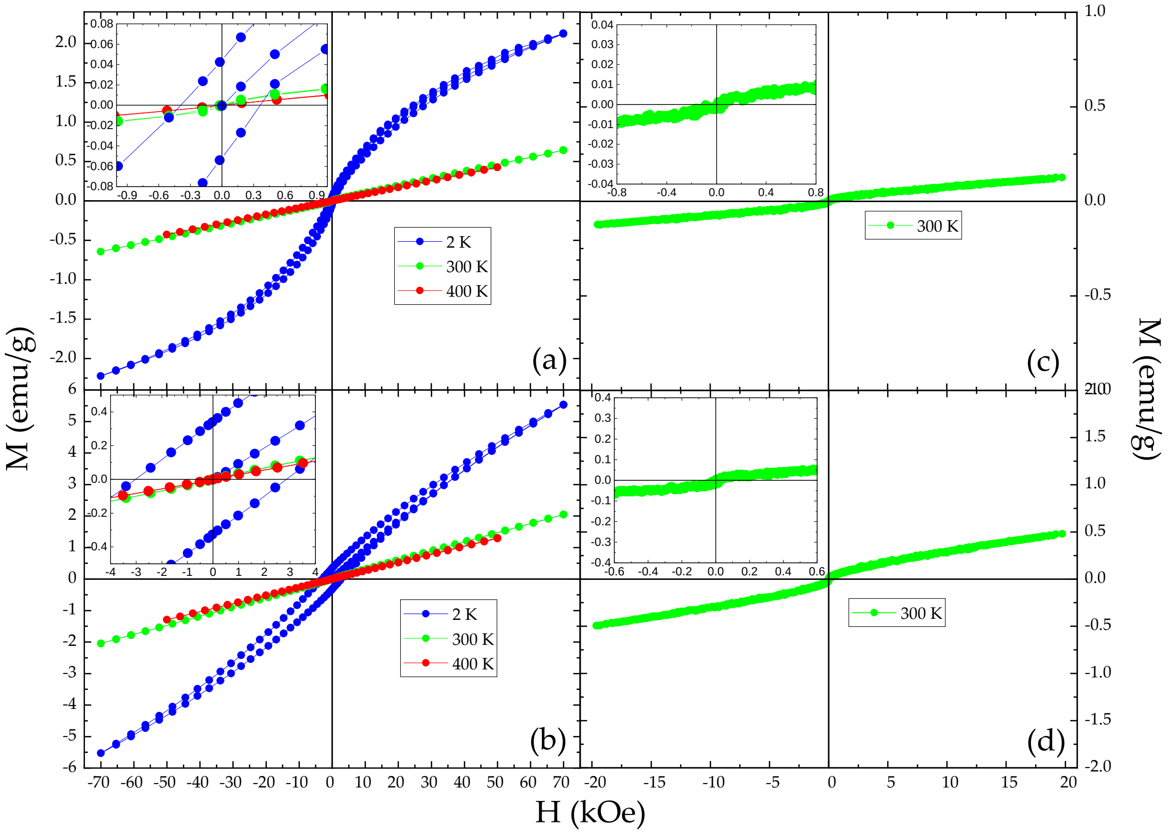

Figure 5.24 Magnetization versus applied magnetic field isothermal loops of the BH-AM1-NHD (a), BH-AM1-NP (b), BH-AM2-NHD (c) and BH-AM2-NP (d) samples measured at different temperatures indicated by different colors 400 (red), 300 K (green) and 2 K (blue). The insets in each set of measurements show the details of the loops' characteristics around zero applied magnetic field for all temperatures (upper left).

The M vs. H isothermal loops of the BH-AM1-NHD sample recorded at 400 K and 300 K reveal a linear paramagnetic (PM) behavior throughout all H values (Figure 5.24a). However, at 2 K a hysteresis with ferro/ferrimagnetic features emerges, superimposed to yet a strong linear PM contribution denoted by the lack of saturation at high H values. The loops' magnetic characteristics are listed in Table 5.5 for all samples. The high positive dM/dH slopes at high fields and the development of coercive fields (Hc) at low T are features that indicate a magnetic NP assembly experiencing strong SPM relaxation at high T, while being partially magnetically blocked at low T [10], [11]. In a similar manner the M vs. H loops of the BH-AM1-NP sample collected at 400 K and 300 K (Figure 5.24b), reveal a clear linear PM behavior, whereas a ferro/ferrimagnetic sigmoidal-shaped curve, like that of the BH-AM1-NHD sample, with non-saturated M values and non-zero Hcs develops at 2 K. However, in this sample the Hc values at 2 K listed in Table 5.5 are about one order of magnitude larger and the area within the loop is quite larger than those of the BH-AM1-NHD sample, indicating 'harder' ferromagnetic characteristics for the BH-AM1-NP sample at low temperatures. Moreover, the M vs. H loop of the BH-AM2-NHD collected at 300 K reveals a similar PM behavior throughout all H values to that observed for the BH-AM1-NHD sample at 300 K. However, the maximum M values of this sample (0.14 emu/gr), which are measured at 20 kOe, are decreased compared to the corresponding M values of the BH-AM1-NHD sample (0.19 emu/g) measured at the same applied field and at the same T (300K). This result may be owed to the presence of a magnetic NP assembly with smaller average NP sizes for the BH-AM2-NHD sample that is influenced from more pronounced fast SPM relaxation phenomena.

Similar to the BH-AM1-NP sample, the M vs. H loop of the BH-AM2-NP sample collected at 300 K predominantly exhibits a PM behavior across all H values, accompanied by a weak FM signal at low H values. However, the loop shows a slight reduction in M values at high fields compared to those observed in the BH-AM1-NP sample. This difference in magnetic behavior can be attributed to the broader nanoparticle size distribution in the BH-AM2-NP sample.

Specifically, a significant portion of the magnetic NPs in the BH-AM2-NP sample have smaller mean sizes, resulting in faster SPM relaxations at RT compared to the magnetic NPs in the BH-AM1-NP sample. Conversely, a subset of larger magnetic NPs within the BH-AM2-NP sample exhibits moderate SPM characteristics, contributing to the weak FM signal at the center of the M vs. H loop.

In all cases, the AM precursor samples share a common tendency towards smaller magnetic NP sizes, whose spatial proximity and interconnection significantly influence their overall magnetic properties.

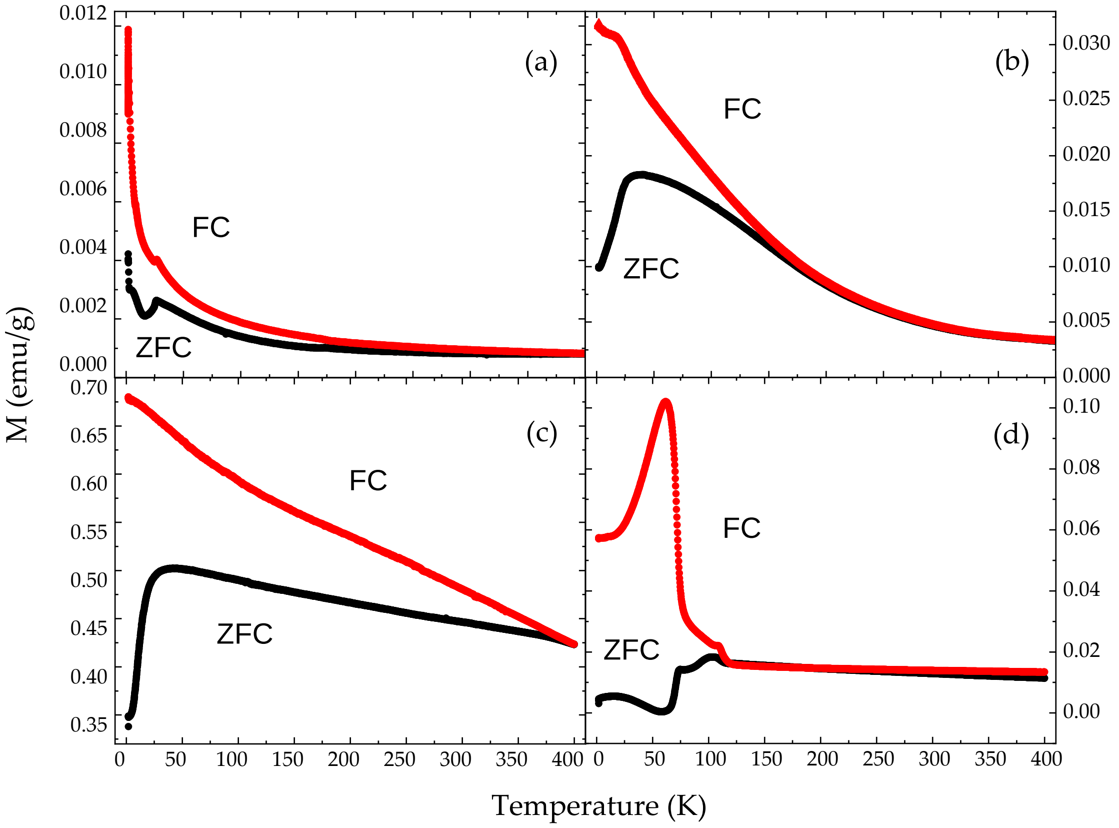

Figure 5.25 Mass magnetic susceptibility versus temperature measurements of the BH-AM1-NHD (a), BH-AM1-NP (b), BH-NHD1-700C,30m (c) and BH-NP1-700C,30m (d) samples measured under an applied external field of 99 Oe following ZFC (black) and FC (red) modes.

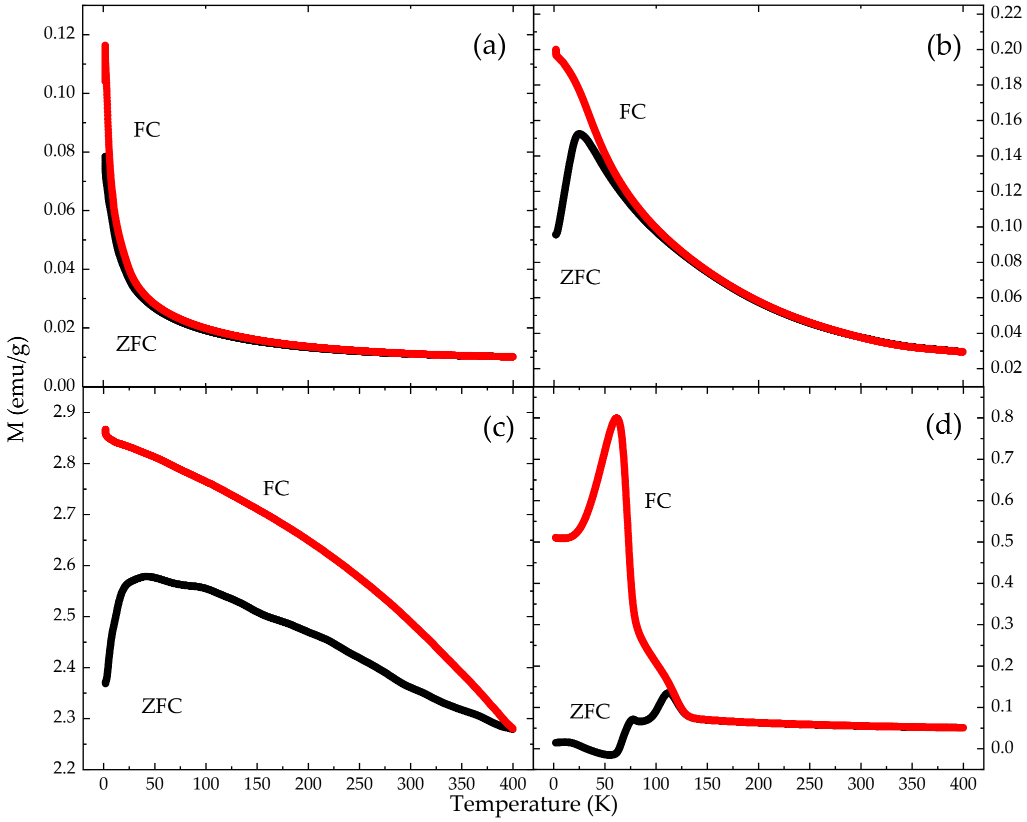

Figure 5.26 Mass magnetic susceptibility versus temperature measurements of the BH-AM1-NHD (a), BH-AM1-NP (b), BH-NHD1-700C,30m (c) and BH-NP1-700C,30m (d) samples measured under an applied external field of 999 Oe following ZFC (black) and FC (red) modes.

The χ_g vs. T ZFC branch for the BH-AM1-NHD sample taken with H_{ap}=99 Oe, appearing in Figure 5.25a, starts descending from an initial χ_g maximum at 2 K and exhibits a local maximum at ~ 27 K, denoting a blocking temperature (T_B) at this point for at least a part of the sample's NPs assembly, followed by a monotonic decrease along the remaining T range. The FC branch follows a similar trend of monotonically increase of χ_g values with decreasing T, disrupted only by a narrow local maximum found again at ~ 27 K. Increasing H to 999 Oe (Figure 5.26) causes the ZFC and FC χ_g vs T branches to virtually coincide in an asymptotic increase of χ_g with reducing T at low temperatures with no sign of saturation or any local maximum, revealing that the strong PM contribution is the dominant factor in this sample, overwhelming any SPM characteristics at high H_{ap} values. These characteristics provide evidence for the existence of an assembly of small SPM NPs experiencing very weak or vanishing interparticle interactions, due to their spatial isolation on the surfaces of the NDs nanotemplates as pointed out by TEM measurements, combined with a strong PM contributing factor [10], [12], [13], [14].

Moreover, Figures 5.25b and 5.26b, exhibit the ZFC and FC branches of the χ_g vs. T variation in the BH-AM1-NP sample presenting more typical characteristics for an assembly of magnetic NPs shaped by the interplay between the magnetic anisotropy, interparticle magnetic interactions and thermal energies. The characteristic large widths around the maxima of the ZFC curves found at T_B=37 K (H_{ap}=99 Oe) and T_B=25 K (H_{ap}=999 Oe), and the bifurcation temperatures found at T_{irr} ~ 200

K (H_{ap}=99 Oe) and T_{irr} ~ 100 K (H_{ap}=999 Oe) reflect the dominant SPM behavior of a magnetic NPs assembly with particle size distribution, which is moreover influenced substantially by interparticle magnetic interactions within it [10], [13], [14].

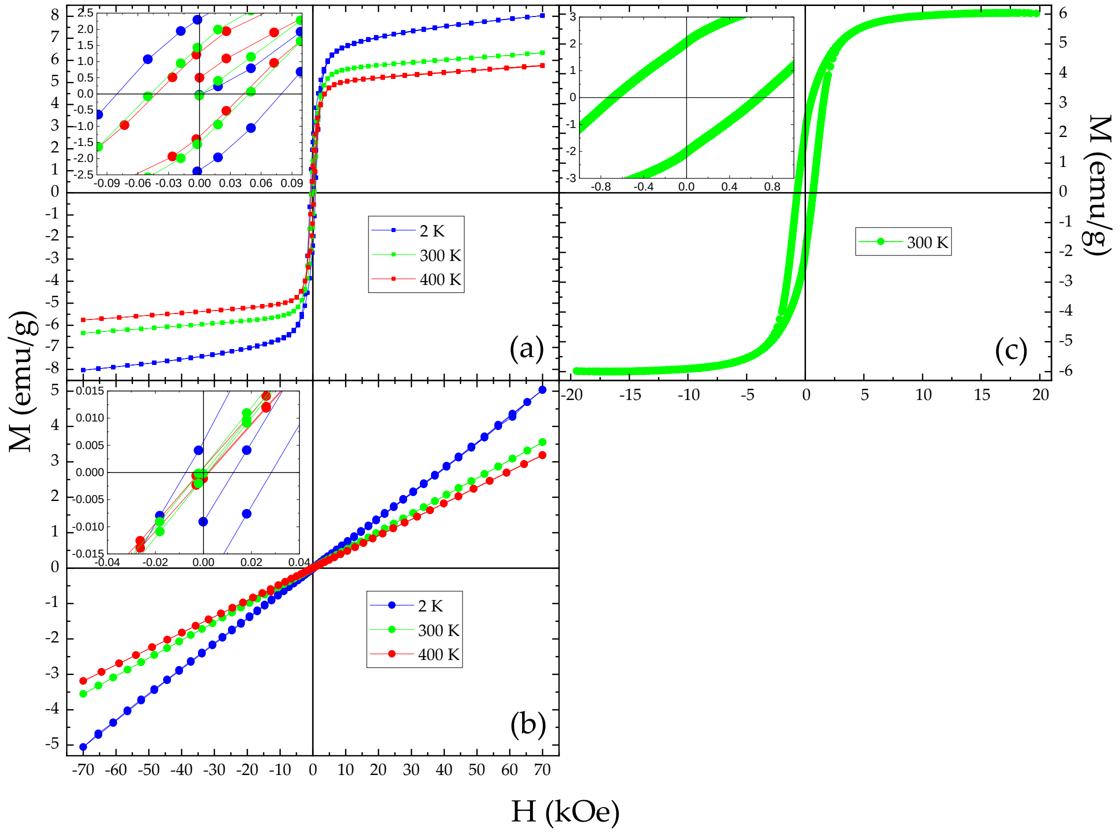

Figure 5.27 Magnetization versus applied magnetic field isothermal loops of the BH-NHD1-700C,30m (a), BH-NP1-700C,30m (b) and BH-NHD2-700C,30m (c) samples measured at different temperatures indicated by different colors 400 K (red), 300 K (green) and 2 K (blue). The insets in each set of measurements show the details of the loops' characteristics around zero applied magnetic field for all temperatures (upper left).

The annealing treatment of the as-made precursors causes different evolutions of magnetic properties between the nanohybrid and unsupported samples to arise. In particular, in Figure 5.27a, the M vs. H loops of the BH-NHD1-700C,30m sample measured at all temperatures reveal clear ferro/ferrimagnetic characteristics with hysteresis, accompanied by constant and non-vanishing dM/dH slopes at high H values that are indicative of the contribution of at least a second PM or SPM phase. The H_C values, which are quite symmetric, regarding their positive and negative values, increase from ~ 425 Oe at 400 K to ~ 800 Oe at 2 K (Table 5.5).

The χ_g vs. T curves of the BH-NHD1-700C,30m sample are characteristic for an assembly of FM NPs showing SPM features with a maximum in the ZFC branch at T_B ~ 40 K both with H_{ap}=99 (Figure 5.25c) and 999 Oe (Figure 5.26c). In addition, the decrease in the χ_g values for these branches is constant and less abrupt for T above T_B, compared to the corresponding curves observed for the BH-AM1-NHD sample. The variation of χ_g in the FC branch shows a continuous increase over the whole temperature range with a very weak tendency for saturation at T below 100 K. The two χ_g vs. T branches coincide only at the highest measured temperature (400 K) for both H_{ap} values, suggesting an increased average size, as well as increased size distribution for the magnetic NPs of the BH-NHD1-700C,30m sample compared to those found for the BH-AM1-NHD sample. Thus, it seems that the assembly of magnetic NPs in this BH-NHD1-700C,30m sample includes contributions from both strong FM characteristics attributed to the magnetically blocked NPs with high magnetic anisotropy and moderate SPM relaxation characteristics due to their reduced particle size.

Table 5.5 Parameters of the magnetic properties of the isothermal loops of **Figures 5.24** and **5.27**. The external field applied for the measurements of the BH-AM1-NHD, BH-AM1-NP, NH-NHD1-700C,30m and BH-NP1-700C,30m samples was 70 kOe, while for the BH-AM2-NHD, BH-AM2-NP and NH-NHD2-700Cm30m samples it was 20 kOe.

Sample	**T (K)**	**M_{max+} (emu/g)**	**M_{max-} (emu/g)**	**M_{R+} (emu/g)**	**M_{R-} (emu/g)**	**H_{C+} (Oe)**	**H_{C-} (Oe)**
BH-AM1-NHD	400	0.43	-0.43	0	0	0	0
	300	0.64	-0.64	0	0	0	0
	2	2.23	-2.22	0.04	-0.05	400	-390
BH-AM1-NP	400	1.29	-1.29	0	0	0	0
	300	2.05	-2.05	0	0	0	0
	2	5.53	-5.53	0.34	-0.33	2870	-3030
BH-AM2-NHD	300	0.14	-0.14	0	0	0	0
BH-AM2-NP	300	0.49	-0.49	0	0	0	0
BH-NHD1-700C,30m	400	5.75	-5.76	1.29	-1.29	-425	425
	300	6.35	-6.35	1.43	-1.56	500	-505
	2	8.03	-8.03	2.29	-2.4	800	-795
BH-NP1-700C,30m	400	3.19	-3.19	0	0	0	0
	300	3.55	-3.55	0	0	0	0
	2	5.03	-5.06	0	0	0	0
BH-NHD2-700C,30m	300	6.02	-6.01	2.01	-2.03	720	-765

These results are in perfect agreement with XRD and TEM-STEM analyses, in which the formation of a well crystallized and size-dispersed assembly of small CsCl-type B2 α'-Fe-Rh magnetic NPs is featured. It is worth mentioning also that no AFM-to-FM metamagnetic transition is observed for this sample, validating thus the contribution of a dominant FM phase with SPM relaxation characteristics along the whole measured temperature length.

On the contrary, in case of BH-NP1-700C,30m sample, from Figure 5.27b and the values of Table 5.5 it is evident that either pure PM or/and AFM behaviors are the only contributions to the loops' measured isothermals at 400, 300 and 2 K. However, the χ_g vs. T measurements reveal a system with PM properties from 400 K down to about 120-110 K, that 'wakes-up' below 114 K and erupts again below 75 K (Figures 5.25d and 5.26d). These late temperatures signal the characteristic transitions from PM to frustrated AFM state at T_N = 114 K and from frustrated AFM to weak-ferromagnetic (WFM) or canted AFM state at T_{WFM}=75 K of the Fe_3BO_5 phase [8], [15], [16]. At low temperatures below 40 K this phase is known to return gradually to a very complex AFM or ferrimagnetic structure with multiple AFM sublattices. These results justify completely the M vs. H measurements and are in line with the results of the XRD and TEM measurements. On the other side, any contribution from a SPM phase existing in the sample is masked below 114 K from the dominant contributions of the bulk Fe_3BO_5 phase's magnetic characteristics.

Moreover, the M vs. H isothermal loop of the BH-NHD2-700C,30m sample collected at 300 K delineates a resembling ferro/ferrimagnetic behavior to that of the BH-NHD1-700C,30m sample with hysteresis (Figure 5.27c), corresponding to an assembly of magnetically blocked NPs, whose H_C values (about 730 Oe at RT), which compared to those found for the BH-NHD1-700C,30m sample, are sufficient high for a typical Fe-Rh alloy at RT [17], [18], [19], [20], [21], [22]. These characteristics are, nevertheless, also accompanied by depleted yet non-vanishing dM/dH slopes at high field values at 300 K, denoting the presence of yet another contribution of smaller IO NPs present in the MNP assembly that undergo very fast SPM relaxations at RT.

5.4 ^{57}Fe Mössbauer Spectroscopy Investigations

The iron-contained phases developed in the samples, their crystal structures, particle size, interconnection and morphology, as well as their magnetic properties are further investigated by means of the atomic-level-probing technique of ^{57}Fe Mössbauer spectroscopy. The ^{57}Fe MS of the as-made nanohybrid and unsupported samples recorded at 300 K, 77 K and 11 K are shown in Figure 5.28 and 5.29, respectively, while those of the annealed samples are presented in Figure 5.30.

The 300 and 77 K MS of the BH-AM1-NHD and BH-AM1-NP samples are almost identical and are composed of a single quadrupole split contribution with relative broad resonant lines. We used one quadrupole split component with a spreading of QS values (ΔQS-Gaussian type) to fit these spectra. The resulting Mössbauer parameters (MPs) values for the RT MS of all samples are listed in Table 5.6, while those of the 77 K and 11 K spectra are given in Table 5.7. The MPs values of this component for both samples indeed coincide, within the experimental error limits. From these values it is evident that this contribution corresponds to high-spin Fe^{3+} ions in oxygen first neighbor environment. However, the evolution of the MS at 11 K is quite different between the BH-AM1-NHD and BH-AM1-NP samples. For the former a broad magnetically split contribution is developed at 11 K, in superposition to the still existing significant quadrupole split contribution, while for the later the broad magnetically split part is the only one contributing to the 11 K spectrum and the quadrupole split part is completely absent. The magnetically split part of the MS for both samples is modeled by a set of magnetic components, for which a spreading (ΔB_{hf}-Gaussian type) of the hyperfine magnetic field (B_{hf}) values, either symmetric or asymmetric with respect to the central B_{hf}^{C} value, was allowed to describe the observed line broadening [23]. The MPs of the magnetically split components in the spectra of both samples (Table 5.7) correspond again to Fe^{3+} ions in oxygen environment, and acquire similar values, as was the case for the quadrupole split components.

It is evident from these results that the iron-bearing phases in both as-made samples are not referring to iron atoms in the metallic or alloyed state. They suggest the presence of IOs or/and iron oxyhydroxides (IOHs), and in particular, the quadrupole splitting (QS) and quadrupole shift (2ε) values, of the corresponding components are characteristic of either SPM γ-Fe_2O_3, or ferrihydrite ($Fe_5HO_8.4H_2O$) NPs [2], [24]. Regardless of the exact stoichiometry of these IO or IOH NPs' phases, the complete magnetically resolved 11 K spectrum for the case of the BH-AM1-NP sample, combined with the corresponding partially magnetically split spectrum of the BH-AM1-NHD sample, reflect the different magnetic interactions experienced by these NPs in each sample at this temperature. More specifically, the spatial isolation of the IO/IOH NPs on the surfaces of the ND nanotemplates, as evident from TEM and magnetization measurements, attributes only weak or vanishing interparticle magnetic interactions that lead to the conservation of the SPM properties for a substantial part (~ 50% according to the absorption area of the quadrupole split component) of these NPs in the BH-AM1-NHD sample at this reduced temperature. On the other hand, the spatial proximity, agglomeration and high interconnection of the corresponding NPs in the BH-AM1-NP sample, ascribes to them strong interparticle magnetic interactions, which cause the complete cease of the SPM relaxation, as "sensed" by the Mössbauer spectroscopy technique, for all NPs at this temperature [4], [5], [10], [12], [13], [14], [25], [26], [27].

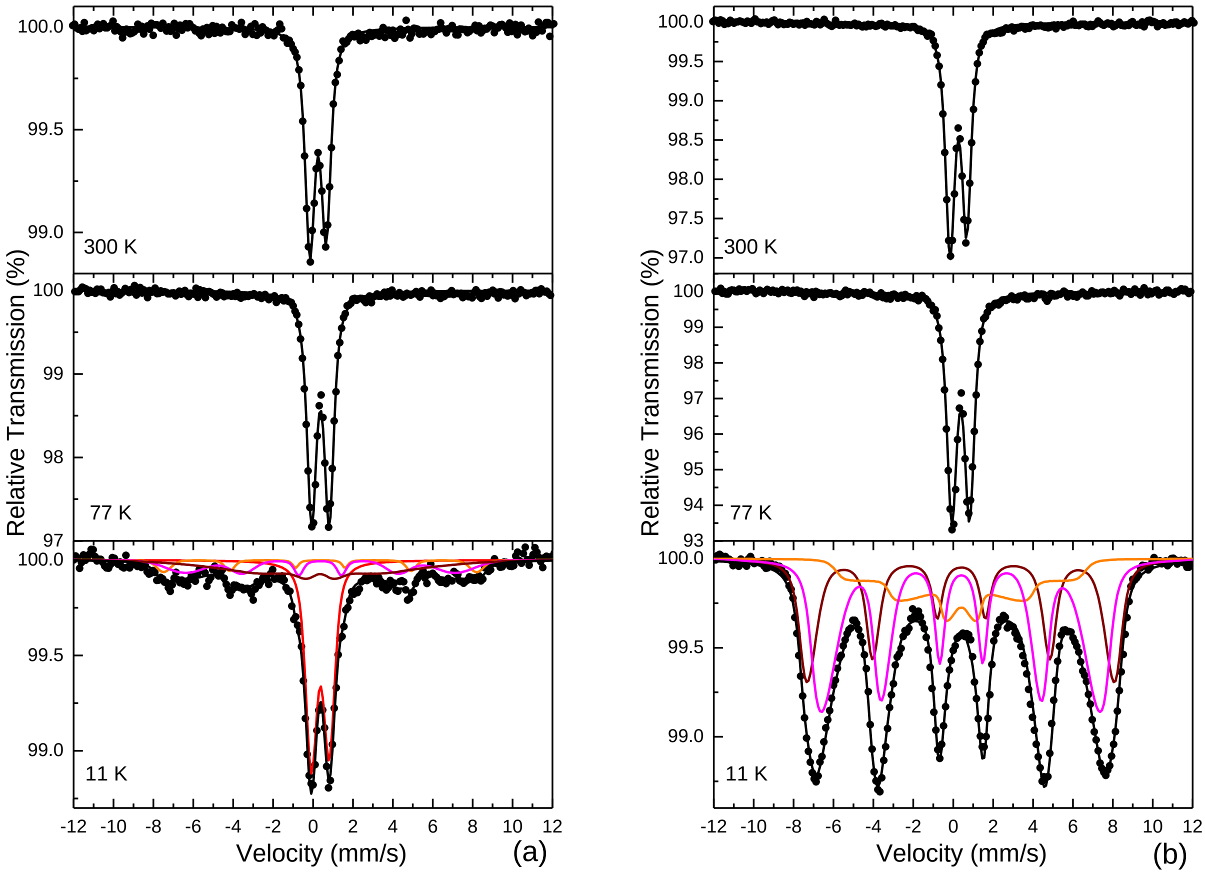

Figure 5.28 ^{57}Fe Mössbauer spectra of the BH-AM1-NHD (a) and BH-AM1-NP (b) samples recorded at different temperatures (room temperature-300 K, 77 K and 11 K).

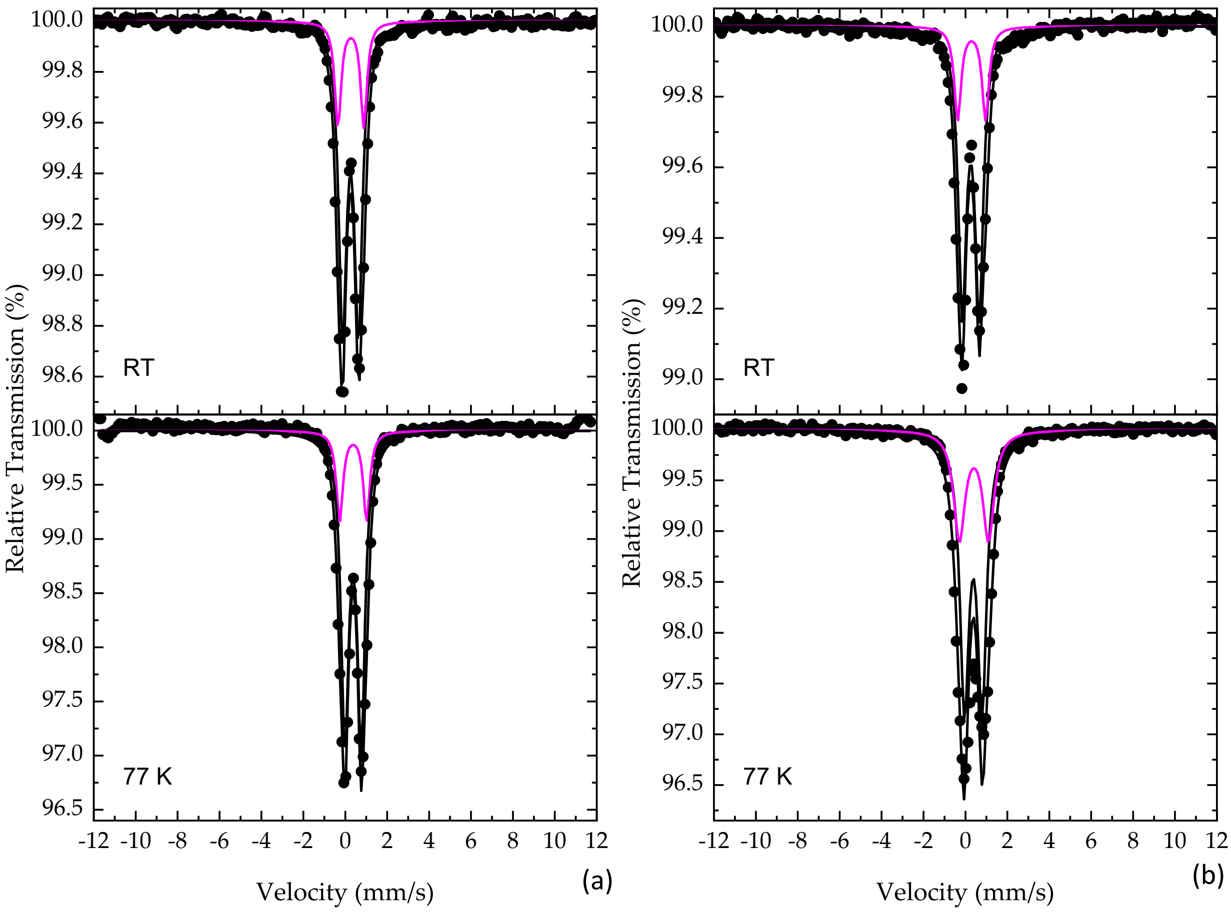

Figure 5.29 ^{57}Fe Mössbauer spectra of the BH-AM2-NHD (a) and BH-AM2-NP (b) samples recorded at different temperatures (room temperature-300K, and 77 K).

The ^{57}Fe MS of the BH-AM2-NHD and BH-AM2-NP precursor samples recorded at RT present similar characteristics to that of the BH-AM1-NHD and BH-AM1-NP samples, respectively. However, these spectra were fitted by two central quadrupole split contributions in order to describe more adequate the central line broadening that is exhibited in both samples. The resulting MPs values from the best fits of these MS are listed in Table 5.6. The MPs values indicate the presence of only Fe^{3+} high-spin states for both precursor samples. In particular, these values are characteristic of Fe^{3+} ions found on IOs or/and iron oxyhydroxides (IOHs) nanostructures, similar to those found in the BH-AM1-NHD and BH-AM1-NP precursors, for which their particle size is so small that it renders them with fast SPM behaviors at RT and 77 K [5], [28], [29]. These results ascribe many structural and magnetic similarities between these different sets of AM precursors, which are in good agreement to those found from the XRD and magnetic measurements studies, and validate for the consistent synthesis of magnetic hybrid nanostructures.

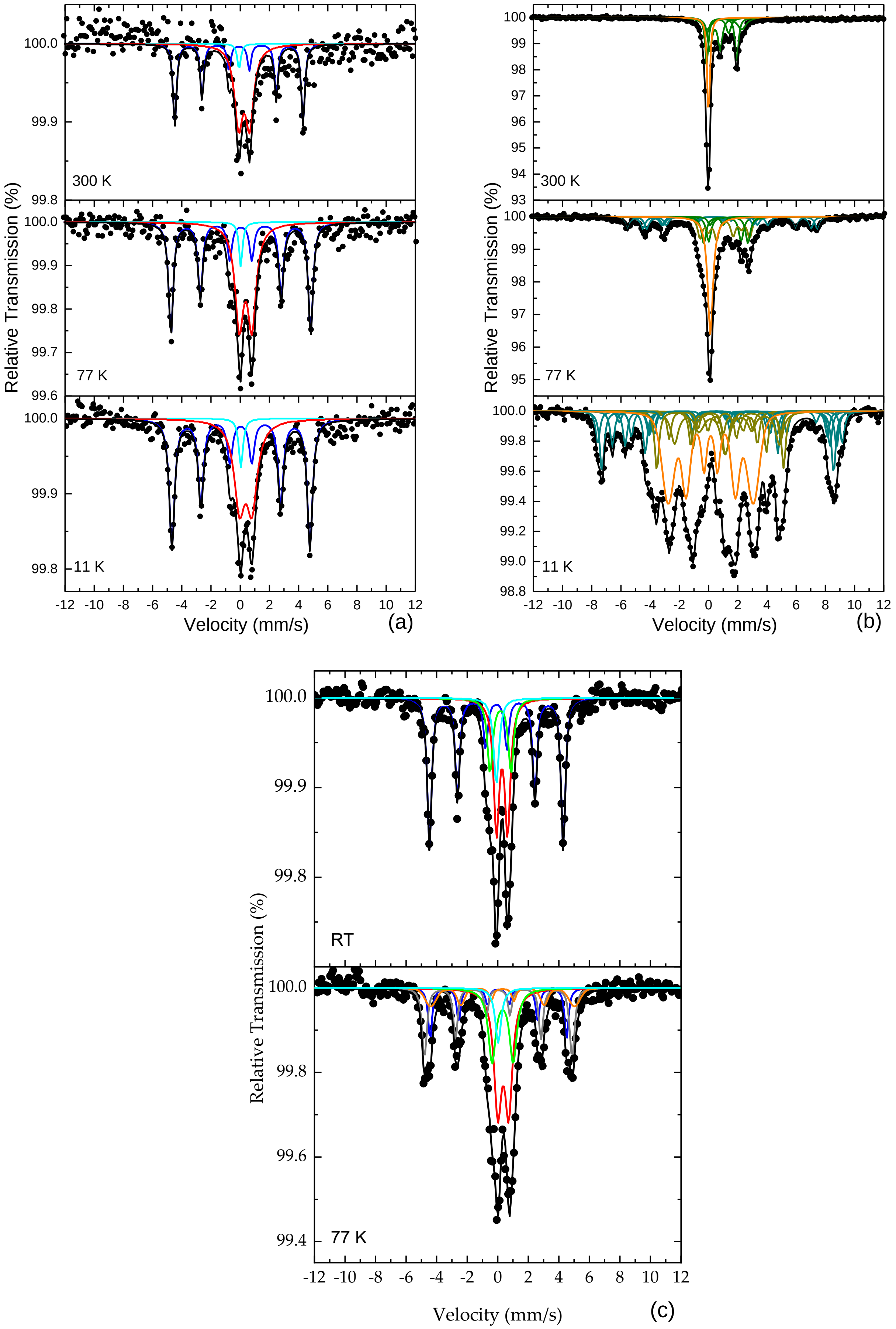

Figure 5.30 ^{57}Fe Mössbauer spectra of the BH-NHD1-700C,30m (a), BH-NP1-700C,30m (b) and BH-NHD2-700C,30m (c) samples recorded at different temperatures (room temperature-300 K, 77 K and 11 K).

Table 5.6 Mössbauer hyperfine parameters as resulting from the best fits of the corresponding spectra of the samples shown on **Figures 5.28, 5.29** and **5.30** recorded at **300 K**. IS the isomer shift (given relative to α-Fe at 300 K), Γ/2 is the half-line width, QS or QS^C is the quadrupole splitting or the central value of the QS, 2ε is the quadrupole shift, B_{hf}^C is the central value of the hyperfine magnetic field, ΔB_{hf} and ΔQS are the total spreading (Gaussian-type) of the B_{hf} and QS values around the central B_{hf}^C and QS^C values respectively, and AA is the relative spectral absorption area of each component used to fit the spectra. Typical errors are ±0.02 mm/s for IS, Γ/2, 2ε and QS or QS^C, ±3 kOe for B_{hf}^C, η ±0.3 at 77 K, θ, φ ±3° at 77 K, and ±3% for AA.

Sample	**Component**	**IS** **(mm/s)**	**Γ/2** **(mm/s)**	**QS, QS^C or 2ε** **(mm/s)**	**$B_{hf}^{(C)}$ or ΔQS** **(kOe or mm/s)**	**ΔB_{hf}** **(kOe)**	**AA** **(%)**	**Color**
BH-AM1-NHD	Fe^{3+} - IO/IHO (SPM)	0.35	0.22	0.81	0.23	0	100	Black
BH-AM1-NP	Fe^{3+} - IO/IHO (SPM)	0.36	0.22	0.83	0.21	0	100	Black
BH-AM2-NHD	Fe^{3+} - IO/IHO (SPM 1)	0.34	0.22	0.76	0	0	78	Black
	Fe^{3+} - IO/IHO (SPM 2)	0.36	0.18	1.29	0	0	22	Magenta
BH-AM2-NP	Fe^{3+} - IO/IHO (SPM 1)	0.35	0.23	0.81	0	0	73	Black
	Fe^{3+} - IO/IHO (SPM 2)	0.38	0.20	1.33	0	0	27	Magenta
BH-NHD1-700C,30m	Fe - bcc B2 α'-FeRh	0.03	0.14	-0.02	273	0	45	Blue
	Fe - bcc B2 α'-FeRh (SPM)	0.03	0.14	0.00	0	0	4	Cyan

	Fe^{3+} - IO/IHO (SPM)	0.38	0.35	0.76	0	0	51	Red
BH-NP1-700C,30m	Fe - fcc γ-FeRh	0.11	0.10	0.00	0	0	25	Orange
	Fe$^{2.\nu+}$ - Fe_3BO_5	0.55	0.17	0.71	0	0	23	Olive
	Fe$^{2.5+}$ - Fe_3BO_5	0.74	0.19	1.49	0	0	13	Olive
	Fe^{2+} - Fe_3BO_5	1.01	0.12	2.06	0	0	22	Olive
	Fe^{2+} - Fe_3BO_5	1.19	0.36	2.39	0	0	17	Olive
BH-NHD2-700C,30m	Fe - bcc B2 α'-FeRh	0.01	0.17	0.01	272	0	38	Blue
	Fe – bcc B2 α'-FeRh (SPM)	0.01	0.21	0.00	0	0	9	Cyan
	Fe^{3+} - IO/IHO (SPM 1)	0.36	0.23	0.75	0	0	33	Red
	Fe^{3+} - IO/IHO (SPM 2)	0.35	0.20	1.31	0	0	20	Green

Table 5.7 ^{57}Fe Mössbauer hyperfine parameters as resulting from the best fits of the corresponding spectra of the samples shown on Figures **5.28, 5.29** and **5.30** recorded at **77 K** and **11 K**. IS the isomer shift (given relative to α-Fe at 300 K), $\Gamma/2$ is the half-line width, QS is the quadrupole splitting, 2ε is the quadrupole shift, B_{hf}^{C} is the central value of the hyperfine magnetic field, ΔB_{hf} is the total spreading (Gaussian-type) of the B_{hf} values around the central B_{hf}^{C} value, and AA is the relative spectral absorption area of each component used to fit the spectra. In some cases, the ΔB_{hf} is asymmetric around the B_{hf}^{C} value and is given as the ΔB_{hf} value lower/higher relative to B_{hf}^{C}. Typical errors are ±0.02 mm/s for IS, $\Gamma/2$, 2ε and QS, ±3 kOe for B_{hf}^{C} and ±3% for AA.

Sample	**Component**	**IS (mm/s)**	**$\Gamma/2$ (mm/s)**	**QS or 2ε (mm/s)**	**B_{hf}^{C} (kOe)**	**ΔB_{hf} (kOe)**	**AA (%)**	**Color**	**T (K)**
BH-AM1-NHD	Fe^{3+} - IO/IHO (SPM)	0.47	0.22	0.88	0	0	100	Black	77
BH-AM1-NP	Fe^{3+} - IO/IHO (SPM)	0.48	0.22	0.89	0	0	100	Black	
BH-AM2-NHD	Fe^{3+} - IO/IHO (SPM 1)	0.46	0.22	0.78	0	0	80	Black	
	Fe^{3+} - IO/IHO (SPM 2)	0.48	0.19	1.29	0	0	20	Magenta	
BH-AM2-NP	Fe^{3+} - IO/IHO (SPM 1)	0.47	0.26	0.84	0	0	70	Black	
	Fe^{3+} - IO/IHO (SPM 2)	0.49	0.33	1.39	0	0	30	Magenta	
BH-NHD1-700C,30m	Fe - bcc B2 α' Fe-Rh	0.15	0.20	-0.02	284	0	46	Blue	
	Fe - bcc B2 α' Fe-Rh (SPM)	0.15	0.16	0.00	0	0	4	Cyan	
	Fe^{3+} - IO/IHO (SPM)	0.49	0.38	0.80	0	0	50	Red	
BH-NP1-700C,30m	Fe - fcc FeRh	0.23	0.22	0.00	0	0	27	Orange	
	Fe^{2+} - Fe_3BO_5	1.23	0.19	2.22	0	0	10	Dark Yellow	
	Fe^{2+} - Fe_3BO_6	1.30	0.19	3.03	0	0	11	Dark Yellow	
	$Fe^{2.v+}$ - Fe_3BO_7	0.66	0.17	0.91	0	0	3	Dark Yellow	
	Fe^{2+} - Fe_3BO_5	1.23	0.19	2.19	47	0	20	Dark Yellow	
	Fe^{3+} - Fe_3BO_5	0.52	0.19	0.82	323	0	10	Dark Cyan	
	$Fe^{2.5+}$ - Fe_3BO_5	0.87	0.19	1.36	347	0	9	Dark Cyan	
	$Fe^{2.5+}$ - Fe_3BO_5	0.81	0.19	1.12	399	0	10	Dark Cyan	

BH-NHD2-700C,30m	Fe - bcc B2 α' Fe-Rh	0.14	0.15	0.01	277	0	16	Blue	
	Fe - bcc B2 α' Fe-Rh (SPM)	0.14	0.17	0.00	0.00	0	9	Cyan	
	Fe - bcc B2 α' Fe-Rh (MRES)	0.14	0.15	0.01	295	11	21	Grey	
	Fe^{3+} - IO/IHO (SPM 1)	0.44	0.30	0.71	0	0	28	Red	
	Fe^{3+} - IO/IHO (MCOL)	0.42	0.15	0	292	19	10	Orange	
	Fe^{3+} - IO/IHO (SPM 2)	0.43	0.23	1.38	0	0	16	Green	
BH-AM1-NHD	Fe^{3+} - IO/IHO (SPM)	0.47	0.20	0.90	0	0	49	Red	11
	Fe^{3+} - IO/IHO	0.47	0.16	-0.01	487	17	7	Magenta	
	Fe^{3+} - IO/IHO	0.47	0.16	0.01	420	57	19	Orange	
	Fe^{3+} - IO/IHO	0.47	0.21	0.01	261	164	25	Brown	
BH-AM1-NP	Fe^{3+} - IO/IHO	0.50	0.31	-0.03	488	12/4	30	Brown	
	Fe^{3+} - IO/IHO	0.50	0.28	-0.03	449	24/6	50	Magenta	
	Fe^{3+} - IO/IHO	0.50	0.14	-0.03	360	135/12	20	Orange	
BH-NHD1-700C,30m	Fe - bcc B2 α' Fe-Rh	0.15	0.22	0.01	294	0	48	Blue	
	Fe - bcc B2 α' Fe-Rh (SPM)	0.15	0.17	0.00	0	0	5	Cyan	
	Fe^{3+} - IO/IHO (SPM)	0.49	0.44	0.86	0	0	47	Red	
BH-NP1-700C,30m	Fe - fcc FeRh	0.26	0.21	0.00	181	20	30	Orange	
	Fe^{2+} - Fe$_3$BO$_5$	1.24	0.17	2.10	94	0	7	Dark Yellow	
	Fe^{2+} - Fe$_3$BO$_8$	1.24	0.17	2.15	249	0	10	Dark Cyan	
	Fe^{2+} - Fe$_3$BO$_8$	1.24	0.17	2.15	205	0	7	Dark Cyan	
	Fe^{2+} - Fe$_3$BO$_8$	1.31	0.31	3.03	161	0	11	Dark Cyan	
	Fe^{3+} - Fe$_3$BO$_5$	0.53	0.17	0.82	491	0	10	Dark Cyan	
	Fe$^{2.5+}$ - Fe$_3$BO$_5$	0.82	0.17	1.14	515	0	6	Dark Cyan	

	$Fe^{2.5+}$ - Fe_3BO_3	0.82	0.17	1.14	474	0	6	Dark Cyan	
	$Fe^{2.5+}$ - Fe_3BO_4	0.88	0.17	1.36	432	0	6	Dark Cyan	
	$Fe^{2.5+}$ - Fe_3BO_5	0.88	0.17	1.36	416	0	4	Dark Cyan	
	$Fe^{2.v+}$ - Fe_3BO_5	0.69	0.17	0.93	414	0	3	Dark Cyan	

The MS of the annealed samples are quite different in shape, both from those of the as-made samples, as well as between each other, as evident from the comparison of Figures 5.28, 5.29 and 5.30. The MS of the BH-NHD1-700C,30m sample in Figure 5.30a combine the contributions of a magnetically split component with relatively sharp resonant lines, which reflects high crystallinity for the corresponding phase represented by this component, and a quadrupole split broad central doublet at all temperatures. Unsuccessful attempts to fit adequately these spectra with only two such components led to the need for the inclusion of an additional minor singlet central component to the fitting model at all temperatures. The resulting MPs values listed in Table 5.6 and Table 5.7, denote that the sextet and the singlet acquire identical ISs, characteristic of a metallic Fe-Rh alloy. In particular, the MPs of the sextet correspond to a well ordered FM CsCl-type B2-bcc α'-Fe-Rh structure [30], [31], [32]. It becomes thus apparent combining the XRD, TEM, magnetization/magnetic susceptibility and current ^{57}Fe Mössbauer spectroscopy measurements that, the main contribution in this sample originates from a well crystallized ordered nanostructured B2 α'-Fe-Rh phase. Due to the existing particle size distribution and their spatial isolation on the surfaces of the NDs nanotemplates however, the smaller B2-type Fe-Rh NPs must experience very strong SPM relaxation that leads to the complete collapse of their B_{hf} values. This part of the Fe-Rh NPs assembly is represented by the minor singlet in the MS of Figure 5.30a. On the other side, the MPs values of the quadrupole split doublet signify also the presence of Fe^{3+} ions in IOs. These IOs could have been developed as native oxides on the surfaces of the Fe-Rh NPs in a core-shell structure, or as stand-alone phases during the annealing procedure. In either case, these IOs experience strong SPM relaxation throughout the whole measured temperature range, as the development of any magnetically split part in the MS presenting their characteristics is suppressed even at temperatures as low as 11 K.

The spectrum of the BH-NP1-700C,30m sample recorded at RT (Figure 5.30b) combines the contributions of a set of quadrupole split doublets and a central singlet. A set of four quadrupole split components and a singlet were used to fit this spectrum adequately. The resulting MPs listed in Table 5.6, suggest that the quadrupole split components correspond to the $Fe^{2.v+}$, $Fe^{2.5+}$ and Fe^{2+} valence states of the mixed-valence oxyborate Fe_3BO_5 phase [8], detected in this sample by XRD and TEM measurements. The singlet acquires MPs that correspond to a PM disordered fcc γ-Fe-Rh phase, also detected by XRD and TEM. The evolution of the MS at lower temperatures confirms the presence of these two phases in this sample. In particular, the fittings at 77 K combine the contributions of the characteristic magnetically split and Fe^{2+} magnetically frustrated components of the Fe_3BO_5 phase, while at 11 K the development of the complex full magnetically split spectrum for this phase is also evident [8]. The Fe-Rh phase retains its PM characteristics at 77 K, but develops magnetic splitting with broad resonant lines, as expected from the magnetic spin-glass properties of this phase [30], [31], [32], [33], [34] at 11 K.

The RT spectrum of the BH-NHD2-700C,30m sample exhibits spectral characteristics like those of the BH-NHD1-700C,30m sample. It shows a dominant magnetically split contribution along with a secondary central quadrupole split contribution. To accurately fit this spectrum, we used the same fitting model we used to describe the BH-NHD1-700C,30m sample. The resulting MPs values for the primary component in the RT spectrum, as listed in Table 5.6, are consistent with those observed for the Fe-bcc B2 α' Fe-Rh phase in the BH-NHD1-700C,30m sample. Meanwhile, the MPs for the secondary contribution suggest the presence of IO nanostructures exhibiting fast SPM relaxation.

Upon lowering the temperature to 77 K, the thermal evolution of the sample's spectrum further confirms the presence of these two phases (see Table 5.7). Specifically, we used two magnetically split components and one single central component to describe the Fe-bcc B2 α' Fe-Rh phase at 77 K: a Fe-bcc B2 α' Fe-Rh component (shown in blue in Figure 5.30c, 77 K) with relatively sharp resonant lines, which reflects high crystallinity for the corresponding phase, a Fe-bcc B2 α' Fe-Rh component with broad lines but magnetically resolved characteristics (shown in cyan in Figure 5.30c, 77 K) indicative of a part of the α' Fe-Rh NPs assembly with smaller average NP sizes compared to those NPs of the Fe-bcc B2 α' Fe-Rh component, but yet, they can be described by different aspects of the SPM relaxation, which refer to the size of the NPs and their interactions through their inter-connection that both influence τ as T is reduced from 300 to 77 K. The minor single central component corresponds to the smaller B2-type Fe-Rh NPs, which retain their very strong SPM relaxation characteristics even at the lower temperature.

The broad central part of the spectrum corresponds to the IO NPs experiencing significant SPM relaxation, represented by the Fe^{3+}-IO/IHO SPM 1 and SPM 2 components (colored red and green in Figure 5.30c, 77 K, respectively). At 77 K, the AA of these SPM components decreases, while a new magnetically collapsing component (Fe^{3+} IO/IHO MCOL, shown in orange in Figure 5.30c, 77 K) appears, reflecting the magnetic behavior of larger IO nanoparticles. This component was necessary to capture the influence of reduced SPM relaxation as the temperature decreased from 300 K to 77 K. The increase in AA for the Fe^{3+} IO/IHO MCOL component at the expense of the SPM components in the RT spectrum indicates a reduction in SPM relaxation time (τ) for the nanostructured IO/IHO particles at low temperatures, as the slowing of rapid SPM relaxation involves a larger portion of this phase [28], [29].

5.5 Discussion

The results of all experimental characterization techniques used in the present study reveal that in the parent AM-NHD and AM-NP samples any Fe-Rh alloy NPs fail to develop directly in the first stage of the synthesis; rather the presence of metallic Rh and IO/IHO NPs separately, however with immediate spatial proximity and interconnection, is confirmed in these samples. The strong resistance, on the one hand, of metallic Rh against, and the high susceptibility, on the other hand, of Fe towards oxidation, should be the main reasons for this outcome, for which the $NaBH_4$ reducing agent seems to succeed in producing Rh NPs from the $RhCl_3$ salt, but misses to construct a Fe-Rh alloy directly. This lack for the development of any Fe-Rh alloyed phase in the first stage is recovered by the application of the second stage in the synthesis, that includes annealing of the parent samples in evacuated quartz ampoules at high temperatures, a procedure which delivers further reduction conditions to the system. It seems that the metallic Rh and IO/IHO NPs due to their spatial proximity are combined in this second stage to deliver Fe-Rh NPs which are grown on the surfaces of the ND nanotemplates of the BH-NHD1-700C,30m and BH-NHD2-700C,30m samples and develop a single alloy FM B2-bcc structure, even though this phase is Rh-rich. As a consequence, the excess iron remains as IO/IHO either as a very thin layer in the Fe-Rh NPs or as separate SPM NPs. On the other hand, the Fe-Rh NPs formed without the support of the NDs nanotemplates in the BH-NP1-700C,30m sample, although also Rh-rich, fail to develop the FM B2-bcc α'-Fe-Rh structure and remain in the PM γ-fcc structure.

It becomes thus clear that the NDs play the most significant role for the development of this FM phase. In particular, since in the parent as-made hybrid and unsupported samples Fe-Rh alloy NPs are not observed, we propose that the source of carbon atoms originating from the graphitic layers natively appearing on the surfaces of the NDs [35], [36], [37], not only provides the desired additional reducing conditions for the growth of the Fe-Rh alloy NPs during the annealing stage [4], [5], [38], but inflict their development in the FM B2-bcc α'-Fe-Rh structure. This could be a consequence of a partial diffusion of C atoms within this Fe-Rh alloy structure e.g. in interstitial positions, forcing its stabilization. The characteristic sign of this behavior could be found through the fact that the lack of this source of C atoms in the parent BH-AM1-NP sample leads to the stabilization of the fcc PM γ-Fe-Rh phase in the corresponding BH-NP1-700C,30m sample treated under the same annealing conditions. Moreover, the restraint of Fe-Rh NP size growth during annealing in the case of the hybrid samples, due to their isolation and uniform distribution on the NDs nanotemplates surfaces, could also provide the appropriate conditions for sustaining the FM B2-bcc α'-Fe-Rh structure within these reduced NPs size limits. In this frame, the lack of saturation for the magnetization values in the M vs. H measurements on those samples, even at temperatures as low as 2 K in case of BH-NHD1-700C,30m sample, could be attributed to the NPs' SPM behavior due to their reduced sizes; the contribution of the SPM B2-bcc-type α'-Fe-Rh singlet in the MS of both annealed nanohybrid samples at all temperatures reinforces this result. This behavior in the M vs. H measurements however, cannot be distinguished by the SPM behavior of the residual IO/IHO NPs at all temperatures as established by ^{57}Fe Mössbauer spectroscopy. On the other hand, the size growth after annealing for the already well interconnected Rh and IO/IHO NPs on the unsupported BH-AM1-NP sample, could also provide the conditions for the development of larger in size Fe-Rh alloyed NPs, for which the PM fcc structure is assumingly more favorable.

Moreover, the results from all experimental characterization techniques indicate that the hybrid and unsupported samples exhibit similar structural and magnetic properties, regardless of the two different synthesis batches used in this study. These findings confirm the reproducibility of magnetic hybrid nanostructure synthesis, validating the proposed synthetic route as a simple, efficient, and reliable procedure.

Another finding of this study that is worth mentioning and analyzing is the existence of only single-phase alloy Fe-Rh NPs in the BH-NHD1-700C,30m, BH-NHD2-700C,30m and BH-NP1-700C,30m annealed samples, however of different crystal structures, although the stoichiometry of the Fe-Rh alloy is found to fall in the Rh-rich side of the phase diagram, where a binary-phase system composed of both FM α'-B2-bcc and PM γ-fcc is predicted for Rh at. compositions up to about 75% [30], [33], [34], [39], [40], [41]. For the Fe-Rh alloys in the α' region, that is at and below -regarding the Rh content- the equiatomic composition, ^{57}Fe Mössbauer spectroscopy studies reveal the presence of two different first neighbor environments for the Fe atoms: one composed of 6-8 Rh and 4-6 Fe atoms, which corresponds to the Fe atoms in the predicted correct CsCl-type positions (FeI) and a second composed of 8 Fe and 6 Rh atoms, which corresponds to the anti-site defects of the CsCl-type structure (FeII) [30], [34]. It is found that the IS and B_{hf} values of the FeII atoms are shifted substantially from those of the FeI atoms [30], [34], so these sites are clearly distinguishable in the Mössbauer spectra. The MS of the annealed BH-NHD1-700C,30m sample at all measured temperatures reveal a sharp magnetically split component attributed to the bcc a′ Fe-Rh phase with FeI characteristics corresponding to the equiatomic composition. In this context, the spectrum of the annealed BH-NHD2-700C,30m sample at room temperature shows a resembling magnetically split contribution with FeI, which, due to size distribution, separates into two magnetically split components with similar FeI characteristics at 77 K. These observations indicate that the local environment of all Fe atoms in the B2-bcc α'-Fe-Rh structure is stable and uniform, consisting exclusively of 8 Rh atoms as nearest neighbors, with no detectable Fe anti-site atoms. Furthermore, XRD measurements confirm that the Fe-Rh phase in the annealed NHD samples is Rh-rich, with a composition of approximately 60–70% Rh. This conclusion is supported by the lattice constants derived from XRD, which align with those reported for alloys in this compositional range [39], [42] and from the results of the ^{57}Fe Mössbauer and STEM EDS analyses. We propose that the growth of this Rh-rich Fe-Rh phase with such distinct Fe first neighbor environment should be again a consequence of the C atoms diffusion from the NDs′ graphitic surface layers. On the other hand, the further increased Rh content, evident by the XRD and STEM EDS measurements found for the alloy Fe-Rh NPs of the BH-NP1-700C,30m sample, and the lack of available C atoms restrain the development of the B2-bcc phase and the NPs remain at the γ-fcc structure even after the thermal annealing at 700 °C.

5.6 Conclusions

This study presents the synthesis, characterization and analysis of a new magnetic nanohybrid material through the growth of ferromagnetic CsCl-type B2-bcc α'-Fe-Rh nanoparticles on nanodiamond nanotemplates. The synthesis follows a two-stage procedure involving wet chemistry, using $NaBH_4$ as the reducing agent, and vacuum thermal annealing. The Fe-Rh nanoparticles averaging 4 nm in size, are uniformly distributed across the surfaces of the nanodiamond nanotemplates. Although these NPs exhibit a rhodium-rich composition (60-70 at. %), they maintain stable ferromagnetic behavior over a wide temperature range, from 2 K to 400 K. Notably, no antiferromagnetic-to-ferromagnetic transition is observed, as such a transition is characteristic only of Fe-Rh alloys near equiatomic stoichiometry. Magnetic measurements also reveal superparamagnetic relaxation effects, which are attributed to the nanoparticles' small size and their isolated distribution on the nanodiamond surfaces.

Attempts to synthesize similarly ferromagnetic Fe-Rh nanoparticles without nanodiamond support, under the same conditions, were unsuccessful, highlighting the crucial role of the nanodiamond substrate. This finding suggests that carbon atoms within the graphitic surface layers of the nanodiamond assemblies may facilitate diffusion processes during the annealing stage, thereby supporting the formation of the ferromagnetic Fe-Rh phase.

Using dense nanodiamond templates as a foundation for this magnetic nanocrystalline system demonstrates the efficacy of these supports and this synthesis approach in developing advanced magnetic hybrid nanostructures. Additionally, by adjusting synthesis parameters, this two-stage method can yield a variety of magnetic nanohybrids tailored for applications across several key technological fields.

5.7 References

[1] B. D. Cullity and S. R. Stock, *Elements of X-ray diffraction*, 3. ed. Upper Saddle River, NJ: Prentice Hall, 2001.

[2] R. M. Cornell and U. Schwertmann, *The Iron Oxides: Structure, Properties, Reactions, Occurences and Uses*. Weinheim: Wiley-VCH Verlag, 2003.

[3] J. P. Ayoub, C. Gatel, C. Roucau, and M. J. Casanove, “Structure and chemical order in FeRh nanolayers epitaxially grown on MgO(001),” *Journal of Crystal Growth*, vol. 314, no. 1, pp. 336–340, Jan. 2011, doi: 10.1016/j.jcrysgro.2010.11.127.

[4] A. P. Douvalis, A. B. Bourlinos, J. Tucek, K. Čépe, T. Bakas, and R. Zboril, “Development of novel FePt/nanodiamond hybrid nanostructures: L10 phase size-growth suppression and magnetic properties,” *J Nanopart Res*, vol. 18, no. 5, p. 115, May 2016, doi: 10.1007/s11051-016-3424-z.

[5] P. Ziogas, A. B. Bourlinos, J. Tucek, O. Malina, and A. P. Douvalis, “Novel Magnetic Nanohybrids: From Iron Oxide to Iron Carbide Nanoparticles Grown on Nanodiamonds,” *Magnetochemistry*, vol. 6, no. 4, p. 73, Dec. 2020, doi: 10.3390/magnetochemistry6040073.

[6] P. Ziogas *et al.*, “Intriguing Prospects of a Novel Magnetic Nanohybrid Material: Ferromagnetic FeRh Nanoparticles Grown on Nanodiamonds,” *Metals*, vol. 12, no. 8, p. 1355, Aug. 2022, doi: 10.3390/met12081355.

[7] P. G. Ziogas, A. B. Bourlinos, P. Chatzopoulou, G. P. Dimitrakopulos, A. Markou, and A. P. Douvalis, “Novel Hybrid Ferromagnetic Fe–Co/Nanodiamond Nanostructures: Influence of Carbon on Their Structural and Magnetic Properties,” *Magnetochemistry*, vol. 10, no. 5, p. 35, May 2024, doi: 10.3390/magnetochemistry10050035.

[8] A. P. Douvalis, A. Moukarika, T. Bakas, G. Kallias, and V. Papaefthymiou, “Mössbauer and magnetization studies of Fe3BO5,” *Journal of Physics: Condensed Matter*, vol. 14, p. 3303, Mar. 2002, doi: 10.1088/0953-8984/14/12/317.

[9] S. He *et al.*, “Room Temperature Ferromagnetic (Fe $_{1-x}$ Co $_{x}$) $_3$ BO $_5$ Nanorods,” *Nano Lett.*, vol. 14, no. 7, pp. 3914–3918, Jul. 2014, doi: 10.1021/nl501193x.

[10] S. Mørup and M. F. Hansen, “Superparamagnetic Particles,” in *Handbook of Magnetism and Advanced Magnetic Materials*, H. Kronmüller and S. Parkin, Eds., Chichester, UK: John Wiley & Sons, Ltd, 2007, p. hmm409. Accessed: Jun. 17, 2021. [Online]. Available: http://doi.wiley.com/10.1002/9780470022184.hmm409

[11] D. Fiorani, Ed., *Surface effects in magnetic nanoparticles*. in Nanostructure science and technology. New York: Springer, 2005.

[12] S. Mørup and E. Tronc, “Superparamagnetic relaxation of weakly interacting particles,” *Phys. Rev. Lett.*, vol. 72, no. 20, pp. 3278–3281, May 1994, doi: 10.1103/PhysRevLett.72.3278.

[13] S. Mørup, M. F. Hansen, and C. Frandsen, “Magnetic interactions between nanoparticles,” *Beilstein J Nanotechnol*, vol. 1, pp. 182–190, 2010, doi: 10.3762/bjnano.1.22.

[14] S. Mørup, C. Frandsen, and M. F. Hansen, “Uniform excitations in magnetic nanoparticles,” *Beilstein J. Nanotechnology*, vol. 1, pp. 48–54, 2010.

[15] J. S. Swinnea and H. Steinfink, “Crystal structure and Mossbauer spectrum of vonsenite, 2FeO . FeBO 3,” *American Mineralogist*, vol. 68, no. 7–8, pp. 827–832, Aug. 1983.

[16] J. Paul Attfield, J. F. Clarke, and D. A. Perkins, “Magnetic and crystal structures of iron borates,” *Physica B: Condensed Matter*, vol. 180–181, pp. 581–584, Jun. 1992, doi: 10.1016/0921-4526(92)90401-D.

[17] J. S. Kouvel and C. C. Hartelius, “Anomalous Magnetic Moments and Transformations in the Ordered Alloy FeRh,” p. 3.

[18] H. Y. Y. Ko, T. Suzuki, N. T. Nam, N. N. Phuoc, J. Cao, and Y. Hirotsu, “Magnetic and structural characterizations on nanoparticles of FePt, FeRh and their composites,” *Journal of Magnetism and Magnetic Materials*, vol. 320, no. 22, pp. 3120–3123, Nov. 2008, doi: 10.1016/j.jmmm.2008.08.089.

[19] J. Ye *et al.*, “Magnetic properties of ordered polycrystalline FeRh thin films,” *RSC Adv.*, vol. 7, no. 70, pp. 44097–44103, 2017, doi: 10.1039/C7RA06738K.

[20] Z. Jia, N. Seetala, and R. D. K. Misra, “Magnetic behavior of chemically synthesized FePt–FeRh nanostructures,” *Physica B: Condensed Matter*, vol. 405, no. 9, pp. 2189–2193, May 2010, doi: 10.1016/j.physb.2010.02.005.

[21] E. M. Hofer and P. Cucka, “Magnetic properties of Rh-rich FeRh alloy,” *Journal of Physics and Chemistry of Solids*, vol. 27, no. 9, Art. no. 9, Sep. 1966, doi: 10.1016/0022-3697(66)90151-X.

[22] H. Y. Y. Ko and T. Suzuki, “Synthesis and magnetic properties of self-organized FeRh nanoparticles,” *Journal of Applied Physics*, vol. 101, no. 9, p. 09J103, May 2007, doi: 10.1063/1.2711285.

[23] A. P. Douvalis, A. Polymeros, and T. Bakas, “IMSG09: A ^{57}Fe-^{119}Sn Mössbauer spectra computer fitting program with novel interactive user interface,” *J. Phys.: Conf. Ser.*, vol. 217, p. 012014, Mar. 2010, doi: 10.1088/1742-6596/217/1/012014.

[24] E. Murad and J. H. Jhonson, “Iron oxides and Oxyhydroxides,” in *Mossbauer Spectroscopy Applied to Inorganic Chemistry*, vol. II, G. J. Long, Ed., New York, USA: Plenum Press, 1987.

[25] U. Herr, J. Jing, R. Birringer, U. Gonser, and H. Gleiter, “Investigation of nanocrystalline iron materials by Mössbauer spectroscopy,” *Appl. Phys. Lett.*, vol. 50, no. 8, pp. 472–474, Feb. 1987, doi: 10.1063/1.98177.

[26] S. Mørup, “Mössbauer effect in small particles,” *Hyperfine Interact*, vol. 60, no. 1, pp. 959–973, Aug. 1990, doi: 10.1007/BF02399910.

[27] S. Mørup, “Magnetic hyperfine splitting in mössbauer spectra of microcrystals,” *Journal of Magnetism and Magnetic Materials*, vol. 37, no. 1, pp. 39–50, Dec. 1983, doi: 10.1016/0304-8853(83)90350-5.

[28] I. S. Lyubutin *et al.*, “Magnetic and Mössbauer spectroscopy studies of hollow microcapsules made of silica-coated $CoFe_2O_4$ nanoparticles,” *Smart Mater. Struct.*, vol. 25, no. 1, p. 015022, Jan. 2016, doi: 10.1088/0964-1726/25/1/015022.

[29] M. Hähsler *et al.*, “Magnetic Properties and Mössbauer Spectroscopy of Fe_3O_4/$CoFe_2O_4$ Nanorods,” *Inorg. Chem.*, vol. 59, no. 6, pp. 3677–3685, Mar. 2020, doi: 10.1021/acs.inorgchem.9b03267.

[30] G. Shirane, C. W. Chen, P. A. Flinn, and R. Nathans, “Hyperfine Fields and Magnetic Moments in the Fe–Rh System,” *Journal of Applied Physics*, vol. 34, no. 4, pp. 1044–1045, Apr. 1963, doi: 10.1063/1.1729362.

[31] Y. Ohtani and I. Hatakeyama, “Antiferro-ferromagnetic transition and microstructural properties in a sputter deposited FeRh thin film system,” *Journal of Applied Physics*, vol. 74, no. 5, pp. 3328–3332, Sep. 1993, doi: 10.1063/1.354557.

[32] L. S.-J. Peng and G. S. Collins, “Point Defects And The B2 To Fcc Transformation In Milled FeRh,” *MRS Proc.*, vol. 481, p. 631, 1997, doi: 10.1557/PROC-481-631.

[33] C. C. Chao, P. Duwez, and C. C. Tsuei, “Metastable fcc Fe–Rh Alloys and the Fe–Rh Phase Diagram,” *Journal of Applied Physics*, vol. 42, no. 11, pp. 4282–4284, Oct. 1971, doi: 10.1063/1.1659766.

[34] M. Rosenberg, V. Kuncser, O. Crisan, A. Hernando, E. Navarro, and G. Filoti, “A Mössbauer spectroscopy and magnetic study of FeRh,” *Journal of Magnetism and Magnetic Materials*, vol. 177–181, pp. 135–136, Jan. 1998, doi: 10.1016/S0304-8853(97)00662-8.

[35] D. Ho, Ed., *Nanodiamonds: Applications in Biology and Nanoscale Medicine*. Boston, MA: Springer US, 2010. doi: 10.1007/978-1-4419-0531-4.

[36] V. N. Mochalin, O. Shenderova, D. Ho, and Y. Gogotsi, “The properties and applications of nanodiamonds,” *Nature Nanotech*, vol. 7, no. 1, pp. 11–23, Jan. 2012, doi: 10.1038/nnano.2011.209.

[37] J. C. Arnault, *Nanodiamonds: Advanced Material Analysis, Properties and Applications.* 2017.

[38] A. Vignes, *Extractive metallurgy*, vol. 2. London : Hoboken, NJ: ISTE ; Wiley, 2011.

[39] L. J. Swartzendruber, “The Fe−Rh (Iron-Rhodium) system,” *Bulletin of Alloy Phase Diagrams*, vol. 5, no. 5, pp. 456–462, Oct. 1984, doi: 10.1007/BF02872896.

[40] H. Okamoto, “Fe-Rh (Iron-Rhodium),” *Journal of Phase Equilibria and Diffusion*, vol. 32, no. 5, p. 472, Jul. 2011, doi: 10.1007/s11669-011-9934-6.

[41] J. van Driel, R. Coehoorn, G. J. Strijkers, E. Brück, and F. R. de Boer, “Compositional dependence of the giant magnetoresistance in FexRh1−x thin films,” *Journal of Applied Physics*, vol. 85, no. 2, pp. 1026–1036, Jan. 1999, doi: 10.1063/1.369224.

[42] J. B. McKinnon, D. Melville, and E. W. Lee, “The antiferromagnetic-ferromagnetic transition in iron-rhodium alloys,” *Journal of Physics C: Solid State Physics*, vol. 3, no. 1S, pp. S46–S58, May 1970, doi: 10.1088/0022-3719/3/1s/306.

Chapter 6. Study of the Fe-Co/NDs system

6.1 XRD

6.1.1 Samples prepared using the sodium borohydride reducing agent

The XRD patterns of pristine NDs, as-made nanohybrid, and unsupported samples prepared with the $NaBH_4$ reducing agent (BH) are shown in Figure 6.1. In Figure 6.1(a), two main broad diffraction peaks at 43.9° (111) and 75.4° (220) in 2θ, corresponding to the cubic ND structure (lattice constant a = 3.567 Å, ICDD PDF 00-006-0675), confirm the crystalline nature of the NDs. Additionally, a diminished diffraction peak observed at 21.6° in 2θ suggests minor impurity residues.

In Figure 6.1(b), the XRD pattern of the BH-AM1-NHD sample exhibits dominant, broad diffraction peaks attributed to ND nanostructures, along with a reduced in intensity and very broad peak at about 36° 2θ. This peak corresponds likely to the diffraction from the (311) atomic planes of a spinel-type $Fe_{3-x}Co_xO_4$ iron-cobalt-oxide (ICO) structure at 35.4° 2θ (lattice constant a = 8.392 Å, ICDD PDF 00-022-1086) [1]. Average crystalline domain sizes, <D>, for the NDs phase were estimated using the Scherrer formula [2], applied to the most resolvable diffraction peaks of each sample, yielding $\langle D_{NDs} \rangle$ = 5 nm.

These findings indicate that both the pristine NDs and the as-made nanohybrid precursor contain highly nanocrystalline ND particles, consistent with the nominal structure and purity provided by Aldrich. However, estimating the average crystalline domain size for the ICO NPs was not feasible due to the non-resolvable nature of the corresponding main diffraction peak.

Figure 6.1(c) presents the XRD pattern of the BH-AM1-NP sample, which shows very broad peaks spanning in a range of angles. These include very broad contributions from the main diffraction peak of a cubic bcc alloy Fe–Co phase at about 45° 2θ (lattice constant a = 2.855 Å, ICDD PDF 00-049-1567 ($Fe_{0.5}Co_{0.5}$)), as well as an ICO phase at 30° (220) and 36° (311) 2θ. The large peak widths and the reduced intensities suggest the formation of very small NPs for both phases that are also affected by low crystallinity.

The retained NDs nanostructured features, alongside with the presence of ICO NPs, render this as-made hybrid sample a promising structural template for the growth of hybrid Fe-Co alloy/NDs samples by the development of the Fe-Co alloy phase after annealing under controlled conditions. The development of the Fe-Co alloy phase is expected to originate from the reduction of the ICO NPs. Conversely, the unsupported sample shows a greater variety of impurity phases, which may hinder the formation of a single crystalline magnetic Fe-Co alloy phase under similar annealing conditions. Instead, the XRD features suggest that the unsupported sample is more likely to adopt a multi-phase nature after annealing, as also seen in the case of the unsupported Fe-Rh system (Chapter 5), diverging from the expected characteristics of intended uniform growth of magnetic nanostructured materials. For this reason, this precursor was not used further in the second annealing step.

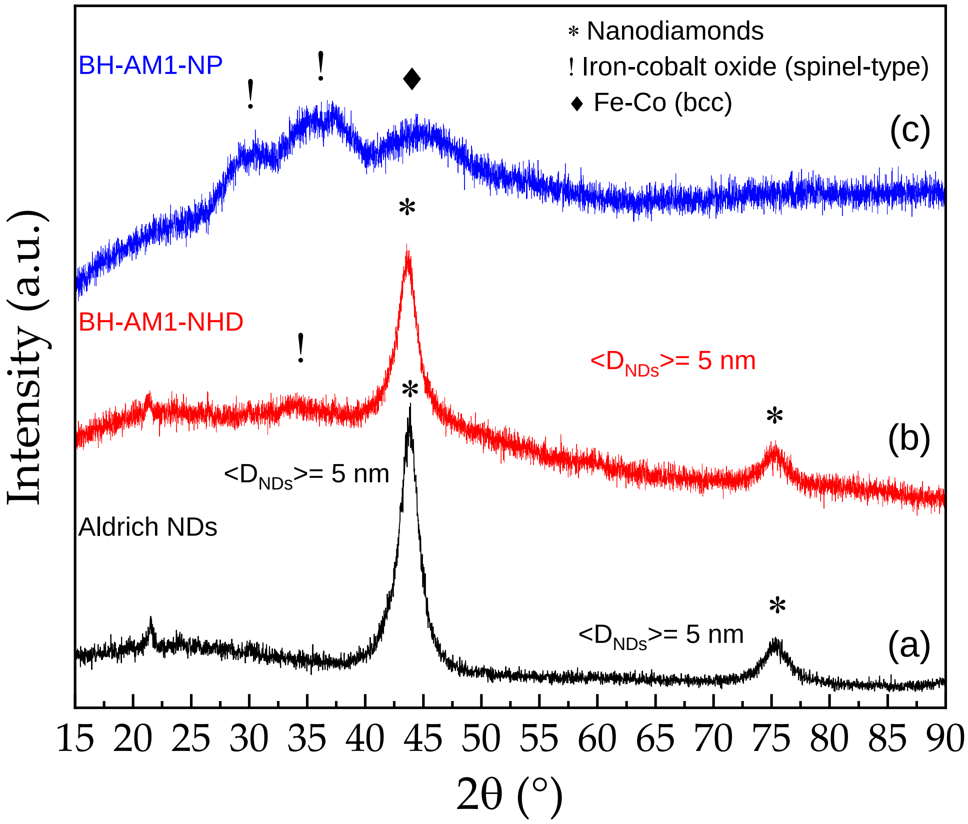

Figure 6.1 XRD patterns of the pristine NDs (a), BH-AM1-NHD (b) and BH-AM1-NP (c) samples. The crystalline phases in the samples are depicted by the respective different symbols denoting the angular positions of their main diffraction peaks. The average crystalline domain size <D> of the nanodiamonds phase for the as-made nanohybrid precursor and pristine NDs samples are denoted in each of these samples' patterns.

6.1.2 Samples prepared using the impregnation method

The XRD patterns of the conventional (non-^{57}Fe enriched) AM-NHD precursor samples prepared using the impregnation (IM) method are shown in Figure 6.2. These patterns exhibit similar structural features among them, as indicated from the presence of the characteristic ND diffraction peaks at 43.9° (111), 75.3° (220), and 91.5° (311) 2θ, and those of the spinel-type ICO structure at 30.1° (220), 35.4° (311), and 63.6° (440) 2θ, respectively [1]. An estimation of the average NP crystalline domain size <D> for the ND and ICO phases based on the most resolvable widths of their main diffraction peaks was made using the Scherrer formula, providing $<D_{NDs}>$ = 5 nm for the NDs NPs and $<D_{ICO}>$ between 2 and 5 nm for the ICO NPs depending on the sample. These results suggest the ability of the first step of the IM synthesis method to produce methodically very small ICO NPs seeds developed on the NDs nanotemplate matrices.

From Figure 6.2, it is also observed that the preparation of the IM-AM1-NHD and IM-AM2-NHD precursors results to more intense diffraction peaks for the corresponding ICO phase, therefore indicating the presence of larger and more crystalline ICO NPs compared to the respective ICO NPs of the other as-made nanohybrid precursor samples.

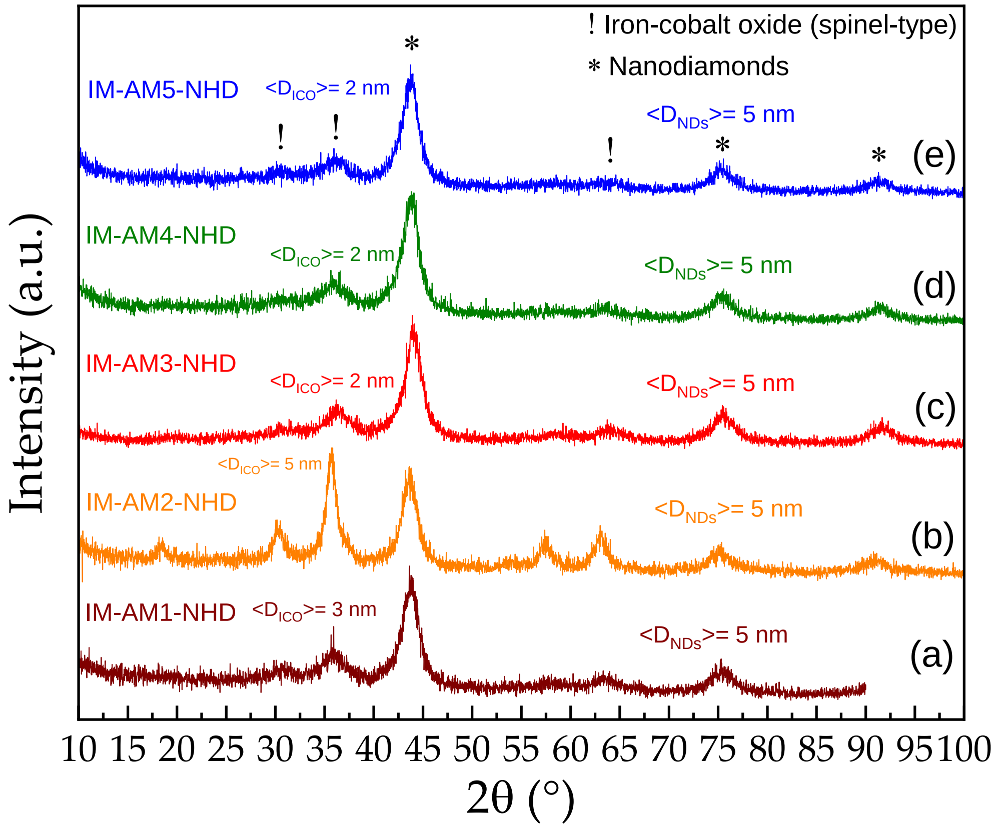

Figure 6.2 XRD patterns of the IM-AM1-NHD (a), IM-AM2-NHD (b), IM-AM3-NHD (c), IM-AM4-NHD (d), IM-AM5-NHD (e) samples. The crystalline phases in the samples are depicted by respective different symbols denoting the angular positions of their main diffraction peaks. The average crystalline domain size <D> of the nanodiamonds and the spinel-type iron-cobalt-oxide phases are denoted in each pattern.

The XRD diagrams of the samples resulting from annealing the as-made nanohybrid precursors using the IM method at different temperatures and heating durations are presented in Figure 6.3. It is evident that the annealing of the AM-NHD precursors at all chosen temperatures and durations can induce the formation of a new nanocrystalline phase. At the same time, the presence of the ICO is completely absent or significantly diminished, and that of the NDs is completely retained. In particular, apart from the presence of the characteristic NDs diffraction peaks, considerable contributions from the broad diffraction peaks of a cubic bcc Fe–Co crystal structure are evident at 44.9° (110), 65.3° (200), and 83.7° (211) 2θ for the measured XRD patterns of all the annealed samples. The high broadening of the diffraction peaks of this phase inhibits a reliable estimation of the atomic Fe–Co stoichiometry to be made only from their angular positions, as three different ICDD PDFs with iron-rich ($Fe_{0.7}Co_{0.3}$ 00-048-1817, lattice constant a = 2.864 Å), equiatomic ($Fe_{0.5}Co_{0.5}$ 00-049-1568, lattice constant a = 2.855 Å), and iron-poor ($Fe_{0.3}Co_{0.7}$ 04-007-3335, lattice constant a = 2.842 Å) stoichiometries can qualitatively match the angular positions of these diffraction peaks equally. The aspects of the nature, morphology, and stoichiometry of this phase in the samples are revealed by TEM analysis (vide infra).

However, an estimation of the average crystalline domain size <D> extracted out of the best resolvable diffraction peaks at 65.3° and 83.7° 2θ for this phase can be made using the Scherrer formula, and the results are depicted in each pattern. It is evident that the average size ranges between 6 and 9 nm in all cases. Moreover, for the samples annealed at 700°C and 650°C, there is no evidence of the presence of ICO in the XRD patterns, but a minor contribution of this phase appears for the samples annealed at 600°C. From these results it is possible to conclude that as regards the formation of the Fe–Co alloy phase originating from the reduction in the ICO NP seeds, the annealing of the precursors can be carried out up to 700°C without any significant increase in the average size of these alloy NPs compared with lower annealing temperatures.

Furthermore, the observation of the residual ICO NPs appearing in the XRD patterns of only the 600 °C annealed samples, in relation to the absence of this phase from the corresponding XRD patterns of the samples annealed at higher temperatures, is attributed to its incomplete reduction towards the metallic Fe–Co phase. It can be thus concluded that 700 °C can be regarded as the optimum annealing temperature for producing the Fe-Co/NDs NHD samples. On the other side, as regards these XRD results, the annealing time does not seem to have a significant effect either in the average particle size of the Fe–Co phase or in the appearance of ICO phases in the samples, except in the case of the 600°C series, where increased time intervals seem to be related to less ICO presence. This means that the Fe–Co phase is rapidly formed from the reduction in the ICO during the annealing procedure.

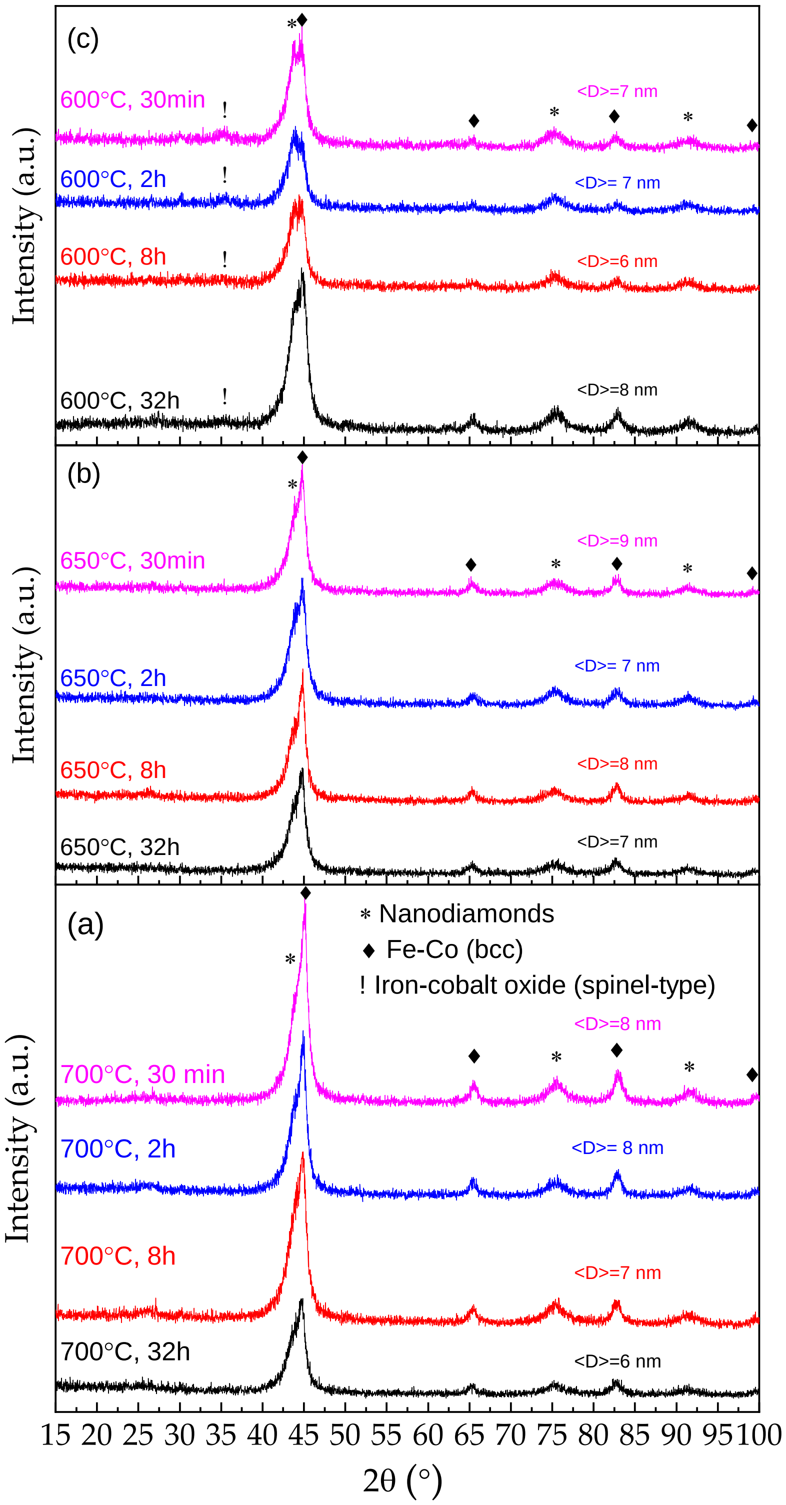

Figure 6.3 XRD patterns of the samples resulting after annealing the impregnated as-made nanohybrid precursors, at 700°C (a), 650°C (b), and 600°C (c) in evacuated quartz ampoules for different durations denoted in each pattern. The crystalline phases in the samples are depicted by respective different symbols denoting the angular positions of their main diffraction peaks. The average crystalline domain size <D> of the nanodiamonds and iron–cobalt oxide phases for the as-made nanohybrid precursor sample and that of the Fe–Co phase for all other annealed samples are denoted in each pattern.

Following this context, Figure 6.4 shows the XRD patterns of the ^{57}Fe enriched as-made precursor (En-IM-AM6-NHD) and the corresponding samples resulting from the annealing of this precursor at different conditions. According to these measurements, the two sets of samples, namely the non-enriched/conventional and enriched with the ^{57}Fe reagent, have many structural similarities. In particular, the XRD pattern of En-IM-AM6-NHD sample in Figure 6.4a depicts the dominant presence of the broad diffraction peaks attributed to NDs, along with the three inferior diffraction peaks referred to the ICO spinel-type phase, while the application of the Scherrer formula in this diagram gives an estimation of the average crystalline domain size of $<D_{NDs}>$ = 4 nm for the NDs, and $<D_{ICO}>$ = 2 nm for the ICO NPs.

Annealing the En-IM-AM6-NHD precursor at 700°C induces the development of Fe–Co bcc nanostructures in addition to the presence of the ND nanotemplates at all durations, as was found also for the conventional precursors. However, there are also some differences; at 26.5° 2θ, a diffraction peak is evident, especially for the samples with the longer annealing durations of 2 and 8 h (Figure 6.4b, c). This peak is attributed to a graphitic carbon-type phase, which has also been found to develop in similar iron carbide/ND hybrid samples prepared by the same synthesis route [3]. As in the case of the annealed samples prepared with the conventional precursors, the aspects of the nature, morphology, and stoichiometry of this, as well as the Fe–Co alloy phase, will be revealed by further TEM analysis (vide infra).

The average crystalline domain size <D> for the Fe–Co phase in most annealing durations lies at 10 nm, which is only slightly higher to those found for the samples prepared with the conventional precursors (6–9 nm), while an increase in <D> to 15 nm for this phase is observed for the longest (8 h) annealed ^{57}Fe enriched sample, suggesting that for this ^{57}Fe enriched precursor, longer durations induce an increase in the Fe–Co particle size. Regarding the cases of the ^{57}Fe enriched annealed samples for 30 min following or not slow cooling rates after the heating procedure (En-IM-NHD6-700C,30m-SC, Figure 6.4d and En-IM-NHD6-700C,30m, Figure 6.4e, respectively), it is found that no major differences are observed in their XRD patterns.

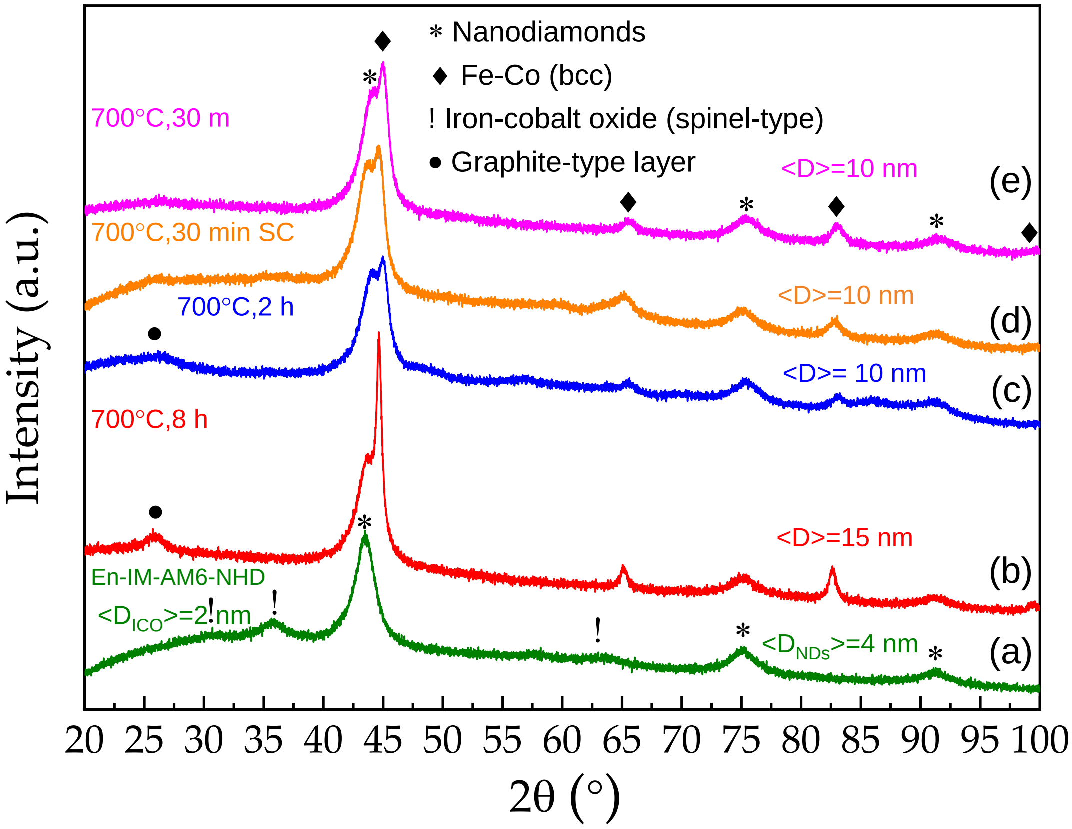

Figure 6.4 XRD patterns of the ^{57}Fe-enriched as-made nanohybrid precursor and the corresponding annealed samples at 700°C. The crystalline phases in the samples are depicted by the respective different symbols denoting the angular positions of their main diffraction peaks. The average crystalline domain size <D> of the nanodiamonds and iron–cobalt oxide phases for the ^{57}Fe-enriched as-made nanohybrid precursor sample and that of the Fe–Co phase for all other samples is denoted in each pattern.

6.2 TEM, STEM and EDS Analysis

6.2.1 TEM Analysis of the impregnated precursor sample

The determination of the dispersion, morphology and structure of the nanophases were revealed by TEM/STEM observations.

TEM images of a representative as-made hybrid sample, namely the conventional IM-AM5-NHD sample are displayed in Figure 6.5. This image reveals a nanohybrid system consisting of relatively circular shaped NPs, appearing in darker contrast than the rest of the material in the bright-field images, that are deposited on the surfaces of close packed ND NPs clusters. The NDs clusters are forming roughly round as well as irregular-shaped nanotemplates with sizes ranging from 30 to 500 nm. Taking into account the XRD results, we can conclude that these darker contrast NPs correspond to the ICO seeds developed on the surfaces of the lower contrast ND NPs clusters.

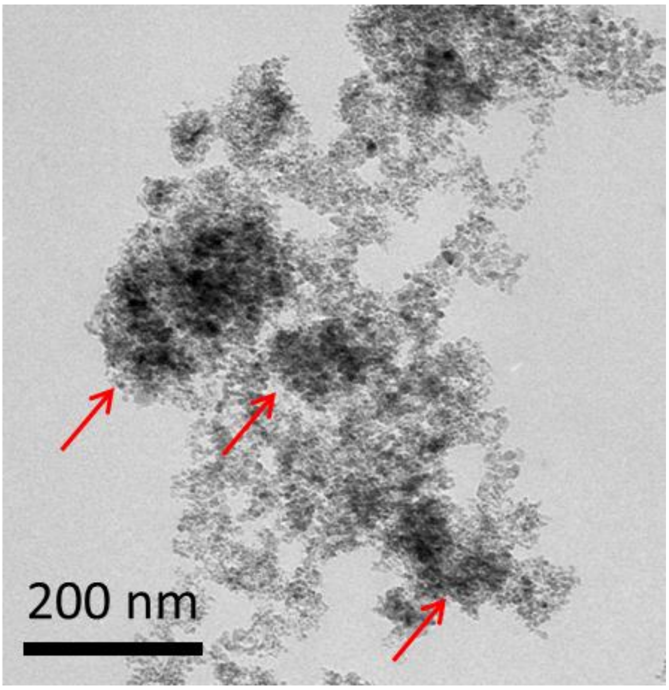

Figure 6.5 Bright-field TEM image of the IM-AM5-NHD sample. Red arrows show some regions in the hybrid cluster, where the formed ICO NPs on the surfaces of the nanodiamonds templates appear denser compared with the total hybrid cluster.

6.2.2 TEM, STEM and EDS analysis of the annealed impregnated samples

Representative TEM images of two annealed samples, namely IM-NHD5-700C,30m and En-IM-NHD6-700C,30m-SC, are displayed in Figures 6.6 and 6.11, respectively. Moreover, HAADF-STEM-EDS and HRTEM images, which thoroughly determine the chemical and structural details of these two respective samples, are given in Figures 6.7-10, and 6.12-6.15, respectively.

Figure 6.6 displays the morphology of the IM-NHD5-700C,30m sample, showing a nanohybrid system consisting of well-dispersed ND clusters with arbitrary shapes and sizes ranging from 20 to 180 nm. These ND cluster nanotemplates contain relatively spherically shaped metallic NPs grown on their surface, which appear in darker contrast relative to the rest of the ND materials in these bright-field images. The ND NPs have an average size of about 5 nm and cluster together to form aggregates. HAADF imaging in STEM mode, shown in Figure 6.7, reveals better the distribution of the metallic NPs on the ND nanotemplates, as the contrast is proportional to the Z-number. A typical counting analysis of their sizes gives an asymmetric distribution, with higher spreading on the higher sizes' side and a mean value of 6 nm (Figure 6.7d).

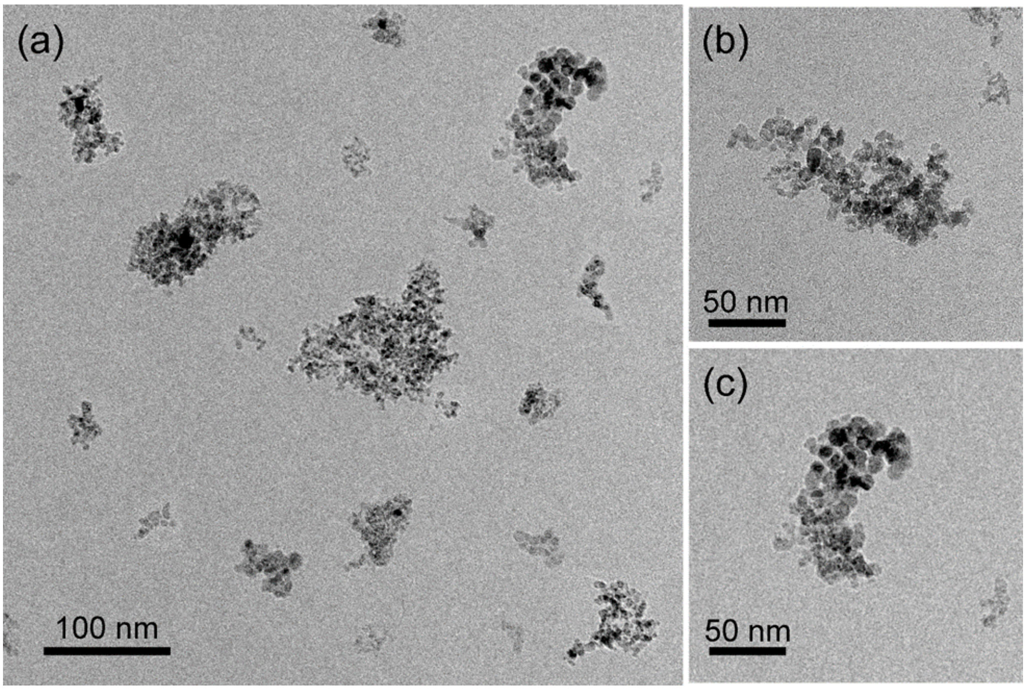

Figure 6.6 Bright-field TEM images of the IM-NHD5-700C,30m sample (a–c) at different magnifications.

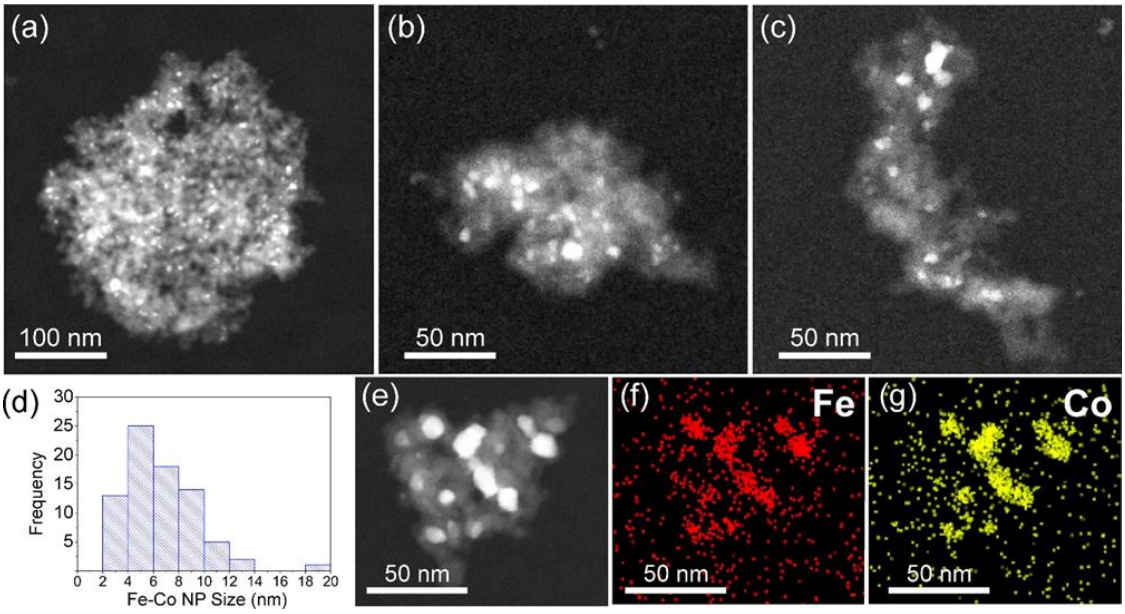

Figure 6.7 HAADF STEM images from different nanohybrid clusters of the IM-NHD5-700C,30m sample (a–c). Distribution of the Fe–Co metallic nanoparticles sizes (d). HAADF STEM image of a particular hybrid Fe–Co nanoparticles/nanodiamonds cluster (e) and the corresponding elemental distribution of Fe (f) and Co (g).

The HAADF STEM image of a hybrid Fe–Co NPs/NDs cluster and the corresponding elemental distribution mapping shown in Figure 6.7e–g reveals that Fe and Co atoms of the metallic NPs reside at the same spatial positions in the cluster, verifying the development of the Fe–Co alloy. Additional point and areal EDS spectra obtained from multiple metallic NPs (Figure 6.8 and Table 6.1) suggest a Co-rich stoichiometry in the Fe–Co alloy phase with an average Fe:Co atomic ratio of about 35:65 ($Fe_{35}Co_{65}$).

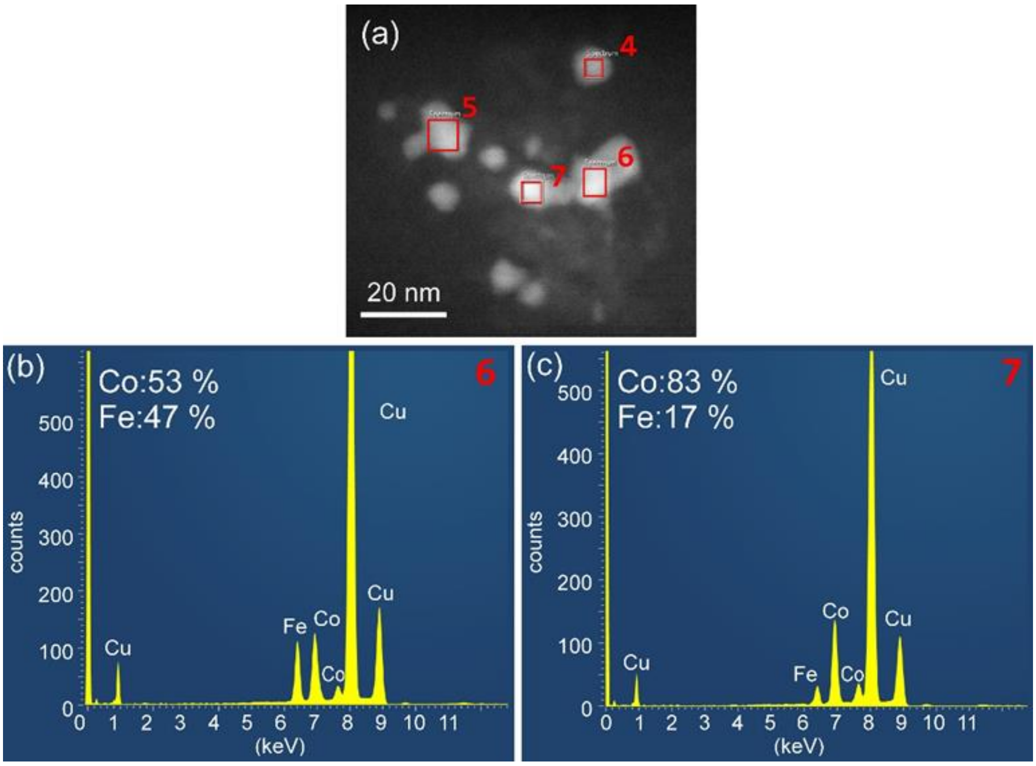

Figure 6.8 (a) HAADF-STEM image from the IM-NHD5-700C,30m sample, illustrating some locations where EDS analysis was conducted. Respective values are listed in Table 6.1. (b, c) spectra #6 and #7 from NPs with high and low Fe-composition respectively (refer to Table 6.1 for results).

Table·6.1 Fe compositions measured on individual Fe-Co NPs of the IM-NHD5-700C,30m sample using EDS analysis.

Point	Fe at. %
1	32
2	46
3	38
4	44
5	32
6	47
7	17
8	15
9	36
10	39
11	36
12	41

13	37
Average:	**35**

Figure 6.9 displays HRTEM images of different metallic Fe–Co NPs grown on the surface of the ND nanotemplates of the IM-NHD5-700C,30m sample, where the characteristic *d*-spacings corresponding to the close-packed {110} and the {200} planes of the bcc $Fe_{35}Co_{65}$ alloy structure are resolved. Moreover, and most importantly, the formation of graphitic-type layered structures partially wrapped around these metallic NPs is evident, and is indicated by the yellow arrows. The presence of these graphitic-type layered structures wrapping to some extend around the metallic Fe–Co NPs is quite systematic, as it is seen regularly in many other Fe–Co NP cases studied using HRTEM on this sample (see also Figure 6.10).

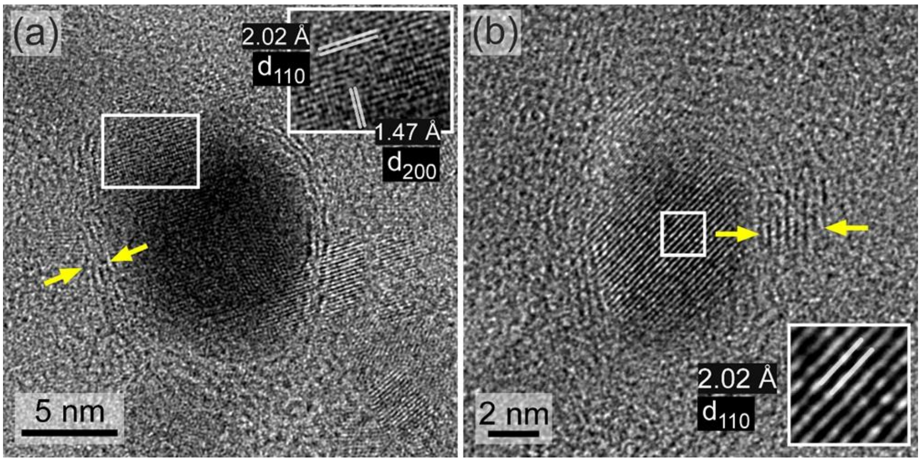

Figure 6.9 HRTEM images of the IM-NHD5-700C,30m sample revealing two different Fe–Co metallic nanoparticles (a, b) grown on nanodiamonds, in which their {110} and {200} planes are resolved in (a) and only the {110} atomic planes in (b). The planes are highlighted in the blown-up white rectangles along with their *d*-spacings. Graphitic-type layered structures wrapped around the metallic nanoparticles are indicated by yellow arrows.

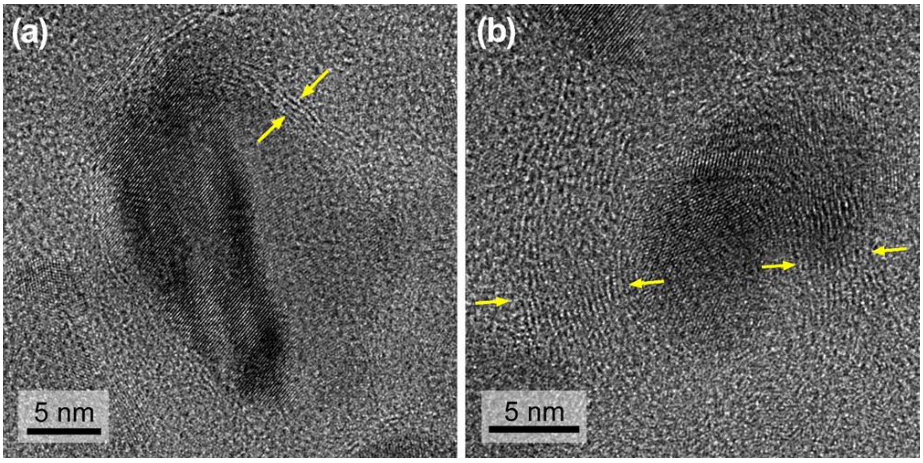

Figure 6.10 HRTEM images obtained from the IM-NHD5-700C,30m sample, showing graphitic-type layers encapsulating partially the Fe-Co NPs (arrows).

Figure 6.11 shows the morphology of the En-IM-NHD6-700C,30m-SC sample. The hybrid Fe–Co/ND clusters are similar in structure, shape, and size to those found for the IM-NHD5-700C,30m sample. The densely-packed individual ND NPs forming the nanotemplates are again, on average, about 5 nm in size, while HAADF-STEM images presented in Figure 6.12(a–c) reveal, for this sample, the same characteristics found for the IM-NHD5-700,30m sample. In this case, the metallic NPs' size distribution seems to be broad but more symmetric, and has a slightly increased 9 nm mean value relative to that of the IM-NHD5-700C,30m sample (Figure 6.12d). These features could be attributed to the slow cooling process which was followed for this sample. The elemental distribution of a hybrid Fe–Co NP/ND cluster shown in Figure 6.12(e–g) reveals that Fe and Co atoms reside at the same spatial positions, verifying again, as in the case of the IM-NHD5-700C,30m sample, the development of the Fe–Co alloy. Moreover, additional point and areal EDS spectra obtained from multiple metallic NPs (Figures 6.13 and Table 6.2) also suggest a Co-rich stoichiometry in the Fe–Co alloy phase with an average Fe:Co atomic ratio of about 33:67 ($Fe_{33}Co_{67}$), very similar to that found for the IM-NHD5-700,30m sample.

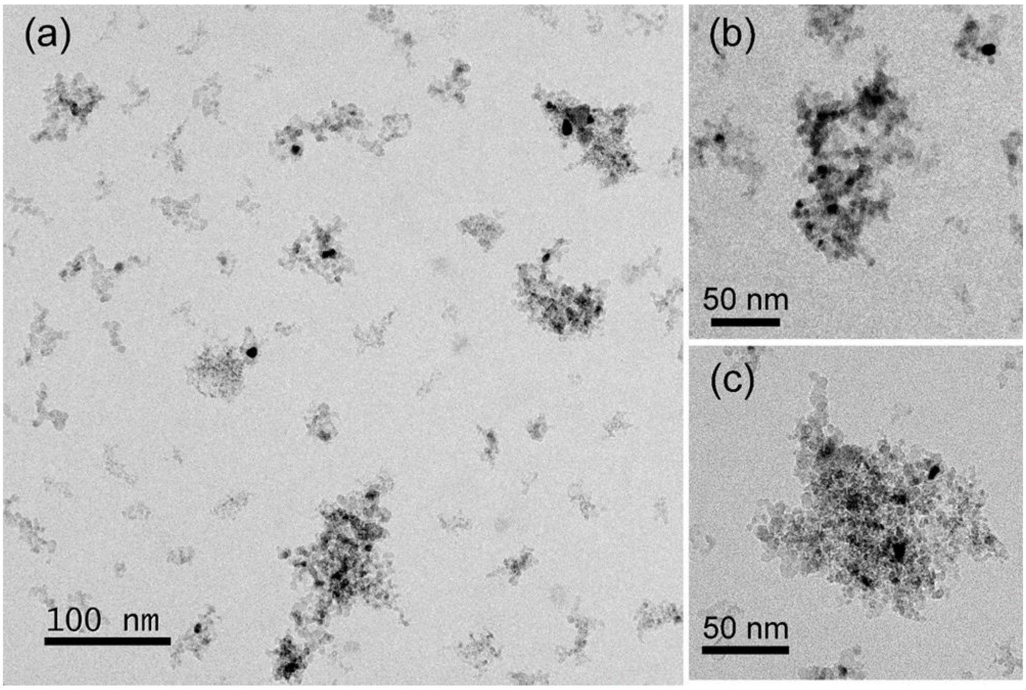

Figure 6.11 TEM images of the En-IM-NHD6-700C,30m-SC sample (a–c) at different magnifications.

The fact that both (^{57}Fe-enriched and non-enriched/conventional) annealed samples possess very similar Co-rich Fe–Co NP compositions reflects the validity and reproducibility of the chosen two-step impregnation synthetic method.

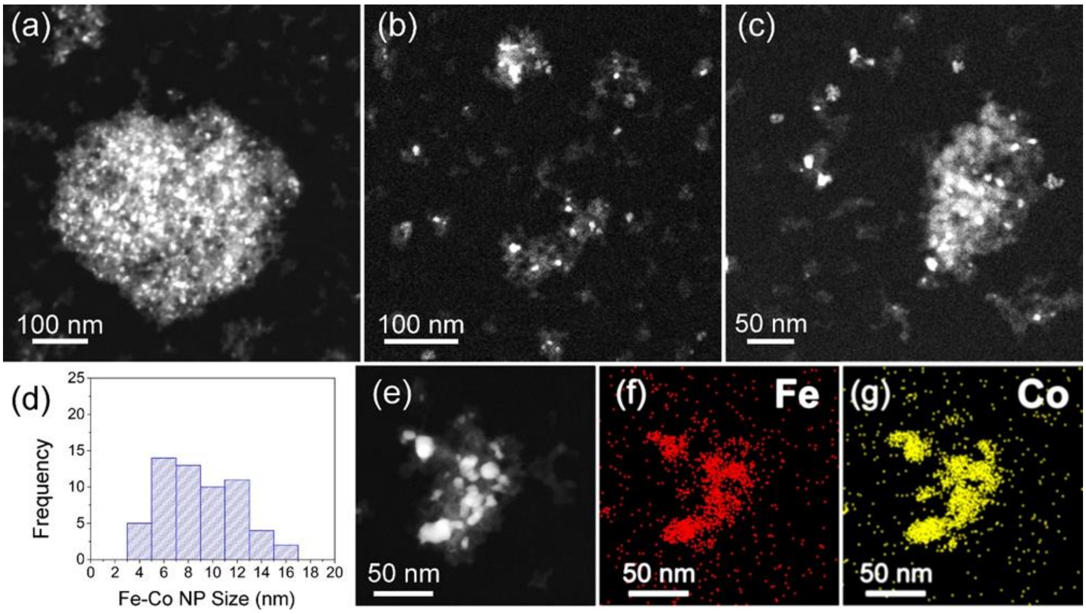

Figure 6.12 HAADF Z-contrast images in STEM mode from different nanohybrid clusters of the En-IM-NHD6-700C,30m-SC sample (a–c). Distribution of the Fe–Co metallic nanoparticles sizes (d). HAADF STEM image of a particular hybrid Fe–Co nanoparticle/nanodiamond cluster (e) and the corresponding elemental distribution-mapping of Fe (f) and Co (g).

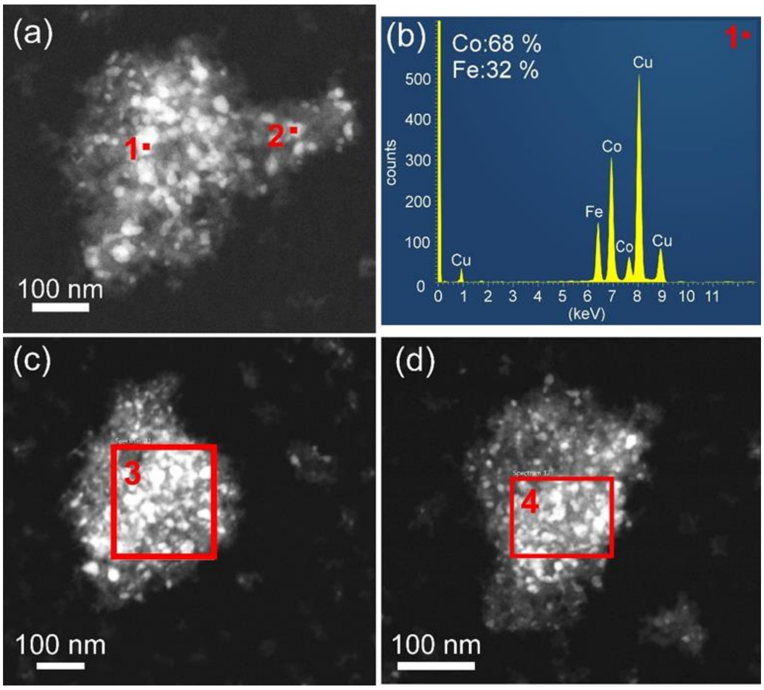

Figure 6.13 HAADF-STEM image from the En-IM-NHD6-700C,30m-SC sample, showing the positions where point-EDX spectra were collected (a). The point spectrum from position 1 and the corresponding relative atomic percentages of Fe and Co are shown in (b). HAADF-STEM images showing other areas where EDX spectra were collected(c, d) (refer to Table 6.2 for all results).

Table 6.2 Fe compositions derived from point and areal EDS spectra obtained from sample En-IM-NHD6-700C,30m-SC.

Point/Area	Fe at %
point 1	32
point 2	33
area 3	35
area 4	33
Average	**33**

Figure 6.14a displays an HRTEM image of a metallic Fe–Co NP at the edge of an ND cluster, as indicated in lower magnification in the inset of this bright-field TEM image. Notably, the lattice spacings from the closely packed {111} planes of the cubic diamond structure and the {110} planes of the metallic bcc B2 Fe–Co structures present a measurable difference. In Figure 6.14b, the HRTEM image reveals a characteristic Fe–Co NP projected along the [100] zone axis, aiding in the definitive identification of the B2 structure. Figure 6.14c illustrates more characteristically the formation of a graphitic-type few-layer structure at the interface between the metallic NPs and the ND support nanotemplate. The inset in Figure 6.14c shows this interface in greater detail with the graphitic-type {0002} planes marked yellow, along with the {110} planes of the adjacent metallic NP marked white. The graphitic layers wrapping around the NPs varied in thickness and degree of coverage, and it is evident that are more pronounced at the neighboring sides where the NDs NPs reside. As shown in Figure 6.15, some graphitic layers were only partially developed around a metallic Fe–Co NP and in another instance, they appear to extend away from the metallic NP.

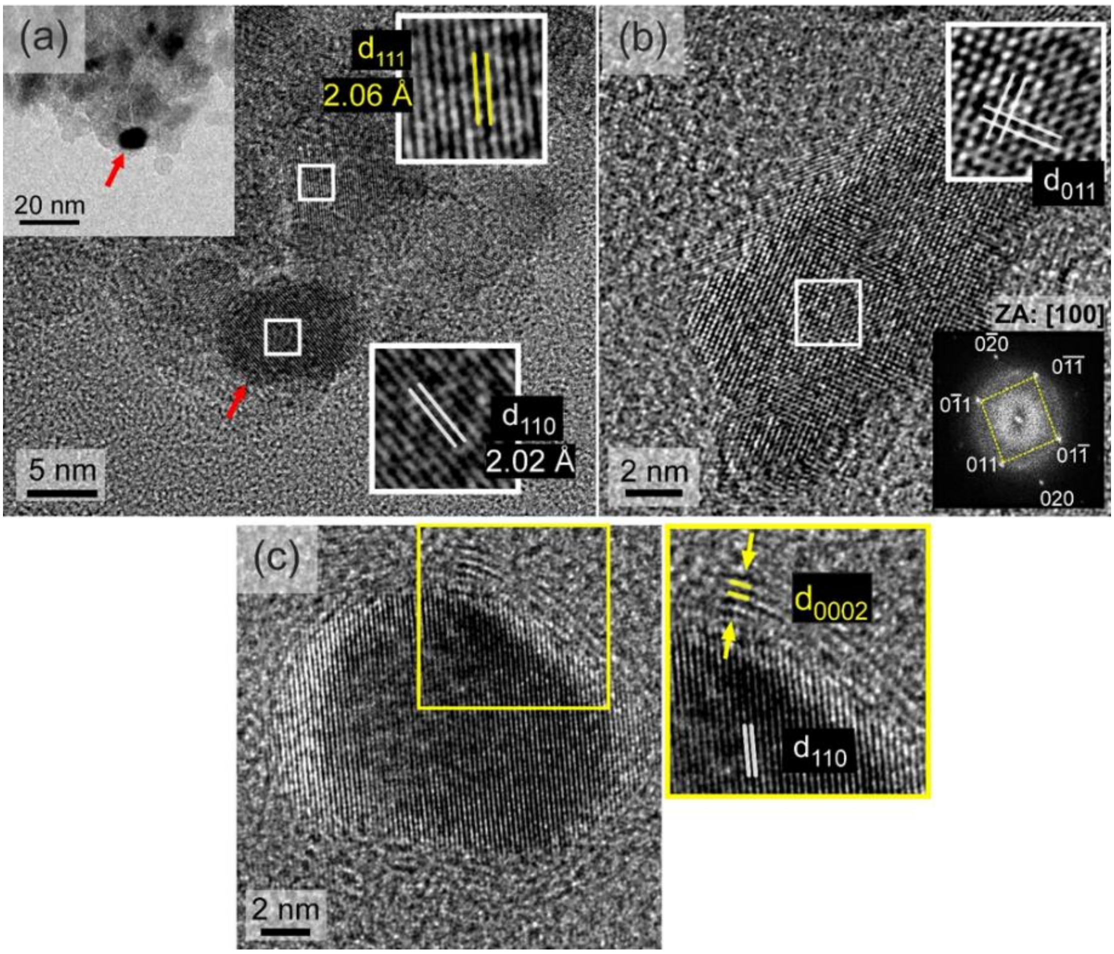

Figure 6.14 HRTEM images of a typical Fe–Co nanoparticle/nanodiamond cluster in the En-IM-NHD6-700C,30m-SC sample. The {111} planes of a nanodiamond nanoparticle and the {110} planes of a bcc Fe–Co metallic nanoparticle are provided. HRTEM image from another metallic Fe–Co nanoparticle projected along [100] (b). HRTEM image showing a Fe–Co nanoparticle surrounded by a graphitic-type few-layer structure (c), with the {110} planes of the metallic bcc and the {0002} planes of the graphitic-type structures indicated by white and yellow fonts.

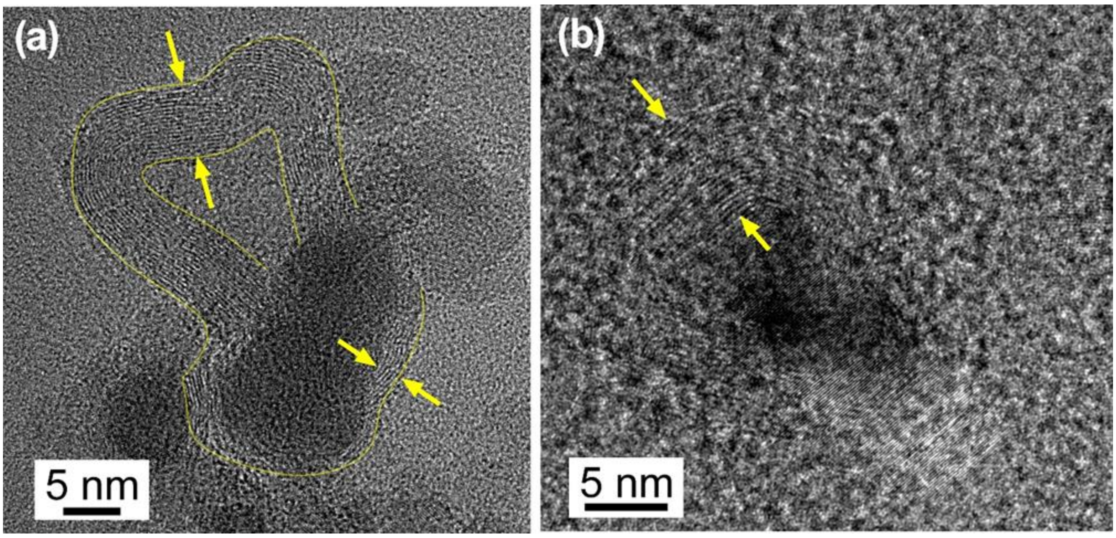

Figure 6.15 HRTEM images obtained from sample En-IM-NHD6-700C,30m-SC, showing graphitic-type layers (arrows) wrapping around Fe-Co NPs. Notably, in (a), these layers are observed to extend partially away from the NP.

From the TEM studies, it is possible to conclude that whatever the sample case (conventional or ^{57}Fe enriched), the development of the graphitic-type layered structures is inherently related to the development of the Fe–Co metallic NPs. By knowing the nature and characteristics of the chemical precursors used to develop the final hybrid nanostructures after vacuum annealing, it becomes apparent that carbon, which is the building element of NDs, is essential for the development of metallic Fe–Co NPs. These metallic NPs are initiated from the corresponding ICO NP seeds; thus, carbon atoms must be interacting with them, and they must be playing a crucial role in their reduction. Following this argument, the verified by TEM measurements presence of these carbon atoms at the interface between the Fe–Co metallic and ND NPs as graphitic-type layers, can also suggest their further possible diffusion within the Fe–Co alloy structure.

6.3 ^{57}Fe Mössbauer Spectroscopy

The atomic-level probing technique of ^{57}Fe Mössbauer spectroscopy offers a unique tool to characterize and study the structural, morphological, electronic, and magnetic properties of the iron-containing phases in the samples.

6.3.1 Samples prepared using the sodium borohydride reducing agent

Figures 6.16 and 6.17 display the ^{57}Fe Mössbauer spectra (MS) of the as-made nanohybrid and unsupported samples prepared using $NaBH_4$ as a reducing agent recorded at RT and 77 K respectively.

At 300 K, the MS of the hybrid and unsupported samples exhibit a prominent, broad, magnetically split contribution combined with a minor central quadrupole split contribution. In the BH-AM1-NP sample (Figure 6.16b), the resonant lines of the magnetically split components are more distinct than in the BH-AM1-NHD sample (Figure 6.16a). Consequently, a set of two broad magnetically split components and a set of two quadrupole-split components were used to fit accurately the spectra of both samples. For the magnetically split components, a Gaussian-type spreading ΔB_{hf} [4] of the hyperfine magnetic field (B_{hf}) values around the central B_{hf}^{C} value was applied in order to describe the line broadening in this part of the spectra. The resulting Mössbauer parameters (MPs) from the best-fits using these models are listed in Table 6.3.

For the RT MS one broad magnetically split component acquires isomer shift (IS) and quadrupole shift (2ε) values which are characteristic of a metallic alloy Fe-Co phase [5], [6], which is however influenced by superparamagnetic (SPM) relaxation that causes the broadening of their resonant lines and the severe reduction of the expected B_{hf}^{C} values, while the MPs values of the other broad magnetically split component are attributed to Fe^{3+} ions in oxygen coordinated environments indicative of spinel-type ICO nanostructures, which are also influenced by SPM relaxation phenomena. Considering the analyses of the XRD patterns of these two samples, these components can be attributed to metallic Fe-Co and ICO NPs that are experiencing fast SPM relaxation due to their very small particle sizes. On the other side, for the BH-AM1-NHD sample, the magnetically split components (MCOL Fe-Co (1) and MCOL Fe-Co (2), in green and magenta, respectively) comprise 66% (21 % and 45% each respective component) of the total absorption area (AA), whereas, for the BH-AM1-NP sample, the two magnetically split components (MCOL ICO and MCOL Fe-Co in cyan and magenta, respectively) account for the 89% of the total AA (27% and 62% each respective component). Moreover, the MCOL Fe-Co component in each sample acquires similar AA values and its weighted (relative to their AAs) average B_{hf} value (236 kOe) in the BH-IM-NP sample is higher than the B_{hf} values of the respective components (139 and 225 kOe) in the BH-IM-NHD sample. These findings suggest that the Fe-Co NPs developed in the BH-AM1-NHD sample during this synthesis are experiencing faster SPM relaxation than the corresponding Fe-Co NPs in the BH-AM1-NP sample. There could be two reasons for this behavior, both of which could be valid simultaneously: first, the Fe-Co NPs of the BH-AM1-NHD sample must be of lower average particle size and crystallinity than those of the BH-AM1-NP sample, and second, the Fe-Co NPs of the BH-AM1-NP sample must experience stronger magnetic interparticle interactions than those of the BH-AM1-NHD sample. The nature of the two samples enforces the second reason, as the interparticle interactions are expected to be enhanced in the unsupported sample where the NPs are well interconnected to each other, while these interactions are expected to be weakened in the NHD sample where these NPs are dispersed on the ND matrices. Evidence on the validity of the first reason can be extracted from the XRD patterns of the two samples, where the presence of the Fe-Co phase, although with a very broad peak is detected for the unsupported sample, while this is not the case for the NHD sample, where the small size and low crystallinity of the Fe-Co NPs could be responsible for the absence of their detection.

The MPs of the quadrupole split components are characteristic for high-spin ($S = 5/2$) Fe^{3+} and high-spin ($S = 2$) Fe^{2+} ions in oxygen-coordinated environments, and suggest the presence of spinel-type ICO nanostructures with additional Fe^{2+} ions incorporated in their lattice [7]. These ICO nanostructures exhibit such small particle sizes that confer them complete SPM properties at RT [3], [7], [8].

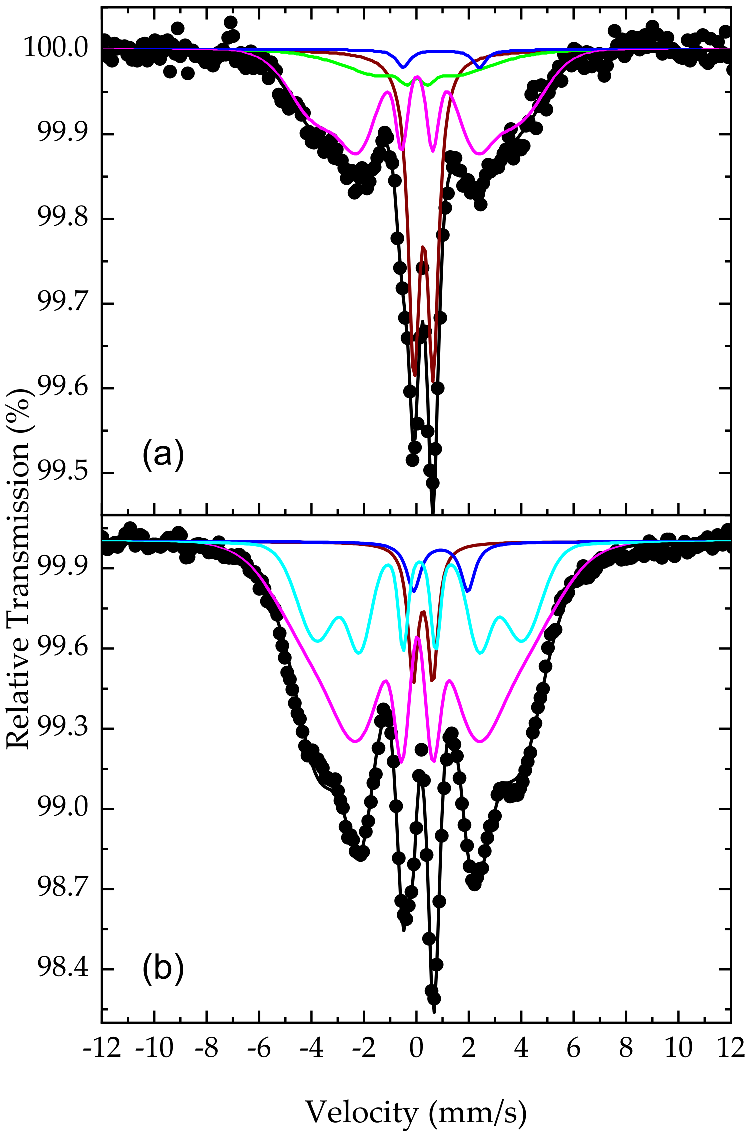

Figure 6.16 ^{57}Fe Mössbauer spectra of the as-made nanohybrid BH-AM1-NHD (a) and the unsupported BH-AM1-NP (b) samples collected at room temperature.

Table 6.3 Mössbauer hyperfine parameters as resulting from the best fits of the corresponding spectra of the samples shown on **Figure 6.16**. IS the isomer shift (given relative to α-Fe at 300 K), Γ/2 is the half-line width, QS is the quadrupole splitting, 2ε is the quadrupole shift, B_{hf}^{C} is the central value of the hyperfine magnetic field, ΔB_{hf} is the total spreading (Gaussian-type) of the B_{hf} values around the central B_{hf}^{C} value, and AA is the relative spectral absorption area of each component used to fit the spectra. Typical errors are ±0.02 mm/s for IS, Γ/2, 2ε and QS, ±3 kOe for B_{hf}^{C} and ±3% for AA.

Sample	**Component**	**I.S. (mm/s)**	**Γ/2 (mm/s)**	**Q.S. or 2ε (mm/s)**	**B_{hf}^{C} (kOe)**	**ΔB_{hf} (kOe)**	**Area (%)**	**Color**
BH-AM1-NHD	SPM Fe^{3+}	0.34	0.26	0.74	0	0	32	Maroon
	SPM Fe^{2+}	1.06	0.30	2.84	0	0	2	Blue
	MCOL Fe-Co (1)	0.14	0.15	0.00	139	90	21	Green
	MCOL Fe-Co (2)	0.14	0.15	0.00	225	62	45	Magenta
BH-AM1-NP	SPM Fe^{3+}	0.35	0.23	0.74	0	0	7	Maroon
	SPM Fe^{2+}	1.03	0.32	2.17	0	0	4	Blue
	MCOL ICO	0.22	0.15	0.00	243	42	27	Cyan
	MCOL Fe-Co	0.15	0.15	0.00	236	91	62	Magenta

The thermal evolution of the MS for these samples at 77 K is shown in Figure 6.17. These spectra can be analyzed using the same fitting models applied at RT, and the resulting MPs are listed in Table 6.4. All components display the expected shifts in their MPs values, while their AA values are similar to those observed at RT, within expected error margins. In the case of BH-AM-NHD sample, the findings indicate minimal changes in the AA values of the ICO SPM and Fe-Co alloy MCOL components at 77 K. This is notable because lower temperatures would typically increase the SPM relaxation time (τ) in all NPs [9], [10]. Such an increase would generally reduce the fast SPM relaxation at low temperatures, affecting a larger fraction of the nanostructured phases [3], [7], [8]. However, for the as-made hybrid sample, the spectral characteristics at 77 K remain consistent with those observed at RT. This stability, suggests robust contributions from both the fast SPM relaxation of smaller ICO NPs and the slower SPM relaxation of larger ICO NPs and the Fe-Co alloy NPs.

The retention of these interactions is likely attributed to the use of $NaBH_4$ as a reducing agent during synthesis, which may introduce undesired structural and morphological characteristics into the hybrid sample after annealing. These effects could detract from the primary objective of developing pure magnetic nanostructured materials with distinct magnetic properties.

In contrast, the BH-AM1-NP sample exhibits a significant difference in the AA values of the dominant MCOL Fe-Co component between RT and 77 K. Specifically, during thermal evolution, the dominant MCOL Fe-Co component (colored magenta in Figure 6.16b) at RT splits into two MCOL Fe-Co components (colored magenta and red in Figure 6.17b) at 77 K, compensating for the reduction in the AA value of the original RT component. These results, combined with the corresponding XRD features, suggest that the unsupported sample could develop a multi-phase character after annealing, similar to the behavior observed in the unsupported Fe-Rh system (Chapter 5). This divergence from the anticipated uniform growth of magnetic nanostructured materials underscores its unsuitability for further processing.

Consequently, this precursor was excluded from the second annealing step. Our will therefore focus on the Fe-Co/NDs system synthesized using the impregnation method.

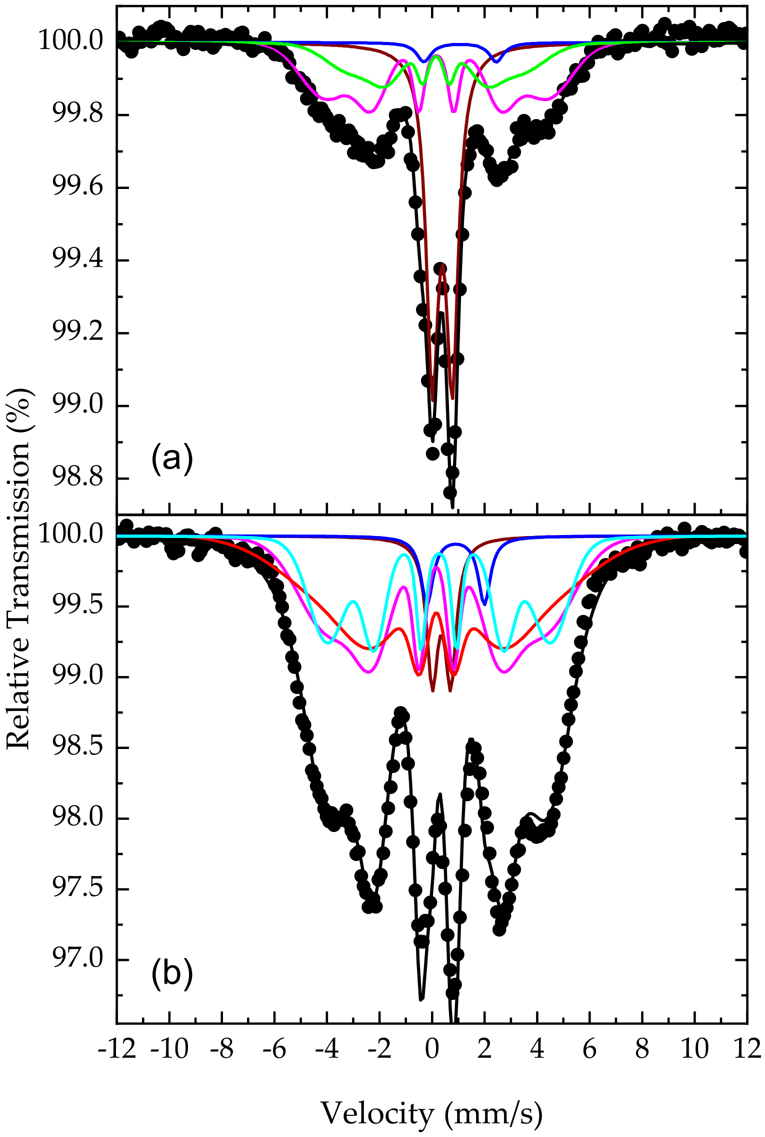

Figure 6.17 ^{57}Fe Mössbauer spectra of the as-made nanohybrid BH-AM1-NHD (a) and the unsupported as-made BH-AM1-NP (b) samples collected at 77 K.

Table 6.4 Mössbauer hyperfine parameters as resulting from the best fits of the corresponding spectra of the samples shown on **Figure 6.17**. IS the isomer shift (given relative to α-Fe at 300 K), $\Gamma/2$ is the half-line width, QS is the quadrupole splitting, 2ε is the quadrupole shift, B_{hf}^{C} is the central value of the hyperfine magnetic field, ΔB_{hf} is the total spreading (Gaussian-type) of the B_{hf} values around the central B_{hf}^{C} value, and AA is the relative spectral absorption area of each component used to fit the spectra. Typical errors are ±0.02 mm/s for IS, $\Gamma/2$, 2ε and QS, ±3 kOe for B_{hf}^{C} and ±3% for AA.

Sample	**Component**	**I.S. (mm/s)**	**$\Gamma/2$ (mm/s)**	**Q.S. or 2ε (mm/s)**	**B_{hf}^{C} (kOe)**	**ΔB_{hf} (kOe)**	**Area (%)**	**Color**
BH-AM1-NHD	SPM Fe^{3+}	0.46	0.28	0.76	0	0	33	Maroon
	SPM Fe^{2+}	1.18	0.33	2.80	0	0	3	Blue
	MCOL Fe-Co (1)	0.26	0.15	0.00	188	46	21	Green
	MCOL Fe-Co (2)	0.27	0.15	0.00	251	44	43	Magenta
BH-AM1-NP	SPM Fe^{3+}	0.47	0.26	0.72	0	0	7	Maroon
	SPM Fe^{2+}	1.15	0.29	2.18	0	0	4	Blue
	MCOL ICO	0.37	0.15	0	264	20	28	Cyan
	MCOL Fe-Co (1)	0.27	0.15	0.00	255	57	32	Magenta
	MCOL Fe-Co (2)	0.27	0.15	0.00	242	117	29	Red

6.3.2 Samples prepared using the impregnation method

6.3.2.1 As-made impregnated precursor samples

The ^{57}Fe MS of conventional as-made nanohybrid precursors, produced via the impregnation synthesis method, are shown in Figure 6.18, with additional spectra collected at 77 K displayed in Figure 6.19. In Figure 6.18, the spectra for all precursor samples at RT are dominated by a broad quadrupole-split contribution. This contribution is effectively modeled by two primary quadrupole-split components across all samples. However, to achieve an accurate fitting model for the IM-AM2-NHD sample an additional set of broad magnetically split components with collapsing B_{hf} characteristics was necessary, all with ionic Fe^{3+} character. For these collapsing B_{hf} components, a Gaussian-type spread, ΔB_{hf} [4], was applied around the central B_{hf}^{C} value to account for line broadening in this part of the MS.

The resulting MPs derived from the best fits of the spectra are listed in Table 6.5. These values reveal the presence of Fe^{3+} high-spin ($S = 5/2$) states for the two SPM main components, SPM Fe^{3+} (1) and SPM Fe^{3+} (2), indicated by dark cyan and purple in Figure 6.18, respectively. These are characteristic of Fe^{3+} ions typically found in spinel-type ICO nanostructures, with particle sizes so small that they exhibit fast SPM behavior at RT [8], [11]. This result aligns with XRD results (Figure 6.2), which estimate an average particle size of 2 to 5 nm for this phase. At RT, the particle size of ICO nanostructured seeds formed on ND nanotemplates during the initial impregnation synthesis step is below the SPM size limit. Consequently, fast SPM relaxation occurs, where, $\tau \ll \tau_{MS}$, resulting in completely collapsed B_{hf} values [12], [13].

In the IM-AM2-NHD sample, MCOL Fe^{3+} (1) and MCOL Fe^{3+} (2) indicated in olive and magenta in Figure 6.18b, suggest that a subset of ICO seeds exceed the SPM size threshold [9], [10]. Here, the slower relaxation ($\tau > \tau_{MS}$) implies increased particle sizes and/or clustering, where strong interparticle interactions prolong τ beyond τ_{MS} [9], [14], [15].

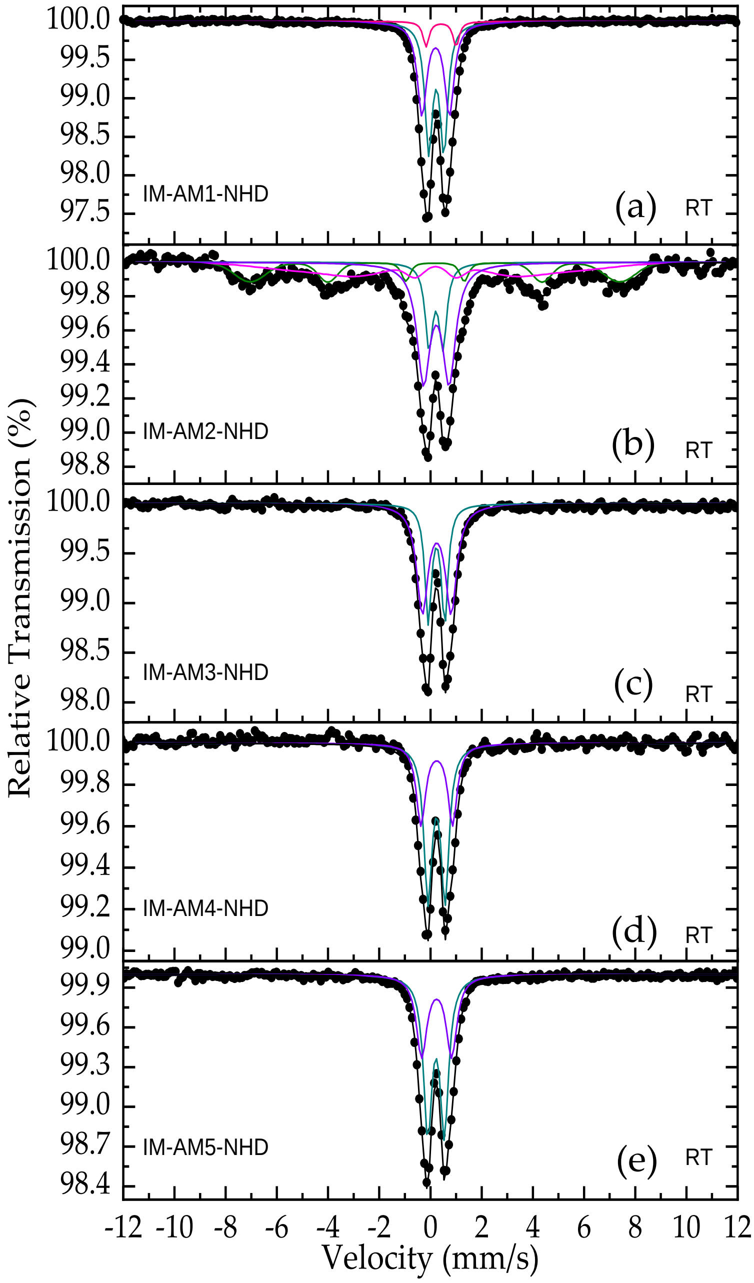

Figure 6.18 ^{57}Fe Mössbauer spectra of the IM-AM1-NHD (a), IM-AM2-NHD (b), IM-AM3-NHD (c), IM-AM4-NHD (d) and IM-AM5-NHD (e) as-made nanohybrid precursor samples, derived from the impregnation synthesis and collected at room temperature.

Table 6.5 Mössbauer hyperfine parameters as resulting from the best fits of the corresponding spectra of the samples shown on **Figure 6.18**. IS the isomer shift (given relative to α-Fe at 300 K), Γ/2 is the half-line width, QS is the quadrupole splitting, 2ε is the quadrupole shift, B_{hf}^{C} is the central value of the hyperfine magnetic field, ΔB_{hf} is the total spreading (Gaussian-type) of the B_{hf} values around the central B_{hf}^{C} value, and AA is the relative spectral absorption area of each component used to fit the spectra. Typical errors are ±0.02 mm/s for IS, Γ/2, 2ε and QS, ±3 kOe for B_{hf}^{C} and ±3% for AA.

Sample	Component	I.S. (mm/s)	Γ/2 (mm/s)	Q.S. (mm/s)	B_{hf}^{C} (kOe)	ΔB_{hf} (kOe)	Area (%)	Color
IM-AM1-NHD	SPM Fe^{3+} (1)	0.34	0.18	0.60	0	0	46	Dark Cyan
	SPM Fe^{3+} (2)	0.31	0.22	1.09	0	0	40	Purple
	SPM Fe^{2+}	0.52	0.14	1.19	0	0	14	Pink
IM-AM2-NHD	SPM Fe^{3+} (1)	0.32	0.18	0.55	0	0	15	Dark Cyan
	SPM Fe^{3+} (2)	0.35	0.32	1.00	0	0	37	Purple
	MCOL Fe^{3+} (1)	0.28	0.15	0.00	449	34	22	Olive
	MCOL Fe^{3+} (2)	0.31	0.15	0.00	312	110	26	Magenta
IM-AM3-NHD	SPM Fe^{3+} (1)	0.34	0.18	0.67	0	0	39	Dark Cyan
	SPM Fe^{3+} (2)	0.35	0.27	1.19	0	0	61	Purple
IM-AM4-NHD	SPM Fe^{3+} (1)	0.34	0.19	0.72	0	0	62	Dark Cyan
	SPM Fe^{3+} (2)	0.35	0.20	1.31	0	0	38	Purple
IM-AM5-NHD	SPM Fe^{3+} (1)	0.32	0.23	0.65	0	0	57	Dark Cyan
	SPM Fe^{3+} (2)	0.35	0.24	1.19	0	0	43	Purple

By lowering the measurement temperature to 77 K, the thermal evolution of the MS for the as-made samples can be examined in greater detail (Figure 6.19). The spectral features at 77 K closely resemble those observed at RT, allowing us to fit the 77 K MS with models similar to those used at RT. The MPs obtained from these fittings are listed in Table 6.6. All spectral components exhibit expected temperature-induced shifts for the values of IS, QS, and B_{hf} relative to those found at RT, while the sum of the AA values for each phase remain consistent (within the expected errors) with those observed at RT. For the IM-AM2-NHD sample the primary difference lies in the AA values of the SPM Fe^{3+} (1) and SPM Fe^{3+} (2) components that decrease at 77 K while the AA values of the MCOL Fe^{3+} (1) and MCOL Fe^{3+} (2) components generally increase relative to those observed for the RT spectra. This shift suggests an increase in the SPM relaxation time τ for a portion of the SPM ICO NPs, indicating magnetic blocking at 77 K [9], [14] [3], [8], [11].

In addition, unique spectral changes can be seen in the IM-AM1-NHD and IM-AM2-NHD samples. In the IM-AM1-NHD sample, as the temperature decreases, the previously fast SPM behavior of the SPM Fe^{2+} component at RT is interrupted. This is reflected in a decrease in the AA value of the SPM

Fe^{2+} quadrupole doublet component (pink in Figure 6.19a), accompanied by an increase in a magnetically collapsing component (orange in Figure 6.19a), suggesting the transition of some Fe^{2+} ions to a magnetically ordered state. The total AA value of these components at 77 K remains comparable to the AA value of the SPM Fe^{2+} component at RT. Meanwhile, in the 77 K spectrum of the IM-AM2-NHD sample, the AA value of the SPM Fe^{3+} (1) component diminishes, fully compensated by an increase in the magnetically split components. This is evidenced by two additional, well-resolved magnetic components (red and blue in Figure 6.19b), alongside the existing magnetically collapsing components.

These results reveal that the majority of the as-made precursor samples are dominated by quadrupole-split contributions, linked to the small ICO NP seeds that exhibit fast SPM behavior at RT and transition to a higher SPM relaxation time regime at 77 K. However, the IM-AM1-NHD and IM-AM2-NHD samples differ in their behavior. These samples contain secondary Fe^{2+} species in the ICO nanostructures and display well-resolved magnetic contributions from larger ICO NPs. These larger NPs, with increased AA values reaching 90% at 77 K (compared to about 76% for IM-AM3-NHD, IM-AM4-NHD, and IM-AM5-NHD), suggest stronger interparticle interactions, leading to larger clusters or agglomerations beyond those defined by the magnetically collapsing components. This high AA value corresponds to a substantial portion of ICO NPs with significant size and strong interparticle interactions, potentially forming non-uniformly on the ND nanotemplate surfaces or as stand-alone seeds near the NDs nanotemplates.

To ensure optimal dispersion and size consistency of ICO NP seeds on the ND nanotemplate surfaces, we have opted to focus further our synthesis and analysis based on the IM-AM3-NHD, IM-AM4-NHD, and IM-AM5-NHD samples, especially as regards the second step of the synthesis that is referred to the annealing procedure in our study. This approach is chosen in order to facilitate a more uniform ICO nanostructured phase dispersion on the NDs surfaces, due to their reduced particle size compared to the rest of the as-made precursor samples. Furthermore, it has been proven to assist further in the comprehensive investigation of the NHD Fe-Co/NDs system using ^{57}Fe Mössbauer spectroscopy (vide infra).

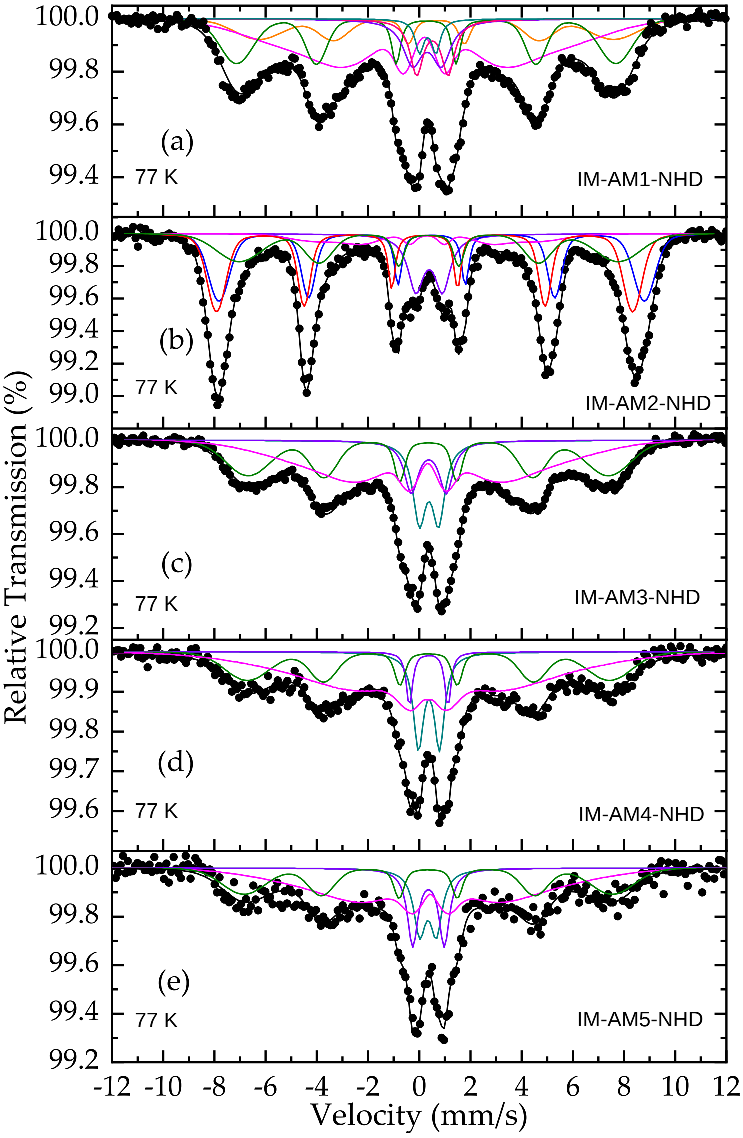

Figure 6.19 ^{57}Fe Mössbauer spectra of the IM-AM1-NHD (a), IM-AM2-NHD (b), IM-AM3-NHD (c), IM-AM4-NHD (d) and IM-AM5-NHD (e) as-made nanohybrid precursor samples, derived from the impregnation synthesis, collected at 77 K.

Table 6.6 Mössbauer hyperfine parameters as resulting from the best fits of the corresponding spectra of the samples shown on **Figure 6.19**. IS the isomer shift (given relative to α-Fe at 300 K), $\Gamma/2$ is the half-line width, QS is the quadrupole splitting, 2ε is the quadrupole shift, B_{hf}^{C} is the central value of the hyperfine magnetic field, ΔB_{hf} is the total spreading (Gaussian-type) of the B_{hf} values around the central B_{hf}^{C} value, and AA is the relative spectral absorption area of each component used to fit the spectra. Typical errors are ±0.02 mm/s for IS, $\Gamma/2$, 2ε and QS, ±3 kOe for B_{hf}^{C} and ±3% for AA.

Sample	**Component**	**I.S. (mm/s)**	**$\Gamma/2$ (mm/s)**	**Q.S. or 2ε (mm/s)**	**B_{hf}^{C} (kOe)**	**ΔB_{hf} (kOe)**	**Area (%)**	**Color**
IM-AM1-NHD	SPM Fe^{3+} (1)	0.45	0.20	0.64	0	0	2	Dark Cyan
	SPM Fe^{3+} (2)	0.42	0.45	1.12	0	0	6	Purple
	MCOL Fe^{3+} (1)	0.38	0.15	0.00	460	36	28	Olive
	MCOL Fe^{3+} (2)	0.30	0.15	0.00	308	120	49	Magenta
	SPM Fe^{2+}	0.63	0.31	1.21	0	0	5	Pink
	MCOL Fe^{2+}	0.68	0.15	0.00	431	55	10	Orange
IM-AM2-NHD	SPM Fe^{3+}	0.47	0.35	1.04	0	0	11	Purple
	MRES Fe^{3+} (1)	0.49	0.15	0.00	511	22	28	Red
	MRES Fe^{3+} (2)	0.37	0.15	0.00	505	19	30	Blue
	MCOL Fe^{3+} (1)	0.41	0.15	0.00	265	65	8	Magenta
	MCOL Fe^{3+} (2)	0.48	0.15	0.00	460	50	23	Olive
IM-AM3-NHD	SPM Fe^{3+} (1)	0.46	0.26	0.72	0	0	14	Dark Cyan
	SPM Fe^{3+} (2)	0.47	0.33	1.22	0	0	10	Purple
	MCOL Fe^{3+} (1)	0.46	0.15	0.00	438	50	31	Olive
	MCOL Fe^{3+} (2)	0.44	0.15	0.00	271	125	45	Magenta
IM-AM4-NHD	SPM Fe^{3+} (1)	0.48	0.24	0.75	0	0	14	Dark Cyan
	SPM Fe^{3+} (2)	0.47	0.18	1.38	0	0	8	Purple
	MCOL Fe^{3+} (1)	0.47	0.15	0.00	440	50	27	Olive
	MCOL Fe^{3+} (2)	0.45	0.15	0.00	251	180	51	Magenta
IM-AM5-NHD	SPM Fe^{3+} (1)	0.44	0.26	0.65	0	0	12	Dark Cyan
	SPM Fe^{3+} (2)	0.46	0.25	1.22	0	0	14	Purple
	MCOL Fe^{3+} (1)	0.49	0.15	0.00	255	141	47	Magenta
	MCOL Fe^{3+} (2)	0.45	0.15	0.00	447	49	27	Olive

In this context, we continue with the study and analysis of the ^{57}Fe MS at RT for the enriched as-made En-IM-AM6-NHD precursor sample. To see the resemblances and differences from the use of ^{57}Fe enriched and conventional reagents, we compare the results found for the En-IM-AM6-NHD precursor to those found for the IM-AM5-NHD precursor, which are shown in Figure 6.20.

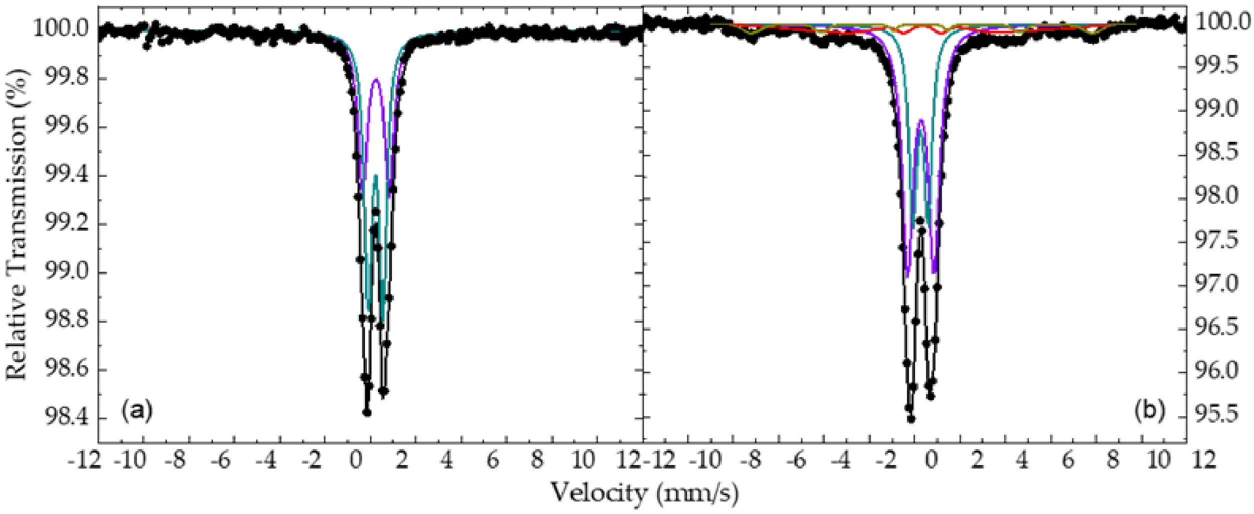

Figure 6.20 ^{57}Fe Mössbauer spectra of the conventional as-made nanohybrid precursor (a) and the ^{57}Fe-enriched nanohybrid precursor (b) samples collected at room temperature.

The spectra show a characteristic central quadrupole-split contribution. This is the sole contribution for the spectrum of the conventional IM-AM5-NHD precursor, whereas, in the spectrum of the enriched En-IM-AM6-NHD precursor, an additional minor, broad magnetically split contribution is evident. Due to the relatively broad resonant lines of the quadrupole-split contributions in both MS, we applied two quadrupole-split components to fit the spectrum of the conventional IM-AM5-NHD precursor. For the enriched En-IM-AM6-NHD precursor, we used a combination of two quadrupole-split and two magnetically split components. For the latter magnetically split components, a Gaussian-type spreading ΔB_{hf} of their B_{hf} values around the central B_{hf}^{C} value was employed to account for the broadening of the resonant lines in this part of the spectrum. The MPs from the best fits of these spectra are provided in Table 6.7.

These MPs indicate only Fe^{3+} high-spin ($S = 5/2$) states for both samples, characteristic of Fe^{3+} ions in ICO spinel-type nanostructures. Their small particle size renders them SPM at RT [3], [7], [8], consistent with the XRD results for these samples. In the IM-AM5-NHD sample, the exclusive presence of the quadrupole-split contribution at RT implies that the ICO NP seeds on the ND nanotemplate surfaces, formed in the initial synthesis stage, are below the SPM size limit at this temperature. Consequently, their SPM relaxation time is shorter than the Mössbauer spectroscopy measurement time ($\tau < \tau_{MS}$), causing their B_{hf} values to collapse entirely [12], [13].

In contrast, the En-IM-AM6-NHD precursor exhibits a broad magnetically split component, represented by two components comprising 18% of the AA. This suggests that part of the ICO NP assembly has a longer SPM relaxation time ($\tau > \tau_{MS}$), possibly due to their larger particle size and/or agglomeration into larger clusters where strong interparticle interactions extend τ beyond τ_{MS} [9], [14], [15].

Table 6.7 Mössbauer hyperfine parameters as resulting from the best fits of the corresponding spectra of the samples shown on **Figure 6.20**. IS the isomer shift (given relative to α-Fe at 300 K), $\Gamma/2$ is the half-line width, QS is the quadrupole splitting, 2ε is the quadrupole shift, B_{hf}^C is the central value of the hyperfine magnetic field, ΔB_{hf} is the total spreading (Gaussian-type) of the B_{hf} values around the central B_{hf}^C value, and AA is the relative spectral absorption area of each component used to fit the spectra. Typical errors are ±0.02 mm/s for IS, $\Gamma/2$, 2ε and QS, ±3 kOe for B_{hf}^C and ±3% for AA.

Sample	**Component**	**IS (mm/s)**	**$\Gamma/2$ (mm/s)**	**QS or 2ε (mm/s)**	**B_{hf}^C (kOe)**	**ΔB_{hf} (kOe)**	**Area (%)**	**Color**
IM-AM5-NHD	SPM Fe^{3+} (1)	0.32	0.23	0.65	0	0	57	Dark Cayn
	SPM Fe^{3+} (2)	0.35	0.24	1.19	0	0	43	Purple
En-IM-AM6-NHD	SPM Fe^{3+} (1)	0.36	0.21	0.67	0	0	31	Dark Cayn
	SPM Fe^{3+} (2)	0.37	0.29	1.17	0	0	51	Purple
	MCOL Fe^{3+} (1)	0.51	0.15	0.14	322	95	12	Red
	MCOL Fe^{3+} (2)	0.39	0.15	0.07	468	22	6	Dark Yellow

6.3.2.2 Annealed impregnated samples

The raw RT MS of the annealed samples, using both the conventional (IM-AM3-NHD, IM-AM4-NHD and IM-AM5-NHD) and the ^{57}Fe enriched (En-IM-AM6-NHD) precursors, are shown in Figure 6.21. Regardless of the samples' synthesis conditions, these MS exhibit certain spectral characteristics that are common in all cases.

These are the following: (i) the presence of a dominant magnetically split contribution with relative sharp resonant lines indicated by blue arrows for the four outer peaks of the six-line pattern; (ii) the presence of minor satellite magnetically split contributions, which are the most pronounced around the two outer peaks of the main magnetically split contribution and are indicated by the green and cyan arrows; and (iii) the presence of a quadrupole split contribution at the center of each MS, indicated by two red arrows. The intensity of the dominant and satellite magnetically split contributions (i) and (ii) are relatively stable in each MS, but that of the quadrupole split contribution (iii) is more pronounced for the samples annealed at 600°C and 650°C with shorter durations and decreases for the samples annealed at 700°C. Moreover, by comparing the MS of the precursors and annealed samples, it is evident that the central quadrupole split contribution (iii) in the annealed samples is reminiscent of the main SPM ICO contribution in the precursor samples.

Thus, a first qualitative conclusion suggests that the samples annealed at 700°C contain less residual part of SPM ICO NPs that could have remained in the annealed samples due to incomplete oxide-to-alloy reduction reactions, compared with the samples annealed at lower temperatures. This result is compatible with the results extracted from the XRD analyses, which suggest some presence of ICO, at least for the samples annealed at the lowest temperature of 600°C.

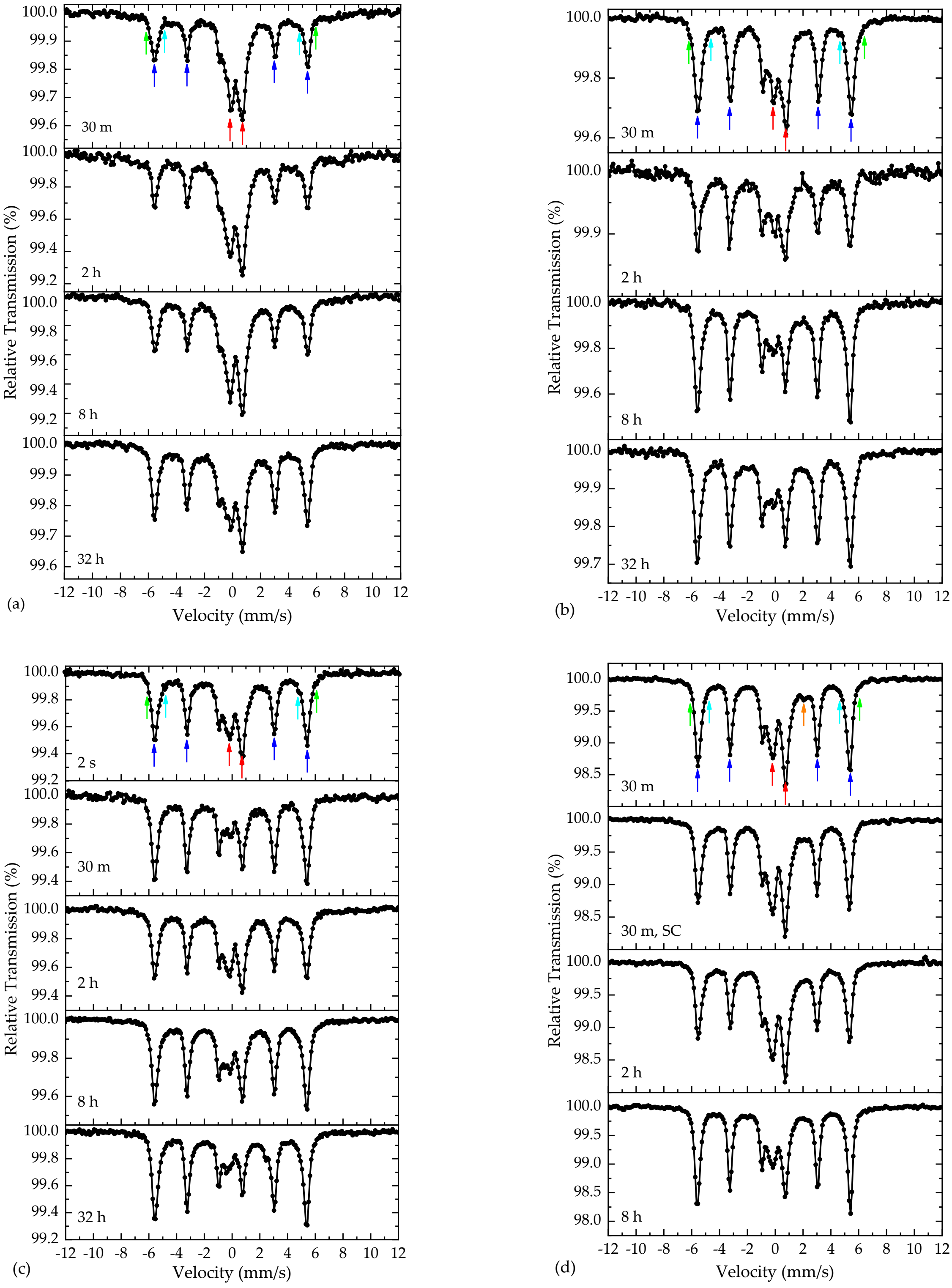

Figure 6.21 Room temperature raw ^{57}Fe Mössbauer spectra of the samples synthesized using the conventional as-made nanohybrid precursors (IM-AM3-NHD, IM-AM4-NHD and IM-AM5-NHD) annealed at 600°C (a), 650°C (b), and 700°C (c) and the ^{57}Fe-enriched as-made nanohybrid precursor (En-IM-AM6-NHD) annealed at 700°C (d). The annealing duration at the specified temperatures is included in each spectrum. The colored arrows denote the positions of the main spectral contributions corresponding to the iron-bearing phases, as discussed in the text.

Consequently, to fit these spectra adequately and taking into account the results from the XRD and TEM analyses as well, we used a model composed of one main magnetically split component to account for the dominant six-line pattern (i), a set of five minor magnetically split components for the satellite contributions (ii), and a set of two quadrupole split components for the central part (iii).

In the cases of the dominant magnetically split component and one of the five minor satellite components, a Gaussian-type spreading ΔB_{hf} of their B_{hf} values was allowed to cover the relative broadening of the resonant lines. In all cases, an additional minor magnetically split component with collapsing B_{hf} characteristics was necessary to be added to the fitting model to cover a broad absorption area residing at and around the center of each spectrum. Representative fits for the MS of the IM-NHD5-700C,30m and of En-IM-NHD6-700C,30m-SC samples are shown in Figure 6.22, and the resulting values of the MPs for these fits are listed in Table 6.8.

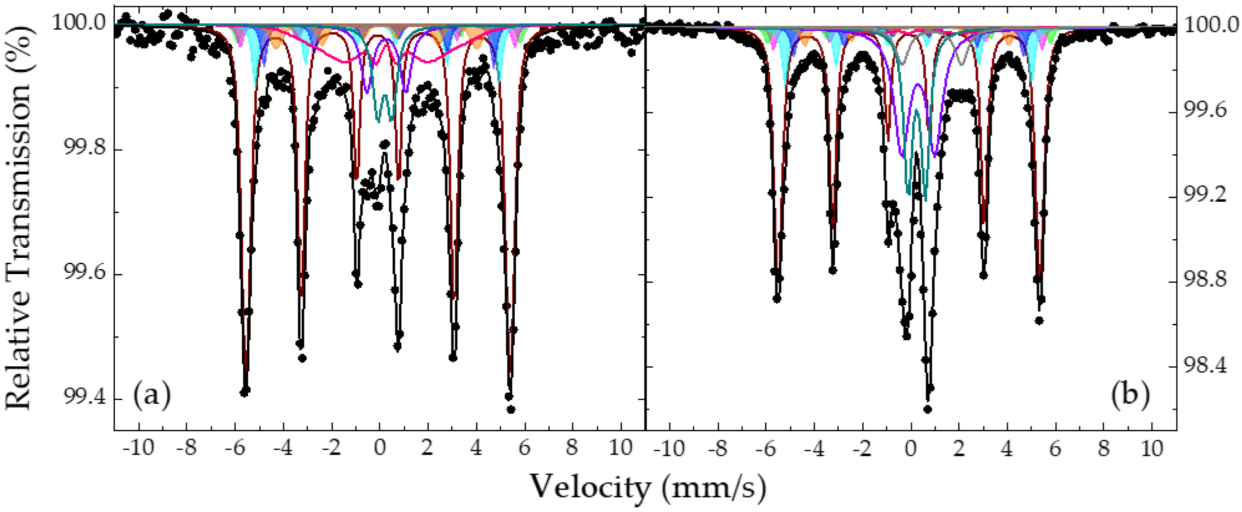

Figure 6.22 Fitted ^{57}Fe Mössbauer spectra of the IM-NHD5-700C,30m (a) and of the En-IM-NHD6-700C,30m-SC (b) samples collected at room temperature.

Table 6.8 Mössbauer hyperfine parameters as resulting from the best fits of the corresponding spectra of the samples shown on **Figure 6.22.** IS the isomer shift (given relative to α-Fe at 300 K), Γ/2 is the half line-width, QS is the quadrupole splitting, 2ε is the quadrupole shift, B_{hf}^{C} is the central value of the hyperfine magnetic field, ΔB_{hf} is the total spreading (Gaussian-type) of the B_{hf} values around the central B_{hf}^{C} value, and AA is the relative spectral absorption area of each component used to fit the spectra. Typical errors are ±0.02 mm/s for IS, Γ/2, 2ε and QS, ±3 kOe for B_{hf}^{C} and ±3% for AA.

Sample	**Component**	**IS (mm/s)**	**Γ/2 (mm/s)**	**QS or 2ε (mm/s)**	**B_{hf}^{C} (kOe)**	**ΔB_{hf} (kOe)**	**Area (%)**	**Color**
IM-NHD5-700C,30m	$Fe_{35}Co_{65}$	0.02	0.14	0.02	340	8	52	Maroon
	Martensitic FeCo (1)	0.09	0.14	0.01	364	0	2	Green
	Martensitic FeCo (2)	0.04	0.14	0.01	354	0	2	Magenta
	Martensitic FeCo (3)	0.00	0.14	0.04	315	0	6	Cyan
	Martensitic FeCo (4)	0.13	0.14	−0.08	296	0	5	Blue
	Martensitic FeCo (5)	0.08	0.14	−0.15	259	13	5	Orange
	MCOL Fe^{3+}	0.28	0.14	0.00	155	65	14	Pink
	SPM Fe^{3+} (1)	0.30	0.22	0.63	0	0	7	Dark Cyan
	SPM Fe^{3+} (2)	0.34	0.28	1.58	0	0	7	Purple
En-IM-NHD6-700,30m-SC (Slow-Cooling)	$Fe_{33}Co_{67}$	0.02	0.14	0.02	337	7	41	Maroon
	Martensitic FeCo (1)	0.09	0.14	0.01	365	0	2	Green
	Martensitic FeCo (2)	0.04	0.14	0.01	346	0	3	Magenta
	Martensitic FeCo (3)	0.05	0.14	0.04	318	0	7	Cyan
	Martensitic FeCo (4)	0.12	0.14	−0.09	296	0	4	Blue
	Martensitic FeCo (5)	0.08	0.14	−0.15	263	5	3	Orange
	MCOL Fe^{3+}	0.43	0.14	0.00	160	60	2	Pink
	SPM Fe^{3+} (1)	0.35	0.21	0.72	0	0	14	Dark Cyan
	SPM Fe^{3+} (2)	0.41	0.38	1.37	0	0	19	Purple
	SPM Fe^{2+}	0.97	0.32	2.46	0	0	5	Grey

Regarding the fit of the IM-NHD5-700C,30m sample's spectrum, the resulting MPs values of the dominant magnetically split component (colored maroon in Figure 6.22a) are characteristic of a cubic FM Fe–Co alloy phase [5], [6]. The IS and B_{hf}^{C} values of 0.02 mm/s and ~340 kOe for this component suggest a stoichiometry in the Co-rich concentration region between 60 and 70 at% Co [16], [17], [18][20], [21], [22].

In addition, the slight line broadening reproduced by the ΔB_{hf} spreading of 8 kOe could suggest contributions from both local stoichiometry and/or Fe–Co atomic-ordering structural fluctuation effects, both of which influence the environment of the iron atoms in the Fe–Co system [5], [6]. For a specific Co-rich concentration above the equiatomic stoichiometry, the increase in atomic Fe–Co ordering contributes lower B_{hf} values compared to decreased ordering levels, while for a certain atomic Fe–Co ordering level, the decrease in Co concentration contributes higher B_{hf} values [16], [17], [18]. To this extent, when both effects are present, which most probably might be the actual situation in these samples, they tend to obscure the clear distinction between an ordered B2 CsCl-type and a disordered A2 Fe–Co structure, thus contributing to the appearance of the resonant line broadening.

The satellite contributions (ii) in this fit are modeled by a set of five minor magnetically split components with colored filled areas as shown in detail in Figure 6.22a. The resulting IS and B_{hf} values of these components listed in Table 6.8 correspond to iron atoms that have a metallic alloy character but are simultaneously influenced by the presence of an additional neighboring atom in their immediate atomic environment. Taking into account the TEM analyses, which suggest the diffusion of carbon atoms in the structure of the Fe–Co NPs, we attribute these components to the iron atoms of a martensitic-type Fe–Co phase forming within the Fe–Co NPs. Each component of this set corresponds to a different iron neighbor environment forming around the interstitial carbon atoms, which induce tetragonal-type distortions in the Fe–Co cubic lattice [19].

Considering the detailed analysis of the structural properties and related MPs of such iron sites emerging in the martensite structure given by Kurdyumov and Gavriljuk [33], we can ascribe certain atomic environments to this set of components. In particular, component Martensitic Fe–Co(1), colored green in Figure 6.22a, acquires the highest B_{hf} value of the set and describes iron atoms in crystal sites placed in dilatated Fe–Co crystal lattice positions at distances relatively far from interstitial carbon atoms. Component Martensitic Fe–Co(2), colored magenta in Figure 6.22a, can be attributed to iron atoms, which are distant third neighbors of the interstitial carbon atoms and are only slightly influenced by the presence of these interstitials. Components Martensitic Fe–Co(3), colored cyan, and Martensitic Fe–Co(4), colored blue in Figure 6.22a, respectively, correspond to iron atoms occupying the closest second- and first-neighbor positions of the interstitial carbon atoms, respectively, which, according to the literature, acquire octahedral Fe/Co coordination in the bcc Fe–Co crystal structure [21], [22]. Finally, component Martensitic Fe–Co(5), colored orange in Figure 6.22a, acquires the lower B_{hf} value of the set and is attributed to Fe atoms with an environment of two carbon atoms as nearest neighbors; such environments (iron atoms with two carbon atoms nearest neighbors) are more probable to appear in increased carbon interstitial concentrations according to relative binomial distribution models [19].

The central part of the spectrum is fitted with two quadrupole split components, SPM Fe^{3+}(1), colored dark cyan, and SPM Fe^{3+}(2), colored purple in Figure 6.22a, respectively, and one broad magnetically split component MCOL Fe^{3+}, colored pink in Figure 6.22a, with collapsing B_{hf} characteristics. These components acquire relative broad resonant lines, and their MPs values listed in Table 6.8 suggest that they correspond to high-spin Fe^{3+} ion sites in oxygen first-neighbor environments, indicative of a spinel-type ICO phase, which, in its majority, experiences fast SPM relaxation phenomena, similar to those found at the precursor samples. This result verifies the qualitative conclusion made earlier in this section that these SPM ICO NPs could have remained in the annealed samples due to incomplete oxide-to-alloy reduction reactions. Although this phase could not be detected by XRD and TEM for this sample, most probably due to its scarceness, the specialized method of ^{57}Fe Mossbauer spectroscopy, which only probes iron, succeeds in detecting it.

To verify the consistency and fidelity of our fitting model, we checked the thermal evolution of the MS for this sample at 11 K. At this temperature, the spectrum of the IM-NHD5-700C,30m sample can be fitted with the same fitting model (see Figure 6.23 and Table 6.9), in which all iron alloy components acquire the expected shifts in their IS and B_{hf} values, while their AA values are very similar (within the expected errors) to those found at RT. A difference can be found only for the AA values of the SPM Fe^{3+} and MCOL Fe^{3+} components, where the increased AA value of the MCOL Fe^{3+} component at the expense of the AA values of the SPM Fe^{3+} components denotes the expected decrease in SPM relaxation time τ for the nanostructured ICO NPs at low temperatures, as the ceasing of the very fast SPM relaxation encompasses a larger portion of this phase [3], [7], [8].

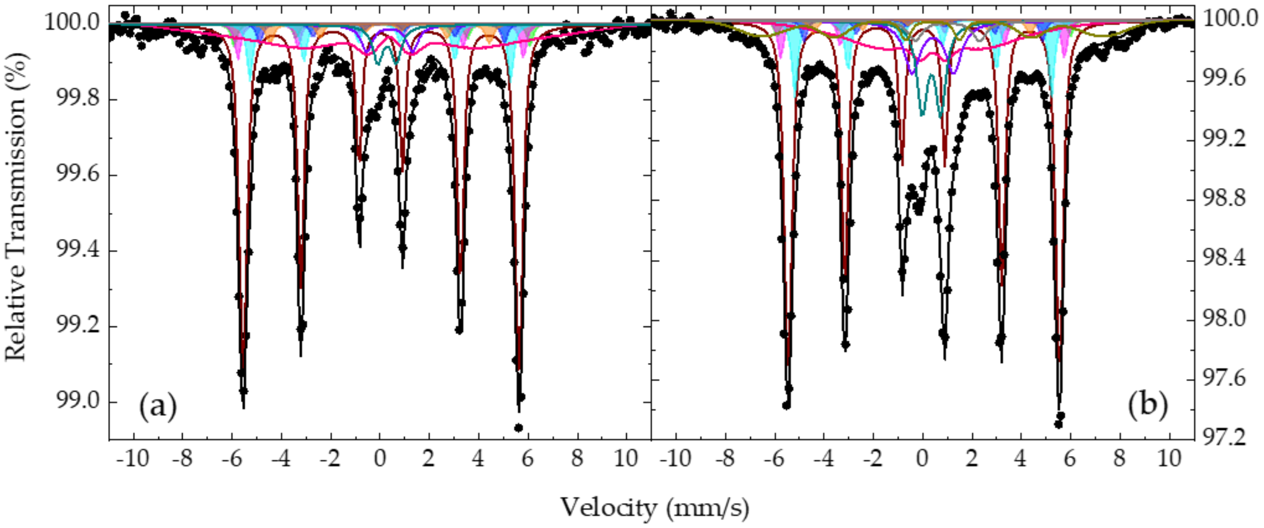

Figure 6.23 Fitted ^{57}Fe Mössbauer spectra of IM-NHD5-700C,30m sample (a) and of En-IM-NHD6-700C,30m-SC (b) collected at 11 K.

Table 6.9 Mössbauer hyperfine parameters as resulting from the best fits of the corresponding spectra of the samples shown on **Figure 6.23**. IS the isomer shift (given relative to α-Fe at 300 K), $\Gamma/2$ is the half line-width, QS is the quadrupole splitting, 2ε is the quadrupole shift, B_{hf}^{C} is the central value of the hyperfine magnetic field, ΔB_{hf} is the total spreading (Gaussian-type) of the B_{hf} values around the central B_{hf}^{C} value, and AA is the relative spectral absorption area of each component used to fit the spectra. Typical errors are ±0.02 mm/s for IS, $\Gamma/2$, 2ε and QS, ±3 kOe for B_{hf}^{C} and ±3% for AA.

Sample	Component	IS (mm/s)	$\Gamma/2$ (mm/s)	QS or 2ε (mm/s)	B_{hf}^{C} (kOe)	ΔB_{hf} (kOe)	Area (%)	Color
IM-NHD5-700,30m	$Fe_{35}Co_{65}$	0.14	0.14	0.02	347	8	53	Maroon
	Martensitic FeCo (1)	0.21	0.14	0.01	375	0	2	Green
	Martensitic FeCo (2)	0.16	0.14	0.01	365	0	2	Magenta
	Martensitic FeCo (3)	0.13	0.14	0.04	325	0	5	Cyan
	Martensitic FeCo (4)	0.26	0.14	-0.08	312	0	5	Blue
	Martensitic FeCo (5)	0.20	0.14	-0.15	277	5	4	Orange
	MCOL Fe^{3+}	0.40	0.14	0.00	240	185	22	Pink
	SPM Fe^{3+} (1)	0.46	0.23	0.67	0	0	3	Dark Cyan
	SPM Fe^{3+} (2)	0.46	0.28	1.63	0	0	3	Purple
En-IM-NHD6-700,30m-SC (Slow-Cooling)	$Fe_{33}Co_{67}$	0.14	0.14	0.02	342	6	41	Maroon
	Martensitic FeCo (1)	0.21	0.14	0.01	370	0	2	Green
	Martensitic FeCo (2)	0.16	0.14	0.01	352	0	3	Magenta
	Martensitic FeCo (3)	0.14	0.14	0.04	323	0	6	Cyan
	Martensitic FeCo (4)	0.26	0.14	-0.09	305	0	4	Blue
	Martensitic FeCo (5)	0.20	0.14	-0.15	267	5	2	Orange
	MCOL Fe^{3+}	0.53	0.14	0.00	130	85	15	Pink
	SPM Fe^{3+} (1)	0.47	0.20	0.73	0	0	4	Dark Cyan
	SPM Fe^{3+} (2)	0.53	0.28	1.42	0	0	4	Purple
	SPM Fe^{2+}	1.08	0.32	2.50	0	0	5	Grey
	MCOL Fe^{3+}	0.47	0.15	0.00	398	72	14	Dark Yellow

By adapting this model, we manage to adequately fit all other RT MS of the annealed samples based on the conventional AM-NHD precursors. The fitted RT MS are shown in Figures 6.24-26, and the resulting MP values are listed in Tables 6.10-6.12.

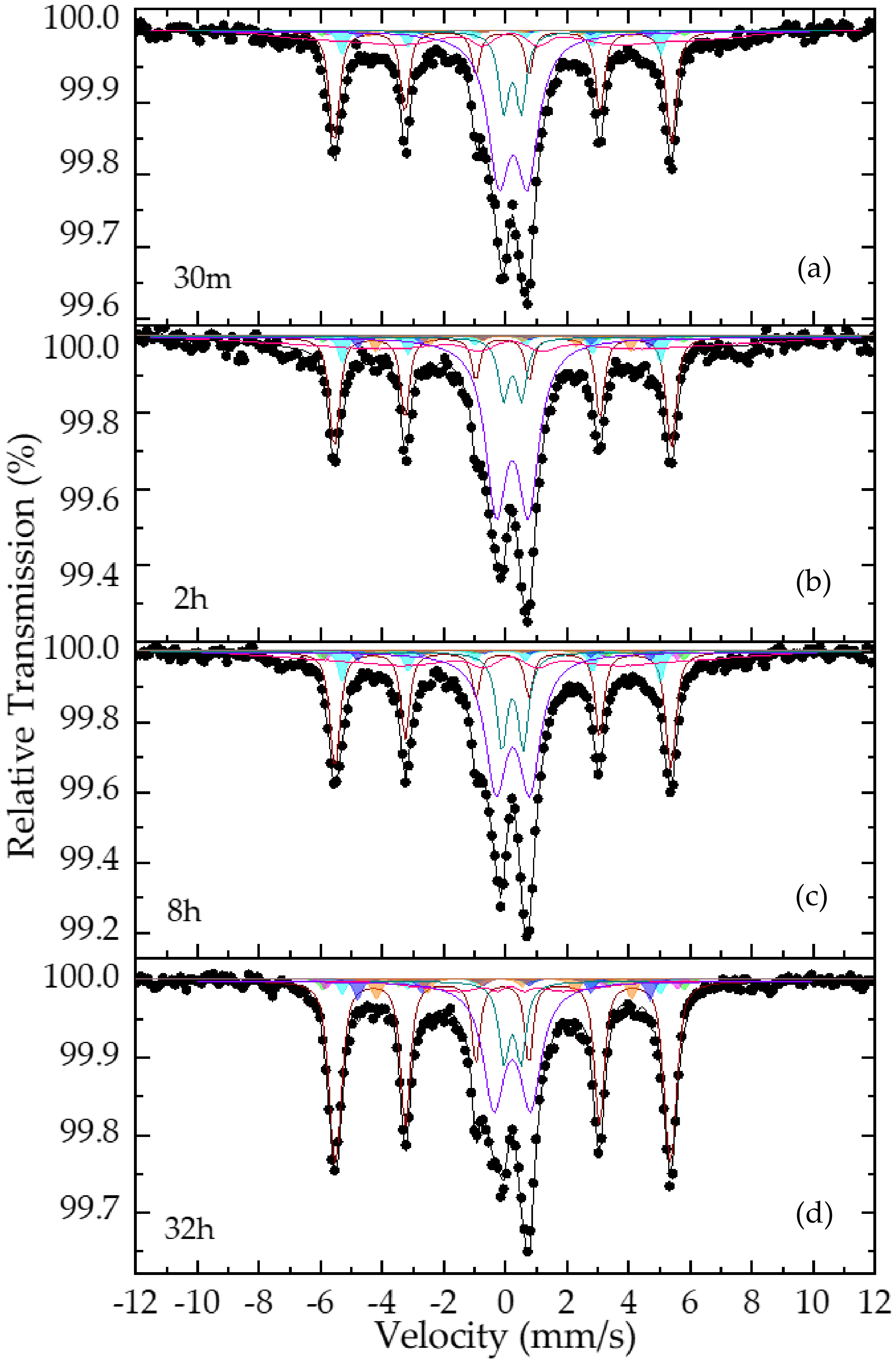

Figure 6.24 Fitted ^{57}Fe Mössbauer spectra of the IM-NHD4-600C,30m (a), IM-NHD5-600C,2h (b), IM-NHD5-600C,8h (c) and IM-NHD4-600C,32h (d) samples collected at RT.

Table 6.10 Mössbauer hyperfine parameters as resulting from the best fits of the corresponding spectra of the samples shown on **Figure 6.24**. IS the isomer shift (given relative to α-Fe at 300 K), $\Gamma/2$ is the half line-width, QS is the quadrupole splitting, 2ε is the quadrupole shift, B_{hf}^{C} is the central value of the hyperfine magnetic field, ΔB_{hf} is the total spreading (Gaussian-type) of the B_{hf} values around the central B_{hf}^{C} value, and AA is the relative spectral absorption area of each component used to fit the spectra. Typical errors are ±0.02 mm/s for IS, $\Gamma/2$, 2ε and QS, ±3 kOe for B_{hf}^{C} and ±3% for AA.

Sample	**Component**	**IS (mm/s)**	**Γ/2 (mm/s)**	**QS or 2ε (mm/s)**	**B_{hf}^{C} (kOe)**	**ΔB_{hf} (kOe)**	**Area (%)**	**Color**
IM-NHD4-600,30m	$Fe_{35}Co_{65}$	0.02	0.15	0.02	340	5	25	Maroon
	Martensitic Fe-Co (1)	0.09	0.15	0.01	366	0	2	Green
	Martensitic Fe-Co (2)	0.04	0.15	0.01	352	0	1	Magenta
	Martensitic Fe-Co (3)	0.00	0.15	0.04	322	0	5	Cyan
	Martensitic Fe-Co (4)	0.15	0.15	-0.08	293	0	1	Blue
	Martensitic Fe-Co (5)	0.05	0.15	-0.15	265	0	1	Orange
	SPM Fe^{3+} (1)	0.34	0.2	0.57	0	0	10	Dark Cyan
	MCOL Fe^{3+}	0.28	0.15	0.00	355	104	18	Pink
	SPM Fe^{3+} (2)	0.36	0.43	0.94	0	0	37	Purple
IM-NHD5-600,2h	$Fe_{35}Co_{65}$	0.02	0.15	0.02	340	5	24	Maroon
	Martensitic Fe-Co (1)	0.09	0.15	0.01	365	0	2	Green
	Martensitic Fe-Co (2)	0.04	0.15	0.01	355	0	1	Magenta
	Martensitic Fe-Co (3)	0.00	0.15	0.04	321	0	5	Cyan
	Martensitic Fe-Co (4)	0.15	0.15	-0.08	295	0	2	Blue
	Martensitic Fe-Co (5)	0.08	0.15	0.01	258	0	2	Orange
	SPM Fe^{3+} (1)	0.34	0.2	0.58	0	0	8	Dark Cyan
	MCOL Fe^{3+}	0.28	0.15	0.00	393	158	17	Pink
	SPM Fe^{3+} (2)	0.33	0.41	1.05	0	0	39	Purple
IM-NHD5-600,8h	$Fe_{35}Co_{65}$	0.02	0.15	0.02	339	5	26	Maroon
	Martensitic Fe-Co (1)	0.09	0.15	0.01	365	0	2	Green
	Martensitic Fe-Co (2)	0.04	0.15	0.01	355	0	2	Magenta
	Martensitic Fe-Co (3)	0.00	0.15	0.04	321	0	6	Cyan
	Martensitic Fe-Co (4)	0.15	0.15	-0.08	295	0	2	Blue

	Martensitic Fe-Co (5)	0.08	0.15	0.09	258	0	1	Orange
	SPM Fe^{3+} (1)	0.34	0.2	0.70	0	0	11	Dark Cyan
	MCOL Fe^{3+}	0.28	0.15	0.00	334	133	17	Pink
	SPM Fe^{3+} (2)	0.35	0.42	1.09	0	0	33	Purple
IM-NHD4-600,32h	Fe$_{35}$Co$_{65}$	0.02	0.15	0.02	338	8	43	Maroon
	Martensitic Fe-Co (1)	0.09	0.15	0.01	365	0	2	Green
	Martensitic Fe-Co (2)	0.04	0.15	0.01	355	0	2	Magenta
	Martensitic Fe-Co (3)	0.00	0.15	0.04	321	0	3	Cyan
	Martensitic Fe-Co (4)	0.15	0.15	-0.08	295	0	4	Blue
	Martensitic Fe-Co (5)	0.08	0.15	0.09	258	3	4	Orange
	SPM Fe^{3+} (1)	0.34	0.20	0.58	0	0	9	Dark Cyan
	MCOL Fe^{3+}	0.28	0.15	0.00	162	60	6	Pink
	SPM Fe^{3+} (2)	0.33	0.42	1.19	0	0	27	Purple

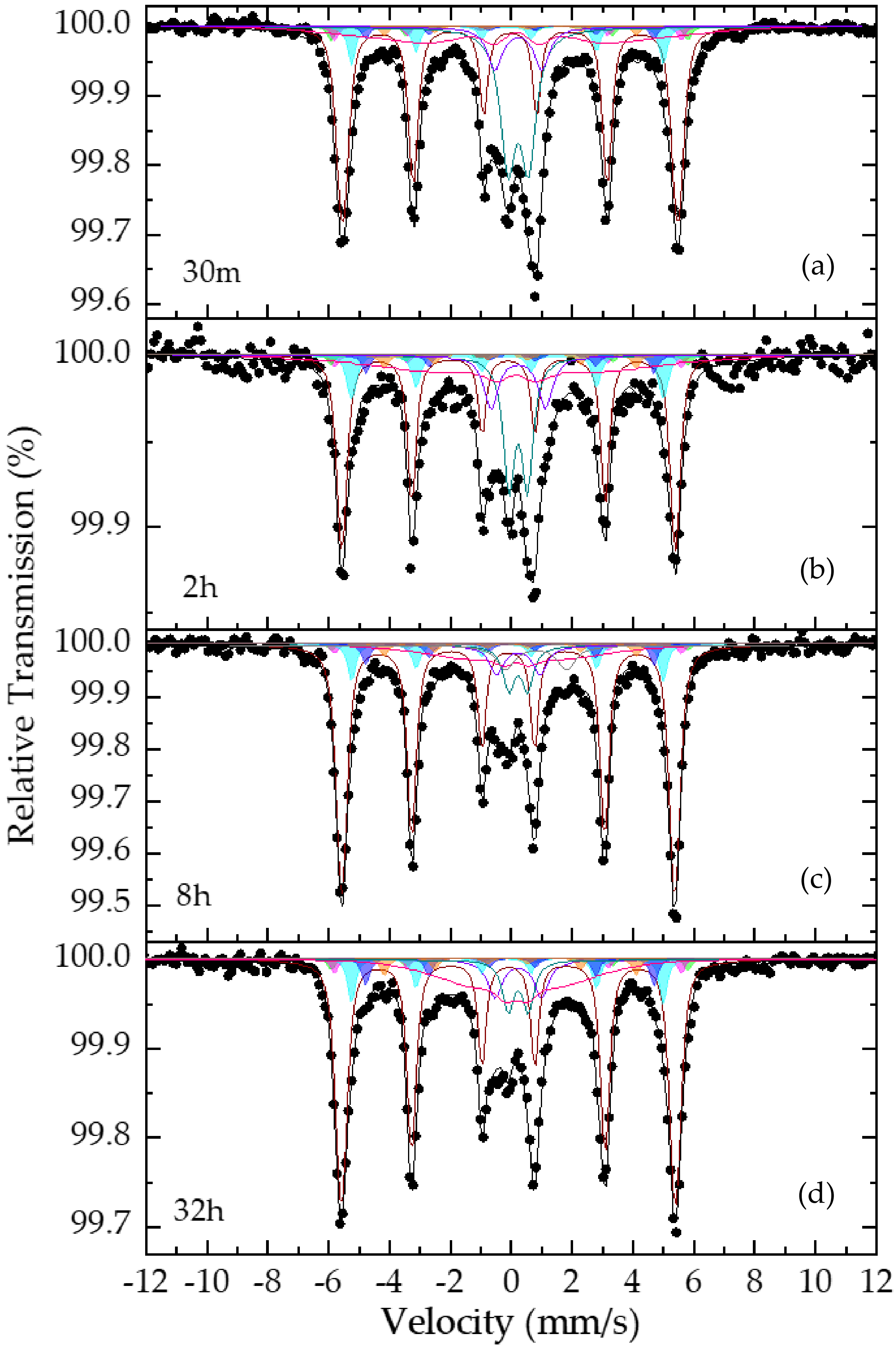

Figure 6.25 Fitted ^{57}Fe Mössbauer spectra of the IM-NHD3-650,30m (a), IM-NHD4-650,2h (b), IM-NHD3-650,8h (c) and IM-NHD4-650,32h (d) samples collected at RT.

Table 6.11 Mössbauer hyperfine parameters as resulting from the best fits of the corresponding spectra of the samples shown on **Figure 6.25**. IS the isomer shift (given relative to α-Fe at 300 K), $\Gamma/2$ is the half line-width, QS is the quadrupole splitting, 2ε is the quadrupole shift, B_{hf}^{C} is the central value of the hyperfine magnetic field, ΔB_{hf} is the total spreading (Gaussian-type) of the B_{hf} values around the central B_{hf}^{C} value, and AA is the relative spectral absorption area of each component used to fit the spectra. Typical errors are ±0.02 mm/s for IS, $\Gamma/2$, 2ε and QS, ±3 kOe for B_{hf}^{C} and ±3% for AA.

Sample	Component	IS (mm/s)	$\Gamma/2$ (mm/s)	QS or 2ε (mm/s)	B_{hf}^{C} (kOe)	ΔB_{hf} (kOe)	Area (%)	Color
IM-NHD3-650,30m	$Fe_{35}Co_{65}$	0.07	0.15	-0.01	342	8	44	Maroon
	Martensitic Fe-Co (1)	0.09	0.15	0.01	365	0	2	Green
	Martensitic Fe-Co (2)	0.04	0.15	0.01	355	0	2	Magenta
	Martensitic Fe-Co (3)	0.00	0.15	0.04	319	0	6	Cyan
	Martensitic Fe-Co (4)	0.15	0.15	-0.08	295	0	2	Blue
	Martensitic Fe-Co (5)	0.08	0.15	0.09	258	0	2	Orange
	SPM Fe^{3+} (1)	0.34	0.30	0.67	0	0	21	Dark Cyan
	MCOL Fe^{3+}	0.28	0.15	0.00	285	105	14	Pink
	SPM Fe^{3+} (2)	0.34	0.30	1.44	0	0	7	Purple
IM-NHD4-650,2h	$Fe_{35}Co_{65}$	0.02	0.15	0.00	341	5	42	Maroon
	Martensitic Fe-Co (1)	0.09	0.15	0.01	365	0	3	Green
	Martensitic Fe-Co (2)	0.04	0.15	0.01	355	0	3	Magenta
	Martensitic Fe-Co (3)	0.00	0.15	0.04	319	3	7	Cyan
	Martensitic Fe-Co (4)	0.15	0.15	-0.08	295	0	3	Blue
	Martensitic Fe-Co (5)	0.08	0.15	0.09	258	0	2	Orange
	SPM Fe^{3+} (1)	0.34	0.22	0.60	0	0	16	Dark Cyan
	MCOL Fe^{3+}	0.28	0.15	0.00	218	160	18	Pink
	SPM Fe^{3+} (2)	0.34	0.28	1.59	0	0	6	Purple
IM-NHD3-650,8h	$Fe_{35}Co_{65}$	0.00	0.15	0.00	340	6	58	Maroon
	Martensitic Fe-Co (1)	0.09	0.15	0.01	365	0	2	Green
	Martensitic Fe-Co (2)	0.04	0.15	0.01	355	0	2	Magenta
	Martensitic Fe-Co (3)	0.00	0.15	0.04	319	0	7	Cyan
	Martensitic Fe-Co (4)	0.15	0.15	-0.08	295	0	3	Blue

	Martensitic Fe-Co (5)	0.08	0.15	0.09	258	0	2	Orange
	SPM Fe^{3+} (1)	0.34	0.22	0.61	0	0	6	Dark Cyan
	MCOL Fe^{3+}	0.28	0.15	0.00	134	105	10	Pink
	SPM Fe^{3+} (2)	0.34	0.28	1.42	0	0	5	Purple
	SPM Fe^{2+}	0.92	0.36	2.00	0	0	5	Grey
IM-NHD4-650,32h	Fe$_{35}$Co$_{65}$	0.01	0.15	0.00	341	7	53	Maroon
	Martensitic Fe-Co (1)	0.09	0.15	0.01	365	0	2	Green
	Martensitic Fe-Co (2)	0.04	0.15	0.01	355	0	3	Magenta
	Martensitic Fe-Co (3)	0.00	0.15	0.04	319	0	7	Cyan
	Martensitic Fe-Co (4)	0.15	0.15	-0.08	295	0	3	Blue
	Martensitic Fe-Co (5)	0.08	0.15	0.09	258	0	3	Orange
	SPM Fe^{3+} (1)	0.34	0.22	0.66	0	0	6	Dark Cyan
	MCOL Fe^{3+}	0.28	0.15	0.00	115	100	17	Pink
	SPM Fe^{3+} (2)	0.34	0.28	1.53	0	0	5	Purple

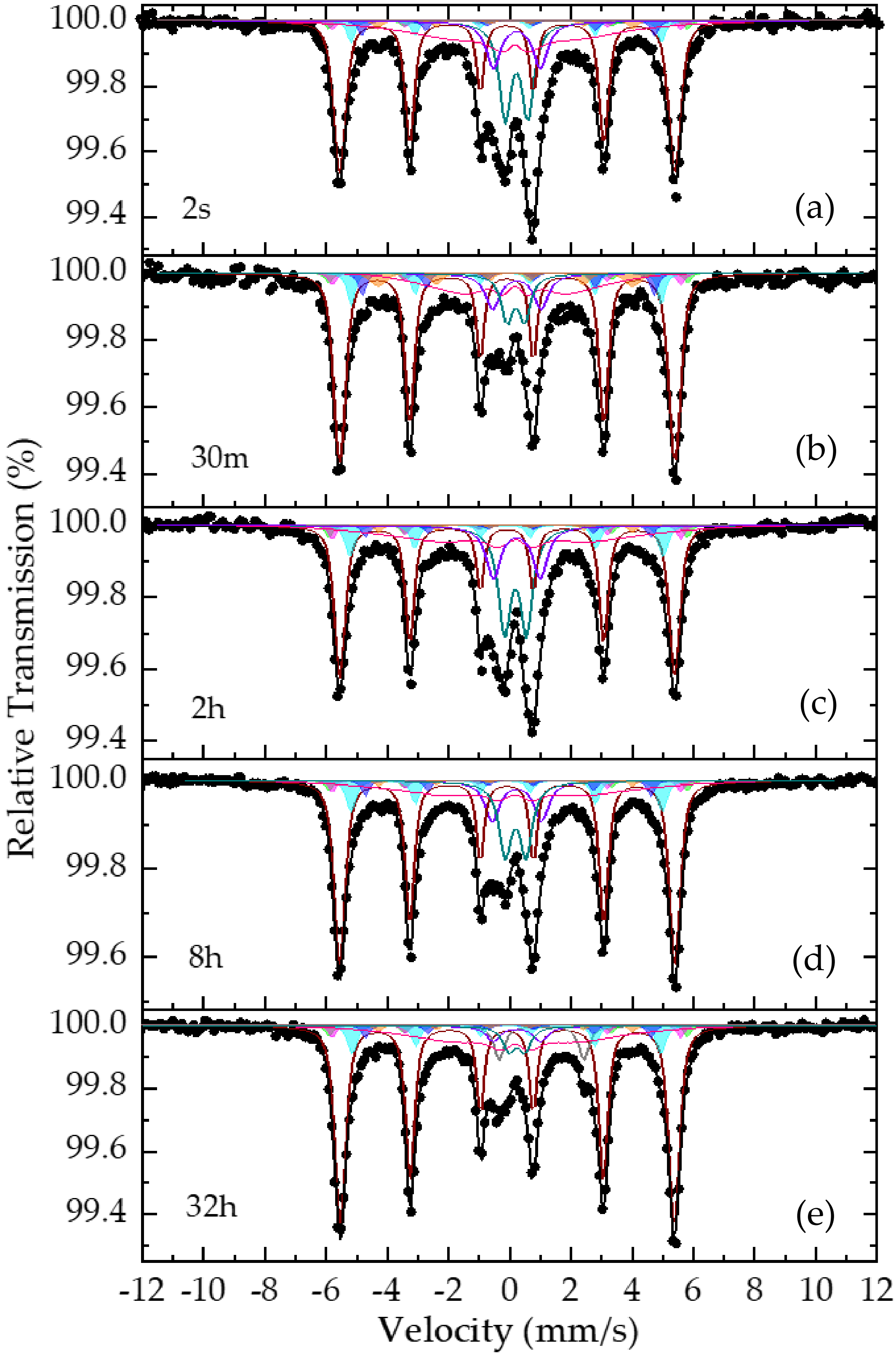

Figure 6.26 Fitted ^{57}Fe Mössbauer spectra of the IM-NHD5-700,2s (a), IM-NHD5-700,30m (b), IM-NHD5-700,2h (c), IM-NHD5-700,8h (d) and IM-NHD5-700,32h (e) samples collected at RT.

Table 6.12 Mössbauer hyperfine parameters as resulting from the best fits of the corresponding spectra of the samples shown on **Figure 6.26**. IS the isomer shift (given relative to α-Fe at 300 K), Γ/2 is the half line-width, QS is the quadrupole splitting, 2ε is the quadrupole shift, B_{hf}^{C} is the central value of the hyperfine magnetic field, ΔB_{hf} is the total spreading (Gaussian-type) of the B_{hf} values around the central B_{hf}^{C} value, and AA is the relative spectral absorption area of each component used to fit the spectra. Typical errors are ±0.02 mm/s for IS, Γ/2, 2ε and QS, ±3 kOe for B_{hf}^{C} and ±3% for AA.

Sample	**Component**	**IS (mm/s)**	**Γ/2 (mm/s)**	**QS or 2ε (mm/s)**	**B_{hf}^{C} (kOe)**	**ΔB_{hf} (kOe)**	**Area (%)**	**Color**
IM-NHD5-700,2s	$Fe_{35}Co_{65}$	0.02	0.14	0.02	340	8	45	Maroon
	Martensitic Fe-Co (1)	0.09	0.14	0.01	364	0	2	Green
	Martensitic Fe-Co (2)	0.04	0.14	0.01	354	0	2	Magenta
	Martensitic Fe-Co (3)	0.00	0.14	0.04	316	0	4	Cyan
	Martensitic Fe-Co (4)	0.13	0.14	-0.08	298	0	2	Blue
	Martensitic Fe-Co (5)	0.08	0.14	-0.15	259	0	2	Orange
	MCOL Fe^{3+}	0.28	0.14	0.00	142	137	19	Pink
	SPM Fe^{3+} (1)	0.33	0.23	0.71	0	0	15	Dark Cyan
	SPM Fe^{3+} (2)	0.34	0.28	1.54	0	0	9	Purple
IM-NHD5-700,30m	$Fe_{35}Co_{65}$	0.02	0.14	0.02	340	8	52	Maroon
	Martensitic Fe-Co (1)	0.09	0.14	0.01	364	0	2	Green
	Martensitic Fe-Co (2)	0.04	0.14	0.01	354	0	2	Magenta
	Martensitic Fe-Co (3)	0.00	0.14	0.04	315	0	6	Cyan
	Martensitic Fe-Co (4)	0.13	0.14	-0.08	296	0	5	Blue
	Martensitic Fe-Co (5)	0.08	0.14	-0.15	259	13	5	Orange
	MCOL Fe^{3+}	0.28	0.14	0.00	155	65	14	Pink
	SPM Fe^{3+} (1)	0.30	0.22	0.63	0	0	7	Dark cyan
	SPM Fe^{3+} (2)	0.34	0.28	1.58	0	0	7	Purple
IM-NHD5-700,2h	$Fe_{35}Co_{65}$	0.02	0.14	0.02	340	6	43	Maroon
	Martensitic Fe-Co (1)	0.09	0.14	0.01	364	0	3	Green
	Martensitic Fe-Co (2)	0.04	0.14	0.01	354	0	3	Magenta
	Martensitic Fe-Co (3)	0.02	0.14	0.04	318	5	7	Cyan
	Martensitic Fe-Co (4)	0.13	0.14	-0.08	290	0	2	Blue

	Martensitic Fe-Co (5)	0.08	0.14	-0.15	258	0	1	Orange
	MCOL Fe^{3+}	0.28	0.14	0.00	212	120	16	Pink
	SPM Fe^{3+} (1)	0.29	0.24	0.64	0	0	15	Dark Cyan
	SPM Fe^{3+} (2)	0.34	0.28	1.53	0	0	10	Purple
IM-NHD5-700,8h	$Fe_{35}Co_{65}$	0.02	0.14	0.02	340	7	49	Maroon
	Martensitic Fe-Co (1)	0.09	0.14	0.01	364	0	2	Green
	Martensitic Fe-Co (2)	0.04	0.14	0.01	354	0	3	Magenta
	Martensitic Fe-Co (3)	0.02	0.14	0.04	316	5	7	Cyan
	Martensitic Fe-Co (4)	0.13	0.14	-0.08	290	0	3	Blue
	Martensitic Fe-Co (5)	0.08	0.14	-0.15	258	0	1	Orange
	MCOL Fe^{3+}	0.28	0.14	0.00	201	120	15	Pink
	SPM Fe^{3+} (1)	0.29	0.24	0.68	0	0	11	Dark Cyan
	SPM Fe^{3+} (2)	0.34	0.28	1.61	0	0	8	Purple
IM-NHD5-700,32h	$Fe_{35}Co_{65}$	0.02	0.14	0.02	339	7	59	Maroon
	Martensitic Fe-Co (1)	0.09	0.14	0.01	364	0	2	Green
	Martensitic Fe-Co (2)	0.04	0.14	0.01	354	0	2	Magenta
	Martensitic Fe-Co (3)	0.02	0.14	0.04	314	5	6	Cyan
	Martensitic Fe-Co (4)	0.13	0.14	-0.08	290	0	3	Blue
	Martensitic Fe-Co (5)	0.08	0.14	-0.15	258	0	1	Orange
	MCOL Fe^{3+}	0.28	0.14	0.00	165	120	13	Pink
	SPM Fe^{3+} (1)	0.34	0.24	0.52	0	0	5	Dark Cyan
	SPM Fe^{3+} (2)	0.34	0.28	1.55	0	0	4	Purple
	SPM Fe^{2+}	1.14	0.19	2.66	0	0	5	Grey

The MPs values from all fits are quite similar to those found for the IM-NHD5-700C,30m sample. In some cases (IM-NHD3-650C,8h and IM-NHD5-700C,32h), an additional SPM quadrupole split component of Fe^{2+} high-spin ($S = 2$) character that indicates the presence of some additional Fe^{2+} ions in the SPM ICO phase [7] was necessary to be included in the fitting model to give a better fitting result for the contributions appearing at about +2 mm/s. For the samples annealed at 600°C in all durations and at 650°C with annealing durations up to 2 h, increased values for the sum of the AAs of the ICO phase components are observed relative to those found for the IM-NHD5-700C,30m sample. The same result holds also for the sample annealed at 700°C in the short duration of 2 s.

These results quantitatively verify our earlier qualitative conclusion on the more prominent presence of residual ICO at lower annealing temperatures and durations.

To ensure the consistency and reliability of the fitting model, we examined the thermal evolution of the samples' MS at all annealing temperatures and durations at 77 K. Additionally, we assessed the model's performance at 11 K for the nanohybrid samples annealed at 700°C for various durations. At lower temperatures, the proposed fitting model satisfactorily describes the spectra for all annealing conditions. In this context, the iron alloy components exhibit the expected shifts in IS and B_{hf} values, while their AA values remain consistent (within the margin of error) with those found in the spectra of the respective samples at RT. The only noticeable difference is in the AA values of the SPM Fe^{3+}/Fe^{2+} and MCOL Fe^{3+}/Fe^{2+} components, where the increase in AA for the MCOL components, at the expense of the SPM components, reflects the expected decrease in SPM relaxation time (τ) for the nanostructured ICO NPs at low temperatures. This indicates that the slowing of the fast SPM relaxation affects a larger portion of these phases [3], [7], [8]. By employing this model, we successfully fitted all the 77 K and 11 K spectra of the annealed samples based on the same model used for the RT spectra. The fitted 77 K MS are presented in Figures 6.27–6.29, with the corresponding MPs values listed in Tables 6.13–6.15. Similarly, the fitted 11 K MS for the samples annealed at 11 K are shown in Figure 6.30, with the resulting MPs values listed in Table 6.16.

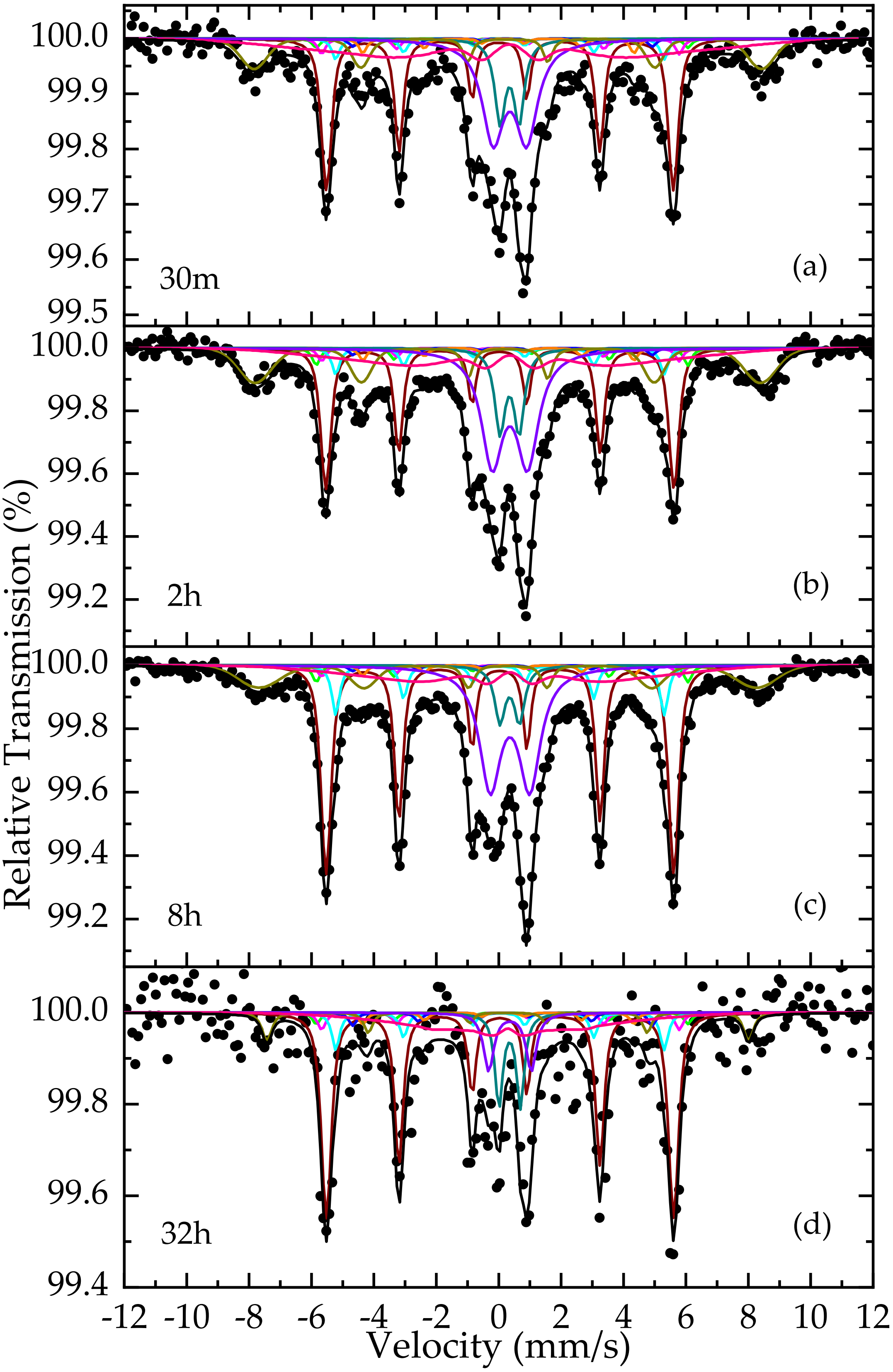

Figure 6.27 Fitted ^{57}Fe Mössbauer spectra of the IM-NHD4-600C,30m (a), IM-NHD5-600C,2h (b), IM-NHD5-600C,8h (c) and IM-NHD4-600C,32h (d) samples collected at 77 K.

Table 6.13 Mössbauer hyperfine parameters as resulting from the best fits of the corresponding spectra of the samples shown on **Figure 6.27**. IS the isomer shift (given relative to α-Fe at 300 K), Γ/2 is the half line-width, QS is the quadrupole splitting, 2ε is the quadrupole shift, B_{hf}^{C} is the central value of the hyperfine magnetic field, ΔB_{hf} is the total spreading (Gaussian-type) of the B_{hf} values around the central B_{hf}^{C} value, and AA is the relative spectral absorption area of each component used to fit the spectra. Typical errors are ±0.02 mm/s for IS, Γ/2, 2ε and QS, ±3 kOe for B_{hf}^{C} and ±3% for AA.

Sample	**Component**	**I.S. (mm/s)**	**Γ/2 (mm/s)**	**QS or 2ε (mm/s)**	**B_{hf}^{C} (kOe)**	**ΔB_{hf} (kOe)**	**Area (%)**	**Color**
IM-NHD4-600C,30m	$Fe_{35}Co_{65}$	0.14	0.15	0.02	347	5	25	Maroon
	Martensitic Fe-Co (1)	0.21	0.15	0.01	370	0	3	Green
	Martensitic Fe-Co (2)	0.16	0.15	0.01	356	0	2	Magenta
	Martensitic Fe-Co (3)	0.13	0.15	0.04	327	0	4	Cyan
	Martensitic Fe-Co (4)	0.27	0.15	-0.08	298	0	1	Blue
	Martensitic Fe-Co (5)	0.17	0.15	-0.15	270	0	2	Orange
	SPM Fe^{3+} (1)	0.46	0.20	0.62	0	0	8	Dark Cyan
	MCOL Fe^{3+} (1)	0.40	0.15	0.00	503	28	16	Pink
	SPM Fe^{3+} (2)	0.47	0.42	1.01	0	0	23	Purple
	MCOL Fe^{3+} (2)	0.47	0.15	0.00	300	121	16	Dark Yellow
IM-NHD5-600C,2h	$Fe_{35}Co_{65}$	0.14	0.15	0.02	347	5	25	Maroon
	Martensitic Fe-Co (1)	0.21	0.15	0.01	370	0	3	Green
	Martensitic Fe-Co (2)	0.16	0.15	0.01	356	0	2	Magenta
	Martensitic Fe-Co (3)	0.13	0.15	0.04	327	0	4	Cyan
	Martensitic Fe-Co (4)	0.27	0.15	-0.08	298	0	1	Blue
	Martensitic Fe-Co (5)	0.17	0.15	-0.15	270	0	2	Orange
	SPM Fe^{3+} (1)	0.46	0.20	0.62	0	0	8	Dark Cyan
	MCOL Fe^{3+} (1)	0.40	0.15	0.00	503	28	16	Pink
	SPM Fe^{3+} (2)	0.47	0.42	1.09	0	0	23	Purple
	MCOL Fe^{3+} (2)	0.47	0.15	0.00	300	121	16	Dark Yellow
IM-NHD5-600C,8h	$Fe_{35}Co_{65}$	0.14	0.15	0.02	346	5	27	Maroon
	Martensitic Fe-Co (1)	0.21	0.15	0.01	370	0	2	Green

	Martensitic Fe-Co (2)	0.16	0.15	0.01	356	0	2	Magenta
	Martensitic Fe-Co (3)	0.13	0.15	0.04	327	0	7	Cyan
	Martensitic Fe-Co (4)	0.27	0.15	-0.08	298	0	2	Blue
	Martensitic Fe-Co (5)	0.17	0.15	-0.15	270	0	1	Orange
	SPM Fe^{3+} (1)	0.46	0.20	0.63	0	0	5	Dark Cyan
	MCOL Fe^{3+} (1)	0.40	0.15	0.00	495	37	18	Pink
	SPM Fe^{3+} (2)	0.47	0.42	1.13	0	0	22	Purple
	MCOL Fe^{3+} (2)	0.47	0.15	0.00	276	112	13	Dark Yellow
IM-NHD4-600C,32h	$Fe_{35}Co_{65}$	0.14	0.15	0.02	346	5	44	Maroon
	Martensitic Fe-Co (1)	0.21	0.15	0.01	370	0	2	Green
	Martensitic Fe-Co (2)	0.16	0.15	0.01	356	0	3	Magenta
	Martensitic Fe-Co (3)	0.13	0.15	0.04	327	0	5	Cyan
	Martensitic Fe-Co (4)	0.27	0.15	-0.08	298	0	3	Blue
	Martensitic Fe-Co (5)	0.17	0.15	-0.15	270	0	3	Orange
	SPM Fe^{3+} (1)	0.46	0.15	0.65	0	0	9	Dark Cyan
	MCOL Fe^{3+} (1)	0.40	0.15	0.00	479	4	7	Pink
	SPM Fe^{3+} (2)	0.47	0.20	1.24	0	0	7	Purple
	MCOL Fe^{3+} (2)	0.40	0.15	0.00	200	120	17	Dark Yellow

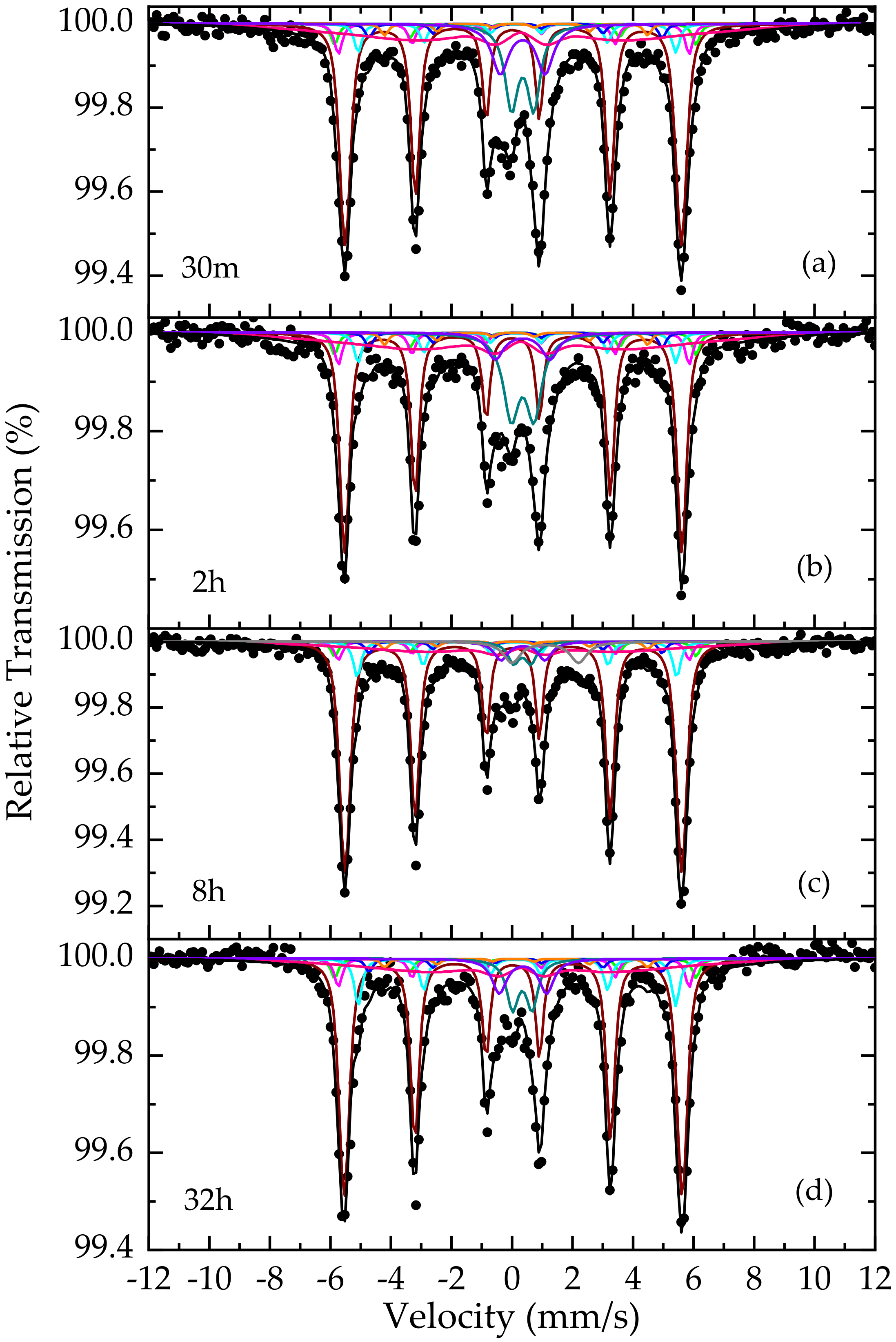

Figure 6.28 Fitted ^{57}Fe Mössbauer spectra of the IM-NHD3-650,30m (a), IM-NHD4-650,2h (b), IM-NHD3-650,8h (c) and IM-NHD4-650,32h (d) samples collected at 77 K.

Table 6.14 Mössbauer hyperfine parameters as resulting from the best fits of the corresponding spectra of the samples shown on **Figure 6.28**. IS the isomer shift (given relative to α-Fe at 300 K), Γ/2 is the half line-width, QS is the quadrupole splitting, 2ε is the quadrupole shift, B_{hf}^{C} is the central value of the hyperfine magnetic field, ΔB_{hf} is the total spreading (Gaussian-type) of the B_{hf} values around the central B_{hf}^{C} value, and AA is the relative spectral absorption area of each component used to fit the spectra. Typical errors are ±0.02 mm/s for IS, Γ/2, 2ε and QS, ±3 kOe for B_{hf}^{C} and ±3% for AA.

Sample	Component	I.S. (mm/s)	Γ/2 (mm/s)	QS or 2ε (mm/s)	B_{hf} (kOe)	ΔB_{hf}^{C} (kOe)	Area (%)	Color
IM-NHD3-650C,30m	$Fe_{35}Co_{65}$	0.14	0.15	0.01	345	6	45	Maroon
	Martensitic Fe-Co (1)	0.21	0.15	0.01	371	0	3	Green
	Martensitic Fe-Co (2)	0.16	0.15	0.01	360	0	3	Magenta
	Martensitic Fe-Co (3)	0.25	0.15	0.04	326	0	5	Cyan
	Martensitic Fe-Co (4)	0.27	0.15	-0.08	301	0	2	Blue
	Martensitic Fe-Co (5)	0.20	0.15	0.09	270	0	2	Orange
	SPM Fe^{3+} (2)	0.46	0.26	0.71	0	0	12	Dark Cyan
	MCOL Fe^{3+}	0.40	0.15	0.00	320	150	20	Pink
	SPM Fe^{3+} (1)	0.46	0.33	1.48	0	0	8	Purple
IM-NHD4-650C,2h	$Fe_{35}Co_{65}$	0.14	0.15	0.01	346	5	43	Maroon
	Martensitic Fe-Co (1)	0.21	0.15	0.01	371	0	4	Green
	Martensitic Fe-Co (2)	0.16	0.15	0.01	360	0	5	Magenta
	Martensitic Fe-Co (3)	0.25	0.15	0.04	326	0	5	Cyan
	Martensitic Fe-Co (4)	0.27	0.15	-0.08	301	0	3	Blue
	Martensitic Fe-Co (5)	0.20	0.15	0.09	270	0	2	Orange
	SPM Fe^{3+} (2)	0.46	0.31	0.66	0	0	13	Dark Cyan

	MCOL Fe^{3+}	0.40	0.15	0.00	320	150	20	Pink
	SPM Fe^{3+} (1)	0.46	0.33	1.61	0	0	5	Purple
IM-NHD3-650C,8h	$Fe_{35}Co_{65}$	0.14	0.15	0.02	346	6	57	Maroon
	Martensitic Fe-Co (1)	0.21	0.15	0.01	371	0	3	Green
	Martensitic Fe-Co (2)	0.16	0.15	0.01	360	0	4	Magenta
	Martensitic Fe-Co (3)	0.25	0.15	0.04	328	0	7	Cyan
	Martensitic Fe-Co (4)	0.27	0.15	-0.08	301	0	2	Blue
	Martensitic Fe-Co (5)	0.20	0.15	0.09	267	0	2	Orange
	SPM Fe^{3+} (2)	0.45	0.23	0.57	0	0	3	Dark Cyan
	MCOL Fe^{3+}	0.41	0.15	0.00	290	150	14	Pink
	SPM Fe^{3+} (1)	0.47	0.28	1.45	0	0	3	Purple
	SPM Fe^{2+}	1.17	0.34	2.07	0	0	5	Grey
IM-NHD4-650C,32h	$Fe_{35}Co_{65}$	0.14	0.15	0.01	347	6	52	Maroon
	Martensitic Fe-Co (1)	0.21	0.15	0.01	371	0	3	Green
	Martensitic Fe-Co (2)	0.16	0.15	0.01	360	0	5	Magenta
	Martensitic Fe-Co (3)	0.25	0.15	0.04	326	0	8	Cyan
	Martensitic Fe-Co (4)	0.27	0.15	-0.08	301	0	2	Blue
	Martensitic Fe-Co (5)	0.20	0.15	0.09	270	0	2	Orange
	SPM Fe^{3+} (2)	0.45	0.23	0.65	0	0	6	Dark Cyan
	MCOL Fe^{3+}	0.41	0.15	0.00	280	145	16	Pink
	SPM Fe^{3+} (1)	0.47	0.29	1.56	0	0	6	Purple

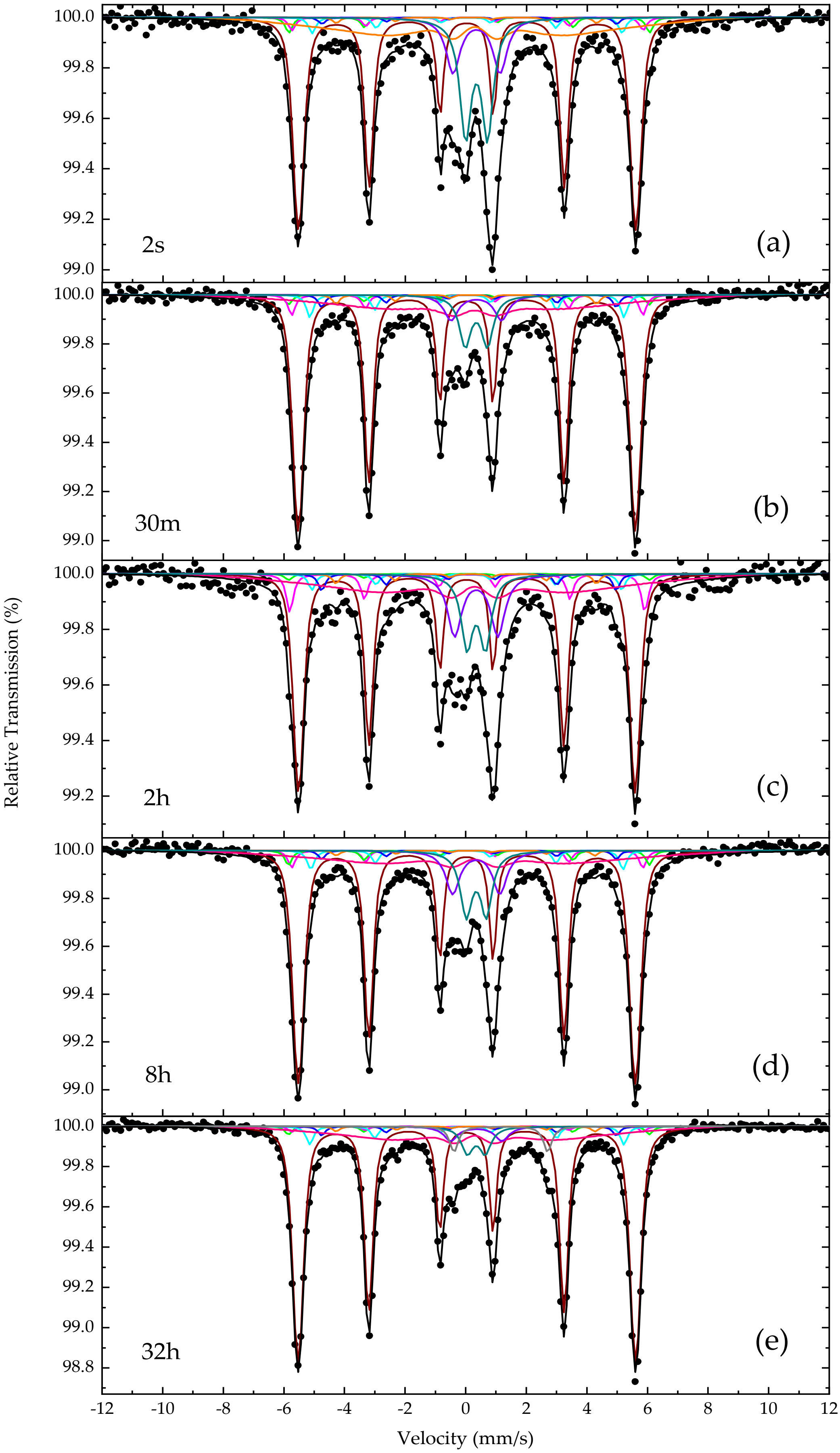

Figure 6.29 Fitted ^{57}Fe Mössbauer spectra of the IM-NHD5-700,2s (a), IM-NHD5-700,30m (b), IM-NHD5-700,2h (c), IM-NHD5-700,8h (d) and IM-NHD5-700,32h (e) samples collected at 77 K.

Table 6.15 Mössbauer hyperfine parameters as resulting from the best fits of the corresponding spectra of the samples shown on **Figure 6.29**. IS the isomer shift (given relative to α-Fe at 300 K), Γ/2 is the half line-width, QS is the quadrupole splitting, 2ε is the quadrupole shift, B_{hf}^{C} is the central value of the hyperfine magnetic field, ΔB_{hf} is the total spreading (Gaussian-type) of the B_{hf} values around the central B_{hf}^{C} value, and AA is the relative spectral absorption area of each component used to fit the spectra. Typical errors are ±0.02 mm/s for IS, Γ/2, 2ε and QS, ±3 kOe for B_{hf}^{C} and ±3% for AA.

Sample	**Component**	**I.S. (mm/s)**	**Γ/2 (mm/s)**	**QS or 2ε (mm/s)**	**B_{hf}^{C} (kOe)**	**ΔB_{hf} (kOe)**	**Area (%)**	**Color**
IM-NHD5-700C,2s	$Fe_{35}Co_{65}$	0.14	0.14	0.02	346	7	46	Maroon
	Martensitic Fe-Co (1)	0.21	0.14	0.01	370	0	3	Green
	Martensitic Fe-Co (2)	0.16	0.14	0.01	360	0	2	Magenta
	Martensitic Fe-Co (3)	0.13	0.14	0.04	318	0	3	Cyan
	Martensitic Fe-Co (4)	0.26	0.14	-0.08	302	0	2	Blue
	Martensitic Fe-Co (5)	0.20	0.14	-0.15	267	0	2	Orange
	MCOL Fe^{3+}	0.40	0.14	0.00	271	120	20	Pink
	SPM Fe^{3+} (1)	0.46	0.23	0.73	0	0	14	Dark Cyan
	SPM Fe^{3+} (2)	0.46	0.28	1.55	0	0	8	Purple
IM-NHD5-700C,30m	$Fe_{35}Co_{65}$	0.14	0.14	0.02	346	7	54	Maroon
	Martensitic Fe-Co (1)	0.21	0.14	0.01	370	0	2	Green
	Martensitic Fe-Co (2)	0.16	0.14	0.01	360	0	3	Magenta
	Martensitic Fe-Co (3)	0.13	0.14	0.04	322	0	5	Cyan
	Martensitic Fe-Co (4)	0.26	0.14	-0.08	302	0	4	Blue
	Martensitic Fe-Co (5)	0.20	0.14	-0.15	267	0	4	Orange
	MCOL Fe^{3+}	0.40	0.14	0.00	240	160	18	Pink
	SPM Fe^{3+} (1)	0.46	0.23	0.65	0	0	6	Dark Cyan
	SPM Fe^{3+} (2)	0.46	0.28	1.63	0	0	4	Purple
IM-NHD5-700C,2h	$Fe_{35}Co_{65}$	0.14	0.14	0.02	345	7	44	Maroon
	Martensitic Fe-Co (1)	0.21	0.14	0.01	370	0	2	Green
	Martensitic Fe-Co (2)	0.16	0.14	0.01	364	0	4	Magenta
	Martensitic Fe-Co (3)	0.13	0.14	0.04	318	0	6	Cyan
	Martensitic Fe-Co (4)	0.26	0.14	-0.08	302	0	3	Blue

	Martensitic Fe-Co (5)	0.20	0.14	-0.15	267	0	2	Orange
	MCOL Fe^{3+}	0.40	0.14	0.00	280	140	21	Pink
	SPM Fe^{3+} (1)	0.46	0.23	0.67	0	0	8	Dark Cyan
	SPM Fe^{3+} (2)	0.46	0.28	1.48	0	0	10	Purple
IM-NHD5-700C,8h	$Fe_{35}Co_{65}$	0.14	0.14	0.02	345	8	52	Maroon
	Martensitic Fe-Co (1)	0.21	0.14	0.01	370	0	3	Green
	Martensitic Fe-Co (2)	0.16	0.14	0.01	360	0	3	Magenta
	Martensitic Fe-Co (3)	0.13	0.14	0.04	320	0	6	Cyan
	Martensitic Fe-Co (4)	0.26	0.14	-0.08	302	0	2	Blue
	Martensitic Fe-Co (5)	0.20	0.14	-0.19	265	0	1	Orange
	MCOL Fe^{3+}	0.40	0.14	0.00	280	140	17	Pink
	SPM Fe^{3+} (1)	0.46	0.23	0.66	0	0	9	Dark Cyan
	SPM Fe^{3+} (2)	0.46	0.28	1.57	0	0	7	Purple
IM-NHD5-700C,32h	$Fe_{35}Co_{65}$	0.14	0.14	0.02	346	7	60	Maroon
	Martensitic Fe-Co (1)	0.21	0.14	0.01	370	0	2	Green
	Martensitic Fe-Co (2)	0.16	0.14	0.01	360	0	2	Magenta
	Martensitic Fe-Co (3)	0.13	0.14	0.04	322	0	6	Cyan
	Martensitic Fe-Co (4)	0.26	0.14	-0.08	302	0	3	Blue
	Martensitic Fe-Co (5)	0.20	0.14	-0.19	265	0	1	Orange
	MCOL Fe^{3+}	0.40	0.14	0.00	240	119	15	Pink
	SPM Fe^{3+} (1)	0.46	0.23	0.57	0	0	4	Dark Cyan
	SPM Fe^{3+} (2)	0.46	0.28	1.62	0	0	3	Purple
	SPM Fe^{2+}	1.21	0.17	2.71	0	0	4	Grey

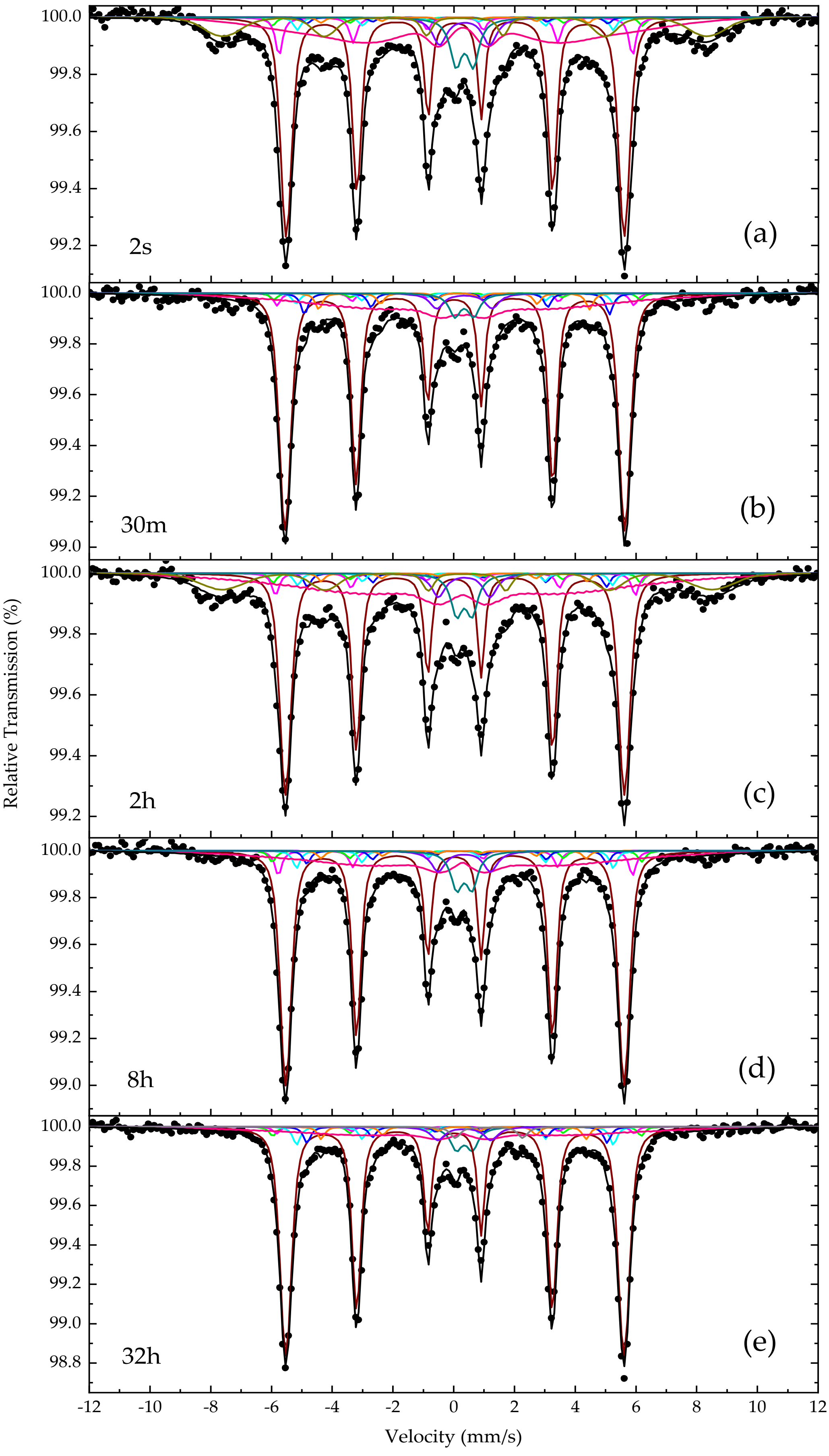

Figure 6.30 Fitted ^{57}Fe Mössbauer spectra of the IM-NHD5-700,2s (a), IM-NHD5-700,30m (b), IM-NHD5-700,2h (c), IM-NHD5-700,8h (d) and IM-NHD5-700,32h (e) samples collected at 11 K.

Table 6.16 Mössbauer hyperfine parameters as resulting from the best fits of the corresponding spectra of the samples shown on **Figure 6.30**. IS the isomer shift (given relative to α-Fe at 300 K), $\Gamma/2$ is the half line-width, QS is the quadrupole splitting, 2ε is the quadrupole shift, B_{hf}^{C} is the central value of the hyperfine magnetic field, ΔB_{hf} is the total spreading (Gaussian-type) of the B_{hf} values around the central B_{hf}^{C} value, and AA is the relative spectral absorption area of each component used to fit the spectra. Typical errors are ±0.02 mm/s for IS, $\Gamma/2$, 2ε and QS, ±3 kOe for B_{hf}^{C} and ±3% for AA.

Sample	**Component**	**I.S. (mm/s)**	**$\Gamma/2$ (mm/s)**	**QS or 2ε (mm/s)**	**B_{hf}^{C} (kOe)**	**ΔB_{hf} (kOe)**	**Area (%)**	**Color**
IM-NHD5-700C,2s	$Fe_{35}Co_{65}$	0.14	0.14	0.02	346	7	45	Maroon
	Martensitic Fe-Co (1)	0.21	0.14	0.01	379	0	2	Green
	Martensitic Fe-Co (2)	0.16	0.14	0.01	361	0	2	Magenta
	Martensitic Fe-Co (3)	0.13	0.14	0.04	323	0	3	Cyan
	Martensitic Fe-Co (4)	0.26	0.14	-0.08	308	0	2	Blue
	Martensitic Fe-Co (5)	0.20	0.14	-0.15	273	0	1	Orange
	MCOL Fe^{3+} (1)	0.40	0.14	0.00	302	120	24	Pink
	MCOL Fe^{3+} (2)	0.46	0.15	0	496	34	12	Dark Yellow
	SPM Fe^{3+} (1)	0.46	0.23	0.68	0	0	5	Dark Cyan
	SPM Fe^{3+} (2)	0.46	0.28	1.59	0	0	4	Purple
IM-NHD5-700C,30m	$Fe_{35}Co_{65}$	0.14	0.14	0.02	347	8	53	Maroon
	Martensitic Fe-Co (1)	0.21	0.14	0.01	375	0	2	Green
	Martensitic Fe-Co (2)	0.16	0.14	0.01	365	0	2	Magenta
	Martensitic Fe-Co (3)	0.13	0.14	0.04	325	0	5	Cyan
	Martensitic Fe-Co (4)	0.26	0.14	-0.08	312	0	5	Blue
	Martensitic Fe-Co (5)	0.20	0.14	-0.15	277	0	4	Orange
	MCOL Fe^{3+}	0.40	0.14	0.00	240	185	22	Pink
	SPM Fe^{3+} (1)	0.46	0.23	0.67	0	0	3	Dark Cyan
	SPM Fe^{3+} (2)	0.46	0.28	1.63	0	0	3	Purple
IM-NHD5-700C,2h	$Fe_{35}Co_{65}$	0.14	0.14	0.02	348	7	45	Maroon
	Martensitic Fe-Co (1)	0.21	0.14	0.01	376	0	2	Green
	Martensitic Fe-Co (2)	0.16	0.14	0.01	368	0	3	Magenta
	Martensitic Fe-Co (3)	0.13	0.14	0.04	322	0	4	Cyan

	Martensitic Fe-Co (4)	0.26	0.14	-0.08	306	0	3	Blue
	Martensitic Fe-Co (5)	0.20	0.14	-0.15	272	0	2	Orange
	MCOL Fe^{3+} (1)	0.40	0.14	0.00	280	196	24	Pink
	MCOL Fe^{3+} (2)	0.55	0.15	0	501	42	10	Dark Yellow
	SPM Fe^{3+} (1)	0.44	0.23	0.59	0	0	4	Dark Cyan
	SPM Fe^{3+} (2)	0.46	0.28	1.50	0	0	3	Purple
IM-NHD5-700C,8h	$Fe_{35}Co_{65}$	0.14	0.14	0.02	349	7	51	Maroon
	Martensitic Fe-Co (1)	0.21	0.14	0.01	378	0	3	Green
	Martensitic Fe-Co (2)	0.16	0.14	0.01	362	0	4	Magenta
	Martensitic Fe-Co (3)	0.13	0.14	0.04	324	0	6	Cyan
	Martensitic Fe-Co (4)	0.26	0.14	-0.08	307	0	3	Blue
	Martensitic Fe-Co (5)	0.20	0.14	-0.19	271	0	1	Orange
	MCOL Fe^{3+}	0.40	0.14	0.00	268	171	22	Pink
	SPM Fe^{3+} (1)	0.45	0.23	0.65	0	0	5	Dark Cyan
	SPM Fe^{3+} (2)	0.46	0.28	1.63	0	0	5	Purple
IM-NHD5-700C,32h	$Fe_{35}Co_{65}$	0.14	0.14	0.02	349	7	61	Maroon
	Martensitic Fe-Co (1)	0.21	0.14	0.01	378	0	2	Green
	Martensitic Fe-Co (2)	0.16	0.14	0.01	362	0	1	Magenta
	Martensitic Fe-Co (3)	0.13	0.14	0.04	324	0	5	Cyan
	Martensitic Fe-Co (4)	0.26	0.14	-0.08	307	0	3	Blue
	Martensitic Fe-Co (5)	0.20	0.14	-0.19	271	0	3	Orange
	MCOL Fe^{3+}	0.40	0.14	0.00	268	171	14	Pink
	SPM Fe^{3+} (1)	0.46	0.23	0.52	0	0	4	Dark Cyan
	SPM Fe^{3+} (2)	0.46	0.28	1.57	0	0	3	Purple
	SPM Fe^{2+}	1.27	0.2	2.59	0	0	4	Grey

For the fit of the RT spectrum of the En-IM-NHD6-700C,30m-SC sample shown in Figure 6.22b, we used the same fitting model as for the IM-NHD5-700,30m sample, with the addition of the SPM quadrupole split component of Fe^{2+} high spin ($S = 2$) character. This was done to cover the necessary absorption area contributing at around +2 mm/s. The resulting MP values of all other components listed in Table 6.8 are very similar to those found for the non-^{57}Fe-enriched IM-NHD5-700C,30m sample. This reveals the high similarity of the Fe–Co NP phase characteristics in the two samples and the reproducibility of the synthesis method, as also verified by the XRD and TEM results.

On the other hand, an increase of about 10% for the sum of the AA values of the components attributed to the ICO phase and a similar decrease in the AA value of the main cubic Fe–Co alloy component is observed for the En-NHD6-700C,30m-SC sample, compared to those AAs found for the IM-NHD5-700C,30m sample. By contrast, the sum of the AA values for the "martensitic" components remains relatively constant in both samples. These results suggest that the En-IM-NHD6-700C,30m-SC sample contains relatively higher amounts of the SPM ICO phase, which is also somehow chemically different, in the sense that it contains additional Fe^{2+} ions, from the corresponding SPM ICO phase found in the IM-NHD5-700C,30m sample, and this reflects some diversification between the two chemical precursor characteristics. The systematic presence of the Fe^{2+} component in the MS of all annealed samples resulting from the annealing of the En-IM-AM6-NHD precursor further enforces this argument, as the presence of this component is only occasional found in the MS of the samples resulting from the annealing of the conventional AM-NHD precursors. The fitted RT MS of all enriched samples are shown in Figure 6.31, and the resulting MPs values are listed in Table 6.17.

By lowering the temperature to 11 K, the evolution of the Mössbauer spectrum of the En-IM-NHD6-700C,30m-SC sample shown in Figure 6.32 follows the same features found for the case of the IM-NHD5-700C,30m sample, verifying again the consistency of the fitting model. The only difference refers to the presence of an additional broad magnetically collapsing component, MCOL Fe^{3+}, colored dark yellow in Figure 6.32b, that corresponds to a part of the ICO phase, whose AA value increases at the expense of the AA values of those SPM Fe^{3+} components found at the respective RT spectrum (Figure 6.31b). This denotes an increase in the characteristic SPM relaxation time τ for a part of the SPM ICO NPs which are becoming magnetically blocked at 11 K [9], [14] [3], [8], [11]. The fitted 11 K MS for all enriched annealed samples are presented in Figure 6.32, with the resulting MPs values listed in Table 6.18.

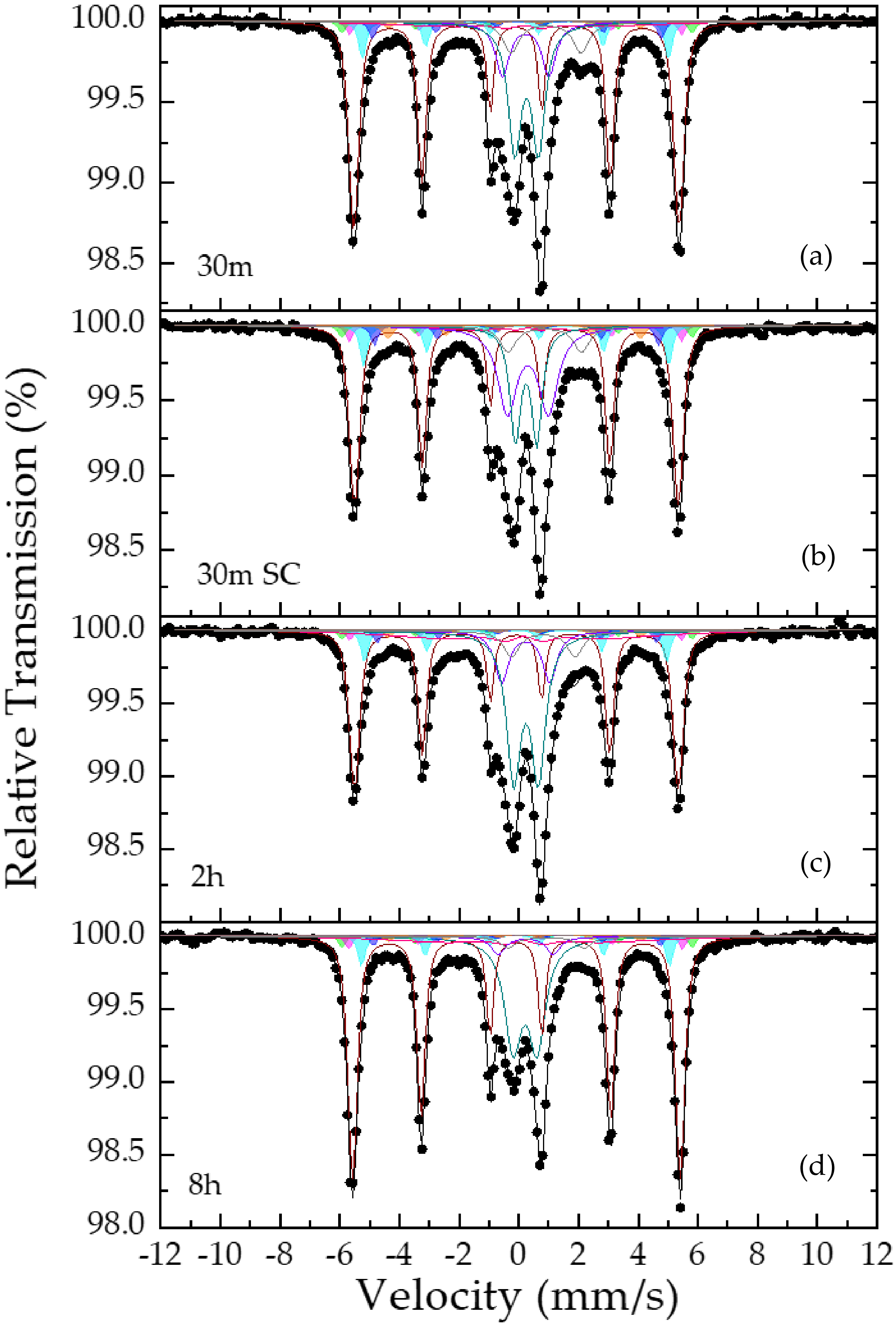

Figure 6.31 Fitted ^{57}Fe Mössbauer spectra of the ^{57}Fe enriched En-IM-NHD6-700,30m (a), En-IM-NHD6-700,30m-SC (b), En-IM-NHD6-700,2h (c) and En-IM-NHD6-700,8h (d) samples collected at RT.

Table 6.17 Mössbauer hyperfine parameters as resulting from the best fits of the corresponding spectra of the samples shown on **Figure 6.31**. IS the isomer shift (given relative to α-Fe at 300 K), $\Gamma/2$ is the half line-width, QS is the quadrupole splitting, 2ε is the quadrupole shift, B_{hf}^{C} is the central value of the hyperfine magnetic field, ΔB_{hf} is the total spreading (Gaussian-type) of the B_{hf} values around the central B_{hf}^{C} value, and AA is the relative spectral absorption area of each component used to fit the spectra. Typical errors are ±0.02 mm/s for IS, $\Gamma/2$, 2ε and QS, ±3 kOe for B_{hf}^{C} and ±3% for AA.

Sample	**Component**	**IS (mm/s)**	**$\Gamma/2$ (mm/s)**	**QS or 2ε (mm/s)**	**B_{hf}^{C} (kOe)**	**ΔB_{hf} (kOe)**	**Area (%)**	**Color**
En-IM-NHD6-700,30m	$Fe_{33}Co_{67}$	0.02	0.14	0.02	339	6	46	Maroon
	Martensitic Fe-Co (1)	0.09	0.14	0.01	365	0	2	Green
	Martensitic Fe-Co (2)	0.04	0.14	0.01	346	0	2	Magenta
	Martensitic Fe-Co (3)	0.02	0.14	0.04	319	0	7	Cyan
	Martensitic Fe-Co (4)	0.13	0.14	-0.09	301	0	3	Blue
	Martensitic Fe-Co (5)	0.08	0.14	-0.15	263	3	1	Orange
	MCOL Fe^{3+}	0.28	0.14	0.00	216	120	5	Pink
	SPM Fe^{3+} (1)	0.36	0.26	0.79	0	0	20	Dark Cyan
	SPM Fe^{3+} (2)	0.34	0.28	1.55	0	0	9	Purple
	SPM Fe^{2+}	1.02	0.32	2.36	0	0	5	Grey
En-IM-NHD6-700,30m-SC	$Fe_{33}Co_{67}$	0.02	0.14	0.02	337	7	41	Maroon
	Martensitic Fe-Co (1)	0.09	0.14	0.01	365	0	2	Green
	Martensitic Fe-Co (2)	0.04	0.14	0.01	346	0	3	Magenta
	Martensitic Fe-Co (3)	0.05	0.14	0.04	318	0	7	Cyan
	Martensitic Fe-Co (4)	0.12	0.14	-0.09	296	0	4	Blue
	Martensitic Fe-Co (5)	0.08	0.14	-0.15	263	5	3	Orange
	MCOL Fe^{3+}	0.43	0.14	0.00	160	60	2	Pink
	SPM Fe^{3+} (1)	0.35	0.21	0.72	0	0	14	Dark Cyan
	SPM Fe^{3+} (2)	0.41	0.38	1.37	0	0	19	Purple
	SPM Fe^{2+}	0.97	0.32	2.46	0	0	5	Grey
	$Fe_{33}Co_{67}$	0.02	0.14	0.02	337	7	39	Maroon
	Martensitic Fe-Co (1)	0.09	0.14	0.01	365	0	2	Green

En-IM-NHD6-700,2h	Martensitic Fe-Co (2)	0.04	0.14	0.01	346	0	2	Magenta
	Martensitic Fe-Co (3)	0.02	0.14	0.04	315	0	6	Cyan
	Martensitic Fe-Co (4)	0.13	0.14	-0.09	292	0	2	Blue
	Martensitic Fe-Co (5)	0.08	0.14	-0.15	263	3	2	Orange
	MCOL Fe^{3+}	0.28	0.14	0.00	234	120	8	Pink
	SPM Fe^{3+} (1)	0.35	0.28	0.83	0	0	25	Dark Cyan
	SPM Fe^{3+} (2)	0.34	0.28	1.66	0	0	9	Purple
	SPM Fe^{2+}	0.93	0.32	2.13	0	0	5	Grey
En-IM-NHD6-700,8h	$Fe_{33}Co_{67}$	0.02	0.14	0.02	341	5	54	Maroon
	Martensitic Fe-Co (1)	0.09	0.14	0.01	365	0	2	Green
	Martensitic Fe-Co (2)	0.04	0.14	0.01	348	0	2	Magenta
	Martensitic Fe-Co (3)	0.02	0.14	0.04	321	0	6	Cyan
	Martensitic Fe-Co (4)	0.13	0.14	-0.09	299	0	2	Blue
	Martensitic Fe-Co (5)	0.08	0.14	-0.15	263	3	1	Orange
	MCOL Fe^{3+}	0.28	0.14	0.00	234	120	6	Pink
	SPM Fe^{3+} (1)	0.31	0.34	0.80	0	0	20	Dark Cyan
	SPM Fe^{3+} (2)	0.34	0.28	1.85	0	0	3	Purple
	SPM Fe^{2+}	1.02	0.32	2.55	0	0	4	Grey

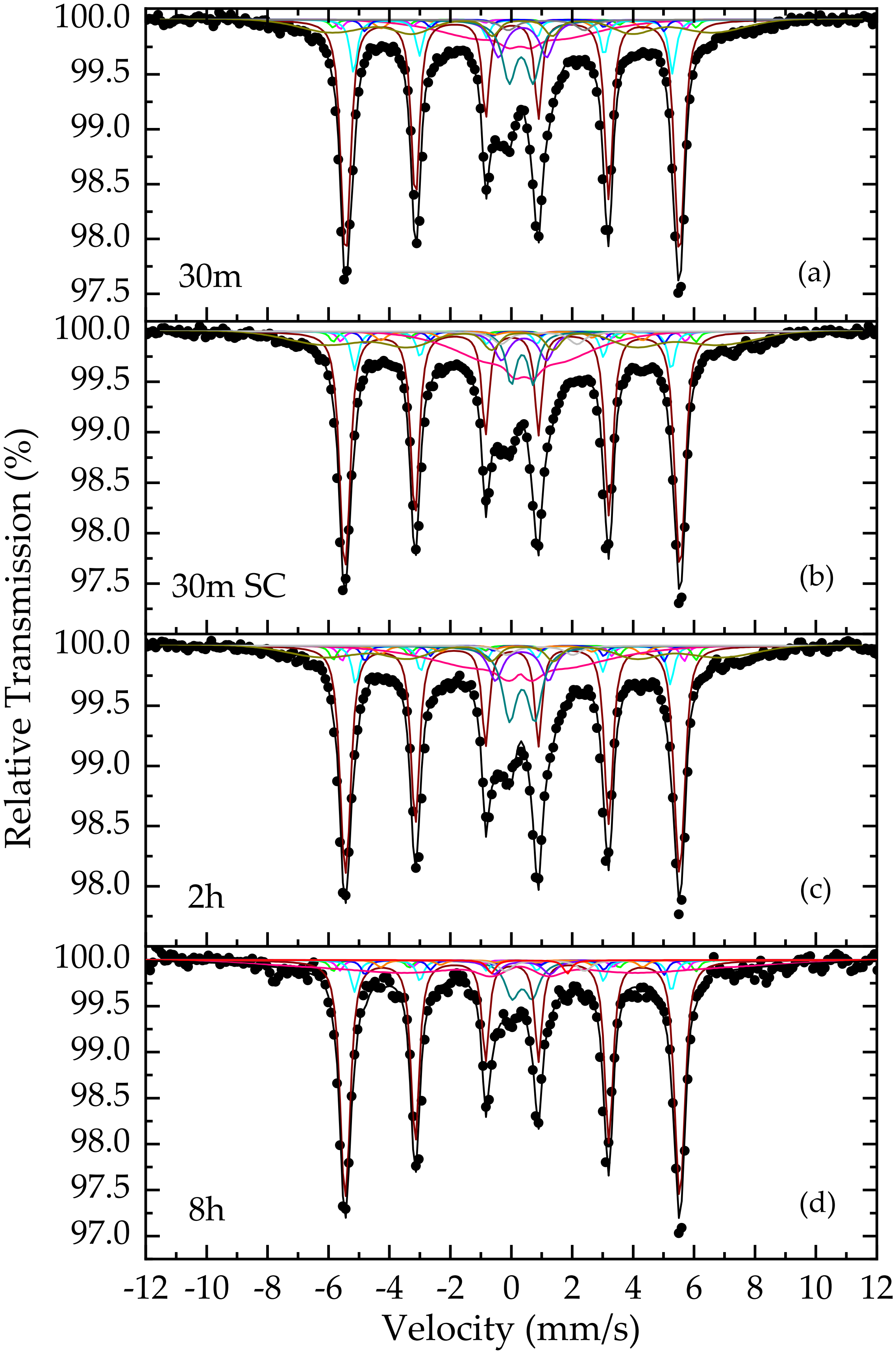

Figure 6.32 Fitted ^{57}Fe Mössbauer spectra of the ^{57}Fe enriched En-IM-NHD6-700,30m (a), En-IM-NHD6-700,30m-SC (b), En-IM-NHD6-700,2h (c) and En-IM-NHD6-700,8h (d) samples collected at 11 K.

Table 6.18 Mössbauer hyperfine parameters as resulting from the best fits of the corresponding spectra of the samples shown on **Figure 6.32**. IS the isomer shift (given relative to α-Fe at 300 K), Γ/2 is the half line-width, QS is the quadrupole splitting, 2ε is the quadrupole shift, B_{hf}^{C} is the central value of the hyperfine magnetic field, ΔB_{hf} is the total spreading (Gaussian-type) of the B_{hf} values around the central B_{hf}^{C} value, and AA is the relative spectral absorption area of each component used to fit the spectra. Typical errors are ±0.02 mm/s for IS, Γ/2, 2ε and QS, ±3 kOe for B_{hf}^{C} and ±3% for AA.

Sample	**Component**	**I.S. (mm/s)**	**Γ/2 (mm/s)**	**QS or 2ε (mm/s)**	**B_{hf}^{C} (kOe)**	**ΔBhf (kOe)**	**Area (%)**	**Color**
En-IM-NHD6-700C,30m	$Fe_{33}Co_{67}$	0.14	0.14	0.02	340	5	46	Maroon
	Martensitic Fe-Co (1)	0.21	0.14	0.01	370	0	1	Green
	Martensitic Fe-Co (2)	0.16	0.14	0.01	352	0	1	Magenta
	Martensitic Fe-Co (3)	0.14	0.14	0.04	325	0	8	Cyan
	Martensitic Fe-Co (4)	0.26	0.14	-0.09	305	0	2	Blue
	Martensitic Fe-Co (5)	0.20	0.21	-0.15	267	3	2	Orange
	MCOL Fe^{3+}	0.40	0.15	0.00	150	93	12	Pink
	MCOL Fe^{3+}	0.47	0.15	0.00	387	60	11	Dark Yellow
	SPM Fe^{3+} (1)	0.43	0.27	0.79	0	0	8	Dark Cyan
	SPM Fe^{3+} (2)	0.48	0.28	1.58	0	0	4	Purple
	SPM Fe^{2+}	1.19	0.32	2.41	0	0	5	Grey
En-IM-NHD6-700C,30m -SC (**S**low Cooling)	$Fe_{33}Co_{67}$	0.14	0.14	0.02	342	6	41	Maroon
	Martensitic Fe-Co (1)	0.21	0.14	0.01	370	0	2	Green
	Martensitic Fe-Co (2)	0.16	0.14	0.01	352	0	3	Magenta
	Martensitic Fe-Co (3)	0.14	0.14	0.04	323	0	6	Cyan
	Martensitic Fe-Co (4)	0.26	0.14	-0.09	305	0	4	Blue
	Martensitic Fe-Co (5)	0.20	0.21	-0.15	267	5	2	Orange
	MCOL Fe^{3+}	0.53	0.14	0.00	130	85	15	Pink

	MCOL Fe^{3+}	0.47	0.15	0.00	398	72	14	Dark Yellow
	SPM Fe^{3+} (1)	0.47	0.20	0.73	0	0	4	Dark Cyan
	SPM Fe^{3+} (2)	0.53	0.28	1.42	0	0	4	Purple
	SPM Fe^{2+}	1.08	0.32	2.50	0	0	5	Grey
En-IM-NHD6-700C,2h	$Fe_{33}Co_{67}$	0.14	0.14	0.02	341	6	41	Maroon
	Martensitic Fe-Co (1)	0.21	0.14	0.01	370	0	2	Green
	Martensitic Fe-Co (2)	0.16	0.14	0.01	349	0	2	Magenta
	Martensitic Fe-Co (3)	0.14	0.14	0.04	321	0	6	Cyan
	Martensitic Fe-Co (4)	0.26	0.14	-0.09	305	0	2	Blue
	Martensitic Fe-Co (5)	0.20	0.21	-0.15	267	3	2	Orange
	MCOL Fe^{3+} (1)	0.40	0.14	0.00	124	117	15	Pink
	MCOL Fe^{3+} (2)	0.44	0.15	0.00	403	67	11	Dark Yellow
	SPM Fe^{3+} (1)	0.47	0.28	0.83	0	0	10	Dark Cyan
	SPM Fe^{3+} (2)	0.46	0.28	1.72	0	0	5	Purple
	SPM Fe^{2+}	1.05	0.32	2.16	0	0	4	Grey
En-IM-NHD6-700C,8h	$Fe_{33}Co_{67}$	0.14	0.14	0.02	347	6	54	Maroon
	Martensitic Fe-Co (1)	0.21	0.14	0.01	370	0	2	Green
	Martensitic Fe-Co (2)	0.16	0.14	0.01	353	0	2	Magenta
	Martensitic Fe-Co (3)	0.14	0.14	0.04	324	0	6	Cyan
	Martensitic Fe-Co (4)	0.26	0.14	-0.09	305	0	3	Blue
	Martensitic Fe-Co (5)	0.20	0.18	-0.15	269	0	2	Orange
	MCOL Fe^{3+}	0.40	0.14	0.00	359	160	19	Pink
	SPM Fe^{3+} (1)	0.47	0.28	0.74	0	0	6	Dark Cyan
	SPM Fe^{3+} (2)	0.46	0.28	1.84	0	0	3	Purple

	SPM Fe^{2+} (1)	1.11	0.28	2.60	0	0	2	Grey
	SPM Fe^{2+} (2)	0.95	0.16	2.55	0	0	1	Red

6.4 Magnetization and Magnetic Susceptibility Measurements

The magnetic properties of both nanohybrid and unsupported samples, prepared using the $NaBH_4$ reducing agent, as well as those of the conventional nanohybrid and ^{57}Fe-enriched samples synthesized via the impregnation method, are further characterized by their M vs. H measurements at constant temperature and χ_g vs. T measurements at constant H. These magnetic measurements reveal the magnetic behavior of the prepared samples, which is influenced by the relative compositions of the contained phases, the types of nanostructures, and the magnetic interactions and interconnections of the NPs present in these samples.

6.4.1 Samples prepared using the sodium borohydride reducing agent

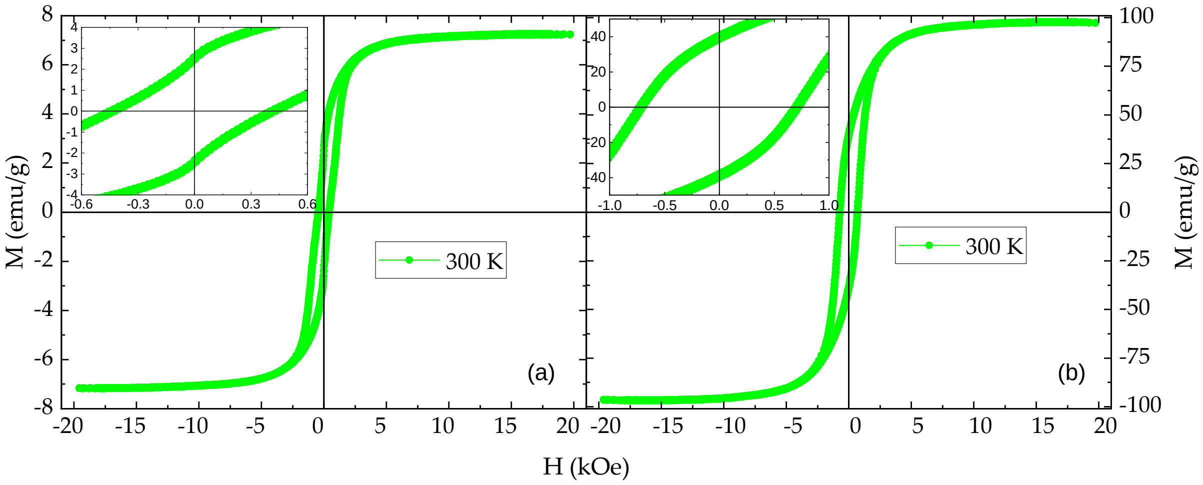

Figure 6.33 Magnetization vs. applied magnetic field isothermal loops of the BH-AM1-NHD (a) and BH- AM1-NP (b) samples measured at RT (300 K). The inset (upper left) in each measurement shows the details of the loops' characteristics around zero applied magnetic field.

The M vs. H loop for the BH-AM1-NHD sample collected at 300 K appearing in Figure 6.33a, demonstrates a distinct ferro/ferrimagnetic response with hysteresis and a coercivity of approximately 430 Oe (see the magnetic characteristics of the loops listed in Table 6.19). There is, however, a slight tendency for incomplete saturation of M at high fields. The inset of Figure 6.33a shows that M fluctuates near H = 0, hinting at two magnetic contributions: one with a harder magnetic characteristic responsible for non-zero coercivity (Hc) values, and another softer component that causes the relative abrupt M variation around H = 0. These features suggest a mixture of ferro/ferrimagnetic Fe-Co/ICO NPs with both hard and soft magnetic characteristics, likely due to variations in composition, particle size and magnetic interparticle interaction strengths [9], [14], [24], [25]. It can also be possible that these magnetic NPs could adopt a core-shell structure, with a ferromagnetic Fe-Co alloy core and a ICO shell, as the BH method is capable to develop NPs with such morphology [26]. The larger or more strongly interacting NPs dominate the total magnetic behavior of the sample, given by the Hc values of ~ 430 Oe found at RT, indicating that the majority of the magnetic NPs are magnetically blocked at this temperature [9], [10]. Moreover, the increased H_C value found for this sample relative to the corresponding values observed for the soft magnetic bulk Fe-Co alloys and ICO that lie in the range of 10–65 Oe [27], suggest that these NPs should be affected by finite size effects, which are known to increase the H_C values as the size of the NPs approaches or reaches the single-magnetic-domain size limit [25]. Meanwhile, the smaller or weakly interacting ICO NPs are identified by their softer magnetic characteristics and the lack of M values saturation, presenting superparamagnetic characteristics at RT. Considering the Mössbauer spectroscopy results for this sample, we can verify by the present M vs. H measurements the existence of the Fe-Co alloy and ICO nanostructured phases and their strong SPM characteristics.

For the FeCo-BH-AM1-NP sample, the M vs. H loop at RT (Figure 6.33b) reveals similar magnetic behavior to the nanohybrid sample, but with smoother M variations around H = 0 and a higher saturation value at high fields. This is expected, however, as the FeCo-BH-AM1-NP sample is designed to contain only the Fe-Co alloy phase. The sample exhibits a symmetric hysteresis loop with a coercivity of 720 Oe at RT (Table 6.19). These observations imply that the ferromagnetic Fe-Co NPs in this sample experience stronger interparticle magnetic interactions. The NPs are likely to be accumulated in agglomerates that contribute to the increased Hc values [9], [25], [26], [28] . These characteristics indicate a system where the magnetic behavior is shaped by strongly interacting Fe-Co NPs with close proximity and interconnection, corroborating the findings from XRD, TEM, and ^{57}Fe Mössbauer spectroscopy analyses.

Table 6.19 Parameters of the magnetic properties derived from the isothermal loops of **Figure 6.33**.

Sample	**T (K)**	**M_{max} (emu/g)**	**M_{min} (emu/g)**	**M_{R+} (emu/g)**	**M_{R-} (emu/g)**	**H_{C+} (Oe)**	**H_{C-} (Oe)**
BH-AM1-ND	300	7.2	-7.2	2.4	-2.5	421	-442
BH-AM1-NP	300	97.6	-97.6	39.4	-39.8	722	-718

6.4.2 Samples prepared using the impregnation method

6.4.2.1 As-made impregnated precursor samples

The M vs. H isothermal loops for all as-made nanohybrid precursor samples prepared via the impregnation method are displayed in Figure 6.34. In general, the loops of all samples at RT exhibit SPM behavior with ferro/ferrimagnetic sigmoidal shape and non-saturating M values. In some cases, non-zero coercive fields are observed. The M values at high fields and other loop properties for each as-made sample are summarized in Table 6.20.

Specifically, the isothermal loops of all but the FeCo-IM-AM2-NHD sample recorded at RT (Figures 6.34a, c, d, e and f) show SPM behavior with M values at 20 kOe not exceeding 1.0 emu/g. On the contrary the FeCo-IM-AM2-NHD sample acquires an M value at 20 kOe which exceeds 5.0 emu/g. These characteristics indicate a system of ferrimagnetic-type ICO NPs in the FeCo-IM-AM2-NHD sample with relatively larger average sizes and broader size distributions, that undergo slower SPM relaxation compared to the assembly of ICO NPs of the other as-made samples which experience faster SPM relaxation. The magnetic behavior in the FeCo-IM-AM2-NHD sample likely results from stronger interparticle interactions due to the increased size of the corresponding ICO NPs [9], [10], [25], [28]. These observations align with findings from previous XRD, TEM and ^{57}Fe Mössbauer spectroscopy characterization techniques.

The coercivity values for all samples lie between ~ 20 and ~120 Oe at RT. These values indicate that most magnetic NPs in these samples are influenced by very fast SPM relaxation, although there must be a distribution of NPs sizes in each sample, which is similar for all but the FeCo-IM-AM2-NHD sample, that gives rise to the variance of the H_C values as a consequence of finite size effects [25]. For the IM-AM5-NHD sample at 2 K, a ferro/ferrimagnetic sigmoidal curve emerges with non-saturating M values and non-zero, asymmetric coercive fields. This characteristic suggests an assembly of ICO NPs that exhibit complete SPM behavior at RT and partial magnetic blocking at 2 K.

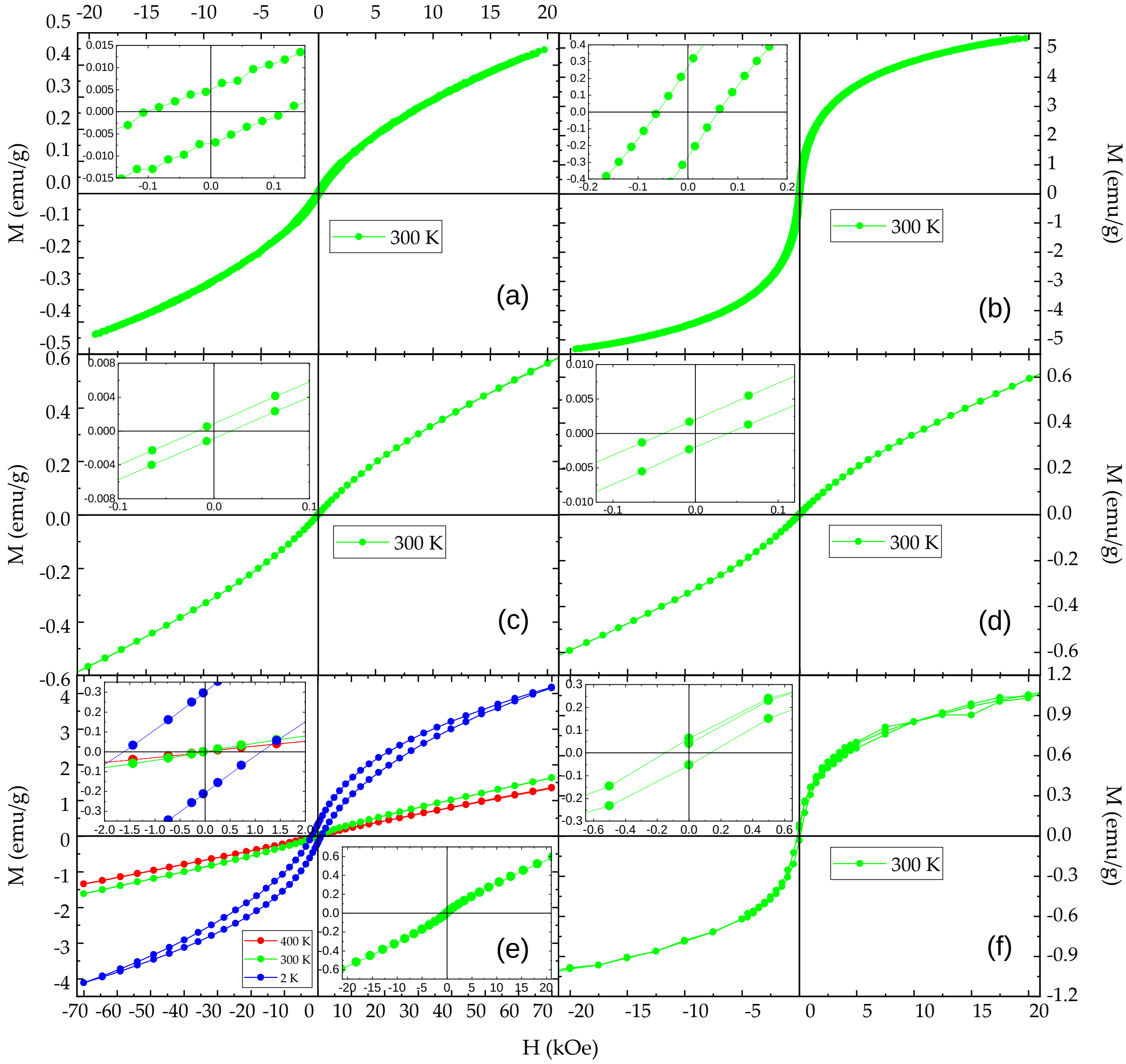

Figure 6.34 Magnetization vs. applied magnetic field isothermal loops of the IM-AM1-NHD (a), IM-AM2-NHD (b), IM-AM3-NHD (c), IM-AM4-NHD (d), IM-AM5-NHD (e) and En-IM-AM6-NHD (f) samples measured at different temperatures indicated by different colors. The insets in each set of measurements show the details of the loops' characteristics around zero applied magnetic field for all temperatures (upper left).

Table 6.20 Parameters of the magnetic properties derived from the isothermal loops of **Figure 6.34**. The external field applied for the measurements of the IM-AM1-NHD (6.34a), IM-AM2-NHD (6.34b), IM-AM3-NHD (6.34c), IM-AM4-NHD (6.34d) and IM-En-AM6-NHD (6.34f) samples was 20 kOe, while for the IM-AM5-NHD (6.34e) sample it was 70 kOe.

Sample	**Figure 6.34**	**T (K)**	**M_{max+} (emu/g)**	**M_{max-} (emu/g)**	**M_{R+} (emu/g)**	**M_{R-} (emu/g)**	**H_{C+} (Oe)**	**H_{C-} (Oe)**
IM-AM1-NHD	a	300	0.45	-0.45	0.005	-0.008	119	-112
IM-AM2-NHD	b	300	5.3	-5.3	0.26	-0.31	62	-64
IM-AM3-NHD	c	300	0.6	-0.6	0.001	-0.001	19	-18
IM-AM4-NHD	d	300	0.6	-0.6	0.002	-0.002	40	-39
IM-AM5-NHD	e	400	1.35	-1.35	0	0	0	0
		300	1.55	-1.55	0	0	0	0
		2	4.1	-4.1	0.3	-0.26	1235	-1670
En-IM-AM6-NHD	f	300	1.1	-1.1	0.001	-0.001	130	-145

6.4.2.2 Annealed impregnated samples

The annealing treatment causes different evolutions of magnetic properties between the as-made nanohybrid and enriched as-made nanohybrid samples to arise. In this respect, in Figures 6.35-6.36, the characteristic M vs. H loops under constant T and the and χ_g vs. T measurements under constant H, respectively, are shown for the IM-NHD5-700C,30m and En-IM-NHD6-700,30m-SC samples.

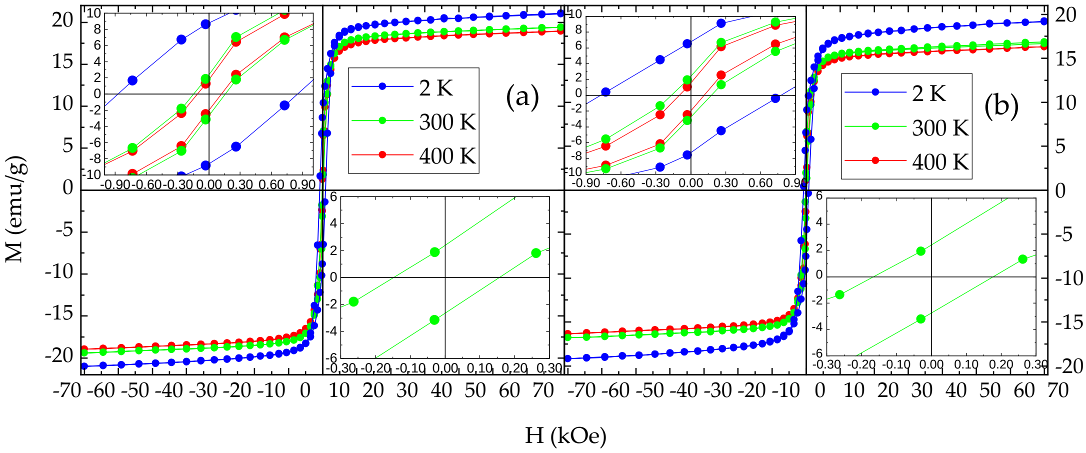

Figure 6.35 Magnetization vs. applied magnetic field isothermal loops of the NHD-700,30m (a) and En-NHD-700,30m-SC (b) samples measured at different temperatures indicated by different colors. The insets in each set of measurements show the details of the loops' characteristics around zero applied magnetic field for all temperatures (upper left) and with even more detail for the 300 K loop (lower right).

The M vs. H isothermal loops of the IM-NHD5-700,30m and En-IM-NHD6-700,30m-SC samples recorded at 400, 300, and 2 K reveal clear FM characteristics with hysteresis, exhibiting coercivities that range from about 100 to about 900 Oe depending on temperature (see Table 6.21). These characteristics are accompanied, however, by constant and non-vanishing dM/dH slopes at high H values at all temperatures. These features correspond to an assembly of Fe–Co NPs with FM order and relative harder magnetic characteristics compared to the nominal coercivities found for typical bulk Fe–Co alloys that reach only about 65 Oe at RT [27]. The non-vanishing dM/dH slopes at high H values denote a second non-FM contribution that can be attributed to the spinel-type ICO NPs found to be present in these samples, which, due to their very small particle size, experience very fast SPM relaxation at all temperatures. Moreover, the large increase in the coercive fields between 400, 300, and 2 K indicates that the assembly of Fe–Co FM NPs should also experience SPM relaxation, which gradually ceases as T decreases, and, in particular—more substantially at 2 K—as the majority of the metallic NPs in the assembly becomes magnetically blocked [29].

Table 6.21 Magnetic characteristics derived from the isothermal loops of **Figure 6.35**.

Sample	**T (K)**	**M_{max+} (emu/g)**	**M_{max-} (emu/g)**	**M_{R+} (emu/g)**	**M_{R-} (emu/g)**	**H_{C+} (Oe)**	**H_{C-} (Oe)**
IM-NHD5-700,30m	400	18.9	−18.9	1.7	−2.0	112	−112
	300	19.4	−19.4	2.3	−2.7	160	−152
	2	21.1	−21.1	8.7	−8.6	856	−881
En-IM-NHD6-700,30m-SC	400	16.3	−16.4	1.6	−1.9	114	−98
	300	16.7	−16.8	2.5	−2.7	177	−169
	2	19.2	−19.2	6.8	−7.2	781	−776

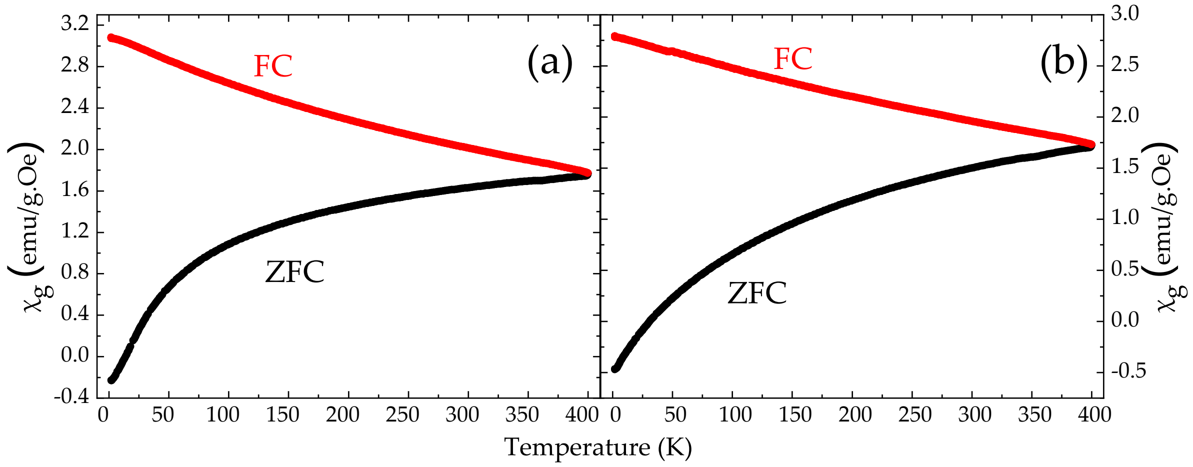

Figure 6.36 Magnetic susceptibility vs. temperature measurements of the non-enriched IM-NHD5-700,30m (a) and ^{57}Fe-enriched En-IM-NHD6-700,30m-SC (b) samples under an applied field of 99 Oe.

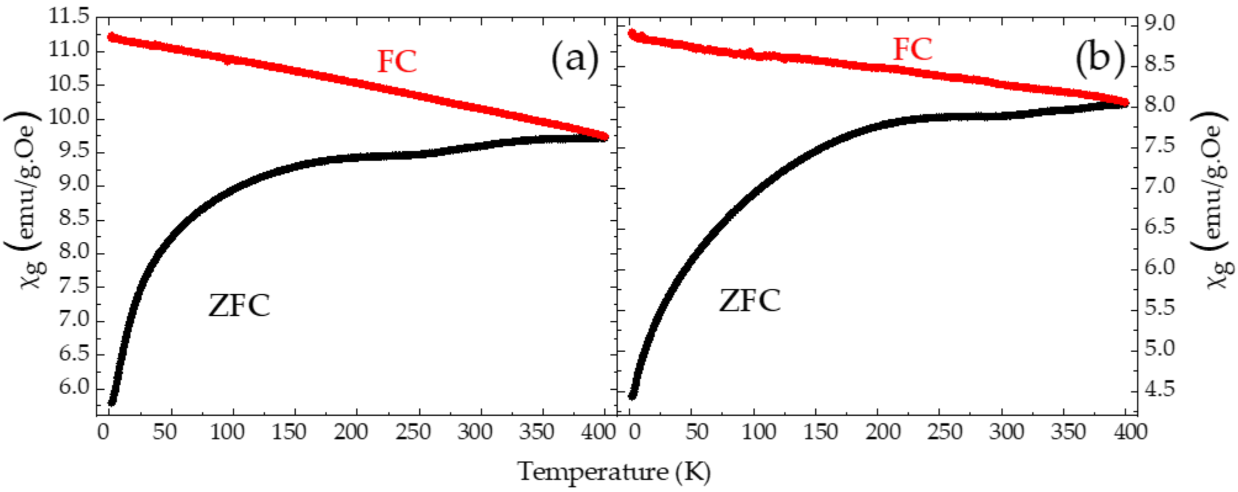

Figure 6.37 Magnetic susceptibility vs. temperature measurements of the non-enriched IM-NHD5-700,30m (a) and ^{57}Fe-enriched En-IM-NHD6-700,30m-SC (b) samples under an applied field of 999 Oe.

The χ_g vs. T measurements of both samples recorded under an applied field of 99 Oe are shown in Figure 6.36 and reflect again the characteristics revealed by the M vs. H measurements, which are attributed to an assembly of Fe–Co FM NPs accompanied by SPM relaxation features. In both diagrams, the χ_g values of the ZFC branches monotonically increase as T increases, with no local maxima up to 400 K, while the FC branches are much smoother and continuously rise as T decreases. The coincidence of the two branches only at the highest measured temperature point of 400 K for both samples suggests a relatively broad size distribution for the magnetically ordered nanophases contained in these samples. The magnetic behavior of the system is clearly determined by the larger-in-size or/and more strongly magnetically interacting metallic Fe–Co NPs, which are magnetically blocked even at 400 K, as demonstrated from the existence of hysteresis in the M vs. H loops [9]. On the other hand, the smaller-in-size or/and weakly magnetically interacting metallic Fe–Co NPs, as well as the SPM ICO NPs, reveal their contribution to the M vs. H and χ_g vs. T measurements mainly through the lack of saturation for the magnetization at high H values recorded in all temperatures. Similar behaviors are obtained in the χ_g vs. T measurements of both annealed samples recorded under an applied field of 999 Oe (Figure 6.37). There, however, the ZFC branches contain a minor local maximum around 200 K for both samples, suggesting a slight diversification in the SPM relaxation behavior for different assemblies of magnetic NPs originating from the differences in the stoichiometry, in the sense of the presence of both Fe–Co and ICO NPs, their size distribution, and interparticle interactions strength, which can be revealed only at higher H values in these measurements [7]. Moreover, the differences in the Fe–Co and ICO NP content in each sample could also justify the slightly higher maximum M and χ_g values observed for the IM-NHD5-700,30m sample relative to those found for the En-IM-6NHD-700,30m-SC sample. As the nominal M values are higher for the Fe–Co phase relative to those of the ICO phase, the higher amount of ICO NPs evident by Mössbauer spectroscopy measurements for the En-IM-NHD6-700,30m-SC sample is proposed to be the cause of its reduced M and χ_g values relative to those found for the IM-NHD5-700,30m sample.

In this context, the characteristic M vs. H and χ_g vs. T measurements, collected for all conventional and enriched samples annealed at various temperatures and durations, display similar magnetic features to those described for the previously mentioned IM-NHD5-700,30m and En-IM-6NHD-700,30m-SC samples. These features include assemblies of larger or more strongly magnetically interacting FM Fe-Co NPs, which exhibit magnetic blocking even at 400 K and predominantly influence the magnetic behavior of each sample. However, the smaller or more weakly interacting metallic Fe-Co NPs, as well as the SPM ICO NPs, contribute to the M vs. H and χ_g vs. T measurements mainly by the absence of saturation of M at high H values, recorded across all temperatures. The characteristic M vs. H and χ_g vs. T measurements of all samples with $H_{ap} = 99$ Oe and $H_{ap} = 999$ Oe are shown in Figures 6.38-6.49, while the resulting parameters of the magnetic properties derived from the respective isothermal loops of all samples at 300 and 2 K are listed in Table 6.22.

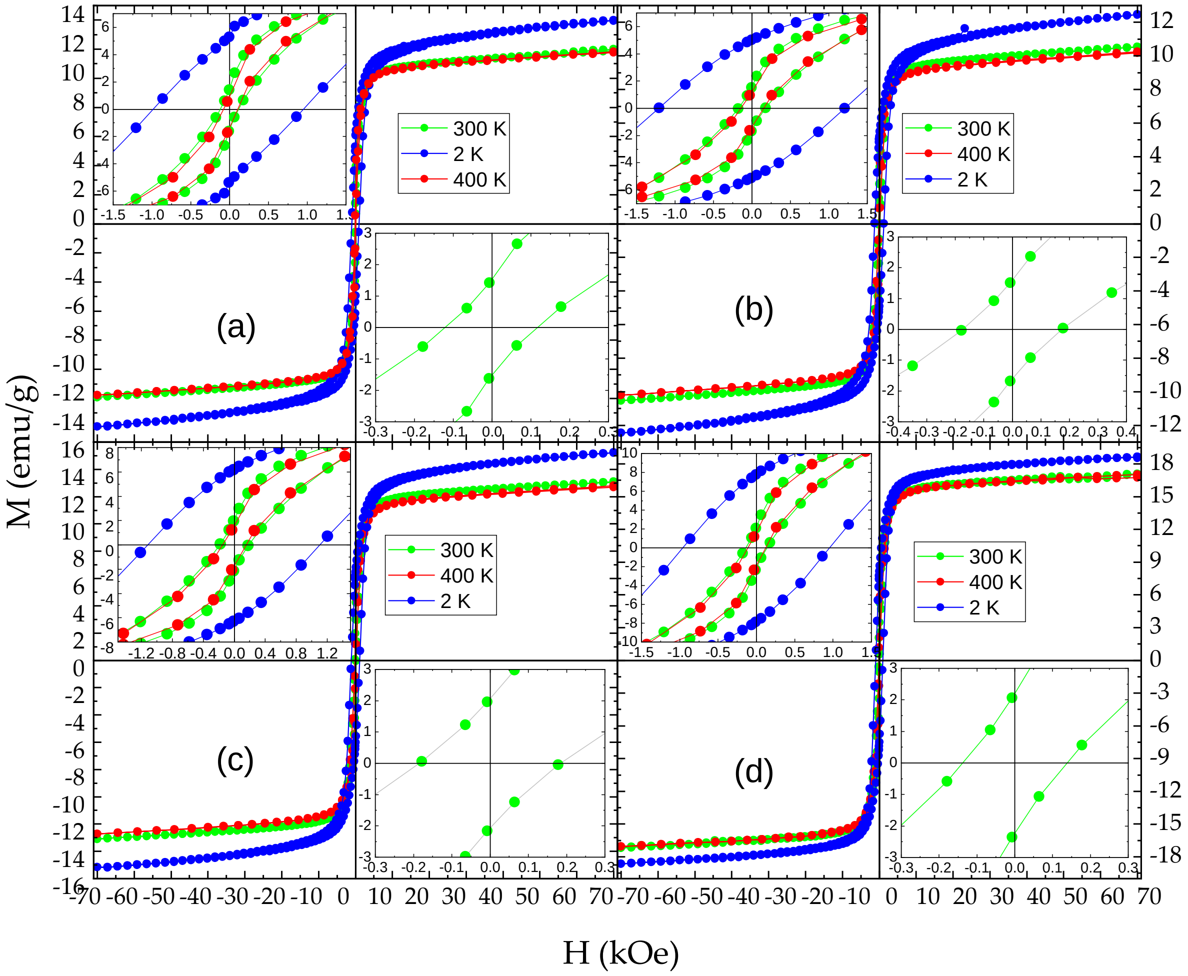

Figure 6.38 Magnetization vs. applied magnetic field isothermal loops of the IM-NHD4-600C,30m (a), IM-NHD5-600C,2h (b), IM-NHD5-600C,8h (c) and IM-NHD4-600C,32h (d) samples measured at different temperatures indicated by different colors. The insets in each set of measurements show the details of the loops' characteristics around zero applied magnetic field for all temperatures (upper left) and with even more detail for the 300 K loop (lower right).

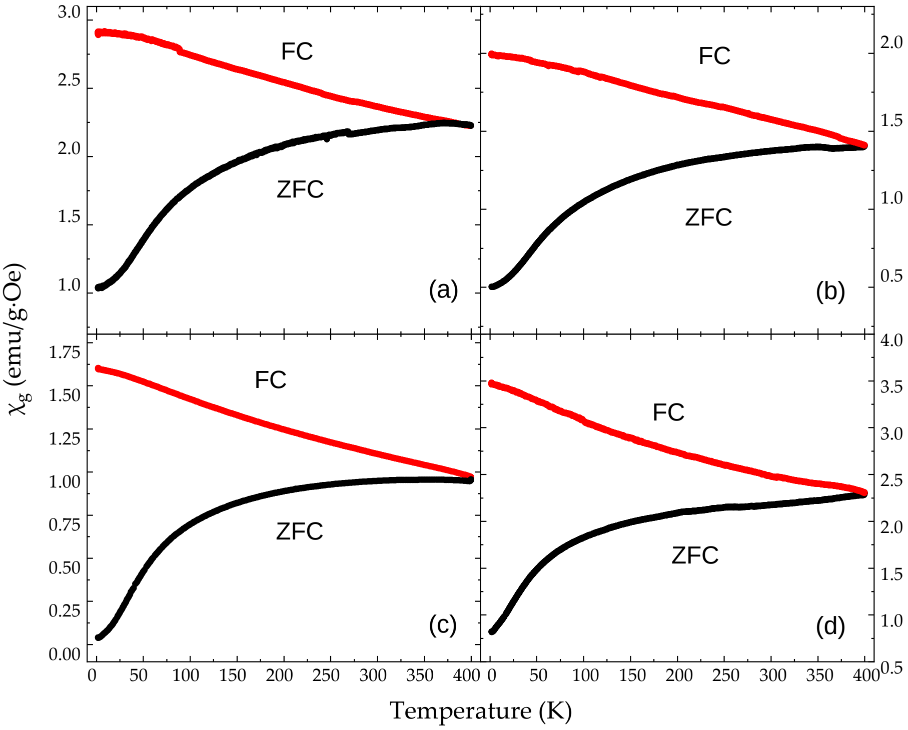

Figure 6.39 Magnetic susceptibility vs. temperature measurements of the IM-NHD4-600C,30m (a), IM-NHD5-600C,2h (b), IM-NHD5-600C,8h (c) and IM-NHD4-600C,32h (d) samples under an applied field of 99 Oe.

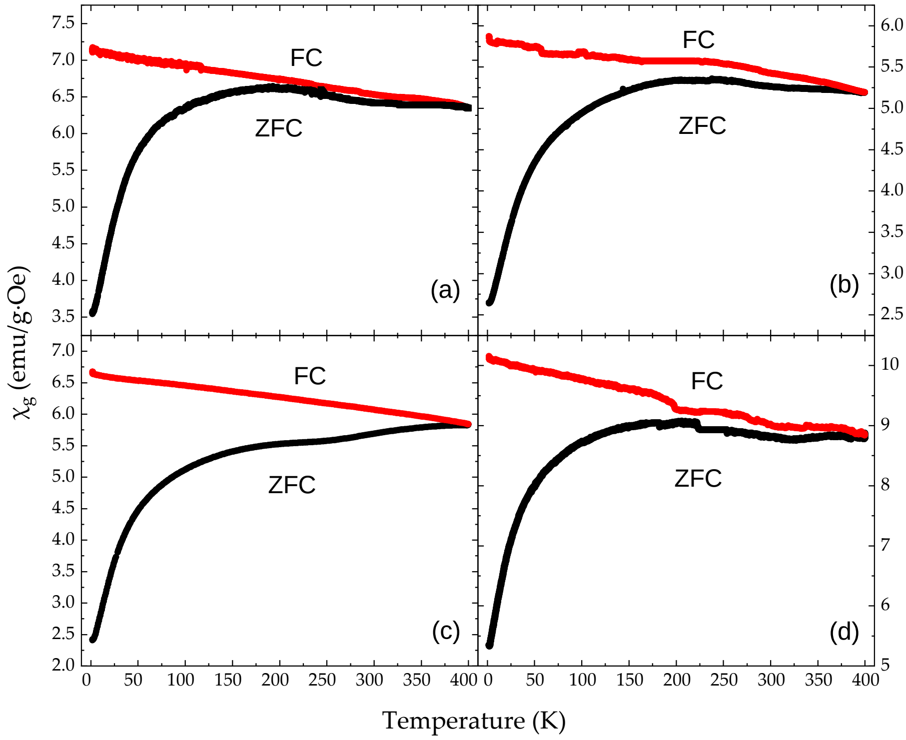

Figure 6.40 Magnetic susceptibility vs. temperature measurements of the IM-NHD4-600C,30m (a), IM-NHD5-600C,2h (b), IM-NHD5-600C,8h (c) and IM-NHD4-600C,32h (d) samples under an applied field of 999 Oe.

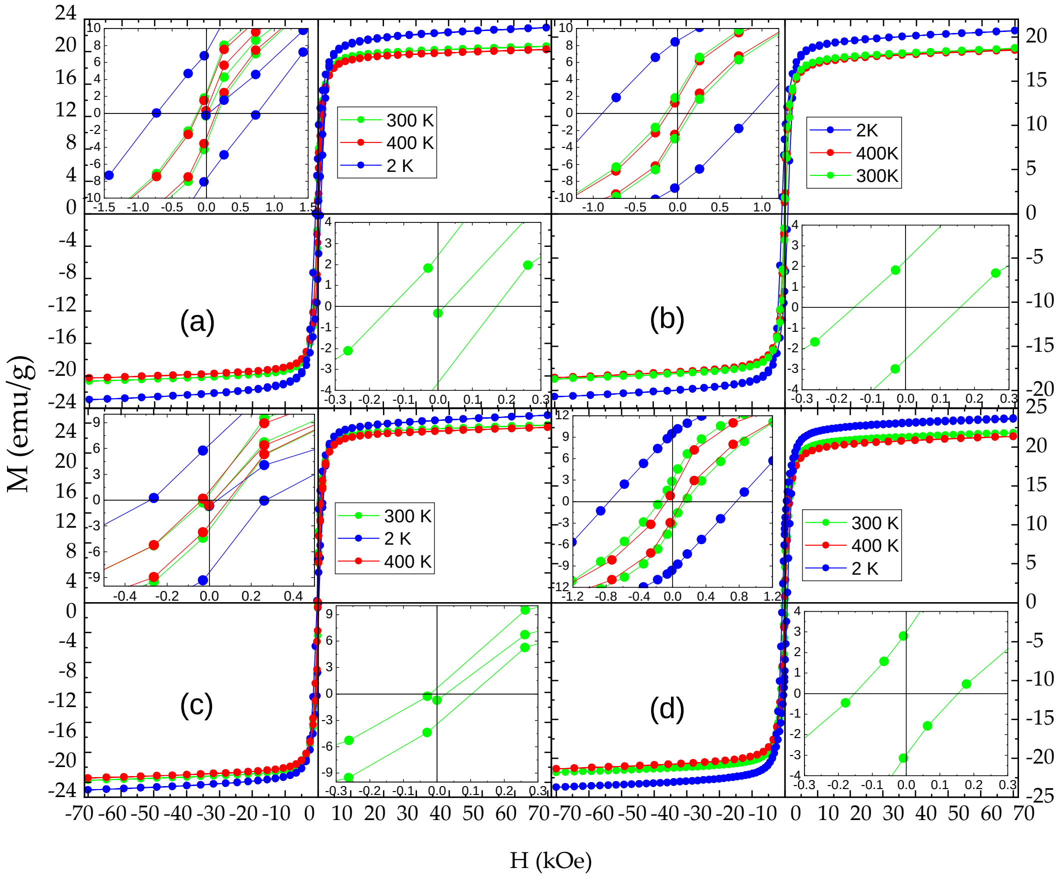

Figure 6.41 Magnetization vs. applied magnetic field isothermal loops of the IM-NHD3-650,30m (a), IM-NHD4-650,2h (b), IM-NHD3-650,8h (c) and IM-NHD4-650,32h (d) samples measured at different temperatures indicated by different colors. The insets in each set of measurements show the details of the loops' characteristics around zero applied magnetic field for all temperatures (upper left) and with even more detail for the 300 K loop (lower right).

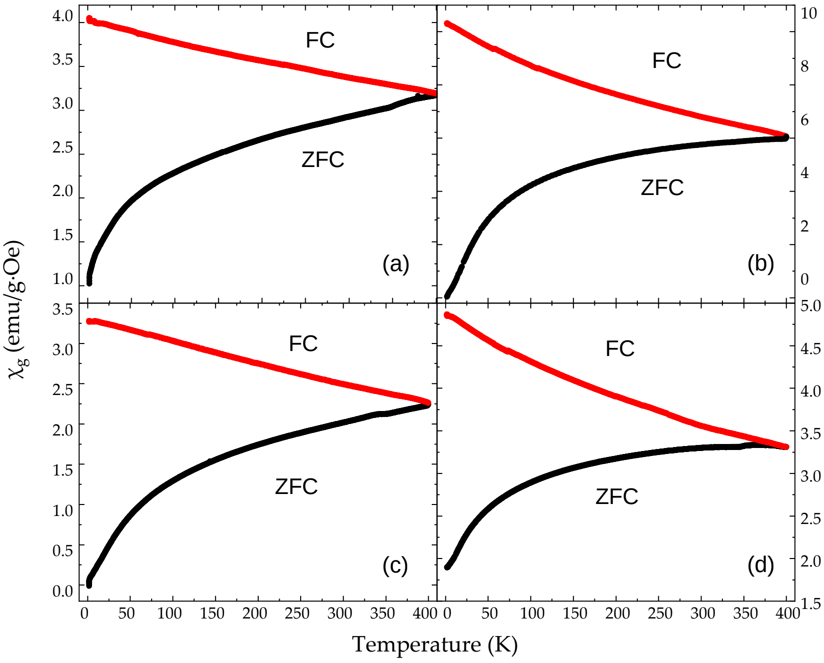

Figure 6.42 Magnetic susceptibility vs. temperature measurements of the IM-NHD3-650,30m (a), IM-NHD4-650,2h (b), IM-NHD3-650,8h (c) and IM-NHD4-650,32h (d) samples under an applied field of 99 Oe.

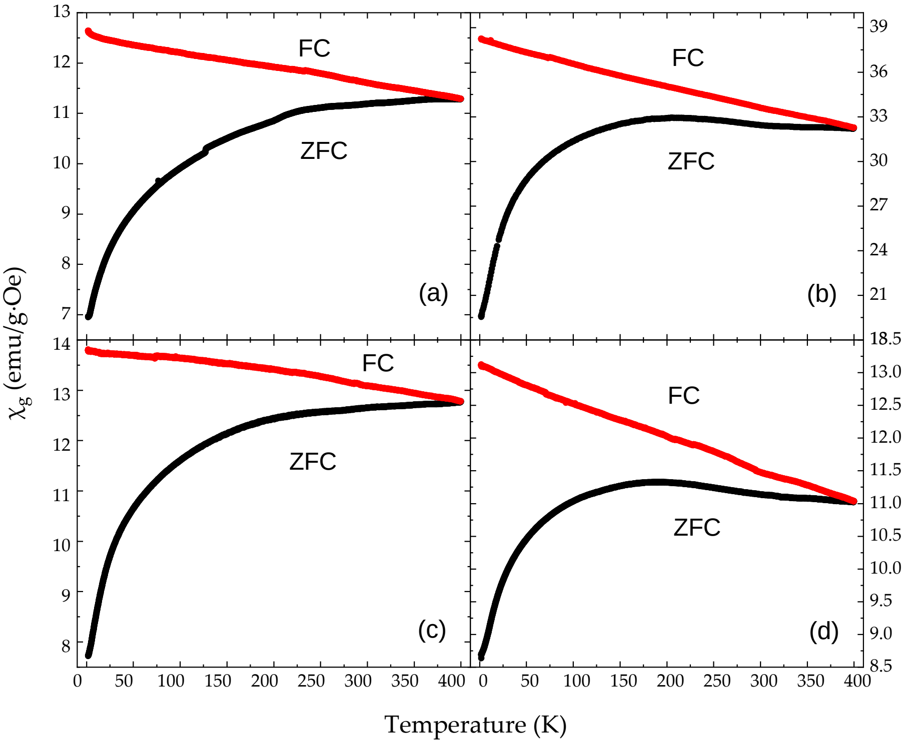

Figure 6.43 Magnetic susceptibility vs. temperature measurements of the IM-NHD3-650,30m (a), IM-NHD4-650,2h (b), IM-NHD3-650,8h (c) and IM-NHD4-650,32h (d) samples under an applied field of 999 Oe.

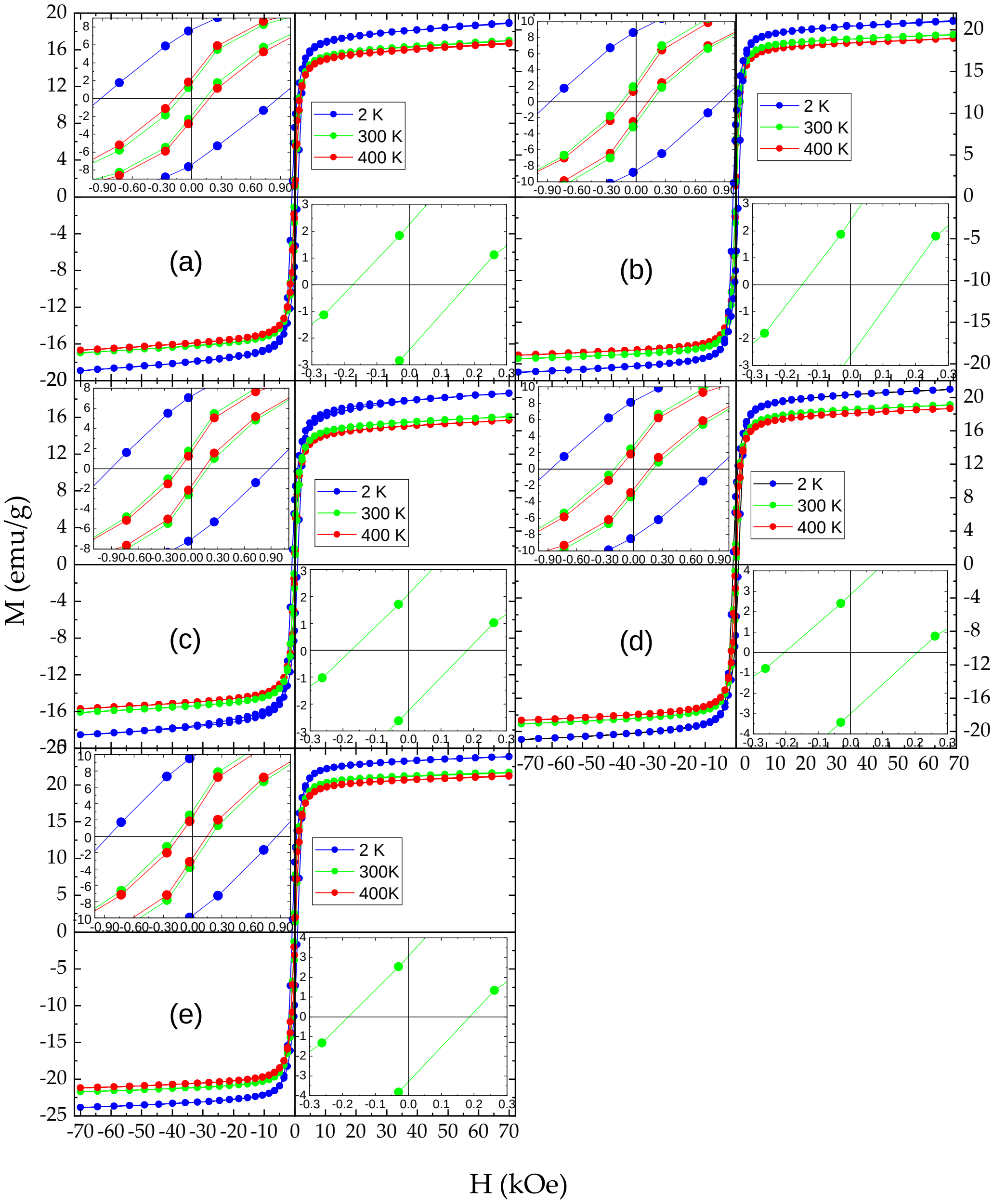

Figure 6.44 Magnetization vs. applied magnetic field isothermal loops of the IM-NHD5-700,2s (a), IM-NHD5-700,30m (b), IM-NHD5-700,2h (c), IM-NHD5-700,8h (d), IM-NHD5-700,32h (e) samples measured at different temperatures indicated by different colors. The insets in each set of measurements show the details of the loops' characteristics around zero applied magnetic field for all temperatures (upper left) and with even more detail for the 300 K loop (lower right).

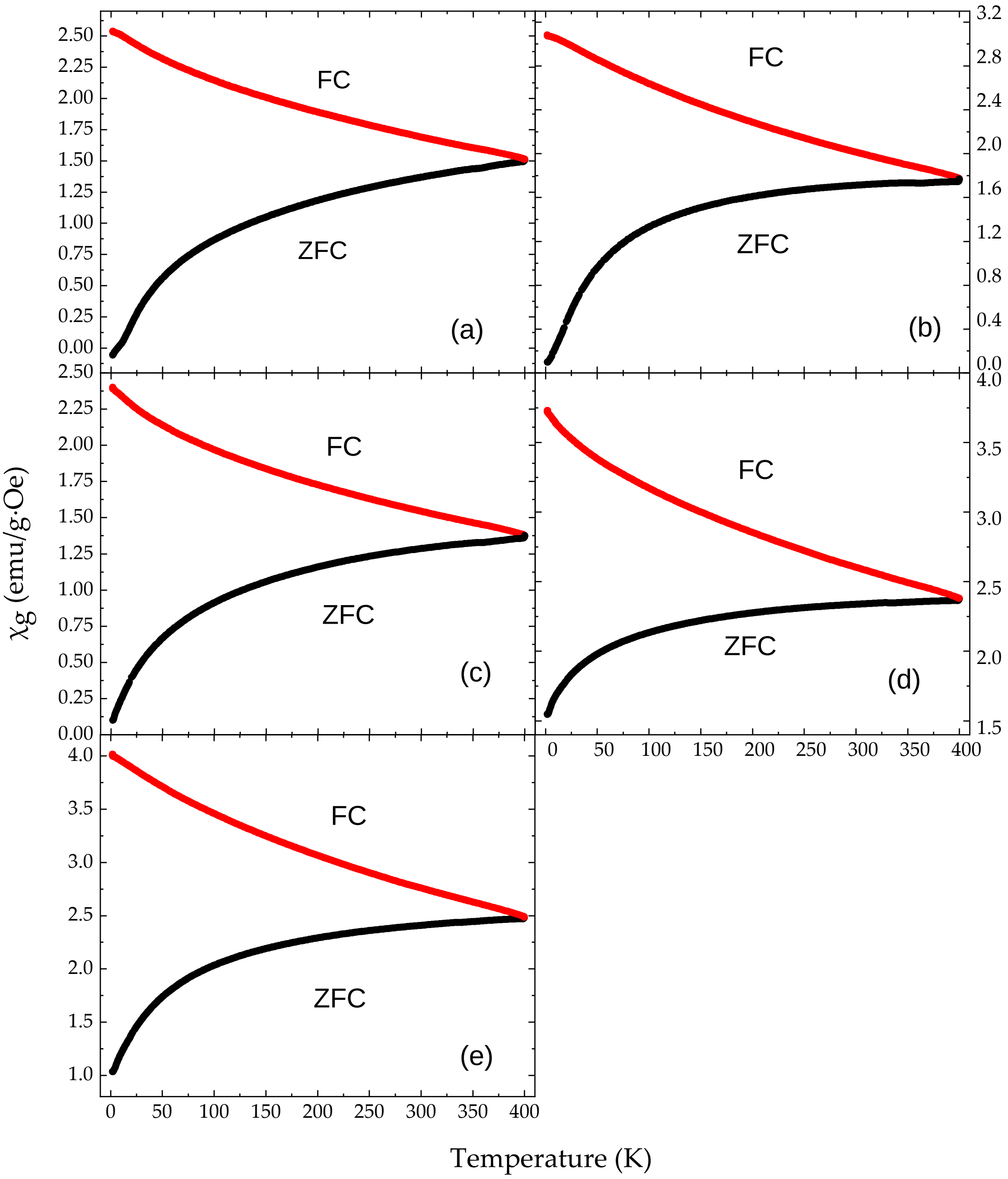

Figure 6.45 Magnetic susceptibility vs. temperature measurements of the IM-NHD5-700,2s (a), IM-NHD5-700,30m (b), IM-NHD5-700,2h (c), IM-NHD5-700,8h (d), IM-NHD5-700,32h (e) samples under an applied field of 99 Oe.

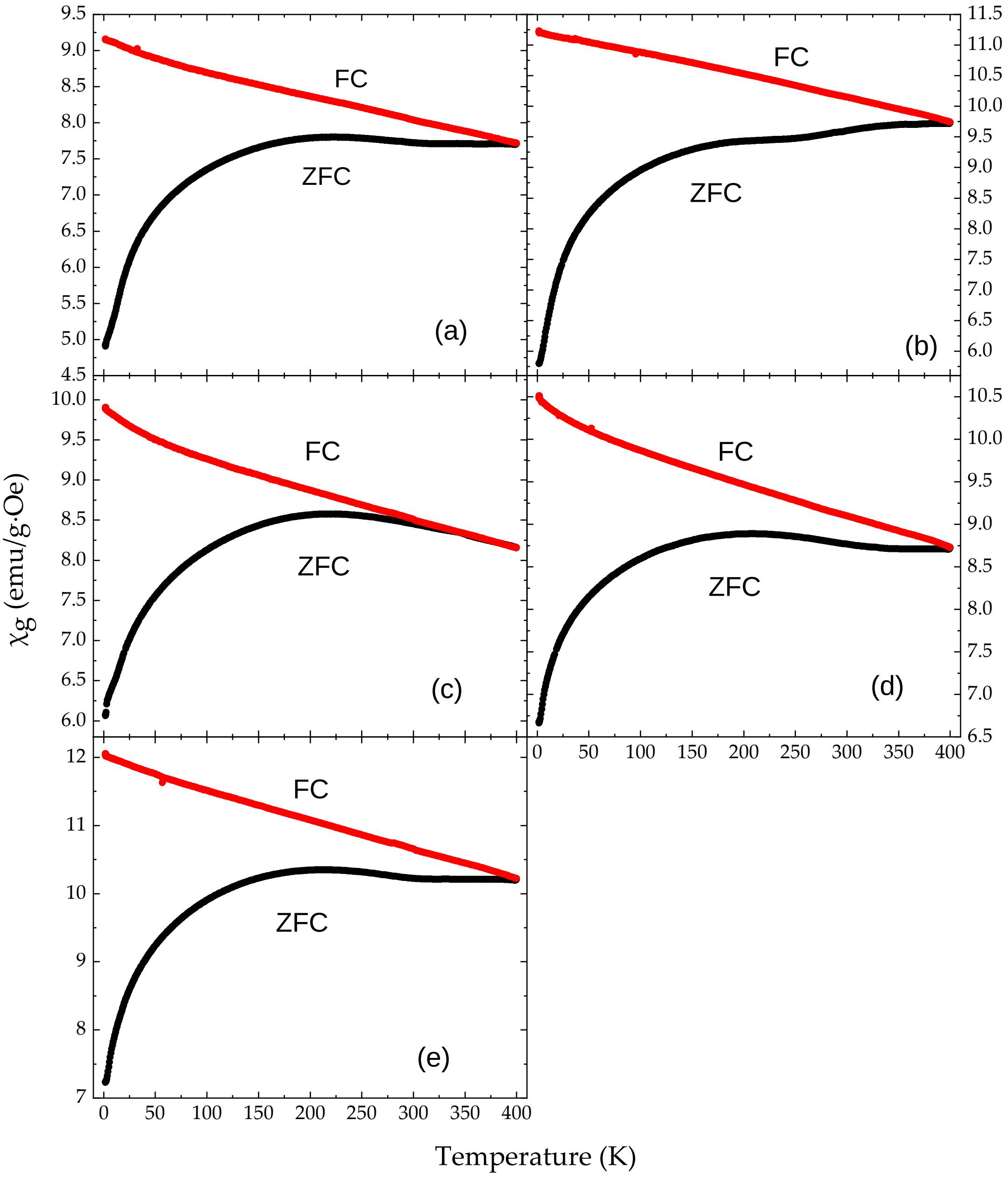

Figure 6.46 Magnetic susceptibility vs. temperature measurements of the IM-NHD5-700,2s (a), IM-NHD5-700,30m (b), IM-NHD5-700,2h (c), IM-NHD5-700,8h (d), IM-NHD5-700,32h (e) samples under an applied field of 999 Oe.

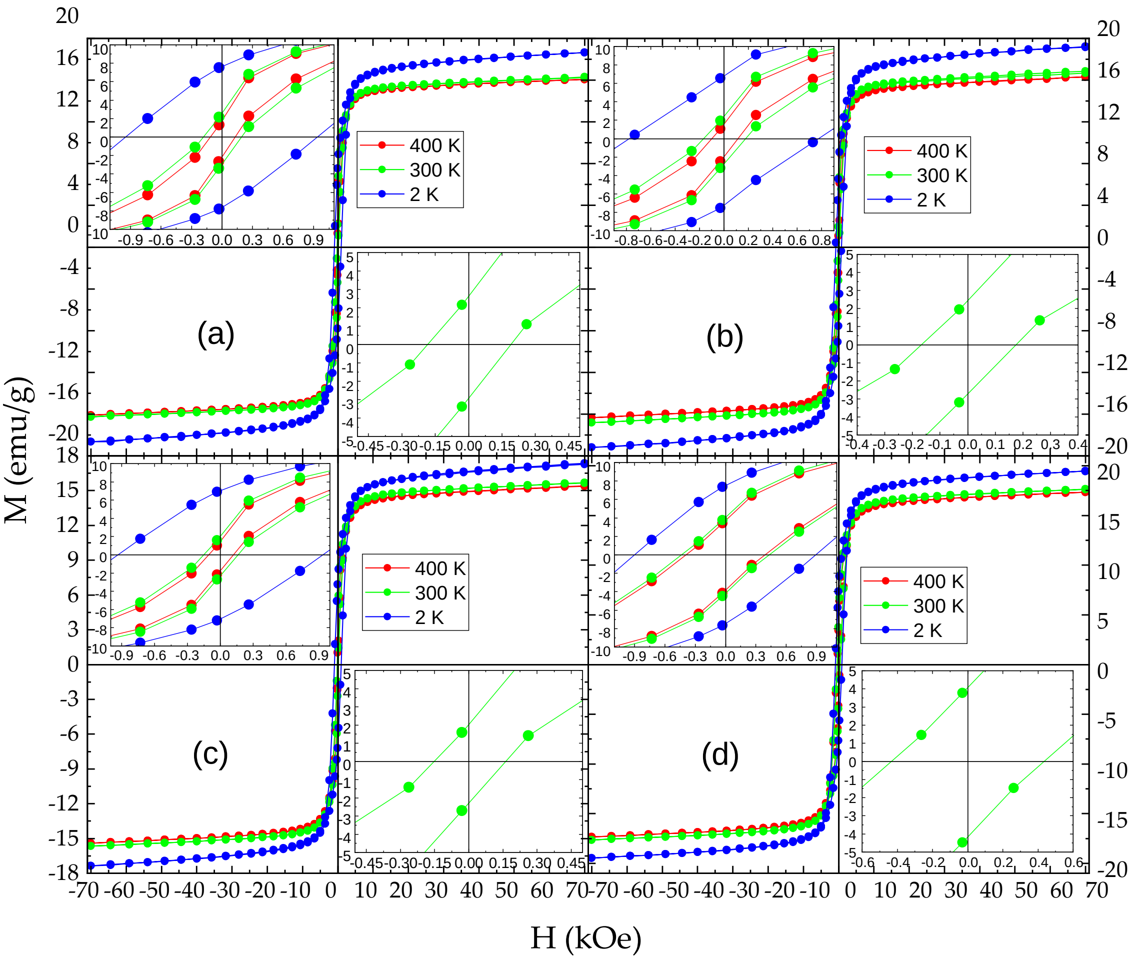

Figure 6.47 Magnetization vs. applied magnetic field isothermal loops of the En-IM-NHD6-700,30m (a), En-IM-NHD6-700,30m-SC (b), En-IM-NHD6-700,2h (c) and En-IM-NHD6-700,8h (d) samples measured at different temperatures indicated by different colors. The insets in each set of measurements show the details of the loops' characteristics around zero applied magnetic field for all temperatures (upper left) and with even more detail for the 300 K loop (lower right).

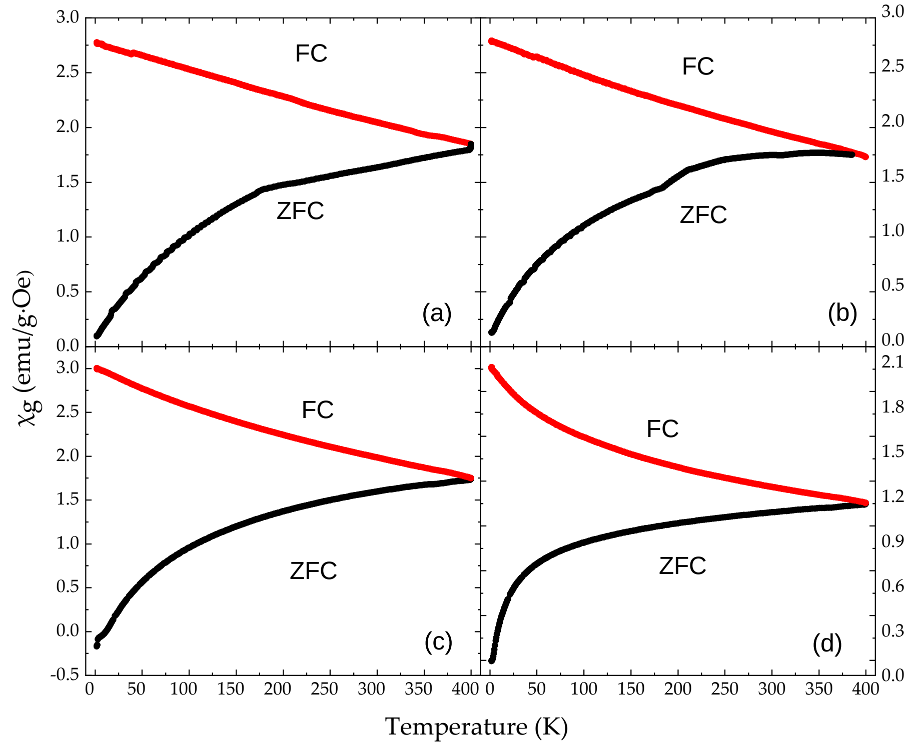

Figure 6.48 Magnetic susceptibility vs. temperature measurements of the En-IM-NHD6-700,30m (a), En-IM-NHD6-700,30m-SC (b), En-IM-NHD6-700,2h (c) and En-IM-NHD6-700,8h (d) samples under an applied field of 99 Oe.

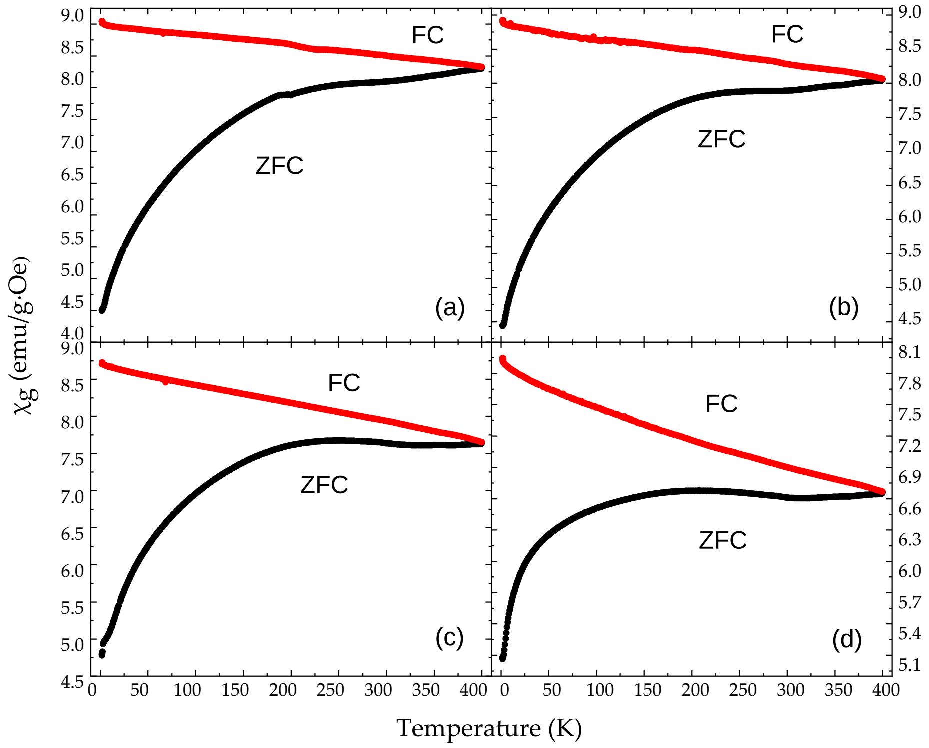

Figure 6.49 Magnetic susceptibility vs. temperature measurements of the En-IM-NHD6-700,30m (a), En-IM-NHD6-700,30m-SC (b), En-IM-NHD6-700,2h (c) and En-IM-NHD6-700,8h (d) samples under an applied field of 999 Oe.

Table 6.22 Magnetic characteristics derived from the respective isothermal loops of all annealed samples at 300 and 2 K (**Figures 6.38, 6.41, 6.44, 6.47**).

Sample	T (K)	M_{max+} (emu/g)	M_{max-} (emu/g)	M_{R+} (emu/g)	M_{R-} (emu/g)	H_{C+} (Oe)	H_{C-} (Oe)
NHD-600,30m	400	12.1	-11.9	0.9	-1.8	103	-84
	300	11.9	-11.9	1.4	-1.6	114	-119
	2	14	-13.9	5.3	-5.3	952	-986
NHD-600,2h	400	10.2	-10.2	1.1	-1.4	126	-121
	300	10.5	-10.6	1.5	-1.6	183	-168
	2	12.4	-12.4	5	-5.1	1221	-1208
NHD-600,8h	400	12.8	-12.8	1.8	-1.9	140	-150
	300	13.1	-13.1	2	-2.1	198	-174
	2	15.2	-15.2	6.2	-6.3	1114	-1114
NHD-600,32h	400	16.2	-16.2	1.4	-1.9	110	-115
	300	17.2	-17.2	2.2	-2.3	140	-130
	2	18.6	-18.7	7.7	-7.8	960	-955
NHD-650,30m	400	20.1	-20.1	2.1	-3.4	90	-75
	300	20.6	-20.6	2.1	-3.9	167	-138
	2	22.9	-22.9	7	-7.8	749	-729
NHD-650,2h	400	17.9	-17.9	1.8	-2.1	105	-95
	300	18.7	-18.7	2.2	-2.6	160	-145
	2	20.7	-20.7	8.6	-8.5	895	-895
NHD-650,8h	400	23.6	-23.6	1.7	-3.1	82	-69
	300	23.8	-23.8	0.8	-3.4	106	-20
	2	25.1	-25.1	6.4	-8.3	265	-271
NHD-650,32h	400	21.1	-21.1	1.5	-2.5	149	-137
	300	21.8	-21.9	2.8	-3.3	162	-154
	2	23.6	-23.8	9.5	-9.6	768	-756
NHD-700,2s	400	16.3	-16.3	2.2	-2.5	165	-175
	300	17	-17	1.6	-1.9	140	-120
	2	18.9	-18.9	7.7	-7.4	880	-921
NHD-700,30m	400	18.9	−18.9	1.7	−2.0	112	−112

	300	19.4	-19.4	2.3	-2.7	160	-152
	2	21.1	-21.1	8.7	-8.6	856	-881
NHD-700,2h	400	15.9	-15.9	1.5	-1.9	110	-130
	300	16	-16.1	2.1	-2.2	177	-181
	2	18.6	-18.5	7.2	-7.1	892	-903
NHD-700,8h	400	18.1	-18.1	2.1	-2.2	165	-155
	300	19.1	-19.2	2.8	-3.2	216	-206
	2	20.9	-20.9	8.3	-8.3	872	-869
NHD-700,32h	400	21.7	-21.6	2.1	-2.5	154	-138
	300	21.7	-21.8	3.1	-3.6	191	-182
	2	23.8	-23.9	9.7	-9.8	866	-857
En-NHD-700,30m	400	16	-16	1.7	-2.1	140	-130
	300	16.3	-16.2	2.6	-2.9	205	-180
	2	18.6	-18.6	7.7	-7.6	940	-947
En-NHD-700,30m-SC	400	16.3	−16.4	1.6	−1.9	114	−98
	300	16.7	-16.8	2.5	-2.7	177	-169
	2	19.2	-19.2	6.8	-7.2	781	-776
En-NHD-700,2h	400	15.2	-15.2	1.6	-2.1	130	-120
	300	15.7	-15.6	2.1	-2.3	168	-148
	2	17.3	-17.4	7.1	-7	945	-932
En-NHD-700,8h	400	17.3	-17.3	3.8	-4.1	390	-385
	300	17.7	-17.7	4.1	-4.2	442	-432
	2	19.4	-19.5	7.5	-7.4	897	-897

6.5 Discussion

The results from all experimental techniques provide a comprehensive understanding of phase development and properties concerning the samples' synthesis conditions. In studying the as-made nanohybrid and unsupported samples synthesized with $NaBH_4$ as a reducing agent, we observed the formation of Fe-Co FM NPs, along with the presence of SPM ICO NP seeds in both precursors. However, secondary impurity phases were present in the unsupported sample. The magnetic behavior of this NP assembly, as confirmed by ^{57}Fe Mössbauer spectroscopy and magnetization measurements at RT, is notably influenced by moderate but primarily slow SPM characteristics at

RT. This behavior arises due to the formation of Fe-Co and ICO NPs, existing either as isolated particles with random dispersion, or as larger agglomerates with magnetic interparticle interactions, or even as core-shell structures. Larger agglomerates of the ICO phase are found in to be more abundant in the unsupported, compared to the hybrid sample.

The as-made nanohybrid sample exhibited magnetic properties similar to those of the unsupported sample, suggesting a strong interconnection of the Fe-Co NPs in both samples. Thus, it is denoted that the morphology and size distribution include large NPs either as individual particles or as larger agglomerates near the ND nanotemplates in the hybrid sample. These structural features likely lead to inadequate Fe-Co NP dispersion on the ND surfaces, combined by the broad size distribution and possible low crystallization and cluster agglomeration of NPs, hindering the formation of a well-defined magnetic hybrid nanostructure. Consequently, it can be concluded that this synthesis approach yields magnetic nanostructures of lower qualities for the desired hybrid samples, prompting a shift toward the impregnation synthesis method.

In the context of the impregnation synthesis procedure, it is essential to consider the role of ND NPs in the conventional and enriched precursor samples, which influence the properties of the final annealed samples. These hybrid nanomaterials comprise fine SPM ICO NPs developed on the surfaces of the NDs nanotemplates. The resulting structural configurations of these nanohybrids are closely connected to the intrinsic properties of the preconceived NDs, which are derived from detonation reactions. These properties activate specific operating mechanisms during the initial steps of the impregnation synthetic procedures followed in our samples. These mechanisms pertain to the attribution of favorable blending and interacting conditions emerging from the development of oxide/hydroxide functional groups present on the NDs' surfaces in the moist mixture, which interact strongly with the corresponding metallic salts dissolved in deionized water during the first step of each sample's synthesis [30]. The advancement of such strong interacting bonds is realized due to the ideal chemical conditions provided by the hygroscopic properties of the metallic salts and the hydrophilic nature of the NDs' surficial functional groups. As a result, a substantial quantity of oxide/hydroxide functional groups is available to interact and form coupling bonds with the respective Fe^{3+} and Co^{2+} metallic ions, ensuring the metal ions have a firm attachment to the NDs' surface. In this respect, it is possible to consider that two types of strong coupling bonds can be developed between the strongly interacting counterparts: (i) Fe-O-C and Co-O-C bonds and (ii) direct Fe-C and Co-C bonds [31], [32], [33].

The experimental data of this work evince the inability to develop any Fe–Co alloy phase during the first step of the samples' synthesis. On the contrary, the development of only very fine ICO NPs that are well dispersed on the nanohybrid clusters can be observed. These characteristics, which conform consistently to the bonding mechanism, were also featured in our previous work based on this wet impregnation method [3]. Nonetheless, the employment of the second step in the synthesis leads to the development of the Fe–Co alloy nanophases. In this second step, the precursor is annealed in vacuum-evacuated quartz ampoules at high temperatures. This procedure induces reduction conditions to the nominal Fe^{3+} and Co^{2+} ions of the ICO NPs in each sample system, forcing these ions to form the Fe–Co alloy nanophases. The spatial proximity between the very small ICO NPs favors their combination and growth into larger clusters during this second annealing step and leads to the development of larger in average size, relative-to-the-original ICO NP seeds, FM bcc Fe–Co cobalt-rich alloy NPs on the surfaces of the ND nanotemplates. However, those ICO NPs that are relatively isolated on the surfaces of the ND nanotemplates fail to develop into metallic Fe–Co alloy NPs and remain on these surfaces as excessive ICO residues.

Similar characteristics are found for the annealed samples originating from both precursor types, conventional and ^{57}Fe-enriched; however, a slightly higher average cobalt concentration for Fe–Co NPs from TEM/EDS measurements is observed for the ^{57}Fe-enriched case. These NPs also appear larger and have a wider dispersion from the equivalent Fe–Co NPs of the non-enriched annealed samples. We consider the idea that these differences can be attributed to the slight modification of the first wet chemistry step procedure followed for the two precursors. The addition of the small amount of metallic ^{57}Fe in an HNO_3 solution during the preparation of the ^{57}Fe-enriched precursor may influence the way the resulting iron ions disperse in the moist mixture during the first step of the synthesis, by prompting aggregation of the Fe^{3+}/$^{57}Fe^{3+}$ ion assemblies, which could possibly lead to their distinctive characteristics. The ^{57}Fe MS of the two precursors indicate some difference regarding the presence of magnetically split contributions for the ^{57}Fe-enriched precursor, which are not observed for the conventional precursor. This difference seems to be passed along partially to the final annealed samples and is reflected through the slight increase in the average Fe–Co NP size/dispersion and amount of ICO AA values in their MS, which include also Fe^{2+} SPM states.

In either case, the annealing procedure triggers the involvement of strong reducing agents in the second step of the synthesis. These are the sp^2-coupled carbon atoms existing already as native species at the surfaces of the ND NPs and are further developed during thermal annealing [31], [34], [35], [36]. These sp^2-hybridized carbon atoms, along with the low O_2 pressure due to the vacuum existing inside the ampules (10^{-3} Torr), provide the appropriate conditions for complete reduction of the Fe^{3+} and Co^{2+} ions in the ICO NPs to the Fe^0 and Co^0 atoms that form the corresponding Fe–Co alloy NPs.

Moreover, the formation of the Fe–Co alloy NPs in our samples is accompanied by the development of graphitic-type layers surrounding these metallic NPs partially or in total, as evidenced by TEM observations. Surface graphitization effects of the ND sp^3 cores can begin to occur at elevated temperatures in the vicinity of 700 °C, and can be further enhanced by the presence of surface structural defects and metallic elements like iron, cobalt, and nickel, which act as catalysts [31], [37]. Metallic nanoparticles can act as catalysts for the graphitization process. Carbon atoms can be preferentially adsorbed onto the surface of the metal nanoparticles, where they undergo rearrangement into graphitic-type structures. Consequently, the metal Fe–Co alloy nanoparticles provide active sites and facilitate the alignment of carbon atoms into the resulting graphitic-type arrangement. It is possible to consider, thus, that the birth of the Fe–Co NPs from the reduction in the ICO NPs with the aid of the surface ND sp^2 carbon atoms, could also serve as an action to promote them as initial metallic alloy nucleation centers for the formation of graphitic-type layered nanostructures, as evidenced by HRTEM observations in both systems.

Furthermore, as the graphitization mechanism occurring on NDs' surfaces at elevated temperatures is favored by structural degradations that could result in low surface energy in the basal layer of the graphitic-type nanostructures, it could, in turn, also lead to low binding energies for the absorbed carbon atoms in the Fe–Co NPs, thus facilitating an easier lateral diffusion of these carbon atoms in the structure of the alloy. Hence, high temperatures not only promote the formation of metallic Fe–Co NPs through reduction in ICO NPs in our samples but also appear to facilitate a partial—at least, lateral—diffusion of carbon atoms across the shared surface and subsurface interfaces of the grown metallic NPs and the NDs in both synthesized systems. This non-extensive mechanism, involving the interstitial diffusion of carbon atoms into the Fe–Co lattice, may be the primary factor contributing to the development of the non-extensive (minor) contribution from the non-cubic tetragonally distorted martensitic-type Fe–Co phase, evidenced by our ^{57}Fe Mössbauer spectroscopy measurements.

With respect to the magnetic properties, the lack of magnetization saturation for all samples' M vs. H measurements, even at 2 K, could be attributed to the SPM behavior of the smaller-in-size metallic Fe–Co alloy NPs superimposed with the SPM behavior of the residual ICO NPs. The presence of this SPM ICO phase was demonstrated by ^{57}Fe Mössbauer spectroscopy at all temperatures in all samples. On the other hand, ^{57}Fe Mössbauer spectroscopy investigations also revealed the contribution from a tetragonally distorted martensitic-type Fe–Co phase encountered in all samples, but its presence is non-extensive. Consequently, no strongly correlated hard magnetic behavior can be confirmed through these M vs. H measurements. Therefore, the magnetic properties of the resulting annealed samples are predominantly influenced by the spatial isolation and well-dispersed placement of the Fe–Co NPs, which provide relative harder FM properties with respect to conventional bulk Fe–Co alloys, which exhibit H_C values ranging between 40 and 70 Oe [27], [38], [39], but are not hard enough to surpass the range of ~200 Oe at RT and 1200 Oe at 2 K.

No significant difference in the magnetic properties was observed between the samples subjected to slow cooling and those cooled conventionally. This includes the comparison of the ^{57}Fe-enriched En-NHD-700,30m and En-NHD-700,30m-SC samples, as well as the conventional NHD-700,30m and ^{57}Fe-enriched En-NHD-700,30m-SC samples. The only notable distinction was the increased presence of the ICO phase in the MS of the En-NHD-700,30m-SC sample compared to the conventional NHD-700,30m sample. Consequently, we conclude that no clear or significant correlation exists between the slow cooling procedure and the crystal ordering of the Fe–Co metallic phase, at least under the specific annealing conditions studied (700 °C, 30 min).

Additionally, it is necessary to evaluate the relevance of the selected annealing conditions (temperature and duration) to the structural and morphological characteristics of the hybrid samples. This assessment also sheds light on how these conditions influence the formation of a hybrid magnetic nanostructured material with optimal properties. The primary objective was to synthesize a hybrid sample that maximizes the yield of the well-ordered CsCl-type bcc Fe–Co alloy phase, derived from the reduction of the ICO NP seeds during annealing. Efficient oxide-to-alloy reduction reactions enhance the purity of the hybrids' structural and magnetic characteristics. Furthermore, a high yield of ferromagnetic nanocrystalline Fe–Co NPs facilitates the development of the martensitic-type Fe–Co phase. This occurs because a greater proportion of metallic Fe–Co NPs can interact with sp^2 graphitic-type layered nanostructures, providing favorable conditions for interstitial carbon atom diffusion within the Fe–Co lattice, which drives the martensitic transformation.

This phenomenon is supported by literature, which emphasizes that inducing a tetragonal distortion in the Fe–Co lattice via the introduction of a third element, such as carbon, requires a pure and well-crystallized CsCl-type Fe–Co alloy with a high chemical ordering parameter [40].

Our experimental results demonstrate that thermal treatment of the as-made conventional samples under all chosen conditions successfully induces the formation of a well-ordered CsCl-type bcc Fe–Co alloy phase from the reduction of ICO NP seeds. However, at 600 °C and 650 °C, shorter annealing durations result in incomplete reduction reactions, leading to a more pronounced presence of ICO nanostructures compared to Fe–Co alloys. In contrast, annealing at 700 °C significantly reduces the prevalence of ICO nanostructures, suggesting that samples processed at this temperature contain fewer residual SPM ICO NPs. This improvement is attributed to the more effective oxide-to-alloy reduction reactions occurring at higher temperatures, as confirmed by ^{57}Fe Mössbauer spectroscopy.

In this context, the thermal treatment of ^{57}Fe-enriched precursors yields structural and magnetic properties comparable to those of the conventionally annealed samples, regardless of the synthesis conditions. Moreover, at a constant annealing temperature of 700 °C, the annealing duration appears to have no significant impact on either the average particle size of the Fe–Co phase or the relative proportions of the ICO and Fe–Co phases.

6.6 Conclusions

In this study, we characterized and analyzed the structural, morphological, electronic, and magnetic properties of Fe-Co/NDs systems synthesized through two wet chemistry approaches: one using the $NaBH_4$ as a reducing agent, and the other employing a two-step preparation process involving an impregnation method followed by controlled annealing. This comparison enabled us to assess each method's effectiveness in producing both hybrid and unsupported magnetic nanostructures and to determine which approach yielded the highest quality magnetic nanoalloy materials.

Our findings show that both hybrid and unsupported samples synthesized with $NaBH_4$ contained iron-cobalt alloy and iron-cobalt-oxide nanoparticles, with the former exhibiting strong interparticle interactions, as revealed by ^{57}Fe Mössbauer spectroscopy. These interactions suggest larger NP sizes and/or aggregation into clusters, which could influence their distribution on the ND nanotemplates in the hybrid sample, which refrained us to further proceed in the annealing process.

Conversely, the impregnation route successfully yielded novel magnetic nanohybrid materials, featuring ferromagnetic bcc Fe–Co NPs grown on NDs nanotemplates. These Fe–Co NPs, with average diameters between 6 and 10 nm, were uniformly distributed on the NDs surfaces and exhibited a high cobalt content (~65 at. % Co). The Fe–Co NPs displayed stable FM behavior across a temperature range from 400 K to 2 K, with coercivity values increasing from approximately 110 Oe at 400 K to around 850 Oe at 2 K. The dominant bcc FM Fe–Co phase was consistently accompanied by a minor, tetragonally distorted, martensitic-type Fe–Co phase and a residual ICO precursor phase.

This distinctive martensitic-type Fe–Co phase likely arose due to the unique morphological properties of the ND growth matrices, which promote surface formations and reconstructions of sp^2 carbon nanostructures that intensify during annealing. These graphitic layers surrounding the Fe–Co NPs created favorable conditions for the diffusion of interstitial carbon atoms within the Fe–Co lattices at elevated temperatures, resulting in the formation of the observed martensitic-type structure. Future work should focus on extending this martensitic phase to achieve enhanced ferromagnetic properties. For example, introducing dual atomic diffusion into interstitial sites, combining carbon and nitrogen from N-doped NDs nanotemplates, could be a promising approach.

These novel nanohybrids, presented here for the first time, expand our group's portfolio of advanced hybrid magnetic nanostructures [3], [41], [42] and hold substantial promise for applications in biomedicine, biopharmaceutics, and related technological fields.

6.7 References

[1] R. M. Cornell and U. Schwertmann, *The Iron Oxides: Structure, Properties, Reactions, Occurences and Uses*, 1st ed. Wiley, 2003. doi: 10.1002/3527602097.

[2] B. D. Cullity and S. R. Stock, *Elements of X-ray diffraction*, 3. ed. Upper Saddle River, NJ: Prentice Hall, 2001.

[3] P. Ziogas, A. B. Bourlinos, J. Tucek, O. Malina, and A. P. Douvalis, "Novel Magnetic Nanohybrids: From Iron Oxide to Iron Carbide Nanoparticles Grown on Nanodiamonds," *Magnetochemistry*, vol. 6, no. 4, Art. no. 4, Dec. 2020, doi: 10.3390/magnetochemistry6040073.

[4] A. P. Douvalis, A. Polymeros, and T. Bakas, "IMSG09: A ^{57}Fe- ^{119}Sn Mössbauer spectra computer fitting program with novel interactive user interface," *J. Phys.: Conf. Ser.*, vol. 217, p. 012014, Mar. 2010, doi: 10.1088/1742-6596/217/1/012014.

[5] B. deMayo, D. W. Forester, and S. Spooner, "Effects of Atomic Configurational Changes on Hyperfine Interactions in Concentrated Iron-Cobalt Alloys," *Journal of Applied Physics*, vol. 41, no. 3, pp. 1319–1320, Mar. 1970, doi: 10.1063/1.1658920.

[6] H. H. Hamdeh, B. Fultz, and D. H. Pearson, "Mössbauer spectrometry study of the hyperfine fields and electronic structure of Fe-Co alloys," *Phys. Rev. B*, vol. 39, no. 16, pp. 11233–11240, Jun. 1989, doi: 10.1103/PhysRevB.39.11233.

[7] I. S. Lyubutin *et al.*, "Magnetic and Mössbauer spectroscopy studies of hollow microcapsules made of silica-coated $CoFe_2O_4$ nanoparticles," *Smart Mater. Struct.*, vol. 25, no. 1, p. 015022, Jan. 2016, doi: 10.1088/0964-1726/25/1/015022.

[8] M. Hähsler *et al.*, "Magnetic Properties and Mössbauer Spectroscopy of Fe_3O_4/$CoFe_2O_4$ Nanorods," *Inorg. Chem.*, vol. 59, no. 6, pp. 3677–3685, Mar. 2020, doi: 10.1021/acs.inorgchem.9b03267.

[9] S. Mørup and M. Hansen, “Superparamagnetic Particles,” 2007. doi: 10.1002/9780470022184.hmm409.

[10] S. Bedanta and W. Kleemann, “Supermagnetism,” *Journal of Physics D: Applied Physics*, vol. 42, p. 013001, Dec. 2008, doi: 10.1088/0022-3727/42/1/013001.

[11] I. S. Lyubutin, C. R. Lin, Yu. V. Korzhetskiy, T. V. Dmitrieva, and R. K. Chiang, “Mössbauer spectroscopy and magnetic properties of hematite/magnetite nanocomposites,” *Journal of Applied Physics*, vol. 106, no. 3, Art. no. 3, Aug. 2009, doi: 10.1063/1.3194316.

[12] N. N. Greenwood and T. C. Gibb, *Mössbauer Spectroscopy*. Dordrecht: Springer Netherlands, 1971. doi: 10.1007/978-94-009-5697-1.

[13] P. Gütlich, E. Bill, and A. X. Trautwein, *Mössbauer Spectroscopy and Transition Metal Chemistry*. Berlin, Heidelberg: Springer Berlin Heidelberg, 2011. doi: 10.1007/978-3-540-88428-6.

[14] S. Mørup, M. F. Hansen, and C. Frandsen, “Magnetic interactions between nanoparticles,” *Beilstein J Nanotechnol*, vol. 1, pp. 182–190, 2010, doi: 10.3762/bjnano.1.22.

[15] H. Kronmüller and S. Parkin, Eds., *Handbook of Magnetism and Advanced Magnetic Materials*, 1st ed. Wiley, 2007. doi: 10.1002/9780470022184.

[16] V. V. Serikov, N. M. Kleinerman, and O. A. Golovnya, “NMR and Mössbauer study of peculiarities of the structure formation in Fe–Co alloys,” *Phys. Metals Metallogr.*, vol. 118, no. 11, pp. 1040–1047, Nov. 2017, doi: 10.1134/S0031918X1711014X.

[17] H. Moumeni, S. Alleg, C. Djebbari, F. Z. Bentayeb, and J. M. Grenèche, “Synthesis and characterisation of nanostructured FeCo alloys,” *Journal of Materials Science*, vol. 39, no. 16/17, pp. 5441–5443, Aug. 2004, doi: 10.1023/B:JMSC.0000039262.37788.b7.

[18] P. A. Montano and M. S. Seehra, “Mössbauer study of the order-disorder and $\alpha - \gamma$ transitions in FeCo,” *Phys. Rev. B*, vol. 15, no. 5, pp. 2437–2441, Mar. 1977, doi: 10.1103/PhysRevB.15.2437.

[19] P. M. Gielen and R. Kaplow, “Mossbauer effect in iron-carbon and iron-nitrogen alloys,” *Acta Metallurgica*, vol. 15, no. 1, pp. 49–63, Jan. 1967, doi: 10.1016/0001-6160(67)90155-1.

[20] V. G. Gavriljuk, A. V. Tarasenko, and A. I. Tyshchenko, “Low temperature ageing of the freshly formed Fe-C and Fe-N martensites,” *Scripta Materialia*, vol. 43, no. 3, pp. 233–238, Jul. 2000, doi: 10.1016/S1359-6462(00)00396-1.

[21] G.V. Kurdyumov Institute for Metal Physics, NAS of Ukraine, 36 Academician Vernadsky Blvd., UA-03680 Kyiv-142, Ukraine *et al.*, “Carbon Distribution in Low-Temperature Isothermal Iron-Based Martensite and Its Tetragonality,” *Metallofiz. Noveishie Tekhnol.*, vol. 38, no. 4, pp. 455–475, Jun. 2016, doi: 10.15407/mfint.38.04.0455.

[22] W. K. Choo and R. Kaplow, “Mössbauer measurements on the aging of iron-carbon martensite,” *Acta Metallurgica*, vol. 21, no. 6, pp. 725–732, Jun. 1973, doi: 10.1016/0001-6160(73)90036-9.

[23] G. V. Kurdjumov and A. G. Khachaturyan, “Nature of axial ratio anomalies of the martensite lattice and mechanism of diffusionless γ → α transformation,” *Acta Metallurgica*, vol. 23, no. 9, pp. 1077–1088, Sep. 1975, doi: 10.1016/0001-6160(75)90112-1.

[24] S. Mørup, C. Frandsen, and M. F. Hansen, “Uniform excitations in magnetic nanoparticles,” *Beilstein J. Nanotechnol.*, vol. 1, pp. 48–54, Nov. 2010, doi: 10.3762/bjnano.1.6.

[25] B. D. Cullity and C. D. Graham, *Introduction to magnetic materials*, 2nd ed. Hoboken, N.J: IEEE/Wiley, 2009.

[26] A. P. Douvalis, R. Zboril, A. B. Bourlinos, J. Tucek, S. Spyridi, and T. Bakas, “A facile synthetic route toward air-stable magnetic nanoalloys with Fe–Ni/Fe–Co core and iron oxide shell,” *J Nanopart Res*, vol. 14, no. 9, p. 1130, Sep. 2012, doi: 10.1007/s11051-012-1130-z.

[27] F. Sánchez-De Jesús, A. M. Bolarín-Miró, C. A. Cortés Escobedo, G. Torres-Villaseñor, and P. Vera-Serna, “Structural Analysis and Magnetic Properties of FeCo Alloys Obtained by Mechanical Alloying,” *Journal of Metallurgy*, vol. 2016, pp. 1–8, Jul. 2016, doi: 10.1155/2016/8347063.

[28] J. M. D. Coey, *Magnetism and Magnetic Materials*, 1st ed. Cambridge University Press, 2001. doi: 10.1017/CBO9780511845000.

[29] D. Fiorani, Ed., *Surface effects in magnetic nanoparticles*. in Nanostructure science and technology. New York: Springer, 2005.

[30] A. B. Bourlinos *et al.*, “Fabrication of fluorescent nanodiamond@C core–shell hybrids via mild carbonization of sodium cholate–nanodiamond complexes,” *J Mater Sci*, vol. 46, no. 24, Art. no. 24, Dec. 2011, doi: 10.1007/s10853-011-5911-z.

[31] X. Duan *et al.*, “sp ^{2} /sp ^{3} Framework from Diamond Nanocrystals: A Key Bridge of Carbonaceous Structure to Carbocatalysis,” *ACS Catal.*, vol. 9, no. 8, Art. no. 8, Aug. 2019, doi: 10.1021/acscatal.9b01565.

[32] J. Tuček, K. C. Kemp, K. S. Kim, and R. Zbořil, “Iron-Oxide-Supported Nanocarbon in Lithium-Ion Batteries, Medical, Catalytic, and Environmental Applications,” *ACS Nano*, vol. 8, no. 8, pp. 7571–7612, Aug. 2014, doi: 10.1021/nn501836x.

[33] X. Fan, H. Gao, X. Kou, B. Zhang, and S. Wang, “Synthesis of FeCo-reduced graphene oxide composite and its magnetic and adsorption properties,” *Materials Research Bulletin*, vol. 65, pp. 320–324, May 2015, doi: 10.1016/j.materresbull.2015.02.007.

[34] M. Zeiger, N. Jäckel, V. N. Mochalin, and V. Presser, “Review: carbon onions for electrochemical energy storage,” *J. Mater. Chem. A*, vol. 4, no. 9, pp. 3172–3196, 2016, doi: 10.1039/C5TA08295A.

[35] O. A. Shenderova and G. E. McGuire, “Science and engineering of nanodiamond particle surfaces for biological applications (Review),” *Biointerphases*, vol. 10, no. 3, p. 030802, Sep. 2015, doi: 10.1116/1.4927679.

[36] A. S. Barnard, “Stability of Diamond at the Nanoscale,” in *Ultananocrystalline Diamond*, Elsevier, 2012, pp. 3–52. doi: 10.1016/B978-1-4377-3465-2.00001-3.

[37] T. Petit, J.-C. Arnault, H. A. Girard, M. Sennour, and P. Bergonzo, “Early stages of surface graphitization on nanodiamond probed by x-ray photoelectron spectroscopy,” *Phys. Rev. B*, vol. 84, no. 23, p. 233407, Dec. 2011, doi: 10.1103/PhysRevB.84.233407.

[38] P. Karipoth, A. Thirumurugan, S. Velaga, J.-M. Greneche, and R. Justin Joseyphus, “Magnetic properties of FeCo alloy nanoparticles synthesized through instant chemical reduction,” *Journal of Applied Physics*, vol. 120, no. 12, Art. no. 12, Sep. 2016, doi: 10.1063/1.4962637.

[39] M. Delshad Chermahini, M. Zandrahimi, H. Shokrollahi, and S. Sharafi, “The effect of milling time and composition on microstructural and magnetic properties of nanostructured Fe–Co alloys,” *Journal of Alloys and Compounds*, vol. 477, no. 1–2, pp. 45–50, May 2009, doi: 10.1016/j.jallcom.2008.10.163.

[40] Y. Kota and A. Sakuma, “Degree of Order Dependence on Magnetocrystalline Anisotropy in Body-Centered Tetragonal FeCo Alloys,” *Appl. Phys. Express*, vol. 5, no. 11, Art. no. 11, Oct. 2012, doi: 10.1143/APEX.5.113002.

[41] A. P. Douvalis, A. B. Bourlinos, J. Tucek, K. Čépe, T. Bakas, and R. Zboril, “Development of novel FePt/nanodiamond hybrid nanostructures: L10 phase size-growth suppression and magnetic properties,” *J Nanopart Res*, vol. 18, no. 5, Art. no. 5, May 2016, doi: 10.1007/s11051-016-3424-z.

[42] P. Ziogas *et al.*, “Intriguing Prospects of a Novel Magnetic Nanohybrid Material: Ferromagnetic FeRh Nanoparticles Grown on Nanodiamonds,” *Metals*, vol. 12, no. 8, p. 1355, Aug. 2022, doi: 10.3390/met12081355.

Chapter 7. Study of the Fe-Ni/NDs system

7.1 XRD

7.1.1 Samples prepared using the sodium borohydride reducing agent

The XRD patterns of pristine NDs, as-made nanohybrid and unsupported samples prepared using the $NaBH_4$ reducing agent (BH) are presented in Figure 7.1. The XRD pattern of pristine NDs (Figure 7.1a) shows two primary broad diffraction peaks corresponding to the cubic ND structure at 43.9° (111) and 75.4° (220) 2θ (lattice constant a = 3.567 Å, ICDD PDF 00-006-0675). Additionally, a diminished diffraction peak at 21.6° 2θ, attributed to residual impurities known to exist from the characterization of the material by the reagent provider (Aldrich 636428-1G), is also visible. The average nanoparticle crystalline domain size <D> for each peak was estimated using the Scherrer formula [1], yielding an average size of $\langle D_{NDs} \rangle$ = 5 nm for the NDs, as shown in the diagram. This result confirms that the ND nanoparticles are indeed very small, validating the nominal nanocrystalline structure and purity specified by Aldrich.

The XRD pattern of the as-made nanohybrid (BH-AM-NHD) sample in Figure 7.1b primarily features broad diffraction peaks associated with ND nanostructures, along with a faint broad peak at ~ 36° 2θ, corresponding to the main diffraction (311) ionic planes of a spinel-type $Fe_{2-x}Ni_xO_4$ iron-nickel-oxide (INO) structure, accompanied by two also faint diffraction peaks at ~ 30° (220), and ~ 63° (440) 2θ (lattice constant a = 8.3337 Å, ICDD PDF 00-054-0964) [2]. The average ND nanoparticle crystalline domain size <D> was similarly estimated to be $\langle D_{NDs} \rangle$ = 5 nm, consistent with the pristine NDs. These findings indicate that both the pristine NDs and the as-made nanohybrid precursor consist of very small ND nanoparticles, maintaining the nanocrystalline structure and purity provided by Aldrich. However, the average crystalline domain size $\langle D_{INO} \rangle$ for the INO nanoparticles could not be determined due to the unresolved diffraction peak of the INO phase as a consequence of its large broadening.

In Figure 7.1c, the XRD pattern of the as-made unsupported (BH-AM-NP) sample displays a broad diffraction peak spanning a wide range of intermediate angles. This broad peak includes the contribution from the primary diffraction peak of the cubic fcc Fe–Ni crystal structure at 43.8° (111), as well as those of the same structure at 51.1° (200), and 75.1° (220) 2θ. There is a faint contribution from additional secondary peaks observed around 31° and 36° 2θ, corresponding to the same spinel-type INO phase detected in the BH-AM-NHD sample. From the width and position of the (111) peak the average crystalline domain size for the Fe-Ni nanoparticles, $\langle D_{Fe\text{-}Ni} \rangle$, was estimated to be approximately 2 nm using the Scherrer formula for the BH-AM1-NP sample.

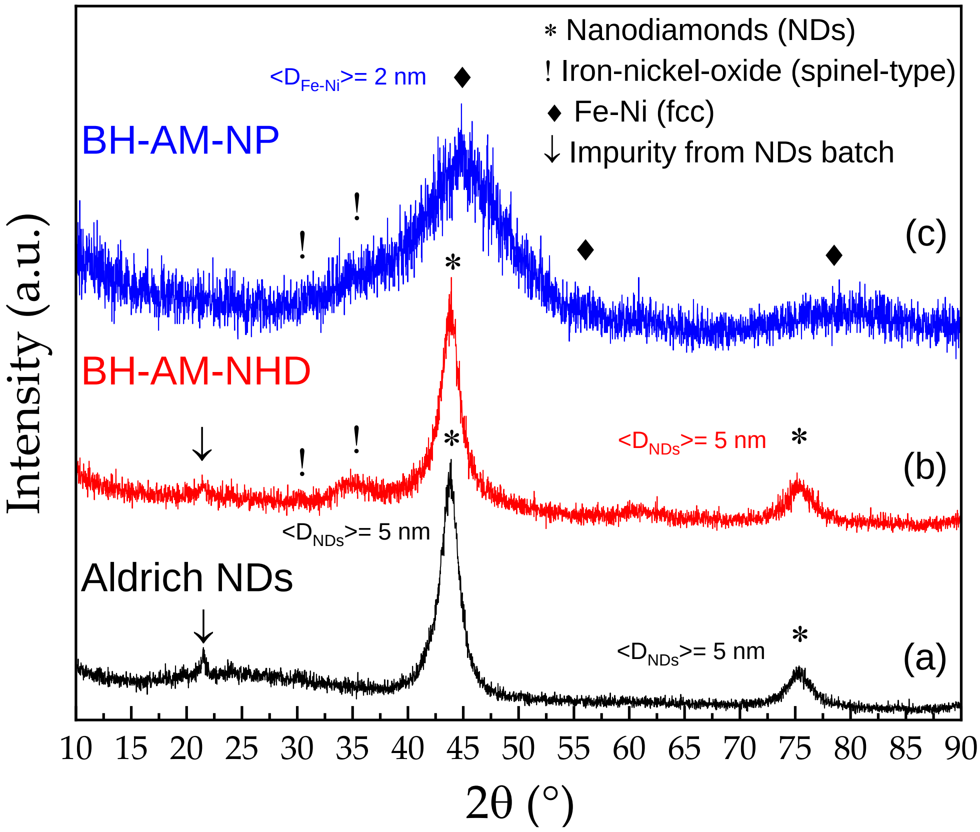

Figure 7.1 XRD patterns of the pristine NDs (a), BH-AM-NHD (b) and BH-AM-NP (c) samples. The crystalline phases in the samples are depicted by respective different symbols denoting the angular positions of their main diffraction peaks. The average crystalline domain size <D> of the nanodiamonds phase for the as-made nanohybrid precursor samples and that of the iron-nickel phase for the as-made unsupported sample are denoted in each pattern.

From these qualitative XRD results, it is suggested that the first synthesis step leads to the formation of small INO NP seeds on the ND nanotemplates in the as-made nanohybrid sample. On the other side, a primary Fe-Ni nanostructured phase, along with secondary INO NP seeds, is developed in the BH-AM-NP sample. The broad widths and reduced intensities of the diffraction peaks in both the as-made nanohybrid and unsupported precursor samples indicate the presence of very small, nanostructured INO NP seeds/NDs and Fe-Ni/INO NPs, which may also exhibit low crystallinity. In the case of the BH-AM-NHD sample, the retention of nanostructured characteristics in the NDs, combined with the development of secondary, very small INO NP seeds, suggests a structural pattern similar to that observed in the Fe-Rh/NDs system (Chapter 5). This resemblance could facilitate the following formation of Fe-Ni NPs when they will be reduced from the INO NP seeds on the surfaces of the ND nanotemplates during annealing under specific conditions at the second step of the synthesis. On the other hand, in the BH-AM-NP sample, the formation of the primary Fe-Ni nanostructure is accompanied by a relatively broad main diffraction peak, making it difficult to accurately determine the atomic Fe-Ni ratio based on the angular position. Therefore, implementing the second synthesis step is necessary to clarify the roles and contributions of these phases and to define the structural properties of the final annealed samples produced by the proposed synthesis method.

In this context, annealing the as-made nanohybrid and unsupported precursor samples at 700°C for 4 hours and at 300°C for 96h (Figure 7.2) induces the formation of new nanocrystalline phases in both samples. The XRD pattern of the BH-NHD-700C,4h sample (Figure 7.2a) shows the retained presence of the ND phase, which is also accompanied by the presence of a set of intense and well-resolved diffraction peaks at 43.8° (111), 51.1° (200), 75.1° (220), and 91.2° (311) 2θ, corresponding to a cubic fcc Fe-Ni rich in nickel phase ($Fe_{0.3}Ni_{0.7}$ ICDD PDF 01-074-5840, lattice constant a = 3.564 Å). Additionally, a secondary impurity phase is observed at 35.1° (240), 37.8° (150), 38.1° (400), 43.7° (321), 46.9° (350), 57.6° (441), 60.2° (002), 61.6° (112), 61.9° (550), 66.7° (601), and 71.5° (281) 2θ, which is attributed to the orthorhombic iron oxyborate (IOB) Fe_3BO_5 (Vonsenite) phase (lattice constants a = 9.452 Å, b = 12.287 Å, c = 3.072 Å, ICDD PDF 00-025-0395). The formation of this phase may be attributed to residual boron (B) precipitates from the $NaBH_4$ reducing agent, likely in the form of amorphous boron oxide (B_2O_3), combined with the presence of INO NPs and the influence of annealing conditions. Moreover, two diminished diffraction peaks at 18.6° 2θ degrees, are attributed to a nickel oxide crystal structure (NiO_2 ICDD PDF 01-085-1977, lattice constant a=b = 2.835 Å, c = 14.332 Å).

Furthermore, the XRD pattern of the BH-NHD-300C,96h sample (Figure 7.2c) exhibits similar structural features to the BH-NHD-700C,4h sample. The dominant diffraction peaks of the fcc NDs phase and the less intense and broader peaks of the Ni-rich Fe-Ni phase appear at the same angular positions as those observed in the BH-NHD-700C,4h sample, while the presence of the INO phase is also detected. An estimation of the average crystalline domain size <D> for the primary phases, calculated using the Scherrer formula, is shown in each pattern. The average size of the fcc Ni-rich Fe-Ni NPs is approximately 16 nm for the BH-NHD-700C,4h sample, whereas for the BH-NHD-300C,96h sample the mean Fe-Ni NP size cannot be determined, due to the unresolvable width and intensity of the 51° 2θ diffraction peak of the Fe-Ni phase. The average size of the IOB phase in the BH-NHD-700C,4h sample is estimated to be 24 nm. In the BH-NHD-300C,96h sample the spinel-type INO phase has an average NP size of about 15 nm. Moreover, a faint diffraction peak can be also observed at approximately 18° 2θ, attributed to the nickel oxide phase.

In contrast, the XRD patterns of the annealed unsupported samples at 700°C for 4h and 300°C for 96h (Figures 7.2b and d, respectively) display the presence of four diffraction peaks attributed to the fcc Ni-rich Fe-Ni phase, together with a set of less-intense diffraction peaks at 44.6°, 64.9° and 82.2° 2θ degrees, attributed to a bcc rich in Fe Fe-Ni phase (Kamacite, ICDD PDF 04-008-8473). The average size of the fcc Fe-Ni NPs ranges between 12 and 10 nm, with the larger sizes observed in the sample annealed for 4 hours, while that of the bcc Fe-Ni phase cannot be determined due to the unresolvable widths and intensities of Kamacite's diffraction peaks in both annealed unsupported samples.

From the analysis of these results it can be suggested that in the case the annealed nanohybrid samples, the formation of the Fe-Ni alloy phase could originate from the reduction of the INO NP seeds, which are present in the precursor, during the second annealing step of the synthesis. However, this phase is accompanied by the formation of secondary impurities of IOB and INO phase these annealed nanohybrid samples. The consistent presence of these impurities suggests that the proposed synthesis method leads to the creation of samples with multi-phase characteristics that may significantly hinder the development of uniquely structured magnetic hybrid nanomaterials.

In contrast, in the annealed unsupported samples the main contribution is owed to nanostructured Fe-Ni phases. These metallic Fe-Ni NPs undergo an expected size growth during the second synthesis step, which is influenced by the annealing temperatures and durations. Moreover, heating the unsupported precursor sample at 700°C for 4h and at 300°C for 96h appears to result in the complete reduction of the INO NP seeds into Fe-Ni nanostructures, indicating that the selection of those temperatures and durations may represent optimal annealing conditions for these samples.

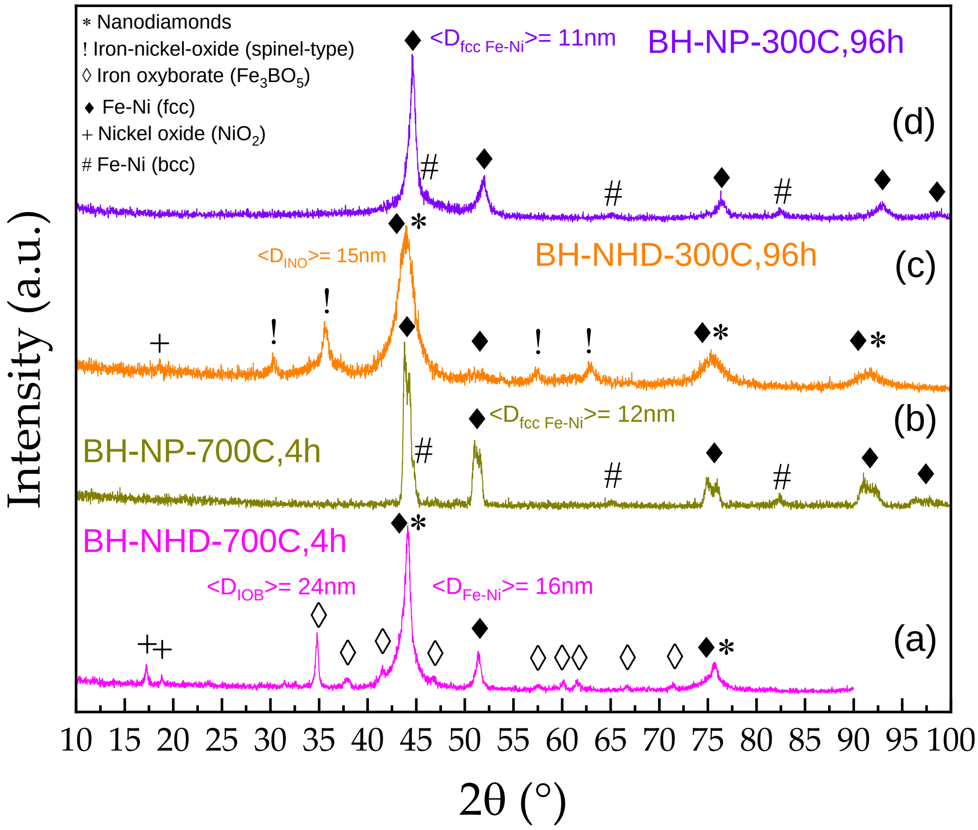

Figure 7.2 XRD patterns of the BH-NHD-700C,4h (a), BH-NP-700C4h (b), BH-NHD-300C,96h (c) and BH-NP-300C,96h (d) samples. The crystalline phases in the samples are depicted by respective different symbols denoting the angular positions of their main diffraction peaks. The average crystalline domain size <D> of the fcc iron–nickel, spinel-type iron-nickel-oxide and iron-oxyborate phases for the annealed nanohybrid samples and that of the fcc iron-nickel phase for the annealed unsupported samples are denoted in the corresponding patterns.

7.1.2 Samples prepared using the impregnation method

The XRD patterns of the conventional AM-NHD precursor samples prepared using the impregnation method (IM) are presented in Figure 7.3. These patterns exhibit structural features similar to the precursor samples using the BH method, as indicated by the presence of the characteristic NDs diffraction peaks at 43.9° (111), 75.3° (220), and 91.5° (311) 2θ, along with those of the spinel-type INO structure at 30.3° (220), 35.7° (311), and 63.1° (440) 2θ, respectively [2]. The average crystalline domain size <D> for the NDs and INO phases was estimated using the Scherrer formula, based on the most resolvable widths of their main diffraction peaks. The NDs were found to have an average size of $<D_{NDs}> = 5$ nm, while the INO NPs had an average size of $<D_{INO}> = 2$ nm. These results demonstrate that the first step of this synthesis method effectively produces very small INO NP seeds on the ND nanotemplate matrices, without the formation of any metallic alloy or secondary impurity phase.

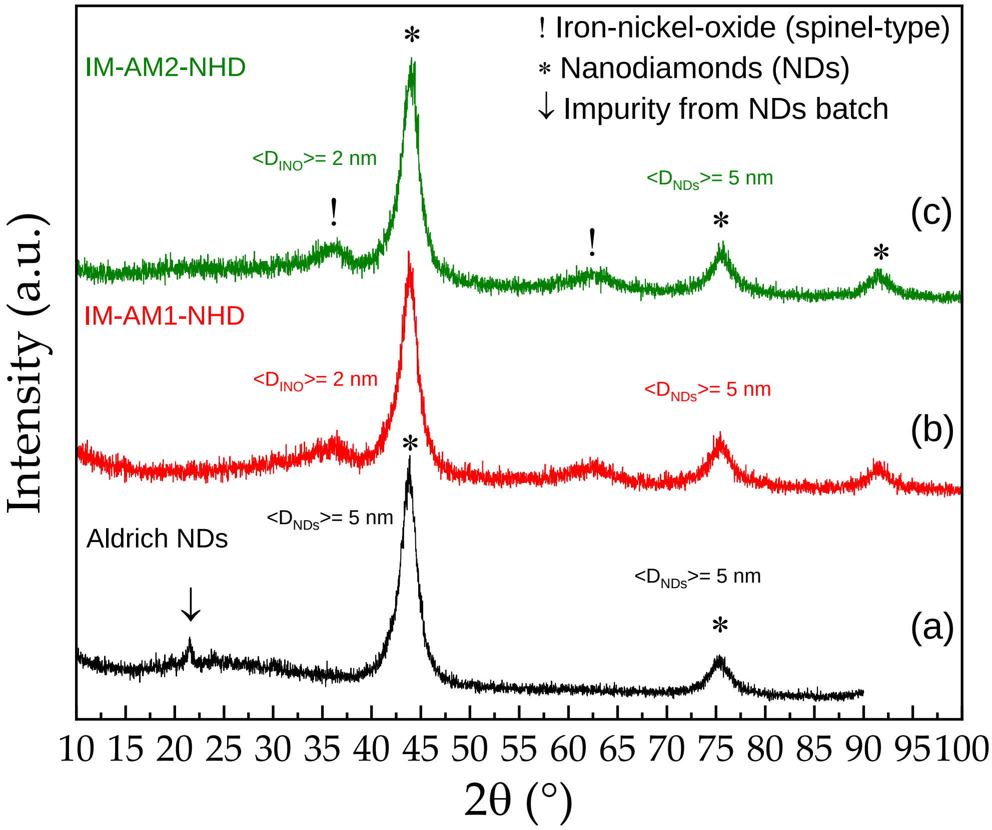

Figure 7.3 XRD patterns of the pristine NDs (a), IM-AM1-NHD (b) and IM-AM2-NHD (c) samples. The crystalline phases in the samples are depicted by respective different symbols denoting the angular positions of their main diffraction peaks. The average crystalline domain size <D> of the nanodiamonds and spinet-type iron-nickel-oxide phases for the pristine nanodiamonds batch and the as-made nanohybrid precursor samples are denoted in each pattern.

The XRD patterns of the annealed samples, derived from annealing these two as-made nanohybrid precursors at 700°C for 30 minutes and 4 hours, are shown in Figure 7.4. It is clear that annealing the impregnated nanohybrid precursors at this temperature and for these durations induces the formation of a new nanocrystalline phase, while the NDs phase is completely preserved, and the INO phase becomes diminished. Notably, no secondary impurity phases are observed in the XRD patterns of the annealed samples.

In particular, in addition to the characteristic ND diffraction peaks, significant contributions from the broad diffraction peaks of a cubic fcc Fe–Ni crystal structure are observed at 43.8° (111), 51.1° (200), 75.1° (220), 91.2° (311), and 96.6° (222) 2θ for all the annealed samples. Due to the relatively broad width of these diffraction peaks, an accurate determination of the atomic Fe-Ni ratio based on their angular positions is challenging. This is because three different ICDD PDFs—representing iron-rich ($Fe_{0.7}Ni_{0.3}$, ICDD PDF 01-071-8325, lattice constant a = 3.575 Å), equiatomic ($Fe_{0.5}Ni_{0.5}$, ICDD PDF 01-071-8322, lattice constant a = 3.575 Å), and iron-poor ($Fe_{0.3}Ni_{0.7}$, ICDD PDF 01-074-5840, lattice constant a = 3.564 Å) Fe-Ni stoichiometries—qualitatively match these diffraction peaks. The exact nature, morphology, and stoichiometry of this phase are further clarified through TEM analysis (vide infra).

Despite the uncertainty in stoichiometry, the average Fe-Ni NPs crystalline domain size <D>, which was estimated using the Scherrer formula from the most resolvable width of the (200) diffraction peak at 51.1° 2θ, falls within a narrow range of 7 to 9 nm for the IM-NHD-700C,30m and IM-NHD-700C,4h samples, respectively, while larger sizes, ranging from 11 to 16 nm, are observed for the IM-NHD2-700C,30m and IM-NHD2-700C,4h samples. The higher NP size consistently seems to be associated with the longer annealing duration. However, the morphology and nature of the INO seeds on the precursor sample could also influence the particle size of the final Fe-Ni NPs developed at the annealed samples.

These results suggest that the formation of the Fe-Ni alloy phase from the reduction of INO NP seeds can be effectively achieved at 700°C, with no residual INO phase remaining, at least as evident from the XRD analysis. Furthermore, the difference in annealing durations—30 minutes versus 4 hours—does not seem to have a significant impact on the average particle size or leave any residual phase, indicating that the Fe-Ni alloy phase can form within a relatively short period of time during the annealing process.

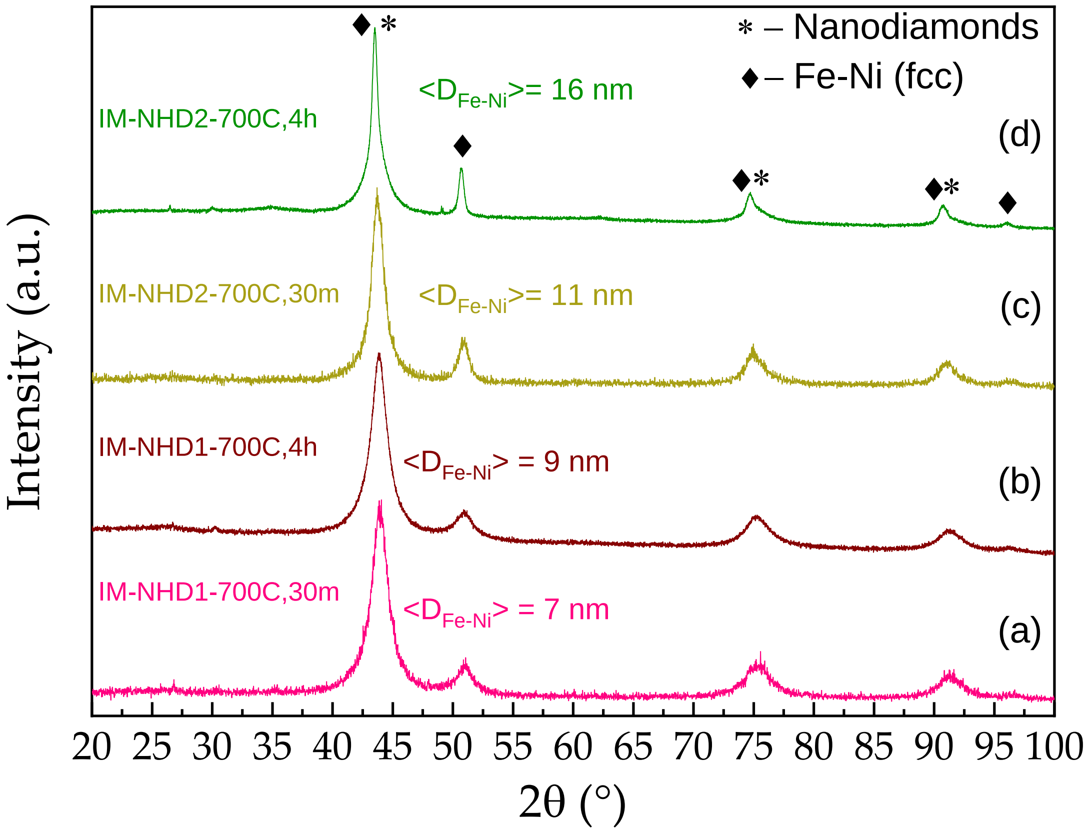

Figure 7.4 XRD patterns of the IM-NHD-700C,30m (a), IM-NHD-700C,4h (b) IM-NHD2-700C,30m (c) and IM-NHD2-700C,4h (d) samples. The crystalline phases in the samples are depicted by respective different symbols denoting the angular positions of their main diffraction peaks. The average crystalline domain size <D> of the nanodiamonds and spinel-type iron-nickel phases for the annealed nanohybrid samples are denoted in each pattern.

In this context, Figure 7.5 shows the XRD patterns of the conventional precursor sample (IM-AM2-NHD) after a two-step thermal treatment procedure. These treatments involve the implementation of the first annealing step, followed by a subsequent-second annealing step, which takes place in situ inside the furnace after the first annealing step's completion. This strategy aimed to the investigation of possible further structural modifications of the respective samples, since it is known that the extended annealing at 300°C could promote the development of hybrid nanostructured magnetic nanomaterials with enhanced long-range chemical ordering [3]. Consequently, we used two approaches: 1) the precursor was annealed at 700°C for 30 minutes and subsequently at 300°C for 64 hours, and 2) the precursor was annealed at 700°C for 4 hours and subsequently at 300°C for 96 hours. The XRD patterns of the resulting samples appear in Figure 7.5.

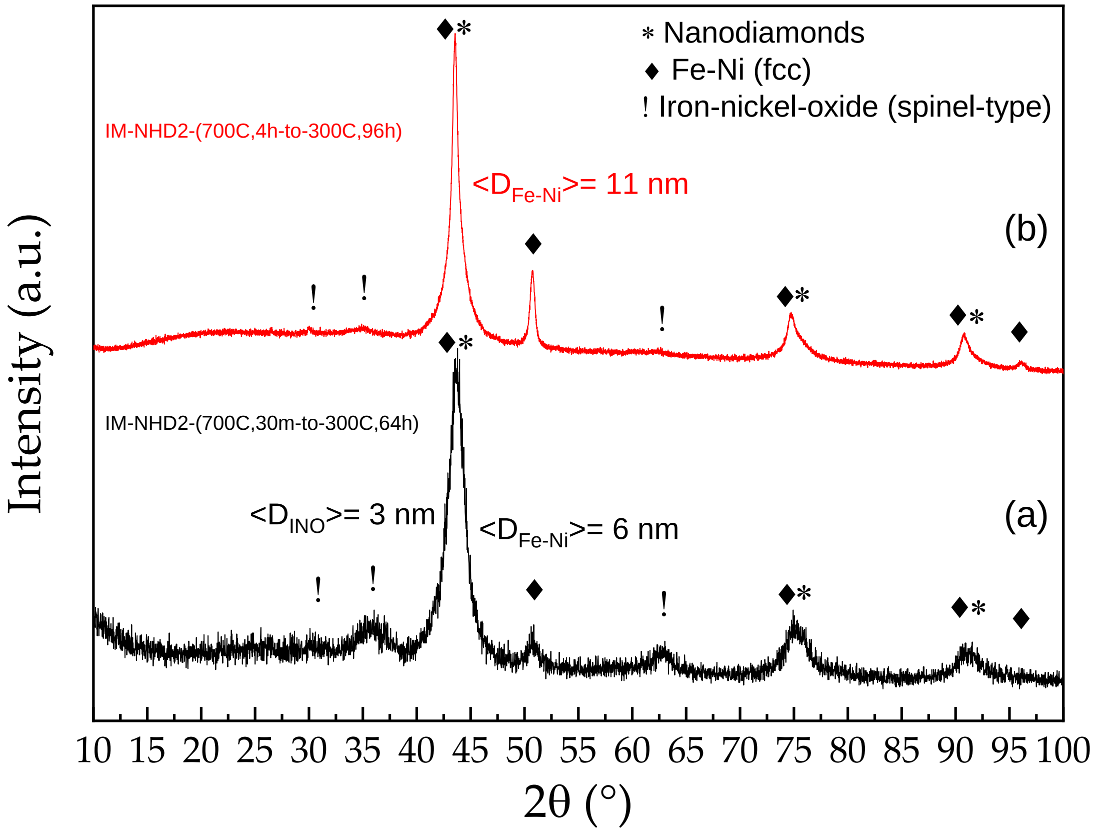

Figure 7.5 XRD patterns of the IM-NHD2-(700C,30m-to-300C,64h) (a) and IM-NHD2-(700C,4h-to-300C,96h) (b) samples. The crystalline phases in the samples are depicted by respective different symbols denoting the angular positions of their main diffraction peaks. The average crystalline domain size <D> of the nanodiamonds and the spinel-type iron-nickel phases for the annealed nanohybrid samples are denoted in each pattern.

The XRD patterns of the two-step annealed samples show similar structural characteristics to those of the annealed samples derived by using the one-step annealing (see also Figures 7.4c, d). These structural features pertain to the presence of the characteristic diffraction peaks attributed to the NDs and Fe-Ni nanostructures. However, these nanostructures are also accompanied by an inferior contribution, attributed to the less intense and broad diffraction peaks of the INO phase.

An estimation of the average crystalline domain size <D> from the most resolvable widths of the nanostructures' diffraction peaks, render to the Fe-Ni NPs an average NP size of 6 nm in the IM-NHD2-(700C,30m-to-300C,64h) sample, which grows larger at 11 nm, as the precursor sample is annealed for longer annealing durations in the second step as observed in the IM-NHD2-(700C,4h-to-300C,96h) sample. On the other hand, the INO NPs obtain an average NP size of 3 nm in case of the IM-NHD2-(700C,30m-to-300C,64h) sample, while its diffraction peaks become unresolvable, but are yet detectable, thus making difficult an estimation of its NPs size.

These results indicate that the formation of the fcc Fe-Ni alloy phase from the reduction of INO NP seeds can be delivered regardless the usage of a subsequent second annealing step, during thermal treatments, indicating the importance and the effectiveness of the first annealing step at a high temperature. However, the second annealing step seems to impair the structural features of both two-step annealed samples, as observed by the presence of the residual INO phase. This formation may be owed to the presence of mild oxidation conditions that could influence the metallic NPs, during the second annealing step at the lower annealing temperature of 300°C and extended durations.

We continue with the study of the XRD patterns of the enriched as-made precursor sample (En-IM-AM3-NHD) alongside its corresponding annealed samples appearing in Figure 7.6. According to these measurements, the two sets of samples— enriched with the ^{57}Fe reagent and conventional (non-enriched)—exhibit similar structural characteristics. Specifically, the XRD pattern of the En-IM-AM3-NHD sample in Figure 7.6a reveals the dominant presence of broad diffraction peaks attributed to NDs, along with two weaker diffraction peaks associated with the INO spinel-type phase. Application of the Scherrer formula to the corresponding peaks of these diagrams provides an estimated average crystalline domain size of $<D_{NDs}>$ = 4 nm for the NDs, while an estimation for the INO phase could not be made due to the unresolved and low-intensity nature of its diffraction peaks.

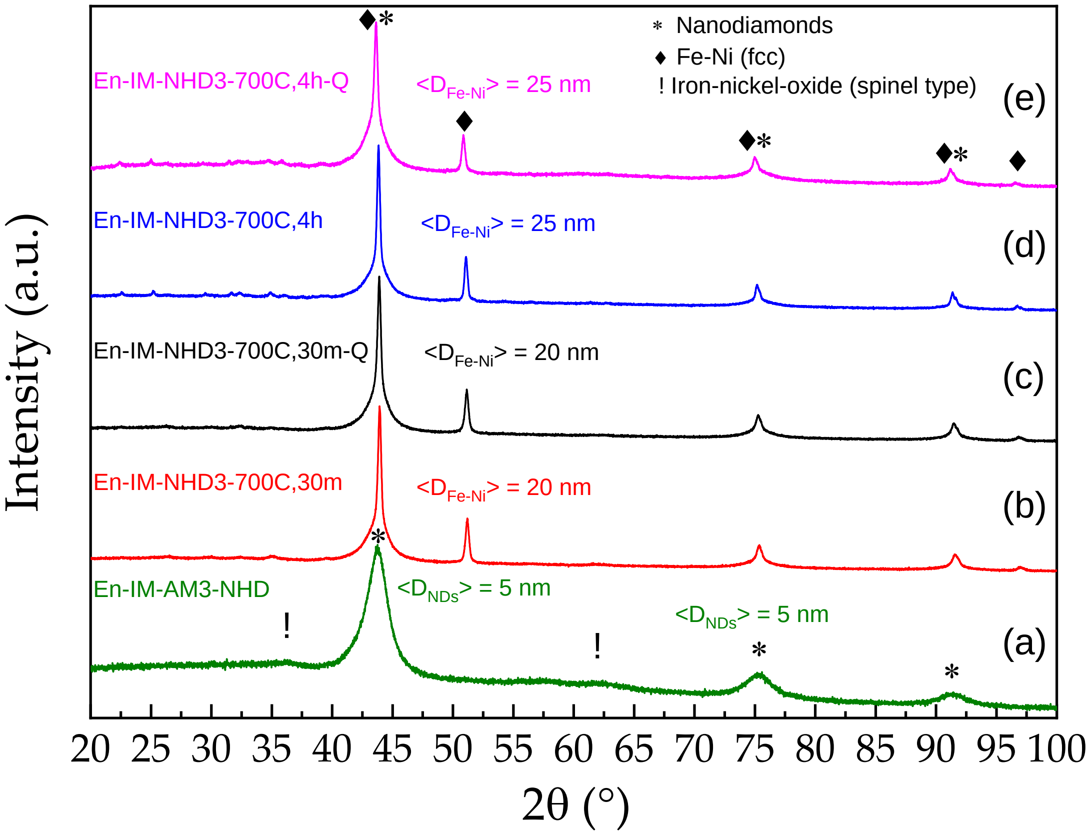

Figure 7.6 XRD patterns of the En-IM-AM3-NHD (a), En-IM-NHD3-700C,30m (b), En-IM-NHD3-700C,30m-Q (c) En-IM-NHD3-700C,4h (d) and En-IM-NHD3-700C,4h-Q (e) samples. The crystalline phases in the samples are depicted by respective different symbols denoting the angular positions of their main diffraction peaks. The average crystalline domain size <D> of the iron-nickel phase for the enriched annealed nanohybrid samples are denoted in each pattern.

Annealing the En-IM-AM3-NHD precursor at 700°C induces the formation of Fe–Ni fcc nanostructures, in addition to retaining the ND nanotemplates, across all durations for the enriched annealed samples, a behavior similar to that observed for the conventionally prepared as-made precursors. As with the annealed samples prepared from the conventional precursors, the nature, morphology, and stoichiometry of this phase, along with that of the Fe–Co alloy phase, will be further elucidated through TEM analysis (vide infra). The average crystalline domain size <D> for the Fe–Ni phase across all annealing durations ranges between 20 and 25 nm, which is significantly larger than those observed for samples prepared from conventional precursors (7–9 nm and 11–16 nm, respectively). Notably, the highest nanoparticle size, 25 nm, is observed for samples annealed for 4 hours, indicating that longer annealing times lead to an increase in Fe–Ni particle size for the enriched precursors.

Regarding the annealed enriched samples influenced by the quenching (Q) process, no significant differences are observed in their XRD patterns appearing in Figure 7.6(c) and (e) for the En-IM-NHD3-700C,30m-Q and En-IM-NHD3-700C,4h-Q respectively, compared to their non-quenched counterparts.

7.2 TEM, STEM and EDS Analysis

7.2.1 TEM Analysis of the impregnated precursor sample

The dispersion, morphology, and structure of the nanophases were characterized through TEM/STEM observations. Figure 7.7 presents TEM images of a representative precursor hybrid sample, specifically the conventional IM-AM1-NHD precursor. The morphological analysis of this sample reveals a nanohybrid system consisting of relatively spherical INO NPs, which appear with darker contrast in the bright-field images. These NPs are dispersed on closely packed NDs, which are forming approximately spherical as well as irregular-shaped nanotemplate clusters with sizes ranging from 30 to 800 nm. The INO NPs themselves exhibit roughly spherical shapes and a broad size distribution, appearing as individual NPs with low interconnection to each other, or in some cases forming more densely packed clusters. The INO NPs situated at the center of the larger NDs hybrid clusters appear sharper and denser, suggesting relatively higher crystallinity and larger sizes compared to the more diffuse INO NPs located at the edges and within smaller hybrid clusters.

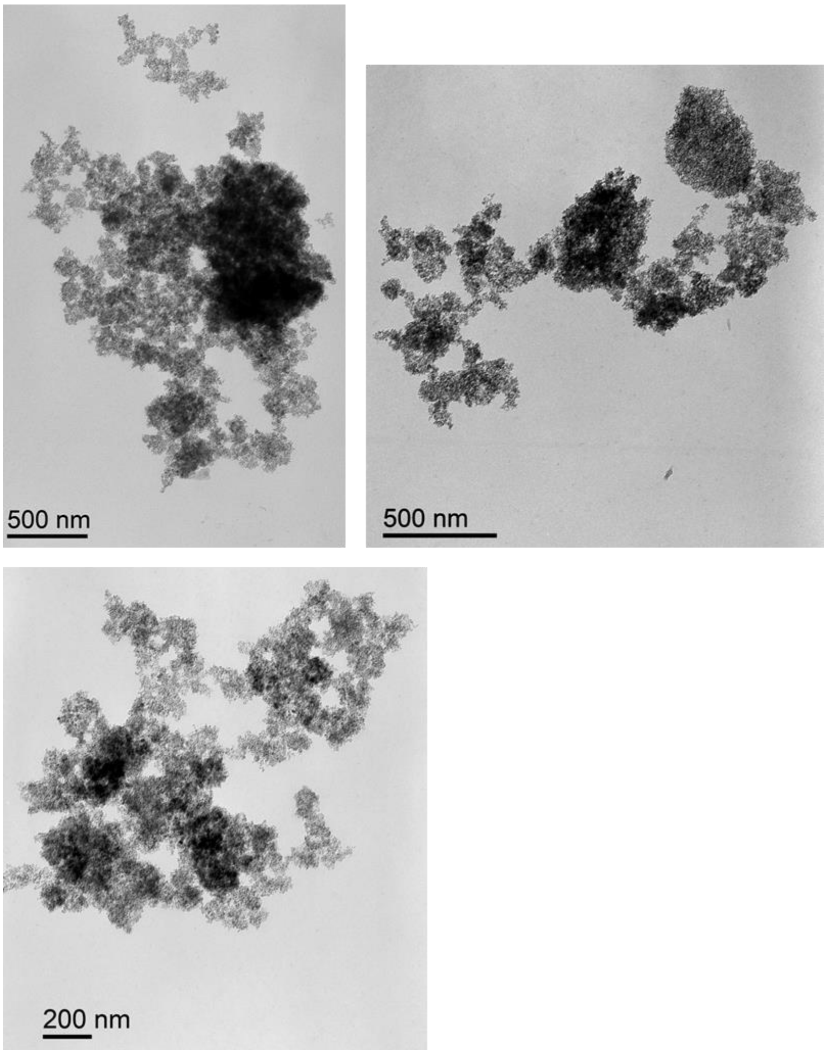

Figure 7.7 Bright-field TEM images of the IM-AM-NHD sample at different magnifications.

7.2.2 TEM, STEM and EDS analysis of the annealed impregnated samples

Representative TEM images of two annealed samples, specifically the IM-NHD-700C,4h and En-IM-NHD3-700C,30m-Q samples, are shown in Figures 7.8 and 7.13, respectively. Furthermore, HAADF-STEM-EDS and HRTEM images, which provide detailed chemical and structural analysis of these two samples, are presented in Figures 7.9-7.12, and 7.14-7.16.

For the IM-NHD-700C,4h sample, Figure 7.8 displays a homogeneous dispersion of coarse NDs agglomerates with arbitrary shapes, ranging from 35 to 120 nm in sizes. These NDs clusters host well-dispersed, roughly spherical metallic NPs on their surfaces, which appear darker due to their higher mass density compared to the NDs.

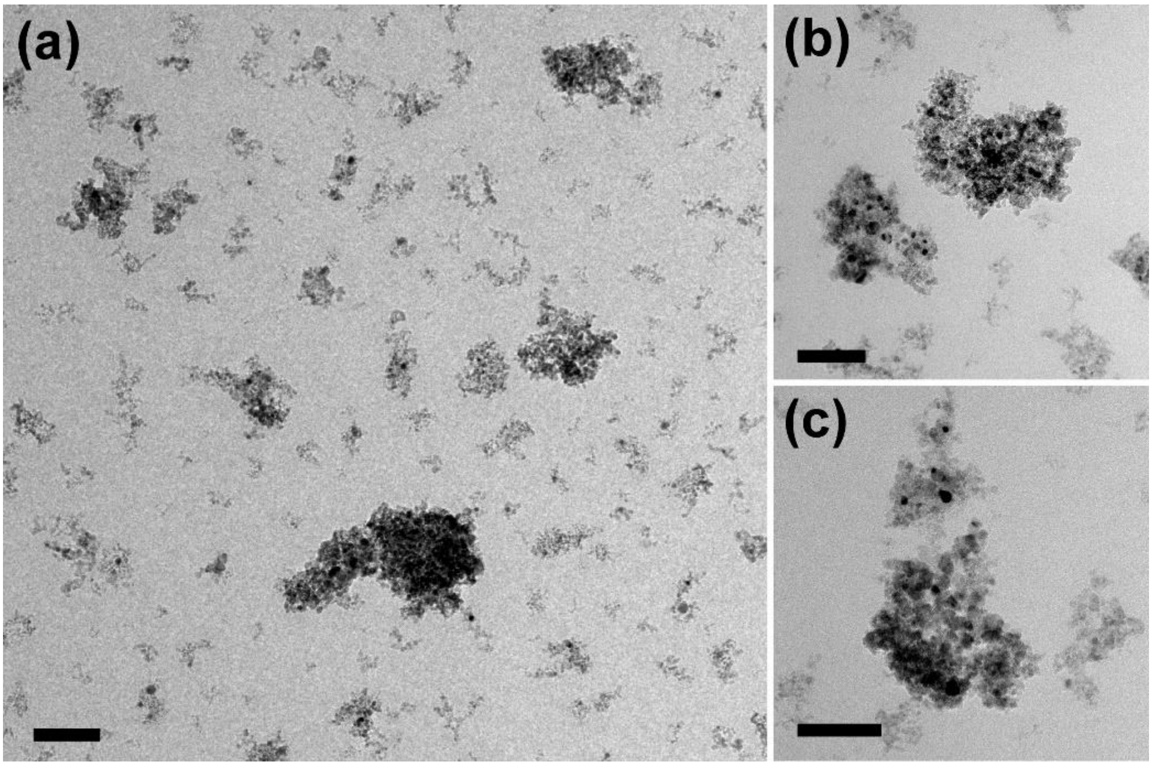

Figure 7.8 Bright-field TEM images of the IM-NHD-700C,4h sample (a-c) at different magnifications. The scalebars correspond to 100 nm.

To better visualize the distribution of metallic NPs within the hybrid structures, HAADF imaging in STEM mode was employed, as its contrast is proportional to atomic number. Figures 7.9a-c present HAADF-STEM images of the IM-NHD-700C,4h sample, illustrating the distribution of metallic NPs across various hybrid clusters. Figure 7.9d shows the metallic Fe-Ni NPs size distribution, which exhibits an asymmetric pattern skewed toward larger sizes, with an average value of 10 nm. Elemental EDS maps from an NHD cluster, presented in Figures 7.9f-g, confirm the co-localization of Fe and Ni atoms, indicating the formation of an Fe-Ni alloy. Additionally, point EDS spectra from individual metallic NPs, shown in Figures 7.10 and Table 7.1, suggest that the Fe-Ni alloy is predominantly Ni-rich, with an average atomic ratio of Fe around 36:64 ($Fe_{36}Ni_{64}$).

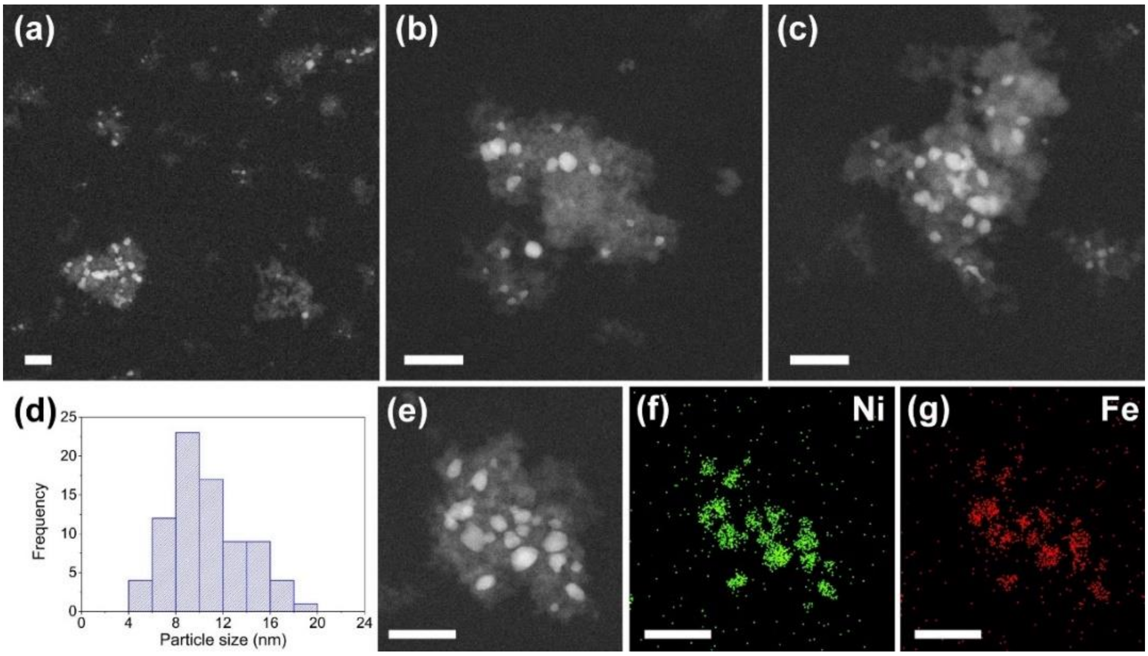

Figure 7.9 HAADF STEM images from different NHD clusters of the IM-NHD-700C,4h sample (a-c). Distribution of the Fe-Ni metallic NPs sizes (d). HAADF STEM image of a particular hybrid Fe-Ni NPs/NDs cluster (e) and the corresponding elemental distribution of Ni (f) and Fe (g). All scalebars correspond to 50 nm.

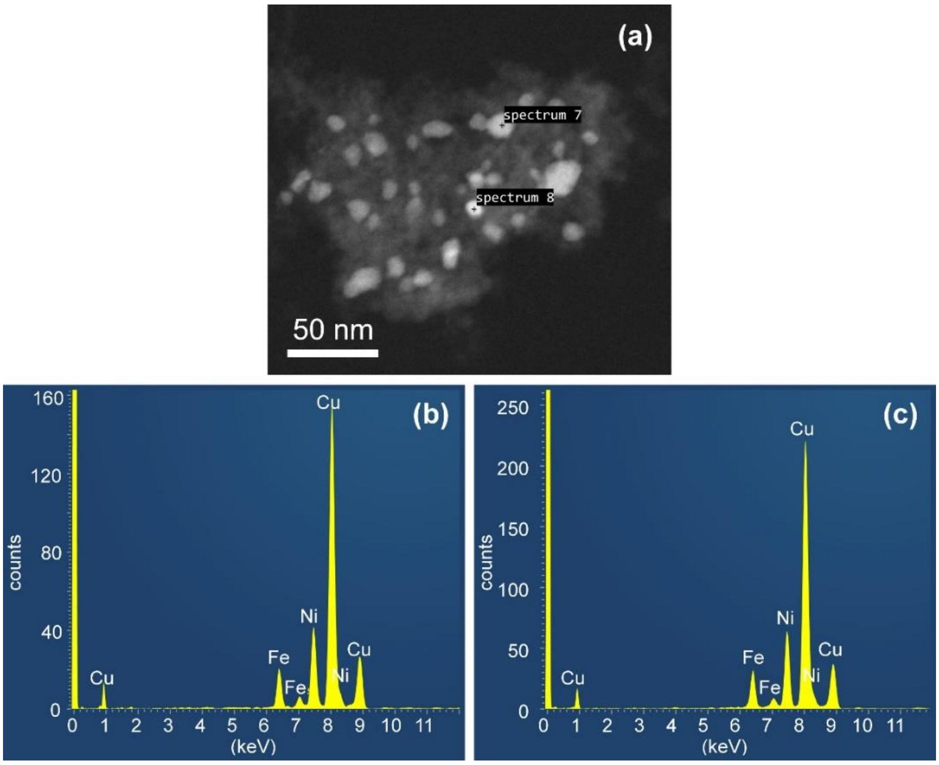

Figure 7.10 (a) HAADF-STEM image from a Fe-Ni NPs/NDs cluster in the IM-NHD-700C,4h sample, illustrating locations where EDS point analysis was conducted. Spectra (b) #7 and (b) #8. Cu peaks are due to the TEM supporting grids.

Table 7.1 Fe compositions measured in IM-NHD-700C,4h sample, using EDS analysis on individual Fe-Ni NPs.

Point	Fe at. %
1	32
2	28
3	30
4	37
5	44
6	44
7	36
8	34
Average:	**36**

Moving forward, Figure 7.11 presents HRTEM images of various metallic Fe-Ni NPs developed on the surfaces of the ND nanotemplates of the IM-NHD-700C,4h sample. The characteristic d-spacings corresponding to the close-packed {111} planes and the {002} planes of the fcc $Fe_{36}Ni_{64}$ alloy are clearly resolved. Additionally, as highlighted by the blue pseudo-color overlay, few-layered graphitic-type structures are observed at the interface between the metallic Fe-Ni NPs and the carbon support assembly. These graphitic-type structures partially envelop the metallic NPs, appearing solely in regions where direct contact occurs between the Fe-Ni NPs and the ND nanostructured template. This phenomenon is further detailed in Figure 7.11a, where the white borderline delineates the edge of the ND support. The formation of graphitic-type layers has been consistently noted in numerous other Fe-Ni NPs examined in this sample, as shown in Figure 7.12.

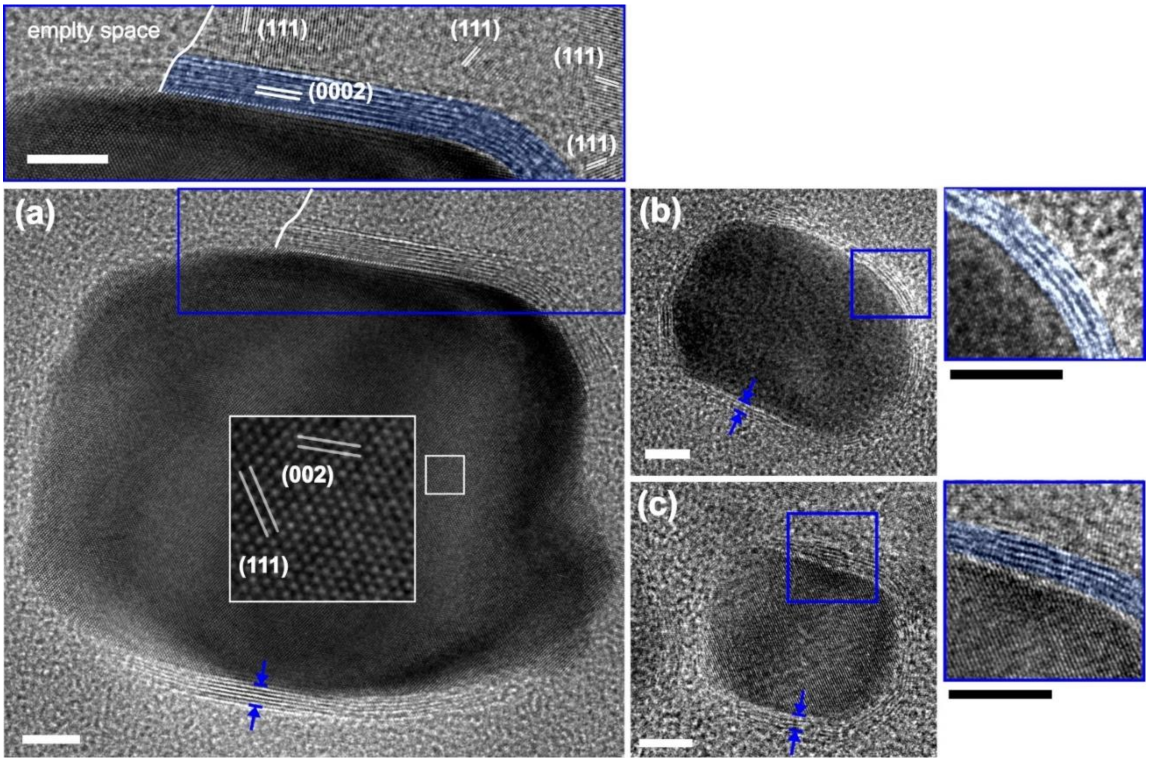

Figure 7.11 HRTEM investigation of the IM-NHD-700C,4h sample. The Fe-Ni NP in (a) sits at the edge of a hybrid cluster and is viewed along the [1$\bar{1}$0] zone axis. The (111) and (002) planes of the fcc FeNi alloy are indicated. In the magnified inset a top, the characteristic (0002) close-packed planes indicate the formation of few-layered graphite (blue pseudo color) at the interface between the Fe-Ni NP and the ND nanotemplate. Close-packed {111} planes, coming from small ND crystallites are also indicated. The white line delineates the boarder of the ND nanotemplate. HRTEM images from other Fe-Ni metallic NPs, showing the formation of few-layered graphite of similar thicknesses (b,c). All scalebars correspond to 5 nm.

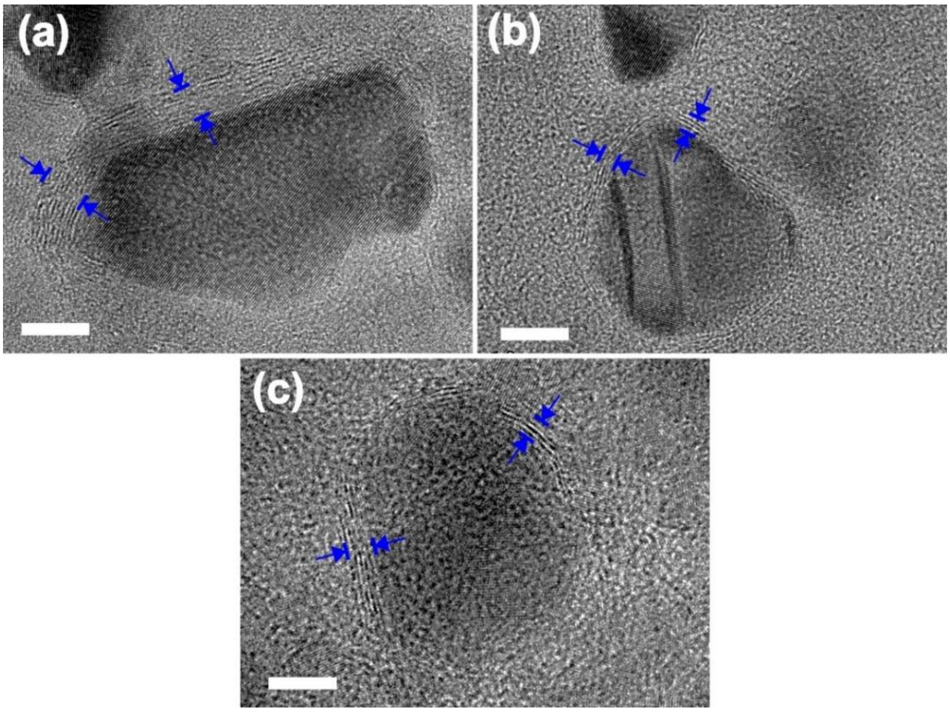

Figure 7.12 HRTEM images obtained from the IM-NHD-700C,4h sample, showing graphitic-type layers wrapping around Fe-Ni NPs (blue arrows).

Based on these TEM observations, it is evident that the formation of graphitic-type layered nanostructures is closely linked to the unique morphological features of the NDs within these nanotemplates, and how they are influenced by temperature as well as their interaction with the growing Fe-Ni NPs. Additionally, the regular occurrence of these graphitic layers on the surfaces of the Fe-Ni NPs, but only in regions where direct contact with the ND NPs is present, indicates a strong affinity of these sp^2 graphitic nanostructures for the metallic compounds. This underscores the critical role of carbon in their development. Furthermore, the consistent TEM observation of these graphitic layers at the interface between the Fe-Ni metallic NPs and the ND NPs, along with their resultant physiochemical interactions, suggests the potential diffusion of carbon atoms into the Fe-Ni alloy structure.

Moving on, Figure 7.13 provides a detailed view of the morphological characteristics of the En-IM-NHD3-700C,30m-Q sample. This figure displays a hybrid system consisting of ND cluster assemblies with roughly spherical nanotemplates evenly dispersed throughout the image. These nanotemplates are accompanied by relatively round metallic Fe-Ni NPs on their surfaces, which appear darker in contrast in the bright-field images. The metallic NPs are developed on closely packed ND NPs, forming coarse agglomerated nanotemplates similar to those observed in the IM-NHD-700C,4h sample. These ND nanotemplates exhibit both spherical and irregular shapes, with sizes ranging from 40 to 150 nm (Figures 7.13a, b). However, several large diamond nanoclusters do not display any metallic NPs on their surfaces. Furthermore, an extensive, presumably amorphous, carbon phase is observed interconnecting with the ND nanotemplates, giving this sample a distinct morphology compared to the conventional IM-NHD-700C,4h sample.

One factor that may have contributed to this morphological variation is owed to the extended sonication time (60 minutes) in ethanol that was applied for the preparation this sample for TEM observations.

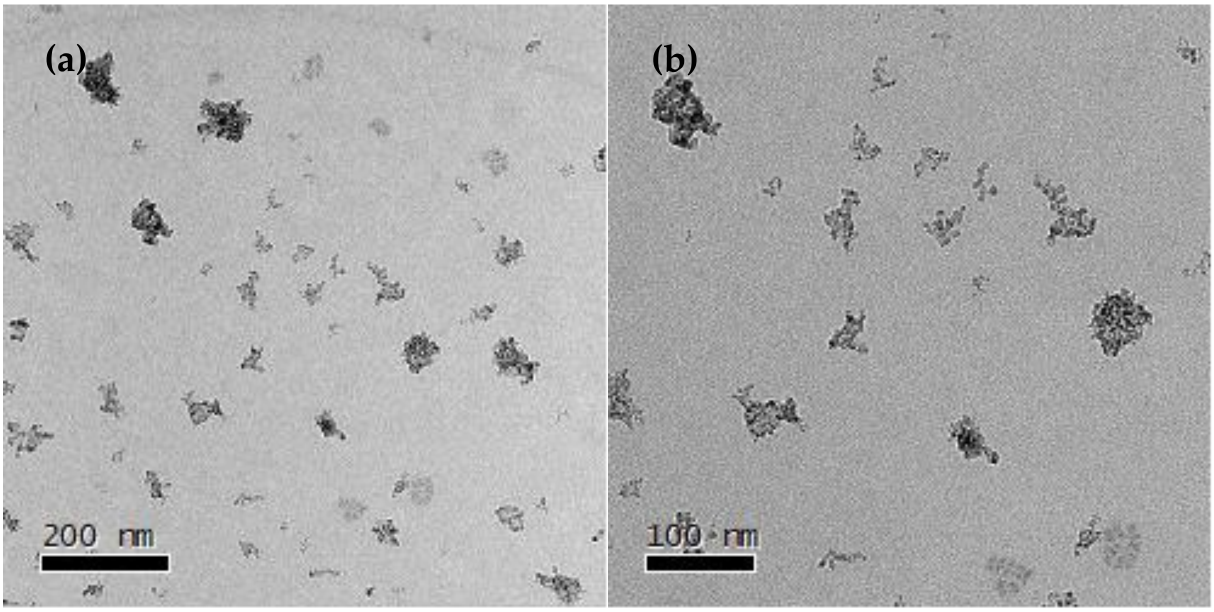

Figure 7.13 TEM images of En-IM-NHD3-700,30m-Q sample at different magnifications (a-b).

HAADF Z-contrast imaging in STEM mode reveals the presence of more cohesive aggregated hybrid clusters in the En-IM-NHD3-700C,30m-Q sample compared to the IM-NHD1-700C,4h sample. The metallic NP density is noticeably reduced in the En-IM-NHD3-700C,30m-Q sample (Figure 7.14a-b). EDS elemental maps from an NHD cluster, displayed in Figures 7.14e and f, confirm that Fe and Ni atoms are co-located, indicating the formation of the Fe-Ni alloy. The size distribution of these metallic NPs is centered around an average of 22 ± 12 nm as shown in Figure 14c. Further point EDS spectra of individual metallic NPs, as shown in Figures 7.15 and Table 7.2, suggest that the Fe-Ni alloy phase is predominantly Ni-rich, with an average atomic ratio of 20:80 ($Fe_{20}Ni_{80}$).

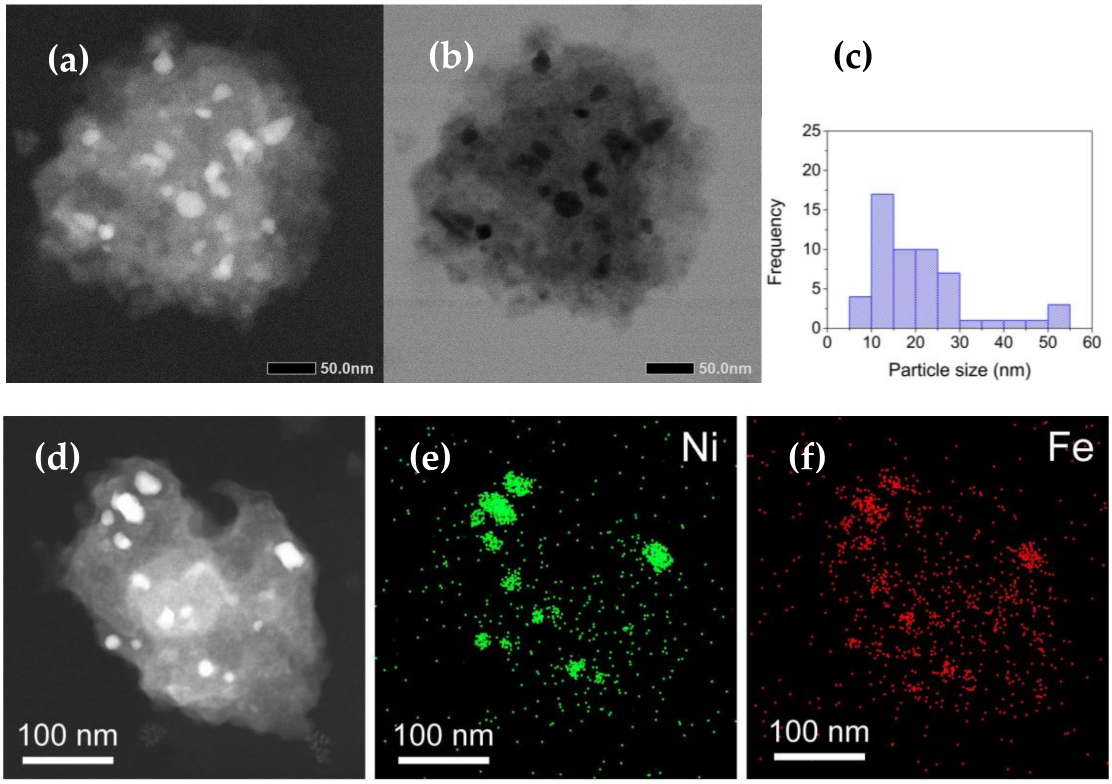

Figure 7.14 HAADF STEM images from different NHD clusters of the En-IM-NHD3-700C,30m-Q sample (a, b). Distribution of the Fe-Ni metallic NPs sizes (c). HAADF STEM image of a particular hybrid Fe-Ni NPs/NDs cluster (d) and the corresponding elemental distribution of Ni (e) and Fe (g).

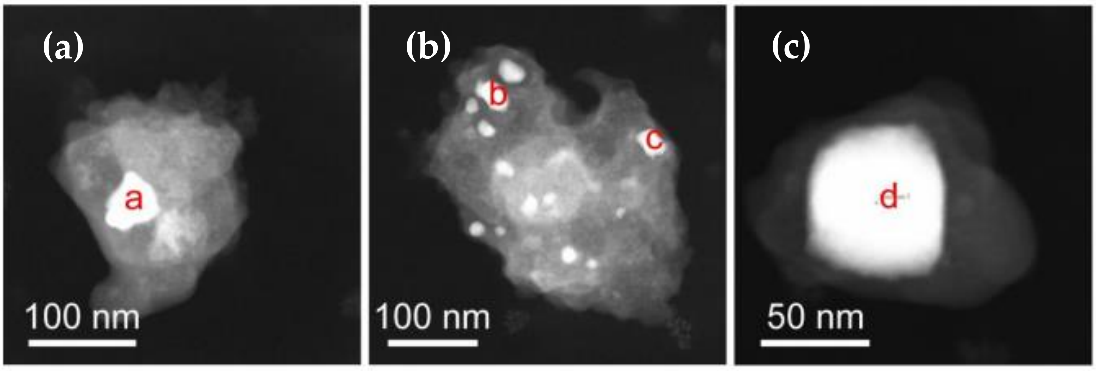

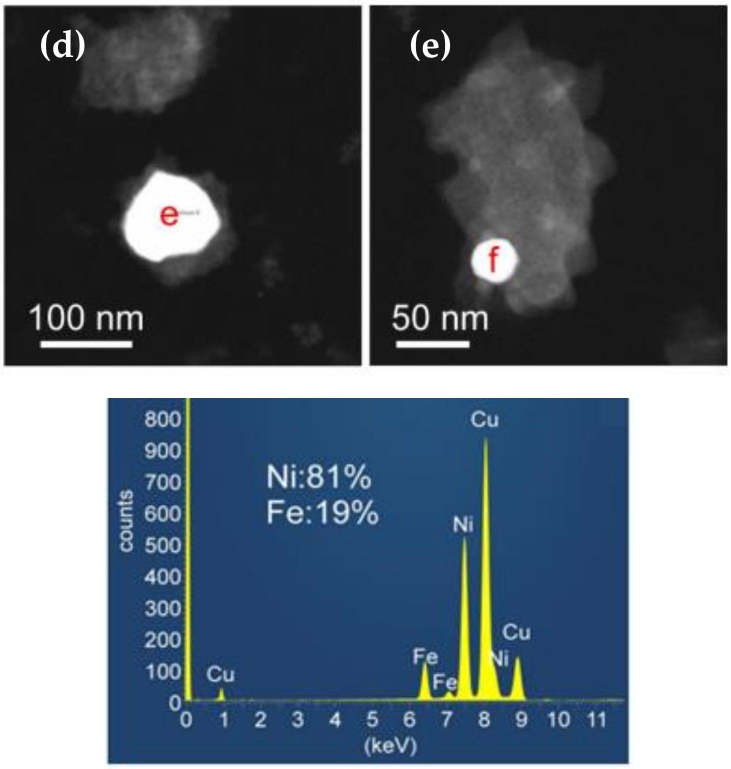

Figure 7.15 HAADF-STEM images from different Fe-Ni NPs/NDs clusters in the En-IM-NHD3-700C,30mQ sample, illustrating locations where EDS point analysis was conducted. Spectra (f) #b. Cu peaks are due to the TEM supporting grids.

Table 7.2 Fe compositions measured in En-IM-NHD3-700C,30m-Q sample, using EDS analysis on individual Fe-Ni NPs.

Point	**Fe at. %**
a	20
b	19
c	20
d	20
e	20
f	23
Average:	**20**

Figure 7.16a-c shows HRTEM images of well-crystallized Fe$_{20}$Ni$_{80}$ NPs with a distinct fcc crystal structure, developed on the surfaces of the NDs clusters. These images also depict a characteristic cubic morphology of the Fe$_{20}$Ni$_{80}$ NPs. HRTEM analysis reveals that the lattice constant α of the Fe$_{20}$Ni$_{80}$ NPs ranges from approximately 3.52 to 3.56 Å, which closely matches the values calculated

for the Fe-Ni phase in the En-IM-NHD3-700C,30mQ sample, which aligns this lattice constant with the ordered fcc FeNi$_3$ γ'-phase with an AuCu$_3$-type structure.

However, in the En-IM-NHD3-700C,30m-Q sample, no graphitic-type nanostructures are observed at the interfaces between the metallic NPs and the ND nanotemplates, a notable difference from the IM-NHD-700C,4h sample. This absence may be attributed to the extended sonication time of 60 minutes for the enriched annealed sample, compared to the 30-40 minutes applied for the conventional annealed sample. It is suggested that the longer sonication duration may have removed the majority of nanostructured species formed within the hybrid material, such as smaller metallic Fe-Ni NPs and/or localized graphitic-type structures that typically envelop metallic NPs at the interfaces where they directly contact the ND NPs. As a result, only the larger or more agglomerated metallic NPs, which developed on the surfaces of the ND nanotemplates, remain.

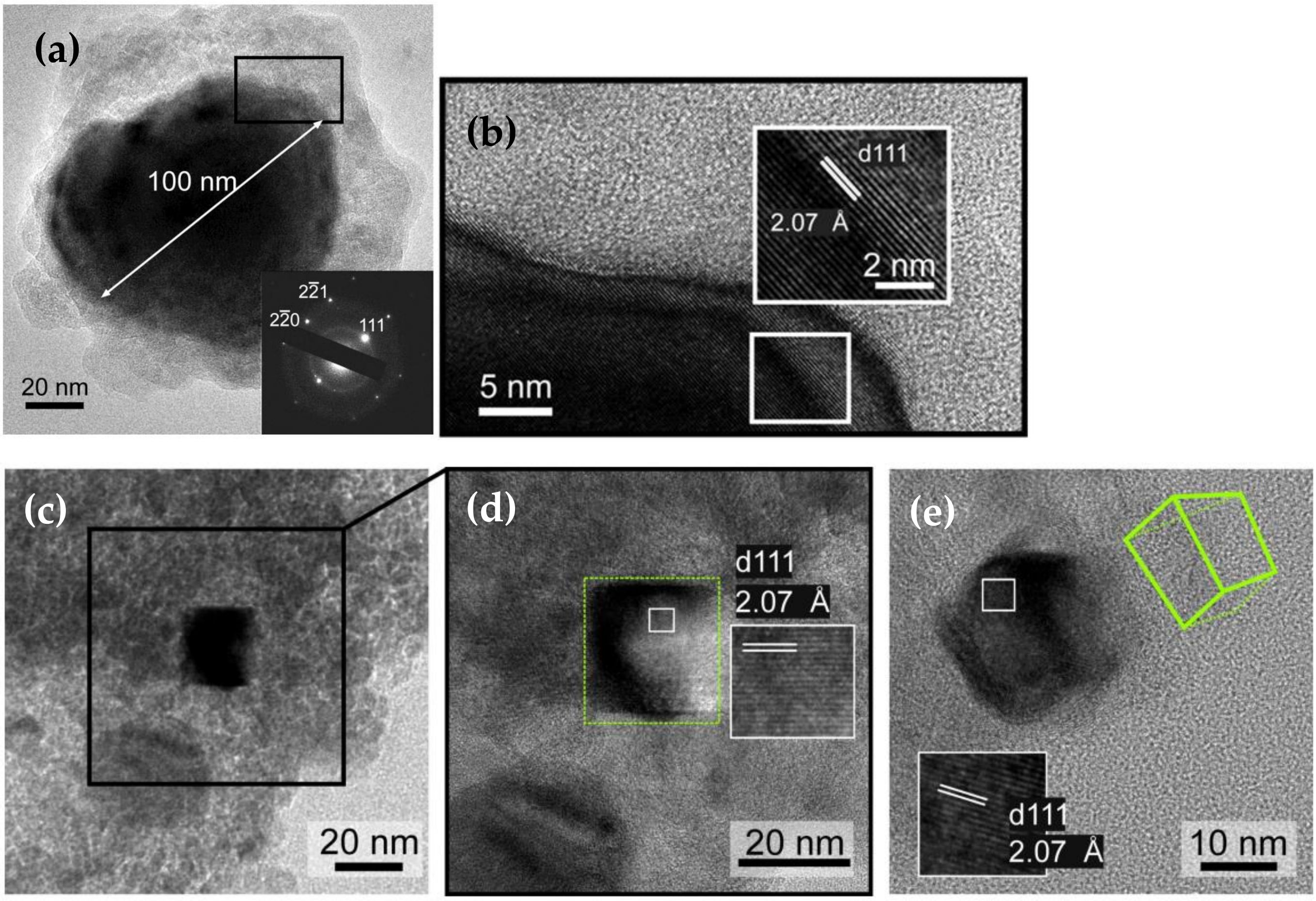

Figure 7.16 HRTEM images of the En-IM-NHD3-700C,30mQ sample. A large Fe-Ni/ND cluster and its selected area electron diffraction pattern is provided as an inset, revealing the $[11\bar{2}]$ zone axis (a). On the right the edge of the particle, is shown in larger magnification and the (111) close packed planes are annotated (b). HRTEM images showing geometric Fe-Ni NPs with characteristic cubic morphologies (c-e).

7.3 ^{57}Fe Mössbauer Spectroscopy

7.3.1 Samples prepared using the sodium borohydride reducing agent

The ^{57}Fe Mössbauer spectroscopy method, an atomic-level probing technique, offers a powerful tool to characterize the structural, morphological, electronic, and magnetic properties of iron-containing phases in the samples. Figures 7.17-18 display the ^{57}Fe Mössbauer spectra (MS) for both as-made nanohybrid and unsupported samples prepared with $NaBH_4$, recorded at RT and 77 K.

In Figure 7.17a, the 300 K spectrum of the as-made nanohybrid precursor sample exhibits a primary quadrupole-split contribution alongside a secondary magnetically split component. To achieve an accurate fit for the BH-AM-NHD sample, three central quadrupole split components and one magnetically split component were employed. For the magnetically split component, a Gaussian-type spreading (ΔB_{hf}) around the central hyperfine magnetic field (B_{hf}^{C}) value was used to account for line broadening in this region [4]. The Mössbauer parameters (MPs) obtained from the best-fit models are summarized in Table 7.3. These values indicate the presence of iron atoms in a Fe-Ni nanostructured phase [3], [5], as well as Fe^{3+} high-spin (S = 5/2) superparamagnetic (SPM) states, with minor contributions from Fe^{2+} high-spin (S = 2) SPM states.

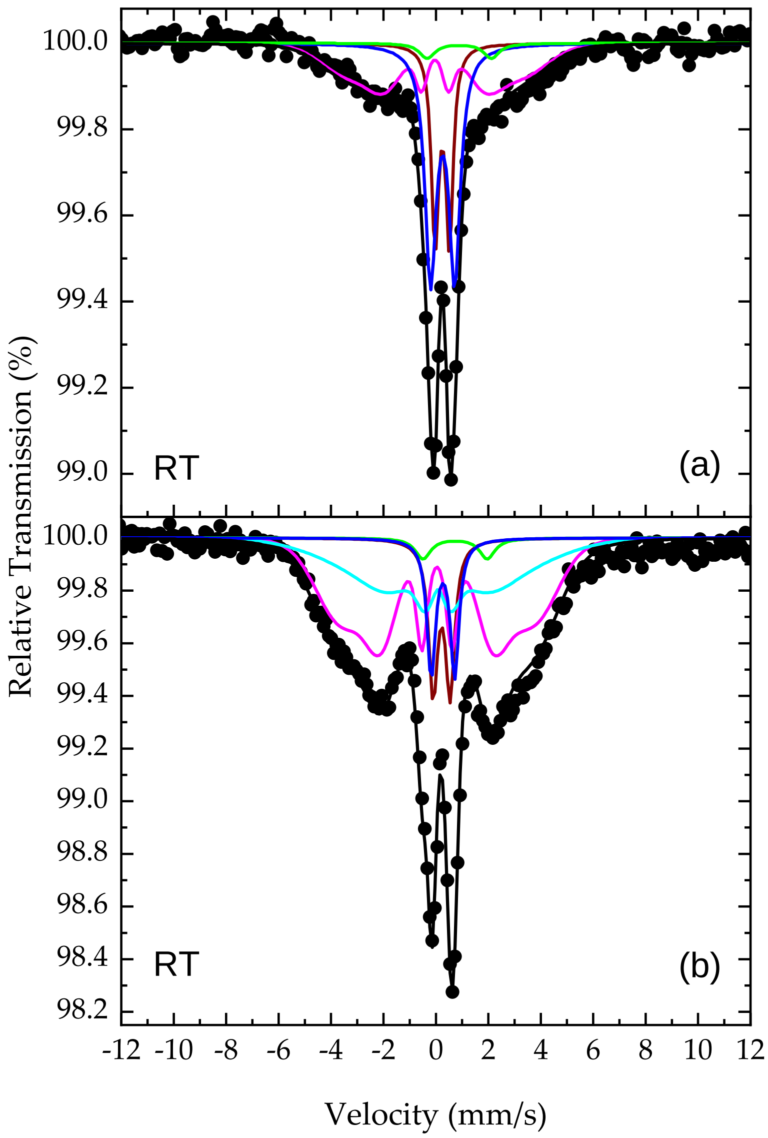

Figure 7.17 ^{57}Fe Mössbauer spectra of the as-made nanohybrid precursor (BH-AM-NHD) (a) and the unsupported precursor (BH-AM1-NP) (b) samples collected at room temperature.

The MPs of the Fe^{3+} and Fe^{2+} ion sites in oxygen-coordinated environments suggest the presence of spinel-type INO nanostructures. This is evidenced by two primary quadrupole doublets (SPM Fe^{3+} (1) and SPM Fe^{3+} (2), colored maroon and blue in Figure 7.17a) at the center of the nanohybrid sample's RT spectrum, alongside some additional Fe^{2+} ions (SPM Fe^{2+}, colored green in Figure 7.17a) in their structure [6]. These features, associated with small NP sizes, are characterized by fast SPM behavior at RT [6], [7]. Furthermore, a magnetically split contribution, comprising 37% of the absorption area (AA), is represented by a single magnetically component (MCOL Fe-Ni, colored magenta in Figure 7.17a) with collapsing B_{hf} behavior. This contribution suggests the presence of an assembly of Fe-Ni alloy NPs developed during the initial synthesis stage, that experience SPM relaxation, slow enough that the characteristic relaxation time (τ) surpasses the Mössbauer spectroscopy measurement time ($\tau_{MS} \sim 10^{-8}$ s) [8], [9]. This may result from larger NP sizes and/or agglomeration into clusters, where interparticle interactions slow relaxation times beyond τ_{MS} [8], [10], [11].

The spectrum of the BH-AM-NP sample in Figure 7.17b is composed of a dominant magnetically split contribution and a secondary quadrupole split contribution, both displaying relatively broad resonance lines. This spectrum was effectively fitted using two magnetically split components, supplemented by three central quadrupole doublets. The MPs derived from this fit are also listed in Table 7.3. Similar to the BH-AM-NHD sample, these values indicate high-spin Fe^{3+} ions typical of INO spinel-type nanostructures with additional Fe^{2+} ions for the SPM components. However, the Fe-Ni NPs here display a more dominant presence than that found in the nanohybrid precursor. Specifically, the main magnetically split contribution is captured by two components (MCOL Fe-Ni (1) in cyan and MCOL Fe-Ni (2) in magenta, Figure 7.17b), comprising up to 76% of AA, while the quadrupole split contribution is represented by three minor central doublets (SPM Fe^{3+} (1) and SPM Fe^{3+} (2) in maroon and blue, and SPM Fe^{2+} in green, Figure 7.17b), totaling 24% of AA. These findings indicate that most of the Fe-Ni NPs formed in the initial synthesis stage exceed the SPM threshold size, showing SPM relaxation phenomena such that $\tau > \tau_{MS}$ [8], [9]. This may stem from an increase in particle size and/or clustering into larger aggregates, where interparticle interactions extend τ beyond τ_{MS} [8], [10], [11].

Table 7.3 Mössbauer hyperfine parameters as resulting from the best fits of the corresponding spectra of the samples shown on **Figure 7.17**. IS the isomer shift (given relative to α-Fe at 300 K), Γ/2 is the half-line width, QS is the quadrupole splitting, 2ε is the quadrupole shift, B_{hf}^{C} is the central value of the hyperfine magnetic field, ΔB_{hf} is the total spreading (Gaussian-type) of the B_{hf} values around the central B_{hf}^{C} value, and AA is the relative spectral absorption area of each component used to fit the spectra. Typical errors are ±0.02 mm/s for IS, Γ/2, 2ε and QS, ±3 kOe for B_{hf}^{C} and ±3% for AA.

Sample	Component	I.S. (mm/s)	Γ/2 (mm/s)	Q.S. or 2ε (mm/s)	B_{hf}^{C} (kOe)	ΔB_{hf} (kOe)	Area (%)	Color
BH-IM-NHD	SPM Fe^{3+} (1)	0.35	0.18	0.64	0	0	20	Maroon
	SPM Fe^{3+} (2)	0.36	0.26	0.92	0	0	37	Blue
	SPM Fe^{2+}	0.94	0.36	2.43	0	0	7	Green
	MCOL Fe-Ni	0.07	0.15	0.00	202	61	36	Magenta
BH-AM-NP	SPM Fe^{3+} (1)	0.33	0.21	0.65	0	0	11	Maroon
	SPM Fe^{3+} (2)	0.35	0.20	0.89	0	0	10	Blue
	SPM Fe^{2+}	0.94	0.33	2.45	0	0	3	Green
	MCOL Fe-Ni (1)	0.15	0.15	0.00	179	110	29	Cyan
	MCOL Fe-Ni (2)	0.17	0.15	0.00	226	56	47	Magenta

The thermal evolution of the MS for the nanohybrid and unsupported precursor samples, measured at 77 K, is shown in Figure 7.18. At this lower temperature, both samples' spectra can be fitted using the same models applied at RT (see Figure 7.18 and Table 7.4). All ionic and iron alloy components exhibit expected shifts in isomer shift (IS) and hyperfine magnetic field (B_{hf}) values, while their AA values remain nearly identical (within expected error) to those at RT. This consistency in AA values between the SPM and MCOL components at 77 K suggests no noticeable changes in the distribution of these components at lower temperature. If we anticipated a decrease in SPM relaxation time (τ) for the nanostructured INO NPs at 77 K, a larger proportion of the nanostructured phases would cease very fast SPM relaxation, which would affect the AA values of the SPM and MCOL components [7].

However, the observed retention of spectral characteristics at 77 K in both samples implies the formation of strongly magnetically interacting Fe-Ni NPs. On the other side the INO NPs are likely to reside on the surfaces of the ND nanotemplates in the nanohybrid sample or as standalone INO NPs in the unsupported sample, or even forming the shell of a core-shell structure having the Fe-Ni NPs as the cores, as found in similar nanophases prepared using the BH method [12], likely due to the influence of the $NaBH_4$ reducing agent used in the initial synthesis step.

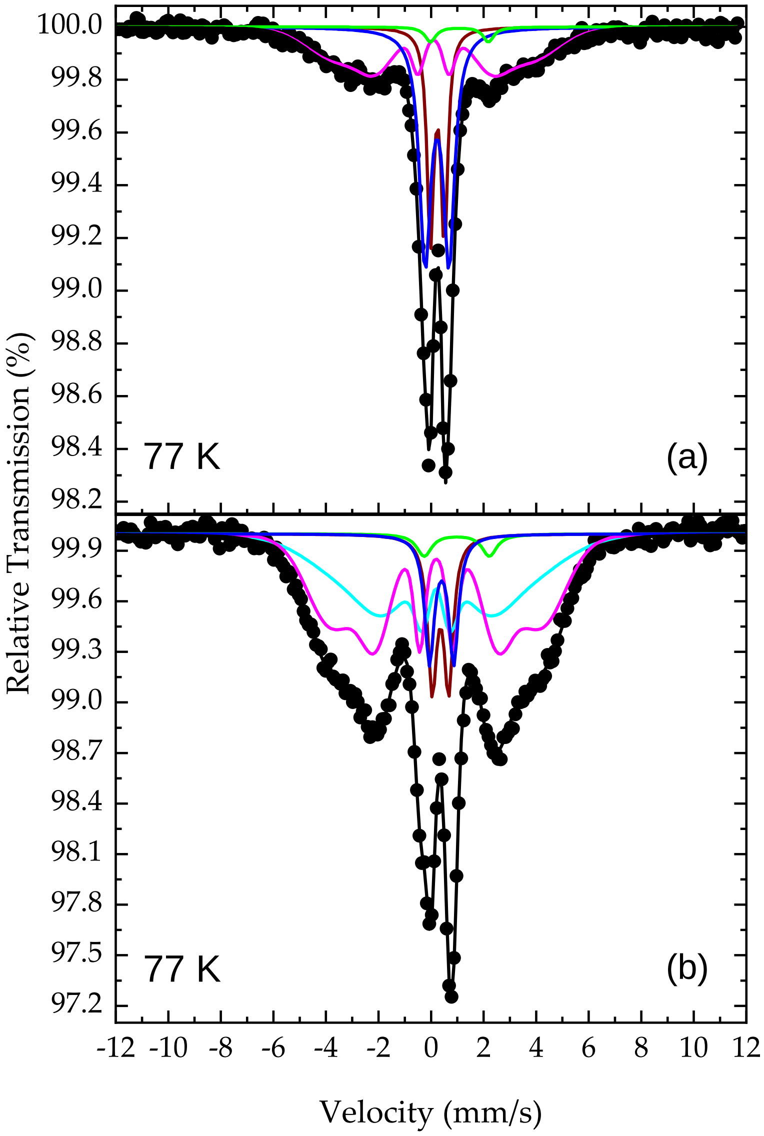

Figure 7.18 ^{57}Fe Mössbauer spectra of the as-made nanohybrid precursor (BH-AM-NHD) (a) and the unsupported precursor (BH-AM1-NP) (b) samples collected at 77 K.

Table 7.4 Mössbauer hyperfine parameters as resulting from the best fits of the corresponding spectra of the samples shown on **Figure 7.18**. IS the isomer shift (given relative to α-Fe at 300 K), Γ/2 is the half-line width, QS is the quadrupole splitting, 2ε is the quadrupole shift, B_{hf}^{C} is the central value of the hyperfine magnetic field, ΔB_{hf} is the total spreading (Gaussian-type) of the B_{hf} values around the central B_{hf}^{C} value, and AA is the relative spectral absorption area of each component used to fit the spectra. Typical errors are ±0.02 mm/s for IS, Γ/2, 2ε and QS, ±3 kOe for B_{hf}^{C} and ±3% for AA.

Sample	**Component**	**I.S. (mm/s)**	**Γ/2 (mm/s)**	**Q.S. or 2ε (mm/s)**	**B_{hf}^{C} (kOe)**	**ΔB_{hf} (kOe)**	**Area (%)**	**Color**
BH-IM-NHD	SPM Fe^{3+} (1)	0.46	0.15	0.63	0	0	20	Maroon
	SPM Fe^{3+} (2)	0.48	0.26	0.92	0	0	36	Blue
	SPM Fe^{2+}	1.08	0.32	2.39	0	0	7	Green
	MCOL Fe-Ni	0.19	0.15	0.00	231	65	37	Magenta
BH-AM-NP	SPM Fe^{3+} (1)	0.45	0.21	0.62	0	0	11	Maroon
	SPM Fe^{3+} (2)	0.47	0.22	0.92	0	0	10	Pink
	SPM Fe^{2+}	1.09	0.34	2.48	0	0	3	Green
	MCOL Fe-Ni (1)	0.27	0.15	0.00	200	95	31	Cyan
	MCOL Fe-Ni (2)	0.29	0.15	0.00	246	55	45	Magenta

The RT Mössbauer spectra of the annealed samples, produced by thermally treating both the as prepared nanohybrid and unsupported precursors at 300°C for 96 hours using $NaBH_4$ as a reducing agent, are shown in Figure 7.19. The spectra exhibit the common feature of a central quadrupole split contribution, but are combined with clear magnetically split contributions for the BH-NHD-300C,96h sample, and broad magnetically split contributions for the BH-NP-300C,96h sample.

For the BH-NHD-300C,96h sample (Figure 7.19a), the resonant lines of the quadrupole split components are more pronounced, while less intense resonant lines appear for the magnetically split components. To model this RT spectrum adequately, we used three primary central quadrupole split components, along with three magnetically resolved (MRES) and two magnetically split component with collapsing Bhf (MCOL) characteristics. For the magnetically split components, a Gaussian-type distribution ΔB_{hf} [4] of hyperfine magnetic field (B_{hf}) values around a central B_{hf}^{C} value was included to capture the broadening of these resonant lines. The resulting MPs values from the best fit of this spectrum (see Table 7.5) indicate that the minor broad magnetically split components (MCOL Fe^{3+}, colored magenta and MCOL Awaruite, colored grey in Figure 7.19) correspond to a INO and a Fe-Ni nanostructured phases [3], [5], respectively, while the rest of the components are attributed to high-spin Fe^{3+} ion sites in oxygen first-neighbor environments, characteristic of a spinel-type INO phase with additional Fe^{2+} ions, experiencing slow for the magnetically split and fast for the quadrupole split SPM relaxation at RT.

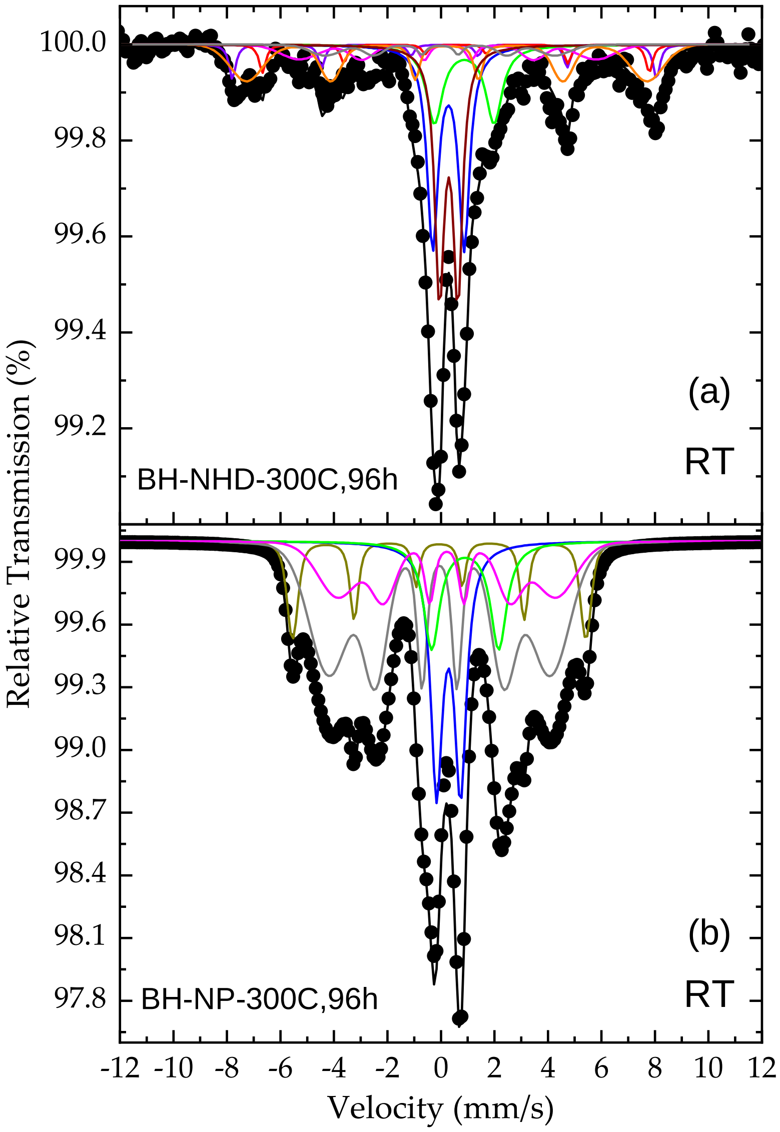

Figure 7.19 ^{57}Fe Mössbauer spectra of the annealed nanohybrid (BH-NHD-300C,96h) (a) and the annealed unsupported (BH-NP-300C,96h) (b) samples collected at room temperature.

The primary contribution in the RT spectrum of the annealed nanohybrid sample arises from the SPM Fe^{3+} (1), SPM Fe^{3+} (2), and SPM Fe^{2+} quadrupole doublet components (maroon, blue, and green in Figure 7.19a, respectively). These components display MPs values similar to the corresponding quadrupole doublets in the nanohybrid precursor (Figure 7.17a) and account for approximately 49% of the total AA, representing about 74% of the AA of the SPM components in the precursor, thus highlighting their strong retention even after annealing at 300°C for 96 hours. By contrast, the three MRES components (MRES Fe^{3+} (1), MRES Fe^{3+} (2), and MRES Fe^{2+}, shown in purple, orange, and red, respectively) make up the remaining 27% of the total AA in the BH-NHD-300C,96h sample. The minor MCOL INO and Fe-Ni components (colored magenta and dark cyan, respectively) corresponds to the INO and Fe-Ni NPs with moderate SPM relaxation, which were retained during the annealing process.

These findings suggest that the majority of NPs formed on the surfaces of the ND nanotemplates are of the INO phase, and possess NP sizes below the SPM size threshold, conferring fast SPM relaxation characteristics at RT [6], [13], [14], [15]. Simultaneously, annealing at 300°C for 96 hours seems to fail to develop further any additional Fe-Ni NPs which might have originated from INO seeds, and affects only a minor fraction of the INO nanostructures, promoting the formation of larger yet still spinel-type INO NPs. The predominant presence of the INO phase in the BH-NHD-300C,96h sample implies that these nanostructures remain in the annealed hybrid sample, likely due to incomplete oxide-to-alloy reduction reactions at this temperature. These results align well with the XRD measurements.

Table 7.5 Mössbauer hyperfine parameters as resulting from the best fits of the corresponding spectra of the samples shown on **Figure 7.19**. IS the isomer shift (given relative to α-Fe at 300 K), $\Gamma/2$ is the half-line width, QS is the quadrupole splitting, 2ε is the quadrupole shift, B_{hf}^C is the central value of the hyperfine magnetic field, ΔB_{hf} is the total spreading (Gaussian-type) of the B_{hf} values around the central B_{hf}^C value, and AA is the relative spectral absorption area of each component used to fit the spectra. Typical errors are ±0.02 mm/s for IS, $\Gamma/2$, 2ε and QS, ±3 kOe for B_{hf}^C and ±3% for AA.

Sample	**Component**	**I.S. (mm/s)**	**$\Gamma/2$ (mm/s)**	**Q.S. or 2ε (mm/s)**	**B_{hf}^C (kOe)**	**ΔB_{hf} (kOe)**	**Area (%)**	**Color**
BH-NHD-300C,96h	SPM Fe^{3+} (1)	0.39	0.21	0.69	0	0	20	Maroon
	SPM Fe^{3+} (2)	0.38	0.25	1.18	0	0	19	Blue
	SPM Fe^{2+}	0.98	0.37	2.36	0	0	10	Green
	MCOL Fe^{3+}	0.36	0.15	0.00	344	39	8	Magenta
	MCOL Awaruite	0.08	0.15	0.00	267	31	15	Grey
	MRES Fe^{3+} (1)	0.24	0.15	0.00	492	0	5	Purple
	MRES Fe^{3+} (2)	0.32	0.15	0.00	465	34	18	Orange
	MRES Fe^{2+}	0.66	0.15	0.00	449	0	4	Red
BH-NP-300C,96h	SPM Fe^{3+}	0.34	0.25	0.82	0	0	16	Blue
	SPM Fe^{2+}	1.01	0.35	2.51	0	0	10	Green
	MCOL Fe^{3+}	0.33	0.15	0.00	253	43	19	Magenta
	Kamacite	0.04	0.15	0.00	341	8	11	Dark Yellow
	MCOL Awaruite	0.05	0.15	0.00	257	42	45	Grey

The RT spectrum of the BH-NP-300C,96h sample (Figure 7.19b) presents a contrasting spectral character compared to the BH-NHD-300C,96h sample. Specifically, the broad magnetically split components dominate the spectrum, while the quadrupole split components play a more secondary role. Accordingly, we modeled this spectrum with three primary magnetically split components (one distinctly magnetically split and two with collapsing magnetic characteristics) and two secondary central quadrupole split components. The MPs resulting from the best fit of this spectrum are shown in Table 7.5.

In the BH-NP-300C,96h spectrum, one broad magnetically split component with collapsing B_{hf} characteristics (MCOL Awaruite, colored grey in Figure 7.19b) is attributed to a cubic, soft FM Fe–Ni alloy phase rich in nickel, known as Awaruite [5], [16], [17], [18]. The broadening reproduced by the ΔB_{hf} spread of 42 kOe suggests moderate SPM relaxation effects, indicating that the high-Ni fcc Fe-Ni NPs may exhibit a range of mean NP sizes at RT. Additionally, the isomer shift (IS) and B_{hf} values of the less intense magnetically split component (Kamacite, colored dark yellow in Figure 7.19b) are characteristic of another cubic, soft FM Fe-Ni phase called Kamacite [18], [19], with a stoichiometry in the Ni-poor concentration region between 4 and 7 atomic % Ni. Another broad magnetically split component (MCOL Fe^{3+}, colored magenta in Figure 7.19b) corresponds to high-spin Fe^{3+} ion sites in oxygen-first-neighbor environments, indicative of a spinel-type INO phase that also exhibits moderate SPM relaxation phenomena at RT.

The central part of the spectrum is fitted with two quadrupole split components—SPM Fe^{3+} and SPM Fe^{2+}—colored blue and green, respectively, in Figure 7.19b. These components display relatively broad resonant lines, with MPs values (listed in Table 7.5) similar to those found for the SPM components in the unsupported precursor, suggesting high-spin Fe^{3+} ions in the spinel-type INO phase with additional Fe^{2+} ions in the nanostructure, affected by fast SPM relaxation at RT.

The results indicate that most nanostructures observed in this sample, comprising ~ 66% of the total AA, are attributed to Fe-Ni NPs developed further from their corresponding Fe-Ni NPs seeds already preformed from the initial step of the synthesis. This development occurred from that part of the Fe-Ni NPs exhibiting magnetically collapsing characteristics in the unsupported precursor, as the fast SPM components of the precursor retained their approximate total AA values after annealing at 300°C for 96 hours.

In summary, annealing both precursor samples at 300°C for 96 hours conserves a significant portion of the initial Fe-Ni or INO phases in both as-made samples, with the INO phase representing the majority of the contribution in the hybrid annealed sample. In contrast, in the annealed unsupported sample, the preformed Fe-Ni phase underwent a formation of Fe-Ni NPs with multiphase characteristics, comprising both a Ni-rich Awaruite and a Ni-poor Kamacite phase. These structural features highlight the differences between the samples, suggesting that this synthetic approach may limit the formation of uniform magnetic nanostructures under the given annealing conditions.

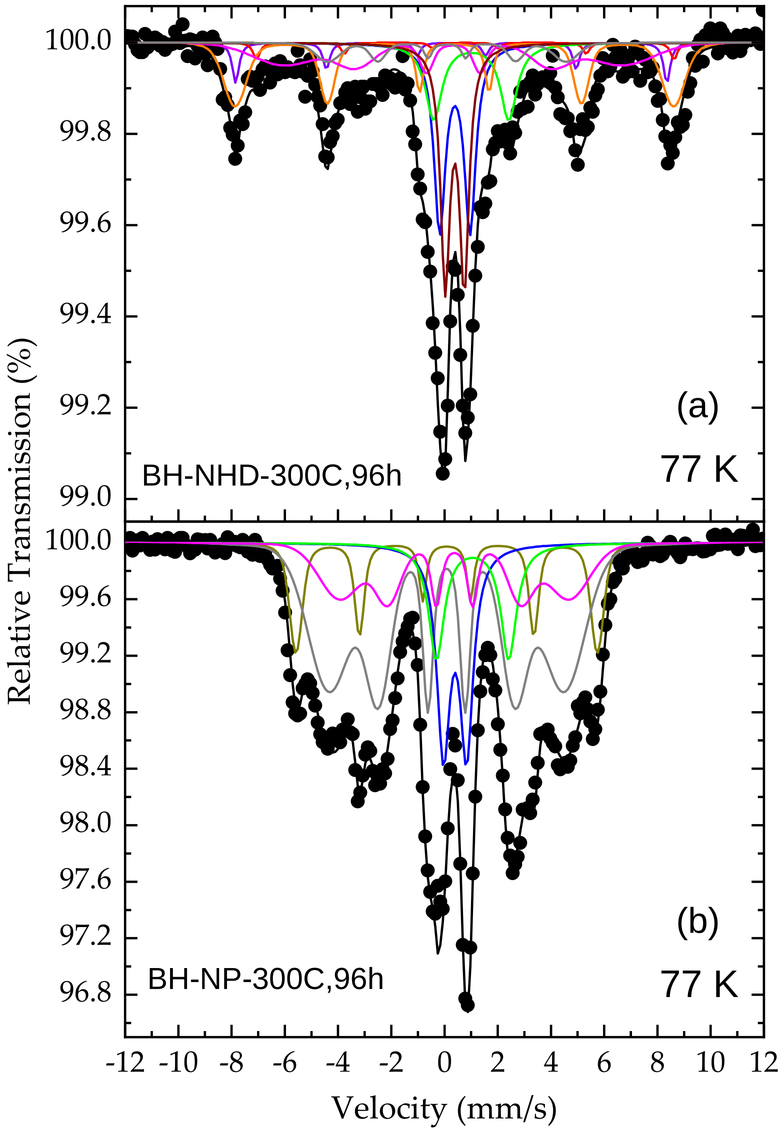

Figure 7.20 ^{57}Fe Mössbauer spectra of the annealed nanohybrid (BH-NHD-300C,96h) (a) and the annealed unsupported (BH-NP-300C,96h) (b) samples collected at 77 K.

The thermal evolution of the MS for the annealed nanohybrid and unsupported samples collected at 77 K is shown in Figure 7.20, with the corresponding MPs values listed in Table 7.6. At this lower temperature, the spectra for both samples can be fitted using the same models applied at RT. All iron alloy components show the expected shifts in IS and B_{hf} values, while their AA values remain very similar to those observed at RT (within the expected error margins).

These findings indicate no significant change in the AA values for the SPM and MCOL components in either sample at 77 K. A reduction in SPM relaxation time (τ) at this temperature would typically reveal a larger fraction of the nanostructured phases [7]. However, both annealed samples retain their original spectral characteristics at 77 K, suggesting that strong magnetic interactions have formed—likely due to the $NaBH_4$ reducing agent used in the initial synthesis step.

Table 7.6 Mössbauer hyperfine parameters as resulting from the best fits of the corresponding spectra of the samples shown on **Figure 7.20**. IS the isomer shift (given relative to α-Fe at 300 K), Γ/2 is the half-line width, QS is the quadrupole splitting, 2ε is the quadrupole shift, B_{hf}^{C} is the central value of the hyperfine magnetic field, ΔB_{hf} is the total spreading (Gaussian-type) of the B_{hf} values around the central B_{hf}^{C} value, and AA is the relative spectral absorption area of each component used to fit the spectra. Typical errors are ±0.02 mm/s for IS, Γ/2, 2ε and QS, ±3 kOe for B_{hf}^{C} and ±3% for AA.

Sample	**Component**	**I.S. (mm/s)**	**Γ/2 (mm/s)**	**Q.S. or 2ε (mm/s)**	**B_{hf}^{C} (kOe)**	**ΔB_{hf} (kOe)**	**Area (%)**	**Color**
BH-NHD-300C,96h	SPM Fe^{3+} (1)	0.48	0.21	0.72	0	0	16	Maroon
	SPM Fe^{3+} (2)	0.49	0.26	1.14	0	0	18	Blue
	SPM Fe^{2+}	1.11	0.38	2.49	0	0	10	Green
	MCOL Fe^{3+}	0.44	0.15	0.00	394	70	14	Magenta
	MCOL Awaruite	0.20	0.15	0	278	24	15	Grey
	MRES Fe^{3+} (1)	0.36	0.15	0.00	503	0	5	Purple
	MRES Fe^{3+} (2)	0.48	0.15	0.00	512	22	18	Orange
	MRES Fe^{2+}	0.89	0.15	0.00	487	0	3	Red
BH-NP-300C,96h	SPM Fe^{3+}	0.46	0.28	0.87	0	0	15	Blue
	SPM Fe^{2+}	1.13	0.36	2.59	0	0	10	Green
	MCOL Fe^{3+}	0.45	0.15	0.00	265	40	18	Magenta
	Kamacite	0.15	0.15	0.00	352	11	12	Dark Yellow
	MCOL Awaruite	0.17	0.15	0.00	271	45	46	Grey

The RT Mössbauer spectra of the nanohybrid and unsupported annealed samples, obtained by thermally treating the precursor samples at 700°C for 4 hours using the $NaBH_4$ reducing agent, are shown in Figure 7.21.

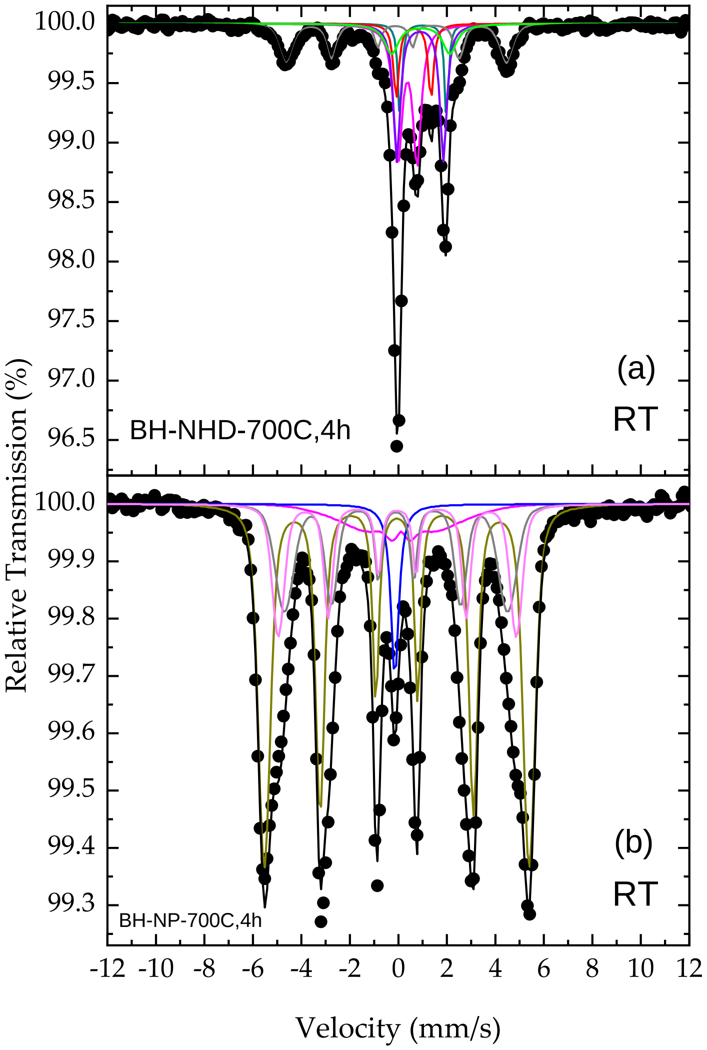

Figure 7.21 ^{57}Fe Mössbauer spectra of the annealed nanohybrid (BH-NHD-700C,4h) (a) and the annealed unsupported (BH-NP-700C,4h) (b) samples collected at room temperature.

In the BH-NHD-700C,4h sample, the RT spectrum is dominated by the intensity of a set of central quadrupole contributions, while a minor magnetically split contribution is also apparent. Conversely, the RT spectrum of the BH-NP-700C,4h sample shows a dominant, broad magnetically split contribution and a secondary, less intense quadrupole split part at the center of the spectrum.

Specifically, to fit the RT spectrum of the BH-NHD-700C,4h sample (Figure 7.21a) spectrum adequately a set of five quadrupole split doublets and one magnetically split sextet were used, which can be described by a broad magnetically split component with B_{hf} characteristics. The resulting MPs listed in Table 7.7 suggest that the four of five quadrupole split components correspond to Fe^{2+}, $Fe^{2.v+}$ and $Fe^{2.5+}$ valence states of the mixed-valence oxyborate Fe_3BO_5 Vonsenite phase [20], which was identified in this sample by XRD measurements. The remaining quadrupole doublet corresponds to Fe^{2+} ions in an oxygen environment, showing similar MPs to the fast SPM components of the INO phase observed in the hybrid precursor sample. One sextet with relatively narrow resonant lines reflects the crystallinity of a corresponding phase, with MPs that indicate a soft FM, Ni-rich fcc Fe-Ni phase (Awaruite), also detected by XRD.

On the other hand, the RT spectrum of the BH-NP-700C,4h sample (Figure 7.21b) is fitted by a set of four magnetically split sextets, with the addition of a minor central singlet. Specifically, one magnetically split component with sharp resonant lines, indicating high crystallinity, is accompanied by three additional magnetically split components with less intense resonant lines exhibiting spreading of their B_{hf} characteristics. The MPs values listed in Table 7.7 indicate that the sextet with the highest absorption area (colored dark yellow in Figure 7.21b) is characteristic of a well-ordered, soft FM, Ni-poor bcc Fe-Ni Kamacite phase. Two of the other sextets (colored grey and light magenta in Figure 7.21b) have MPs corresponding to an ordered, soft FM, Ni-rich fcc Fe-Ni Awaruite and a disordered, soft FM Ni-rich fcc γ_2-Taenite phase [3], [5], respectively. The relative low dispersion in the B_{hf} values of these two components may be due to a distribution in particle sizes, leading to moderate SPM relaxation effects at RT [8], [9]. The fourth sextet's MPs values (MCOL Fe^{3+} colored magenta) correspond to Fe^{3+} ions associated with the INO phase, with spectral characteristics similar to those of the corresponding component observed in the unsupported precursor sample, showing moderate SPM characteristics at RT. The singlet's MPs indicate a disordered PM Ni-poor fcc γ_1-Fe-Ni phase (colored blue), known as Anti-Taenite [21], [22].

Table 7.7 Mössbauer hyperfine parameters as resulting from the best fits of the corresponding spectra of the samples shown on **Figure 7.21**. IS the isomer shift (given relative to α-Fe at 300 K), Γ/2 is the half-line width, QS is the quadrupole splitting, 2ε is the quadrupole shift, B_{hf}^C is the central value of the hyperfine magnetic field, ΔB_{hf} is the total spreading (Gaussian-type) of the B_{hf} values around the central B_{hf}^C value, and AA is the relative spectral absorption area of each component used to fit the spectra. Typical errors are ±0.02 mm/s for IS, Γ/2, 2ε and QS, ±3 kOe for B_{hf}^C and ±3% for AA.

Sample	**Component**	**I.S. (mm/s)**	**Γ/2 (mm/s)**	**Q.S. or 2ε (mm/s)**	**B_{hf}^C (kOe)**	**ΔB_{hf} (kOe)**	**Area (%)**	**Color**
BH-NHD-700C,4h	Fe^{2+} - Fe_3BO_5 (1)	1.08	0.15	1.97	0	0	9	Dark Cyan
	$Fe^{2.v+}$ - Fe_3BO_5	0.48	0.18	0.80	0	0	20	Magenta
	$Fe^{2.5+}$ - Fe_3BO_5	0.73	0.16	1.53	0	0	10	Red
	Awaruite	0.00	0.15	0.03	282	14	28	Grey
	Fe^{2+} - Fe_3BO_5 (2)	1.07	0.17	1.97	0	0	22	Purple
	Fe^{2+} SPM	1.03	0.35	2.40	0	0	11	Green
BH-NP-700C,4h	Kamacite	0.04	0.15	0.00	339	11	53	Dark Yellow
	Awaruite	0.01	0.15	0.00	286	19	18	Grey
	γ_2 Taenite	0.06	0.15	0.00	305	11	16	Light Magenta
	γ_1 Taenite	-0.04	0.20	0.00	0	0	4	Blue
	MCOL Fe^{3+}	0.29	0.15	0.00	123	81	8	Magenta

To further examine the thermal evolution of the MS for both annealed samples, the 77 K MS were analyzed (Figure 7.22). The 77 K MS were fitted using the appropriate models containing the relative components of the phases detected at RT. The resulting MPs are listed in Table 7.8. Notably, all spectral components exhibited the expected shifts in IS, quadrupole splitting (QS), and B_{hf} due to the temperature decrease, while the total AA values for each phase remained consistent (within the expected error margins) with those observed at RT.

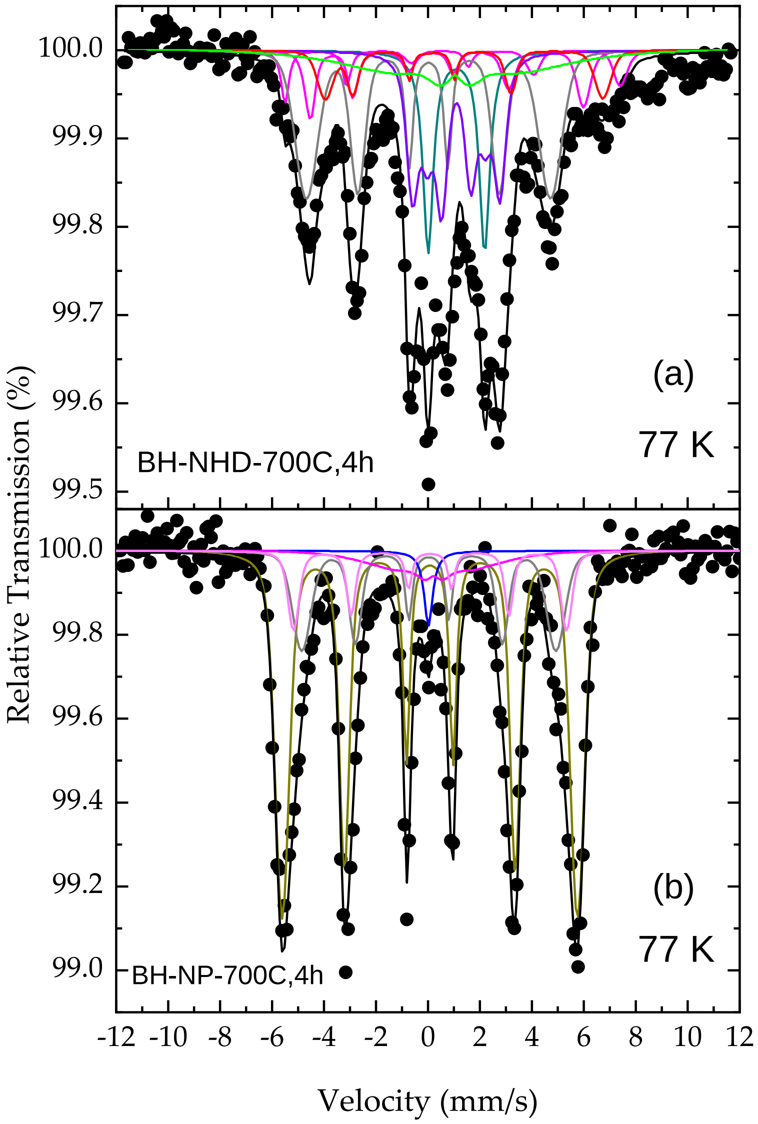

Figure 7.22 ^{57}Fe Mössbauer spectra of the annealed nanohybrid (BH-NHD-700C,4h) (a) and the annealed unsupported (BH-NP-700C,4h) (b) samples collected at 77 K.

Table 7.8 Mössbauer hyperfine parameters as resulting from the best fits of the corresponding spectra of the samples shown on **Figure 7.22**. IS the isomer shift (given relative to α-Fe at 300 K), Γ/2 is the half-line width, QS is the quadrupole splitting, 2ε is the quadrupole shift, B_{hf}^{C} is the central value of the hyperfine magnetic field, ΔB_{hf} and ΔQS are the total spreading (Gaussian-type) of the B_{hf} and QS values around the central B_{hf}^{C} and QS or 2ε values respectively, η is an asymmetry parameter and θ,φ are the polar and azimuthal angles (degrees), and AA is the relative spectral absorption area of each component used to fit the spectra. Typical errors are ±0.02 mm/s for IS, Γ/2, 2ε and QS, ±3 kOe for B_{hf}^{C} , η ±0.3 at 77 K, θ, φ ±3° at 77 K, and ±3% for AA.

Sample	Component	I.S. (mm/s)	Γ/2 (mm/s)	Q.S. or 2ε (mm/s)	B_{hf}^{C} (kOe)	ΔB_{hf} or ΔE_Q (kOe) or (mm/s)	η	θ (deg.)	φ (deg.)	Area (%)	Color
BH-NHD-700C, 4h	Fe^{2+} Fe_3BO_5 (1)	1.20	0.18	2.17	0	0	0	0		10	Dark Cyan
	Fe^{3+} Fe_3BO_5	0.53	0.18	0.81	325	0.4	0	22		9	Magenta
	$Fe^{2.5+}$ - Fe_3BO_5	0.82	0.18	1.10	395	0.5	0.3	35	236	8	Magenta
	Awaruite	0.13	0.15	0.00	292	23	0	0		31	Grey
	Fe^{2+} Fe_3BO_5 (2)	1.20	0.18	2.17	47	0.2	0.3	53	57	23	Purple
	$Fe^{2.5+}$ Fe_3BO_5	0.88	0.15	1.35	350	15	0.2	11	40	8	Red
	MCOL Fe^{2+}	1.15	0.15	0	200	150	0	0		11	Green
BH-NP-700C, 4h	Kamacite	0.18	0.15	0.00	353	13	-	-	-	55	Dark Yellow
	Awaruite	0.14	0.15	0.00	304	18	-	-	-	21	Grey
	γ_2 Taenite	0.19	0.15	0.00	326	9	-	-	-	15	Light Magenta
	γ_1 Taenite	0.13	0.20	0.00	0	0	-	-	-	2	Blue
	MCOL Fe^{3+}	0.32	0.15	0.00	136	90	-	-	-	7	Cyan

These results suggest that annealing both precursor samples at a higher temperature, 700°C for 4 hours, led to the formation of secondary impurity phases. These phases correspond to residual components of the INO phase seen in the precursor samples, as well as an iron oxyborate (Fe_3BO_5 Vonsenite) phase and Fe-Ni multi-phase configurations. The formation of the Vonsenite phase in the annealed hybrid sample is likely due to residual boron from the $NaBH_4$ reducing agent, possibly in the form of amorphous boron oxide (B_2O_3) in the hybrid sample combined with iron oxides (IOs) and the effects of the higher annealing temperature. In contrast, the Fe-Ni multi-phase structures in the annealed unsupported sample emerged from the development of the preformed Fe-Ni NPs phase in the precursor during the second annealing step at 700°C for 4 hours. This treatment produced Fe-Ni nanostructures with a range of crystal structures, magnetic ordering, and stoichiometries in both hybrid and unsupported samples.

These structural and compositional characteristics introduce undesired properties in the synthesized materials, which deviate from the primary goal of developing pure magnetic nanostructured materials with distinct magnetic characteristics. To address this, we have decided to continue our investigation into the Fe-Ni/NDs system using the impregnation synthesis method.

7.3.2 Samples prepared using the impregnation method

The ^{57}Fe MS of the conventionally synthesized non-enriched nanohybrid precursors prepared via the impregnation synthesis method recorded at RT and at 77 K are shown in Figure 7.23. In Figures 7.23a, b, the RT spectra for all as-made precursor samples are primarily characterized by a dominant quadrupole split contribution with relatively broad resonant lines. This feature can be sufficiently described using two main quadrupole split components in the spectra for both impregnated precursors. Additionally, a minor third quadrupole component was necessary to accurately fit the RT spectrum of the IM-AM2-NHD sample.

The best-fit MPs are listed in Table 7.9. These parameters indicate high-spin ($S = 5/2$) Fe^{3+} ionic states for both main quadrupole split components, labeled SPM Fe^{3+} (1) and SPM Fe^{3+} (2), shown in dark cyan and purple in Figure 7.23, respectively. These Fe^{3+} states are typical of INO spinel-type nanostructures. Additionally, minor contributions of high-spin ($S = 2$) Fe^{2+} states were observed, represented by the SPM Fe^{2+} component (colored green) in the IM-AM2-NHD spectrum. The particle sizes of these nanostructures are sufficiently small to exhibit very fast SPM behavior at RT [6], [13], [14], [15], [23]. This finding verifies the respective results regarding the average particle size of 2 nm previously deduced for this phase from XRD measurements (Figure 7.3). At RT, the INO NP seeds developed on the surface of the ND nanotemplates are below the SPM size limit, where fast SPM relaxation renders their characteristic relaxation time τ quite shorter than the Mössbauer measuring time τ_{MS}, which is approximately 10^{-8} s, resulting in complete averaging of their B_{hf} values to zero (collapse of B_{hf}) [24], [25].

At 77 K, for a subset of the INO NP assembly, τ can be increased to comparable or slightly higher values relative to τ_{MS}, allowing these particles to exhibit magnetic splitting with collapsing B_{hf} characteristics in the MS (Figure 7.23c, d). This subset is represented by the MCOL Fe^{3+} component, shown in red in both MS in Figure 7.23c, d. These are likely the larger NPs in the particle size distribution or those situated in close proximity to each other [8], [10]. For the remaining NPs, which are smaller in size or more isolated, the SPM characteristics are preserved at 77 K, as represented by the two quadrupole-split SPM Fe^{3+} (1) and SPM Fe^{3+} (2) components (dark cyan and purple in Figure 7.23c,d), similar to the RT findings.

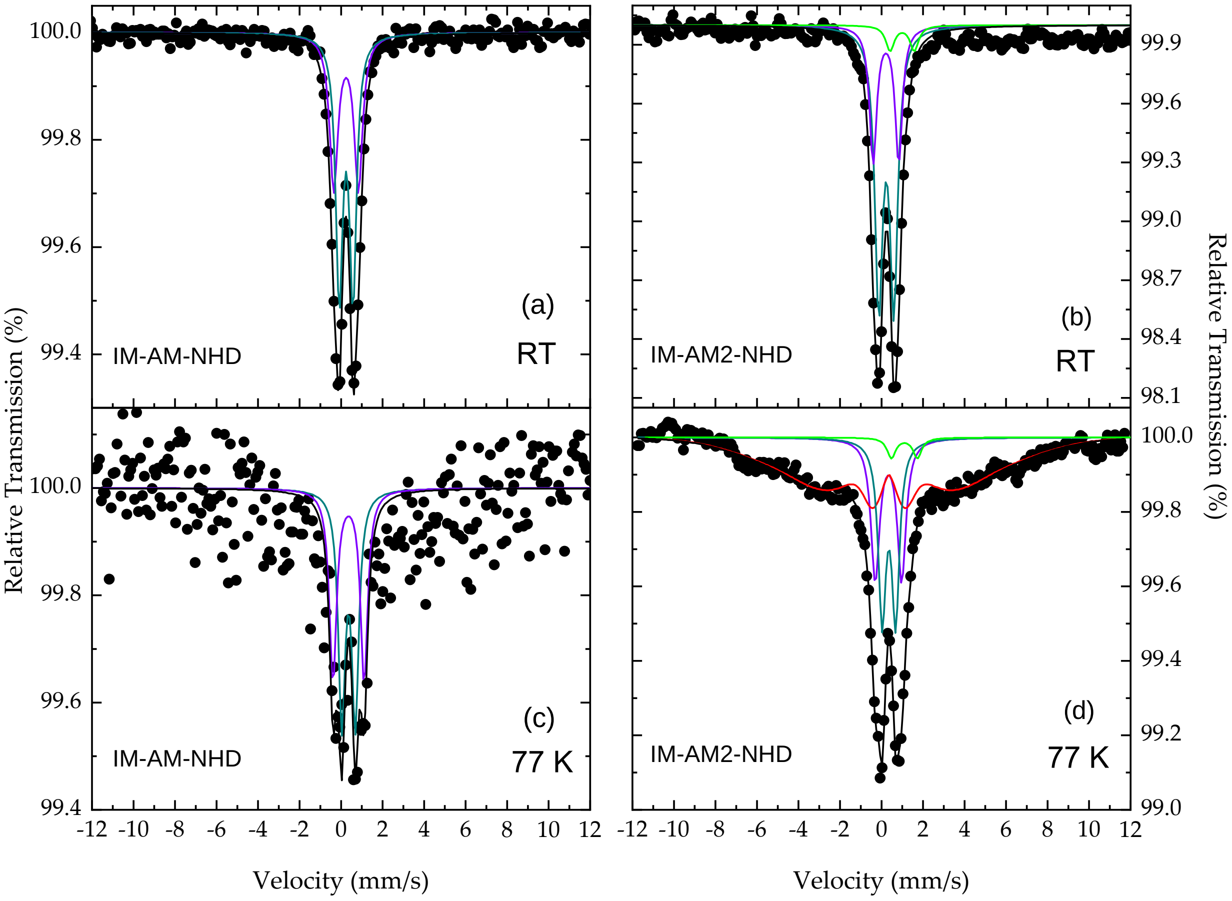

Figure 7.23 ^{57}Fe Mössbauer spectra of the as-made nanohybrid precursor samples (IM-AM-NHD and IM-AM2-NHD) collected at room temperature (a, b), their respective spectra collected at 77 K (c, d).

Table 7.9 Mössbauer hyperfine parameters as resulting from the best fits of the corresponding spectra collected at room temperature of the samples shown on **Figures 7.23a, b**. IS the isomer shift (given relative to α-Fe at 300 K), $\Gamma/2$ is the half-line width, QS is the quadrupole splitting, 2ε is the quadrupole shift, B_{hf}^{C} is the central value of the hyperfine magnetic field, ΔB_{hf} is the total spreading (Gaussian-type) of the B_{hf} values around the central B_{hf}^{C} value, and AA is the relative spectral absorption area of each component used to fit the spectra. Typical errors are ±0.02 mm/s for IS, $\Gamma/2$, 2ε and QS, ±3 kOe for B_{hf}^{C} and ±3% for AA.

Sample	Component	I.S. (mm/s)	Γ/2 (mm/s)	Q.S. or 2ε (mm/s)	B_{hf}^{C} (kOe)	ΔB_{hf} (kOe)	Area (%)	Color
IM-AM-NHD	SPM Fe^{3+} (1)	0.32	0.22	0.57	0	0	46	Dark Cyan
	SPM Fe^{3+} (2)	0.34	0.25	1.14	0	0	54	Purple
IM-AM2-NHD	SPM Fe^{3+} (1)	0.34	0.23	0.71	0	0	62	Dark Cyan
	SPM Fe^{3+} (2)	0.32	0.21	1.23	0	0	32	Purple
	SPM Fe^{2+}	1.14	0.25	1.19	0	0	6	Green

Table 7.10 Mössbauer hyperfine parameters as resulting from the best fits of the corresponding spectra collected at 77 K of the samples shown on **Figures 7.23c, d**. IS the isomer shift (given relative to α-Fe at 300 K), $\Gamma/2$ is the half-line width, QS is the quadrupole splitting, 2ε is the quadrupole shift, B_{hf}^C is the central value of the hyperfine magnetic field, ΔB_{hf} is the total spreading (Gaussian-type) of the B_{hf} values around the central B_{hf}^C value, and AA is the relative spectral absorption area of each component used to fit the spectra. Typical errors are ±0.02 mm/s for IS, $\Gamma/2$, 2ε and QS, ±3 kOe for B_{hf}^C and ±3% for AA.

Sample	Component	I.S. (mm/s)	$\Gamma/2$ (mm/s)	Q.S. or 2ε (mm/s)	B_{hf}^C (kOe)	ΔB_{hf} (kOe)	Area (%)	Color
IM-AM-NHD	SPM Fe^{3+} (1)	0.47	0.23	0.62	0	0	21	Dark Cyan
	SPM Fe^{3+} (2)	0.46	0.25	1.20	0	0	22	Purple
	MCOL Fe^{3+}	0.46	0.15	0.00	163	140	57	Red
IM-AM2-NHD	SPM Fe^{3+} (1)	0.46	0.22	0.69	0	0	21	Dark Cyan
	SPM Fe^{3+} (2)	0.44	0.25	1.22	0	0	19	Purple
	MCOL Fe^{3+}	0.47	0.15	0.00	284	157	56	Red
	SPM Fe^{2+}	1.26	0.25	1.25	0	0	5	Green

The MS of the annealed samples derived from thermal treatments of the IM-AM-NHD precursor at 700°C for 30m and 4h are shown in Figures 7.24 and 7.25, respectively. Regardless of the annealing duration, both spectra display similar characteristics, which can be described qualitatively by: (i) a set of rather broad but distinct magnetically split contributions accompanied by (ii) a set of minor magnetically split contributions detected mainly as satellites around the outer resonant peaks of the distinct magnetically split contributions, and (iii) a set of quadrupole split contributions observed at the center of the MS. The intensity of the distinct and satellite magnetically split contributions (i) and (ii) is relatively stable in each of these MS, but that of the quadrupole split contributions (iii) is more pronounced for the sample annealed for the shorter annealing duration (30 minutes), compared to that found for the sample annealed for the longer annealing duration (4 hours).

Analyzing adequately such complex MS is a challenging endeavor, since different sets of fitting models can be used. To reach a solid choice on the fitting model, we considered the facts already gained from the other experimental characterization techniques in this study, namely XRD and TEM. The main evidences given from these two experimental methods are: a) there is a dominant presence of an fcc Fe-Ni nanostructured alloy phase which corresponds to the Fe-Ni NPs grown on the surfaces of the NDs nanotemplates, b) this phase has a Fe:Ni stoichiometry close to 1:3, which could correspond either to intermetallic $FeNi_3$ or/and to γ_2-Taenite, c) the development of graphitic-type layers encapsulating the Fe-Ni NPs is suggesting further diffusion of C atoms within the fcc alloy structure, and d) a minor INO nanostructured phase should also be present in the samples.

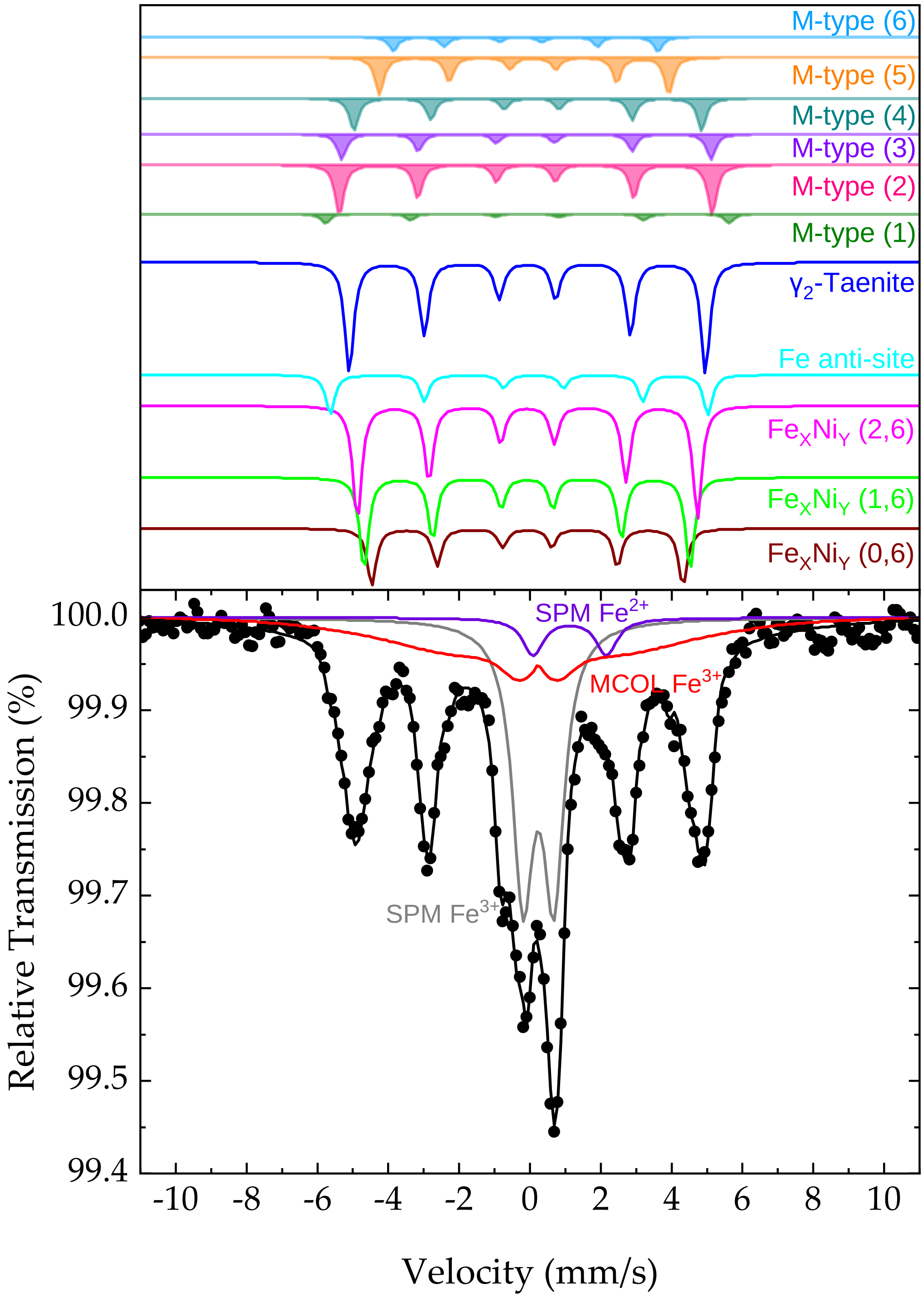

Figure 7.24 ^{57}Fe Mössbauer spectrum of the IM-NHD-700C,30m sample collected at room temperature.

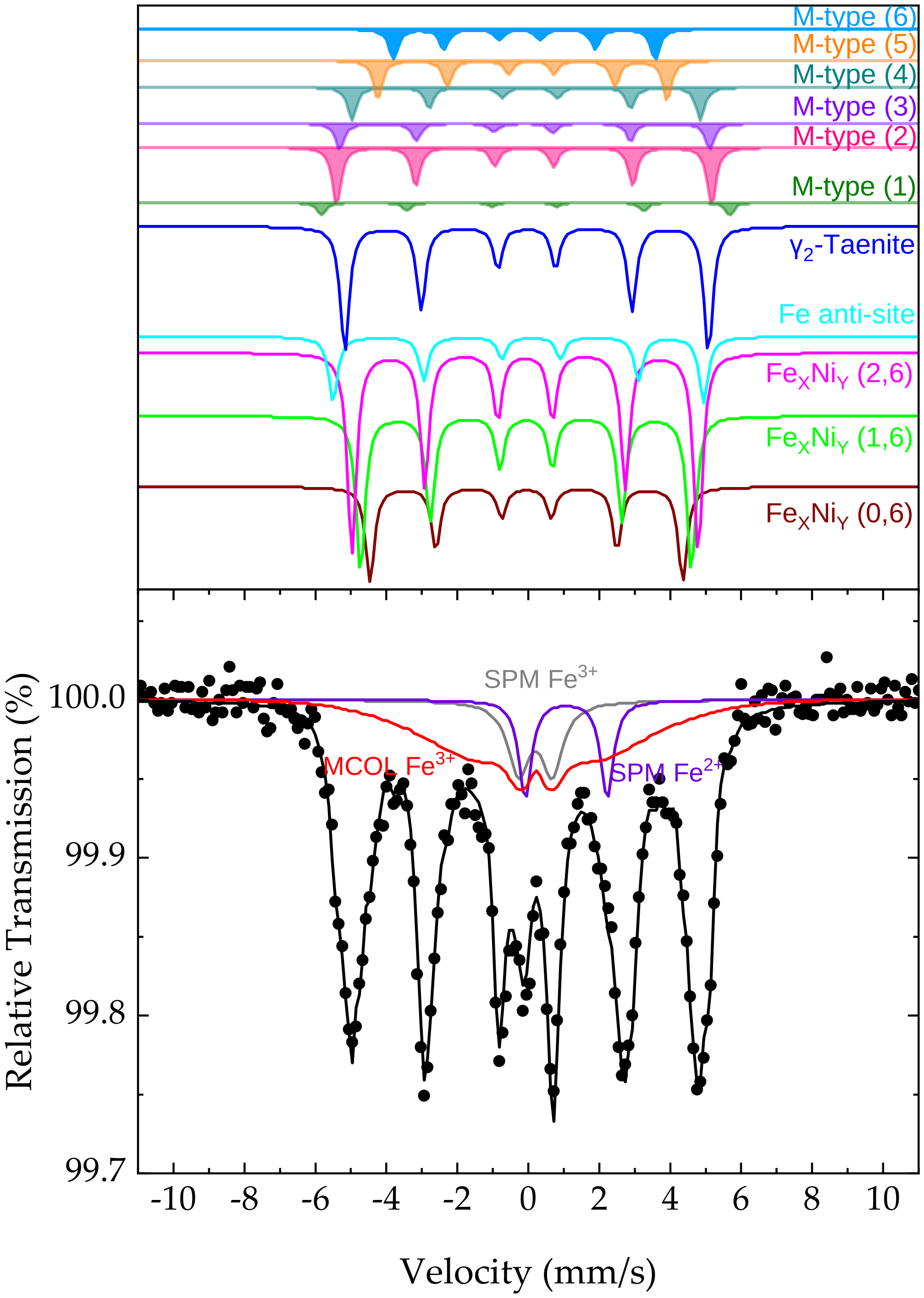

Figure 7.25 ^{57}Fe Mössbauer spectrum of the IM-NHD-700C,4h sample collected at room temperature.

Table 7.11. Mössbauer hyperfine parameters as resulting from the best fits of the corresponding spectra of the samples shown on **Figures 7.24** and **7.25**. IS the isomer shift (given relative to α-Fe at 300 K), Γ/2 is the half-line width, QS is the quadrupole splitting, 2ε is the quadrupole shift, B_{hf}^{C} is the central value of the hyperfine magnetic field, ΔB_{hf} is the total spreading (Gaussian-type) of the B_{hf} values around the central B_{hf}^{C} value, and AA is the relative spectral absorption area of each component used to fit the spectra. Typical errors are ±0.02 mm/s for IS, Γ/2, 2ε and QS, ±3 kOe for B_{hf}^{C} and ±3% for AA.

Sample	Components	I.S. (mm/s)	Γ/2 (mm/s)	Q.S. or 2ε (mm/s)	B_{hf}^{C} (kOe)	ΔB_{hf} (kOe)	Area (%)	Color
IM-NHD-700C,30m	Fe_xNi_Y (0,6)	0.03	0.15	0.00	273	0	5	Maroon
	Fe_xNi_Y (1,6)	0.02	0.15	0.00	286	0	8	Green
	Fe_xNi_Y (2,6)	0.03	0.15	0.00	298	0	9	Magenta
	Fe anti-site	0.00	0.15	-0.41	331	0	3	Cyan
	γ_2-Taenite	0.03	0.15	0.00	312	0	7	Blue
	M-type (1)	0.04	0.15	0.01	354	0	2	Olive
	M-type (2)	0.00	0.15	0.00	327	0	4	Pink
	M-type (3)	0.00	0.15	0.04	324	0	3	Purple
	M-type (4)	0.11	0.15	-0.11	305	0	3	Dark Cyan
	M-type (5)	0.08	0.15	-0.25	254	0	3	Orange
	M-type (6)	-0.07	0.15	0.13	232	0	1	Light blue
	SPM Fe^{3+}	0.34	0.36	0.87	0	0	28	Grey
	SPM Fe^{2+}	1.23	0.36	2.06	0	0	4	Dark purple
	MCOL Fe^{3+}	0.34	0.15	0.00	174	179	21	Red
IM-NHD-700C,4h	Fe_xNi_Y (0,6)	0.05	0.15	0.00	274	0	7	Maroon
	Fe_xNi_Y (1,6)	0.04	0.15	0.00	290	0	12	Green
	Fe_xNi_Y (2,6)	0.01	0.15	0.00	303	0	14	Magenta

	Fe anti-site	0.00	0.15	-0.36	324	0	5	Cyan
	γ_2-Taenite	0.06	0.15	0.00	318	0	10	Blue
	M-type (1)	0.04	0.15	0.01	357	0	1	Olive
	M-type (2)	0.00	0.15	0.00	328	0	5	Pink
	M-type (3)	0.00	0.15	0.04	324	0	2	Purple
	M-type (4)	0.11	0.15	-0.11	305	0	3	Dark Cyan
	M-type (5)	0.08	0.15	-0.25	253	0	3	Orange
	M-type (6)	-0.07	0.15	0.13	229	0	2	Light blue
	SPM Fe^{3+}	0.31	0.36	0.95	0	0	8	Grey
	SPM Fe^{2+}	1.17	0.22	2.31	0	0	6	Dark purple
	MCOL Fe^{3+}	0.33	0.15	0.00	147	116	22	Red

To include the contribution of Fe-Ni nanostructured phase in our fitting model we take into account the relative literature on the analyses of the MS of $FeNi_3$. $FeNi_3$ or Awaruite, is considered as one of the two ordered phases encountered in the Fe-Ni system's phase diagram (the other being the $L1_0$ FeNi Tetrataenite), which orders from the disordered state with very slow diffusion rates below 500 °C to form an ordered $AuCu_3$-type soft FM (γ'-fcc crystal $L1_2$) structure with a nominal iron-to-nickel atomic ratio of 1:3 [5], [26], [27]. However, it is known that below the Curie temperature of 600 °C, the hyperfine magnetic field (B_{hf}) at the iron nuclei shows always a distribution around the B_{hf} value of the perfectly ordered $FeNi_3$ alloy, depending on the degree of Fe-Ni atomic order and/or local stoichiometry contributions. Therefore, the existence of a distribution of B_{hf} values entails the presence of incomplete ordering and/or deviation of the nominal (Fe:Ni=1:3) stoichiometry, leading to different surrounding configurations of the iron atoms as pointed out by J.W. Drijver et al. [27]. In this work, J.W. Drijver et al. report that a great determinant for understanding in thorough the B_{hf} distribution exhibited in the nearly completely ordered $FeNi_3$ system, is the relation of the B_{hf} with the local environment of the iron atoms around their first and second neighboring shells, when these iron atoms occupy the nominal Fe crystallographic sites in the ordered structure.

Many scientists tried to study this effect in nearly completely ordered $FeNi_3$ alloys. In a typical perfectly ordered fcc $FeNi_3$ alloy, an iron atom is surrounded by twelve nickel atoms and zero iron atoms in the first neighboring shell, and by six iron atoms and zero nickel atoms in the second neighboring shell. In terms of iron atoms occupancy in these first and second neighboring shells around the nominal Fe crystallographic sites of the $FeNi_3$ system, M. Kanashiro et al. used the notation (n_1,n_2), where n_1 corresponds to the iron atoms occupancy in the first neighboring shell and n_2 to the iron atoms occupancy in the second neighboring shell [28], [29]. Moreover, the probability of finding such configurations is given by the relation:

$$W(n_1) = \frac{12!}{(12-n_1)!n_1!}\left(\frac{3+\theta+S}{4}\right)^{12-n_1}\left(\frac{1-\theta-S}{4}\right)^{n_1} \quad (1)$$

where θ/4 is the fractional deviation of the Fe concentration from the nominal Fe:Ni=1:3 stoichiometry (Fe_XNi_Y, where X=(1-θ)/4, Y=(3+θ)/4 and X+Y=1), and S is the long range order parameter defined as $S = \frac{3}{4}(p - \frac{1}{4})$ [27], with p being the probability of finding an iron atom at the nominal Fe crystallographic sites of the ordered $FeNi_3$ system.

M. Kanashiro et al. [28], [29] suggested that there are three main magnetically split contributions to be considered for analyzing the MS of a nearly completely ordered $Fe_{1+z}Ni_{3-z}$ (or Fe_XNi_Y) alloy. Each one of these contributions corresponds to a different local atom configuration (n_1,n_2) ascribed as (n_1,6), with n_1 ranging only from 0 to 2, namely (0,6), (1,6) and (2,6), since for n_1>3 all other configurations can be neglected due to vanishing W(n_1) probabilities when the order parameter S is high enough to reach 0.7.

However, a subsequent study on this matter introduced by T.E. Cranshaw et al. [30], highlighted the importance of considering also the occupancy of the iron atom located at the nominal nickel crystallographic site, thus forming an Fe anti-site configuration, as an additional and effective contribution to the interpretation of B_{hf} distribution in a nearly completely ordered $FeNi_3$ environment. More specific, T.E. Cranshaw and his co-workers concluded that a systematic ordering of defects can be developed in both non-stoichiometric and disordered $FeNi_3$-type alloys, where apart from the statistically prominent iron sites Fe_XNi_Y (0,6), Fe_XNi_Y (1,6) and Fe_XNi_Y (2,6), an Fe anti-site configuration with equivalent statistical contribution, notated there as Fe_XNi_Y (4,0), should be included in the fitting model. The notation Fe_XNi_Y (4,0) to describe the Fe anti-site configuration, is given by T.E. Cranshaw et al. due to its identical environment with an Fe atom located at a nominal Fe crystallographic site that has 4 Fe anti-site atoms on the first neighboring shell and 6 Ni anti-site atoms on the second neighboring shell.

To this extent, and in order to elucidate the B_{hf} distribution phenomena contributing to the appearance of a resonant line broadening in the spectra of our annealed samples, which most probably might be the actual situation, we conveniently accept M. Kanashiro's and T.E. Cranshaw's arguments. Therefore, we use the notations Fe_XNi_Y (0,6), Fe_XNi_Y (1,6), Fe_XNi_Y (2,6) and Fe anti-site, corresponding to a set of four components colored maroon, green, magenta and cyan respectively, to model the contribution of the Fe_XNi_Y phase in our spectra shown in Figures 7.24 and 7.25.

Accepting an average Fe_XNi_Y stoichiometry of Fe:Ni=0.34:0.66 as indicated by TEM for the NHD-700C,4h sample, from the definition of the fractional deviation of the Fe concentration from the nominal Fe:Ni=0.25:0.75 (1:3) stoichiometry $\frac{Fe}{Ni} = \frac{0.34}{0.66} = \frac{\frac{1-\theta}{4}}{\frac{3+\theta}{4}}$ we can calculate θ to be –0.36. Furthermore, the probability 1-p of finding an Fe anti-site atom in such a $Fe_{0.34}Ni_{0.66}$ alloy is given by the relation $W_{Fe,w} = (1-\theta-S)/4(1-\theta)$ [29]. This probability is equal to the ratio of the absorption area (AA) of the Fe anti-site component relative to the total AA of all components describing this phase in the NHD-700C,4h sample spectrum. This ratio is ~ 0.13 (5%/38%), which together with $\theta = -0.36$ leads to estimate the order parameter value for the $Fe_{0.34}Ni_{0.66}$ alloy phase in the NHD-700C,4h sample to be S=0.67. A similar ratio of 0.12 (3%/25%) is found for the corresponding components of the NHD-700C,30min sample spectrum.

This set of components provides AA to cover the characteristic contributions (i) of the MS, but, on the other hand, it is not the only case of an Fe-Ni fcc phase that can do so. This is because the fcc FM disordered γ_2-Taenite (nickel-rich) Fe-Ni phase, whose presence is more prominent in the range of 500 to 650 °C according to the Fe-Ni phase diagram [31], [32], modeled by a single magnetically split component, can also supply AA to cover this characteristic contributions (i) [5], [33]. Consequently, we must consider this component as well in our fitting model. This component appears colored blue in Figures 7.24 and 7.25.

We now turn our attention to the satellite contributions (ii) of the MS. For this part of the spectra, we take into account the TEM analyses which show the development of graphitic-type layers surrounding the Fe-Ni NPs and suggest further the diffusion of carbon atoms at interstitial sites in their structure. This pattern has been found to exist almost identically in the similar Fe-Co NPs/NDs NHD system developed and studied in this thesis (see Chapter 6) [34]. There, this part was attributed to iron atoms arranged on a non-extensive martensitic-type Fe-Co phase formed in the interface between the Fe-Co NPs and the developed graphitic-type layers surrounding them. Following the similarity of the TEM and Mössbauer experimental data observed for these two iron-based binary alloy NHD systems, we attribute the satellite contributions (ii) of the current MS to a martensitic-type Fe-Ni phase forming within the Fe-Ni NPs, in the interface between them and the supporting NDs nanotemplate growth platforms.

We utilized six minor magnetically split components for this purpose, which correspond to iron atoms exhibiting a metallic alloy character while also being influenced by an adjacent neighboring atom in their immediate vicinity [35]. Based on detailed analyses of the structural properties and related MPs of these iron sites within the martensite structure as reported in the literature [36], [37], [38], [39], [40], [41], [42], [43], we can assign specific atomic environments to these components that model the satellite contributions (ii). Specifically, component M-type (1), shown in olive in Figures 7.24 and 7.25, has the highest B_{hf} value and represents iron atoms in dilated Fe-Ni crystal lattice positions far from interstitial carbon atoms. Component M-type (2), depicted pink in Figures 7.24 and 7.25, corresponds to iron atoms that are distant third neighbors to interstitial carbon atoms, slightly influenced by their presence. Components M-type (3) and M-type (4), shown in purple and dark cyan in Figures 7.24 and 7.25, respectively, represent iron atoms in the closest second- and first-neighbor positions to interstitial carbon atoms. Lastly, components M-type (5) and M-type (6), shown in orange and light blue in Figures 7.24 and 7.25, respectively, have the lowest B_{hf} values and are associated with Fe atoms that have two nearest-neighbor carbon atoms. These environments, with two interstitial carbon atoms as nearest neighbors, are more likely in higher carbon concentrations according to relative binomial distribution models [39], [40], [41], [44], [45].

Subsequently, the central part (iii) of the MS, is fitted with two quadrupole split components and one very broad magnetically split component with collapsing B_{hf} characteristics, all having ionic Fe character. In the cases of the collapsing B_{hf} components, a Gaussian-type spreading ΔB_{hf} [4] of their B_{hf} values around the central B_{hf}^{C} value was allowed to cover the line broadening at this part of the MS.

Assembling in the fitting model the components corresponding to the three sets of contributions for the annealed samples' MS described above, we got back quite adequate fitting results. The resulting MPs values of all components are listed in Table 7.11. The MPs values of the $Fe_{1+z}Ni_{3-z}$ (Fe_XNi_Y) and γ_2-Taenite are very close to those found in the literature for these phases [5], [28], [29], [30], [33]. The same holds also for the set of components used to fit the martensitic-type Fe-Ni phase [36], [37], [38], [39], [40], [41], [42], [43]. Regarding the set of components used to fit contribution (iii) of the MS, we observe that their MPs values correspond to high-spin Fe^{3+} and Fe^{2+} ion sites in oxygen first-neighbor environments, indicating the presence of a spinel-type INO phase with some additional Fe^{2+} ions in its structure [23], which experiences fast SPM relaxation phenomena similar to those found at the precursor sample. From these results, it is evident that the existence of the quadrupole split contributions (iii) in the annealed samples are remnants of the main SPM INO contributions observed in the precursor sample, most probably as a result of incomplete oxide-to-alloy reduction reactions.

The resulting MPs values of the set of components corresponding to the $Fe_{1+z}Ni_{3-z}$, γ_2-Taenite, martensitic-type Fe-Ni and INO phases are very similar for the two annealed samples. This finding emphasizes the high resemblance and iterability of all phases developed in these samples, as also verify the XRD and TEM results. However, a significant change is observed for the total AA value found for the components describing the INO phase. In particular, this value drops from 53% for the NHD-700C,30m sample to 36% for the NHD-700C,4h sample. In contrast, the total AA values for the components of the $Fe_{1+z}Ni_{3-z}$ and γ_2-Taenite phases increase from 25% to 38% and from 7% to 10% respectively for these samples. On the other hand, the sum of the AA values for the components of the martensitic-type Fe-Ni phase remains constant in both samples. These findings indicate that the sample with longer annealing duration contains relatively higher amounts of the fcc Fe-Ni phases and lower amounts of INO phase. Thus, increasing the annealing time seems to favor the formation of the fcc Fe-Ni phases as a result of the reduction of the INO seeds emerging from the precursor sample.

To verify the accuracy and consistency of our fitting model, we inspected the thermal evolution of the MS at 77 K (see Figure 7.26). The features of these spectra are very similar to those found for the RT MS. Consequently, the 77 K MS can be fitted with the same fitting model as that used for the RT spectra. The resulting MPs values are listed in Table 7.12. We observe that all components acquire the expected shifts in their IS, QS, 2ε and B_{hf} values due to the temperature drop, while the sum of the AA values for the components of each phase are very similar (within the expected errors) to those found at RT. The only difference refers to the individual AA values for the components of the INO phase. In particular, the AA value of the MCOL Fe^{3+} component increases at the expense of the AA value of the SPM Fe^{3+} component, relative to those found at the RT MS. This denotes an increase in the characteristic SPM relaxation time τ for a part of the SPM INO NPs which are becoming magnetically blocked at 77 K [8], [10] [7], [23], [46].

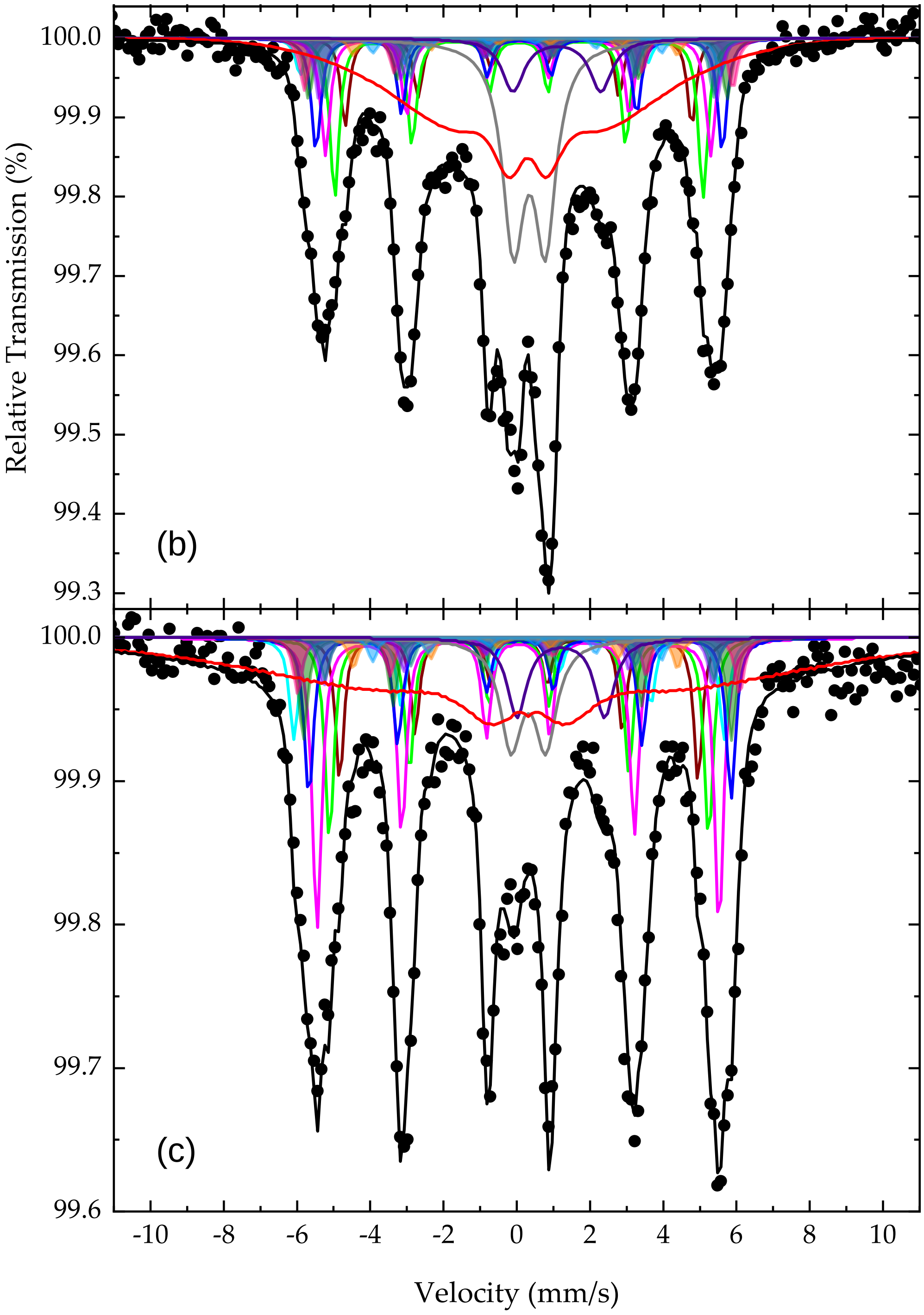

Figure 7.26 Fitted ^{57}Fe Mössbauer spectra of the IM-NHD-700C,30m (a) and of IM-NHD-700C,4h (b) samples collected at 77 K.

Table 7.12. Mössbauer hyperfine parameters as resulting from the best fits of the corresponding spectra of the samples shown on **Figure 7.26**. IS the isomer shift (given relative to α-Fe at 300 K), Γ/2 is the half line-width, QS is the quadrupole splitting, 2ε is the quadrupole shift, B_{hf}^C is the central value of the hyperfine magnetic field, ΔB_{hf} is the total spreading (Gaussian-type) of the B_{hf} values around the central B_{hf}^C value, and AA is the relative spectral absorption area of each component used to fit the spectra. Typical errors are ±0.02 mm/s for IS, Γ/2, 2ε and QS, ±3 kOe for B_{hf}^C and ±3% for AA.

Sample	Components	I.S. (mm/s)	Γ/2 (mm/s)	Q.S. or 2ε (mm/s)	B_{hf}^C (kOe)	ΔB_{hf} (kOe)	Area (%)	Color
IM-NHD-700C,30m	Fe_xNi_Y (0,6)	0.15	0.14	0.00	294	0	5	Maroon
	Fe_xNi_Y (1,6)	0.16	0.15	0.00	313	0	9	Green
	Fe_xNi_Y (2,6)	0.14	0.15	0.00	327	0	8	Magenta
	Fe anti-site	0.15	0.15	-0.42	357	0	2	Cyan
	γ_2-Taenite	0.17	0.15	0.00	344	0	7	Blue
	M-type (1)	0.16	0.15	0.01	363	0	3	Olive
	M-type (2)	0.14	0.15	0.00	355	0	4	Pink
	M-type (3)	0.13	0.15	0.04	337	0	4	Purple
	M-type (4)	0.23	0.15	-0.11	330	0	4	Dark Cyan
	M-type (5)	0.20	0.15	-0.25	275	0	1	Orange
	M-type (6)	0.05	0.15	0.13	245	0	1	Light blue
	SPM Fe^{3+}	0.45	0.36	0.88	0	0	15	Grey
	SPM Fe^{2+}	1.33	0.36	2.14	0	0	4	Dark purple
	MCOL Fe^{3+}	0.44	0.15	0.00	174	135	32	Red
IM-NHD-700C,4h	Fe_xNi_Y (0,6)	0.16	0.14	0.00	304	0	7	Maroon
	Fe_xNi_Y (1,6)	0.17	0.15	0.00	321	0	11	Green
	Fe_xNi_Y (2,6)	0.14	0.15	0.00	341	0	14	Magenta
	Fe anti-site	0.13	0.15	-0.46	365	0	5	Cyan
	γ_2-Taenite	0.20	0.15	0.00	358	0	8	Blue
	M-type (1)	0.16	0.15	0.01	374	0	3	Olive
	M-type (2)	0.13	0.15	0.00	363	0	5	Pink
	M-type (3)	0.13	0.15	0.04	329	0	3	Purple
	M-type (4)	0.23	0.15	-0.11	330	0	2	Dark Cyan
	M-type (5)	0.20	0.15	-0.25	275	0	2	Orange
	M-type (6)	0.05	0.15	0.13	245	0	1	Light blue

	SPM Fe^{3+}	0.43	0.36	0.95	0	0	6	Grey
	SPM Fe^{2+}	1.31	0.32	2.39	0	0	4	Dark purple
	MCOL Fe^{3+}	0.43	0.15	0.00	326	283	28	Red

In this context, we continue with the study of the RT Mössbauer spectra of the annealed samples derived from thermal treatments of the IM-AM2-NHD precursor at 700°C for 30 minutes and 4 hours, as shown in Figures 7.27 and 7.28, respectively. Using the fitting models previously applied to the IM-NHD-700C,30m and IM-NHD-700C,4h samples, we successfully fit the RT MS for these annealed samples derived from the conventional IM-AM2-NHD precursor. The fitted RT MS are presented in Figures 7.27-28, and the corresponding MPs values are listed in Table 7.14.

The MPs values from these fittings closely resemble those for the IM-NHD-700C,30m and IM-NHD-700C,4h models, respectively. However, in the IM-NHD2-700C,30m and IM-NHD2-700C,4h samples, an additional SPM quadrupole-split component (SPM Fe^{2+} (2), shown in brown in Figures 7.27 and 7.28) was necessary to account for additional Fe^{2+} ions in the SPM INO phase [47]. The combined AA values for the INO phase components in each annealed sample—56% for the 30-minute and 51% for the 4-hour treatments—are comparable to the IM-NHD-700C,30m sample's AA value of 53%. Conversely, for the IM-NHD-700C,4h sample, the INO phase components underwent greater reduction due to the extended 4-hour duration, averaging a total AA value of 36%.

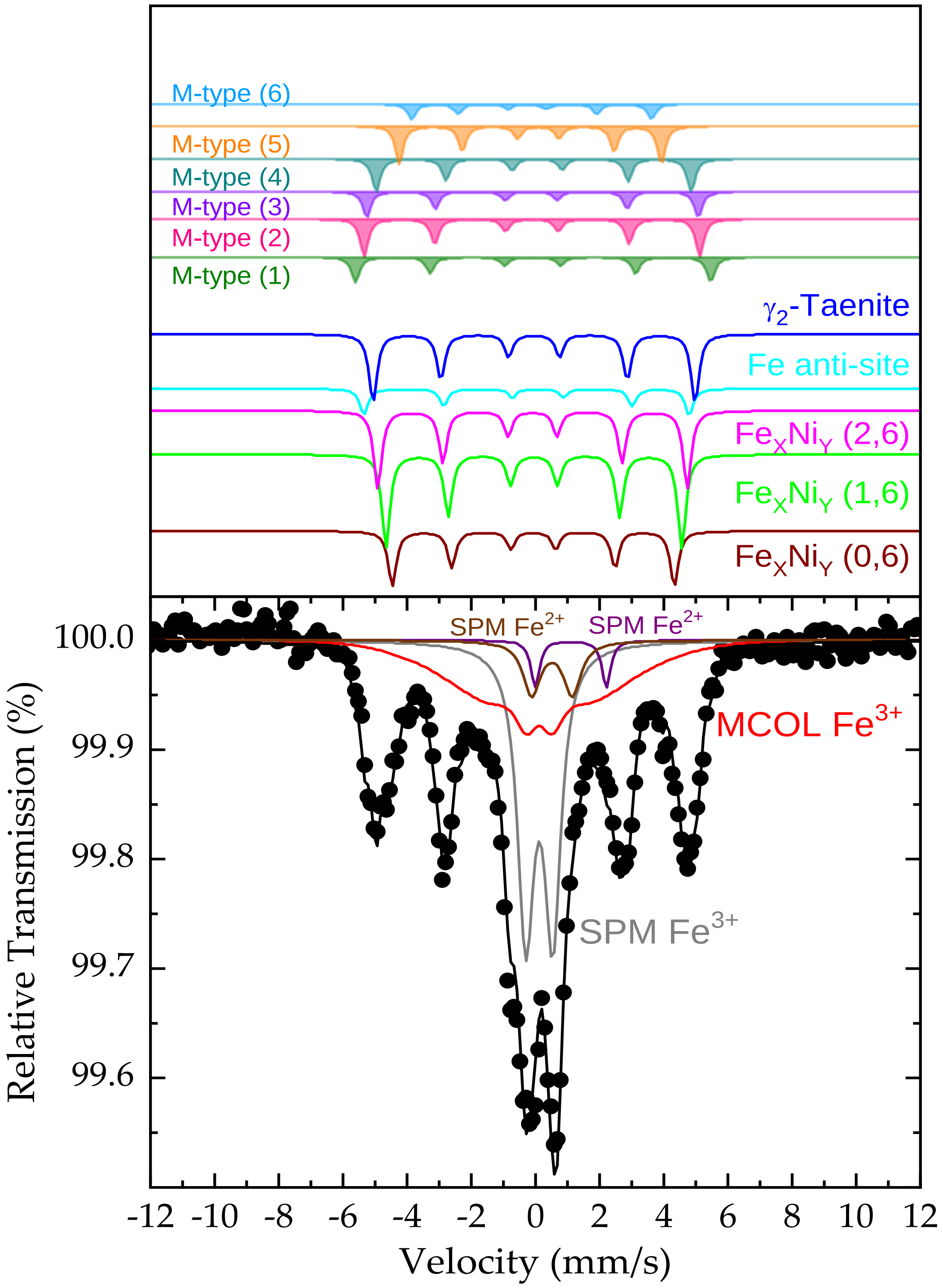

Figure 7.27 ^{57}Fe Mössbauer spectrum of the IM-NHD2-700C,30m sample collected at room temperature.

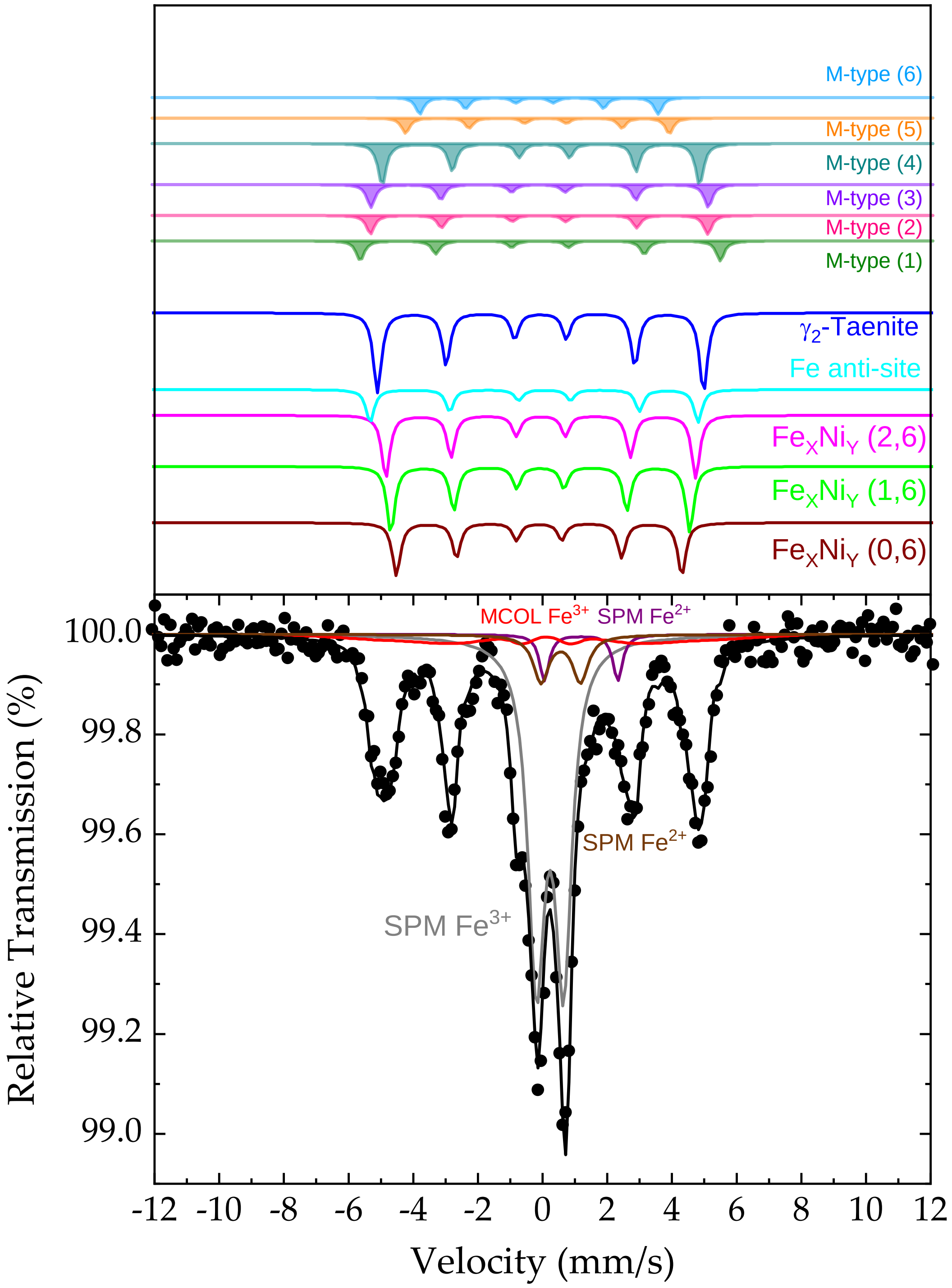

Figure 7.28 ^{57}Fe Mössbauer spectrum of the IM-NHD2-700C,4h sample collected at room temperature.

Table 7.14 Mössbauer hyperfine parameters as resulting from the best fits of the corresponding spectra of the samples shown on **Figures 7.27** and **7.28**. IS the isomer shift (given relative to α-Fe at 300 K), Γ/2 is the half line-width, QS is the quadrupole splitting, 2ε is the quadrupole shift, B_{hf}^{C} is the central value of the hyperfine magnetic field, ΔB_{hf} is the total spreading (Gaussian-type) of the B_{hf} values around the central B_{hf}^{C} value, and AA is the relative spectral absorption area of each component used to fit the spectra. Typical errors are ±0.02 mm/s for IS, Γ/2, 2ε and QS, ±3 kOe for B_{hf}^{C} and ±3% for AA.

Sample	Component	I.S. (mm/s)	Γ/2 (mm/s)	Q.S. or 2ε (mm/s)	BhfC (kOe)	ΔBhf (kOe)	Area (%)	Color
IM-NHD2-700C,30m	Fe_xNi_Y (0,6)	0.04	0.15	0.00	273	0	5	Maroon
	Fe_xNi_Y (1,6)	0.06	0.15	0.00	286	0	8	Green
	Fe_xNi_Y (2,6)	0.01	0.15	0.00	300	0	7	Magenta
	Fe anti-site	0.00	0.15	-0.36	315	0	3	Cyan
	γ_2-Taenite	0.06	0.15	0.00	312	0	6	Blue
	M-type (1)	0.04	0.15	0.01	344	0	2	Olive
	M-type (2)	0.00	0.15	0.00	325	0	3	Pink
	M-type (3)	0.00	0.15	0.04	321	0	2	Purple
	M-type (4)	0.11	0.15	-0.11	305	0	3	Dark Cyan
	M-type (5)	0.08	0.15	-0.25	254	0	3	Orange
	M-type (6)	-0.07	0.15	0.13	232	0	2	Light Blue
	SPM Fe^{3+}	0.30	0.31	0.89	0	0	29	Grey
	MCOL Fe^{3+}	0.28	0.15	0.00	135	110	20	Red
	SPM Fe^{2+} (1)	1.21	0.16	2.22	0	0	2	Dark Purple
	SPM Fe^{2+} (2)	0.62	0.33	1.26	0	0	5	Brown
IM-NHD2-700C,4h	Fe_xNi_Y (0,6)	0.00	0.15	0.00	274	0	6	Maroon
	Fe_xNi_Y (1,6)	0.04	0.15	0.00	287	0	7	Green
	Fe_xNi_Y (2,6)	0.05	0.15	0.00	298	0	7	Magenta
	Fe anti-site	0.00	0.15	-0.32	315	0	4	Cyan
	γ_2-Taenite	0.04	0.15	0.00	313	0	8	Blue
	M-type (1)	0.04	0.15	0.01	346	0	2	Olive
	M-type (2)	0.00	0.15	0.00	324	0	3	Pink
	M-type (3)	0.00	0.15	0.04	324	0	3	Purple
	M-type (4)	0.11	0.15	-0.11	305	0	5	Dark Cyan
	M-type (5)	0.08	0.15	-0.25	253	0	2	Orange

	M-type (6)	-0.07	0.15	0.13	229	0	2	Light Blue
	SPM Fe^{3+}	0.29	0.36	0.83	0	0	37	Grey
	MCOL Fe^{3+}	0.28	0.15	0.00	289	95	6	Red
	SPM Fe^{2+} (1)	1.19	0.18	2.28	0	0	3	Dark Purple
	SPM Fe^{2+} (2)	0.59	0.22	1.22	0	0	5	Brown

To ensure the consistency and reliability of the fitting model, we examined the thermal evolution of the IM-NHD2-700C,30m sample's spectrum at 77 K. The fitting model applied at RT satisfactorily describes the spectrum at this lower temperature. In this context, the iron alloy components exhibit the expected shifts in IS and B_{hf} values, while their AA values remain consistent (within the margin of error) with those found in the RT spectrum of the respective sample.

The only notable difference lies in the AA values of the SPM Fe^{3+}/Fe^{2+} and MCOL Fe^{3+}/Fe^{2+} components. Specifically, the increase in AA for the MCOL components, at the expense of the SPM components, reflects the expected decrease in the SPM relaxation time (τ) for the nanostructured INO NPs at lower temperature. This finding indicates that the ceasing of the fast SPM relaxation affects a larger portion of this phase [7], [46], [47]. The fitted 77 K spectrum is presented in Figure 7.29, with the corresponding MPs values listed in Table 7.15.

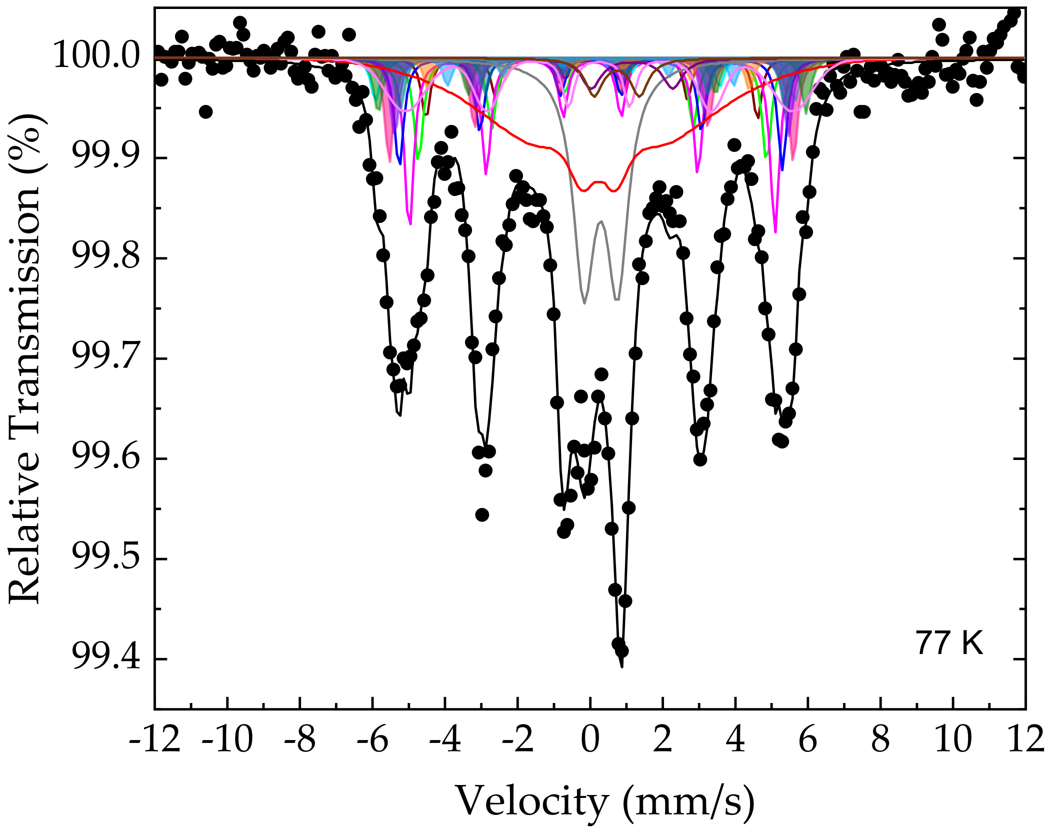

Figure 7.29 ^{57}Fe Mössbauer spectrum of the IM-NHD2-700C,30m sample collected at 77 K.

Table 7.15 Mössbauer hyperfine parameters as resulting from the best fits of the corresponding spectra of the samples shown on **Figures 7.29**. IS the isomer shift (given relative to α-Fe at 300 K), Γ/2 is the half line-width, QS is the quadrupole splitting, 2ε is the quadrupole shift, B_{hf}^C is the central value of the hyperfine magnetic field, ΔB_{hf} is the total spreading (Gaussian-type) of the B_{hf} values around the central B_{hf}^C value, and AA is the relative spectral absorption area of each component used to fit the spectra. Typical errors are ±0.02 mm/s for IS, Γ/2, 2ε and QS, ±3 kOe for B_{hf}^C and ±3% for AA.

Sample	**Component**	**I.S. (mm/s)**	**Γ/2 (mm/s)**	**Q.S. or 2ε (mm/s)**	**B_{hf}^C (kOe)**	**ΔB_{hf} (kOe)**	**Area (%)**	**Color**
IM-NHD2-700C,30m	Fe_xNi_Y (0,6)	0.14	0.14	0.00	284	0	4	Maroon
	Fe_xNi_Y (1,6)	0.17	0.15	0.00	298	0	6	Green
	Fe_xNi_Y (2,6)	0.16	0.15	0.00	313	0	7	Magenta
	Fe anti-site	0.15	0.15	-0.36	359	0	2	Cyan
	γ_2-Taenite	0.12	0.15	0.00	328	0	6	Blue
	M-type (1)	0.16	0.15	0.01	366	0	3	Olive
	M-type (2)	0.14	0.15	0.00	346	0	5	Pink
	M-type (3)	0.13	0.15	0.04	337	0	4	Purple
	M-type (4)	0.23	0.15	-0.11	330	0	3	Dark Cyan
	M-type (5)	0.20	0.15	-0.25	275	0	2	Orange
	M-type (6)	0.05	0.15	0.13	245	0	2	Light Blue
	SPM Fe^{3+}	0.36	0.36	0.93	0	0	13	Grey
	MCOL Fe^{3+}	0.34	0.15	0.00	150	124	24	Red
	MCOL Fe^{3+} (2)	0.35	0.15	0.00	332	30	13	Light Magenta
	SPM Fe^{2+} (1)	1.32	0.32	2.25	0	0	2	Dark Purple
	SPM Fe^{2+} (2)	0.79	0.29	1.25	0	0	4	Brown

In addition, we examined the case where the IM-AM2-NHD precursor underwent a two-step annealing procedure. This approach involved a typical annealing step at 700°C, which could lead to the formation of hybrid samples with well-established structural characteristics, as previously discussed. This was followed by a subsequent thermal treatment at a lower temperature of 300°C. The aim was to investigate any further structural modifications in the spectral patterns of the respective samples. Extended annealing at 300°C could promote the development of hybrid nanostructured magnetic materials with enhanced long-range chemical ordering. Furthermore, literature suggests that γ_2-Taenite may decompose into an ordered ferromagnetic equiatomic FeNi Tetrataenite phase at this temperature, which possesses unique hard magnetic characteristics [3], [48], [49]. This transformation could rekindle interest in studying the Fe-Ni/NDs system.

Figures 7.30-31 present the RT Mössbauer spectra of the annealed samples derived from two-step treatments of the IM-AM2-NHD precursor: one at 700°C for 30 minutes followed by 300°C for 64 hours (IM-NHD-(700C,30m-to-300C,64h)) and another at 700°C for 4 hours followed by 300°C for 96 hours (IM-NHD-(700C,4h-to-300C,96h)). Unfortunately, this approach resulted in distinct spectral configurations of nanostructured phases in each sample's RT spectrum, which could not be adequately described using the fitting models applied to the IM-NHD2-700C,30m and IM-NHD2-700C,4h samples.

Despite the different annealing durations, both spectra exhibit similar characteristics, described qualitatively by a set of broad but distinct magnetically split contributions alongside quadrupole split contributions observed at the center of the RT MS. The intensity of the distinct magnetically split contributions is diminished in the spectrum of the IM-NHD-(700C,30m-to-300C,64h) sample, while it is more pronounced in the IM-NHD-(700C,4h-to-300C,96h) spectrum. Conversely, the intensity of the quadrupole split contributions is more pronounced in the shorter annealing duration sample (30 minutes at 700°C and 64 hours at 300°C) compared to the longer duration sample (4 hours at 700°C and 96 hours at 300°C).

To select a suitable fitting model for analyzing these RT MS, we referenced data from XRD and ^{57}Fe Mössbauer spectroscopy analyses of the IM-NHD2-700C,30m and IM-NHD2-700C,4h samples. These analyses indicated the presence of a fcc Fe-Ni nanostructured alloy phase, corresponding to Fe-Ni NPs grown on the surfaces of the ND nanotemplates, with a Fe:Ni stoichiometry close to 1:3. This could correspond to either intermetallic $FeNi_3$ Awaruite or γ_2-Taenite, alongside an INO nanostructured phase.

For the IM-NHD-(700C,30m-to-300C,64h) sample, we employed three main central quadrupole split components and three broad magnetically split components with B_{hf} characteristics to fit the RT spectrum (Figure 7.30). The resulting MPs values from this fit, listed in Table 7.16, correspond to high-spin Fe^{3+} ion sites in oxygen first-neighbor environments, indicative of a spinel-type INO phase with additional Fe^{2+} ions, which experience fast SPM relaxation phenomena at RT. The main contributions to the RT spectrum are attributed to the SPM Fe^{3+} (1), SPM Fe^{3+} (2), and SPM Fe^{2+} quadrupole split doublet components (colored dark cyan, purple, and green in Figure 7.30, respectively), collectively accounting for approximately 80% of the area under the curve (AA). Additionally, a broad magnetically split component with resolved B_{hf} characteristics (MRES Awaruite, colored grey in Figure 7.30) corresponds to a cubic soft FM Fe–Ni alloy Awaruite phase. The IS and B_{hf} values of the magnetically split component with less intense resonant lines (MRES γ_2-Taenite component, colored blue in Figure 7.30) are characteristic of a cubic soft FM Fe-Ni γ_2-Taenite phase. Another broad magnetically split component (MCOL Fe^{3+}, colored red in Figure 7.30) exhibits collapsing B_{hf} characteristics and corresponds to high-spin Fe^{3+} ion sites in oxygen first-neighbor environments, indicative of a spinel-type INO phase, experiencing moderate SPM relaxation at RT.

For the RT spectrum of the IM-NHD-(700C,4h-to-300C,96h) sample, we used the same fitting model as before but included an additional SPM Fe^{2+} component (colored brown in Figure 7.31) to better describe the central part of this spectrum. In this case, the magnetically collapsing contribution attributed to the aforementioned nanostructured phases has a greater AA value (54%) compared to the quadrupole split contribution (46%) (see Table 7.17). This may be due to the influence of the longer annealing durations for this sample.

Nevertheless, these results indicate that the second annealing step at 300°C impairs the structural patterns established during the first annealing step at 700°C in both samples. This is evident from the reappearance of the SPM Fe^{3+}/SPM Fe^{2+} and MCOL Fe^{3+} INO components, suggesting that the extended annealing at 300°C creates favorable oxidation conditions detrimental to the Fe-Ni nanostructures.

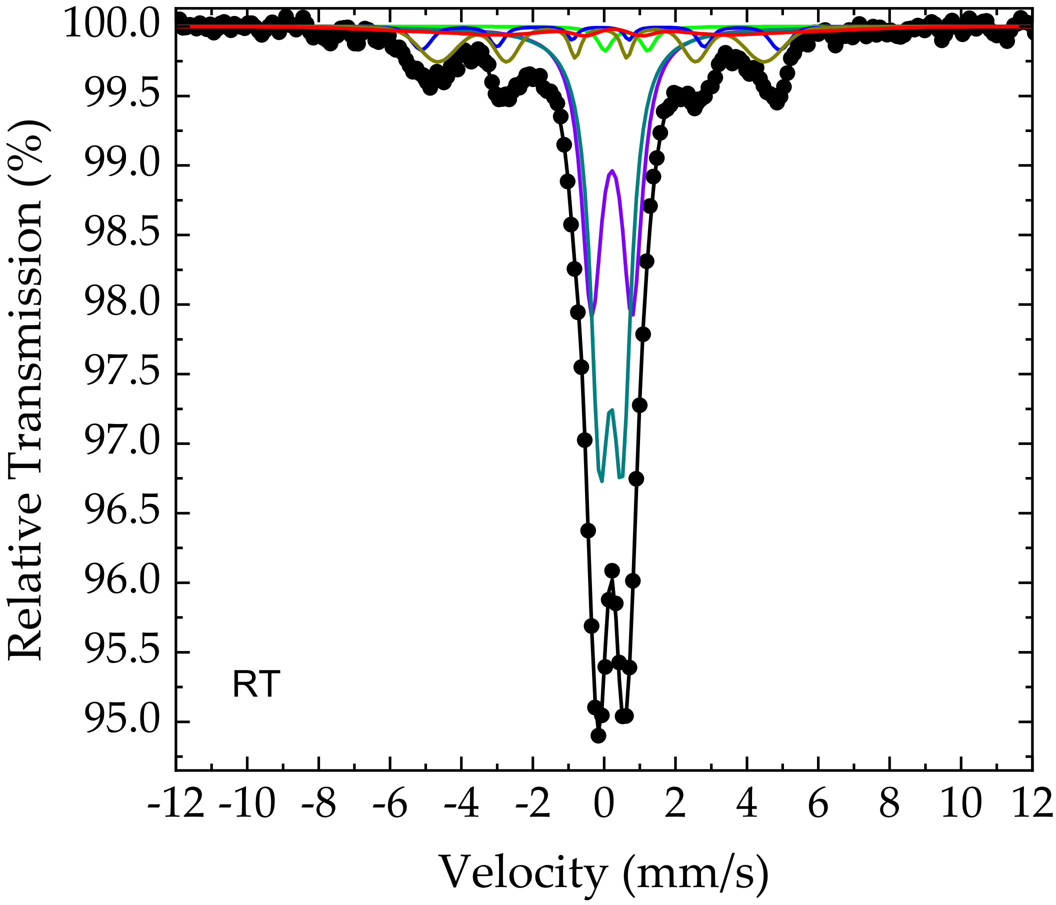

Figure 7.30 ^{57}Fe Mössbauer spectrum of the IM-NHD2-(700C,30m-to-300C,64h) sample collected at room temperature.

Table 7.16 Mössbauer hyperfine parameters as resulting from the best fits of the corresponding spectra of the samples shown on **Figures 7.30**. IS the isomer shift (given relative to α-Fe at 300 K), Γ/2 is the half line-width, QS is the quadrupole splitting, 2ε is the quadrupole shift, B_{hf}^C is the central value of the hyperfine magnetic field, ΔB_{hf} is the total spreading (Gaussian-type) of the B_{hf} values around the central B_{hf}^C value, and AA is the relative spectral absorption area of each component used to fit the spectra. Typical errors are ±0.02 mm/s for IS, Γ/2, 2ε and QS, ±3 kOe for B_{hf}^C and ±3% for AA.

Sample	**Component**	**I.S. (mm/s)**	**Γ/2 (mm/s)**	**Q.S. or 2ε (mm/s)**	**B_{hf}^C (kOe)**	**ΔB_{hf} (kOe)**	**Area (%)**	**Color**
FeNi-IM-AN(700C,30m-to-300C,64h) from AM(10-04-20)	SPM Fe^{3+} (1)	0.29	0.31	0.63	0	0	44	Dark Cyan
	SPM Fe^{3+} (2)	0.32	0.36	1.13	0	0	33	Purple
	MCOL Fe^{3+}	0.37	0.15	0.00	307	112	4	Red
	SPM Fe^{2+}	0.73	0.24	1.20	0	15	3	Green
	MRES Awaruite	0.02	0.15	0.00	284	28	11	Grey
	MRES γ_2-Taenite	0.01	0.15	0.00	310	13	5	Blue

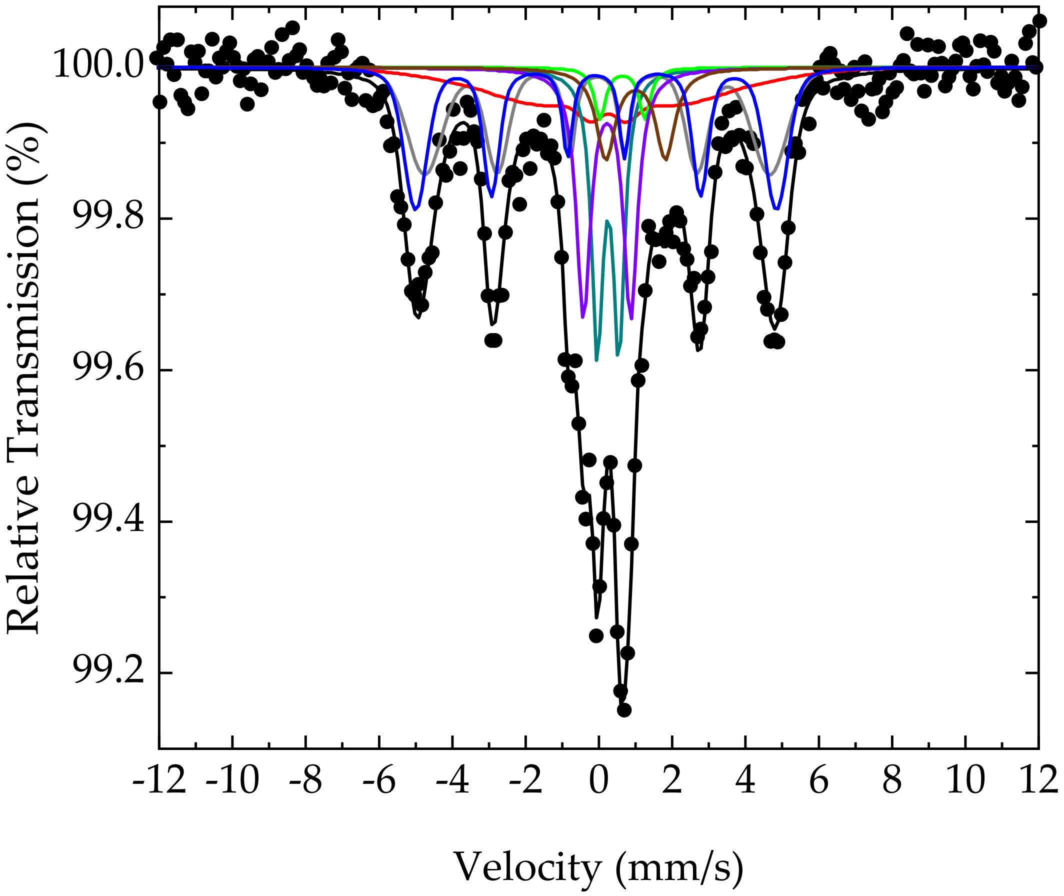

Figure 7.31 ^{57}Fe Mössbauer spectrum of the IM-NHD2-(700C,4h-to-300C,96h) sample collected at room temperature.

Table 7.17 Mössbauer hyperfine parameters as resulting from the best fits of the corresponding spectra of the samples shown on **Figures 7.31**. IS the isomer shift (given relative to α-Fe at 300 K), $\Gamma/2$ is the half line-width, QS is the quadrupole splitting, 2ε is the quadrupole shift, B_{hf}^{C} is the central value of the hyperfine magnetic field, ΔB_{hf} is the total spreading (Gaussian-type) of the B_{hf} values around the central B_{hf}^{C} value, and AA is the relative spectral absorption area of each component used to fit the spectra. Typical errors are ±0.02 mm/s for IS, $\Gamma/2$, 2ε and QS, ±3 kOe for B_{hf}^{C} and ±3% for AA.

Sample	**Component**	**I.S. (mm/s)**	**$\Gamma/2$ (mm/s)**	**Q.S. or 2ε (mm/s)**	**B_{hf}^{C} (kOe)**	**ΔB_{hf} (kOe)**	**Area (%)**	**Color**
FeNi-IM-AN(700C,4h-to-300C,96h) from AM(10-04-20)	SPM Fe^{3+} (1)	0.36	0.183	0.59	0	0	13	Dark Cyan
	SPM Fe^{3+} (2)	0.33	0.23	1.29	0	0	15	Purple
	MCOL Fe^{3+}	0.37	0.15	0.00	169	121	15	Red
	SPM Fe^{2+} (1)	0.75	0.18	1.22	0	0	3	Green
	SPM Fe^{2+} (2)	1.11	0.31	1.63	0	0	7	Brown
	MRES Awaruite	0.06	0.15	0.00	293	26	24	Grey
	MRES γ_2-Taenite	0.03	0.15	0.00	306	15	23	Blue

Now, we shift our study's focus to the enriched as-made precursor sample and its annealed derivatives. The MS of the enriched as-made nanohybrid precursor, recorded at RT and at 77 K, are presented in Figure 7.32.

In Figure 7.32a, the RT spectrum of the as-made precursor is dominated by a quadrupole split contribution with relatively broad resonant lines. This contribution can be adequately described using two main quadrupole split components. Additionally, a minor contribution from another quadrupole split component has been included to enhance the fitting model for the RT spectrum of the En-IM-AM3-NHD sample. The resulting MPs from the best fit of these spectra are listed in Table 7.18. These values indicate the presence of high-spin Fe^{3+} ($S = 5/2$) ionic states for both components (SPM Fe^{3+} (1) and SPM Fe^{3+} (2), shown in grey and dark purple in Figure 7.32a, respectively), which are typical of Fe^{3+} sites commonly found in INO spinel-type nanostructures. Subtle contributions from Fe^{2+} high-spin ($S = 2$) states, represented by the SPM Fe^{2+} component colored dark yellow in the En-IM-AM3-NHD spectrum, are also observed. The small particle size of these nanostructures results in fast SPM behavior at RT [6], [13], [14], [15], [23]. At RT, the sizes of all INO NP seeds developed on the surfaces of the ND nanotemplates during the first stage of synthesis drop below the SPM size limit, causing their B_{hf} values to average to zero [24], [25].

Upon lowering the temperature to 77 K, the relaxation time τ for some of the INO NP seeds increases to values comparable to or slightly exceeding τ_{MS}. This change confers magnetic splitting and collapsing B_{hf} characteristics to their contributions in the corresponding Mössbauer spectra (Figure 7.32b). These contributions are represented by the MCOL Fe^{3+} components (colored red, light orange, and light magenta) in Figure 7.32b, likely corresponding to the larger INO NPs in the particle size distribution or NPs that are in closer proximity [8], [10]. For the remaining smaller or more isolated INO NP seeds, the SPM characteristics are retained in the 77 K spectrum, represented by the two quadrupole split SPM Fe^{3+} (1) and SPM Fe^{3+} (2) components, similar to those observed at RT (see Table 7.19).

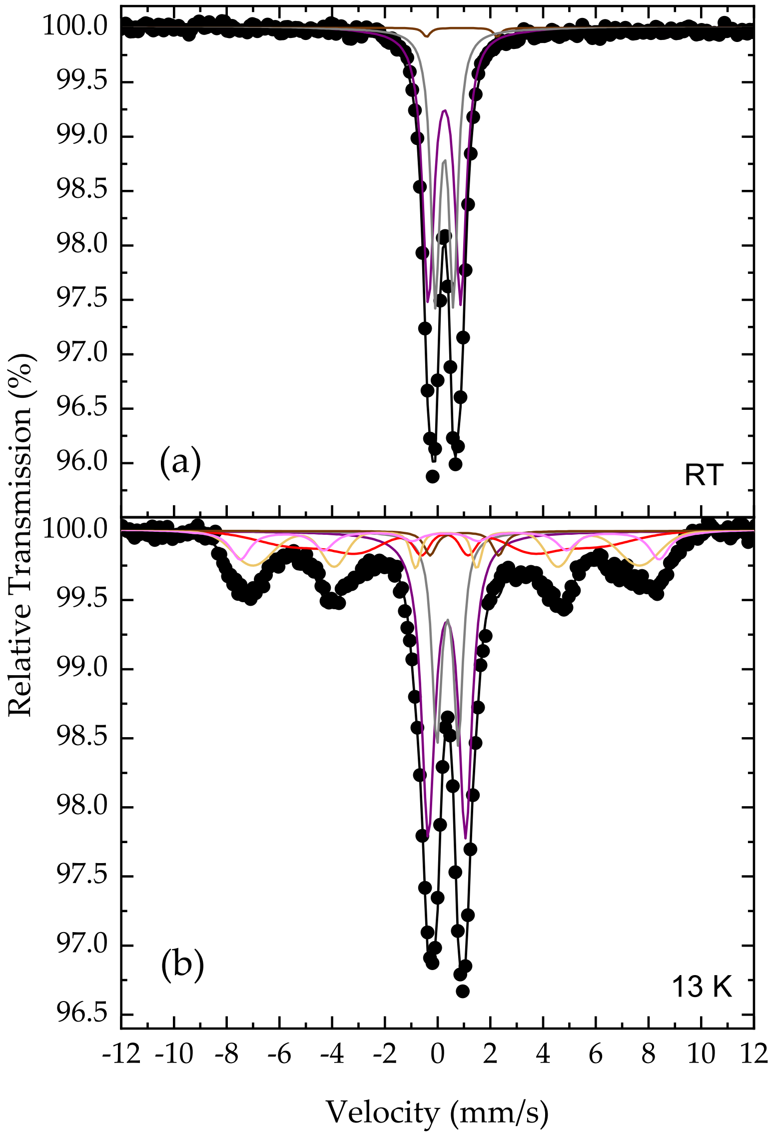

Figure 7.32 ^{57}Fe Mössbauer spectrum of the En-IM-AM3-NHD sample collected at room temperature (a) and 13 K (b).

Table 7.18 Mössbauer hyperfine parameters as resulting from the best fits of the corresponding spectra of the samples shown on **Figures 7.32a**. IS the isomer shift (given relative to α-Fe at 300 K), Γ/2 is the half line-width, QS is the quadrupole splitting, 2ε is the quadrupole shift, B_{hf}^{C} is the central value of the hyperfine magnetic field, ΔB_{hf} is the total spreading (Gaussian-type) of the B_{hf} values around the central B_{hf}^{C} value, and AA is the relative spectral absorption area of each component used to fit the spectra. Typical errors are ±0.02 mm/s for IS, Γ/2, 2ε and QS, ±3 kOe for B_{hf}^{C} and ±3% for AA.

Sample	**Component**	**I.S. (mm/s)**	**Γ/2 (mm/s)**	**Q.S. or 2ε (mm/s)**	**B_{hf}^{C} (kOe)**	**ΔB_{hf} (kOe)**	**Area (%)**	**Color**
En-IM-AM3-NHD	SPM Fe^{3+} (1)	0.36	0.20	0.72	0	0	42	Grey
	SPM Fe^{3+} (2)	0.37	0.26	1.28	0	0	55	Dark Purple
	SPM Fe^{2+}	1.14	0.16	2.68	0	0	3	Brown

Table 7.19 Mössbauer hyperfine parameters as resulting from the best fits of the corresponding spectra of the samples shown on **Figures 7.32b**. IS the isomer shift (given relative to α-Fe at 300 K), Γ/2 is the half line-width, QS is the quadrupole splitting, 2ε is the quadrupole shift, B_{hf}^{C} is the central value of the hyperfine magnetic field, ΔB_{hf} is the total spreading (Gaussian-type) of the B_{hf} values around the central B_{hf}^{C} value, and AA is the relative spectral absorption area of each component used to fit the spectra. Typical errors are ±0.02 mm/s for IS, Γ/2, 2ε and QS, ±3 kOe for B_{hf}^{C} and ±3% for AA.

Sample	**Component**	**I.S. (mm/s)**	**Γ/2 (mm/s)**	**Q.S. or 2ε (mm/s)**	**B_{hf}^{C} (kOe)**	**ΔB_{hf} (kOe)**	**Area (%)**	**Color**
En_IM-AM3-NHD	SPM Fe^{3+} (1)	0.48	0.22	0.78	0	0	18	Grey
	SPM Fe^{3+} (2)	0.46	0.30	1.33	0	0	36	Dark Purple
	MCOL Fe^{3+} (1)	0.38	0.15	0.00	346	88	16	Red
	MCOL Fe^{3+} (2)	0.43	0.15	0.00	456	42	18	Light Orange
	MCOL Fe^{3+} (3)	0.48	0.45	0.00	494	66	10	Light Magenta
	SPM Fe^{2+}	1.26	0.28	2.72	0	0	3	Brown

The RT MS of the annealed samples using the enriched precursor are displayed in Figure 7.33. Regardless of the synthesis conditions, these MS exhibit spectral characteristics similar to those observed in the RT MS of the conventional annealed samples. A representative fit for the RT spectrum of the En-IM-NHD3-700C,30m-Q sample is shown in Figure 7.33b, with the resulting MPs values listed in Table 7.20.

To fit this spectrum, we employed the same fitting model used for the IM-NHD-700C,4h sample, with the addition of two secondary SPM quadrupole split components (one SPM Fe^{3+} (2) and one SPM Fe^{2+} (2), colored dark purple and brown in Figure 7.33b). These components represent secondary Fe^{3+} species of the INO phase accompanied by Fe^{2+} ions. Notably, the MCOL Fe^{3+} component (colored red in Figure 7.25), which was included in the RT spectrum fit of IM-NHD-

700C,4h, was excluded from the En-IM-NHD3-700C,30m-Q sample's RT fit. The MPs values of all other components listed in Table 7.20 are very similar to those found for the non-^{57}Fe-enriched IM-NHD-700C,4h sample, demonstrating the high similarity of the Fe–Ni NP phase characteristics between the two samples and confirming the reproducibility of the synthesis method, as also corroborated by the XRD and TEM results. In contrast, a 13% increase in the total AA values attributed to the INO phase and a 7% decrease in the total AA values of the cubic Fe–Ni alloy components are observed for the En-NHD3-700C,30m-Q sample compared to the IM-NHD-700C,4h sample. Additionally, a similar 5% decrease in the sum of the AA values for the "martensitic" components is observed for the enriched annealed sample compared to the conventional annealed sample. These results suggest that the En-IM-NHD3-700C,30m-Q sample contains relatively higher amounts of the SPM INO phase, which also appears to be chemically distinct, as it contains additional Fe^{2+} ions compared to the SPM INO phase in the IM-NHD-700C,4h sample. This reflects some diversification in the chemical characteristics of the two precursors. The consistent presence of the SPM Fe^{3+} (2) and SPM Fe^{2+} (2) components in the MS of all annealed samples derived from the En-IM-AM3-NHD precursor (Figure 7.33 and Table 7.20) reinforces this argument, as these components are absent in the MS of annealed samples derived from the conventional precursors.

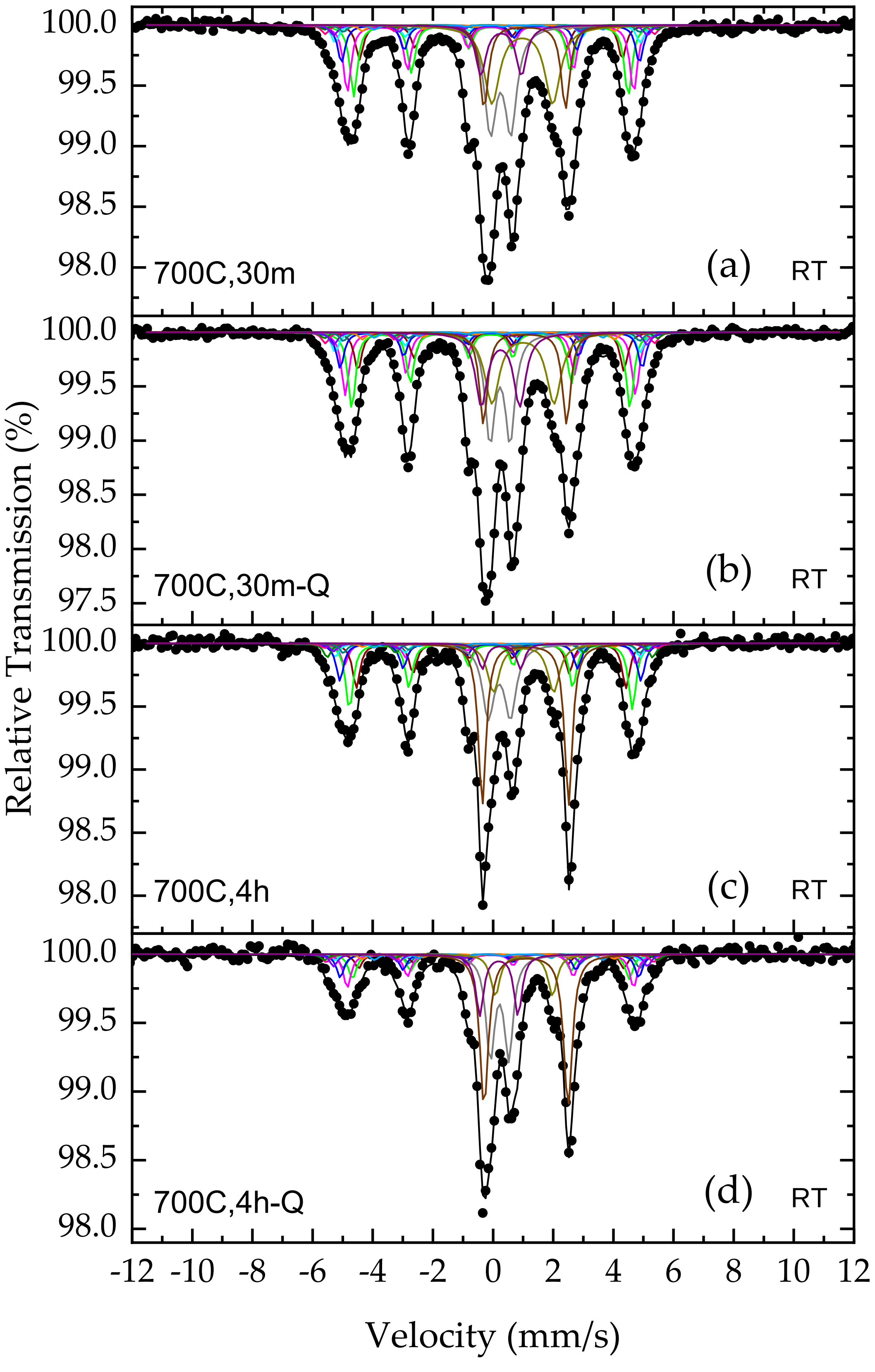

Figure 7.33 ^{57}Fe Mössbauer spectrum of the ^{57}Fe enriched En-IM-NHD3-700,30m (a), En-IM-NHD3-700,30m-Q (b), En-IM-NHD3-700,4h (c) and En-IM-NHD3-700,4h-Q (d) samples collected at room temperature.

Table 7.20 Mössbauer hyperfine parameters as resulting from the best fits of the corresponding spectra of the samples shown on **Figures 7.33**. IS the isomer shift (given relative to α-Fe at 300 K), Γ/2 is the half line-width, QS is the quadrupole splitting, 2ε is the quadrupole shift, B_{hf}^C is the central value of the hyperfine magnetic field, ΔB_{hf} is the total spreading (Gaussian-type) of the B_{hf} values around the central B_{hf}^C value, and AA is the relative spectral absorption area of each component used to fit the spectra. Typical errors are ±0.02 mm/s for IS, Γ/2, 2ε and QS, ±3 kOe for B_{hf}^C and ±3% for AA.

Sample	Component	I.S. (mm/s)	Γ/2 (mm/s)	Q.S. or 2ε (mm/s)	B_{hf}^C (kOe)	ΔB_{hf} (kOe)	Area (%)	Color
En-IM-NHD3-700C,30m	Fe_xNi_y (0,6)	0.03	0.15	0.00	271	0	8	Maroon
	Fe_xNi_y (1,6)	0.03	0.15	0.00	284	0	12	Green
	Fe_xNi_y (2,6)	0.02	0.15	0.00	296	0	12	Magenta
	Fe anti-site	0.03	0.15	-0.20	315	0	3	Cyan
	γ_2-Taenite	0.02	0.15	0.00	308	0	7	Blue
	M-type (1)	0.04	0.15	0.01	354	0	2	Olive
	M-type (2)	0.03	0.15	0.00	340	0	1	Pink
	M-type (3)	0.02	0.15	0.04	324	0	2	Purple
	M-type (4)	0.11	0.15	-0.11	306	0	1	Dark Cyan
	M-type (5)	0.08	0.15	-0.25	260	0	1	Orange
	M-type (6)	-0.11	0.15	0.13	236	0	1	Light blue
	SPM Fe^{3+} (1)	0.36	0.24	0.68	0	0	16	Grey
	SPM Fe^{2+} (1)	1.08	0.31	2.02	0	0	15	Dark Yellow
	SPM Fe^{2+} (2)	1.16	0.17	2.70	0	0	10	Brown
	SPM Fe^{3+} (2)	0.37	0.23	1.35	0		7	Dark Purple
En-IM-NHD3-700C,30m-Q	Fe_xNi_y (0,6)	0.03	0.15	0.00	275	0	8	Maroon
	Fe_xNi_y (1,6)	0.03	0.15	0.00	287	0	12	Green
	Fe_xNi_y (2,6)	0.02	0.15	0.00	300	0	10	Magenta
	Fe anti-site	0.03	0.15	-0.20	315	0	4	Cyan
	γ_2-Taenite	0.04	0.15	0.00	312	0	7	Blue
	M-type (1)	0.04	0.15	0.01	349	0	2	Olive
	M-type (2)	0.03	0.15	0.00	340	0	1	Pink
	M-type (3)	0.02	0.15	0.04	320	0	2	Purple
	M-type (4)	0.11	0.15	-0.11	306	0	2	Dark Cyan
	M-type (5)	0.08	0.15	-0.25	260	0	2	Orange

	M-type (6)	-0.11	0.15	0.13	236	0	1	Light blue
	SPM Fe^{3+} (1)	0.34	0.20	0.67	0	0	15	Grey
	SPM Fe^{2+} (1)	1.10	0.29	2.06	0	0	13	Dark Yellow
	SPM Fe^{2+} (2)	1.17	0.16	2.76	0	0	10	Brown
	SPM Fe^{3+} (2)	0.36	0.24	1.28	0	0	11	Dark Purple
En-IM-NHD3-700C,4h	Fe_xNi_Y (0,6)	0.04	0.15	0.00	279	0	9	Maroon
	Fe_xNi_Y (1,6)	0.03	0.15	0.00	292	0	13	Green
	Fe_xNi_Y (2,6)	0.02	0.15	0.00	301	0	7	Magenta
	Fe anti-site	0.03	0.15	-0.20	315	0	3	Cyan
	γ_2-Taenite	0.02	0.15	0.00	311	0	8	Blue
	M-type (1)	0.04	0.15	0.01	344	0	2	Olive
	M-type (2)	0.01	0.15	0.00	336	0	3	Pink
	M-type (3)	0.01	0.15	0.04	324	0	2	Purple
	M-type (4)	0.11	0.15	-0.11	306	0	2	Dark Cyan
	M-type (5)	0.08	0.15	-0.25	260	0	1	Orange
	M-type (6)	-0.11	0.15	0.13	236	0	1	Light blue
	SPM Fe^{3+} (1)	0.33	0.23	0.74	0	0	15	Grey
	SPM Fe^{2+} (1)	1.12	0.24	2.00	0	0	9	Dark Yellow
	SPM Fe^{2+} (2)	1.18	0.16	2.79	0	0	20	Brown
	SPM Fe^{3+} (2)	0.35	0.16	1.27	0	0	4	Dark Purple
En-IM-NHD3-700C,4h-Q	Fe_xNi_Y (0,6)	0.04	0.15	0.00	274	0	4	Maroon
	Fe_xNi_Y (1,6)	0.03	0.15	0.00	286	0	7	Green
	Fe_xNi_Y (2,6)	0.02	0.15	0.00	296	0	6	Magenta
	Fe anti-site	0.03	0.15	-0.20	315	0	3	Cyan
	γ_2-Taenite	-0.01	0.15	0.00	308	0	6	Blue
	M-type (1)	0.04	0.15	0.01	344	0	2	Olive
	M-type (2)	0.00	0.15	0.00	338	0	2	Pink
	M-type (3)	0.01	0.15	0.04	324	0	3	Purple
	M-type (4)	0.11	0.15	-0.11	306	0	4	Dark Cyan
	M-type (5)	0.08	0.15	-0.25	260	0	1	Orange
	M-type (6)	-0.11	0.15	0.13	236	0	2	Light blue
	SPM Fe^{3+} (1)	0.32	0.18	0.62	0	0	19	Grey

	SPM Fe^{2+} (1)	1.17	0.18	1.99	0	0	7	Dark Yellow
	SPM Fe^{2+} (2)	1.20	0.17	2.77	0	0	24	Brown
	SPM Fe^{3+} (2)	0.34	0.16	1.28	0	0	9	Dark Purple

Upon lowering the temperature to 13 K, the evolution of the Mössbauer spectrum of the En-IM-NHD3-700C,30m-Q sample (Figure 7.34b and Table 7.21) exhibits spectral features consistent with those of the IM-NHD-700C,4h sample at 77 K, further verifying the fitting model's consistency. We observe that all components of the enriched sample shift in their IS, QS, 2ε, and B_{hf} values due to the temperature drop, while the sum of the AA values for each phase's components remains very similar (within the expected errors) to those at RT. The only notable difference is the emergence of two broad magnetically collapsing components, MCOL Fe^{3+} and MCOL Fe^{2+}, colored light magenta and red in Figure 7.34b, respectively, whose AA values increase at the expense of the SPM Fe^{3+} and SPM Fe^{2+} components found in the corresponding RT spectrum (Figure 7.33b). This indicates an increase in the characteristic SPM relaxation time τ for some of the SPM INO NPs, which become magnetically blocked at 13 K [8], [10] [7], [23], [46]. The fitted 13 K MS for all enriched annealed samples is presented in Figure 7.34, with the resulting MPs values listed in Table 7.21.

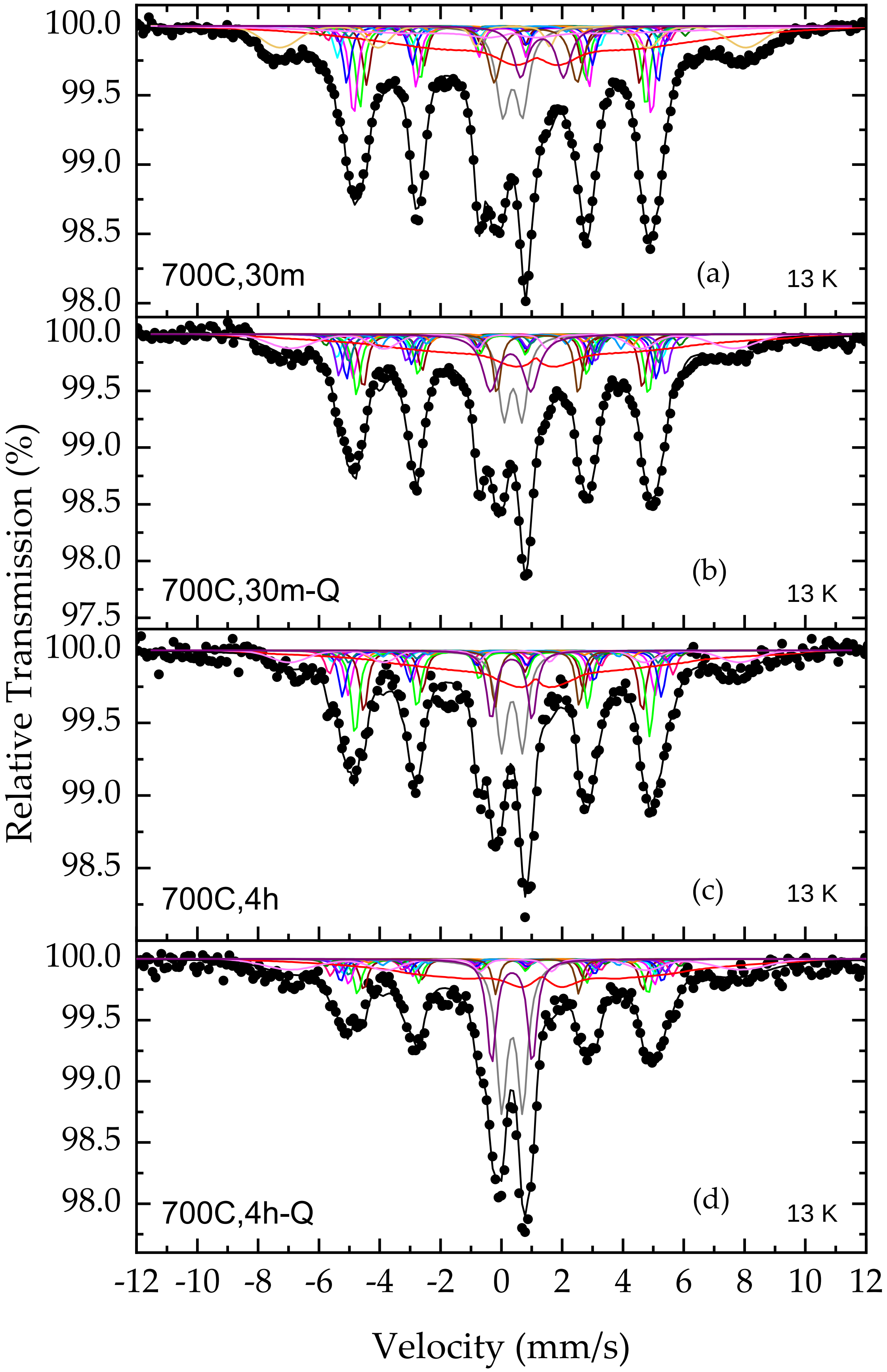

Figure 7.34 ^{57}Fe Mössbauer spectrum of the ^{57}Fe enriched En-IM-NHD3-700,30m (a), En-IM-NHD3-700,30m-Q (b), En-IM-NHD3-700,4h (c) and En-IM-NHD3-700,4h-Q (d) samples collected at 13 K.

Table 7.21 Mössbauer hyperfine parameters as resulting from the best fits of the corresponding spectra of the samples shown on **Figures 7.34**. IS the isomer shift (given relative to α-Fe at 300 K), $\Gamma/2$ is the half line-width, QS is the quadrupole splitting, 2ε is the quadrupole shift, B_{hf}^{C} is the central value of the hyperfine magnetic field, ΔB_{hf} is the total spreading (Gaussian-type) of the B_{hf} values around the central B_{hf}^{C} value, and AA is the relative spectral absorption area of each component used to fit the spectra. Typical errors are ±0.02 mm/s for IS, $\Gamma/2$, 2ε and QS, ±3 kOe for B_{hf}^{C} and ±3% for AA.

Sample	Component	I.S. (mm/s)	$\Gamma/2$ (mm/s)	Q.S. or 2ε (mm/s)	B_{hf}^{C} (kOe)	ΔB_{hf} (kOe)	Area (%)	Color
En-IM-NHD3-700C,30m	Fe$_x$Ni$_Y$ (0,6)	0.16	0.15	0.00	279	0	7	Maroon
	Fe$_x$Ni$_Y$ (1,6)	0.16	0.15	0.00	293	0	12	Green
	Fe$_x$Ni$_Y$ (2,6)	0.15	0.15	0.00	305	0	12	Magenta
	Fe anti-site	0.15	0.15	-0.20	331	0	3	Cyan
	γ_2-Taenite	0.14	0.15	0.00	318	0	7	Blue
	M-type (1)	0.16	0.15	0.01	372	0	2	Olive
	M-type (2)	0.15	0.15	0.00	350	0	1	Pink
	M-type (3)	0.12	0.15	0.04	331	0	2	Purple
	M-type (4)	0.23	0.15	-0.11	314	0	1	Dark Cyan
	M-type (5)	0.20	0.15	-0.25	270	0	1	Orange
	M-type (6)	0.02	0.15	0.13	246	0	1	Light blue
	SPM Fe^{3+} (1)	0.48	0.25	0.65	0	0	7	Grey
	SPM Fe^{2+} (1)	1.29	0.25	2.72	0	0	5	Brown
	MCOL Fe^{2+} (1)	1.23	0.15	0.00	234	190	21	Red
	MCOL Fe^{3+} (1)	0.49	0.15	0.00	476	53	6	Light Orange
	MCOL Fe^{3+} (2)	0.47	0.15	0.00	278	229	5	Light Magenta
	SPM Fe^{3+} (2)	0.49	0.25	1.39	0	0	7	Dark Purple
En-IM-NHD3-700C,30m-Q	Fe$_x$Ni$_Y$ (0,6)	0.16	0.15	0.00	285	0	8	Maroon
	Fe$_x$Ni$_Y$ (1,6)	0.15	0.15	0.00	298	0	12	Green
	Fe$_x$Ni$_Y$ (2,6)	0.15	0.15	0.00	309	0	9	Magenta
	Fe anti-site	0.15	0.15	-0.20	331	0	4	Cyan
	γ_2-Taenite	0.14	0.15	0.00	318	0	7	Blue
	M-type (1)	0.16	0.15	0.01	363	0	2	Olive
	M-type (2)	0.16	0.15	0.00	354	0	1	Pink
	M-type (3)	0.12	0.15	0.04	329	0	3	Purple

	M-type (4)	0.23	0.15	-0.11	316	0	4	Dark Cyan
	M-type (5)	0.20	0.15	-0.25	270	0	2	Orange
	M-type (6)	0.02	0.15	0.13	246	0	2	Light blue
	SPM Fe^{3+} (1)	0.45	0.21	0.62	0	0	8	Grey
	SPM Fe^{2+} (1)	1.30	0.15	2.72	0	0	3	Brown
	MCOL Fe^{2+} (1)	1.26	0.15	0.00	227	186	20	Red
	MCOL Fe^{3+} (2)	0.47	0.15	0.00	453	41	8	Light Magenta
	SPM Fe^{3+} (2)	0.47	0.32	1.33	0	0	8	Dark Purple
En-IM-NHD3-700C,4h	Fe_xNi_Y (0,6)	0.16	0.15	0.00	284	0	10	Maroon
	Fe_xNi_Y (1,6)	0.14	0.15	0.00	301	0	13	Green
	Fe_xNi_Y (2,6)	0.12	0.15	0.00	314	0	7	Magenta
	Fe anti-site	0.15	0.15	-0.20	342	0	2	Cyan
	γ_2-Taenite	0.13	0.15	0.00	326	0	7	Blue
	M-type (1)	0.16	0.15	0.01	362	0	2	Olive
	M-type (2)	0.10	0.15	0.00	351	0	3	Pink
	M-type (3)	0.12	0.15	0.04	334	0	2	Purple
	M-type (4)	0.23	0.15	-0.11	316	0	2	Dark Cyan
	M-type (5)	0.20	0.15	-0.25	270	0	1	Orange
	M-type (6)	0.02	0.15	0.13	241	0	1	Light blue
	SPM Fe^{3+} (1)	0.46	0.21	0.71	0	0	10	Grey
	SPM Fe^{2+} (1)	1.29	0.14	2.78	0	0	4	Brown
	MCOL Fe^{2+} (1)	1.23	0.15	0.00	196	179	23	Red
	MCOL Fe^{3+} (2)	0.49	0.15	0.00	460	33	6	Light Magenta
	SPM Fe^{3+} (2)	0.47	0.18	1.32	0	0	6	Dark Purple
En-IM-NHD3-700C,4h-Q	Fe_xNi_Y (0,6)	0.17	0.15	0.00	285	0	6	Maroon
	Fe_xNi_Y (1,6)	0.15	0.15	0.00	297	0	7	Green
	Fe_xNi_Y (2,6)	0.13	0.15	0.00	312	0	5	Magenta
	Fe anti-site	0.15	0.15	-0.20	318	0	3	Cyan
	γ_2-Taenite	0.11	0.15	0.00	329	0	6	Blue
	M-type (1)	0.16	0.15	0.01	362	0	2	Olive
	M-type (2)	0.11	0.15	0.00	350	0	2	Pink
	M-type (3)	0.12	0.15	0.04	334	0	2	Purple

	M-type (4)	0.23	0.15	-0.11	316	0	3	Dark Cyan
	M-type (5)	0.20	0.15	-0.25	270	0	1	Orange
	M-type (6)	0.02	0.15	0.13	241	0	1	Light blue
	SPM Fe^{3+} (1)	0.45	0.21	0.67	0	0	14	Grey
	SPM Fe^{2+} (1)	1.32	0.13	2.74	0	0	5	Brown
	MCOL Fe^{2+} (1)	1.34	0.15	0.00	244	175	26	Red
	MCOL Fe^{3+} (2)	0.45	0.15	0.00	460	50	9	Light Magenta
	SPM Fe^{3+} (2)	0.46	0.18	1.32	0	0	8	Dark Purple

7.4 Magnetization and Magnetic Susceptibility Measurements

7.4.1 Samples prepared using the sodium borohydride method

The magnetic properties of both nanohybrid and unsupported samples, prepared using the $NaBH_4$ reducing agent, as well as those of the conventional nanohybrid and ^{57}Fe-enriched samples synthesized via the impregnation method, are further characterized by their M vs. H measurements at constant temperature and χg vs. T measurements at constant H. These magnetic measurements reveal the magnetic behavior, which is influenced by the relative compositions, types of nanostructures, and the magnetic interactions and interconnections of the NPs present in the samples.

The isothermal M vs. H loop of the BH-AM1-NHD sample recorded at 300 K, as shown in Figure 7.35, displays clear ferro/ferrimagnetic characteristics with hysteresis (Figure 7.35a), exhibiting a coercivity (Hc) of approximately 430 Oe (see Table 7.22). However, these characteristics are accompanied by constant and non-saturated M values at high external fields. Additionally, the inset of Figure 7.35a shows that the variation of M around H = 0 is not smooth; instead, it appears to consist of two contributions: one with magnetically harder characteristics that contributes to the non-vanishing Hc values in the loops, and another with magnetically softer characteristics that accounts for the fluctuations in M values at H = 0. These results indicate a system of ferro/ferrimagnetic INO NP seeds, as corroborated by XRD and ^{57}Fe Mössbauer measurements, exhibiting a combination of hard and soft magnetic characteristics that may arise from size dispersion and/or variations in the strength of magnetic interparticle interactions [8], [10], [50], [51].

Moreover, the behavior of the system appears to be dominated by larger and/or strongly magnetically interacting NPs, as the presence of coercivity values at room temperature implies the involvement of magnetic NPs that are magnetically blocked at this temperature [8], [9]. In contrast, smaller and/or weakly interacting INO NPs exhibit softer magnetic characteristics, revealing their presence through a slight tendency to achieve non-saturated M values.

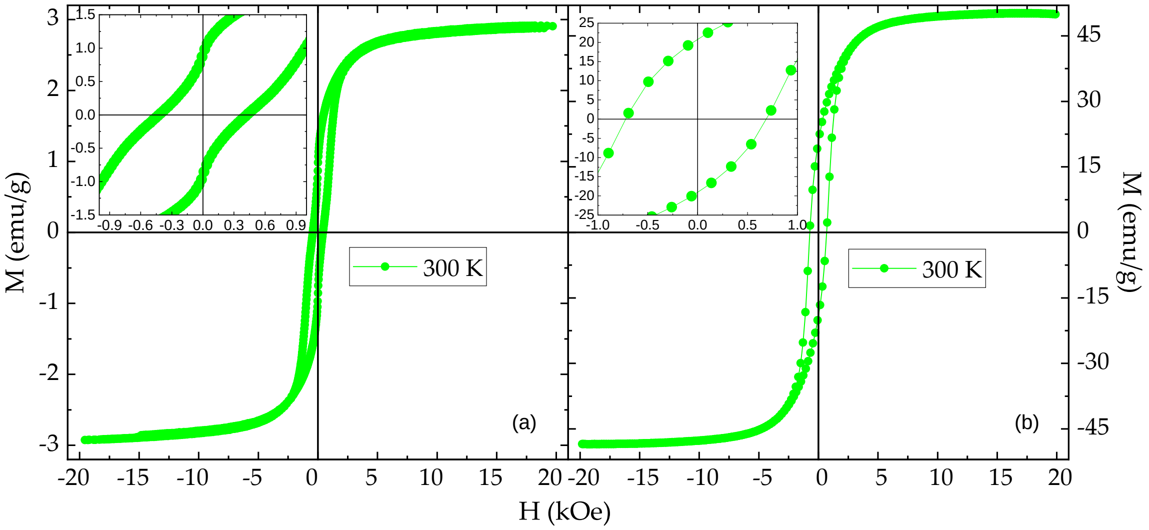

Figure 7.35 Magnetization vs. applied magnetic field isothermal loops of the BH-AM1-NHD (a) and BH- AM1-NP (b) samples measured at RT indicated by green colors. The insets in each set of measurements show the details of the loops' characteristics around zero applied magnetic field for the 300 K loop (upper left).

For the BH-AM1-NP sample, the M vs. H isothermal loop at RT (Figure 7.35b) exhibits magnetic characteristics similar to those of the as-made nanohybrid sample. However, this loop demonstrates greater saturation at high fields and is smoother around H = 0, showing clear symmetric hysteresis, with coercivity values reaching 700 Oe at RT (see Table 7.22). These findings suggest that, on average, the system of ferro/ferrimagnetic INO NP seeds in the unsupported sample comprises magnetic NPs with larger particle sizes that experience stronger magnetic interparticle interactions. The morphology and size of the NPs may lead to the formation of larger Fe-Ni alloy NPs either as stand-alone particles or as larger agglomerates, likely contributing to the increased Hc values [8], [51], [52]. These characteristics reflect a magnetic system in which the close proximity and interconnection of larger NPs shape the overall magnetic behavior.

Table 7.22 Parameters of the magnetic properties derived from the isothermal loops of **Figure 7.35**.

Sample	**T (K)**	**M_{max} (emu/g)**	**M_{min} (emu/g)**	**M_{R+} (emu/g)**	**M_{R-} (emu/g)**	**H_{C+} (Oe)**	**H_{C-} (Oe)**
BH-AM1-NHD	300	2.92	-2.93	0.96	-0.95	434	-414
BH-AM1-NP	300	50.3	-49.7	20.8	-19.6	695	-712

The annealing treatments applied to the nanohybrid and unsupported precursors promote similar developments in the magnetic properties of the corresponding annealed samples. In this context, Figure 7.36 illustrates the characteristic M vs. H loops at constant H for the BH-NHD-300C,96h, BH-NP-300C,96h, BH-NHD-700C,4h, and BH-NP-700C,4h samples.

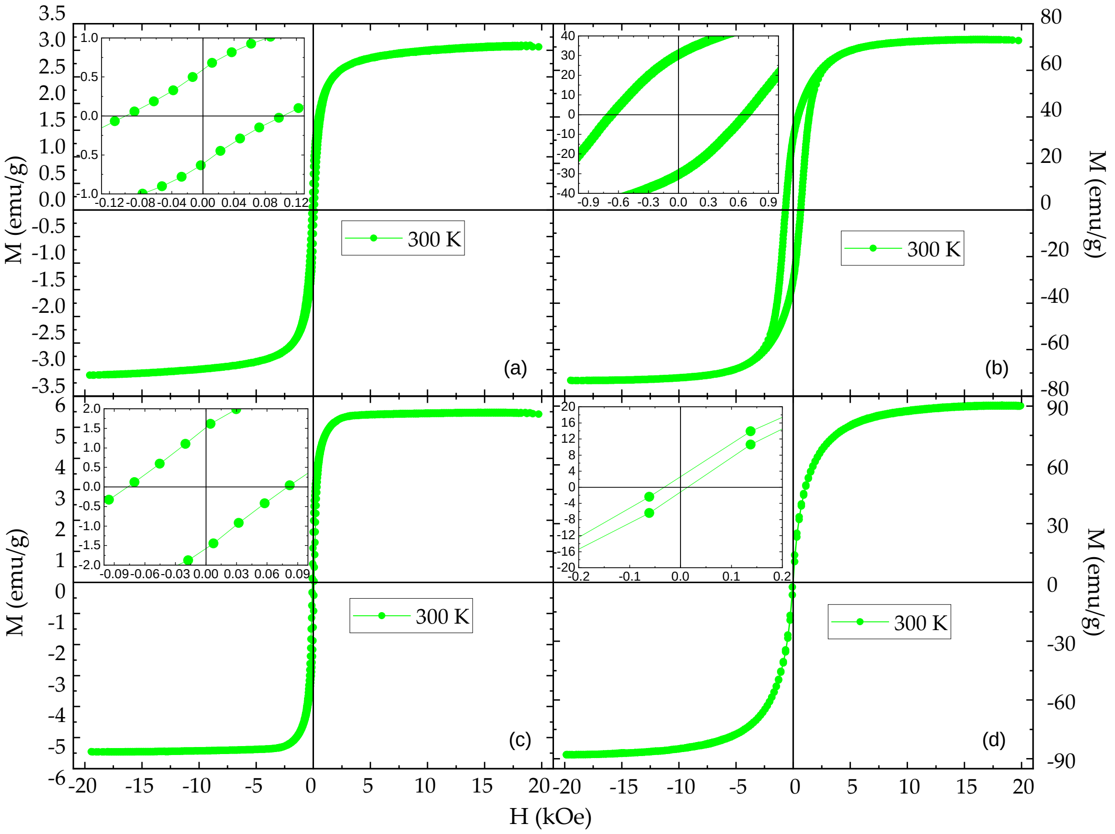

Figure 7.36 Magnetization vs. applied magnetic field isothermal loops of the BH-NHD-300C,96h (a), BH-NP-300C,96h (b), BH-NHD-700C,4h (c) and BH-NP-700C,4h (d) samples measured at RT indicated by green colors. The insets in each set of measurements show the details of the loops' characteristics around zero applied magnetic field for the 300 K loop (upper left).

Specifically, Figure 7.36a displays the isothermal M vs. H loop of the BH-NHD-300C,96h sample recorded at RT. This loop exhibits clear ferro/ferrimagnetic characteristics with hysteresis, accompanied by diminished dM/dH slopes at high H values, which can be attributed to a secondary contribution with SPM characteristics. The Hc values are more symmetric compared to those of the nanohybrid precursor, with positive and negative values acquiring a total of 100 Oe at 300 K (Table 7.23). Furthermore, the magnetization of the annealed nanohybrid sample retains similar M values to those of the nanohybrid precursor, indicating that the annealing procedure at 300°C for 96 hours was insufficient to reduce the parent ferro/ferrimagnetic INO NP seeds on the surfaces of the NDs nanotemplates into metallic Fe-Ni NPs with well-defined ferromagnetic characteristics. These results suggest that the magnetic system of the BH-NHD-300C,96h sample consists of INO NPs arranged on the surfaces of the ND nanotemplates, indicating an increased size distribution for the magnetic NPs. Some NPs may be configured into larger and/or agglomerated NPs on the surfaces of the ND nanoplatforms, contributing to the ferrimagnetic order of the system. In contrast, other NPs remain below the SPM size limit, leading to rapid SPM relaxation characteristics at RT, which accounts for the non-vanishing dM/dH slopes at high H values. These findings align well with the results from XRD and ^{57}Fe Mössbauer spectroscopy measurements.

Conversely, Figure 7.36b shows the M vs. H loop of the BH-NP-300C,96h sample at RT, reflecting an assembly of magnetic NPs exhibiting high saturation M values, which are greater than those of the unsupported precursor. These values are associated with the soft ferromagnetic Fe-Ni nanostructures, which can achieve saturation magnetization values of up to 125 emu/g and coercivities ranging from 35 to 60 Oe at RT [31], [53], [54], [55]. However, these M values are affected by an additional contribution, likely from the INO phase. Moreover, the synthesis method may influence the morphology and size of these NPs, potentially leading to the formation of larger Fe-Ni alloy NPs that experience stronger magnetic interparticle interactions, thereby contributing to the increased Hc values observed [8], [51], [52].

Table 7.23 Parameters of the magnetic properties derived from the isothermal loops of **Figure 7.36**.

Sample	**T (K)**	**M_{max} (emu/g)**	**M_{min} (emu/g)**	**M_{R+} (emu/g)**	**M_{R-} (emu/g)**	**H_{C+} (Oe)**	**H_{C-} (Oe)**
BH-NHD-300C,96h-NHD	300	3.12	-3.13	0.57	-0.61	104	99
BH-NHD-300C,96h-NP	300	73.8	-74.2	30.9	-30.8	686	-677
BH-NHD-700C,4h-NHD	300	5.53	-5.49	1.50	-1.53	81	77
BH-NHD-700C,4h-NP	300	90.9	-89.7	2.54	-1.69	20	-26

Furthermore, thermal treatments of both nanohybrid and unsupported precursors at 700°C for 4 hours result in samples that exhibit magnetic characteristics similar to those of their counterparts annealed at 300°C for 96 hours. Specifically, Figure 7.36c illustrates the M vs. H loop of the BH-NHD-700C,4h sample at RT, reflecting an assembly of ferro/ferrimagnetic NPs that demonstrate higher saturation M values compared to the BH-NHD-300C,96h sample. This sample exhibits also greater saturation at high fields, with coercivity reaching 100 Oe (Table 7.23). These results indicate that the higher annealing temperature facilitates the partial formation of Fe-Ni nanostructures, along with the presence of the IOB (Fe_3BO_5) paramagnetic phase, as indicated by confirmed by XRD and ^{57}Fe Mössbauer spectroscopy investigations. Due to sintering, these NPs achieve sizes that exceed the SPM size limit, resulting in slower SPM relaxation phenomena compared to the assembly of phases present in the BH-NHD-300C,96h sample.

The M vs. H loop of the BH-NP-700C,4h sample at RT shows clear soft FM characteristics with no hysteresis. The coercivity values are decreased relative to those of the BH-NP-300C,96h sample, reaching only 20 Oe at RT (Table 7.23). These findings suggest that the magnetic behavior of this system is predominantly influenced by the soft ferromagnetic Fe-Ni nanostructures, as confirmed by XRD and ^{57}Fe Mössbauer spectroscopy investigations.

7.4.2 Samples prepared using the impregnation method

The magnetic properties of the conventional, non-enriched, as-made nanohybrid precursor samples prepared using the IM method are characterized by their M vs. H measurements under constant temperature, as shown in Figure 7.37. The isothermal loops of both conventional precursors recorded at RT exhibit linear SPM characteristics. The M values at high fields, along with all other magnetic properties of the loops for all as-made samples, are summarized in Table 7.24. Specifically, the isothermal loops of the IM-AM-NHD and IM-AM2-NHD samples recorded at RT (Figures 7.37a and b) display distinctly linear SPM behaviors throughout all H values. The absence of coercivity suggests that the majority of the INO NP seeds in the precursor samples are subject to very rapid SPM relaxation phenomena.

Moreover, the M vs. H loop of the IM-AM2-NHD sample shows a weak diamagnetic contribution around H=0, attributed to the ND nanotemplates, as detailed in the inset of Figure 7.37b. In the case of the IM-AM-NHD sample, a ferro/ferrimagnetic sigmoidal-type curve develops with non-saturated M values and non-vanishing, asymmetric coercive fields at 2 K, superimposed on a strong linear SPM contribution, indicated by the lack of saturation at high H values. The high positive dM/dH slopes at high fields and the emergence of coercive fields at low temperatures suggest a magnetic NP assembly experiencing strong SPM relaxation at high temperatures while being partially magnetically blocked at low temperatures [56], [57].

The χ_g vs. T ZFC branch for the IM-AM-NHD sample, measured with H_{ap} of 99 Oe, is shown in Figure 7.38a. This branch starts to decline from an initial χ_g maximum at 2 K and exhibits a small plateau at approximately 50 K, followed by a decrease with two more local maxima appearing at ~ 175 and 225 K, indicating a set of blocking temperatures (T_B) for different parts of the NP assembly according to their sizes. The FC branch follows a similar trend, showing a more smother increase in χ_g with decreasing temperature. Increasing H to 999 Oe (Figure 7.38b) causes the ZFC and FC χ_g vs. T branches to virtually coincide from 400 down to ~ 150 K, exhibiting an asymptotic increase of χ_g with decreasing temperature at low temperatures, with no signs of saturation or local maxima—only a hump at approximately 50 K. This observation reveals that the strong SPM contribution dominates in this sample. These characteristics provide evidence for the presence of an assembly of small SPM INO NPs with a variety of interparticle interactions (from weak to negligible), attributed to their partial clustering as well as spatial isolation on the surfaces of the ND nanotemplates, as indicated by TEM measurements [56], [58], [59], [60].

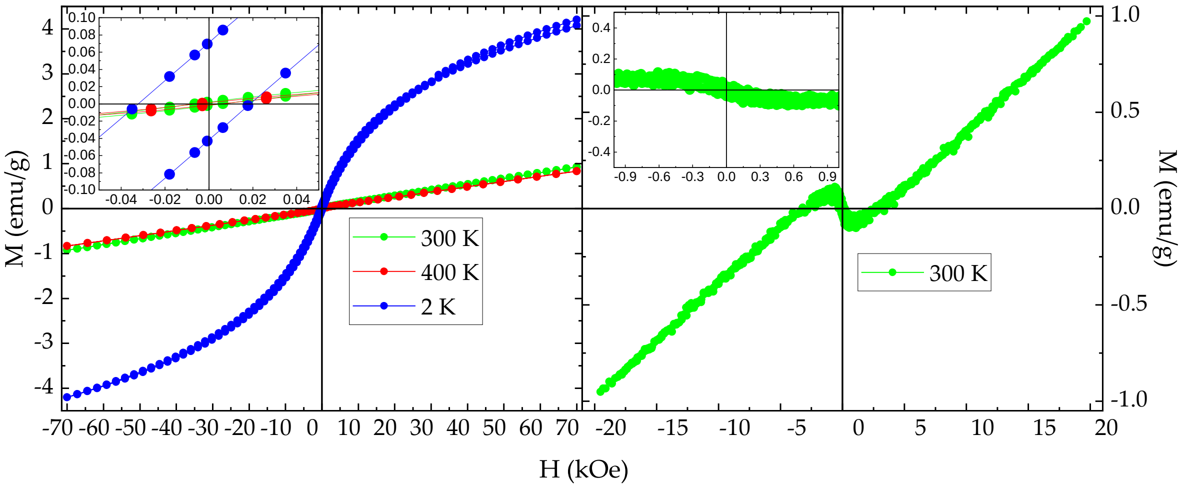

Figure 7.37 Magnetization vs. applied magnetic field isothermal loops of the IM-AM-NHD (a) and IM-AM2-NHD (b) precursor samples measured at different temperatures indicated by different colors. The insets in each set of measurements show the details of the loops' characteristics around zero applied magnetic field for all temperatures (upper left).

Table 7.24 Parameters of the magnetic properties derived from the isothermal loops of **Figure 7.37**.

Sample	**T (K)**	**M_{max} (emu/g)**	**M_{min} (emu/g)**	**M_{R+} (emu/g)**	**M_{R-} (emu/g)**	**H_{C+} (Oe)**	**H_{C-} (Oe)**
IM-AM1-NHD	400	0.82	-0.87	0	0	0	0
	300	0.93	-0.96	0	0	0	0
	2	4.11	-4.17	0.07	-0.05	20	-33
IM-AM2-NHD	300	0.98	-0.96	0	0	0	0

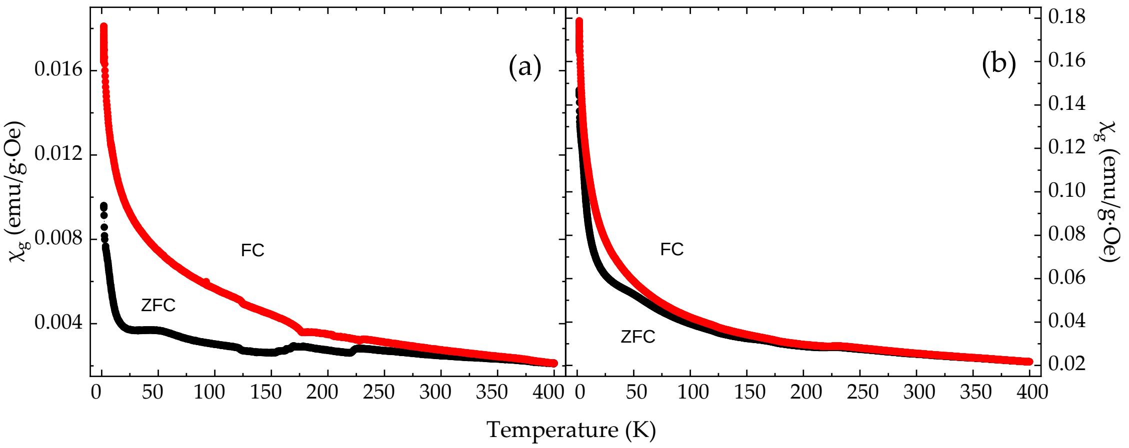

Figure 7.38 Magnetic susceptibility vs. temperature measurements of the conventional non-enriched IM-AM-NHD precursor sample under an applied field of 99 Oe (a) and under an applied field of 999 Oe.

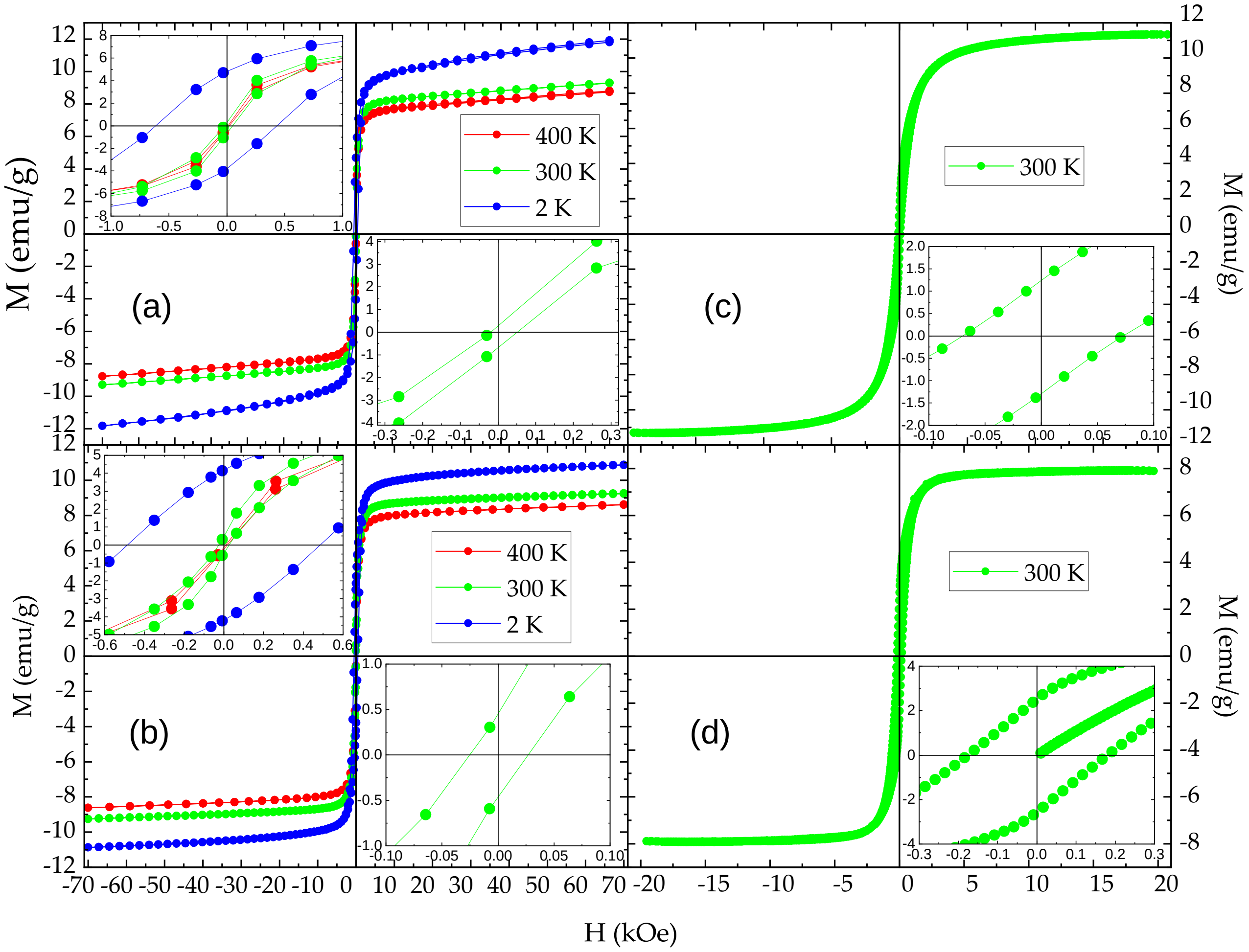

Figure 7.39 Magnetization vs. applied magnetic field isothermal loops of the IM-NHD-700C,30m (a), IM-NHD-700C,4h (b), IM-NHD2-700C,30m (c) and IM-NHD2-700C,4h (d) samples measured at different temperatures indicated by different colors. The insets in each set of measurements show the details of the loops' characteristics around zero applied magnetic field for all temperatures (upper left) and with even more detail for the 300 K loop (lower right).

Treating thermally the precursors synthesized using the IM method at 700°C for different time durations causes evolution of magnetic properties of the nanohybrid samples to arise. To this regard, the M vs. H isothermal loops of IM-NHD-700C,30m and IM-NHD-700C,4h samples recorded at 400, 300 and 2 K (Figure 7.39a and c, respectively) reveal clear FM characteristics with hysteresis, exhibiting coercivities that range from about 10 to about 600 Oe depending on temperature (see Table 7.25). These characteristics are accompanied, however, by constant and non-vanishing dM/dH slopes at high H values at all temperatures. These slopes denote a SPM contribution that can be attributed to the spinel-type INO NPs found to be present in these annealed samples, which, due to their very small particle size, experience very fast SPM relaxation at all temperatures. Similarly, the M vs. H loops of the IM-NHD2-700C,30m and IM-NHD2-700C,4h samples recorded at RT (Figure 7.39b and d, respectively) exhibit resembling magnetic characteristics to former samples, presenting however higher Hc values. This may be owed to the presence of greater amounts of the INO phase in their concentrations, as indicated by their respective MS at RT (see Figures 7.27 and 7.28, respectively). Typical soft FM Fe-Ni alloys present M_S values that reach 125 emu/g and coercivities of about 35 to 60 Oe at RT [31], [53], [54], [55]. It is evident that the maximum M values found in our samples are in the range of 10% of the M_S values of the soft FM Fe-Ni alloys, and this can be justified by the fact that we have scheduled a 10 wt.% of Fe, Ni metals loading in our synthesis. Furthermore, the large increase in the coercive fields from 300 K to 2 K, in case of the IM-NHD-700C,30m and IM-NHD-700C,4h samples, indicates that the assembly of Fe–Ni FM NPs should also experience SPM relaxation, which gradually changes its characteristic relaxation time as T decreases [8], [61].

Table 7.25 Magnetic characteristics derived from the isothermal loops of **Figure 7.39.**

Sample	**T (K)**	**M_{max+} (emu/g)**	**M_{max-} (emu/g)**	**M_{R+} (emu/g)**	**M_{R-} (emu/g)**	**H_{C+} (Oe)**	**H_{C-} (Oe)**
IM-NHD-700,30m	400	8.8	-8.8	-0.1	-0.2	21	10
	300	9.3	-9.3	0.3	-0.6	50	-21
	2	11.9	-11.8	4.8	-3.8	433	-611
IM-NHD2-700C,30m	300	11.5	-11.4	1.2	-1.3	74	-71
IM-NHD-700,4h	400	8.6	-8.6	-0.1	-0.2	18	9
	300	9.2	-9.2	0.4	-0.5	27	-25
	2	10.9	-10.9	4.1	-4.2	487	-488
IM-NHD2-700C,4h	300	7.9	-8.0	2.5	-2.6	173	-175

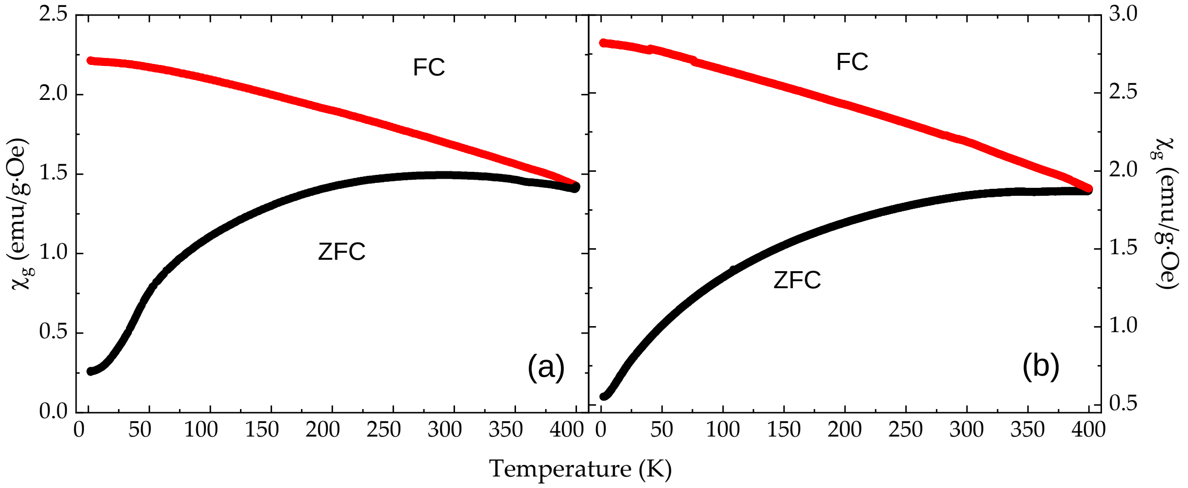

Figure 7.40 Magnetic susceptibility vs. temperature measurements of the IM-NHD-700C,30m (a) and IM-NHD-700C,4h (b) samples under an applied field of 99 Oe.

The χ_g vs. T measurements of both samples, recorded under an applied field of 99 Oe, are shown in Figure 7.40 and reflect the SPM relaxation features of the FM NPs. In both diagrams, the χ_g values of the ZFC branches monotonically increase as T increases, with no local maxima up to 400 K, while the FC branches are much smoother and continuously rise as T decreases. The two branches coincide only at the highest measured temperature point at 400 K for both samples suggesting a relative broad size distribution for the magnetically ordered nanophases involved in these samples. These results reflect a system, whose magnetic behavior is clearly influenced by the larger in size and/or more strongly magnetically interacting metallic Fe-Ni NPs, which are magnetically blocked even at 400 K, as delineated by the presence of small hysteresis in the M vs. H loops [8]. Similar behaviors are obtained in the χ_g vs. T measurements of both annealed samples recorded under an applied field of 999 Oe (Figure 7.41). There, however, the ZFC branches sample display a minor local maximum around 167 K and 147 K for the IM-NHD-700C,30m and IM-NHD-700C,4h samples, respectively, suggesting a slight diversification in the SPM relaxation behavior for different assemblies of magnetic NPs originating from the differences in NPs size distribution, which can be revealed by the higher H values in these measurements [61]. Moreover, the differences in the Fe–Ni and INO NP content in each sample could also justify the slightly higher maximum χ_g values observed for the IM-NHD-700C,4h sample relative to those found for the IM-NHD-700C,30m sample. As the nominal M values are higher for the Fe–Ni phase relative to those of the INO phase [62], the higher amount of INO NPs evident by the ^{57}Fe Mössbauer spectroscopy measurements for the IM-NHD-700C,30m sample, should contribute to its reduced χ_g values relative to those found for the IM-NHD-700C,4h sample at relative low fields (up to 1 kOe). On the other hand, as the SPM contribution to the total M values for the INO phase is higher in high fields (> 10 kOe), the characteristics of the M vs. H isothermal loops are influenced significantly by this contribution at these fields region, as evident by the higher dM/dH slope and maximum M values recorded for the IM-NHD-700C,30m sample in comparison to the IM-NHD-700C,4h sample (Figure 7.39, Table 7.25).

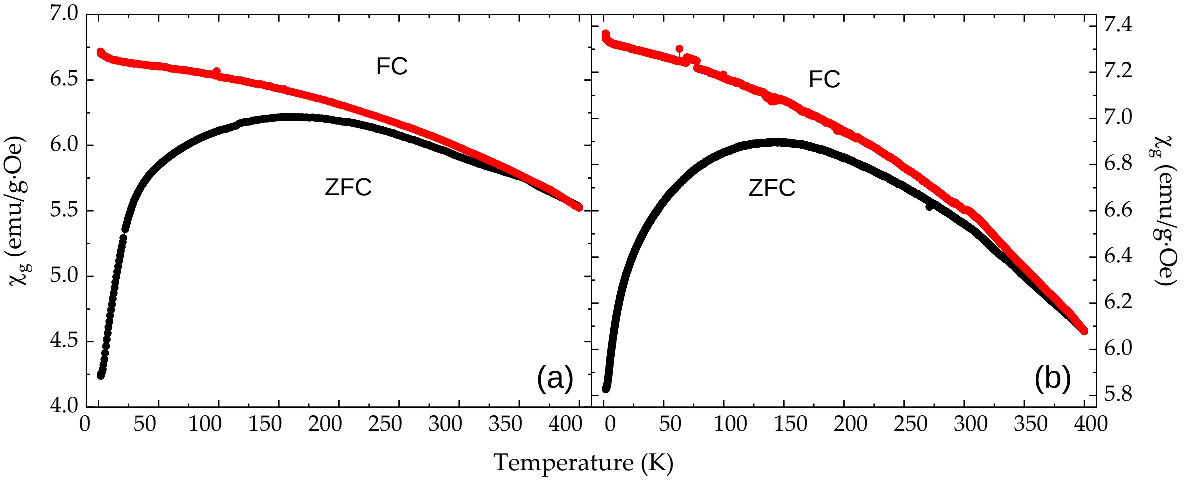

Figure 7.41 Magnetic susceptibility vs. temperature measurements of the IM-NHD-700C,30m (a) and IM-NHD-700C,4h (b) samples under an applied field of 999 Oe.

The RT M vs. H loops of the conventional as-made precursors subjected to a two-step annealing procedure, specifically the IM-NHD2-(700C,30m-to-300C,64h) and IM-NHD2-(700C,4h-to-300C,96h) samples, are depicted in Figure 7.42. In both samples, the M vs. H loops recorded at RT exhibit clear FM characteristics, attributed to the formation of soft FM Fe-Ni nanostructures, accompanied however by slight hysteresis. This hysteresis is more pronounced in the IM-NHD2-(700C,30m-to-300C,64h) sample, which presents coercivities of 180 Oe and 50 Oe at RT for each sample, respectively (Table 7.26).

As previously noted, these high coercivity values can be attributed to contributions from retained spinel-type INO nanostructures that are present in the annealed samples, whose magnetic properties can exhibit saturation M values reaching 15 emu/g and coercivities of approximately 700 Oe at RT [53], depending on their size and morphology. This contribution is evident in the M vs. H loops of the annealed samples, as indicated by the diminished, yet still observable, dM/dH slopes at high fields.

Nonetheless, the dominant contribution to the magnetic behavior of these two-step annealed systems arises from the Fe-Ni nanostructures developed in each hybrid sample during the initial annealing step of the synthesis. This is corroborated by XRD and ^{57}Fe Mössbauer studies. The lower M values and higher coercivities observed in both two-step annealing magnetic systems indicate a greater contribution from the INO phase in these samples compared to the INO phase content affecting the magnetic properties of samples subjected to a single annealing step.

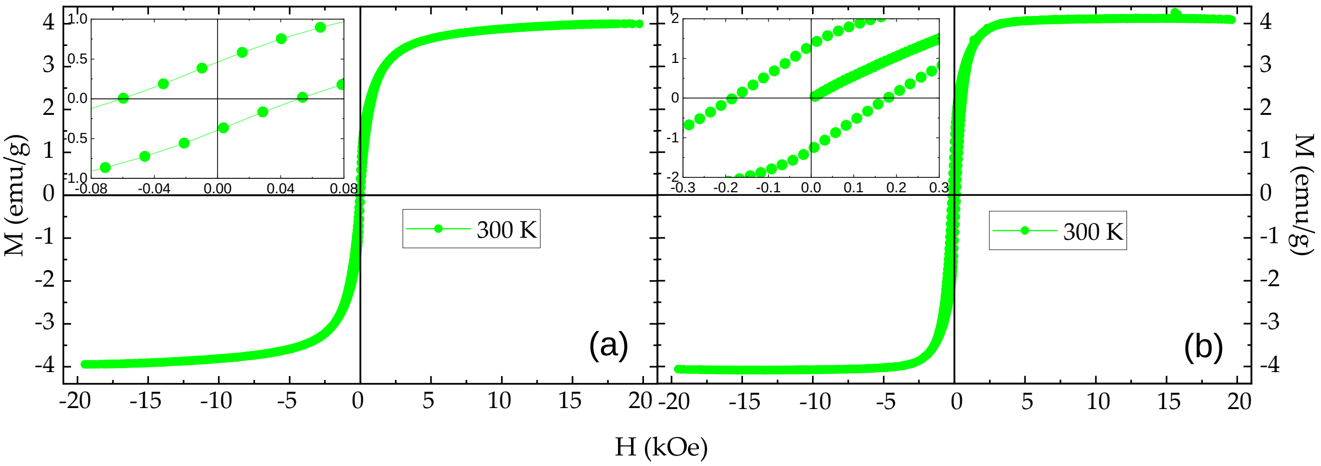

Figure 7.42 Magnetization vs. applied magnetic field isothermal loops of the IM-NHD2-(700C,30m-to-300C,64h) (a) and IM-NHD2-(700C,4h-to-300C,96h) (b) samples measured at room temperature, as indicated by the green color. The insets in each set of measurements show the details of the loops' characteristics around zero applied magnetic field with even more detail for the 300 K loop (upper left).

Table 7.26 Parameters of the magnetic properties derived from the isothermal loops of **Figure 7.42**.

Sample	**T (K)**	**M_{max} (emu/g)**	**M_{min} (emu/g)**	**M_{R+} (emu/g)**	**M_{R-} (emu/g)**	**H_{C+} (Oe)**	**H_{C-} (Oe)**
IM-NHD2-(700C,30m-to-300C,64h)	300	4.0	-3.9	0.46	-0.43	53	-57
IM-NHD2-(700C,4h-to-300C,96h)	300	4.1	-4.1	1.3	-1.3	177	-182

Figure 7.43 illustrates the M vs. H isothermal loop for the En-IM-AM3-NHD sample recorded at RT. The magnetic behavior of this enriched as-made precursor sample exhibits characteristics similar to those of the conventional as-made precursor samples (see Figure 7.37). Notably, it displays a distinct linear SPM behavior across all applied magnetic field values, indicating that the majority of the magnetic INO NP seeds in the enriched precursor sample are influenced by fast SPM relaxation phenomena (Table 7.27). The presence of coercive fields around H = 0 can be attributed to standard deviations influenced by the moment of the gelatin holder encapsulating the magnetic material.

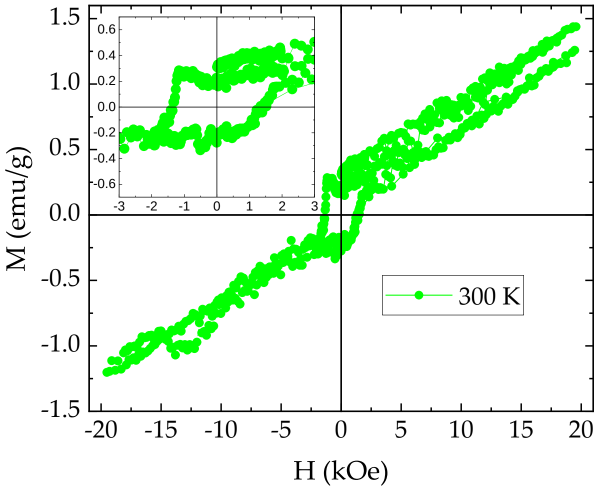

Figure 7.43 Magnetization vs. applied magnetic field isothermal loops of the En-IM-AM3-NHD sample measured at room temperature, as indicated by the green color. The inset shows the details of the loops' characteristics around zero applied magnetic field with even more detail for the 300 K loop (upper left).

Moreover, the characteristic M vs. H and χ_g vs. T measurements obtained for all enriched samples annealed at various temperatures and durations exhibit magnetic features akin to those described for the previously mentioned conventional annealed samples. These features include assemblies of large or strongly magnetically interacting FM Fe-Ni NPs, which demonstrate magnetic blocking even at 400 K, particularly in the En-IM-NHD-700C,30m and En-IM-NHD-700C,30m-Q samples (Figure 7.44a and b). This behavior predominantly influences the magnetic properties of each annealed enriched sample.

Conversely, the smaller or more weakly interacting metallic Fe-Ni NPs, along with the SPM INO NPs, primarily contribute to the M vs. H and χ_g vs. T measurements by exhibiting a lack of saturation in magnetization at high H values, recorded across all temperatures. Additionally, they show the presence of high coercive fields, reaching values similar to those typical of the INO phase. The characteristic M vs. H and χ_g vs. T measurements for the En-IM-NHD-700C,30m and En-IM-NHD-700C,30m-Q samples with applied fields of 99 Oe and 999 Oe, respectively, are presented in Figures 7.45-46. The resulting parameters of the magnetic properties derived from the respective isothermal loops of all samples at 300 K and 2 K are summarized in Table 7.27.

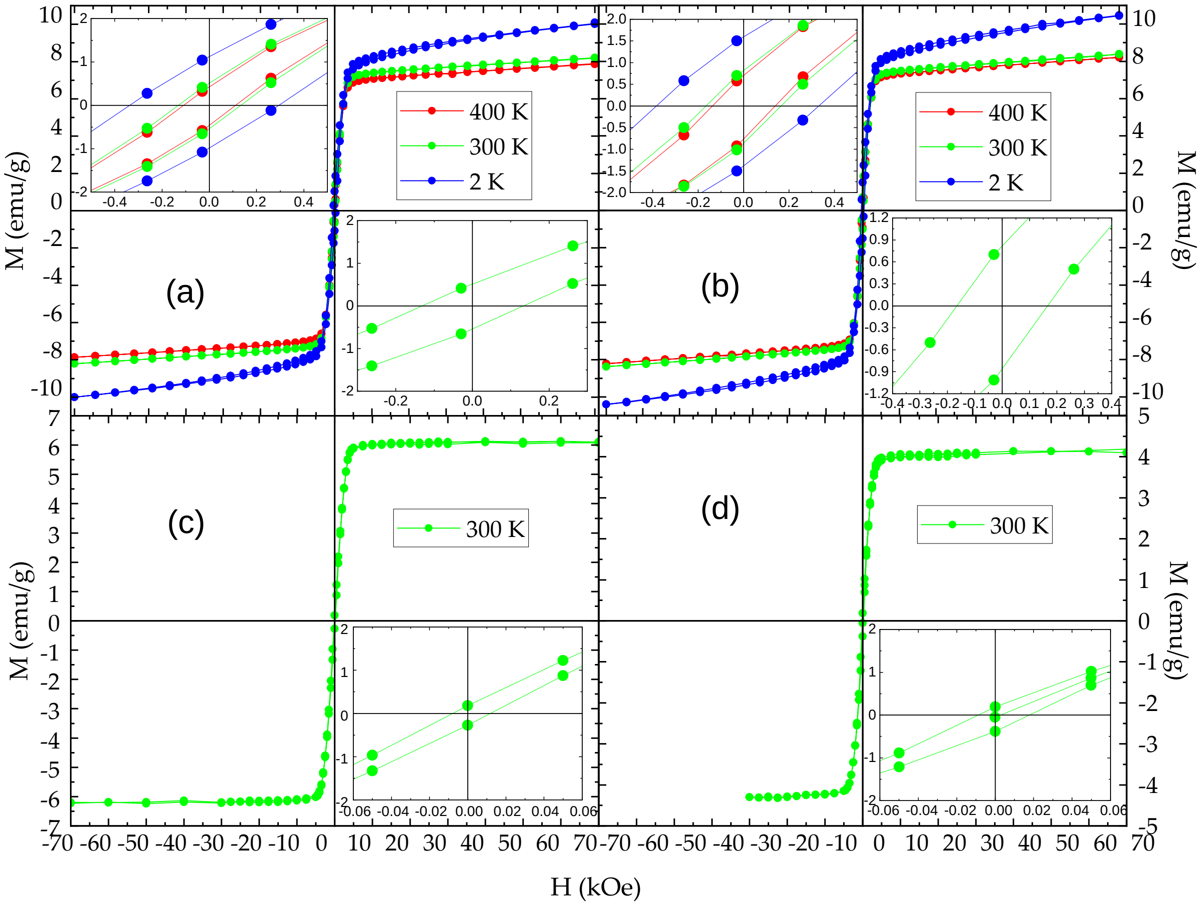

Figure 7.44 Magnetization vs. applied magnetic field isothermal loops of the En-IM-NHD3-700C,30m (a), En-IM-NHD3-700C,30m-Q (b), En-IM-NHD3-700C,4h (c) and En-IM-NHD3-700C,4h-Q (d) samples measured at different temperatures indicated by different colors. The insets in each set of measurements show the details of the loops' characteristics around zero applied magnetic field for all temperatures (upper left) and with even more detail for the 300 K loop (lower right).

Table 7.27 Magnetic characteristics derived from the isothermal loops of **Figure 7.43-44.**

Sample	**T (K)**	**M_{max+} (emu/g)**	**M_{max-} (emu/g)**	**M_{R+} (emu/g)**	**M_{R-} (emu/g)**	**H_{C+} (Oe)**	**H_{C-} (Oe)**
En-IM-AM3-NHD	300	1.3	-1.2	0	0	0	0
En-IM-NHD3-700,30m	400	7.8	-7.9	0.48	-0.51	110	-103
	300	8.1	-8.2	0.51	-0.56	134	-129
	2	10	-10.1	1.14	-1.08	298	-317
En-IM-NHD3-700,30m-Q	400	8.1	-8.2	0.65	-0.72	131	-132
	300	8.4	-8.5	0.78	-0.86	161	-168
	2	10.5	-10.5	1.6	-1.4	338	-361
En-IM-NHD3-700,4h	300	6.1	-6.2	0.02	-0.01	11	-9
En-IM-NHD3-700,4h-Q	300	4.1	-4.2	0.03	-0.03	18	-13

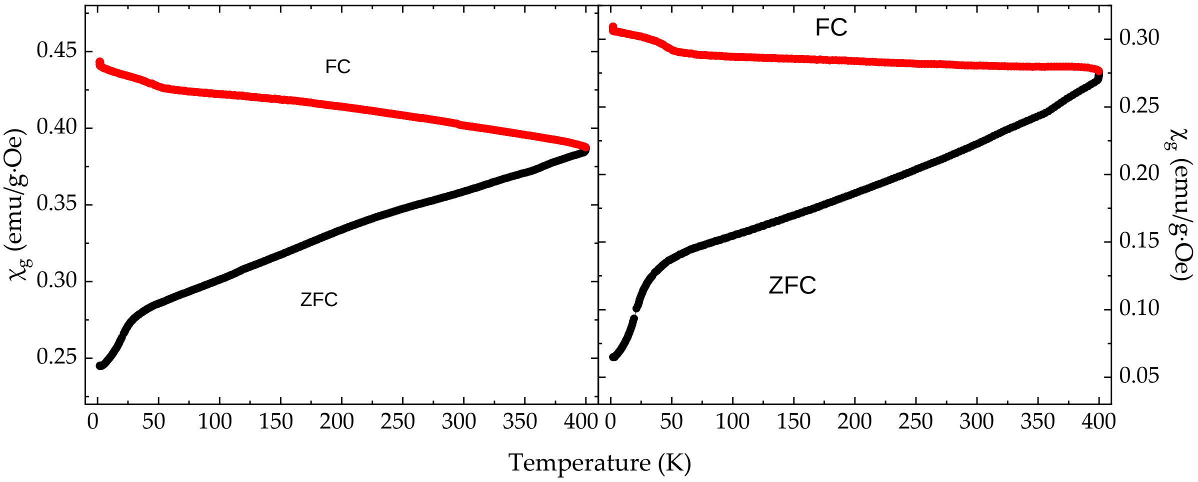

Figure 7.45 Magnetic susceptibility vs. temperature measurements of the En-IM-NHD3-700C,30m (a) and En-IM-NHD3-700C,30m-Q (b) samples under an applied field of 99 Oe.

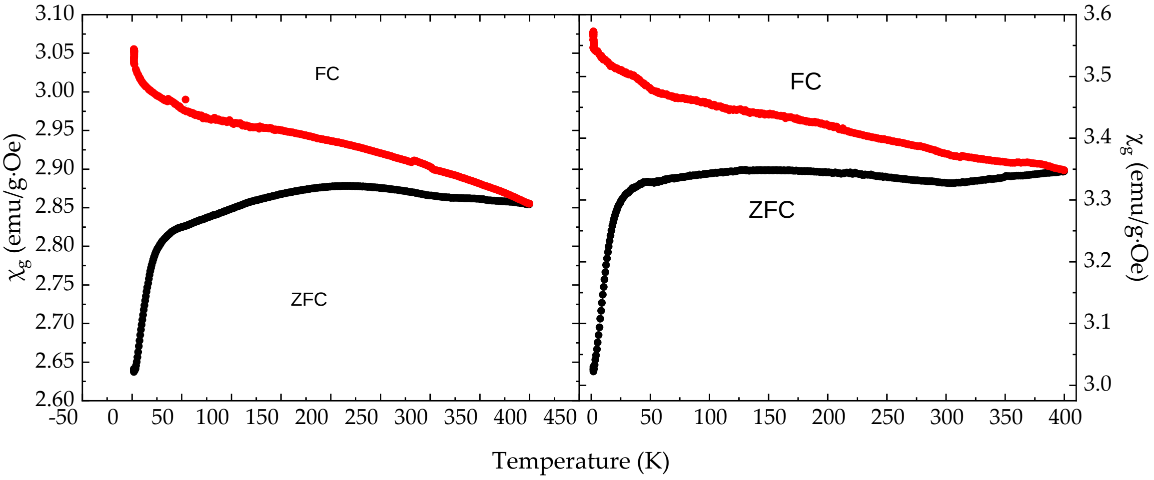

Figure 7.46 Magnetic susceptibility vs. temperature measurements of the En-IM-NHD3-700C,30m (a) and En-IM-NHD3-700C,30m-Q (b) samples under an applied field of 999 Oe.

7.5 Discussion

The results from the various experimental techniques employed in this study reveal a comprehensive understanding of the interconnections between the developed phases in both precursor and annealed samples, alongside their properties. Analysis of the as-made nanohybrid and unsupported samples, synthesized using $NaBH_4$ as a reducing agent during the initial synthesis step, indicated the presence of SPM fcc Fe-Ni alloy and INO NP seeds formed on the surfaces of NDs nanotemplates and as stand-alone NPs, respectively. These characteristics influenced significantly the properties of the final annealed samples.

Specifically, the annealed samples were primarily affected by residual INO or IOB NPs, resulting from incomplete oxide-to-metal reduction reactions during high-temperature annealing. Additionally, the pre-existed Fe-Ni NPs, which present retained morphological characteristics as a result of using the $NaBH_4$ agent in the initial synthesis step, contributed to the final properties of the annealed samples by exhibiting stoichiometric distributions in the annealed samples, as confirmed by XRD and ^{57}Fe Mössbauer spectroscopy.

According to the Fe-Ni phase diagram, these stoichiometric distributions resulted in the formation of polycrystalline magnetic materials. However, this introduced unwanted properties, diverging from the initial goal of producing pure magnetic nanostructures with distinct magnetic characteristics. As a result, the focus of our work shifted toward implementing the impregnation synthesis procedure to achieve the desired outcomes.

In this revised context, the significant role of ND NPs in the conventional and enriched precursor samples is crucial to understanding the properties observed in the final annealed samples. These hybrid nanomaterials consist of fine SPM INO NPs formed on the ND nanotemplate surfaces. The structure and morphology of the ND NPs, which are generated through detonation reactions, are critical for both the initial growth and anchoring of INO seeds during the impregnation step and the subsequent development of Fe-Ni NPs in the final synthesis phase.

It is known that the initial process drives specific mechanisms observed in similar systems of NDs substrates [46], [34], which involve blending and interaction among these nanostructures. In particular, the native presence of carboxyl/hydroxyl functional groups on the NDs NPs surfaces in the moist mixture at the initial impregnation process, facilitates strong attractive interactions with the dissolved metallic salts, due to the hygroscopic nature of the salts and the hydrophilic functional groups on the NDs [63]. These interactions lead to the formation of strong coupling between the Fe^{3+} and Ni^{2+} ions and the functional groups, resulting in their firm attachment on the NDs' surfaces, by the formation of (i) iron-oxide-carbon and nickel-oxide-carbon and (ii) direct iron-carbon and nickel-carbon bonds [64], [65], [66].

Furthermore, the thermal treatment of the precursor samples in vacuum-evacuated quartz ampoules at high temperatures triggers the involvement of strong reducing agents in this second step of the synthesis of the final NHD samples in each system. These agents are the sp^2-coupled carbon atoms existing already as native species at the surfaces of the NDs NPs, and are further developed during thermal annealing in close proximity to the growing metallic nanoparticles [64], [67], [68], [69]. These sp^2-hybridized carbon atoms, along with the low O_2 pressure due to the vacuum existing inside the ampules (10^{-3} Torr), provide the appropriate conditions for the full reduction of the AM-NHDs' and En-AM-NHDs' Fe^{3+} and Ni^{2+} ions in the INO NPs to the Fe^0 and Ni^0 atoms that form the Fe-Ni alloy NPs. Moreover, TEM observations, in case of the annealed samples originating from the conventional precursor, verified that the native sp^2 carbon atoms are assembled into graphitic-type layered nanostructures that are encapsulating the metallic NPs partially or in total. Their supply and further development are proposed to emerge from the ND sp^3 cores, as the later undergo a surface graphitization procedure at elevated temperatures, of 700 °C and above. This process is known to be further enhanced by the presence of defects, such as carbon atom vacancies and dislocations, as well as by the presence of metallic elements like iron, cobalt, and nickel on the surfaces of the NDs NPs, that can act as catalysts, and therefore can facilitate the rearrangement of carbon atoms into graphitic-type structures [35], [64], [70]. Thus, carbon atoms initially participate in the formation and further development of the Fe-Ni NPs through their reduction capacity, while in sequence the Fe-Ni NPs can mutually serve as nucleation centers for the initiation and further construction of graphitic-type layers on their surfaces, as evidenced by HRTEM. Moreover, the graphitization process of these layers leads to low binding energies for the sp^2-type carbon atoms, inducing their further lateral diffusion within the structure of the Fe–Ni NPs. Therefore, high temperatures combined with the NDs' morphology appear not only to promote the formation of Fe-Ni NPs, but also to favor a partial lateral diffusion of carbon atoms in the regions across the interfaces between the metallic NPs and NDs NPs, where the source of carbon atom is originating. We propose that this diffusion mechanism is responsible for the development of the minor tetragonally distorted martensitic-type Fe-Ni phase that has non-extensive characteristics, in the sense that its appearance in the Fe-Ni NPs is related to the presence of the adjacent ND NPs. We support this proposal to the evidences provided by ^{57}Fe Mössbauer spectroscopy, which is an atomic-level probe technique, while XRD, TEM and magnetization measurements, being more collective and due to the high similarity of the fcc and martensitic-type Fe-Ni crystal structures provide their average characteristics, which cannot distinguish clearly these two phases.

Similar characteristics are found from the ^{57}Fe Mössbauer spectroscopy investigations for the annealed samples derived from the ^{57}Fe-enriched precursor sample; however, a slightly higher average nickel concentration for Fe–Ni NPs from TEM/EDS measurements is observed for the ^{57}Fe-enriched case. These NPs also appear larger, having a wider dispersion from the equivalent Fe–Ni NPs of the non-enriched annealed samples, while no graphitic-type nanostructures are observed at the interfaces between the metallic NPs and the ND nanotemplates, a notable difference from the IM-NHD-700C,4h sample. These morphological characteristics may be attributed to the extended sonication time of 60 minutes for the enriched annealed sample, compared to the 30-40 minutes applied for the conventional annealed sample. As mentioned before, the longer sonication duration may has removed the more confined nanostructured species formed within the enriched hybrid material, such as smaller metallic Fe-Ni NPs and/or localized graphitic-type structures that typically envelop metallic NPs at the interfaces where they directly contact the ND NPs. We suggest that the En-IM-NHD3-700C,30m-Q sample exhibits resembling morphological and structural properties like those observed in the annealed conventional IM-NHD-700C,4h sample, prior to TEM observations as indicated by XRD and ^{57}Fe Mössbauer spectroscopy investigations, however, as a result of the extended sonication duration applied for the enriched annealed sample, only the larger or more agglomerated metallic NPs conserved on the surfaces of the ND nanotemplates, which in several cases do not display any metallic NPs on their surfaces.

Moreover, based on the ^{57}Fe Mössbauer spectroscopy investigations we consider the idea that the structural differences can be attributed primarily to the slight modification of the first wet chemistry step procedure followed for the two precursors. The addition of the small amount of metallic ^{57}Fe in an HNO_3 solution during the preparation of the ^{57}Fe-enriched precursor may influence the way the resulting iron ions disperse in the moist mixture during the first step of the synthesis, by prompting aggregation of the $Fe^{3+}/^{57}Fe^{3+}$ ion assemblies, which could possibly lead to their distinctive characteristics. The ^{57}Fe MS of the two precursors indicate some difference regarding the presence of magnetically split contributions for the ^{57}Fe-enriched precursor, which are not observed for the conventional precursor. This difference seems to be passed along partially to the final annealed samples and is reflected through the slight increase in the average Fe–Ni NP size/dispersion and amount of INO AA values in their MS, which include also Fe^{2+} SPM states.

Another issue that needs further clarification refers to the fcc Fe-Ni phases present in the NHD annealed samples. The results indicate that two closely related phases regarding their structural and magnetic properties, namely γ' $Fe_{1+z}Ni_{3-z}$ and γ_2-Taenite are developed, that can be distinguished only by ^{57}Fe Mössbauer spectroscopy. TEM observations and EDS measurements suggest that both iron-alloy based phases are rich in the second alloying element (Ni), without however distinguishing between the two phases. On the other hand, the presence of the residual SPM INO phase with a $NiFe_2O_4$ stoichiometry in both annealed samples, declares that a portion of the total iron contained in the system appears as Fe^{3+} ions in this Ni poor INO phase. This could justify the average Ni rich stoichiometry of the Fe-Ni alloy system ($Fe_{0.34}Ni_{0.66}$) relative to the nominal equiatomic stoichiometry considered in the synthesis, by accepting that the amount of iron missing in the alloy phase is located in the oxide phase.

Furthermore, no significant difference could be deducted from the employment of the quenching procedure in the magnetic properties between either the ^{57}Fe-enriched En-IM NHD3-700,30m and En-IM-NHD3-700,30m-Q, as well as the En-IM NHD3-700,4h and En-IM NHD3-700,4h-Q samples or the conventional IM-NHD-700,30m and IM-NHD-700,4h samples, apart from the already mentioned increased presence of the INO phase in the MS of the enriched samples relative to the conventional IM-NHD-700,4h sample. Therefore, we have to conclude that there is no significant and straightforward interconnection between the quenching procedure and the crystal order of the Fe–Ni metallic phase, at least between the chosen specific annealing conditions (700 °C, 30 min or 4 hours).

Consequently, the combination of these steps, as well as the internal mechanisms that are accompanying them, leads to the synthesis of a unique hybrid metallic compound conventional system. However, as we mentioned earlier, similar characteristics have been found in the study of the Fe-Co/NDs system, leading to a formation of a recurring morphological pattern for these two systems. One could easily relate the repetitiveness of these characteristics to the step-by-step impregnation routine synthesis that both systems share. Therefore, it would be expected to see the formation of metallic NPs on the surfaces of ND NPs, as well as the formation of graphitic-type layered nanostructures at the interface between the metallic and ND NPs, as this is directly related to the graphitization process of native sp^2-type carbon atoms existing on the surfaces of ND NPs at high temperatures. This process is favored by the presence of similar metallic elements, like Fe, Co and Ni, that are known to catalyze this process and are used in the two systems [35], [64].In contrast, the Fe-Rh/NDs system deviates from this trend, as it does not exhibit morphological characteristics analogous to those found in the Fe-Co/NDs and Fe-Ni/NDs systems. Specifically, the formation of graphitic-layered nanostructures at the interface between Fe-Rh nanoparticles and ND surfaces is absent. This divergence can be attributed to the influence of Rh in the iron-based alloy during synthesis.

Rhodium, a noble metal, differs significantly from Fe, Co, and Ni, as it is generally not recognized for catalytic activity in graphitization [71]. Instead, Rh is considered less reactive in carbon-carbon bonding processes compared to transition metals [71], [72], [73], [74]. During thermal treatment, the interaction between Fe and Rh in Fe-Rh nanoparticles could modify the catalytic behavior. While Fe is capable of catalyzing the graphitization process by interacting with carbon atoms, Rh offers little to no enhancement of this process. In fact, the presence of Rh may inhibit the catalytic activity of Fe, as Rh's lower reactivity toward carbon diminishes the overall catalytic efficiency [75].

The effectiveness of Fe-Rh nanoparticles in facilitating graphitization likely depends on specific synthesis parameters, such as temperature, the type of carbon precursor, and the Fe:Rh atomic ratio. Analyses of the Fe-Rh/NDs system revealed that the Fe-Rh nanoparticles formed on ND surfaces are predominantly Rh-rich, with an Fe:Rh atomic ratio of approximately 3:7. Consequently, the Rh-rich composition of the alloy appears to suppress the catalytic activity of Fe, as Rh's influence predominates. This suppression limits both Fe's and Rh's contributions to the formation of graphitic-layered nanostructures at the Fe-Rh/ND interface.

Additionally, the appearance of the martensitic-type phase in the Fe-Co/NDs and Fe-Ni/NDs systems should be expected, as this is favored during the graphitization process in the second part of the synthesis procedure. This is proposed, because from the above results we understand that the configuration of the morphological environment that includes the interconnected martensitic-type and graphitic-type-layered phases of the two iron alloy systems (Fe-Ni and Fe-Co), is determined by the actions of both the ND NPs and the second element of iron-based alloy, whose presence is catalytic. To understand these arguments, it is important to consider some other very significant aspects that the presence of the martensitic-type phase and the absence of other related phases indicate.

According to the literature, the appearance of martensitic-type phases could be observed when the concentration of carbon atoms in the iron alloy is relatively small and does not exceed 2-5 at.%. In this way, one could say that on the one hand the strong affinity of the carbon atoms to form direct bonds easier with iron atoms than with cobalt and nickel atoms [76], and on the other hand the affinity of the formation of stronger metallic bonds between iron and the second metallic element in the two alloy systems (Ni and Co), can lead to the avoidance of the establishment of direct bonds between the carbon atoms and the metallic elements. These bonds favor the formation of either iron, or iron-nickel or iron-cobalt carbides [77], [78], [79], [80], [81], which are phases that we have not observed in any of these two iron alloy systems. We propose that this mechanism leads to the conservation of the alloyed crystal structure for the metallic NPs with the retainment of the carbon atoms at the interstitial sites, where their presence constitutes the configuration of the martensitic-type phase. This conclusion is further confirmed by considering the situation where the second element of the iron alloy in the NHD system is absent. In this case the second part of the developed NHD composite material should be related to the reduction of only iron oxide NPs seeds in the precursor during the annealing process. This synthesis and study of the resulting material has been done following the same procedures at similarly high temperatures (750 °C, 4h), that led however to the solely formation of the nanostructured iron carbide (Fe_3C) phase [7]. There, it was concluded that the iron carbide formation resulted from the direct interaction of a significant portion of the sp^2-type carbon atoms with the reduced part of metallic iron. Thus, under the certain synthesis conditions, iron alone, and not alloyed with Co or Ni, is led to the direct formation of iron carbide upon interaction with carbon atoms, rather than the formation of iron alloy NPs and the martensitic-type phase. This is driven most probably by the easier and faster diffusion of the carbon atoms within the pure iron than the alloyed with Ni or Co structures [82], [83], [84].

7.6 Conclusions

In this study, we characterized and analyzed the structural, morphological, electronic, and magnetic properties of Fe-Ni/NDs systems synthesized using a two-step preparation process combining wet chemical techniques and controlled annealing. Two different wet chemistry approaches were employed: one utilizing $NaBH_4$ as a reducing agent and the other an impregnation method. This comparison enabled us to assess each method's effectiveness in producing hybrid and unsupported magnetic nanostructures and to determine which approach yielded the highest quality magnetic nanoalloy materials.

Our results show that both hybrid and unsupported annealed samples synthesized with $NaBH_4$ were affected by the presence of multiphase soft ferromagnetic Fe-Ni nanostructures with variable nickel concentrations, along with significant contributions from residual iron-nickel-oxide nanoparticles originating from the precursor material.

Conversely, the impregnation route successfully facilitated the formation of a novel magnetic nanohybrid material, featuring soft FM fcc Fe-Ni NPs grown on NDs nanotemplates. These Fe-Ni NPs, with an average size of about 7-9 nm, are uniformly distributed across the surfaces of the ND nanotemplates and exhibit a nickel-rich composition (~64 at.% Ni), likely corresponding to a combination of Awaruite ($FeNi_3$) and γ_2-Taenite phases. They display FM behavior across a temperature range from 2 K to 400 K, with coercivity values increasing from ~20 Oe at 400 K to 490 Oe at 2 K. Formation of the predominant fcc Fe-Ni phases is consistently accompanied by a minor, non-extensive, tetragonally distorted martensitic-type Fe-Ni phase.

The emergence of this unique martensitic-type Fe-Ni phase is attributed to the distinctive morphological properties of the ND growth matrices, which facilitate the formation of carbon sp^2-type nanostructures on the surfaces of the Fe-Ni NPs during the annealing stage. These graphitic layers envelop the Fe-Ni NPs on the NDs surfaces, creating an ideal environment for interstitial carbon atom diffusion within the Fe-Ni lattices at elevated temperatures, thereby inducing the localized formation of martensitic-type Fe-Ni structures.

These findings deepen our understanding of iron alloy-based nanohybrid magnetic systems and underscore the critical role of NDs NPs in fostering unique magnetic phases, particularly in promoting magnetic metallic NPs that combine FM cubic phases with tetragonally distorted martensitic characteristics. The goals of this work are to elucidate the mechanisms underlying the formation of these distinctive hybrid magnetic nanostructures and to lay a foundation for further development and exploration of similar systems.

7.7 References

[1] B. D. Cullity and S. R. Stock, *Elements of X-ray diffraction*, 3. ed. Upper Saddle River, NJ: Prentice Hall, 2001.

[2] R. M. Cornell and U. Schwertmann, *The Iron Oxides: Structure, Properties, Reactions, Occurences and Uses*, 1st ed. Wiley, 2003. doi: 10.1002/3527602097.

[3] J. F. Albertsen, H. P. Nielsen, and V. F. Buchwald, “On the Fine Structure of Meteoritical Taenite/Tetrataenite and its Interpretation,” *Phys. Scr.*, vol. 27, no. 4, pp. 314–320, Apr. 1983, doi: 10.1088/0031-8949/27/4/015.

[4] A. P. Douvalis, A. Polymeros, and T. Bakas, “IMSG09: A ^{57} Fe- ^{119} Sn Mössbauer spectra computer fitting program with novel interactive user interface,” *J. Phys.: Conf. Ser.*, vol. 217, p. 012014, Mar. 2010, doi: 10.1088/1742-6596/217/1/012014.

[5] J. F. Albertsen, J. M. Knudsen, and G. B. Jensen, “Structure of taenite in two iron meteorites,” *Nature*, vol. 273, no. 5662, pp. 453–454, Jun. 1978, doi: 10.1038/273453a0.

[6] L. K. Bogart, I. G. Morozov, I. P. Parkin, and M. V. Kuznetcov, “57Fe Mössbauer study of NiFe2O4 nanoparticles produced by the levitation-jet aerosol technique,” *J Mater Sci: Mater Electron*, vol. 29, no. 16, pp. 14347–14352, Aug. 2018, doi: 10.1007/s10854-018-9569-z.

[7] P. Ziogas, A. B. Bourlinos, J. Tucek, O. Malina, and A. P. Douvalis, “Novel Magnetic Nanohybrids: From Iron Oxide to Iron Carbide Nanoparticles Grown on Nanodiamonds,” *Magnetochemistry*, vol. 6, no. 4, Art. no. 4, Dec. 2020, doi: 10.3390/magnetochemistry6040073.

[8] S. Mørup and M. Hansen, “Superparamagnetic Particles,” 2007. doi: 10.1002/9780470022184.hmm409.

[9] S. Bedanta and W. Kleemann, “Supermagnetism,” *Journal of Physics D: Applied Physics*, vol. 42, p. 013001, Dec. 2008, doi: 10.1088/0022-3727/42/1/013001.

[10] S. Mørup, M. F. Hansen, and C. Frandsen, “Magnetic interactions between nanoparticles,” *Beilstein J Nanotechnol*, vol. 1, pp. 182–190, 2010, doi: 10.3762/bjnano.1.22.

[11] H. Kronmüller and S. Parkin, Eds., *Handbook of Magnetism and Advanced Magnetic Materials*, 1st ed. Wiley, 2007. doi: 10.1002/9780470022184.

[12] A. P. Douvalis, R. Zboril, A. B. Bourlinos, J. Tucek, S. Spyridi, and T. Bakas, “A facile synthetic route toward air-stable magnetic nanoalloys with Fe–Ni/Fe–Co core and iron oxide shell,” *J Nanopart Res*, vol. 14, no. 9, p. 1130, Sep. 2012, doi: 10.1007/s11051-012-1130-z.

[13] T. Komatsu and N. Soga, “Mössbauer study of the NiFe2O4 precipitation process from a silicate glass,” *Journal of Applied Physics*, vol. 51, no. 1, pp. 601–606, Jan. 1980, doi: 10.1063/1.327312.

[14] J. H. Liu, L. Wang, and F. S. Li, “Magnetic properties and Mössbauer studies of nanosized NiFe2O4 particles,” *J Mater Sci*, vol. 40, no. 9–10, pp. 2573–2575, May 2005, doi: 10.1007/s10853-005-2077-6.

[15] M. V. Ushakov, B. Senthilkumar, R. Kalai Selvan, I. Felner, and M. I. Oshtrakh, “Mössbauer spectroscopy of NiFe2O4 nanoparticles: The effect of Ni2+ in the Fe3+ local microenvironment in both tetrahedral and octahedral sites,” *Materials Chemistry and Physics*, vol. 202, pp. 159–168, Dec. 2017, doi: 10.1016/j.matchemphys.2017.09.011.

[16] C.-W. Yang, D. B. Williams, and J. I. Goldstein, “Low-temperature phase decomposition in metal from iron, stony-iron, and stony meteorites,” *Geochimica et Cosmochimica Acta*, vol. 61, no. 14, pp. 2943–2956, Jul. 1997, doi: 10.1016/S0016-7037(97)00132-4.

[17] R. B. Scorzelli and J. Danon, “Mössbauer Spectroscopy and X-Ray Diffraction Studies of Fe-Ni Order-Disorder Processes in a 35% Ni Meteorite (Santa Catharina),” *Phys. Scr.*, vol. 32, no. 2, pp. 143–148, Aug. 1985, doi: 10.1088/0031-8949/32/2/010.

[18] R. B. Scorzelli, “A study of phase stability in invar Fe–Ni alloys obtained by non-conventional methods,” *Hyperfine Interactions*, vol. 110, no. 1/2, pp. 143–150, 1997, doi: 10.1023/A:1012679517295.

[19] E. Lima, V. Drago, P. F. P. Fichtner, and P. H. P. Domingues, “Tetrataenite and other Fe–Ni equilibrium phases produced by reduction of nanocrystalline NiFe2O4,” *Solid State Communications*, vol. 128, no. 9–10, pp. 345–350, Dec. 2003, doi: 10.1016/j.ssc.2003.08.046.

[20] A. P. Douvalis, A. Moukarika, T. Bakas, G. Kallias, and V. Papaefthymiou, “Mössbauer and magnetization studies of Fe3BO5,” *Journal of Physics: Condensed Matter*, vol. 14, p. 3303, Mar. 2002, doi: 10.1088/0953-8984/14/12/317.

[21] D. G. Rancourt and R. B. Scorzelli, “Low-spin γ-Fe⍰Ni(γLS) proposed as a new mineral in Fe⍰Ni-bearing meteorites: epitaxial intergrowth of γLS and tetrataenite as a possible equilibrium state at ∼20–40 at% Ni,” *Journal of Magnetism and Magnetic Materials*, vol. 150, no. 1, pp. 30–36, Sep. 1995, doi: 10.1016/0304-8853(95)00089-5.

[22] J. F. Albertsen, J. M. Knudsen, N. O. Roy-Poulsen, and L. Vistisen, “Meteorites and Thermodynamic Equilibrium in f.c.c. Iron-Nickel Alloys (25-50% Ni),” *Phys. Scr.*, vol. 22, no. 2, pp. 171–175, Jan. 1980, doi: 10.1088/0031-8949/22/2/014.

[23] I. S. Lyubutin, C. R. Lin, Yu. V. Korzhetskiy, T. V. Dmitrieva, and R. K. Chiang, “Mössbauer spectroscopy and magnetic properties of hematite/magnetite nanocomposites,” *Journal of Applied Physics*, vol. 106, no. 3, Art. no. 3, Aug. 2009, doi: 10.1063/1.3194316.

[24] N. N. Greenwood and T. C. Gibb, *Mössbauer Spectroscopy*. Dordrecht: Springer Netherlands, 1971. doi: 10.1007/978-94-009-5697-1.

[25] P. Gütlich, E. Bill, and A. X. Trautwein, *Mössbauer Spectroscopy and Transition Metal Chemistry*. Berlin, Heidelberg: Springer Berlin Heidelberg, 2011. doi: 10.1007/978-3-540-88428-6.

[26] A. Kovács *et al.*, “Discovery and Implications of Hidden Atomic-Scale Structure in a Metallic Meteorite,” *Nano Lett.*, vol. 21, no. 19, pp. 8135–8142, Oct. 2021, doi: 10.1021/acs.nanolett.1c02573.

[27] J. W. Drijver, K. De Groot, and F. Van Der Woude, “DETERMINATION OF LONG RANGE ORDER IN Ni $_3$ Fe USING THE MOSSBAUER EFFECT TECHNIQUE,” *J. Phys. Colloques*, vol. 35, no. C6, pp. C6-465-C6-468, Dec. 1974, doi: 10.1051/jphyscol:1974696.

[28] M. Kanashiro and N. Kunitomi, “Environment effect on the hyperfine field distributions in ordered Ni3Fe,” *Solid State Communications*, vol. 19, no. 11, pp. 1127–1130, Sep. 1976, doi: 10.1016/0038-1098(76)90114-9.

[29] M. Kanashiro and N. Kunitomi, “Non-Linear Local Environment Effect in Ni $_3$ Fe Observed by Mössbauer Effect of Fe ^{57},” *J. Phys. Soc. Jpn.*, vol. 48, no. 1, pp. 93–101, Jan. 1980, doi: 10.1143/JPSJ.48.93.

[30] T. E. Cranshaw, “The electronic and magnetic structure of ordered Ni $_3$ Fe studied by Mossbauer spectroscopy,” *J. Phys. F: Met. Phys.*, vol. 17, no. 4, pp. 967–984, Apr. 1987, doi: 10.1088/0305-4608/17/4/022.

[31] B. Zhang, N.-E. Fenineche, H. Liao, and C. Coddet, “Magnetic properties of in-situ synthesized FeNi3 by selective laser melting Fe-80%Ni powders,” *Journal of Magnetism and Magnetic Materials*, vol. 336, pp. 49–54, Jun. 2013, doi: 10.1016/j.jmmm.2013.02.014.

[32] C.-W. Yang, D. B. Williams, and J. I. Goldstein, “A revision of the Fe-Ni phase diagram at low temperatures (<400 °C),” *JPE*, vol. 17, no. 6, pp. 522–531, Dec. 1996, doi: 10.1007/BF02665999.

[33] E. Dos Santos, J. Gattacceca, P. Rochette, R. B. Scorzelli, and G. Fillion, “Magnetic hysteresis properties and 57Fe Mössbauer spectroscopy of iron and stony-iron meteorites: Implications for mineralogy and thermal history,” *Physics of the Earth and Planetary Interiors*, vol. 242, pp. 50–64, May 2015, doi: 10.1016/j.pepi.2015.01.004.

[34] P. G. Ziogas, A. B. Bourlinos, P. Chatzopoulou, G. P. Dimitrakopulos, A. Markou, and A. P. Douvalis, “Novel Hybrid Ferromagnetic Fe–Co/Nanodiamond Nanostructures: Influence of Carbon on Their Structural and Magnetic Properties,” *Magnetochemistry*, vol. 10, no. 5, p. 35, May 2024, doi: 10.3390/magnetochemistry10050035.

[35] M. Alahmadi and M. Siaj, “Graphene-Assisted Magnetic Iron Carbide Nanoparticle Growth,” *ACS Appl. Nano Mater.*, vol. 1, no. 12, pp. 7000–7005, Dec. 2018, doi: 10.1021/acsanm.8b01794.

[36] G. V. Kurdjumov and A. G. Khachaturyan, “Nature of axial ratio anomalies of the martensite lattice and mechanism of diffusionless γ → α transformation,” *Acta Metallurgica*, vol. 23, no. 9, pp. 1077–1088, Sep. 1975, doi: 10.1016/0001-6160(75)90112-1.

[37] G.V. Kurdyumov Institute for Metal Physics, NAS of Ukraine, 36 Academician Vernadsky Blvd., UA-03680 Kyiv-142, Ukraine *et al.*, “Carbon Distribution in Low-Temperature Isothermal Iron-Based Martensite and Its Tetragonality,” *Metallofiz. Noveishie Tekhnol.*, vol. 38, no. 4, pp. 455–475, Jun. 2016, doi: 10.15407/mfint.38.04.0455.

[38] V. G. Gavriljuk, A. V. Tarasenko, and A. I. Tyshchenko, “Low temperature ageing of the freshly formed Fe-C and Fe-N martensites,” *Scripta Materialia*, vol. 43, no. 3, pp. 233–238, Jul. 2000, doi: 10.1016/S1359-6462(00)00396-1.

[39] R. N. Panda and N. S. Gajbhiye, “Magnetic properties of nanocrystalline γ-Fe–Ni–N nitride systems,” *Journal of Applied Physics*, vol. 86, no. 6, pp. 3295–3302, Sep. 1999, doi: 10.1063/1.371205.

[40] T. Sohmura and F. E. Fujita, “Mossbauer effect in hydrogenated Fe-Ni alloys,” *J. Phys. F: Met. Phys.*, vol. 8, no. 9, pp. 2061–2071, Sep. 1978, doi: 10.1088/0305-4608/8/9/027.

[41] J. Foct, P. Rochegude, and C. Cordier-Robert, “Atom distributions in mixed interstitial-substitutional solid solution: The case of Fe1−xNixNy austenite,” *Hyperfine Interact*, vol. 45, no. 1–4, pp. 359–364, Mar. 1989, doi: 10.1007/BF02405900.

[42] V. M. Nadutov, “Mössbauer analysis of the effect of substitutional atoms on the electronic charge distribution in nitrogen and carbon austenites,” *Materials Science and Engineering: A*, vol. 254, no. 1–2, pp. 234–241, Oct. 1998, doi: 10.1016/S0921-5093(98)00663-7.

[43] L. Vergara, J. Desimoni, K. Laneri, A. Fernández Guillermet, and G. J. Zarragoicoechea, “Distribution of interstitial atoms in FCC Fe–N alloys: A Mössbauer, thermodynamic and Monte Carlo approach,” *Physica B: Condensed Matter*, vol. 363, no. 1–4, pp. 178–189, Jun. 2005, doi: 10.1016/j.physb.2005.03.019.

[44] P. M. Gielen and R. Kaplow, “Mossbauer effect in iron-carbon and iron-nitrogen alloys,” *Acta Metallurgica*, vol. 15, no. 1, pp. 49–63, Jan. 1967, doi: 10.1016/0001-6160(67)90155-1.

[45] W. K. Choo and R. Kaplow, “Mössbauer measurements on the aging of iron-carbon martensite,” *Acta Metallurgica*, vol. 21, no. 6, pp. 725–732, Jun. 1973, doi: 10.1016/0001-6160(73)90036-9.

[46] M. Hähsler *et al.*, “Magnetic Properties and Mössbauer Spectroscopy of Fe $_3$ O $_4$ /CoFe $_2$ O $_4$ Nanorods,” *Inorg. Chem.*, vol. 59, no. 6, pp. 3677–3685, Mar. 2020, doi: 10.1021/acs.inorgchem.9b03267.

[47] I. S. Lyubutin *et al.*, “Magnetic and Mössbauer spectroscopy studies of hollow microcapsules made of silica-coated CoFe $_2$ O $_4$ nanoparticles,” *Smart Mater. Struct.*, vol. 25, no. 1, p. 015022, Jan. 2016, doi: 10.1088/0964-1726/25/1/015022.

[48] M. Gong and S. Ren, “Phase Transformation-Driven Surface Reconstruction of FeNi Nanostructures,” *Chem. Mater.*, vol. 27, no. 22, pp. 7795–7800, Nov. 2015, doi: 10.1021/acs.chemmater.5b03736.

[49] A. M. Montes-Arango *et al.*, “Discovery of process-induced tetragonality in equiatomic ferromagnetic FeNi,” *Acta Materialia*, vol. 116, pp. 263–269, Sep. 2016, doi: 10.1016/j.actamat.2016.06.050.

[50] S. Mørup, C. Frandsen, and M. F. Hansen, “Uniform excitations in magnetic nanoparticles,” *Beilstein J. Nanotechnol.*, vol. 1, pp. 48–54, Nov. 2010, doi: 10.3762/bjnano.1.6.

[51] B. D. Cullity and C. D. Graham, *Introduction to magnetic materials*, 2nd ed. Hoboken, N.J: IEEE/Wiley, 2009.

[52] J. M. D. Coey, *Magnetism and Magnetic Materials*, 1st ed. Cambridge University Press, 2001. doi: 10.1017/CBO9780511845000.

[53] M. Nirouei, A. Jafari, and K. Boustani, “Magnetic and Structural Study of FeNi3 Nanoparticles: Effect of Calcination Temperature,” *J Supercond Nov Magn*, vol. 27, no. 12, pp. 2803–2811, Dec. 2014, doi: 10.1007/s10948-014-2727-5.

[54] G. Hongxia, C. Hua, L. Fan, Q. Zhenping, C. Suping, and N. Zuoren, “Shape-controlled synthesis of FeNi $_3$ nanoparticles by ambient chemical reduction and their magnetic properties,” *J. Mater. Res.*, vol. 27, no. 11, pp. 1522–1530, Jun. 2012, doi: 10.1557/jmr.2012.67.

[55] X.-M. Zhou and X.-W. Wei, “Single Crystalline FeNi $_3$ Dendrites: Large Scale Synthesis, Formation Mechanism, and Magnetic Properties,” *Crystal Growth & Design*, vol. 9, no. 1, pp. 7–12, Jan. 2009, doi: 10.1021/cg8000976.

[56] S. Mørup and M. F. Hansen, “Superparamagnetic Particles,” in *Handbook of Magnetism and Advanced Magnetic Materials*, H. Kronmüller and S. Parkin, Eds., Chichester, UK: John Wiley & Sons, Ltd, 2007, p. hmm409. Accessed: Jun. 17, 2021. [Online]. Available: http://doi.wiley.com/10.1002/9780470022184.hmm409

[57] D. Fiorani, Ed., *Surface effects in magnetic nanoparticles*. in Nanostructure science and technology. New York: Springer, 2005.

[58] S. Mørup and E. Tronc, “Superparamagnetic relaxation of weakly interacting particles,” *Phys. Rev. Lett.*, vol. 72, no. 20, pp. 3278–3281, May 1994, doi: 10.1103/PhysRevLett.72.3278.

[59] S. Mørup, M. F. Hansen, and C. Frandsen, “Magnetic interactions between nanoparticles,” *Beilstein J Nanotechnol*, vol. 1, pp. 182–190, 2010, doi: 10.3762/bjnano.1.22.

[60] S. Mørup, C. Frandsen, and M. F. Hansen, “Uniform excitations in magnetic nanoparticles,” *Beilstein J. Nanotechnology*, vol. 1, pp. 48–54, 2010.

[61] D. Fiorani, Ed., *Surface effects in magnetic nanoparticles*. in Nanostructure science and technology. New York: Springer, 2005.

[62] B. D. Cullity and C. D. Graham, *Introduction to Magnetic Materials*, 1st ed. Wiley, 2008. doi: 10.1002/9780470386323.

[63] A. B. Bourlinos *et al.*, “Fabrication of fluorescent nanodiamond@C core–shell hybrids via mild carbonization of sodium cholate–nanodiamond complexes,” *J Mater Sci*, vol. 46, no. 24, Art. no. 24, Dec. 2011, doi: 10.1007/s10853-011-5911-z.

[64] X. Duan *et al.*, “sp ^{2} /sp ^{3} Framework from Diamond Nanocrystals: A Key Bridge of Carbonaceous Structure to Carbocatalysis,” *ACS Catal.*, vol. 9, no. 8, Art. no. 8, Aug. 2019, doi: 10.1021/acscatal.9b01565.

[65] J. Tuček, K. C. Kemp, K. S. Kim, and R. Zbořil, “Iron-Oxide-Supported Nanocarbon in Lithium-Ion Batteries, Medical, Catalytic, and Environmental Applications,” *ACS Nano*, vol. 8, no. 8, pp. 7571–7612, Aug. 2014, doi: 10.1021/nn501836x.

[66] X. Fan, H. Gao, X. Kou, B. Zhang, and S. Wang, “Synthesis of FeCo-reduced graphene oxide composite and its magnetic and adsorption properties,” *Materials Research Bulletin*, vol. 65, pp. 320–324, May 2015, doi: 10.1016/j.materresbull.2015.02.007.

[67] M. Zeiger, N. Jäckel, V. N. Mochalin, and V. Presser, “Review: carbon onions for electrochemical energy storage,” *J. Mater. Chem. A*, vol. 4, no. 9, pp. 3172–3196, 2016, doi: 10.1039/C5TA08295A.

[68] O. A. Shenderova and G. E. McGuire, “Science and engineering of nanodiamond particle surfaces for biological applications (Review),” *Biointerphases*, vol. 10, no. 3, p. 030802, Sep. 2015, doi: 10.1116/1.4927679.

[69] A. S. Barnard, “Stability of Diamond at the Nanoscale,” in *Ultananocrystalline Diamond*, Elsevier, 2012, pp. 3–52. doi: 10.1016/B978-1-4377-3465-2.00001-3.

[70] T. Petit, J.-C. Arnault, H. A. Girard, M. Sennour, and P. Bergonzo, “Early stages of surface graphitization on nanodiamond probed by x-ray photoelectron spectroscopy,” *Phys. Rev. B*, vol. 84, no. 23, p. 233407, Dec. 2011, doi: 10.1103/PhysRevB.84.233407.

[71] E. V. Rut’kov, A. V. Kuz’michev, and N. R. Gall’, “Carbon interaction with rhodium surface: Adsorption, dissolution, segregation, growth of graphene layers,” *Phys. Solid State*, vol. 53, no. 5, pp. 1092–1098, May 2011, doi: 10.1134/S1063783411050246.

[72] K. Fagnou and M. Lautens, “Rhodium-Catalyzed Carbon−Carbon Bond Forming Reactions of Organometallic Compounds,” *Chem. Rev.*, vol. 103, no. 1, pp. 169–196, Jan. 2003, doi: 10.1021/cr020007u.

[73] N. Lal Verma *et al.*, “Transition-metal-mediated C-C bond activation: Recent advances and its applications in organic synthesis,” *Results in Chemistry*, vol. 6, p. 101130, Dec. 2023, doi: 10.1016/j.rechem.2023.101130.

[74] M. D. R. Lutz, S. Roediger, M. A. Rivero-Crespo, and B. Morandi, “Mechanistic Investigation of the Rhodium-Catalyzed Transfer Hydroarylation Reaction Involving Reversible C–C Bond Activation,” *J. Am. Chem. Soc.*, vol. 145, no. 49, pp. 26657–26666, Dec. 2023, doi: 10.1021/jacs.3c07780.

[75] W. J. Arnoult and R. B. McLellan, “The solubility of carbon in rhodium ruthenium, iridium and rhenium,” *Scripta Metallurgica*, vol. 6, no. 10, pp. 1013–1018, Oct. 1972, doi: 10.1016/0036-9748(72)90163-9.

[76] P. W. Atkins, J. De Paula, and J. Keeler, *Atkins’ physical chemistry*, Twelfth edition. New York, NY: Oxford University Press, 2023.

[77] A. Wiltner and Ch. Linsmeier, “Formation of endothermic carbides on iron and nickel,” *phys. stat. sol. (a)*, vol. 201, no. 5, pp. 881–887, Apr. 2004, doi: 10.1002/pssa.200304362.

[78] A. M. Sherman, G. T. Eldis, and M. Cohen, “The Aging and Tempering of Iron-Nickel-Carbon Martensites,” *Metall Trans A*, vol. 14, no. 5, pp. 995–1005, May 1983, doi: 10.1007/BF02659847.

[79] J. Gautam, T. D. Thanh, K. Maiti, N. H. Kim, and J. H. Lee, “Highly efficient electrocatalyst of N-doped graphene-encapsulated cobalt-iron carbides towards oxygen reduction reaction,” *Carbon*, vol. 137, pp. 358–367, Oct. 2018, doi: 10.1016/j.carbon.2018.05.042.

[80] K. Y. Kim *et al.*, “Cobalt Ferrite Nanoparticles to Form a Catalytic Co–Fe Alloy Carbide Phase for Selective CO $_2$ Hydrogenation to Light Olefins,” *ACS Catal.*, vol. 10, no. 15, pp. 8660–8671, Aug. 2020, doi: 10.1021/acscatal.0c01417.

[81] E. R. D. Scott, “New Carbide, (Fe,Ni)23C6, found in Iron Meteorites,” *Nature Physical Science*, vol. 229, no. 2, pp. 61–62, Jan. 1971, doi: 10.1038/physci229061a0.

[82] *Diffusion Bonding of Materials*. Elsevier, 1985. doi: 10.1016/C2013-0-03774-7.

[83] R. Filipek, M. Danielewski, and R. Bachorczyk Nagy, “Interdiffusion Studies in Co-Fe-Ni Alloys,” *DDF*, vol. 237–240, pp. 408–413, Apr. 2005, doi: 10.4028/www.scientific.net/DDF.237-240.408.

[84] K. L. Crispin, S. Saha, D. Morgan, and J. A. Van Orman, “Diffusion of transition metals in periclase by experiment and first-principles, with implications for core–mantle equilibration during metal percolation,” *Earth and Planetary Science Letters*, vol. 357–358, pp. 42–53, Dec. 2012, doi: 10.1016/j.epsl.2012.09.023.

Chapter 8. Conclusive Remarks & Future Research Perspectives

In this thesis, emphasis was given on the synthesis, characterization, and study of the properties of novel hybrid magnetic nanostructured materials composed of bimetallic iron alloys (Fe-Rh, Fe-Co, Fe-Ni) grown on nanodiamond nanotemplates. Nanohybrid materials—combinations of different nanomaterials designed to integrate their favorable properties into a single hybrid structure, or even to provide novel properties—emerge as a promising class of advanced, high-performance materials, since they offer more effective solutions for meeting the demands of modern technologies compared to traditional materials. This endeavor, reported here for the first time, emphasizes the synthesis and investigation of magnetic metal compound nanohybrids, exploring the synergistic effects of iron-based bimetallic alloys and the physical properties of nanodiamond nanotemplates, thereby enhancing their structural and magnetic characteristics and broadening their application prospects (**Chapter 1**).

Characterization of the samples involved techniques such as X-ray diffraction, electron microscopy, magnetization measurements, and ^{57}Fe Mössbauer spectroscopy, with foundational principles outlined in **Chapter 2**. A key focus is on understanding how particle size affects the magnetic properties of nanoparticles. As the size decreases to a critical threshold, notable phenomena like changes in magnetization reversal mechanisms emerge, which are critical for technological advancements. At this size, thermal energy influences magnetization direction, leading to superparamagnetic behavior, a phenomenon explained through distinct features of the characterization techniques used (**Chapter 3**).

The synthesis process consisted of a two-step procedure: an initial wet chemistry step to produce precursors, followed by controlled thermal treatments. Two methods were tested: one using $NaBH_4$ as a reducing agent and another employing an impregnation technique. This comparison allowed for the evaluation of each method's effectiveness in generating hybrid and unsupported magnetic nanostructures, maintaining a nominal atomic ratio of Fe:X (X = Rh, Co, Ni) at 1:1, and a combined metal-to-nanodiamond mass ratio of approximately 10 wt.%. Comparing the magnetic and structural properties of the hybrid and unsupported samples was essential for understanding the role of the ND matrix, providing insights into how NDs influence the growth and stability of the nanoalloy phases during synthesis (**Chapter 4**).

The study of the Fe-Rh/NDs system resulted in the successful synthesis of a novel nanohybrid material composed of ferromagnetic CsCl-type B2-bcc α'-Fe-Rh nanoparticles on nanodiamond nanotemplates. Employing a two-stage synthesis approach—wet chemistry reduction with $NaBH_4$ followed by controlled vacuum thermal annealing—resulted in Fe-Rh nanoparticles (~4 nm in diameter) uniformly dispersed on nanodiamond surfaces. Despite a rhodium-rich composition (60-70 at.%), these nanoparticles exhibit stable ferromagnetic behavior from 2 K to 400 K. The unsuccessful attempts to replicate similarly ferromagnetic Fe-Rh nanoparticles without nanodiamond support further highlight the critical role of nanodiamond substrates. This finding suggests that carbon atoms from the graphitic surface layers of nanodiamonds may promote diffusion processes during annealing, stabilizing the ferromagnetic Fe-Rh phase.

The use of dense nanodiamond templates in this context proves to be an effective strategy for fabricating magnetic nanocrystalline systems with enhanced stability and uniformity. However, during thermal treatments, the formation of graphitic-layered nanostructures from the NDs at the interface between Fe-Rh nanoparticles and ND surfaces is inhibited. This phenomenon can be attributed to the influence of Rh in the iron-based alloys during synthesis. Unlike Fe, Rh lacks significant catalytic activity for graphitization. In fact, the presence of Rh may suppress the catalytic activity of Fe, as Rh's lower reactivity toward carbon reduces the overall catalytic efficiency.

As a result, the Rh-rich Fe-Rh alloy nanoparticles formed on the ND surfaces appear to diminish Fe's catalytic potential, with Rh's influence predominating. This suppression limits the contributions of both Fe and Rh to the development of graphitic-layered nanostructures at the Fe-Rh/ND interface.

The two-stage synthesis method, characterized by its adaptable parameters—including metal composition and annealing conditions such as atmosphere (vacuum), duration, and temperature—offers a versatile pathway for designing a wide range of magnetic nanohybrids. These systems hold significant potential for diverse technological applications (**Chapter 5**).

The study of the Fe-Co/NDs system demonstrated the successful synthesis of novel magnetic nanohybrid materials by growing ferromagnetic bcc Fe-Co nanoparticles on nanodiamond nanotemplates, using the combination of a wet chemistry impregnation method followed by controlled annealing. The Fe-Co NPs, uniformly distributed on ND surfaces with cobalt-rich compositions (~65 at.% Co) and average sizes of 6 to 10 nm, exhibit stable ferromagnetic behavior over a broad temperature range from 2 K to 400 K. Alongside the dominant bcc ferromagnetic Fe-Co phase, we consistently observe a secondary, non-extensive tetragonally distorted martensitic-type Fe-Co phase and a residual ICO precursor phase.

The formation of this unique martensitic-type Fe-Co phase can be attributed to the ND templates' specific morphological characteristics. During the annealing step, these NDs develop sp^2 graphitic-type layered nanostructures that surround the Fe-Co NPs, creating a conducive environment for carbon atom diffusion into the Fe-Co lattice at high temperatures. This interstitial diffusion process facilitates the emergence of the martensitic-type structural configuration, adding distinct properties to the synthesized nanohybrid materials **(Chapter 6)**.

Finally, the study of the Fe-Ni/NDs system presents the successful synthesis of a novel magnetic nanohybrid material by growing soft ferromagnetic fcc Fe-Ni nanoparticles on nanodiamond nanotemplates through a two-step process of wet chemical impregnation synthesis and controlled annealing. The Fe-Ni NPs, averaging 10 nm in size and exhibiting a nickel-rich composition (~64 at.% Ni), are uniformly distributed on ND surfaces. They exhibit a stable FM response from 2 K to 400 K, with coercivity values increasing from ~20 Oe at 400 K to 490 Oe at 2 K. This FM behavior is primarily attributed to Awaruite ($FeNi_3$) and γ_2-Taenite phases, consistently accompanied by a secondary, non-extensive tetragonally distorted martensitic-type Fe-Ni phase.

The development of this unique martensitic-type Fe-Ni phase is closely linked to the ND matrix properties, which enable the formation of carbon sp^2-type nanostructures on Fe-Ni NP surfaces during annealing. These graphitic layers enshroud the Fe-Ni NPs, creating an optimal environment for carbon diffusion within the Fe-Ni lattices at elevated temperatures, thereby promoting the formation of this distinctive martensitic-type configuration **(Chapter 7)**.

This study examines the effects of two wet chemistry synthetic routes, the $NaBH_4$ reducing agent and the impregnation method, on the synthesis and properties of Fe-Rh/NDs, Fe-Co/NDs, and Fe-Ni/NDs systems. The $NaBH_4$ method generates a recurring morphological pattern across all three systems, that is the formation of metallic and spinel-type iron-based oxide NPs with distinct morphological patterns. For the Fe-Rh/NDs system, metallic Rh and IO/IHO NPs form during the first synthesis stage, while annealing promotes Fe-Rh alloy formation, influenced by the interaction and combination of the Rh catalysts and the sp^2 carbon atoms originating from the ND surfaces, stabilizing the ferromagnetic B2-bcc α'-Fe-Rh structure.

In the Fe-Co/NDs and Fe-Ni/NDs systems, the $NaBH_4$ route produces Fe-Co alloys and spinel-type ICO NPs and Fe-Ni alloys and INO NPs accordingly. Retained morphological features from the initial synthesis include core-shell structures and strong magnetic interactions between the metallic alloy NPs, which thermal treatments do not fully homogenize. In the Fe-Ni/NDs system, annealing yields multiphase Fe-Ni NPs, including Ni-rich Awaruite and Ni-poor Kamacite phases, limiting uniformity.

In contrast, the implementation of the impregnation method in the Fe-Co/NDs and Fe-Ni/NDs systems promotes the formation of fine ICO and INO NPs seeds anchored to ND surfaces of each system respectively, avoiding strong magnetic interactions. This approach enhances seed growth and supports controlled development of Fe-Co and Fe-Ni NPs in the final synthesis phase of each system, yielding more uniform nanostructures compared to the $NaBH_4$ method.

Overall, this research enhances our understanding of iron alloy-based nanohybrid magnetic systems and underscore the pivotal role of NDs nanotemplates in promoting unique magnetic phase development. These studies aim to illuminate the mechanisms underlying the formation of such hybrid magnetic nanostructures and to establish a foundation for future work in designing similar magnetic nanohybrids. The insights gained here could lay the groundwork for future studies and applications for such tailored hybrid nanostructures across various technological fields.

In terms of future research perspectives, one promising avenue for further exploration involves maintaining the nominal equiatomic stoichiometries of the metallic magnetic nanoparticles on the nanodiamond nanotemplates by carefully controlling the first step of the synthesis. This can be achieved either by regulating the nominal Fe:X (where X = Rh, Co, Ni) atomic ratio of the respective metal salts or by adjusting the total weight percent (wt.%) loading of the combined Fe and X (X = Rh, Co, Ni) metal-to-nanodiamond mass ratio used in each nanohybrid system.

Another aspect worthy of investigation is the enhancement of the contribution of martensitic-type phases within the respective magnetic hybrid nanostructured systems. Based on extensive studies in the literature, one effective approach to achieving this goal is to introduce an additional third element, such as nitrogen atoms. This addition could facilitate their diffusion into the crystal lattice of the metallic magnetic nanoparticles, similar to the mechanisms exhibited by the native sp^2 carbon atoms in the existing nanohybrid systems. By promoting the diffusion of interstitial carbon atoms in conjunction with the introduction of nitrogen atoms, it may be possible to trigger extensive formations of martensitic-type configurations within the systems under investigation. This could be implemented by utilizing an inert nitrogen gas presence in the ampoule during the annealing process, or with flow within a closed system that circulates in the solenoid furnace during the second annealing step of each nanohybrid system's synthesis.

Publications

i. Novel Hybrid Ferromagnetic Fe–Co/Nanodiamond Nanostructures: Influence of Carbon on Their Structural and Magnetic Properties. **Ziogas, P.**; Bourlinos, A.B.; Chatzopoulou, P.; Dimitrakopulos G., Markou, A.; Douvalis, A.P. Magnetochemistry 2024, 10(5), 35; https://doi.org/10.3390/magnetochemistry10050035.

ii. Intriguing Prospects of a Novel Magnetic Nanohybrid Material: Ferromagnetic FeRh Nanoparticles Grown on Nanodiamonds. **Ziogas, P.**; Bourlinos, A.B.; Chatzopoulou, P.; Dimitrakopulos G., Kehagias Th., Markou, A.; Douvalis, A.P. Metals 2022, 12, 1355; https://doi.org/10.3390/met12081355.

iii. Isolation, Characterization and Hydrogen Sulfide H_2S Sorption Properties at Room Temperature of Magnetite Sludge from Radiator. **Ziogas, P.**; Douvalis, A.P.; Bourlinos, A.B.; Papachristodoulou C.; Chalmpes N.; Karakassides M.A.; Giannakas A.; Salmas C. J Nanotechnol Res 2022; 4 (2): 97-110; DOI: 10.26502/jnr.2688-85210032.

iv. Novel Magnetic Nanohybrids: From Iron Oxide to Iron Carbide Nanoparticles Grown on Nanodiamonds. **Ziogas, P.**; Bourlinos, A.B.; Tucek J., Ondrej Malina; Douvalis, A.P. Magnetochemistry 2020, 6 (4), 73; doi:10.3390/magnetochemistry6040073.

v. Impact of the solidification path of FeO_x–SiO_2 slags on the resultant inorganic polymers. Siakati C.; Douvalis A.P.; **Ziogas P.**; Peys A.; Pontikes Y. Am Ceram Soc. 2020; 103:2173–2184. DOI: 10.1111/jace.16869.

vi. Growing Ferromagnetic Fe-Ni Alloy Nanoparticles on Nanodiamonds Nanotemplates: the Role of sp^2-type Carbon in their Development and in the Appearance of a Martensitic-Type Phase. **Ziogas, P.**; Bourlinos, A.B.; Chatzopoulou, P.; Dimitrakopulos G., Markou, A.; Douvalis, A.P. Metals 2024, in final stage and under submission in an accredited international journal.

Presentations to National Conferences

Poster Presentations

i. **New Magnetic Iron Carbide/Nanodiamond Hybrid Nanostructures: Synthesis, Characterization and Examination of their Performance on Cr^{6+} Removal from Aqueous Solutions**,
P.Ziogas, A.B. Bourlinos, J. Tucek, R. Zboril, M. Baiskousi, M. Karakassides and A.P. Douvalis, XXXIV Panhellenic Conference on Solid State Physics and Materials Science, September 2019, University of Patras, Patras Greece.

ii. **Probing the Properties of Magnetic Nanophases in Nanodiamond-Based Hybrid Nanostructures with Mössbauer Spectroscopy**,
P.Ziogas, A.B. Bourlinos and A.P. Douvalis, March 2019, ESRF-NRS Workshop, Grenoble France.

Oral Presentations

i. **Synthesis, characterization and study of the properties of new magnetic nanostructured materials (NanoDiamonds/FeRh NanoParticles),**
P.Ziogas, A.B. Bourlinos, P. Chatzopoulou, G. Dimitrakopoulos, A. Markou and A.P. Douvalis, XXXV Panhellenic Conference on Solid State Physics and Materials Science, September 2021, NCSR 'Demokritos', Athens Greece.

ii. **Novel Fe-Co Nanoalloy Phases Grown on Nanodiamonds: Insights from ^{57}Fe Mössbauer spectroscopy,**
P.Ziogas, A.B. Bourlinos and A.P. Douvalis, XXXVII Panhellenic Conference on Solid State Physics & Materials Science, September 2023, Aristotle University of Thessaloniki, Thessaloniki Greece.

iii. **Novel Hybrid Ferromagnetic Fe-Ni Nanoalloys Grown on Nanodiamonds,**
P.Ziogas, A.B. Bourlinos and A.P. Douvalis, XXXVIII Panhellenic Conference on Solid State Physics and Materials Science", September 2024, University of Ioannina, Ioannina Greece.